Transactions of the ASME

The Journal of Fluids Engineering (ISSN 0098-2202) is published quarterly for $100 per year by The American Society of Mechanical Engineers, 345 East 47th Street, New York, NY 10017. Second class postage paid at New York, NY and additional mailing offices. POSTMASTER: Send address changes to The Journal of Fluids Engineering, c/o THE AMERICAN SOCIETY OF MECHANICAL ENGINEERS, 22 Law Drive, Box 2300, Fairfield, NJ 07007-2300.
CHANGES OF ADDRESS must be received at Society headquarters seven weeks before they are to be effective. Please send old label and new address.
PRICES: To members, $24.00, annually: to nonmembers, $100. Add $6.00 for postage to countries outside the United States and Canada.
STATEMENT from By-Laws. The Society shall not be responsible for statements or opinions advanced in papers or . . . printed in its publications (B7.1, Par. 3).

INDEXED by the Engineering Index, Inc.

Journal of Fluids Engineering

Published Quarterly by The American Society of Mechanical Engineers

VOLUME 107 • NUMBER 1 • MARCH 1985

REVIEW—Computational Methods for Internal Flows With Emphasis on Turbomachinery

William D. McNally

Peter M. Sockol

NASA Lewis Research Center, Cleveland, Ohio

A review is given of current computational methods for analyzing flows in turbomachinery and other related internal propulsion components. The methods are divided primarily into two classes, inviscid and viscous. The inviscid methods deal specifically with turbomachinery applications. Viscous methods, on the other hand, due to the state-of-the-art, deal with generalized duct flows as well as flows in turbomachinery passages. Inviscid methods are categorized into the potential, stream function, and Euler approaches. Viscous methods are treated in terms of parabolic, partially parabolic, and elliptic procedures.

Introduction

The subject of internal flows is a very broad and complex one, encompassing a wide variety of geometries and flow situations. There are many examples of machinery in which internal flows play an important part. One such example is the modern turbofan engine, such as that depicted in Fig. 1. Here the understanding of internal flows is very important in predicting the performance of many key components. These include the inlets and exhaust nozzles at the extremeties of the engine, the rotating and stationary turbomachinery blade rows in both the compressor and turbine sections of the engine, the interconnecting ducts, and the combustor portion of the engine. In this paper, in order to make the subject more manageable, we have chosen to treat in detail a subset of the total class of internal flows. We will be speaking specifically about flows through turbomachinery blade rows of all types, as well as viscous flows through ducts of various geometries.

The paper will be divided primarily into descriptions of inviscid flow methods and then viscous flow methods. Inviscid flow methods will be described in the context of turbomachinery blade row applications because a large number of analyses have been developed for these situations. For viscous flow methods the state-of-the-art is less well advanced. Here the treatment will be expanded beyond turbomachinery to also encompass duct flows. The analyses discussed in the paper will also be limited to steady flows. Although some do have the capability to predict unsteady flow phenomena, they have been developed primarily as predictors for steady flows. A wide variety of flow characteristics exist in the various types of turbomachinery. The objective of the analyses to be discussed later will be to predict as many of these flow features as possible. First of all, large axial, radial and centrifugal pressure gradients exist within the flow passages due to the turning of the fluid within the blade rows. Secondly, this turning redistributes the incoming vorticity field and generates cross flows. At higher velocities strong shocks exist within the blade passages. These can be complex and interacting, and can in turn generate their own vorticity fields. These shocks, of course, interact with the blade surfaces and endwall boundary layers, often causing separation and additional blade loss.

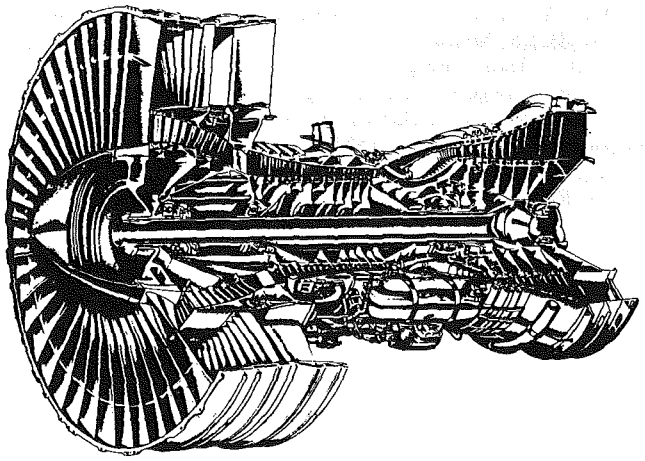

Fig. 1 Pratt & Whitney JT9D turbofan engine

There are also a wide variety of viscous flow phenomena existing in the blade passages. Primarily there are the boundary layers which exist on all blade and endwall surfaces as well as on the surfaces of midspan dampers. Such boundary layers can have laminar, transitional, and turbulent regions. When pressure gradients are strong, of course, separation can also occur. Some separations may experience reattachment. Finally, there are the wakes which exist downstream of all blade rows.

The resultant flow picture is extremely complex (Fig. 2), particularly in multistage turbomachinery. No single analysis can hope to model all of these flow phenomena. In the methods to be described here, a number of approaches are used to divide this overall problem into one of manageable

Contributed by the Fluids Engineering Division for publication in the JOURNAL OF FLUIDS ENGINEERING. Manuscript receveived by the Fluids Engineering Division, December 3, 1982.

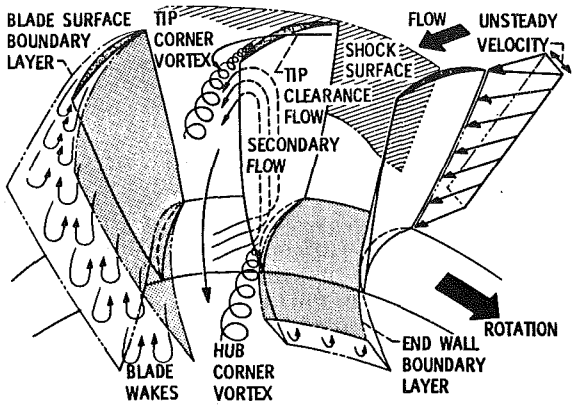

Fig. 2 Turbomachinery blade row flow features

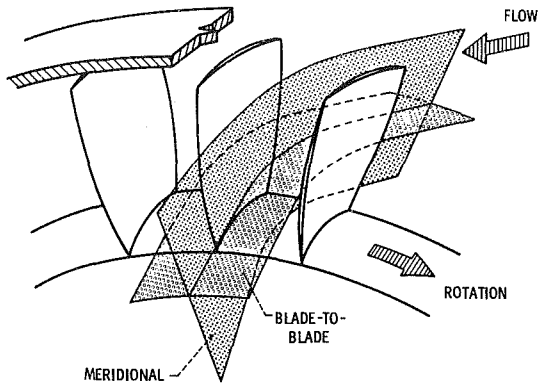

Fig. 3 Turbomachinery two-dimensional flow surfaces

size. We have separated these models into two major groups, inviscid and viscous analyses. Within these classifications many other assumptions are made. First, the solution is usually limited to a single blade row, either stationary or rotating. Next, for a steady solution, the flow in all blade passages is taken to be identical. Within a passage the solution may be limited to two dimensions, on one of two types of flow surfaces. The first is a meridional surface, an average or mean flow surface between the suction and pressure sides of the blade (Fig. 3). The second is a blade-to-blade surface, generally formed by rotating one of the calculated meridional streamlines around the blade row in the circumferential direction. Such surfaces are axisymmetric and may have radius change from inlet to outlet. Quasi-three-dimensional effects can also be considered on such a surface by giving it a thickness which varies in the meridional flow direction from inlet to outlet.

Finally, a number of decisions can be made in the process of reducing the full flow equations to a reasonable subset. Some of the assumptions and approaches used in the past will be summarized in the following.

Historical Perspective. A number of articles have appeared in the literature reviewing the methods and theories which have been used to describe the fluid flow through turbomachinery [1–7]. These do an excellent job of reviewing the early work in the field, as well as some of the more recent approaches.

In the 1950s and 60s, singularity methods were often used to compute two-dimensional incompressible potential flows through cascades. These have been reviewed by Gostelow [1], and Perkins and Horlock [3] and will not be discussed here.

Also in the 50s and 60s classical secondary flow theory was developed to predict three dimensional incompressible rotational or vortical flow in cascades. Such methods have been reviewed by Horlock and Lakshminarayana [2] and likewise will not be discussed.

In the 60s and early 70s finite difference approaches began to gain prominence, and were used to calculate two-dimensional, subsonic, inviscid flows. Both streamline curvature and stream function approaches were applied on both meridional and blade-to-blade flow surfaces. These approaches are reviewed by Gostelow [1], Perkins and Horlock [3], and Japikse [4]. Stream function methods will be discussed later.

During the 1970s time-marching solutions of the Euler equations began to be used to solve both two-dimensional and three-dimensional transonic flows in blade rows. In the 2D cases such methods were applied on both meridional and blade-to-blade surfaces. Some of these methods are reviewed by Japikse [4], and Habashi [5]. They will be discussed and updated in this paper.

Also during the 1970s numerical solutions to the full potential equations for two dimensional transonic flow in turbomachinery began to appear. A great deal of work has been done to extend such methods to the present time. Early full potential solutions were reviewed by Habashi [5], and the later approaches will be discussed and updated here.

During the 70s many of the above methods, as well as some early viscous approaches, began to be applied to flows in centrifugal impellers. These methods are reviewed in the paper by Adler [6] and are also discussed and updated here. In 1977 all of the turbomachinery computational methods to date were discussed by Klein in an update of Scholz's classic work [7]. Finally the state-of-the-art in the computation of a wide variety of turbulent flows was addressed at the recent AFOSR-HTTM-Stanford Conference on Complex Turbulent Flows [8]. The relevant findings from this conference will also be discussed.

Grid Generation. Numerical solution of fluid dynamic problems involves discretizing the governing equations on a network of points, or grid, throughout the physical domain. The accuracy of the resultant solution depends to a great degree on the properties of this grid. The subject of grid generation has become an active area of research, with many investigators and many different approaches. Coverage of this subject is beyond the scope of the present paper. However a number of reviews of the area have been published recently. We cite two review articles [9, 10] together with the proceedings of a conference devoted primarily to grid generation [11].

Outline of Paper. Inviscid flow methods are considered first. The Euler equations are introduced, and the difficulties in solving the primitive variable form are discussed. The stream function formulation for two dimensional flows and the scalar potential approximation are both presented, and the advantages and limitations of each described. The various methods currently in use for turbomachinery flow analysis are then reviewed.

The next section considers viscous methods. The time-averaged Navier-Stokes equations are introduced and the difficulties associated with their solution are discussed. Parabolic and partially parabolic approximations are presented, along with the advantages and limitations of each. The various methods in use for both turbomachinery and generalized duct flow analyses are then reviewed.

Finally a short discussion on the status of turbulence modelling is given. The paper concludes with comments on future directions.

Inviscid Methods

Euler Equations. The ultimate equations to be solved in most internal flows are the viscous Navier-Stokes equations. However, since solving these equations on modern day

computers is still quite time consuming, they are often reduced to a simpler form, the Euler equations, by neglecting the viscous terms.

These equations in two-dimensional, Cartesian, conservation law form are as follows:

$$\frac{\partial U}{\partial t}+\frac{\partial F}{\partial x}+\frac{\partial G}{\partial y}=0 \tag{1}$$

where

$$U=\begin{bmatrix}\rho\\ \rho u\\ \rho v\\ e\end{bmatrix},\quad F=\begin{bmatrix}\rho u\\ \rho u^2+p\\ \rho uv\\ (e+p)u\end{bmatrix},\quad G=\begin{bmatrix}\rho v\\ \rho uv\\ \rho v^2+p\\ (e+p)u\end{bmatrix} \tag{2}$$

ρ and p are the static density and pressure, u and v are the Cartesian velocity components in the x and y directions, and e is the total energy per unit volume. The system is completed by an equation of state relating p, ρ, and internal energy ϵ. These equations permit variation in entropy, total pressure, and total temperature throughout the field, and cover the entire range from subsonic to supersonic flows.

In most instances the solution to the first order steady equations is desired. These equations change character depending upon the local Mach number. In a totally supersonic flow some very efficient methods exist for their solution. The method of characteristics or a simple marching procedure are two common approaches. In subsonic domains, however, no generally accepted method has yet been devised for solving this system. One approach used for both subsonic or transonic flows is to reintroduce the time terms to the equations. The resultant set of equations is everywhere hyperbolic. A steady solution can be obtained by marching from some initial guessed flow field through time until an axymptotic steady-state is achieved.

Over the past fifteen years, a number of algorithms have been developed for marching the time-dependent Euler equations to a steady state. The initial conditions give rise to perturbation waves which move through the field as the solution progresses in time. The inviscid equations have no inherent dissipation and, therefore, these waves must either be radiated from open boundaries or absorbed by the addition of artificial damping terms. Generally, to reach a steady state requires a large number of iterations and a long computational time.

A second problem with these equations is the large storage required on the computer. There are four primitive variables in 2D, five in 3D, and all four (or five) must be stored in each grid point. This is a major disadvantage compared to less general alternative methods, in which only a single unknown must be stored at each grid point.

A final source of difficulty is in the boundary conditions. Conditions are required for all of the primitive variables on each of the boundaries. Some of these are supplied by the physics of the problem; however, other auxiliary relations must be obtained, e.g., through application of the method of characteristics at the boundary. Typically this leads to a rather cumbersome treatment, and in most methods approximations are made to the full characteristic relationships.

A number of approaches to solving the full Euler equations will be surveyed later in this paper. The conventional approach to circumventing the above difficulties for steady inviscid flow is to treat a less general problem by defining either a stream function or a potential function and to solve the resultant second order equations.

Stream Function Equation. This equation is derived by postulating that the mass flow components, ρu and ρv, are obtained from a scalar function as follows

$$\rho u=\frac{\partial \psi}{\partial y},\quad \rho v=-\frac{\partial \psi}{\partial x} \tag{3}$$

where ψ is the stream function.

Substitution of these relations into the definition of vorticity yields a second order equation for ψ with vorticity a known function of velocity, e.g., [12]. Extensive experience exists in the application of relaxation procedures to such equations. The stream function formulation retains the generality contained in the full Euler equations. However, it is limited to two-dimensional or axisymmetric flows, and made difficult by the fact that the density in the transonic regime is a double-valued function of the unknown ψ. Solution for ψ in the transonic regime is possible, and has recently been obtained by Hafez [12] for an isentropic isolated airfoil application. The cascade version of such a development is currently underway.

A number of different subsonic stream function solutions have been obtained for meridional plane and blade-to-blade plane regions. Working in terms of the stream function solves many of the problems cited previously for the full Euler equations. The stream function gives a single second order partial differential equation, for which robust and well understood relaxation methods exist. These solutions can therefore be obtained in much less computer time. The computer storage required is likewise much lower, necessitating only the storage of the stream function at each mesh point. Finally, the boundary conditions are more natural and are smaller in number. Generally Dirichlet boundary conditions are used at solid surfaces, and either Dirichlet or Neumann conditions are imposed at open surfaces. The solution can be obtained in an order of magnitude less time than for the primitive-variable Euler equations.

Full Potential Equations. Another approach to circumventing the problems inherent in the full Euler equations is to assume that the velocity components u and v are derivatives of a scalar function, φ.

$$u=\frac{\partial \varphi}{\partial x},\quad v=\frac{\partial \varphi}{\partial y} \tag{4}$$

Such a flow is automatically isentropic with constant total temperature and zero vorticity (irrotational). Substitution of these relations into the continuity equations yields a second order equation in φ.

As with the stream function, the potential equation can be solved by efficient relaxation techniques, and requires storage of only a single variable. Furthermore, it permits the solution of three-dimensional as well as two-dimensional flows. The primary disadvantages are the limitation to isentropic and irrotational flows. The isentropic assumption implies that shock waves captured in the transonic regime must be limited in Mach number to a value less than 1.3. The irrotationality condition requires a uniform incoming flow in two-dimensional situations, and a free vortex condition in three-dimensional turbomachinery flows.

The potential equation will admit the existence of discontinuities in the flow field. However, these discontinuities are isentropic shocks, which do not represent true physical shock waves because they do not satisfy the Rankine-Hugoniot jump conditions. However, these shocks will be approximately of the proper strength and will exist in the proper position in the flow field if the Mach number of the flow approaching the shock is less than or equal to 1.3.

With regard to boundary conditions for the potential function, Neumann or mixed conditions will exist at solid surfaces, and either Dirichlet or Neumann conditions at open surfaces. These are easier to incorporate than the more complicated conditions for the Euler equations.

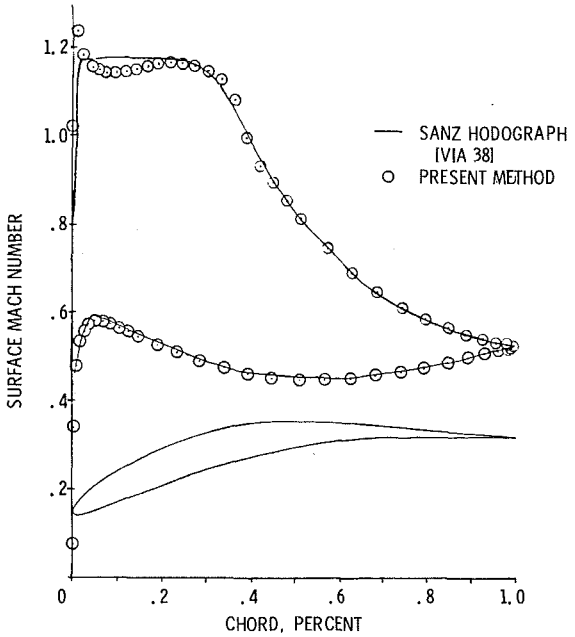

Fig. 4 Supercritical stator comparison with Sanz—after Farrell [26]

Analyses for the inviscid equations are described next. Methods for the potential equation will be covered first, followed by those for the stream function equation, and finally those for the Euler equations. In most cases the solutions have been obtained on curvilinear meshes such as those discussed above.

Potential Equation Analyses

A great deal of progress has been made in the last ten years in the development of solutions to the potential equation. At the beginning of this period Murman and Cole [13] demonstrated a way to properly account for the domain of dependence in supersonic regions by introducing a special backward or upwind differencing. This had the effect of stabilizing solutions and permitting the first real transonic flow calculations using the small disturbance potential equation.

Several major advances were also made by Jameson. The first of these [14] generalized the concepts introduced by Murman and Cole to the full potential equation in nonconservation form. Solutions to the equation in this form now routinely use Jameson's rotated difference scheme, which introduces artificial damping in the supersonic region. Hafez et al. [15] later introduced the concept of artificial compressibility to accomplish the same objective when the conservation form of the full equation is used. In this case the density is evaluated upstream of the point at which it is applied, in order to stabilize the solution in the supersonic zone. Jameson [16] also proposed a method for introducing artificial damping when the conservation form of the potential equation is used.

A number of different authors, applying these numerical techniques, and using either finite difference, finite area (or volume), or finite element methods to discretize the potential equation have devised stable and accurate methods for solving 2D transonic flows on the blade-to-blade surfaces of turbomachinery.

Many of these analyses also incorporate quasi-3D effects through radius change and stream channel convergence. A number of three-dimensional applications of these methods, not only to turbomachinery problems but also to propeller, wing-body, and nacelle problems, are under development.

Discretizing the Equation. There are several ways in which the equation is discretized to obtain a set of algebraic equations for solution. The three major approaches are: finite differences, finite areas or volumes, and finite elements.

In the finite difference method the terms in the partial differential equation are discretized using standard central and backward (or upwind) differencing. The resultant system of algebraic equations is solved by standard techniques. This approach was applied in the early work of Dodge [17], Ives [18, 19], and Rae [20]. More recently this method has been used by Caspar [21, 22], who applies it to discrete areas throughout the physical domain.

The finite volume approach is a hybrid between a finite difference method and a finite element method, with more of the latter. In this method, a local transformation is done on each of the volumes which discretize the flow field. The unknowns and the coordinates are then represented by some functional representation on each of these discrete volumes. This method is described more fully in the paper by Caughey and Jameson [23], and has been applied recently in the analyses of Dulikravich [24, 25], Farrell and Adamczyk [26], and Fruhauf [27].

The third approach is the finite element method. In this method the physical space is discretized with triangular or quadrilateral shaped elements generated in an arbitrary fashion. The potential function is approximated within each element by a linear combination of mesh point values for the function based on locally defined shape functions assigned to the element. One of the standard weighted residuals methods, usually the Galerkin method, is then used to reduce the partial differential equation to an algebraic system which is solved directly during each iteration.

Finite element methods have been used extensively in the blade-to-blade calculation methods of Laskaris [28, 29], Ecer and Akay [30, 31], and Hirsch and Deconinck [32]. The Laskaris work is primarily subsonic, with a three-dimensional application presented in [29]. The Ecer and Hirsch algorithms have been extended to the transonic range for turbomachinery applications.

Stabilization in the Supersonic Zone. As mentioned previously, there are two principal techniques which are used to stabilize the solution in the supersonic zone, the artificial viscosity approach of Jameson [14], and the artificial compressibility approach of Hafez et al. [15]. The intent of these approaches is to modify the differencing in the critical flow regions such that the grid points contributing to the solution at a given point lie primarily within its zone of influence. Jameson's rotated scheme identifies both hyperbolic and elliptic operators in supersonic zones. Upwind differences are used for the former and central differences for the latter. This has the effect of introducing an artificial viscosity to the solution procedure, which assures its stability in supersonic regions. This artificial viscosity approach is employed principally by investigators using the nonconservation form of the full potential equation, Dulikravich [24], Ives [18], Rae [20], and Fruhauf [27]. Dodge [17], who also solves the nonconservation form, constructs hyperbolic and elliptic operators on a near-characteristic grid, updated during the course of calculation. The artificial compressibility scheme of Hafez, which achieves the same objectives as the artificial viscosity approach, has been employed by investigators solving the conservation form of the full potential equation, Caspar [21], Farrell [26], Ecer [30], and Hirsch [32].

Solution of the Algebraic Equations. Several different techniques have been used to solve the algebraic system. The first, and most common, is successive line over relaxation (SLOR). This is employed by Farrell [26], Dulikravich [24, 25], Ives [18, 19], Fruhauf [27], Rae [20], and Hirsch [32]. Other approaches employ a direct solver, typically Gaussian

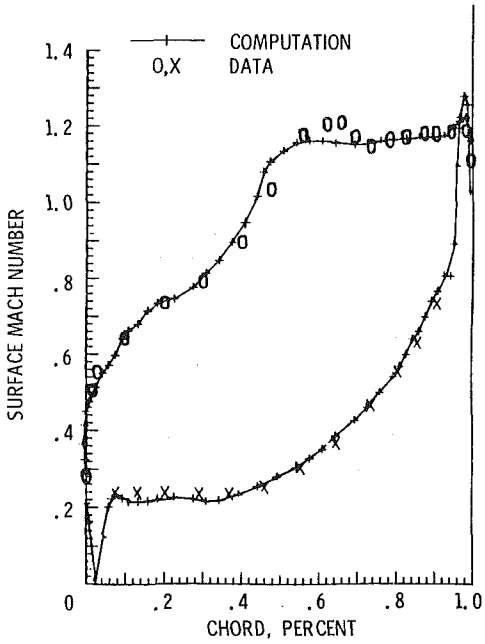

Fig. 5 VKI turbine cascade comparison with experiment—after Hirsch [32]

elimination, as the noniterative part of an overall solution scheme. Ecer [30, 31], Laskaris [28, 29], and Caspar [21, 22] employ this approach. The final method is approximate factorization or ADI, as applied by Holst [33, 34]. This approach can be an order of magnitude faster than traditional relaxation. However, it has only been applied to turbomachinery problems by Hirsch [32].

Another approach for solving the difference equations even more rapidly than approximate factorization is the use of multi-grid techniques. Such techniques were demonstrated for external flow applications by South and Brandt [35] and Jameson [36], who extended the methods initially developed by Brandt [37]. To date Hirsch [32] is the only one to apply the multi-grid approach to the solution of the potential equation for turbomachinery.

Results for Potential Equation. The results presented are for 2D and quasi-3D blade-to-blade stream surfaces, as well as complete 3D flow passage analyses. Most of the references discussed do an excellent job of predicting transonic flows in compressor and turbine blade rows with Mach numbers below 1.3.

Results of Farrell [26] are shown in Fig. 4 for a supercritical compressor stator tip section designed for NASA Lewis by Sanz using a hodograph technique based on Bauer et al. [38]. The trailing edge of this blade ends in a cusp. The inlet Mach number is 0.71, and inlet flow angle 31.16 deg. The results show good agreement with the hodograph solution with some evidence of a weak shock in the recompression region. This might have been more pronounced with a finer grid.

The results shown in Fig. 5 were obtained by Hirsch [32] using a finite element blade-to-blade code. They show Mach number calculated for a VKI-LS59 gas turbine cascade. The inlet Mach number is 0.281, inlet flow angle 30.0 deg, outlet Mach number 0.975, and outlet flow angle −65.89 deg. The stream channel convergence in the through flow direction is unity. The comparison with experimental data in this accelerating flow situation is extremely good, even in the transonic region at the rear end of the blade.

Finally, results computed with the 3D code of Dulikravich [25, 39] are presented in Fig. 6. These are for an idealized rotor with upstream axial Mach number of 0.62 and rotational speed of 1000 rpm. This corresponds to an upstream relative tip Mach number of 0.87. Hub and tip radii were one and two meters, respectively. The code cannot treat cases with supersonic upstream flow relative to the rotor. Regions of supersonic flow are present on all blade surfaces from hub to shroud, with fairly strong shocks in the tip region. Peak Mach numbers reach values of approximately 1.5 at the tip. Two grids were used to obtain this solution, with coarse grid results interpolated to provide initial values on the fine grid. The coarse grid used 24 points around the blade by 6 normal and 6 radial and the fine grid used double those mesh dimensions in all directions.

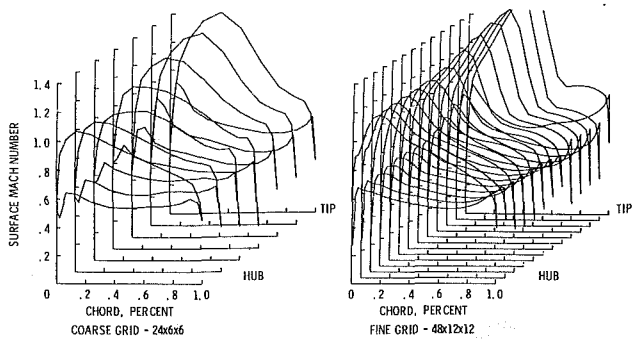

Fig. 6 3D full potential rotor calculation—after Dulikravich [39]

Stream Function Equation Analyses

Stream function equation applications to turbomachinery occurred about ten years prior to those for the full potential equation. A major development paving the way for analyses of turbomachinery flows was the series of early papers by Wu, particularly [40], which derived the stream function equations for hub-to-shroud and blade-to-blade stream surfaces of turbomachinery. Derivation of the equations on the two intersecting surfaces is complex, and the reader is referred to details in Wu and the other references to be given.

Historical Development and Applications. The two earliest developers of stream function analyses for turbomachinery worked independently, Katsanis in the United States and Marsh in England. Katsanis [41] published a method for isentropic blade-to-blade flows applicable to any fixed or rotating axial, radial or mixed flow turbomachinery blade row. Quasi-3D effects were incorporated through a stream channel thickness. Wood [42] has since devised methods for extending Katsanis's approaches into the low transonic region. Katsanis and McNally [43] also published anlayses for slotted or tandem blade rows, as well as a method [44] to magnify the solution around the blade edges.

Marsh [45] developed a stream function analysis for hub-shroud surfaces. His non-rectangular grid was composed of parallel lines in the radial direction and through-flow lines following the shape of the hub and shroud boundaries. This is in contrast to the rectangular grid employed by Katsanis. Marsh's technique also applied to axial, radial and mixed flow turbomachines. Smith [46] contrasted results from Marsh's code to those of established streamline curvature methods, and showed significant advances in the calculation of quasi-3D flows using stream function methods.

In 1970 Smith [47] and Frost applied these methods to compute flow on general blade-to-blade stream surfaces. Smith [48] also described both the meridional and the blade-to-blade analyses in use at N.G.T.E. This was the first description of the meridional and blade-to-blade methods used together.

Other codes for both hub-to-shroud and blade-to-blade analyses were developed at Carleton University by Davis and Millar [49–52]. In 1975 Davis [53] presented the first hub-to-shroud stream function solution for flow in a centrifugal

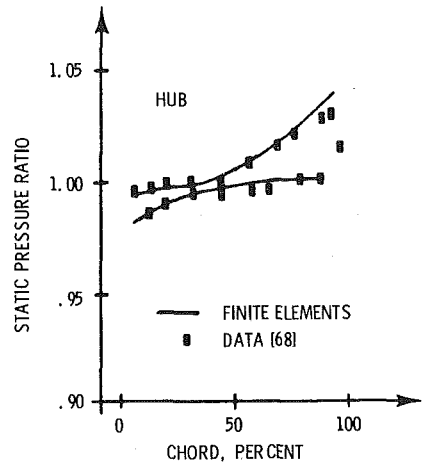

Fig. 7 Calculated and experimental static pressure on impeller hub—after Hirsch [66]

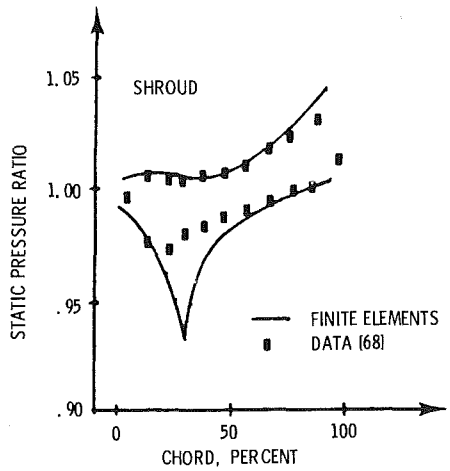

Fig. 8 Calculated and experimental static pressure on impeller shroud—after Hirsch [66]

compressor. He used a special form of through-flow grid which remained quasi-orthogonal throughout the solution domain. Davis also incorporated a turbulent endwall calculation, using an integral method based on the entrainment theory of Head [54].

In 1974 Katsanis and McNally [55] described their hub-to-shroud stream function code for use with the blade-to-blade analysis of [41]. This code applied to single axial or mixed flow compressor and turbine blade rows. In 1977, the same authors [56, 57] extended this code to radial or centrifugal blade rows.

Marsh in 1976 [58] compared his stream function method to streamline curvature techniques for the hub-shroud problem. He concluded that both these techniques could be viewed as two methods for solving the same governing equations on the same mean surface, but did not find any definite superiority of one method over the other.

Multi-Surface Iterative Approaches. In 1976 Bosman [59], presented an iterative approach to couple hub-to-shroud and blade-to-blade analyses. Locations of the axisymmetric blade-to-blade surfaces are taken from streamlines on a single hub-to-shroud surface. The blade-to-blade solutions are then used to redefine the hub-to-shroud surface. This process is iterated to convergence. Bosman applied his techniques to calculate flows in a low speed centrifugal compressor and a radial inflow turbine.

A second, more elaborate iterative procedure was described by Adler and Krimerman [60–62]. The method is initiated by normal applications of meridional and blade-to-blade calculations on axisymmetric stream surfaces. A number of different hub-to-shroud stream surfaces are then obtained from corresponding streamlines in the blade-to-blade surfaces. Multiple hub-shroud solutions are then used to obtain blade-to-blade surfaces by connecting corresponding streamlines. These surfaces are no longer axisymmetric. Iteration between the two families of surfaces is continued to convergence. Adler applies this technique to a centrifugal impeller, and shows that the results clearly deviate from those obtained using a single meridional surface.

Hirsch [63] presented the first solution of the meridional stream function equation based on the finite element method. Later, Hirsch developed an iterated analysis [64] in which meridional and blade-to-blade finite element analyses were combined for application to axial turbomachinery. Second-order isoparametric quadrilateral elements were used to permit accurate simulation of blade curvature. Results compared favorably with the LDV data obtained by DFVLR in Germany [65]. In 1980 Hirsch [66] presented an iterative analysis for centrifugal compressors, and applied it to the radial compressor mapped with LDV by Eckardt [67]. The viscous and secondary flow effects were not well reproduced with the through-flow calculations particularly in the back end of the compressor. Hirsch also presented a quasi-3D calculation on the Type-B centrifugal compressor described in reference [68]. Figures 7 and 8 show calculated and experimental static pressure distributions on the hub and shroud sections for a flow coefficient of 0.5. The inviscid calculations predict a stronger local acceleration along the shroud suction surface than experimentally determined.

Finally, in 1980 Goulas [69] presented a stream function analysis for the blade-to-blade flow in a centrifugal compressor with splitter blades. The analysis can either calculate isentropically, or simulate turbulent flow with the addition of a simple turbulence model. The method treats stagnation points as well as the formation of small recirculation zones at the front of the splitter blades. The method was applied to a centrifugal compressor, and various axial locations for the leading edge of the splitter were studied.

Multi-Stage Meridional Capability. Of the methods just described for anlayzing hub-shroud flow with stream function analyses, the methods of Marsh [45], Smith [48], Davis [49, 51], and Hirsch [63, 64] all permit the analysis of multi-stage machines. The method of Davis, however, was only demonstrated [49, 51] for a single full stage machine. On the other hand, the methods of Katsanis [55, 56], and Bosman [59] apply to a single blade row.

Transonic and Three-Dimensional Flows. Recently Hafez [12] has extended the solution of the stream function equation to transonic flows by using techniques developed for the potential equation. His methods circumvent the fact that the density is not a unique function of the mass flux, having both subsonic and supersonic solutions. The method is applied to transonic flows over a NACA 0012 airfoil, a 10% parabolic airfoil, and a cylinder. These results are compared to both potential and Euler solutions. Hafez has likewise investigated the application of stream function methods to three-dimensional flows through the use of two stream functions. This work is ongoing.

Euler Equation Analyses

Explicit Time Marching Methods. Explicit solutions to the Euler equations have been under development for a number of years, with applications for internal flow situations dating back to the 1950s. An explicit method is one in which all spatial derivatives are evaluated using known conditions at an old time level. The resultant methods are simple and easy to code. All such methods, however, are limited by the so-called

Courant, Friedrichs, and Lewy (CFL) stability limit, which states that the domain of dependence of the numerical scheme must contain the domain of dependence of the original equations.

MacCormack [71] introduced a two-step predictor-corrector method, which alternates between forward and backward differencing on the two steps. The ease with which this method can be applied has led to many applications in the turbomachinery field. An early application of the MacCormack scheme by Gopalakrishnan and Bozzola [72] was for a transonic compressor cascade with supersonic inlet and subsonic outlet. Kurzrock and Novick [73] have applied this scheme to a rotating blade-to-blade stream surface, with radius change and stream channel convergence. They calculated transonic flow in a 2D compressor cascade and also flow on a quasi-3D stream surface of a compressor rotor. Thompkins [74] has applied the MacCormack algorithm to flow through a three-dimensional transonic compressor rotor. Calculations can be made for any general blade shape, including those with part-span shrouds. Computed results will be presented later.

Another set of explicit methods is obtained by writing the conservation laws in integral form and applying them to local control volumes surrounding each grid point. The fluxes of mass, momentum, and energy crossing the control surfaces are evaluated using the values from surrounding points. A first order integration in time is then used to advance the dependent variables forward to a steady state. McDonald [75] applied this approach to 2D transonic flow in axial turbine cascades. His method includes the use of hexagonal elements surrounding each grid point and the replacement of the energy equation by assuming constant total enthalpy. Computed and experimental results were compared for a number of high-turning turbine cascades with supersonic exits.

Denton [76–78] has developed a somewhat simpler method for both 2D and 3D turbomachinery flows. Denton employs quadrilateral elements in two dimensions and six-sided elements in 3D, which lead to simpler expressions for his surface flux integrals. In order to ensure stability he uses upwind differencing in the streamwise direction for the fluxes of mass and momentum, while using downwind differencing for pressure. Central differencing is used for all quantities in the pitchwise direction. This scheme has the property that stability depends only on the axial Mach number, as opposed to the absolute Mach number. This method has been applied to a wide variety of both axial and mixed flow compressor and turbine geometries.

Bosman and Highton [79] have developed a method for 3D flows which employes two overlapping grids with density and internal energy evaluated at one set of nodes and velocities evaluated at the second set. Primitive variables are updated in a sequential fashion. The method has been applied to both radial inflow turbines [79] and to centrifugal compressor impellers [80].

Recent efforts have been devoted to improving both the accuracy and the speed of explicit methods. One example is Moretti's λ-scheme [81] which exploits concepts from the method of characteristics. The Euler equations are rewritten so that the right-hand sides involve derivatives of one-dimensional Riemann invariants. These derivatives are approximated by one-sided differences in characteristic directions and unknowns are updated in time by a two-step predictor-corrector scheme. This results in improved accuracy as evidenced by very sharp shocks captured with modest numbers of grid points. The method produces isentropic shocks unless it is corrected with a shock fitting procedure, as in De Neef and Moretti [82]. A modified version has been applied to simple compressor and turbine cascades by Pandolfi and Zannetti [83]. A similar method to the λ-scheme has been developed by Chakravarthy et al. [84].

Ni [85] has developed a new method that is equivalent to the second-order Lax-Wendroff procedures (see Richtmyer and Morton [86]). By spatially varying the time-step to be everywhere near the CFL limit, a significant increase in overall speed is obtained. In addition, this effectively biases the differencing such that the numerical scheme has a domain of dependence close to that of the underlying hyperbolic system. Ni's method has been coupled with a multiple-grid procedure which greatly speeds convergence to a final steady state. Applications in [85] were for transonic flow in a turbine cascade as well as an axisymmetric nacelle with centerbody.

Improved convergence rates can also be obtained by adding pseudo-unsteady terms to the steady equations. When properly constructed, these artificial terms can introduce a strong internal damping into the resulting unsteady system. Essers [87] added artificial unsteady terms to the continuity and irrotationality equations. This results in two equations in the unknown velocities, with density obtained from the isentropic relationship. These equations are solved by a predictor-corrector scheme. Results are presented for two-dimensional flow through a turbine rotor blade section with supersonic exit.

Another pseudo-unsteady method has been developed by Viviand and Veuillot [88, 89]. The energy equation is replaced by constant total enthalpy, and the pressure expressed as a function of density and velocity. The reduced system is solved by a predictor-corrector scheme. Since the system has no unusual damping mechanism the method relies on careful treatment of waves at the boundaries in order to reach a steady state. A three-dimensional version has been developed by Brochet [90, 91] and applied to flow in a supersonic compressor cascade with converging endwalls and to transonic flow in a fan rotor.

Implicit Time Marching Methods. Implicit time-marching methods for both the Euler and the Navier-Stokes equations date from the mid-1970s. In these methods the equations are backward differenced in time, and the nonlinear terms at the new time are linearized about their values at the previous time level. Introduction of differences gives a large system of algebraic equations for the unknowns at the new time level. In each of the methods to be discussed here, these equations are solved by block alternating-direction-implicit (block ADI) techniques.

The first of these methods was introduced by Briley and McDonald [92, 93], primarily for the compressible Navier-Stokes equations. Beam and Warming [94] independently developed a similar method for the Euler equations. Briley and McDonald [95] have since shown that when the Beam and Warming algorithm is written in the "delta" form to solve for the corrections to the unknowns, the two methods have identical matrix structures.

Steger [96, 97] has developed a curvilinear coordinate version of the Beam-Warming algorithm for viscous as well as inviscid flows, and has applied it to both isolated airfoils and cascades in two dimensions. Shamroth et al. [98] have applied the Briley-McDonald procedure to laminar and turbulent flow through a cascade. Finally, Fruhauf [27] has applied the Beam-Warming algorithm to solve the Euler equations for both subsonic and supercritical flow through cascades.

New Methods Under Development. A number of methods are under development in order to achieve more accurate and faster solutions for the Euler equations. Delaney [99] has developed a hopscotch method for solving the Euler equations for application to cascades. The method appears to be significantly faster than the original MacCormack algorithm.

Denton [100] has extended his earlier Euler method by employing a simpler more accurate differencing scheme. He has also increased the convergence speed through the use of a simple multiple-grid procedure. He has applied the method to

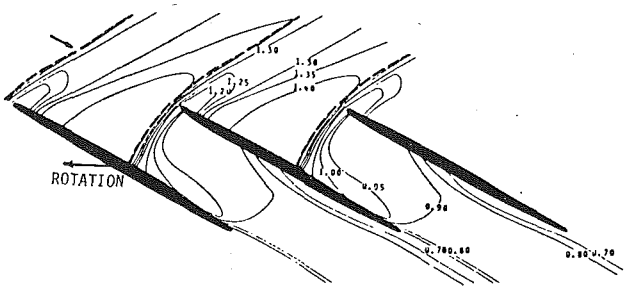

Fig. 9 Measured Mach number contours near tip of NASA transonic compressor rotor—after Chima [105]

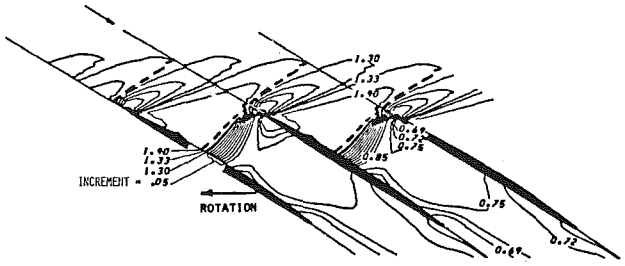

Fig. 10 Calculated Mach number contours near tip of NASA transonic compressor rotor—Thompkins method—after Chima [105]

2D transonic flow in both compressor and turbine blade rows. Johnson [101] has developed a new technique in which the first-order steady Euler equations are imbedded in a second-order system. Published results to date include both subcritical and supercritical flow in a two-dimensional channel with a bump on one wall.

Both Ecer and Akay [102] and Lacor and Hirsch [103] have developed methods for solving the steady Euler equations. The velocity is split into potential and rotational parts and the system of equations is reduced to a second order equation for a potential function and a pair of first order convective equations describing the evolution of two scalars which together determine the rotational part of the velocity field. Both methods employ finite element techniques. Ecer has analyzed 2D transonic flow in a channel with a bump and flow around a 2D cylinder. Hirsch calcualted 3D flow in a rectangular elbow with 90 deg of turning.

Finally Chang and Adamczyk [104] have developed a new semi-direct algorithm for computing three-dimensional inviscid shear flows. The velocity and density fields are evaluated for known vorticity, total enthalpy and entropy from the solution of a pair of Poisson equations by three-dimensional, fast, direct solvers. The vorticity, total enthalpy and entropy are updated by solving convective equations for a pair of scalars. In the present work, finite difference procedures are used throughout. To date the method has been applied to study the development of inviscid shear flows in turning channels.

Applications of Euler Methods. Results are presented to indicate the kinds of calculations which are being performed with the Euler methods. Thompkins' code [74] has been applied at NASA by Chima and Strazisar [105] to calculate the three-dimensional flow in a transonic axial compressor rotor for which laser anemometer measurements were also obtained. Figure 9 shows Mach number contours for the measured results at a section 15Δ from the tip of the blade. These results can be compared to the calculated contours at the same location in Fig. 10. These figures indicate a pronounced bowwave and passage shock system, and show good agreement between the measured and calculated results for this feature.

The method of Ni [85] has been applied to flow past a VKI

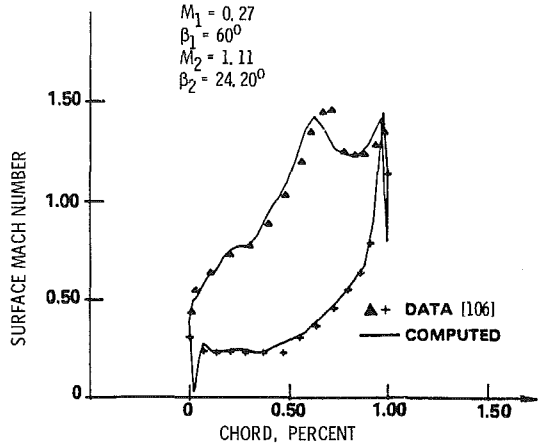

Fig. 11 Calculated and measured surface Mach number on VKI turbine rotor—after Ni [85]

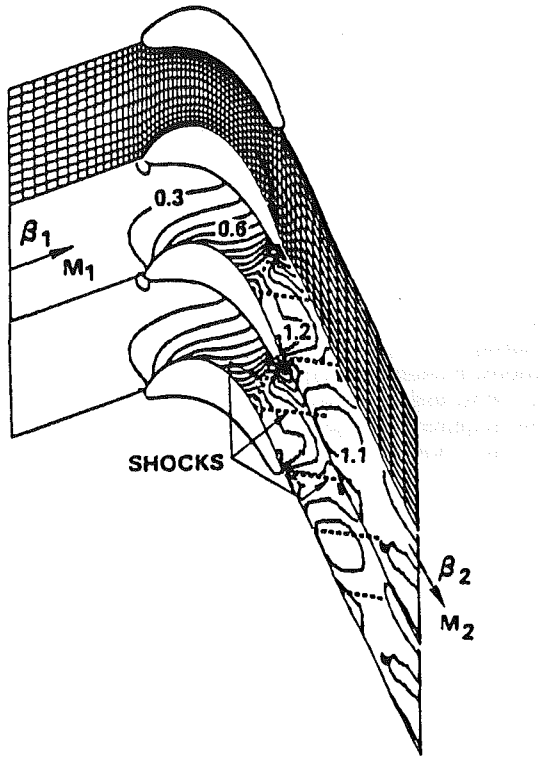

Fig. 12 Mach number contours for VKI turbine rotor—after Ni [85]

gas turbine rotor blade, and compared to data by Sieverding [106]. Figure 11 presents calculated and experimental surface Mach numbers for this turbine rotor. The agreement is excellent on both blade surfaces. Figure 12 indicates the mesh used in the calculation and shows the calculated Mach number contours.

Viscous Methods

Full Viscous Equations. Most flows of engineering interest are adequately described by the compressible Navier-Stokes equations. These equations, in two-dimensional conservation form and Cartesian (x, y) coordinates, are written

$$\frac{\partial U}{\partial t} + \frac{\partial F}{\partial x} + \frac{\partial G}{\partial y} = \frac{\partial R}{\partial x} + \frac{\partial S}{\partial y} \tag{5}$$

where U, F, and G are the same as for the Euler equations, and

$$R=\begin{bmatrix}0\\ \tau_{xx}\\ \tau_{yx}\\ R_4\end{bmatrix},\quad S=\begin{bmatrix}0\\ \tau_{xy}\\ \tau_{yy}\\ S_4\end{bmatrix} \tag{6}$$

with

$$\tau_{xx}=2\mu\frac{\partial u}{\partial x}-\frac{2}{3}\mu\theta,\quad \tau_{yy}=2\mu\frac{\partial v}{\partial y}-\frac{2}{3}\mu\theta$$

$$\tau_{xy}=\tau_{yx}=\mu\left(\frac{\partial u}{\partial y}+\frac{\partial v}{\partial x}\right),\quad \theta=\frac{\partial u}{\partial x}+\frac{\partial v}{\partial y}$$

$$R_4=\tau_{xx}u+\tau_{xy}v+\kappa\frac{\partial \epsilon}{\partial x},\quad S_4=\tau_{yx}u+\tau_{yy}v+\kappa\frac{\partial \epsilon}{\partial y} \tag{7}$$

Here μ is the viscosity coefficient and κ is the coefficient of thermal conductivity.

These equations are valid for turbulent flows, but such computations are impractical today due to the large range of length scales in the turbulent spectra. The equations are replaced by time-averaged equations and the Reynolds stresses, e.g. $-\rho\,\overline{u'v'}$, are modelled through the addition of auxiliary algebraic or differential relations. If an "eddy viscosity" model is adopted for the Reynolds stresses, the above equations will hold for the mean fluid variables $\bar{\rho}$, $\bar{u}$, $\bar{v}$, $\bar{\epsilon}$, with μ and κ replaced by their effective turbulent values. For practical engineering flows with curved boundaries, the Cartesian equations are transformed to curvilinear body-fitted coordinates and, for steady flows, the time derivatives are often retained as an aid in the solution process. The resulting equations are quite difficult to solve for a number of reasons. First, many disparate length scales must be resolved, e.g., those associated with boundary layers and shock waves. This requires a large number of grid points even for a minimum description. Second, a large number of quantities are needed at every grid point. For example, in three-dimensional flow, one might need five primitive variables, two turbulence properties, and nine or more metric derivatives. Hence a very large computer memory and long running times are needed. Third, the numerical problems associated with the Euler equations are still present. One such problem often occurs when the local cell Reynolds number, $\rho u\Delta x/\mu$, exceeds 2 and the solution becomes either unstable or highly inaccurate. The common "fix" of locally switching from central to first order upwind differencing of the convective term can introduce excessive numerical diffusion.

Many techniques have been developed over the years for viscous problems which solve simpler sets of equations. We consider only those for steady flows, and group them into two categories.

Partially Parabolic Approximation. The partially parabolic approximation assumes the existence of a main flow direction, known a priori. In general, flow separation is excluded. The viscous terms are simplified by neglecting diffusion in this direction. This is much like the boundary layer approximation. In two dimensions, if x is the flow direction, R, τ_{yy}, and $\partial v/\partial x$ are set to zero in equations (5) to (7). For three dimensions see Caretto, Curr, and Spalding [107]. One variable, usually the pressure, is treated as elliptic and stored at every grid point. The remaining variables, e.g., u, v, ϵ in 2D, are treated as parabolic and stored on only two or three cross-sections at a time. Given an approximate pressure field the momentum and energy equations are marched in the flow direction and the variables are corrected locally to satisfy continuity. After each marching sweep, the pressure field is updated by solving an elliptic equation on the entire grid. This sequence of marching followed by pressure update is repeated until convergence. The approximation is applicable to many internal flows including those in turning ducts and turbomachinery blade rows as long as the details of the flow in the leading and trailing edge regions are not critical and separation is negligible.

Fully Parabolic Approximation. The fully parabolic approximation uses the same assumptions as the above with regard to the main flow direction and the neglect of streamwise viscous diffusion. In addition, upstream transmission of pressure disturbances generated during the calculation is assumed negligible. An initial pressure field, stored on the full grid, is assumed to contain all of the effects of boundary curvature. The remaining variables are stored on only two or three cross sections at a time. The momentum and energy equations, or an equivalent set, are marched once in the flow direction, and the variables are corrected at each cross section in order to satisfy continuity. This procedure should be applicable to flows in duct-like geometries with moderate turning in the absence of streamwise separation. Since only a single marching sweep is employed, these computations should be orders of magnitude faster than time marching procedures.

Both parabolic approximations are capable in principle of predicting strong secondary flows provided local continuity is well satisfied. Both can also treat modest amounts of streamwise separation if the Flugge-Lotz and Rehyner approximation is adopted, i.e., streamwise velocity is artificially prevented from becoming negative in the convective term only.

Methods are now discussed in each of the above categories starting with the fully parabolic approximation. Within each category, the main elements of a solution procedure are presented along with the distinguishing features of each method.

Fully Parabolic Methods

Main Parabolizing Assumption. All of the methods in this category require an additional assumption, beyond the neglect of streamwise viscous diffusion, in order to obtain a fully parabolic system. In the usual procedure a bulk pressure correction, $\bar{p}_c$, uniform over each cross section, is introduced into the streamwise momentum equation and determined so as to ensure the correct total mass flux. The cross flow equations retain a separate pressure correction p_c which is permitted to vary over the cross section. This procedure is employed by Patankar and Spalding [108], Briley [109], Ghia et al. [110], Roberts and Forester [111], and Briley and McDonald [112].

A different procedure is employed by Anderson [113] in 2D and Anderson and Hankins [114] in 3D. The equations are parabolized by writing them in an intrinsic coordinate system which could be obtained for example from an incompressible potential flow solution. The assumption of small velocities normal to the streamwise grid lines eliminates convective derivatives and viscous terms in the transverse momentum equations. The resulting system is fully parabolic with characteristic surfaces coincident with the cross-planes. Hence, no bulk pressure correction is required.

Satisfaction of Local Continuity. To satisfy local continuity, Patankar and Spalding [108] introduce approximate relations between the velocities and pressure corrections obtained from the transverse momentum equations. Substitution into continuity gives a 2D elliptic equation over the cross-section. Another approach, adopted by Briley [109] and Ghia et al. [110], assumes a 2D potential φ for the transverse velocity corrections. Continuity yields a 2D elliptic equation for φ in the cross-plane, and the divergence of the transverse momentum equations provides a second elliptic equation for

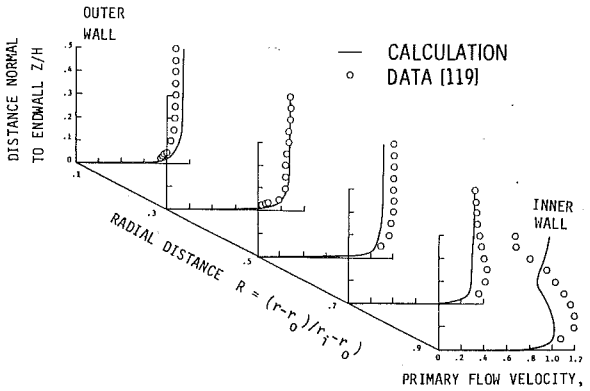

Fig. 13 Computed and measured axial velocity profiles after 77.5 deg turning in circular arc square duct—after Kreskovsky [118]

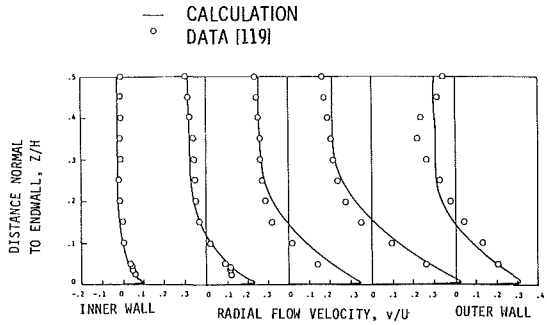

Fig. 14 Computed and measured radial flow velocity profiles after 77.5 deg turning in circular arc square duct—after Kreskovsky [118]

the pressure correction. Roberts and Forester [111] work directly with the divergence of the transverse momentum equations which gives a 2D elliptic equation with a source term related to the non-satisfaction of local continuity. This equation is solved iteratively with the momentum equations until continuity is satisfied. This technique is related to that of Harlow and Welch [115] for 2D time-dependent flows. Briley and McDonald [112] split the transverse velocity into irrotational and rotational parts described by a 2D potential φ and stream function ψ, respectively. Substitution into continuity and the definition of streamwise vorticity ω_s gives 2D elliptic equations for φ and ψ. The latter is solved coupled with the transport equation for ω_s which replaces both transverse momentum equations. Anderson [114] uses the same splitting as Briley and McDonald and solves for φ, ψ, and ω_s. However, the Poisson equation for pressure p is added to the system.

Approximation by Algebraic System. All of the methods use finite difference techniques to approximate the viscous equations by an algebraic system. First order upwind differences are used in the main flow direction and second order central differences in the cross-plane. Within this common framework, a few variations deserve comment. Patankar and Spalding [108] use a staggered grid similar to that of Harlow and Welch [115]. Velocity components and pressures are stored at different locations within a grid cell in order to simplify differencing of the convective terms. The other methods store all variables at common locations within the grid. For large transverse velocities both Patankar and Spalding [108] and Ghia et al. [110] switch to upwind differencing in the cross-plane. Roberts and Forester [111] add explicit local damping to deal with this problem. The other methods have not encountered this problem. Anderson [113] in his 2D method applied Keller's box scheme to a system of first order partial differential equations. In the current version [114] for 3D flows, a system of second order equations with differencing similar to the other methods is employed.

Solution of Algebraic System. To solve the algebraic equations at each cross-section, Patankar and Spalding [108] obtain provisional velocity components from the momentum equations by an ADI technique, and the bulk correction $\tilde{p}_c$ from a global mass balance over the section. The local correction p_c is obtained from the 2D elliptic equation by several ADI sweeps, and the velocities are corrected using the approximate velocity-pressure correction relation. Finally, the energy equation is solved by ADI. The procedures of Briley [109] and Ghia et al. [110] are similar to the above, except that $\tilde{p}_c$ is determined iteratively with the streamwise velocity, and the 2D elliptic equations for φ and p_c are solved by point SOR. Roberts and Forester [111] follow a sequence similar to that of Briley, without the equation for φ. However, the entire sequence is repeated iteratively at each cross-section using updated pressures in the momentum equations until convergence is achieved. Briley and McDonald [112] solve for the streamwise velocity, density, and total enthalpy with a coupled block ADI technique and iterate to determine $\tilde{p}_c$. Scalar ADI is then used to find the potential φ. Finally, a coupled block ADI scheme is used to find ψ and ω_s. Anderson [114] solves a fully coupled system for primary velocity, φ, ψ, ω_s, p, and total enthalpy. Point SOR is used at present with 6 $\times$ 6 block inversion at each point.

Application of Methods. The methods of this section have been applied to a variety of flows. Patankar and Spalding [108] have analyzed developing laminar flow in a square duct with a moving wall [108] and in a round turning duct [116]. Briley [109] calculated the developing laminar flow in rectangular ducts and included the effects of transverse buoyancy. The method of Ghia et al. [110] has been applied to developing laminar flow in straight ducts of polar cross-section [110] and to turning ducts of rectangular cross-section [117]. Roberts and Forester [111] computed the turbulent flow in a rectangular-to-round diffusing transition duct. The method of Briley and McDonald [112] has been used for laminar flows in a turning duct similar to a turbine blade passage [112] and for turbulent flow in a rectangular turning duct [118]. Finally, Anderson [113] has computed several 2D turbulent flows in axisymmetric ducts with curved walls, and Anderson and Hankins [114] have applied their 3D method to the hot turbulent flow in a turbofan forced mixer nozzle.

To illustrate the capability of these methods we present results obtained by Kreskovsky, Briley, and McDonald [118] for turbulent flow in a rectangular duct with a 90 deg bend. Figures 13 and 14 show computed primary and radial velocity profiles, for a cross-section 77.5 deg around the bend, compared with the LDV measurements of Taylor et al. [119]. Note the very large radial velocity near the suction side of the channel.

Finally, we note that Baker and Orzechowski [120] have developed a finite element parabolic method. Like the methods of Briley and Ghia et al., it solves 2D elliptic equations for φ and p. Like that of Anderson it uses the small transverse velocity assumption to parabolize the system.

Partially Parabolic Methods

Satisfaction of Local Continuity. Three of the four methods considered in this section are similar to fully parabolic methods. To satisfy local continuity, both Pratap and Spalding [121] and Moore and Moore [122] employ approximate velocity-pressure correction relations and adjust these variables at each cross-section in the same manner as Patankar and Spalding. In successive passes, as the pressure field is refined, these corrections should approach zero. Chilukuri and Pletcher [123] correct the local velocity field

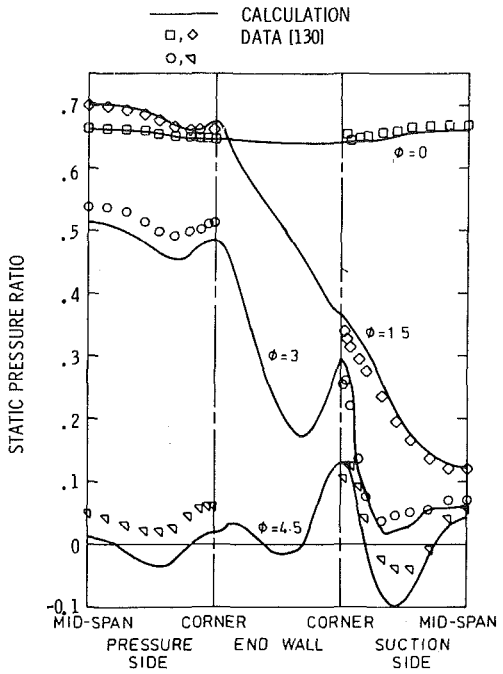

Fig. 15 Calculated and measured wall static pressure on suction, pressure, and end wall surfaces of Stanitz elbow—after Moore [127]

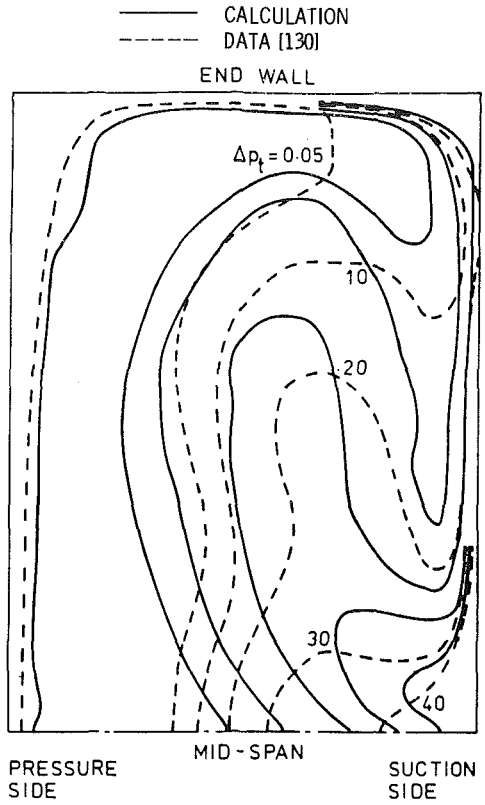

Fig. 16 Calculated and measured total pressure loss contours at exit of Stanitz elbow—after Moore [127]

through a potential φ in a manner similar to that of Briley [109] and Ghia [110]. φ should also approach zero in successive passes. Dodge [124] splits the velocity into viscous and potential parts **U** and $\nabla\varphi$. **U** is obtained by marching the momentum equations and φ is updated after each full sweep by solving a three-dimensional elliptic equation obtained from continuity.

Elliptic Pressure Update. The technique for updating the elliptic pressure field after each march is the distinguishing feature of these methods. Pratap and Spalding [121] use the pressure field obtained from the continuity corrections during the march. An ad hoc means of distributing these corrections upstream is mentioned in the paper but not discussed. Moore and Moore [122] use an elliptic pressure correction equation obtained from an approximation to the divergence of the momentum equations. The corrections approach zero after many marching passes through the field. Chilukuri and Pletcher [123] use the pressure Poisson equation obtained from the divergence of the full momentum equations. Dodge [124, 125] introduces an approximate relation between pressure and the potential φ. Once the 3D elliptic equation is solved for φ, the pressure is obtained from this relation.

Approximation by Algebraic System. Finite difference techniques are again used in each method. In the marching equations first or second order upwind differences are used in the primary flow direction and second order central differences in the cross-plane. Pratap and Spalding [121] and Chilukuri and Pletcher [123] use the staggered grid of Patankar and Spalding. The velocity components and the pressure are stored at different locations in a grid cell. Moore and Moore [122] use a staggered scheme with velocity components stored at one set of grid locations and the pressure corrections stored at another. Dodge [125] stores all variables at common grid locations. He introduces subgrids near the walls to resolve the viscous layers. The elliptic pressure equations of both Moore and Moore [122] and Chilukuri and Pletcher [123] use central differences. The global potential equation of Dodge [125] uses the mixed upwind-central differencing of reference [18].

Solution of Algebraic System. To solve these algebraic systems ADI techniques are used in all methods to obtain the velocity components from the momentum equations during the march. Since Chilukuri and Pletcher [123] solve 2D problems, they perform a tridiagonal matrix inversion in only one direction. Pratap and Spalding [121] and Moore and Moore [122] use ADI to solve the pressure correction equations at each cross-plane. Only the Moore's, however, iterate with the momentum equations until the pressure corrections are acceptably small. Both Moore and Moore [122] and Chilukuri and Pletcher [123] use point relaxation procedures to solve the elliptic pressure equations. The Moores omit points in the near wall region of the boundary layer. Dodge [124, 125] obtains separate marching solutions on each of his near wall subgrids and couples these to the interior marching solution at their common boundaries. The global potential equation for φ is solved by the transonic relaxation technique of reference [18], with the near wall subgrid points omitted.

Application of Methods. The partially parabolic methods have been applied to a somewhat broader range of flows than those of the previous section. Pratap and Spalding [121] have analyzed 3D turbulent flow in rectangular turning ducts [126]. Moore and Moore have computed 3D turbulent flow in an accelerating rectangular elbow [127] and two centrifugal impellers [128, 129]. Chilukuri and Pletcher [123] computed 2D laminar flow in the inlet of a straight channel over a broad range of Reynolds numbers. Dodge [125] has calculated 3D turbulent flow in a rectangular diffuser and a low aspect ratio turbine stator. We show results from two of these computations as examples of the state-of-the-art.

Stanitz et al. [130] measured the turbulent flow in an accelerating rectangular elbow designed by means of potential flow theory. Moore and Moore [127] computed this flow for cases with low exit Mach numbers in which spoilers were used to thicken the incoming endwall boundary layers. Figure 15

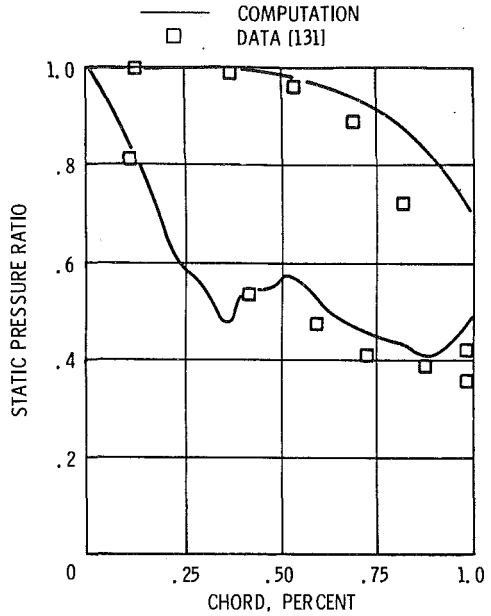

Fig. 17 Calculated and measured static pressures for turbine stator hub section—after Dodge [125]

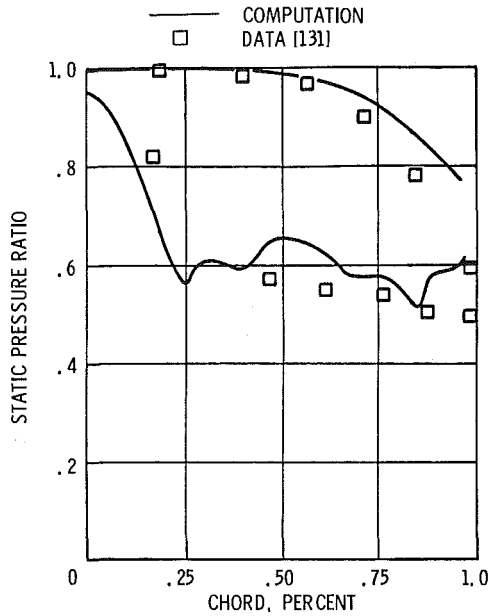

Fig. 18 Calculated and measured static pressures for turbine stator tip section—after Dodge [125]

shows computed and measured wall static pressure on four cross sections located upstream, inside, and downstream of the bend. Figure 16 shows computed and measured total pressure loss contours at the exit plane downstream of the bend.

Dodge [125] has computed 3D turbulent flow through a highly-loaded low-solidity high-aspect-ratio turbine stator. His results are compared to the measurements of Waterman [131]. Figures 17 and 18 show computed and measured static pressures for the hub and tip blade sections, respectively.

Elliptic Methods

All methods in this category are capable of computing separated flows. Those which solve the compressible equations in conservation-law form also have shock-capturing capability. This is not generally available in the parabolic methods. In the absence of separation or shock waves, the elliptic methods may or may not be more accurate than the parabolic ones. If the elliptic method requires locally first-order upwind differencing for stability or a coarse grid because of storage limitations, it may suffer in comparison. Most of the methods now in use for internal flows are adaptions of techniques discussed here. However, other methods, especially those now under development for external aerodynamic applications, will undoubtedly be adapted for internal flows in the near future.

Methods for Steady Equations. A popular method introduced by Caretto et al. [132] is based on that of Patankar and Spalding [109]. The method uses the so-called SIMPLE algorithm for Semi Implicit Method for Pressure Linked Equations. The steady momentum equations, with an assumed pressure field, are solved for provisional values of the velocities. An approximate velocity-pressure correction relation is then combined with continuity to give a 3D equation for pressure. The corrected pressure field, underrelaxed for stability, is substituted into the momentum equations to continue the process. Many variants of this method have been studied by Raithby and Schneider [133]. They found that reintroduction of the time derivatives into the momentum equations, with implicit time differencing and a local time step proportional to volume, increased the convergence rate of the algorithm.

A different procedure has been used by Walitt et al. [134]. The 3D steady equations are transformed to a 2D unsteady system by treating one direction as time-like and evaluating derivatives in this direction from a previous solution. The equations are solved by marching in the time-like direction. After one sweep, the time-like direction is switched and the equations are marched in this new direction. Since an explicit procedure is used on each cross-plane, very small marching steps are required to assure stability. This method has been applied to a centrifugal impeller [134] and to flow in a supersonic compressor cascade with splitter vanes [135].

Methods for Unsteady Equations. The methods for the unsteady viscous equations are closely related to explicit and implicit time marching methods for the Euler equations. In an explicit technique all spatial derivatives are evaluated at a previous time. The solution procedure is unchanged by the addition of viscous terms. The boundary conditions on the velocity are changed to enforce no-slip at solid walls. The close mesh spacing, necessary to resolve the boundary layers, imposes severe time step restrictions to maintain numerical stability (CFL limit). Bosman and Highton [136] have developed an explicit viscous method closely related to their Euler method [79]. The application was to 3D subsonic flow in rotating machinery. Shang et al. [137] have implemented a 3D version of MacCormack's explicit predictor-corrector scheme [71] on a vector computer. The application here was to supersonic shocked flow in a rectangular wind tunnel. Spradley et al. [38] have also implemented a 3D explicit method on a vector computer. The time updating is similar to the MacCormack scheme, but the spatial discretization used the general interpolants method (GIM), [139]. The application was to supersonic flow in an exhaust nozzle.

In an implicit technique, the nonlinear spatial derivatives are linearized about the previous time, and backward differencing is used on the time derivative. The resulting linear system is modified by the addition of the viscous terms. However, for central differencing of both inviscid and viscous terms, the matrix structure remains the same as for the Euler equations. These implicit techniques permit high resolution of the viscous layers without severe time-step restrictions. Briley and McDonald [92, 93] and Beam and Warming [94] have developed similar implicit techniques which were described earlier. Briley and McDonald have concentrated on viscous

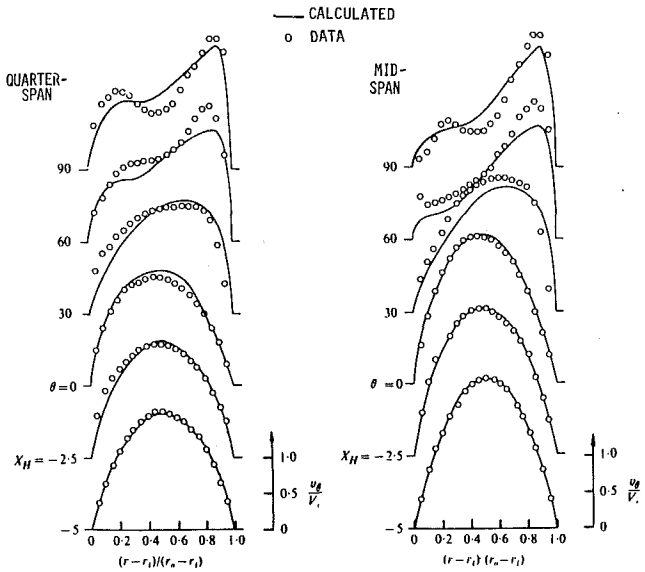

Fig. 19 Calculated and measured profiles at quarter-span and mid-span around curved rectangular duct—after Humphrey [142]

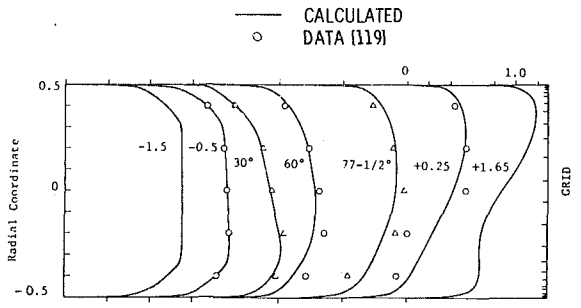

Fig. 20 Computed and measured axial velocity profiles along symmetry plane of curved square duct—after Buggeln [144]

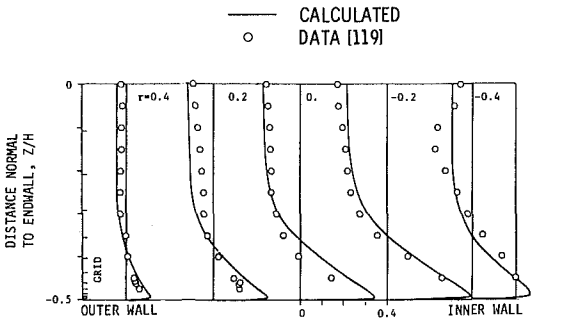

Fig. 21 Computed and measured radial flow velocity profiles after 77.5 deg turning in circular arc square duct—after Buggeln [144]

flows from the outset. Steger [96] has implemented the Beam and Warming procedure in a 2D curvilinear-coordinate, viscous code, which is applicable to a broad range of flow conditions including those in turbomachinery. In this "thin layer" approximation, Steger drops the streamwise viscous diffusion terms.

Ghia et al. [140] have developed a semi-elliptic implicit method for 2D incompressible flow. They first present a fully elliptic method that solves the complete momentum equations together with a Poisson equation for the pressure. Continuity is enforced by driving one of the source terms in the Poisson equation to zero in the manner of Harlow and Welch [115]. The semi-elliptic method is obtained by dropping the streamwise viscous diffusion terms. This permits a simpler solution procedure for the momentum equations.

Approximation by Algebraic System. All but one of the elliptic methods use finite difference techniques to approximate the differential equations by an algebraic system. Spradley et al. [138] use the GIM formulation which is similar to the finite volume approaches discussed earlier. The dependent variables are represented by interpolating functions over the interior of local mesh volumes, and an algebraic system is obtained from weighted integrals of the differential equation over each mesh volume. Only Caretto et al. [132] use the staggered grid of Patankar and Spalding [108]. Bosman and Highton [136] employ the staggered arrangement used in their Euler method [79]. All the other methods store the dependent variables at common grid locations. The hybrid central-upwind differencing used by Patankar and Spalding has also been used by Caretto et al. [132] and Briley and McDonald [93]. Ghia et al. [140] have used upwind differencing of the streamwise convective term everywhere in the flow field.

Solution of Algebraic System. The algebraic solution techniques have been discussed earlier, either for the Euler methods or the parabolic methods. The explicit time marching procedures as well as the explicit spatial marching method of Walitt et al. [134] use local update schemes somewhat akin to point Jacobi relaxation. Values at the new time depend only on a few values at the previous time. This is a slowly converging process, but it is easily coded and vectorized. All the implicit time marching procedures as well as the steady method of Caretto et al. [132] use ADI techniques to solve the momentum equations. These techniques can be fast, especially if the time-step is permitted to vary both in time and space, see e.g. McDonald and Briley [141]. Finally, for completeness, we note that the elliptic pressure equation has been solved by ADI, Caretto et al. [132], and by point SOR, Ghia et al. [140].

Application of Elliptic Methods. To illustrate the state-of-the-art for elliptic methods in internal viscous flows, we present results from three of the analyses discussed above. The actual range of applications of the methods is too broad to be covered here.

Humphrey et al. [142] have computed laminar flow in a square turning duct using a method based on that of Caretto et al. [132]. Results were compared with LDV measurements by the same authors. Figure 19 compares calculated and measured (circles) streamwise velocity profiles at quarter (up from end wall) span and mid-span for several cross-sections progressing from five hydraulic diameters upstream to completion of the 90 deg bend. The disagreement at the last three stations may be due to inadequate grid resolution (10 × 15) over the cross-section. A similar computation and comparison with data for turbulent flow in the same duct is presented in reference [143].

Buggeln et al. [144] have used the method of Briley and McDonald [93] to compute both laminar and turbulent flow in curved ducts, channels and pipes. We present comparisons with the data of Taylor et al. [119] for the same turbulent flow case computed by Kreskovsky et al. [118] with the parabolic method of [112]. Figure 20 shows comparisons for streamwise velocity profiles at the symmetry plane for several stations upstream of, around, and downstream of the bend. Figure 21 shows comparisons for several radial velocity profiles at the 77.5 deg station. Comparing Fig. 21 with Fig. 14 shows considerable agreement between the two methods.

Finaly, Ghia et al. [140] have computed 2D laminar flow in a channel with a large constriction using both their fully elliptic and semi-elliptic methods. Figure 22 shows computed streamline contours for a case with a large separation zone on the downstream side of the constriction. The upper part of the

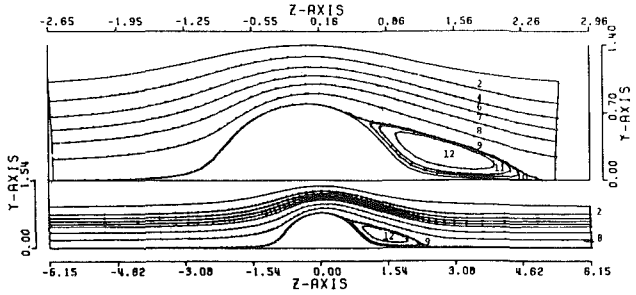

Fig. 22 Computed streamline contours for channel with constriction Re = 100—after Ghia [140]

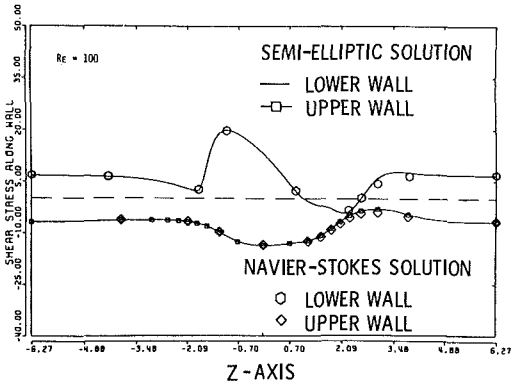

Fig. 23 Comparison of semi-elliptic and elliptic computations for wall shear—after Ghia [140]

figure shows an enlargement of the central portion of the full channel shown below. Figure 23 shows computed results of both methods for wall shear. The agreement between methods is excellent in the separated region on the lower wall.

In general these methods all perform quite well. The disagreement with experiment where it exists is probably due to inadequate grid resolution. However, much work remains to be done to determine the numerical accuracy of all these methods.

Turbulence Modeling

The recently completed AFOSR-HTTM-Stanford Conference on Complex Turbulent Flows was organized for the purpose of providing an assessment of the state-of-the-art in turbulent flow prediction, especially that of turbulence modeling. A wide range of test flows with reliable experimental data was assembled and computational groups were invited to submit computed results for these flows to the Conference. The comparisons of these results with the data together with the findings of the Evaluation Committee will be presented in reference [8].

The current focus in turbulent modeling seems to have shifted from the one and two equation eddy viscosity models of a few years ago to methods which predict the Reynolds stresses themselves. Many results obtained with these models were presented at the Conference. However, while the promise of these models is considerable, at the present they show little or no advantage over the simpler treatments. This is especially true for separated flows.

The results of any turbulent flow prediction depend at least as much on the numerical technique as they do on the turbulence model. For most of the flows included in the conference, it was not possible to separate the limitations of the numerics from those of the turbulence models. Grid refinement studies were presented in only a few cases and many of these were inadequate.

In many internal flows, and especially in those through turbomachinery components, as a result of the rapid turning of the fluid, the evolution of the flow is dominated by the balance between strong pressure gradients and centrifugal forces. Turbulent mixing, though present, plays a lesser role. Indeed the development of complex secondary flows in these components, while dependent on the presence of shear layers due to upstream viscous effects, is an essentialy inviscid phenomenon. Hence, if one can develop a sufficiently accurate and efficient numerical technique for solving the partial differential equations of fluid dynamics, good predictions of such flows should be possible even with a realtively simple turbulence model. This view is supported by the observations of Humphrey et al. [143] in their studies of turbulent flow in turning ducts.

Concluding Remarks

The current status of potential flow methods for turbomachinery is quite advanced. A large number of codes have been developed for analyzing two-dimensional transonic flow with shocks on blade-to-blade surfaces. While an order of magnitude speed up in computing time may be possible with the latest procedures, many of these codes run fast enough for routine use by designers. In addition, at least three codes can compute three-dimensional potential flow in rotors. One of these has demonstrated transonic shock-capturing ability. Most of the stream function codes for turbomachinery applications are based on classical relaxation or matrix inversion techniques. They solve for subcritical flow on blade-to-blade or hub-to-shroud surfaces. Recently, however, a transonic stream function method has been developed and one application to a cascade is under development. In the case of the primitive variable Euler equations a larger number of codes have been developed for turbomachinery applications. Most of these solve for two-dimensional, blade-to-blade flow with shocks. There are, in addition, at least three codes which analyze three-dimensional shocked flows in rotors. With few exceptions, however, these codes utilize older long-running numerical algorithms. Since solution of the Euler equations is now one of the most active areas of research in computational fluid mechanics and since a number of promising new methods are under development, this situation should be much improved in a few years.

The state-of-the-art for viscous methods is much less developed than for inviscid ones. A few single-pass parabolic marching codes have been developed for three-dimensional flows in ducts and turning passages. These methods are relatively fast and fairly accurate in the absence of strong secondary flows. When strong secondary flows are present at high Reynolds numbers, either excessive grid or implicit numerical dissipation may be needed to maintain stability in inviscid regions of the flow. A few multi-pass partially parabolic codes have been developed for three-dimensional flows in turning passages and at least two of these have been applied to turbomachinery rotors. In these methods the pressure field is treated as elliptic and is updated as the computation proceeds. Much work remains to be done to speed up these methods and to extend the pressure correction techniques into the transonic regime. A number of codes have been developed which solve the full time-averaged Navier-Stokes equations in either two or three dimensions, in both ducts and turbomachinery, for both subsonic and transonic flow. The comments on accuracy and computational efficiency which were made for the Euler equation methods are equally valid here except that the computer times are even longer. It is likely that the status of Navier-Stokes codes will be improved substantially with the advent of new improved Euler solvers since most regions of viscous flows are dominated by inviscid effects. Finally, although it is not true that turbulence models are becoming much more accurate, in many flows in turning passages and turbomachinery the velocity field is determined primarily by the balance between

centrifugal forces and pressure gradients and the effects of turbulence are relatively weak. Hence, if one has a sufficiently accurate numerical procedure, one can hope to adequately compute such flows even with a relativley simple turbulence model.

References

1 Gostelow, J. P., "Review of Compressible Flow Theories for Airfoil Cascades," ASME *Journal of Engineering for Power*, Oct. 1973, pp. 281–292.

2 Horlock, J. H., and Lakshminarayana, B., "Secondary Flows: Theory, Experiment, and Application in Turbomachinery Aerodynamics," *Annual Review of Fluid Mechanics*, Vol. 5, 1973, pp. 247–280.

3 Perkins, H. J., and Horlock, J. H., "Computation of Flows in Turbomachines," *Finite Elements in Fluids*, Vol. 2, Gallagher, et al., eds., John Wiley, 1975, pp. 141–157.

4 Japikse, D., "REVIEW—Progress in Numerical Turbomachinery Analysis," ASME JOURNAL OF FLUIDS ENGINEERING, Dec. 1976, pp. 592–606.

5 Habashi, W. G., "Numerical Methods of Turbomachinery," *Recent Advances in Numerical Methods in Fluids*, Vol. 1, Pineridge Press, Ltd., 1980, pp. 245–287.

6 Adler, D., "Status of Centrifugal Impeller Internal Aerodynamics, Part I: Inviscid Flow Prediction Methods," ASME *Journal of Engineering for Power*, July 1980, pp. 728–737; Part II: Experiments and Influence of Viscosity," ASME *Journal of Engineering for Power*, July 1980, pp. 738–746.

7 Scholz, N., "Aerodynamics of Cascades," AGARD-AG-220-1977.

8 Kline, S. J., Cantwell, B. J., and Ferziger, J. H., "Proceedings of the 1980–81 AFOSR-HTTM-Stanford Conference on Complex Turbulent Flows: Comparison of Computation and Experiment," Stanford University Press (to be published), 1982.

9 Thompson, J. F., Warsi, Z. U. A., and Mastin, C. W., "Boundary Fitted Coordinate Systems for Numerical Solution of Partial Differential Equations—A Review," *Journal of Computational Physics*, Vol. 47, 1982, pp. 1–108.

10 Thompson, J. F., "A Survey of Grid Generation Techniques in Computational Fluid Dynamics," AIAA Paper 83-0447, 1983.

11 Thompson, J. F. ed., *Numerical Grid Generation*, North-Holland Publishers, New York, 1982.

12 Hafez, M., and Lovell, D., "Numerical Solution of Transonic Stream Function Equation," AIAA Paper 81-1017, AIAA Computational Fluid Dynamics Conference, Palo Alto, 1981.

13 Murman, E. M., and Cole, J. D., "Calculation of Plane, Steady Transonic Flows," *AIAA Journal*, Vol. 9, 1971, p. 114.

14 Jameson, A., "Iterative Solution of Transonic Flows Over Airfoils and Wings Including Flows at Mach 1," *Communications of Pure and Applied Math*, Vol. 27, 1974, pp. 283–304.

15 Hafez, M., South, J., and Murman, E., "Artificial Compressibility Methods for Numerical Solution of Transonic Full Potential Equations," *AIAA Journal*, Vol. 17, 1979, p. 838.

16 Jameson, A., "Transonic Potential Flow Calculations in Conservation Form," *Proceedings AIAA Second Computational Fluid Dynamics Conference*, Hartford, Conn., 1975, p. 148.

17 Dodge, P. R., "A Non-Orthogonal Numerical Method for Solving Transonic Cascade Flows," ASME Paper 76-GT-63, 1976.

18 Ives, D. C., and Liutermoza, J. F., "Second-Order Accurate Calculation of Transonic Flow Over Turbomachinery Cascades," *AIAA Journal*, Vol. 17, 1978, p. 870; also AIAA Paper 78-1149.

19 Ives, D. C., and Liutermoza, J. F., "Analysis of Transonic Cascade Flow Using Conformal Mapping and Relaxation Techniques," AIAA Paper 76-370, AIAA Ninth Fluid and Plasma Dynamics Conference, San Diego, 1976.

20 Rae, W. J., and Homicz, G. F., "A Rectangular-Coordinate Method for Calculating Nonlinear Transonic Potential Flow Fields in Compressor Cascades," AIAA Paper 78-248, AIAA Sixteenth Aerospace Sciences Meeting, Huntsville, Ala., 1978.

21 Caspar, J. R., "Unconditionally Stable Calculation of Transonic Potential Flow Through Cascades Using An Adaptive Mesh for Shock Capture," ASME Paper 82-GT-238, 1982.

22 Caspar, J. R., Hobbs, D. E., and Davis, R. L., "The Calculation of Two-Dimensional Compressible Potential Flow in Cascades Using Finite Area Techniques," AIAA Paper 79-0077, 17th Aerospace Sciences Meeting, New Orleans, La., 1979.

23 Caughey, D. A., and Jameson, A., "Numerical Calculation of Transonic Potential Flow About Wing-Body Combinations," *AIAA Journal*, Vol. 17, No. 2, p. 175, 1979; also AIAA Paper 77-677.

24 Dulikravich, D. S., "Numerical Calculation of Transonic Axial Turbomachinery Flows," *Proceedings of Seventh International Conference on Numerical Methods in Fluid Dynamics*, Stanford, Calif., 1980, p. 164.

25 Dulikravich, D. S., and Caughey, D. A., "Finite Volume Calculation of Transonic Potential Flow Through Rotors and Fans," FDA-80-03 Report, Cornell University, Mar. 1980.

26 Farrell, C. A., and Adamczyk, J. J., "Full Potential Solution of Transonic Quasi-3-Dimensional Flow Through A Cascade Using Artificial Compressibility," ASME Paper 81-GT-70, ASME Gas Turbine Conference, Houston, Texas, Mar. 1981.

27 Fruhauf, H. H., "Numerical Computation of Compressible Cascade Flows," *Fifth International Symposium on Airbreathing Engines*, Bangalore, India, Feb. 1981.

28 Laskaris, T. E., "Finite-Element Analysis of Compressible and Incompressible Viscous Flow and Heat Transfer Problems," *The Physics of Fluids*, Vol. 18, 1975, p. 1639.

29 Laskaris, T. E., "Finite-Element Analysis of 3-Dimensional Potential Flow in Turbomachines," *AIAA Journal*, Vol. 16, 1978, p. 717.

30 Akay, H. U., and Ecer, A., "Transonic Flow Computations in Cascades Using Finite Element Method," ASME Paper 81-GT-4, ASME International Gas Turbine Conference, Houston, Texas, 1981.

31 Ecer, A., and Akay, H. U., "Investigation of Transonic Flow in a Cascade Using An Adaptive Mesh," AIAA Paper 80-1430, AIAA 13th Fluid and Plasma Dynamics Conference, Snowmass, Colo., 1980.

32 Deconinck, H., and Hirsch, C., "Finite Element Methods for Transonic Blade-to-Blade Calculation in Turbomachines," ASME Paper 81-GT-5, ASME International Gas Turbine Conference, Houston, Texas, 1981.

33 Holst, T. L., "Implicit Algorithm for Conservative Transonic Full Potential Equation Using An Arbitrary Mesh," *AIAA Journal*, Vol. 17, 1979, p. 1038.

34 Holst, T. L., and Ballhaus, W. F., "Conservative Implicit Schemes for the Full Potential Equation Applied to Transonic Flows," *AIAA Journal*, Vol. 17, 1979, p. 145.

35 South, J. C., and Brandt, A., "Application of a Multi-Level Grid Method to Transonic Flow Calculations," *Transonic Flow Problems in Turbomachinery*, Adamson, T. C. and Platzer, M. F., Ed., Hemisphere Publishers, Washington, 1977, pp. 180–207.

36 Jameson, A., "A Multi-Grid Scheme for Transonic Potential Calculations on Arbitrary Grids," *Proceedings of AIAA Fourth Computational Fluid Dynamics Conference*, Williamsburg, Va., 1979, p. 122.

37 Brandt, A., "Multi-Level Adaptive Grid Technique (MLAT) for Fast Numerical Solution to Boundary Value Problems," *Proceedings of Third International Conference on Numerical Methods and Fluid Mechanics*, Paris, France, 1972, p. 82.

38 Bauer, F., Garabedian, P., Korn, D., and Jameson, A., "Supercritical Wing Sections II," *Lecture Notes in Economics and Mathematical Systems*, Vol. 108, Springer-Verlag, New York, 1975.

39 Dulikravich, D. S., "CAS30—FORTRAN Program for Analysis of 3D, Steady, Transonic, Potential, Axial Turbomachinery Flows Using O-Type Grids," to be published as NASA CR, 1983.

40 Wu, C. H., "A General Theory of Three-Dimensional Flow In Subsonic and Supersonic Turbomachines of Axial, Radial and Mixed-Flow Types," NASA TN 2604, 1952.

41 Katsanis, T., "FORTRAN Program for Calculating Transonic Velocities on a Blade-to-Blade Stream Surface of a Turbomachine," NASA TN D-5427, 1969.

42 Wood, J. R., "Improved Method for Calculating Transonic Velocities on Blade-to-Blade Stream Surfaces of a Turbomachine," NASA Technical Paper 1772, 1981.

43 Katsanis, T., and McNally, W. D., "FORTRAN Program for Calculating Velocities and Stream Lines on a Blade-to-Blade Stream Surface of a Tandem Blade Turbomachine," NASA TN D-5044, 1969.

44 Katsanis, T., and McNally, W. D., "FORTRAN Program for Calculating Velocities in a Magnified Region on a Blade-to-Blade Stream Surface of a Turbomachine," NASA TN D-5091, 1969.

45 Marsh, H., "A Digital Computer Program for the Through-Flow Fluid Mechanics in an Arbitrary Turbomachine Using a Matrix Method," Aeronautical Research Council R&M 3509, 1968.

46 Smith, D. J. L., and Barnes, J. F., "Calculation of Fluid Motion in Axial Flow Turbomachines," ASME Paper 68-GT-12, 1968.

47 Smith, D. J. L., and Frost, D. H., "Calculation of the Flow Past Turbomachine Blades," *Proceedings of the Institution of Mechanical Engineers*, Vol. 184, 1970, p. 72.

48 Smith, D. J. L., "Computer Solutions of Wu's Equations for the Compressible Flow Through Turbomachines," Fluid Mechanics, Acoustics, and Design of Turbomachinery, Part I, NASA SP-304, 1974.

49 Davis, W. R., and Millar, D. A. J., "A Discussion of the Marsh Matrix Technique Applied to Fluid Flow Problems," *Canadian Aeronautics and Space Journal*, Vol. 5, 1972, p. 64.

50 Davis, W. R., and Millar, D. A. J., "A Matrix Method Applied to the Analysis of the Flow Past Turbomachine Blades," Carleton University Report ME/A72-7, 1972.

51 Davis, W. R., and Millar, D. A. J., "Axial Flow Compressor Analysis Using a Matrix Method," Carleton University Report ME/A73-1, 1973.

52 Davis, W. R., and Millar, D. A. J., "A Comparison of the Matrix and Stream Line Curvature Methods of Axial Flow Turbomachinery Analysis, from a User's Point of View," ASME Paper 74-WA/GT-4, ASME *Journal of Engineering for Power*, 1974.

53 Davis, W. R., "A General Finite Difference Technique for the Compressible Flow in the Meridional Plane of Centrifugal Turbomachinery," ASME Paper 75-GT-121, 1975.

54 Head, M. R., "Entrainment in the Turbulent Boundary Layer," Aeronautical Research Council R&M 3152, 1958.

55 Katsanis, T., and McNally, W. D., "Quasi-3-Dimensional Flow Solution by Meridional Plane Analysis," SAE Paper 740850, 1974.

56 Katsanis, T., and McNally, W. D., "Revised FORTRAN Program for Calculating Velocities and Streamlines on the Hub-Shroud Midchannel Stream

Surface of an Axial, Radial, or Mixed-Flow Turbomachine or Annular Duct, I—User's Manual," NASA TN D-8430, 1977.

57 Katsanis, T., and McNally, W. D., "Revised FORTRAN Program for Calculating Velocities and Streamlines on the Hub-Shroud Midchannel Stream Surface of Axial, Radial, or Mixed-Flow Turbomachine or Annular Duct, II—Programmer's Manual," NASA TN D-8431, 1977.

58 Marsh, H., "Through-Flow Calculation in Axial Turbomachinery: A Technical Point of View," AGARD Propulsion and Energetics Panel, 47th Meeting, Paper Number 2, 1976.

59 Bosman, C., and El-Shaarawi, M. A. I., "Quasi-3-Dimensional Numerical Solution of Flow in Turbomachines," ASME Paper 76-FE-23, 1976.

60 Adler, D., and Krimerman, Y., "The Complete 3-Dimensional Calculation of the Compressible Flow Field in Turbo Impellers," *Journal of Mechanical Engineering Science*, Vol. 20, 1978, p. 149.

61 Adler, D., and Krimerman, Y., "The Numerical Calculation of the Meridional Flow Field in Turbomachines Using the Finite Element Method," *Israel Journal of Technology*, Vol. 12, No. 3/4, 1974.

62 Adler, D., and Krimerman, Y., "The Numerical Calculation of the Blade-to-Blade Flow Field in Turbo Impellers Using the Finite Element Method," *Journal of Mechanical Engineering Sciences*, Vol. 19, 1977, p. 108.

63 Hirsch, C., and Warzee, G., "A Finite Element Method for Through-Flow Calculation in Turbomachines," ASME Paper 76-FE-12, 1976.

64 Hirsch, C., and Warzee, G., "An Integrated Quasi-3-D Finite Element Calculation Program for Turbomachinery Flows," ASME *Journal of Engineering for Power*, Vol. 101, 1979, p. 141.

65 Dunker, R. J., Strinning, P. E., and Weyer, H. B., "Experimental Study of the Flow Field within a Transonic Axial Compressor Rotor by Laser Velocimetry and Comparison with Through-Flow Calculation," ASME Paper 77-GT-28, 1977.

66 Hirsch, C., and Warzee, G., "Quasi-3-D Finite Element Computation of Flows in Centrifugal Compressors," *Symposium on Performance Prediction of Centrifugal Pumps in Compressors*, p. 69, ASME 25th International Gas Turbine Conference, New Orleans, La., Mar. 1980.

67 Eckardt, D., "Detailed Flow Investigations within a High-Speed Centrifugal Compressor Impeller," ASME Paper 76-FE-13, ASME JOURNAL OF FLUIDS ENGINEERING, Vol. 98, 1976, p. 390.

68 Mizuki, S., Ariga, I., and Watanabe, I., "Investigation Concerning the Blade Loading of Centrifugal Impellers," ASME Paper 74-GT-143, 1974.

69 Goulas, A., "A Blade-to-Blade Solution of the Flow in a Centrifugal Compressor Impeller with Splitters," ASME *Journal of Engineering for Power*, Vol. 102, 1980, p. 632.

70 McNally, W. D., "FORTRAN Program for Generating a Two-Dimensional Orthogonal Mesh Between Arbitrary Boundaries," NASA TN D-6766, 1972.

71 MacCormack, R. W., "The Effect of Viscosity in Hypervelocity Impact Cratering," AIAA Paper 69-345, 1969.

72 Gopalakrishnan, S., and Bozzola, R., "Computation of Shocked Flows in Compressor Cascades," AIAA Paper 72-GT-31, 1972.

73 Kurzrock, J. W., and Novick, A. S., "Transonic Flow Around Rotor Blade Elements," ASME JOURNAL OF FLUIDS ENGINEERING, Vol. 97, 1975, p. 598.

74 Thompkins, W. T., "A FORTRAN Program for Calculating Three-Dimensional, Inviscid, Rotational Flows with Shock Waves in Axial Compressor Blade Rows. I-User's Manual," NASA CR 3560, 1982.

75 McDonald, P. W., "The Computation of Transonic Flow Through Two-Dimensional Gas Turbine Cascades," ASME Paper 71-GT-89, 1971.

76 Denton, J. D., "A Time Marching Method for Two- and Three-Dimensional Blade-to-Blade Flow," Aeronautical Research Council R&M 3775, 1975.

77 Denton, J. D., "Extension of the Finite Area Time Marching Method to Three Dimensions," *VKI Lecture Series*, Vol. 84, 1976.

78 Denton, J. D., and Singh, U. K., "Time Marching Methods for Turbomachinery Flow Calculation. Part I Basic Principles and 2D Applications, and Part II Three-Dimensional Flows," *VKI Lecture Series*, 1979-7, 1979.

79 Bosman, C., and Highton, J., "A Calculation Procedure for Three-Dimensional, Time-Dependent, Inviscid, Compressible Flow Through Turbomachine Blades of Any Geometry," *Journal of Mechanical Engineering Science*, Vol. 21, 1979, p. 39.

80 Bosman, C., "An Analysis of Three-Dimensional Flow in a Centrifugal Compressor Impeller," ASME *Journal of Engineering for Power*, Vol. 102, 1980, p. 619.

81 Moretti, G., "The λ-Scheme," *Computers and Fluids*, Vol. 7, 1979, p. 191.

82 De Neef, T., and Moretti, G., "Shock Fitting for Everybody," *Computers and Fluids*, Vol. 8, 1980, p. 327.

83 Pandolfi, M., and Zannetti, L., "A Physical Approach to Solve Numerically Complicated Hyperbolic Flow Problems," *Proceedigns of Seventh International Conference on Numerical Methods in Fluid Mechanics*, Palo Alto, Springer-Verlag, 1980.

84 Chakravarthy, S. R., Anderson, D. A., and Salas, M. D., "The Split-Coefficient Matrix Method for Hyperbolic Systems of Gas Dynamic Equations," AIAA Paper 80-0268, AIAA 18th Aerospace Sciences Meeting, Pasadena, 1980.

85 Ni, R. H., "A Multiple Grid Scheme for Solving the Euler Equations," AIAA 5th Computational Fluid Dynamics Conference, Palo Alto, AIAA Paper 81-1025, 1981.

86 Richtmyer, R. D., and Morton, K. W., *Difference Methods for Initial Value Problems*, 2nd Edition, Interscience Publishers, New York, 1967.

87 Essers, J. A., and Kafyeke, F., "Application of Fast Pseudo-Unsteady Method to Steady Transonic Flows in Turbine Cascades," ASME Paper 81-GT-124, 1981.

88 Viviand, H., and Veuillot, J. P., "Methodes Pseudo-Instation-Naires Pour Le Calcul D'Ecoulements Transsoniques," ONERA Publication 1978-4, English Translation ESA.TT.561, 1978.

89 Veuillot, J. P., and Viviand, H., "A Pseudo-Unsteady Method for the Computation of Transonic Potential Flows," *AIAA Journal*, Vol. 17, No. 7, July 1979.

90 Brochet, J., "Numerical Computation of Three-Dimensional Transonic Internal Flows," Rech. Aerosp. Number 1980-5, 1980.

91 Enselme, M., Brochet, J., and Boisseau, J. P., "Low Cost Three-Dimensional Flow Computations Using a Mini-System," AIAA 5th Computational Fluid Dynamics Conference, Palo Alto, AIAA Paper 81-1013, 1981.

92 Briley, W. R., and McDonald, H., "Solution of the Three-Dimensional Compressible Navier-Stokes Equations By An Implicit Techniques," *Proceedings 4th International Conference on Numerical Methods In Fluid Dynamcis*, Boulder, Springer-Verlag, 1975, p. 105.

93 Briley, W. R., and McDonald, H., "Solution of the Multidimensional Compressible Navier-Stokes Equations by a Generalized Implicit Method," *Journal of Computational Physics*, Vol. 24, 1977, p. 372.

94 Beam, R. M., and Warming, R. F., "An Implicit Finite-Difference Algorithm for Hyperbolic Systems in Conservation-Law Form," *Journal of Computational Physics*, Vol. 22, 1976, p. 87.

95 Briley, W. R., and McDonald, H., "On the Structure and Use of Linearized Block Implicit Schemes," *Journal of Computational Physics*, Vol. 34, 1980, p. 54.

96 Steger, J. L., "Implicit Finite-Difference Simulation of Flow About Arbitrary Two-Dimensional Geometries," *AIAA Journal*, Vol. 16, 1978, p. 679.

97 Steger, J. L., Pulliam, T. H., and Chima, R. V., "An Implicit Finite Difference Code for Inviscid and Viscous Cascade Flow," AIAA Paper 80-1427, AIAA 13th Fluid and Plasma Dynamics Conference, Snowmass, 1980.

98 Shamroth, S., Gibeling, H. J., and McDonald, H., "A Navier-Stokes Solution for Laminar and Turbulent Flow Through a Cascade of Airfoils," AIAA Paper 80-1426, AIAA 13th Fluid and Plasma Dynamics Conference, Snowmass, 1980.

99 Delaney, R. A., "Time-Marching Analysis of Steady Transonic Flow in Turbomachinery Cascades Using the Hopscotch Method," ASME Paper 82-GT-152, 1982.

100 Denton, J. D., "An Improved Time-Marching Method for Turbomachinery Flow Calculation," ASME Paper 82-GT-239, 1982.

101 Johnson, G. M., "Relaxation Solution of the Full Euler Equations," *Proceedings of the Eighth International Conference on Numerical Methods in Fluid Dynamics*, Aachen, Germany, 1982.

102 Ecer, A., and Akay, H. U., "Solution of Steady Euler Equations for Flows Using a Variational Finite Element Formulation," Open Forum, AIAA 5th Computational Fluid Dynamics Conference, Palo Alto, 1981.

103 Lacor, C., and Hirsch, C., "Rotational Flow Calculations In Three-Dimensional Blade Passages," ASME Paper 82-GT-316, 1982.

104 Chang, S. C., and Adamczyk, J. J., "A Semi-Direct Algorithm for Computing 3-D Inviscid Shear Flows," AIAA 5th Computational Fluid Dynamics Conference, Palo Alto, 1981.

105 Chima, R. V., and Strazisar, A. J., "Comparison of Two- and Three-Dimensional Flow Computations with Laser Anemometer Measurements in a Transonic Compressor Rotor," NASA TP 1931, 1982.

106 Sieverding, C. H., "Experimental Data on Two Transonic Turbine Blade Sections in Comparison with Various Theoretical Methods," von Karman Institute, LS 59, 1973.

107 Caretto, L. S., Curr, R. M., and Spalding, D. B., "Two Numerical Methods for Three-Dimensional Boundary Layers," *Computer Methods in Applied Mechanics and Engineering*, Vol. I, 1972, pp. 39–57.

108 Patankar, S. V., and Spalding, D. B., "A Calculation Procedure for Heat, Mass and Momentum Transfer In Three-Dimensional Parabolic Flows," *International Journal of Heat and Mass Transfer*, Vol. 15, 1972, pp. 1787–1806.

109 Briley, W. R., "Numerical Method for Predicting Three-Dimensional Steady Viscous Flow in Ducts," *Journal of Computational Physics*, Vol. 14, No. 1, 1974, pp. 8–28.

110 Ghia, U., Ghia, K. N., and Studerus, C. J., "Three-Dimensional Laminar Incompressible Flow In Straight Polar Ducts," *Computers and Fluids*, Vol. 5, 1977, pp. 205–218.

111 Roberts, D. W., and Forester, C. K., "Parabolic Procedure for Flows In Ducts with Arbitrary Cross-Sections," *AIAA Journal*, Vol. 17, No. 1, 1979, pp. 33–40.

112 Briley, W. R., and McDonald, H., "Analysis and Computation of Viscous Subsonic Primary and Secondary Flows," AIAA Paper 79-1453, July 1979.

113 Anderson, O. L., "Calculation of Internal Viscous Flows in Axisymmetric Ducts at Moderate to High Reynolds Numbers," *Computers and Fluids*, Vol. 8, 1980, pp. 391–411.

114 Anderson, O. L., and Hankins, G. B., Jr., "Development of a Parabolic Finite Difference Method for 3-D High Reynolds Number Viscous Internal Flows," ASME Paper Winter Annual Meeting, Nov. 1981.

115 Harlow, F. H., and Welch, J. E., "Numerical Calculation of Time-Dependent Viscous Incompressible Flow of Fluid with Free Surface," *Physics of Fluids*, Vol. 8, 1965, pp. 2182–2189.

116 Patankar, S. V., Pratap, V. S., and Spalding, D. B., "Prediction of Laminar Flow and Heat Transfer in Helically-Coiled Pipes," *Journal of Fluid Mechanics*, Vol. 62, Part III, 1974, pp. 539–551.

117 Ghia, K. N., and Sokhey, J. S., "Laminar Incompressible Viscous Flow in Curved Ducts of Regular Cross-Sections," ASME JOURNAL OF FLUIDS ENGINEERING, Vol. 99, 1977, pp. 640–648.

118 Kreskovsky, J. P., Briley, W. R., and McDonald, H., "Prediction of Laminar and Turbulent Primary and Secondary Flows in Strongly Curved Ducts," NASA CR-3388, Feb. 1981.

119 Taylor, A. M. K. P., Whitelaw, J. H., and Yianneskis, M., "Measurements of Laminar and Turbulent Flow in a Curved Duct with Thin Inlet Boundary Layers," NASA CR-3367, Jan. 1981.

120 Baker, A. J., and Orzechowski, J. A., "A Continuity-Constraint Finite Element Algorithm for Three-Dimensional Parabolic Flow Prediction," ASME Paper, Winter Annual Meeting, Nov. 1981.

121 Pratap, V. S., and Spalding, D. B., "Fluid Flow and Heat Transfer and Three-Dimensional Duct Flows," *International Journal of Heat and Mass Transfer*, Vol.19, 1976, pp. 1183–1188.

122 Moore, J., and Moore, J. G., "A Calculation Procedure for Three-Dimensional, Viscous, Compressible Duct Flow. Part I—Inviscid Flow Considerations," ASME Paper 79-WA/FE-4, Dec. 1979.

123 Chilukuri, R., and Pletcher, R. H., "Numerical Solutions to the Partially Parabolized Navier-Stokes Equations for Developing Flow in a Channel," *Numerical Heat Transfer*, Vol. 3, 1980, pp. 169–188.

124 Dodge, P. R., "Numerical Method for 2D and 3D Viscous Flows," *AIAA Journal*, Vol. 15, No. 7, 1977, pp. 961–965.

125 Dodge, P. R., "3-D Heat Transfer Analysis Program," AFAPL-TR-77-64, Oct. 1977.

126 Pratap, V. S., and Spalding, D. B., "Numerical Computations of the Flow In Curved Ducts," *The Aeronautical Quarterly*, Vol. 26, 1975, pp. 219–228.

127 Moore, J., and Moore, J. G., "A Calculation Procedure for Three-Dimensional, Viscous, Compressible Duct Flow. Part II—Stagnation Pressure Losses in a Rectangular Elbow," ASME Paper 79-WA/FE-5, Dec. 1978.

128 Moore, J., and Moore, J. G., "Calculations of Three-Dimensional, Viscous Flow and Wake Development in a Centrifugal Impeller," *Symposium on Performance Prediction of Centrifugal Pumps and Compressors*, ASME 25th International Gas Turbine Conference, New Orleans, 1980.

129 Moore, J., and Moore, J. G., "Three-Dimensional, Viscous Flow Calculations for Assessing the Thermodynamic Performance of Centrifugal Compressors—Study of the Eckardt Compressor," AGARD Conference, Brussels, May 1980.

130 Stanitz, J. D., Osborn, W. M., and Mizisin, J., "An Experimental Investigation of Secondary Flow in An Accelerating Rectangular Elbow with 90° of Turning," NACA TN-3015, Oct. 1953.

131 Waterman, W. F., "Low-Aspect-Ratio Turbine Technology Program Final Report for Phase II," AiResearch Report 75-211701 (2), Mar. 1977.

132 Caretto, L. S., Gosman, A. D., Patankar, S. V., and Spalding, D. B., "Two Calculation Procedures for Steady, Three-Dimensional Flows with Recirculation," Third International Conference on Numerical Methods in Fluid Mechanics,' Paris, 1972, Springer-Verlag, New York,

133 Rathby, G. D., and Schneider, G. E., "Numerical Solution of Problems in Incompressible Fluid Flow: Treatment of the Velocity-Pressure Coupling," *Numerical Heat Transfer*, Vol. 2, 1979, pp. 417–440.

134 Walitt, L., Harp, J. L., Jr., and Liu, C. Y., "Numerical Calculation of the Internal Flow Field in a Centrifugal Compressor Impeller," NASA CR-134984, Dec. 1975.

135 Walitt, L., and Liu, C. Y., "Numerical Calculations of the Viscous Flow In a Supersonic Compressor Cascade with Splitter Vanes," AFAPL-TR-78-2, Feb. 1978.

136 Bosman, C., and Highton, J., "The Computation of Three-Dimensional Viscous, Compressible Flow," *Numerical Methods in Laminar and Turbulent Flow*, Editors Taylor, C., Morgan, K., and Brebbia, C. A., *Proceedings of the International Conference*, University of Swansea, 1978, Halsted Press, John Wiley and Sons.

137 Shang, J. S., Buning, P. G., Hankey, W. L., and Wirth, M. C., "Performance of a Vectorized Three-Dimensional Navier-Stokes Code on the CRAY-1 Comptuer," *AIAA Journal*, Vol. 18, No. 9, 1980, pp. 1073–1079.

138 Spradley, L. W., Stalnaker, J. F., and Ratliff, A. W., "Solution of the Three-Dimensional Navier-Stokes Equations on a Vector Processor," *AIAA Journal*, Vol. 19, No. 10, 1981, pp. 1302–1307.

139 Prozan, R. J., Spradley, L. W., Anderson, P. G., and Pearson, M. L., "The General Interpolants Method," AIAA Paper 77-642, June 1977.

140 Ghia, U., Ghia, K. N., Rubin, S. G., and Khosla, P. K., "Study of Incompressible Flow Separation Using Primitive Variables," *Computers and Fluids*, Vol. 9, 1981, pp. 123–142.

141 McDonald, H., and Briley, W. R., "Computational Fluid Dynamic Aspects of Internal Flows," AIAA Paper 79-1445, July 1979.

142 Humphrey, J. A. C., Taylor, A. M. K., and Whitelaw, J. H., "Laminar Flow In a Square Duct of Strong Curvature," *Journal of Fluid Mechanics*, Vol. 83, Part III, 1977, pp. 509–527.

143 Humphrey, J. A. C., Whitelaw, J. H., and Yee, G., "Turbulent Flow in a Square Duct with Strong Curvature," *Journal of Fluid Mechanics*, Vol. 103, 1981, pp. 443–463.

144 Buggeln, R. C., Briley, W. R., and McDonald, H., "Computation of Laminar and Turbulent Flow in Curved Ducts, Channels, and Pipes Using the Navier-Stokes Equations," ONR Report R80-920006-F, Dec. 1980.

Tah-teh Yang
Professor.

Francois Ntone
Graduate Student.

Tong Jiang
Research Assistant.

Department of Mechanical Engineering,
Clemson University,
Clemson, S.C. 29631

D. R. Pitts
Professor,
Department of Mechanical and
Aerospace Engineering,
University of Tennessee,
Knoxville, Tenn. 37996-2210

An Investigation of High Performance, Short Thrust Augmenting Ejectors

The design of air-to-air, thrust augmenting ejectors having short curved wall diffusers utilizing boundary layer control is discussed. The design is achieved by an inverse method which uses the vorticity at the diffuser inlet as a flow parameter in the analysis. Three diffusers having ejector length-to-mixing chamber diameter ratios of approximately 6:1 and mixing chamber inlet area-to-primary nozzle area ratios of 20:1 and 40:1 were designed and tested. A new high level of performance was analytically predicted and achieved experimentally. Comparisons between predicted and observed performances, velocity distributions and pressure distributions are presented.

Introduction

The use of a jet ejector for augmenting thrust offers solution to some critical problem areas in the design of V/STOL propulsion systems. The benefit of using ejectors, however, is seriously offset by its complexities. The criteria for using such a thrust system are: (*a*) it has to be short enough to satisfy space-limitations, and (*b*) it must provide high thrust augmentation to yield a substantial net gain in a practical application.

There exists a large body of literature on ejectors for thrust augmentation. Among the early efforts are those of Von Karman [1] for theoretical treatment and the experimental studies of Jacobs and Shoemaker [2]. In the recent open literature Fabri and Siestrunck [3] and Addy [4] reported work on supersonic ejectors, Bevilaqua [5, 6] treated entrainment mechanisms and mixing, and Quinn discussed the effects of jet temperature [7] and aeroacoustic interaction [8]. More recently, J. L. Porter and R. A. Squyers [9] published an overview on ejector theory and performance. A comprehensive listing of 1619 references was presented as volume II of their report. In the following discussion, attention will be directed only to previous work related to the current investigation.

Previous exploratory work by the first author [10] had indicated a surprisingly high thrust augmentation to be possible by the use of a highly effective, short, curved-wall diffuser incorporating boundary layer control. A diffuser of this type will be referred to as a Griffith diffuser [11]. A typical Griffith diffuser has a wall velocity distribution exhibiting a high velocity inlet region, slightly accelerating flow up to a narrow slot region and a sudden drop in velocity taking place across the narrow slot region. Downstream of the slot region, there is an exit of the diffuser. The sudden drop of the velocity takes place over the slot where boundary layer control is applied so that no flow separation takes place. Because no adverse pressure gradient is involved along the stationary wall of a Griffith diffuser, the potential flow approximation has been used successfully in the inverse design method for determining the diffuser wall geometry. The analytical formulation and the algorithms for that method are presented in reference [11] and the references cited in reference [11], respectively.

In the study of reference [10], ejectors having diffusers with length-to-diameter ratio (l/D) of 4.9:1 and 6.5:1, and mixing chamber inlet area-to-primary nozzle area ratio (λ) of 150, were tested with steam as the primary flow and ambient air as the entrained flow. The experimentally observed mass ratio of entrained-to-primary fluid appeared to be several times higher than that of conventially designed ejectors. However, lack of data concerning λ for early studies in the literature precludes more precise comparison. The maximum value of thrust augmentation ratio ϕ achieved in reference [10] was 2.81. This did not account for the penalty of boundary layer control and was higher than could be expected if air were to be used as the primary fluid. Nevertheless, these early results together with the compactness of the ejector presented a strong attraction for further study of short diffusers employing boundary layer control.

In 1973 Gilbert and Hill [12] published their two-dimensional ejector analysis and test results. Both compressibility and viscosity were accounted for in their analysis. The pressure gradient across the flow passage throughout the

Contributed by the Fluids Engineering Division and presented at the Winter Annual Meeting, New Orleans, La., December 9–14, 1984 of THE AMERICAN SOCIETY OF MECHANICAL ENGINEERS. Manuscript received by the Fluids Engineering Division, May 12, 1983. Paper No. 84-WA/FE-10.

ejector was neglected. In 1977, Tai [13] of the David W. Taylor Naval Ship R&D Center utilized Gilbert and Hill's analysis up to the exit of the mixing chamber. Then he implemented a diffuser design sub-program based on an argument that the boundary layer can withstand a nearly infinite pressure gradient for a very short distance without separation. Tai referred to his diffuser design criterion as the "incipient separation criterion." At the exit of the mixing chamber, an infinite pressure gradient is imposed. After that, the pressure gradient along the diffuser is so adjusted to satisfy an incipient separation criterion by keeping the wall frictional velocity between 1 to 6 ft/s, according to Tai. Note that larger values lead to longer diffusers which are less desirable. The diffuser geometry is determined through an iterative procedure of adjusting the local pressure gradient to satisfy this range of wall frictional velocity. The boundary condition on the exit of the ejector is satisfied by terminating the computation when the local static pressure reaches the ambient value.

Tai, op. cit., has shown that an optimum thrust augmentation ratio of 1.42:1 may be reached with the diffuser section of the ejector designed with the "incipient stall criterion" and for an overall L/D of 6:1 and $\lambda = 19$. The obvious question is whether or not the use of Griffith-type diffuser sections would significantly improve ejector performance. In 1980, work by the authors of this paper was resumed under sponsorship of the U.S. Navy, David Taylor Naval Ship Research Development Center (DTNSRDC). Specific goals were (*i*) to verify the observed ejector performance of reference [10], and (*ii*) to develop a design procedure for short, efficient ejectors.

In the Ejector Design-Inverse Method presented in the following section, owing to the fact that the Griffith diffuser wall curvature is large, particularly around the suction slot, Gilbert and Hill's program can not be used in analyzing the flow within the Griffith diffuser. On the other hand, because of no deceleration along the solid wall portion of the diffuser, the inviscid flow approximation should be acceptable. Segment-wide the Bernoulli equation is applicable along each streamline where dissipation is not severe. This is the case both in the nozzle and along the diffuser wall. The design method outlined in the next section is somewhat cumbersome. A more elegant analytical method, however, would require the inverse solution of the Navier-Stokes equations. Such a solution is not currently available.

Ejector Design—Inverse Method

Figure 1 shows the major steps in analyzing an axisymmetrical ejector with a short, curved-wall diffuser. The mixing chamber is shaped like a circular pipe and may have a contraction toward the end of the mixing chamber. To initiate the analysis, the area ratio of the primary nozzle to the mixing chamber inlet and the ratio of the mixing chamber length to its diameter (l/D) are specified. The diffuser length usually is restricted to about one exit diameter of the diffuser. In addition, the static pressure at the mixing chamber inlet and stagnation pressure of the primary air are also specified. Both the entrained secondary flow from the stagnant ambient and the primary flow within the nozzle are isentropic up to the mixing chamber inlet. Analytically, specification of the static pressure at the mixing chamber inlet in fact implies that the ratio of the secondary mass flow to the primary mass flow is defined. Starting from the inlet, there are heat and momentum transfer between the primary flow and the entrained secondary flow.

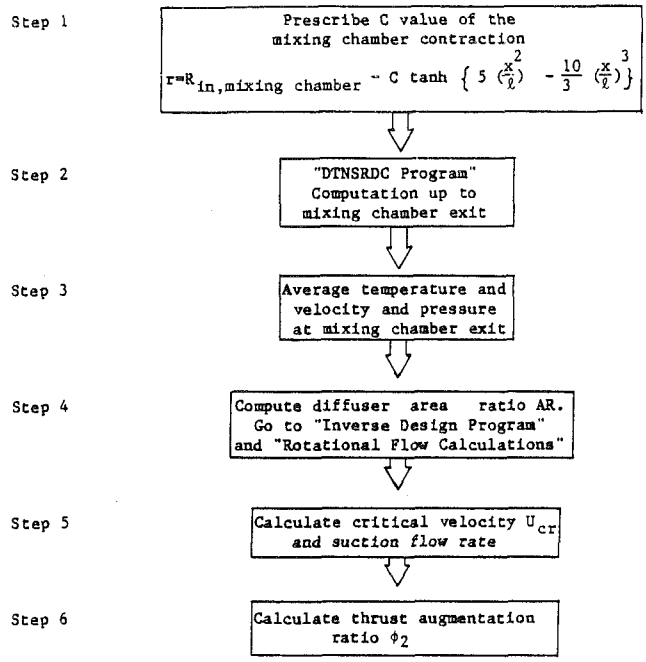

Fig. 1 Block-diagram showing the major steps in ejector analysis

The first step is to specify the mixing chamber geometry by a selected dimensional value of C in the radius distribution equation of Fig. 1 along with other mixing chamber geometric parameters. In step two, the computer program originally devised by Gilbert and Hill [12] is used to compute velocity and temperature profiles and pressure values up to the exit of the mixing chamber. Governing equations for the flow are of the boundary layer type; therefore pressure variations only exist along the flow direction and not across the streamlines.

In the third step, the mass-averaged flow velocity and temperature are computed. These are employed in the fourth step, which uses one-dimensional, compressible isentropic flow to determine the necessary area ratio to yield the diffuser exit pressure at the atmospheric level (or the ambient level).

Nomenclature

A = area
AR = area ratio
C = constant used in Fig. 1, Step 1
D = constant diameter
$f.s.$ = ratio of slot suction to total flow rate
l = mixing chamber length
l/D = mixing chamber length to diameter ratio
L = overall length
$\dot{m}$ = mass flow rate
P = pressure
r = radius, $f(x)$
u, V = velocity
x = length, general
λ = mixing chamber inlet to nozzle area ratio
ϕ = thrust augmentation ratio $(\dot{m}V)_e/\dot{m}V)_p$
ϕ_2 = modified thrust augmentation ratio (see equation (1))
ω = vorticity

Subscripts

amb = ambient condition
aux = auxiliary ejector
e = exit of diffuser, primary ejector
e' = exit of diffuser, auxiliary ejector
mc = mixing chamber
0 = stagnation condition
p = primary flow, primary ejector
p' = primary flow auxiliary ejector
$s1$ = secondary entrained flow at inlet
suc = suction

For other computations in this step, inviscid incompressible axisymmetric flow is assumed within the diffuser. As long as the flow along the solid wall is maintained without deceleration, the inviscid flow approximation can be justified. The Inverse design Program reported by Nelson and Yang [14] is used to obtain the geometry of the short, curved-wall diffuser for a specified area ratio at the length approximately equal to one exit diameter. This length specification is somewhat arbitrary, yet experience suggests that it should not be difficult to achieve.

Immediately after the determination of the diffuser geometry, a computer program based on a rotational flow analysis is used in step 4 to examine the velocity distribution along the diffuser wall. As an objective, there should be no deceleration along the solid diffuser wall. If necessary, the input for the Inverse Design Program is revised to generate a new diffuser geometry. This process is repeated until there is no indicated deceleration along the diffuser wall. It is sometimes necessary to revise the analysis from the very first step where the mixing chamber inlet pressure is specified. An increase of the static pressure at the inlet implies a reduction in mass ratio and therefore a reduction in diffuser area ratio. Usually this revision can eliminate the problem of deceleration along the solid wall. For a configuration with no deceleration, no flow separation will take place. It is recommended that the velocity from the diffuser inlet to the suction slot be kept slightly accelerated.

The fifth step is to estimate the amount of fluid to be removed for boundary layer control. For this purpose it is necessary to know the boundary layer profile immediately upstream of the suction slot. It is reasonable to assume that this profile is the same as that at the exit of the mixing chamber, and by using that profile, the critical velocity determined by Taylor's criterion [15] can be calculated and the rate of boundary layer removal can then be determined.

In step 6, the modified thrust augmentation ratio ϕ_2 is computed. The consideration of the mass flow of primary fluid used in auxiliary ejector, which provides the necessary boundary layer control, and the thrust contribution from the discharge of the boundary layer removal are included in the definition of ϕ_2 viz,

$$\phi_2 = \frac{1}{(\dot{m}V)_p + (\dot{m}V)_{p'}} \left(\int_e \rho V^2 dA + \int_{e'} \rho V^2 dA \right) \quad (1)$$

But due to small numerical contribution of the second integral term, this equation was approximated by

$$\phi_2 = \frac{1}{(\dot{m}V)_p + (\dot{m}V)_{p'}} \left((\dot{m}V)_{e'} + \int_e \rho V^2 dA \right) \quad (1.a)$$

In step 3, the velocity profile across the mixing chamber exit was computed, and in step 4 an inviscid rotational flow analysis was approximated. Therefore, the momentum term represented by the integral in equation (1.*a*) can be readily determined. One-dimensional compressible flow analysis, using specified primary and auxiliary mass flow rates together with the mass ratio in the auxiliary ejector, were used to compute the non-integral momentum terms.

In the present study, an ejector was first fabricated based on the design using the approximation of constant vorticity in the diffuser for rotational flow calculation. It had a diffuser area ratio of 2.2:1, and it was found that this ejector could not be operated without flow separation. A refined analytical procedure which requires no constant vorticity approximation was subsequently devised. Results of the refined anlaysis indicated that the flow reversal within the first ejector was inevitable regardless of the amount of flow removal for boundary layer control. We call this flow phenomenon "inviscid flow reversal," a consequence of the continuity equation and vorticity equation requirements. The allowable area ratio of the diffuser without flow reversal obtained using refined analytical procedures is smaller than that resulting from a constant vorticity analysis. An outline of the "refined rotational flow calculation" is presented in the appendix of reference [16].

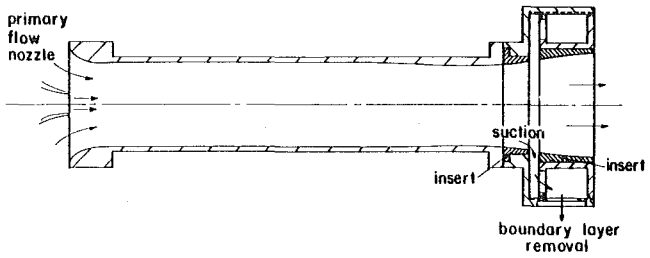

Fig. 2 Geometry of the ejector with diffuser area ratio for 1.33, $\lambda = 40$, $(L/D)_{overall} = 6.09$

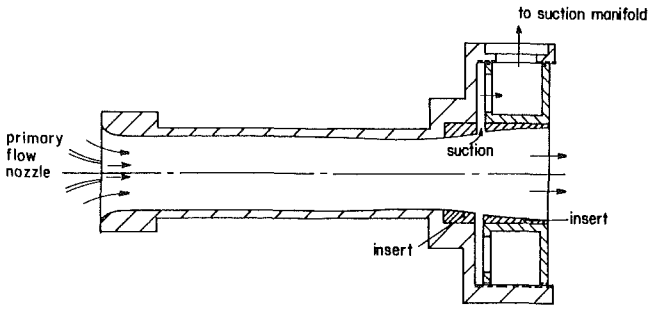

Fig. 3 Geometry of the ejector with diffuser area ratio of 1.26, $\lambda = 20$, $(L/D)_{overall} = 6.02$

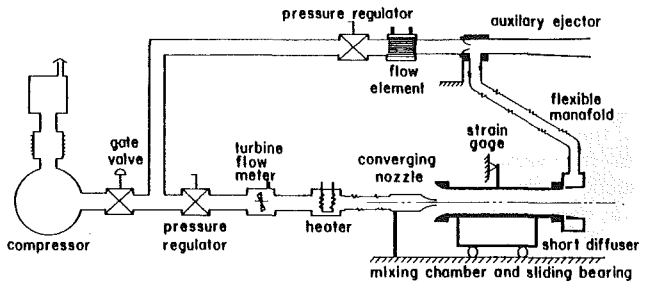

Fig. 4 Schematic of test setup

Experimental Investigation

A. Test Models. Figure 2 shows an ejector which has a λ value of 40, mixing chamber ratio (l/D) of 4.82:1 and diffuser area ratio of 1.33:1. The diffuser of this ejector can be changed to an area ratio of 1.46:1 by changing the curved-wall inserts to thus form a second ejector but having the same mixing chamber and λ value.

A third ejector wth a λ value of 20, mixing chamber length-to-diameter ratio (l/D) of 4.75:1 and a diffuser area ratio of 1.26:1 is shown as Fig. 3. Systematical tests were conducted to determine the effective thrust augmentation ratio ϕ_2 for these three ejectors (diffuser area ratios 1.26:1, 1.33:1 and 1.46:1). Two types of primary nozzles, single-jet and multiple-jet, were used. These were convergent nozzles located so that the primary nozzle exit plane coincided with the mixing chamber inlet plane.

The auxiliary ejector used for boundary layer removal in the ejectors studied is of conventional design and the primary nozzle size was optimized for the operational conditions of the main ejectors.

B. Test Facility. Figure 4 shows a schematic of the test setup. The compressed air used as the primary fluid for the ejector and for the auxiliary ejector was supplied by an oil-less

Ingersoll-Rand type ESH compressor which has a maximum capacity of 204 ACFM at 90 psig. The compressed air was cooled by using an aftercooler and then routed to a 3-ft diameter, 8-ft tall surge tank. From there the air was delivered through a 2-in. pipeline to the laboratory. A gate valve was used to control the air flow into the test loop. Either a Fisher model 95L (10–30 psig) or model 95H (25–75 psig) regulator was used to regulate the pressure of the primary flow for the ejector nozzle, depending upon required test pressure range. A Cox Turbine Flowmeter was installed downstream of the pressure regulator and an electrical resistance heater, rated 5.6 Kw and controlled by a voltage regulator, was placed downstream of the flowmeter. A metal flexible hose was used to connect the heater and the converging nozzle plenum. This allowed easy alignment during installation. In the other branch of the test loop, compressed air was supplied to a converging nozzle of the auxiliary ejector. A C. A. Norgren model R-17-800 regulator was used upstream of a Meriam laminar flow element. The latter was used to meter the primary flow rate of the auxiliary ejector. The primary nozzle and the mixing chamber of the test ejector were mounted on an alignment device to ensure that the centerlines of the primary nozzle and mixing chamber were precisely aligned. A set of eight sliding ball bearings was used to allow the mixing chamber to move freely in the axial direction. A force measuring device utilizing a set of strain gages was mounted rigidly on the mixing chamber to provide a direct measurement of the thrust force on the mixing chamber. The mixing chamber and the diffuser were assembled together as one integral part which moved freely relative to the alignment rig. The alignment rig was mounted firmly on a stationary supporting stand. The curved wall diffuser insert downstream of the suction slot could be adjusted relative to the upstream insert to vary the slot size or the gap between the inserts. Four suction ports were provided, and a featherweight flexible hose was used as the suction mainfold which led to the inlet of the auxiliary ejector. The primary jet, mixing chamber and the diffuser of the auxiliary ejector were all firmly mounted to the stationary stand. The featherweight flexible hose minimized errors in the thrust force measurement on the mixing chamber of the ejector. Conventional instruments and well-accepted laboratory procedures were employed in measurements of pressure, temperature, momentum, mass flow rates and force.

C. Test Conditions. Three ejectors (two with λ equal to 40 and diffuser area ratios of 1.46:1 and 1.33:1 and one with λ equal to 20 and diffuser area ratio of 1.26:1) were successfully operated, mostly without flow separation in their diffuser sections. These ejectors were systematically tested. The plenum pressure of each ejector was set at five levels 10, 17.4, 23.2, 29.0, and 35.5 psig, 10 psig being the design value. The ambient static and also the stagnation pressure were approximately 14.5 psia which resulted in pressure ratios of the stagnation pressures to ambient pressure (P_0/P_{amb}) of 1.67:1, 2.21:1, 2.61:1, 3.02:1 and 3.47:1. The plenum pressure of the primary flow of the auxiliary ejector was selected at five levels, 7.5, 10, 12.5, 15, and 17.5 psig, for each of the following ejector primary flow plenum pressures, 10, 17.5, and 23.2 psig. The auxiliary plenum pressure was selected at four levels, 12.5, 15, 17.5, and 20 psig at each primary flow plenum pressure of 29.0 and 35.5 psig. The temperature of the primary air of the ejector was elevated to 164°F by passing the air through a 6-in. pipe containing suspended electrical heating elements. The heated air expanded through a converging nozzle to reach a static temperature of about 80°F, approximately the static temperature of the entrained secondary fluid.

The gap size between two curved-wall sections of the diffuser was adjusted to yield a maximum vacuum of the first

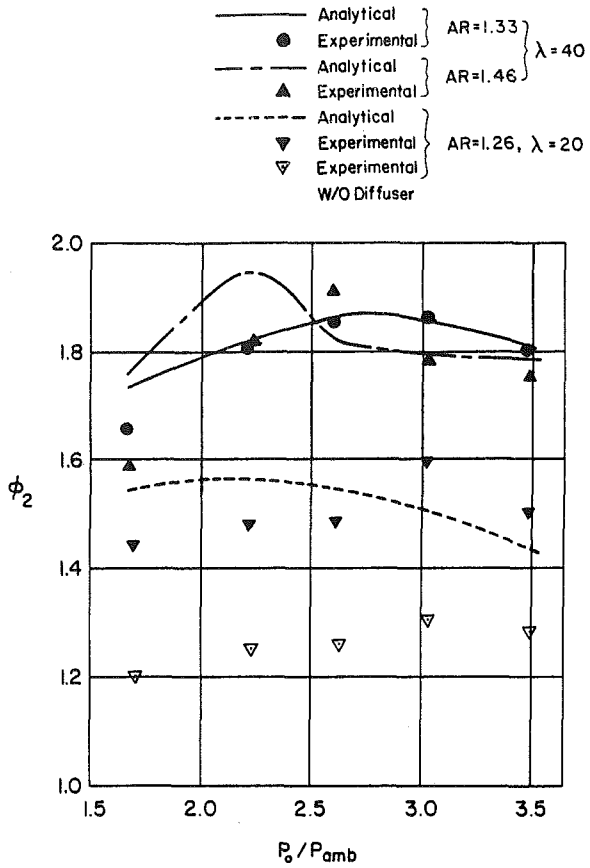

Fig. 5 Comparison of analytically and experimentally determined $(\phi_2)_{max}$ values at various P_0/P_{amb} ratios

mixing chamber static pressure reading. This resulted in a gap size ranging between 1/4 in. and 3/16 in. for all the tested ejectors.

D. Test Procedures. Ejector components test rigs were designed to obtain flow velocity profiles at the mixing chamber exit and to obtain the performance of the auxiliary ejector. These rigs were designed and operated at a simulated diffuser condition of no flow separation in the diffuser. Using the rotational flow analysis, a diffuser was designed with an area ratio of 1.64:1. This area ratio was too large because the computed vorticity used in rotational flow analysis was lower than the value derived from measured velocity at low pressure ratios of the stagnation pressures. Until the diffuser area ratio was reduced to 1.46:1, flow separation within the diffuser persisted. A considerable effort was devoted to eliminating flow separation in the short, curved-wall diffuser, and this was achieved largely on the ejector performance test stand rather than using components testing.

The mixing chamber length for λ of 40 was initially 15.5 in. This was reduced to 13.5 in. on the ejector performance test stand. The first mixing chamber wall static pressure tap was used to monitor the flow rate of the entrained secondary flow, and tufts attached at the diffuser exit were used as indicators for flow attachment. In this length reduction process, no secondary flow reduction was detected in the first one inch of trimming. A reduction of 0.2 in water was observed in the wall static pressure reading when the length was reduced to 13.5 in. No flow separation was indicated by tufts inside the diffuser. These improvements were carried out at a plenum pressure of 10 psig for the primary flow of the ejector.

For each test run the plenum pressure levels for the primary and auxiliary ejectors were adjusted to the pre-selected values via pressure regulators and monitored by manometers. The

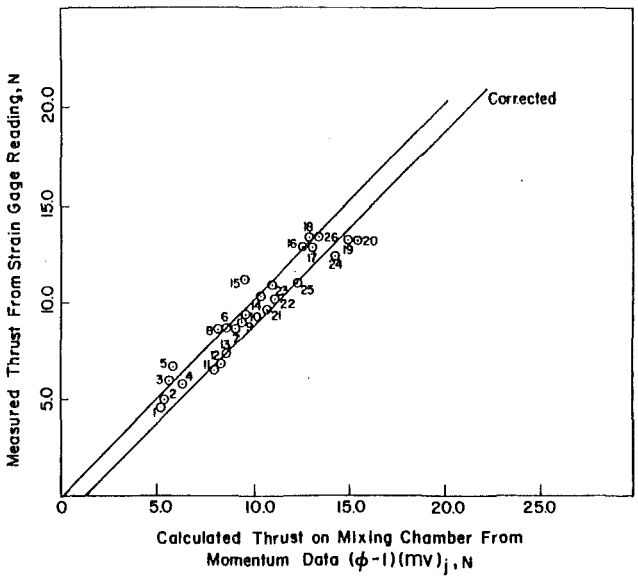

Fig. 6 Comparison of measured and computed thrust on mixing chamber, AR = 1.26, λ = 20, single-jet nozzle

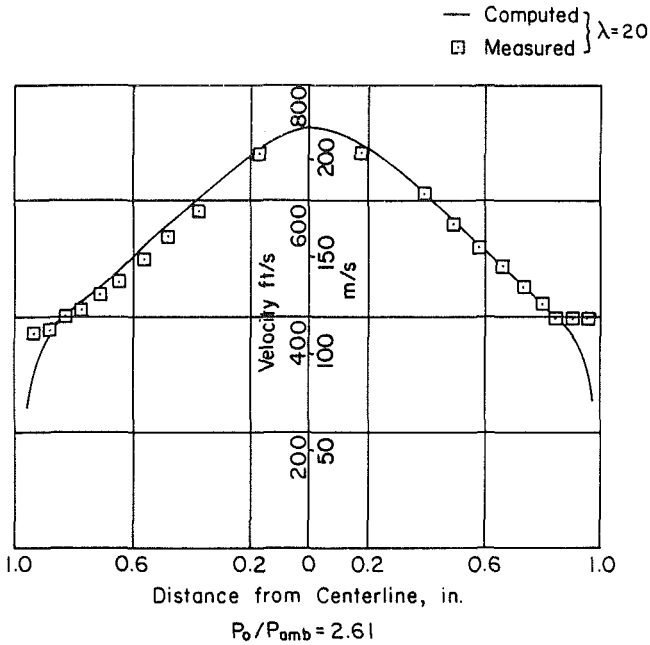

Fig. 7 Typical velocity distributions at the mixing chamber exit, computed and measured, AR = 1.26, λ = 20

plenum temperature of the primary air of the main ejector was regulated to yield a pre-selected temperature by adjusting the voltage regulator of the electrical heater. A miniature Kiel-probe was used to traverse the auxiliary ejector exit. A Keil-probe and a static pressure probe were used to traverse the main ejector exit. A 10-point method was used for traversing the entire diameter yielding 20 stations for both stagnation and static pressure readings. These pressure readings and the wall pressure readings of the mixing chambers and the diffusers were recorded either via (*i*) pressure transducer-scanning valve to a tele-type arrangement or (*ii*) pressure transducer-scanning valve to an Apple computer for data storing and data reduction. Strain gage output was read as a direct measurement of the force on the mixing chamber. Normally it required 30–40 minutes to complete one test run. Care was exercised to ensure that the pressure levels of the primary flows, the temperature of the heated air and the strain gage output reading did not "drift" during the test period. Therefore, those readings were repeated at the end of each test run.

E. Test Results. The most important results of this investigation pertain to the optimization of the modified thrust augmentation ratio ϕ_2 as a function of the pressure ratio, P_0/P_{amb}. These results are summarized in Fig. 5. A discrete point on this figure represents an experimentally obtained maximum ϕ_2 value for a given pressure ratio. Each ϕ_2 value was optimized by varying the flow to the auxiliary ejector. Using the experimentally measured values of f.s., $(MR)_{aux}$ and vorticity ω at the diffuser inlet and the analytical procedure outlined in Fig. 1, three performance curves, one for each tested ejector, were obtained. Figure 5 shows those three curves of predicted ϕ_2 versus pressure ratio P_0/P_{amb}. The open circles represent the ϕ values of the ejectors with diffuser removed. These values should serve as base line performance to indicate the thrust augmentation gained by the use of the diffuser. Good agreement is observed between analytically computed and experimentally observed ϕ_2 values over a major part of the P_0/P_{amb} range.

The thrust augmentation of the type of ejectors studied in this investigation is the thrust force on the mixing chamber. The values of this force were obtained from two approaches: (1) the difference between the momentum of the ejector at diffuser exit and the momentum of the primary nozzle at its exit, and (2) the direct force measurement using a strain gage arrangement. Figure 6 shows a typical comparison of these forces determined from the two different approaches for the ejector of AR = 1.26:1 and λ = 20. The numbers next to the data points denote the test run number listed in Table 1 of reference [16]. A large majority of the data points fall on a line of 45 degrees, but displaced up to 0.3 lb to indicate higher values of thrust force derived from momentum measurements. It is believed that the experimental apparatus was not totally free to move before the cantilever arm of the mixing chamber came into contact with motion stop. There appears to be a small but systematic error in the strain gage force measurements introduced by the presence of the suction manifold of the auxiliary ejector. Allowing for this, the thrust forces determined from the two different sources agree well for most of the data in the low and medium range of tested pressure ratio of P_0/P_{amb}. Greater deviations were observed at high pressure ranges; this increased deviation could be attributed to the fact that the static pressure across the mixing chamber inlet may not have been constant as was assumed.

Whereas the maximum ϕ_2 values of the present study are in the neighborhood of 1.6, a study reported as reference [9] indicates maximum thrust augmentation values ranging from 1.4 to 2.0. The high value utilized a "hyper-mixing" nozzle ejector, whereas the lower value was obtained with a single, axisymmetric ejector nozzle comparable to the designs of the present study. Their reported ϕ value of 1.4 is comparable to the computed optimum value reported by Tai [13] and is less than the optimum value observed in the present work. Recently, Alperin and Wu [17] published an analytical prediction of ejector thrust augmentation ratios for both subsonic and supersonic, mixed flows. Reference [16] deals with the subsonic case. They have shown that for a stationary ejector with ideal mixing and no frictional losses, ϕ can reach a value of 3.5 for a nozzle pressure ratio of 1.67 and a ϕ value of 2.4 for a nozzle pressure ratio of 3.47. Of course in their ideal analysis, length is not a pertinent geometrical parameter. This is in contrast to the current study where length is of major importance.

Figure 7 shows a typical set of normalized velocity distributions at the diffuser inlet. The distribution shown by solid line was obtained by using the computer program of reference [12]. Experimentally measured mass ratio MR and

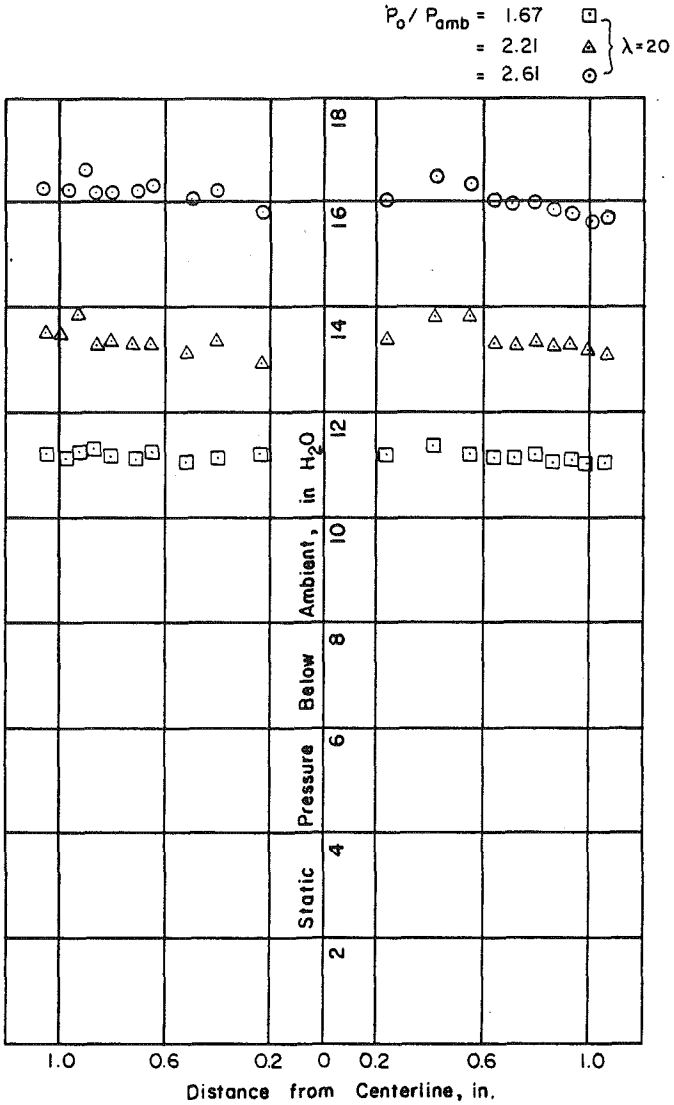

Fig. 8 Typical static pressure distributions across the exit of the mixing chamber AR = 1.26, λ = 20

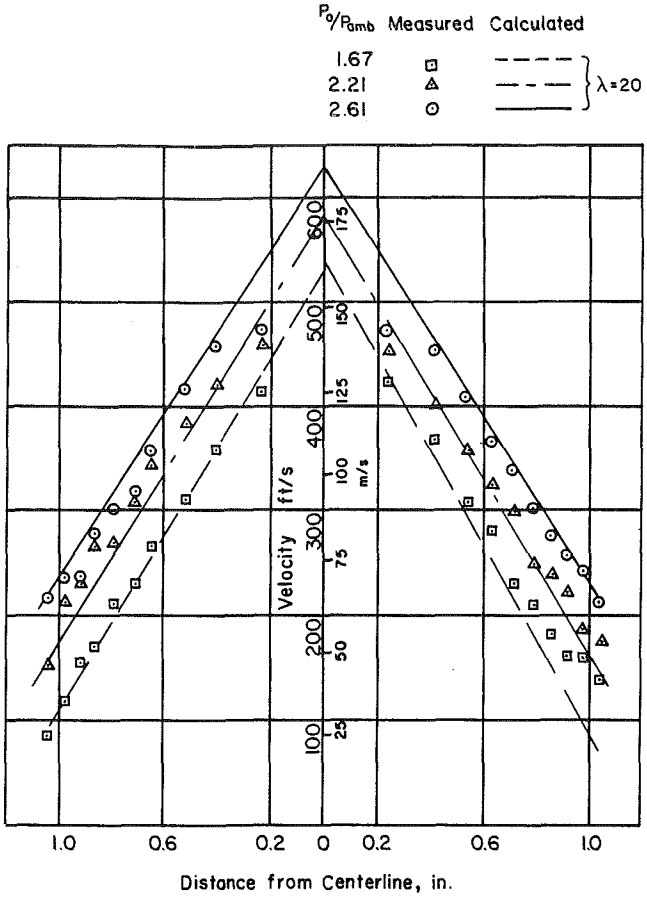

Fig. 9 Typical velocity distributions at the diffuser exit, computed and measured, AR = 1.26, λ = 20

pressure ratio P_0/P_{amb} were used as inputs for this computation. This mixing chamber exit is located 4.82 diameters downstream from its inlet. The velocity distribution shown by discrete points was obtained with a miniature Kiel-probe and a static pressure probe. Basic features of a shear flow were observed in both profiles. Owing to the sizes of the probes, no measurements were taken closer than 1/16 in. from the wall. The vorticity values derived from the measured velocity are about 10 percent higher than those derived from the computed distribution at P_0/P_{amb} = 1.67. Better agreement in vorticity values was observed at higher pressure ratios. Fifteen sets of velocity distribution were examined for this investigation. In static pressure measurements the centerline pressure usually was 1.0 to 2.0 in. of water lower than that at the wall. Figure 8 shows three sets of static pressure distributions across the exit of the mixing chamber of the ejector with λ = 20. These were measured for pressure ratios of 1.67, 2.21 and 2.61. These pressure ratios correspond approximately to subsonic, sonic and supersonic primary flow within the mixing chamber, respectively.

The velocity measurements at the exit of the mixing chamber provided information for correcting the vorticity ω used in computing the diffuser exit velocity for the rotational flow analysis. The velocity measurements also provided an independent source from which the entrained flow rate $\dot{m}_{sl}$ was determined.

Figure 9 shows typical exit velocity distributions for an ejector having AR = 1.26:1. The lines represent the velocity distribution computed with the rotational flow analysis of reference [16]. The features of shear flow are preserved in both the computed and the experimentally measured velocity distributions.

The velocity measurements at the diffuser exit provided one of the key elements of information for evaluation of thrust augmentation ratio ϕ_2, mass flow rate $\dot{m}_e$ and mass flow ratio MR. The ratio MR is defined as $\dot{m}_{s1}/\dot{m}_p$ and the entrained mass flow rate $\dot{m}_{sl}$ was determined from the following

$$\dot{m}_{s1} = \dot{m}_e + \dot{m}_{suc} - \dot{m}_p$$

where

$$\dot{m}_{suc} = \dot{m}_{e,aux} - \dot{m}_p{}'$$

Independent checks on $\dot{m}_{sl}$ were made by using the following equation

$$\dot{m}_{s1} = \dot{m}_{mc} - \dot{m}_p$$

The values of $\dot{m}_{s1}$ determined from the above two independent approaches differed by no more than 4 percent.

Steady-flow prevailed in this ejector over most of the operating ranges of P_0 and $P_{0,aux}$, except when P_0 was around 30 psig. In all velocity profiles the measured peak velocities fall below computed values. During the tests for the ejector having AR = 1.26:1 and λ = 20, much more uniform velocity distributions were observed both at the exit of the mixing chamber and at the exit of the diffuser when the primary nozzle plenum pressure was set between a narrow range of 30–31 psig. Quinn [7, 8] attributes such profiles to aeroacoustic interactions. For the other two ejectors tested,

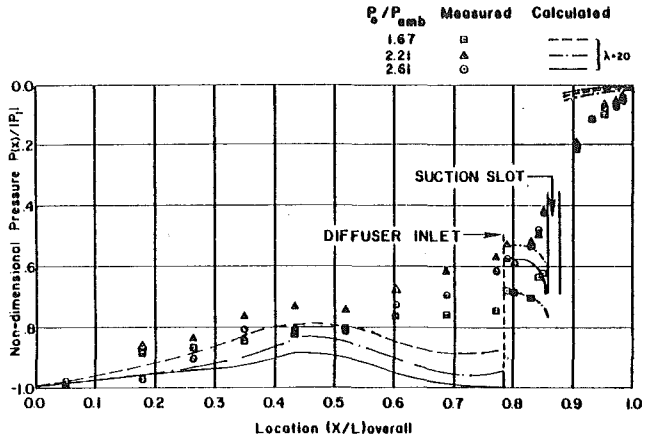

Fig. 10 Comparison of diffuser wall pressure distributions, measured and computed, AR = 1.26 λ = 20

steady flow prevailed over the entire test ranges of P_0 and $P_{0,aux}$.

Figure 10 shows the typical measured and computed pressure distributions along the mixing chamber wall and the diffuser wall for an ejector having AR = 1.26:1. In the mixing chamber the computed pressure distribution was obtained by using Gilbert and Hill's analysis along with the measured inlet static pressure as input. The computed diffuser wall pressure distribution was obtained by using measured diffuser inlet conditions (or mixing chamber exit conditions) together with the rotational flow analysis for wall velocity and the Bernoulli equation for corresponding pressure. The wall pressure readings throughout the ejectors were below ambient pressure. The static pressure at the end of the bell month inlet was used as the normalizing factor. The discontinuity of the computed pressure distribution at the diffuser inlet is a result of the use of experimental pressure data at the mixing chamber exit for the diffuser wall velocity computation. Plotted on gage pressure readings, the computed pressure is significantly lower than the measured pressure. In terms of absolute pressure level, however, the difference amounts to only 2 to 3 percent of the absolute pressure. Therefore good correlation between the experimental and computed velocity distributions at both the diffuser and mixing chamber exits is not contradicted by the large difference between experimental and computed gage pressure distributions along the mixing chamber wall. It has been pointed out by Nagamatsu [18] that under most of the tested nozzle pressure ratios there were "shock bottles" within the mixing chamber which could explain why the measured pressure readings are higher than the computed values from the analysis of reference [12], which assumes that no expansion and shock waves exist in the mixing chamber. For further discussion on the mixing of subsonic and supersonic jet flow from convergent nozzle with the ambient air one should refer to the articles by Love et al. [19] and Nagamatsu and Sheer [20].

Within the diffuser, favorable pressure gradients were prescribed initially to the solid wall portion (upstream and downstream of the suction slot) of the diffuser designed with the irrotational flow, inverse design program. The rotational flow computation also predicted favorable pressure gradients. Owing to low diffuser area ratio, attached flows were maintained even though experimental data exhibited deceleration both upstream and downstream of the suction slot. The diffuser was designed for P_0/P_{amb} = 1.67. The computed pressure distribution curves along the diffuser walls show that the curve for P_0/P_{amb} = 2.21 is above instead of below that for P_0/P_{amb} = 2.61 as the trend indicated in the mixing chamber. This reverse trend is caused by using the experimentally observed diffuser inlet static pressures as the input of the rotational flow computations and no special significance should be attached.

F. Accuracy Statement. The accuracy of the experimental value of ϕ_2 presented in Fig. 5 was analyzed. Based on the accuracy of the instruments and the uncertainty of the readings, the following maximum errors wre encountered. At the ejector exit plane errors of 1 percent in area due to probe locations, 0.4 percent in density due to temperature measurements, and 0.8 percent in velocity due to pressure measurements existed. Similarly at the exit plane of the auxiliary ejector, maximum errors of 4 percent in area, 0.4 percent in density and 2 percent in velocity were assessed. In addition, a one percent maximum error in both primary fluid mass flow rates for the ejector and the auxiliary ejector, and 1 and 2 percent maximum errors in their respective jet velocities were assessed. Based on these values and the definition of the modified thrust augmentation ratio (equation (1)), a maximum error of 6.8 percent and a probable error of 4.3 percent in ϕ_2 were estimated.

Conclusions

Two important features were brought out in this investigation:

1. The vorticity at the diffuser inlet was introduced as a flow parameter in ejector analysis.
2. A new level of performance for ejector thrust augmentation was established.

From inviscid rotational flow consideration, a flow reversal will take place regardless of the amount of boundary layer removal when the diffuser area ratio is too large for the inlet vorticity. This inviscid flow reversal is a consequence of flow continuity and vorticity requirements. Therefore, for each inlet vorticity level there is a maximum value of the diffuser area ratio. Beyond this ratio, flow reversal is inevitable regardless of the amount of boundary layer removal. This feature was demonstrated for the first time both analytically and experimentally.

T. C. Tai has previously shown in reference [13] that an optimum thrust augmentation ratio value of 1.42:1 may be reached when the ejector diffuser was designed with the incipient stall criterion for an overall l/D ratio of 6:1 and λ = 19. In the present investigation using a Griffith type diffuser, an even higher thrust augmentation ratio of 1.60:1 was observed for similar conditions. For λ = 40 and l/D 6:1, no thrust augmentation value was predicted by Tai, but in the present work an effective thrust augmentation ratio of 1.91:1 was attained.

In most of the test runs the thrust augmentation determined by using momentum measurements correlates well with independent force measurements on the mixing chamber. This correlation suggests that both the ejector inlet and diffuser exit pressure can be approximated by the ambient pressure. At higher flow ratios, the inlet pressure deviated more from the ambient pressure, therefore the momentum measurements deviated from the force measurements slightly as expected.

This investigation has shown that λ is an important parameter in attainment of thrust augmentation ratio. A decrease in the thrust augmentation ratio can be expected if there is a decrease in λ. Therefore, whenever possible a larger λ or a larger mixing chamber should be used for a given size of primary jet.

Acknowledgments

This investigation was supported by the David W. Taylor Naval Ship Research and Development Center (DTNSRDC) and the Naval Air Systems Command (NAVAIR) under Navy

contract N00167-81-C-0087. The work was technically under the cognizance of D. G. Kirkpatrick (NAVAIR-311D) and T. C. Tai (DTNSRDC 1606). The authors wish to acknowledge the support of the South Carolina Energy R & D Center for the preparation of this paper.

References

1 Von Karman, T., "Theoretical Remarks on Thrust Augmentation," Reissner Anniversary Volume, Contribution to Applied Mechanics, 1949.

2 Jacobs, E. N., and Shoemaker, J. M., "Test on Thrust Augmentation for Jet Propulsion," TN 431, NACA, 1932.

3 Fabri, J., and Siestrunck, R., "Supersonic Air Ejectors," *Advances in Applied Mechanics*, Vol. 5, Sec. 1, Academic Press, 1958, pp. 1-34.

4 Addy, A. L., "The Analysis of Supersonic Ejector Systems," Supersonic Ejectors, AGARDO Graph No. 163, 1972.

5 Bevilaqua, P. M., and Lykondis, P. S., "Mechanisms of Entrainment in Turbulent Wakes," *AIAA Journal*, Vol. 9, No. 8, Aug. 1971.

6 Bevilaqua, P. M., "Evaluation of Hypermixing for Thrust Augmenting Ejectors," *Journal of Aircraft*, Vol. 11, No. 6, June 1973.

7 Quinn, B., "Ejector Performance at High Temperatures and Pressures," *Journal of Aircraft*, Vol. 13, Dec. 1976.

8 Quinn, B., "Effects of Aeroacoustic Interactions on Ejector Performance," *Journal of Aircraft*, Vol. 12, Nov. 1975.

9 Porter, J. L., and Squyers, R. A., "A Summary/Overview of Ejector Augmentor Theory and Performance," ATC Report No. R-91100/9CR-47A, April 1981, Vought Corporation Advanced Technology Center, Dallas, Texas.

10 Yang, T., and El-Nasher, A. M., "Ejector Peformance with a Short Diffuser," *Proceedings of the Symposium on Jet Pumps and Ejectors*, The British Hydromechanism Research Association, England, Nov. 1972.

11 Yang, T., and Nelson, C. D., "Griffith Diffusers," ASME JOURNAL OF FLUIDS ENGINEERING, Vol. 101, No. 4, Dec. 1979.

12 Gilbert, G. B., and Hill, P. G., "Analysis and Testing of Two-Dimensional Slot Nozzle Ejectors with Variable Area Mixing Sections," NASA CR-2251, May 1973.

13 Tai, T. C., "Optimization of Axisymmetric Thrust Augmenting Ejectors," AIAA Paper 77-707, June 1977.

14 Nelson, C. D., and Yang, T., "Inverse Problem Design Method for Branched and Unbranched Axially Symmetric Ducts," AIAA Journal, Sept. 1977.

15 Gregory, N., "Note on Sir Geoffery Taylor's Criterion for the Rate of Boundary Layer Suction at a Velocity Discontinuity," R & M No. 2496, 1947.

16 Yang, T., Ntone, F., and Jiang, Tong, "Experimental Investigation of High Performance, Short, Thrust Augmenting Ejectors," DTNSRDC-ASED-CR-2-83, Mechanical Engineering Department, Clemson University, Jan. 1983.

17 Alperin, Morton and Wu, Jium-Jenq, "Thrust Augmenting Ejectors, Part 1," *AIAA Journal*, Nov. 1983.

18 Nagamatsu, H. T., private communication, Dec. 1983.

19 Love, E. S., Grisby, C. E., Lee, L. P., and Woodling, M., "Experimental and Theoretical Studies of Axisymmetric Free Jets," *J. of Aeronautical Sciences*, Vol. 25, 1958, pp. 791-799.

20 Nagamatsu, H. T., and Sheer, R. E., Jr., "Subsonic and Supersonic Jets and Supersonic Suppressor Characteristics." *Aeroacoustics: Jet and Combustion Noise: Duck Acoustics*, Editor H. T. Nagamatsu, Vol. 37 of the *Progress in Aeronautics and Astronautics Series*, MIT Press, 1975, pp. 125-151.

A Simplified Method of Using Four-Hole Probes to Measure Three-Dimensional Flow Fields

N. Sitaram[1]
A. L. Treaster[2]

Applied Reasearch Laboratory,
State College, Pa. 16801

A simplified method of using four-hole probes to measure three-dimensional flow-fields is presented. This method is similar to an existing calibration and application procedure used for five-hole probes. The new method is demonstrated for two four-hole probes of different geometry. These four-hole probes and a five-hole probe are used to measure the turbulent boundary layer on a flat plate. The results from the three probes are in good agreement with theoretical predictions. The major discrepancies occur near the surface of the flat plate and are attributed to wall vicinity and velocity gradient effects.

Introduction

In a recent paper [1], Shepard described a four-hole probe for three-dimensional flow measurements. The advantages of four-hole probes over five-hole probes, such as fewer measurements and reduced instrumentation during calibration and application of the probe, a simpler probe with a smaller head, and smaller errors due to wall vicinity effect and shear gradient effect, are offset by the complex method of Shepherd.

The purpose of this paper is to present a simplified calibration and interpolation method of using four-hole probes for three-dimensional flow measurements. This method is similar to that developed for five-hole probes by Treaster and Yocum [2]. This new method is demonstrated for two four-hole probes of different configuration. These four-hole probes and a five-hole probe are used to measure the turbulent boundary layer on a flat plate and the results are compared with theoretical predictions.

Probe Geometry

The two miniature probes used in this study are shown in Figs. 1 and 2, respectively. Both probe tips were fabricated from 0.55 mm (0.022 in.) outer diameter and 0.30 mm (0.012 in.) inner diameter stainless steel hypodermic tubing. Tangential silver solder fillets are faired between the tubes. The probe tips are machined to a 50 degree half angle cone and located approximately four local support diameters upstream to reduced support interference effects. The probe support configuration in Fig. 1 is the same for both probe tips.

The four-hole probe tip shown in Fig. 1 is similar to that used by Shepherd. The probe shown in Fig. 2 was used both in the four-hole and five-hole probe modes. In the four-hole probe mode, tube 5 was not used. Tube 5 could be eliminated or used to mount a thermocouple. This probe has a smaller error due to velocity gradient effect, as the probe height in the pitch plane is equal to two tube diameter only. The four-hole probe shown in Fig. 1 and five-hole probe have larger errors due to velocity gradient effect, as their heights in the pitch plane are two and one-half diameters and three tube diameters, respectively. It should be noted that these probes are smaller than any commercially available probes, so that spatial and velocity gradient effects are minimized.

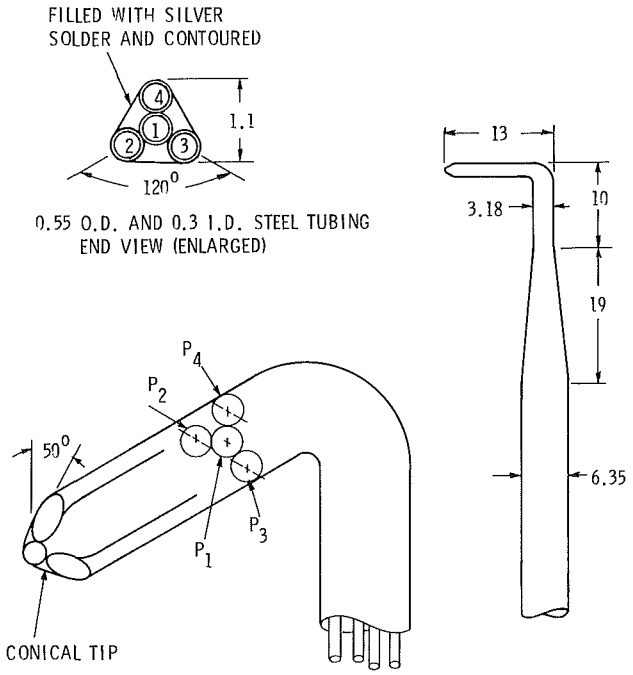

Fig. 1 Four-hole probe 1 geometry

Contributed by the Fluids Engineering Division for publication in the JOURNAL OF FLUIDS ENGINEERING. Manuscript received by the Fluids Engineering Division, January 24, 1983.

[1]Former graduate student, Aerospace Engineering Dept., The Pennsylvania State University.

[2]Research Associate, Applied Research Laboratory, The Pennsylvania State University.

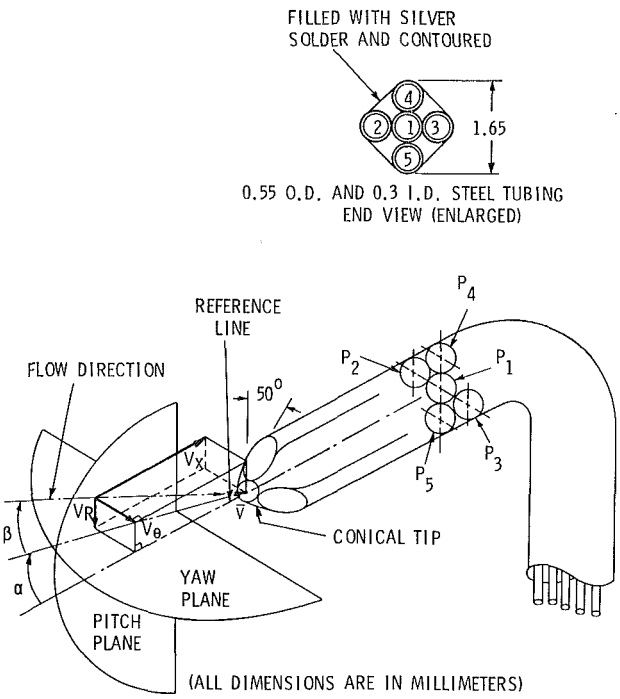

Fig. 2 Four-hole probe 2 geometry

Calibration and Application Techniqes

Calibration. The probes were calibrated in the open air jet tunnel of the Applied Research Laboratory [3] at the Pennsylvania State Unversity at air velocities of 34, 26 and 17 m/sec (112, 85 and 56 fps), respectively, to evaluate Reynolds number effects. The calibration was carried out at all combinations of pitch and yaw from −20 degrees to 20 degrees in 10 degree increments. At each angular setting the desired pressures from the subject probe and the reference stagnation and static pressures were measured. A set of calibration coefficients for each probe were computed according to the definitions in the following sections.

Calibration Coefficients. For four-hole probe 1 (Fig. 1) the following calibration coefficients are defined:

$$C_{p_{\text{pitch}}} = [P_4 - (P_2 + P_3)/2]/D, \quad C_{p_{\text{yaw}}} = (P_2 - P_3)/D,$$
$$C_{p_{\text{static}}} = (\bar{P} - P_s)/D \text{ and } C_{p_{\text{total}}} = (P_1 - P_0)/D,$$

where $\bar{P} = (P_2 + P_3 + P_4)/3$ and $D = (P_1 - \bar{P})$.

For four-hole probe 2, the five-hole probe used in the four-hole probe mode (Fig. 2), the following calibration coefficients are defined:

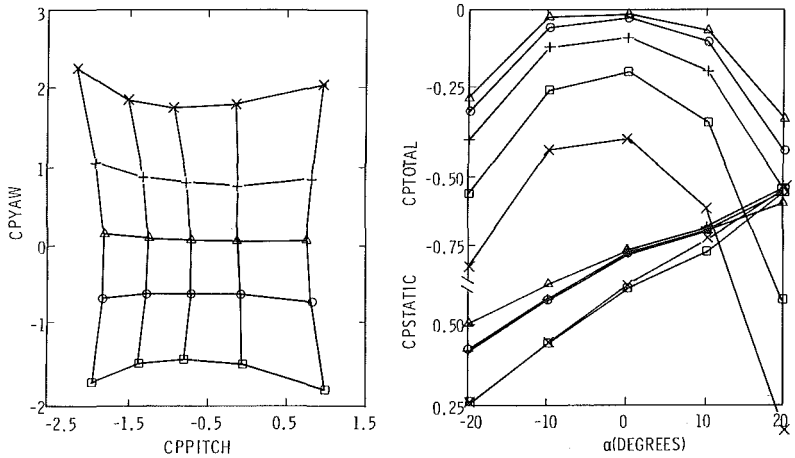

Fig. 3 Calibration curves of four-hole probe 1 (for legend see Fig. 4)

Nomenclature

$C_{p_{\text{pitch}}}$ = pitch coefficient, defined in text (CPITCH in figures)
$C_{p_{\text{static}}}$ = static pressure coefficient, defined in text (CPSTATIC in figures)
$C_{p_{\text{total}}}$ = total pressure coefficient, defined in text (CPTOTAL in figures)
$C_{p_{\text{yaw}}}$ = yaw coefficient, defined in text CPYAW in figures)
D = $(P_1 - \bar{P})$, N/m² (psi)
d = probe diameter, m (ft)
P = pressure, N/m² (psi)
$\bar{P}$ = mean pressure, N/m² (psi), defined in text
R = Reynolds number = $V_e d/\nu$, dimensionless
V = velocity, m/s (fps)
X = distance from flat plate leading edge, m (ft)
Z = distance between flat plate and probe axis, m (ft)
α = pitch angle, degrees (see Fig. 2)
β = yaw angle, degrees (see Fig. 2)
δ = boundary layer thickness, m (ft)
η = nondimensionalized distance between flat plate and probe axis = Z/δ
θ = flow angle = $\tan^{-1}(V_\theta/V_x)$, degrees
ν = kinematic viscosity of air, m²/s (ft²/s)
ρ = air density, kg/m³ (slug/ft³)
ϕ = meridional angle = $\sin^{-1}(V_r/V_m)$, degrees
ψ = pressure coefficient

Subscripts

a = atmosphere
e = boundary layer edge
0 = stagnation quantities
m = meridional direction, direction of resultant of the velocity components in x and r directions
r,θ,x = along the cylindrical (r,θ,x) coordinate directions
s = static quantities
1,2,3,4,5 = refer to tube numbers of the probe (see Figs. 1 and 2)

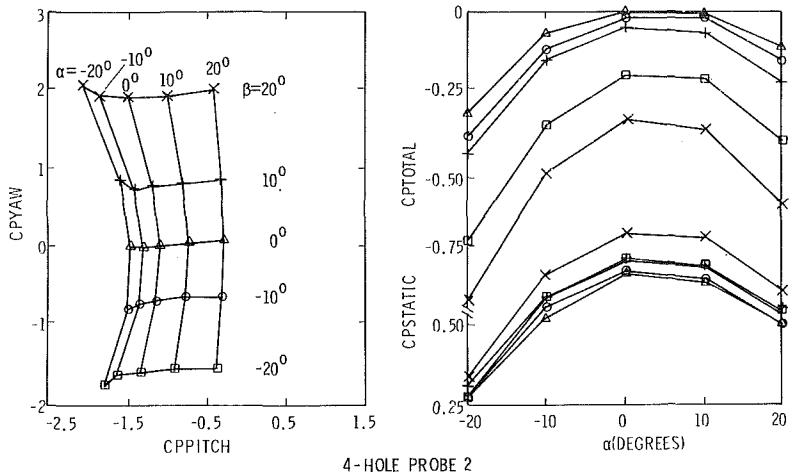

Fig. 4 Calibration curves of four-hole probe 2

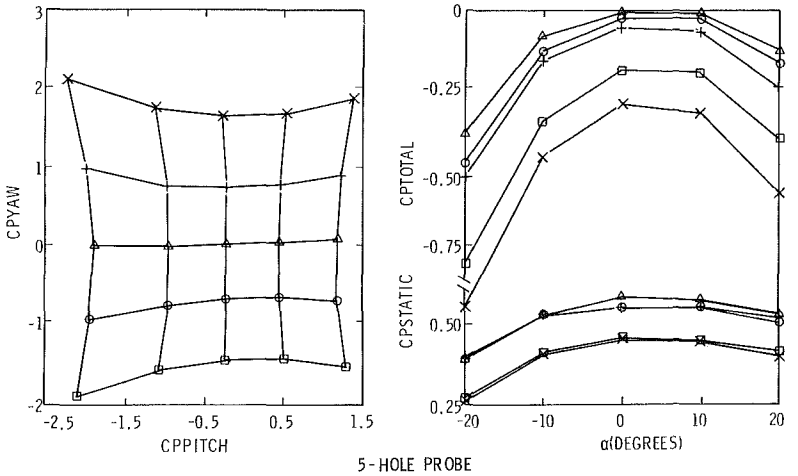

Fig. 5 Calibration curves of five-hole probe (for legend see Fig. 4)

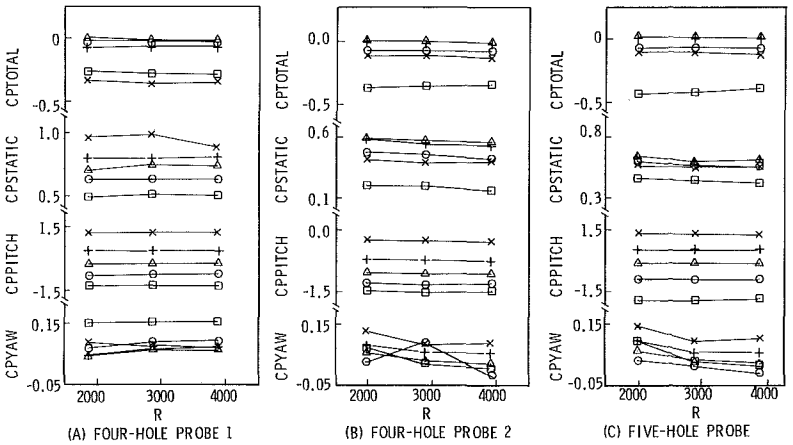

Fig. 6 Reynolds number effect on calibration curves

$C_{p_{\text{pitch}}} = (P_3 - P_1)/D$, $C_{p_{\text{yaw}}} = (P_2 - P_3)/D$,
$C_{p_{\text{static}}} = (\bar{P} - P_s)/D$ and $C_{p_{\text{total}}} = (P_1 - P_0)/D$,

where $\bar{P} = (P_2 + P_3)/2$ and $D = (P_1 - \bar{P})$.

For the five-hole probe (Fig. 2) the calibration coefficients are defined in the same manner as presented in reference [2]:

$C_{p_{\text{pitch}}} = (P_4 - P_5)/D$, $C_{p_{\text{yaw}}} = (P_2 - P_3)/D$,
$C_{p_{\text{static}}} = (\bar{P} - P_s)/D$ and $C_{p_{\text{total}}} = (P_1 - P_0)/D$,

where $\bar{P} = (P_1 + P_2 + P_3 + P_4)/4$ and $D = (P_1 - \bar{P})$.

The preceeding sets of calibration coefficients were found to be the most convenient and to have high sensitivities.

Calibration Results. The calibration coefficients, at an air velocity of 34 m/s (112 fps) are presented in Figs. 3 to 5, for

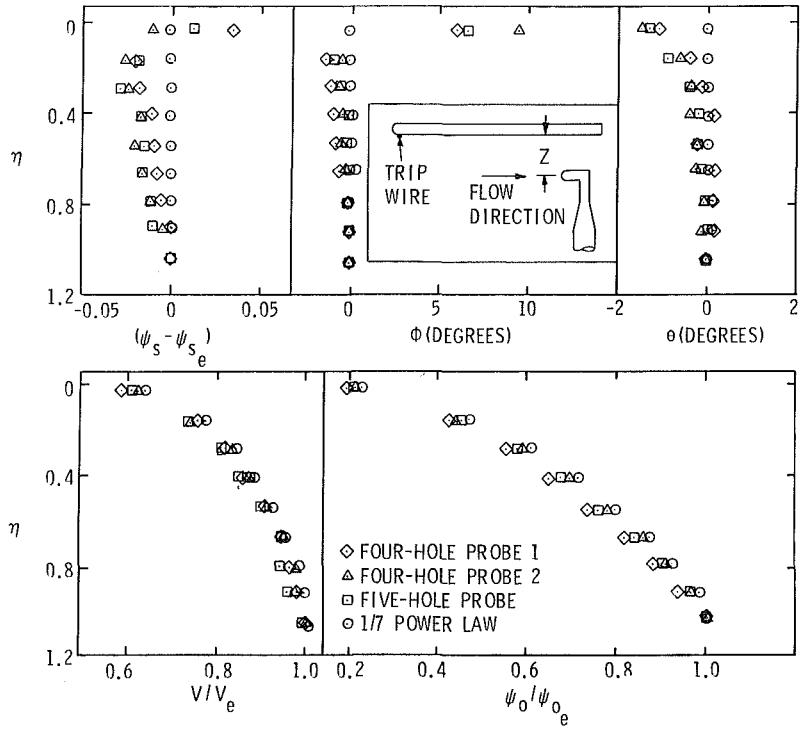

Fig. 7 Comparison of flow properties at X = 0.954 m and 0 deg yaw angle

the four-hole probe 1, four-hole probe 2, and five-hole probe, respectively. They are presented in the following forms:

(i) $C_{p_{\text{pitch}}}$ vs $C_{p_{\text{yaw}}}$ at various α and β

(ii) $C_{p_{\text{static}}}$ vs α at various β

(iii) $C_{p_{\text{total}}}$ vs α at various β

From Figs. 3 to 5, it is evident that the sensivities of the four-hole probes are comparable to those of the five-hole probe. For example, in the region of zero yaw and pitch angles, $C_{p_{\text{yaw}}}$ and $C_{p_{\text{pitch}}}$ have sensivities of 0.070 and 0.055 per degree, respectively, for the four-hole probe 1. For the four-hole probe 2, the corresponding values are 0.038 and 0.072 per degree, respectively. For the five-hole probe, $C_{p_{\text{yaw}}}$ and $C_{p_{\text{pitch}}}$ have sensivities of 0.075 and 0.075 per degree, respectively. The sensivities of $C_{p_{\text{yaw}}}$ and $C_{p_{\text{pitch}}}$ obtained from the proposed method for all probes are slightly higher than the sensivities of the corresponding calibration coefficients of Shepherd's method.

The negligible effect of Reynolds number variation at $\beta = 0$ deg is demonstrated in Fig. 6 for these probes.

Application Technique. By incorporating the appropriate set of the previously defined calibration coefficients the application technique is the same as that presented in reference [2].

A brief comparison of the proposed method with Shepherd's method [1] is in order. In Shepherd's method, the space immediately upstream of the probe tip was divided into six similar zones, to utilize the symmetry of the tip of four-hole probe 1. In each zone, the pressures, in decreasing magnitude, are evaluated. In determining the flow field from the measured pressures, the corresponding set of calibration coefficients has to be used. In the present method, such complexity is avoided, by using the same set of calibration coefficients for every zone.

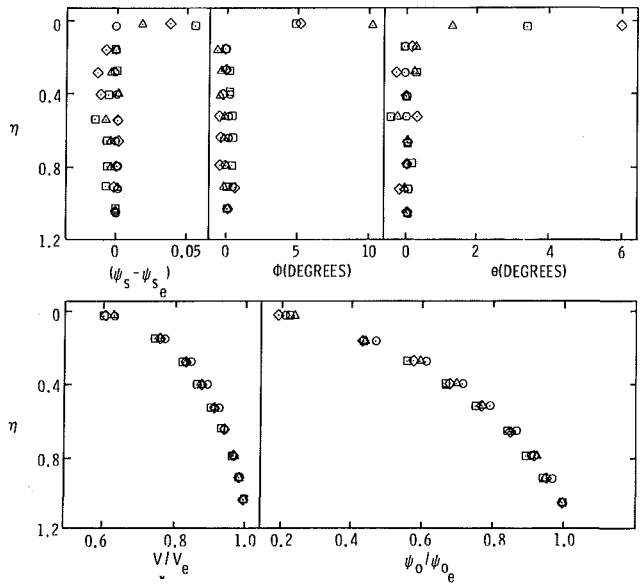

Fig. 8 Comparison of flow properties at X = 0.954 m and 20 deg yaw angle (for legend see Fig. 7)

Application. To determine the accuracy of the interpolation program, the following method was employed for all the probes. The calibration data at three velocities were used as measured data and the calibration coefficients at a velocity of 34 m/s (112 fps) were used in the interpolation programs. By comparing the interpolated values with the measured data the accuracy was determined. From this analysis the following accuracy can be expected for measurements with any of the three probes:

yaw and pitch angles:	± 0.5 degree
velocites:	± 1% of total velocity
static and stagnation pressures:	± 1% of dynamic head based on total velocity

These estimates are valid only when the probes are in uniform and nearly uniform flows. When they are measuring flows, which are affected by errors due to wall vicinity and large velocity gradient (such as boundary layers on a flat plate), the magnitude of errors, especially in pitch angles and static pressures, is larger near the surface. For a five-hole probe used in reference [4], which is similar to that used in this investigation, the maximum errors in pitch angle and static pressure, which occur very near the surface, are less than 3 degrees and 5 percent of dynamic head based on the total velocity, respectively. As the probe moves away from the surface, the errors decrease in magnitude. Beyond two probe diameters, these errors are negligible. The same order of magnitude of errors may be expected for the probes employed in the present investigation. These wall effects are in agreement with those documented by Treaster and Yocum [2].

To further investigate the accuracy of the probe, the probes were employed to measure the turbulent boundary layer on a flat plate, at a distance of 0.954 m (37.5 in.) from the leading edge of a flat plate. A trip wire was attached near the leading edge of the flat plate, to ensure that the boundary layer developed on the flat plate was turbulent. The results from this experiment at 24.4 m/s (80 fps) with the probes oriented at 0° and 20° relative to the flow in the yaw plane are shown in Figures 7 and 8, respectively. The arrangement is shown as an inset in Fig. 7. The resulting data from each probe are compared with theoretical predictions for a turbulent boundary layer, assuming a 1/7 power law for the velocity profile [5].

The following relationships can be derived for a two-dimensional boundary layer on the flat plate, with zero pressure static gradient.

$$\left.\begin{aligned} V/V_e &= \eta^{1/7} \\ \psi_0 - \psi_s &= 2(P_0 - P_s)/\rho V_e^2 \\ &= (V/V_e)^2 = \eta^{2/7} \end{aligned}\right\} \text{for } Z \le \delta$$

$$\left.\begin{aligned} V/V_e &= 1 \\ \psi_0 - \Psi_s &= 1 \end{aligned}\right\} \text{for } Z \ge \delta$$

$$\left.\begin{aligned} \psi_s - \psi_{s_e} &= 0 \\ \text{Flow angle } \theta &= 0° \\ \text{Meridional angle } \phi &= 0° \end{aligned}\right\} \text{for all } Z$$

The calculated boundary layer thickness at the measurement position [5] is 20.2 mm (0.795 in.), which corresponds to 12.1 times the probe diameter.

From the figures, it is evident that the results from all the probes, in the region away from the surface, compare well with the theoretical prediction. Within two probe diameters from the surface, the errors in the static and stagnation pressures, flow and meridional angles, and velocities are considerable due to the wall vicinity effect.

When the probes are at a yaw angle of 20 degrees relative to the flow direction, the errors are of the same magnitude of those when the probes are at zero angle with the flow direction.

Conclusions

The following conclusions are drawn from the present investigation.

1. Because of its simplicity and versatility, the proposed method to determine three-dimensional flow using four-hole probes is very attractive. The same method can be used for four-hole probes of different configuration and five-hole probes with minor modifications.

2. The proposed method is much simpler to use than Shepherd's method [1]. The sensivities of $C_{p_{\text{yaw}}}$ and $C_{p_{\text{pitch}}}$ obtained from the proposed method are slightly higher than sensivities of the corresponding calibration coefficients of Shepherd's method.

3. The results obtained from the probes compare very well with the theoretical predictions, except within two probe diameters from the wall where wall-proximity effects are present.

References

1 Shepherd, I. C., "A Four-Hole Pressure Probe for Fluid Flow Measurements in Three Dimensions," ASME JOURNAL OF FLUIDS ENGINEERING, Vol. 103, No. 4, 1981, pp. 590–594.

2 Treaster, A. L., and Yocum, A. M., "The Calibration and Application of Five-Hole Probes," *ISA Transactions*, Vol. 18, No. 3, pp. 23–24.

3 Lehman, A. F., "The Garfield Thomas Water Tunnel," ORL TM NOrd 16597-56, Sept. 1959.

4 Lakshminarayana, B., and Sitaram, N., "Wall Boundary Layer Development near the Tip Region of an IGV of an Axial Flow Compressor," ASME Paper No. 83-GT-177, 1983.

5 Schlichting, H., *Boundary Layer Theory*, 7th edition, McGraw-Hill, 1979.

Orifice Contraction Coefficient for Inviscid Incompressible Flow

R. D. Grose
InterNorth, Inc.,
Research Center
Omaha, Neb. 68117

The theory for steady flow of an incompressible fluid through an orifice has been semi-empirically established for only certain flow conditions. In this paper, the development of a more rigorous theory for the prediction of the orifice flow contraction effect is presented. This theory is based on the conservation of momentum and mass principles applied to global control volumes for continuum flow. The control volumes are chosen to have a particular geometric construction which is based on certain characteristics of the Navier-Stokes equations for incompressible and, in the limit, inviscid flow. The treatment is restricted to steady incompressible, single phase, single component, inviscid Newtonian flow, but the principles that are developed hold for more general conditions. The resultant equations predict the orifice contraction coefficient as a function of the upstream geometry ratio for both axisymmetric and two-dimensional flow fields. The predicted contraction coefficient values agree with experimental orifice discharge coefficient data without the need for empirical adjustment.

Introduction

The flow of fluids through orifices is of practical importance to industry, especially with regard to flow rate measurement of the fluid being transported. Over the past several decades, various standards have been established for flow measurement methods utilizing orifices so that reliable results could be obtained. It is interesting to note that despite such investigation and standardization, the flow behavior or orifices has been established universally only for certain flow conditions and the relationships between governing variables remains largely empirical. In this work, the theory of orifice flow behavior is expanded and a more detailed mathematical treatment of the representation for the flow conditions in an orifice that exist at very high Reynolds numbers are presented.

The orifice discharge coefficient, C, is conventionally defined to be the ratio of the actual flow rate through an orifice to that predicted by an equation derived from one-dimensional inviscid flow theory. In a previous paper, the author showed that it is possible to represent the orifice discharge coefficient by the product of three independent coefficients termed the *contraction* coefficient, the *viscosity* coefficient, and the *flow profile* coefficient [1]:

$$\dot{\omega} = CA_0\sqrt{2g_c\rho'\Delta p/(1-\lambda)^2} \quad (1a)$$

$$C = C_pC_cC_v \quad (1b)$$

In the previous paper, attention was focused on predicting the *viscosity* coefficient, C_v, which corrects the theoretical equation for streamwise viscous effects. It is the dominant coefficient of the three at extremely low Reynolds numbers ($\mathrm{Re}_o < 16$). In this paper, the focus is on the prediction of the *contraction* coefficient, C_c, which is the dominant coefficient at the other extreme – very high Reynolds numbers ($\mathrm{Re}_o > 10^5$; $\beta < .7$). The contraction coefficient corrects the theoretical equation for the convergence of the flow as it issues from the orifice. A future paper will deal with the profile coefficient, C_p, which tends to be of secondary importance for the standard orifice geometry under common flow conditions, but becomes more important for orifice flows near transition or as the orifice diameter ratio approaches unity. The profile coefficient corrects for wall induced viscous effects on the flow field and as a consequence it usually is the dominant coefficient for flow through pipes, nozzles, venturis, and similar geometries.

The Contraction Coefficient Uncertainty

Determination of the orifice contraction effect has attracted the attention of analysts and experimentalists for many decades. When viewed broadly, the results of these investigations have been in good agreement but, when viewed from the contemporary requirement for high accuracy (e.g., ± 1 percent), especially for metering orifice applications, then a rather large disparity is found to exist.

Early on, analysts were able to show that an orifice in a plane of infinite extent, when fitted with a Borda mouthpiece, has a theoretical discharge coefficient of 0.5 under inviscid-flow conditions due to contraction effects [2]. In inviscid orifice flow, the contraction solely determines the flow field structure so that the *contraction coefficient* and the discharge coefficient are identical. One of the successes of potential flow theory (also inviscid) has been the prediction of the discharge (contraction) coefficient for the two dimensional orifice in an infinite plane (without a mouthpiece) using conformal transformation techniques [3]. This classic result:

$$C_c = \frac{\pi}{\pi+2} = 0.611 \quad \text{(2-d)} \quad (2)$$

Contributed by the Fluids Engineering Division of The American Society of Mechanical Engineers and presented at the Winter Annual Meeting, New Orleans, La., December 9-14, 1985. Manuscript received by the Fluids Engineering Division, March 22, 1983.

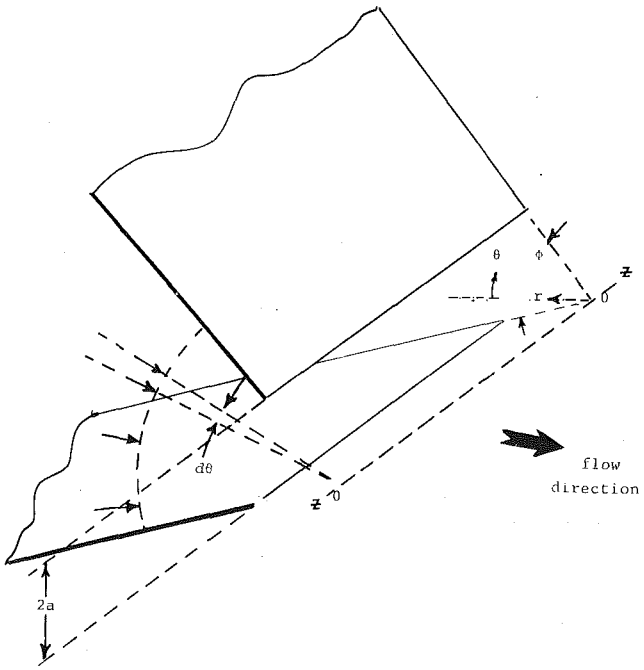

Fig. 1 Two-dimensional orifice flow

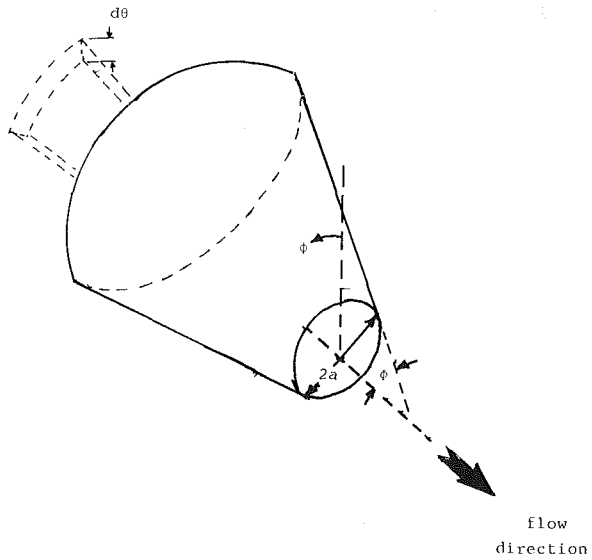

Fig. 2 Axisymmetric orifice flow

is in *good* agreement with experimental orifice discharge coefficient data (better than with the Borda mouthpiece result). On the other hand, there is an extensive body of experimental orifice data taken at high Reynolds numbers for which the discharge coefficient is less than 0.611 [4]. Since, as noted, the classic result is for inviscid flow (i.e., for a Reynolds number indefinitely high), this disparity is somewhat unsettling. Moreover, analysis based on complex numerical schemes have more recently confirmed that the theoretical value for the orifice contraction coefficient for very high Reynolds numbers is indeed less than what conventional potential flow theory predicts [5].

It is also interesting to note that most potential flow theories have been developed for the two-dimensional geometry and not the axisymmetric orifice geometry – the geometry type for which most of the orifice discharge coefficient data have been accumulated. While it has never been proven *in general* that the contraction coefficient is the same for the two flow types, it is possible, in the case of the Borda mouthpiece geometry mentioned previously, to show that the same theoretical result is obtained. In order to shed additional light on this matter, both two-dimensional and axisymmetric contraction coefficient theories are presented in this paper.

Approach

The basic approach uses the well accepted global-control-volume momentum-balance technique, an elementary version of which was used in the Borda mouthpiece orifice theory [6]. In the particular approach used here, the conservation of mass and momentum equations are written for control volumes having non-planar imaginary "surfaces." The basis for this approach can be traced to the Navier-Stokes (N-S) equations. The complete set of N-S equations for the three common coordinate systems are readily found in the literature and are not repeated here.

Consider first the N-S equations in the cylindrical coordinate system suitably simplified by presuming the flow to be time invariant, the density and viscosity to be constant, with body forces nonexistent, and where the flow is invariant for all values of the z coordinate. Under these conditions, the r-component equation is:

$$\rho\left[v_r\frac{\partial v_r}{\partial r}+\frac{v_\theta}{r}\frac{\partial v_r}{\partial \theta}-\frac{{v_\theta}^2}{r}\right]=-\frac{\partial p}{\partial r}+\mu\left[\frac{\partial}{\partial r}\left(\frac{1}{r}\frac{\partial}{\partial r}(rv_r)\right)+\right.$$
$$\left.+\frac{1}{r^2}\frac{\partial^2 v_r}{\partial \theta^2}-\frac{2}{r^2}\frac{\partial v_\theta}{\partial \theta}\right] \quad (3)$$

and the θ-component equation is:

$$\rho\left[v_r\frac{\partial v_\theta}{\partial r}+\frac{v_\theta}{r}\frac{\partial v_\theta}{\partial \theta}-\frac{v_r v_\theta}{r}\right]=-\frac{1}{r}\frac{\partial p}{\partial \theta}+\mu\left[\frac{\partial}{\partial r}\left(\frac{1}{r}\frac{\partial}{\partial r}(rv_\theta)\right)+\right.$$
$$\left.+\frac{1}{r^2}\frac{\partial^2 v_\theta}{\partial \theta^2}+\frac{2}{r^2}\frac{\partial v_r}{\partial \theta}\right] \quad (4)$$

Nomenclature

C = discharge coefficient
C_i = integration constant
C_c = contraction coefficient
C_p = profile coefficient
C_v = viscosity coefficient
D = diameter
ρ = density
v = velocity
r = radius (radial coordinate)
y = normal to the axis coordinate
ω = flow rate
λ = general approach factor
θ = angular coordinate
p = pressure
μ = viscosity
Φ = convergence angle
ϕ = azimuth angle
U = bulk velocity
α = potential surface area ratio (surface to base)
A = area
κ = orifice to upstream channel width ratio = a/b
γ = orifice to upstream area ratio
β = orifice to upstream diameter ratio = $a/b = D_0/D_u$
$\bar{p}_w$ = mean wall pressure
a = orifice half width or radius
b = upstream channel half width or pipe radius
p^0 = stagnation pressure
Re = reynolds number
∇ = differential operator

Subscripts

u = upstream
s = imaginary potential "surface"
d = downstream
o = orifice plane
w = wall (upstream face of the orifice plane)
r = coordinate component
θ = coordinate component

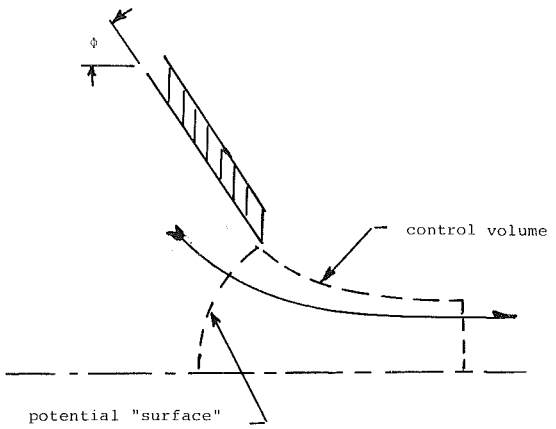

Fig. 3 Control volume

These equations describe the incompressible, constant viscosity flow in a two-dimensional convergent channel as depicted in Fig. 1. If it is asserted that streamlines are coincident with rays emanating from the line origin (equivalent to a sink in potential flow theory) then the velocity components in the θ-direction also disappear (along with the z components). Equations (3) and (4) accordingly simplify to the following set:

$$\rho v_r \frac{\partial v_r}{\partial r} = -\frac{\partial p}{\partial r} + \mu\left[\frac{\partial}{\partial r}\left(\frac{1}{r}\frac{\partial}{\partial r}(rv_r)\right) + \frac{1}{r^2}\frac{\partial^2 v_r}{\partial \theta^2}\right] \tag{5}$$

$$0 = -\frac{1}{r}\frac{\partial p}{\partial \theta} + \mu\left[\frac{2}{r^2}\frac{\partial v_r}{\partial \theta}\right] \tag{6}$$

At very high Reynolds numbers where viscous forces become relatively unimportant, equations (5) and (6) show that the pressure is constant on constant radius circular arcs as depicted in Fig. 1. With pressure constant, it follows that velocity must also be constant on these arcs. For a fixed orifice opening (dimension 2a in Fig. 1), the distance to the origin from the opening becomes infinitely large as the convergence angle, Φ, approaches zero. In the limit, the constant potential circular arcs appear as straight vertical lines normal to the r-coordinate axis. Under these conditions, the r-coordinate is equivalent to the Cartesian x-coordinate and accordingly there is no pressure gradient in the y-direction. (This is in agreement with the commonly held and experimentally verified notion for one-dimensional flow fields.) Also under these conditions equation (5), with viscosity, μ, equal to zero, is identical to the Euler equation or the differential form of the Bernoulli equation.

A similar approach can be taken for the spherical coordinate system equation set. Under the same flow conditions, and with invariance in the azimuthal coordinate, ϕ, this equation set describes the axisymmetric orifice flow situation as depicted in Fig. 2. Again, with the assertion that the streamlines are coincident with rays emanating from the origin as depicted in Fig. 2, the θ-velocity components disappear and the spherical equation set becomes:

$$\rho v_r \frac{\partial v_r}{\partial r} = -\frac{\partial p}{\partial r} + \mu\left[\nabla^2 v_r - \frac{2}{r^2}v_r\right] \tag{7}$$

$$0 = -\frac{1}{r}\frac{\partial p}{\partial \theta} + \mu\frac{2}{r^2}\frac{\partial v_r}{\partial \theta} \tag{8}$$

When viscous effects vanish, equations (7) and (8) show that pressure (and hence velocity) is constant on curved-imaginary-potential "surfaces" of constant radius from the origin, which are, in fact spherical sectors. And again, for a fixed opening size, as the convergence angle, Φ, diminishes, the distance to the origin becomes increasingly large until in the limit for Φ arbitrarily small, the spherical sector approaches a planar circle on which pressure and velocity are constant. This is in concert with inviscid, axisymmetric pipe flow usually described in the cylindrical coordinate system.

The Spherical Sector Control Volume Analysis and the Borda Mouthpiece

A number of useful deductions can be made from a flow analysis which uses the control volume method when it is constructed around the spherical/circular sector potential "surface" concept. For the first of the analyses presented here, the control volume is constructed downstream of the spherical sector, which, for ease of analysis, is located at the exit plane of the orifice. The free streamlines of the jets outer boundary as it issues from the orifice form the control volumes boundaries as depicted in Fig. 3. The downstream closure "surface" is chosen at a point where the streamlines are parallel which, following the previous arguments, causes it to be a planar circle. Figure 3 depicts a generalized orifice geometry formed by an axisymmetric conical body, unlimited in extent, having a convergence angle Φ with respect to the axis of symmetry. When Φ equals $\pi/2$, the conventional (infinite) planar orifice geometry results. For Φ approaching π, the geometry models the Borda mouthpiece orifice[1]. It is important to note that Fig. 3 can represent either the two-dimensional or the axisymmetric flow situation, the latter when viewed in the meridional plane.

Before beginning the analysis in detail, it is well to re-emphasize that the analysis is for inviscid flow even though the N-S equations are fundamental to it. Accordingly, the velocities and pressures are constant on each control volume surface which in turn implies that a "fully slipped" condition prevails on any solid surface and on appropriate control volume "surfaces."

We begin by denoting the ratio of the spherical sector surface area to the orifice opening area by α. Then, referring to Fig. 3, the global-mass-flow-continuity equation for the control volume can be expressed as:

$$\rho U_s \alpha A_0 = \rho U_d A_d \tag{9}$$

Equation (9) can be normalized and rearranged to obtain an equation for the velocity ratio.

$$\frac{U_s}{U_d} = \frac{C_c}{\alpha} \tag{10}$$

where C_c is the downstream normal "surface" to orifice opening area ratio which is conventionally termed the contraction and in this paper is termed the *contraction coefficient*. Utilizing the momentum theorem, the axial force balance on the control volume produces the following equation:

$$\rho U_s^2 A_0 + (p_s - p_d)A_0 - \rho U_d^2 A_d = 0 \tag{11}$$

Dividing through by A_0 and replacing the area ratio by the contraction coefficient yields:

$$\rho U_s^2 + p_s - p_d - \rho U_d^2 C_c = 0 \tag{12}$$

At this point it is convenient to introduce the Bernoulli equation. This equation can be used to relate the stagnation pressure, p^0, to the local velocity and pressure at any point in the flow field, viz:

$$p^0 - p_s = \frac{1}{2}\rho U_s^2 \tag{13}$$

$$p^0 - p_d = \frac{1}{2}\rho U_d^2 \tag{14}$$

[1] Strictly speaking, the Borda mouthpiece has a rounded entrance lip.

Using the mathematical ploy of both adding and subtracting p^0 in equation (12), it is possible to substitute equations (13) and (14) into equation (12) with the result:

$$\frac{1}{2}\rho U_s^2 + \frac{1}{2}\rho U_d^2 - \rho U_d^2 C_c = 0 \tag{15}$$

Dividing equation (15) through by U_d yields:

$$\frac{1}{2}\left(\frac{U_s}{U_d}\right)^2 + \frac{1}{2} - C_c = 0 \tag{16}$$

It is now possible to substitute equation (10) for the velocity ratio in equation (16) to produce:

$$\frac{1}{2}\left(\frac{C_c}{\alpha}\right)^2 - C_c + \frac{1}{2} = 0 \tag{17}$$

Equation (17) is obviously quadratic in the contraction coefficient C_c, and the solution for C_c is given by the quadratic formula, viz:

$$C_c = \alpha^2 - [\alpha^4 - \alpha^2]^{1/2} \tag{18}$$

where only the root for a negative radical is found to have physical significance ($C_c > 1$ has no meaning). Equation (18) is a geometrically general result for any situation in which the theoretical constraints can be satisfied. In particular, given the arguments put forth in the preceding section, it is valid for both two-dimensional and axisymmetric orifice geometries.

Two-Dimensional Solutions and the Wall Pressure Problem. Some interesting two dimensional solutions of equation (18) can be obtained when the area ratio α, is given by the circular relation:

$$\alpha = \frac{\Phi}{\sin\Phi} \quad (\Phi \text{ in radians}) \tag{19}$$

Substitution into equation (18) yields:

$$C_c = \frac{\Phi^2}{\sin^2\Phi} - \left(\frac{\Phi^4}{\sin^4\Phi} - \frac{\Phi^2}{\sin^2\Phi}\right)^{1/2} \tag{20}$$

While equation (20) appears to be indeterminate at $\Phi = 0$ and at $\Phi = \pi$, it can be shown through the application of L'Hospital's rule that as $\Phi \to 0$, equation (20) has the limiting value of unity (a satisfactory result since a contraction is not expected when fluid emanates from a constant width channel). A second application of the rule for $\Phi \to \pi$ yields $C_c = 0.5$, which is in accord with the classical Borda Mouthpiece result (as well it should since the same theoretical approach has been used). However, when the angle $\Phi = \pi/2$, equation (20) predicts the contraction coefficient has a value of 0.5646, a value substantially less than the potential flow prediction of 0.611. But, agreement can be obtained between the two theoretical techniques at $\Phi = \pi/2$ by fitting the orifice with a Borda mouthpiece when the orifice plane is finite in extent. Application of the conformal transformation theory to this two-dimensional Borda mouthpiece geometry yields the following result [7]:

$$C_c = \frac{1}{\kappa} - \left[\frac{1}{\kappa^2} - \frac{1}{\kappa}\right]^{1/2} \tag{21}$$

where κ designates the orifice to upstream channel width ratio. Interestingly enough, not only does this equation predict the same contraction coefficient value at the limit $\kappa = 0$ (e.g., $C_c = 0.5$), but has the same form as equation (18). It can be seen that equation 21 approaches the value of unity as the width ratio, κ, approaches unity. With this cornerstone of agreement established, the next question is – can the control volume theory be made to yield equation (21).

To show that it can, it is first necessary to bring the upstream geometry into the equations through the use of a control volume upstream of, and adjacent to, the previously considered control volume. The situation is depicted in Fig. 4.

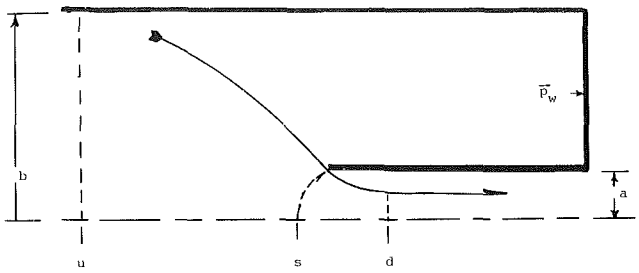

Fig. 4 Borda mouthpiece geometry

The upstream control volume is used to obtain the constraint for the area ratio, α, instead of equation (19), since equation (18) retains its validity. The continuity theorem applied to this control volume yields:

$$\rho U_u A_u = \rho U_s A_s \tag{22}$$

which, upon rearrangement, can be expressed in analogy to equation (16) as:

$$\frac{U_u}{U_s} = \alpha\gamma \tag{23}$$

where γ is the orifice-opening-to-upstream-conduit area ratio. Again using the momentum theorem, an axial force balance on the upstream control volume produces the following equation:

$$\rho U_u^2 A_u + p_u A_u - \bar{p}_w (A_u - A_0) - p_s A_0 - \rho U_s^2 A_0 = 0 \tag{24}$$

where $\bar{p}_w$ is the average area (area weighted mean) pressure acting on the end closure surface as shown in Fig. 4. Dividing equation (24) through by the upstream area, A_u, and again using γ to represent the area ratios thus formed, produces:

$$\rho U_u^2 + p_u - \bar{p}_w(1-\gamma) - p_s\gamma - \rho U_s^2\gamma = 0 \tag{25}$$

Once again simplification can be gained by the addition and subtraction of the stagnation pressure and a substitution of the Bernoulli equation, followed by the appropriate nondimensionalization. The result of these operations is:

$$\frac{U_u^2}{U_s} - \gamma + \left[\frac{p^0 - \bar{p}_w}{p^0 - p_s}\right](1-\gamma) = 0 \tag{26}$$

Substitution of equation (23) into equation (26) and solving for the area ratio, α, produces:

$$\alpha^2 = \frac{1}{\gamma} - \frac{(1-\gamma)}{\gamma^2}\left[\frac{p^0 - \bar{p}_w}{p^0 - p_s}\right] \tag{27}$$

Equation (27), like equation (18), is a geometrically general result. For the two dimensional case, γ is replaced by the width ratio, κ. With this replacement, and substituting equation (27) into equation (18), and comparing the resultant equation to equation (21), it can be seen that the two equations from the two different theories are identical if, and only if, the mean wall pressure, $\bar{p}_w$, is equal to the stagnation pressure, p^0. The important point about this finding is that agreement between control volume theory and potential flow theory can be obtained when pressure distributions on relevant surfaces are made the same for both.

The Elliptical Theorem and the Wall Pressure Postulate

Of special importance to this paper is the fact that equation (27), with $\bar{p}_w = p^0$, shows that the shape of the potential surface between the upstream and downstream control volumes is determined by the upstream area ratio. As κ approaches unity so does the "surface" area ratio, α, and this can occur only through a distortion of the "surface" shape from a spherical or circular configuration. Since the surface is considered a true potential, it must be normal to flow vectors at the orifice lip, which vectors are parallel to the orifice plane at that point. An elementary geometric construct which

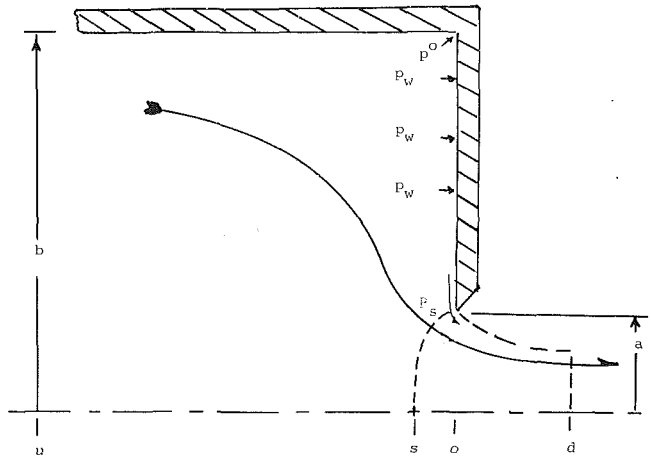

Fig. 5 Orifice with finite upstream geometry

satisfies these conditions is the ellipse. Accordingly, it is postulated that the potential surface is either an ellipse for two-dimensional orifices or an ellipsoid for circular orifices. The surface area to base area for both can be shown to be a function only of the eccentricity. In this light the eccentricity of the potential surface is related to the pressure distribution on the adjacent orifice plane. The question now arises as to the correct theoretical description of the orifice plane pressure distribution and the resultant mean pressure.

Both the spherical/circular sector control volume and the potential flow theories can provide clues to the nature of the pressure distribution. Returning first to equation (19) (the two dimensional circular sector area ratio equation); for the conventional orifice case, $\Phi = \pi/2$, this equation yields an α^2 value of $\pi^2/4$. Now equation (27), with $\gamma = \kappa$, will also yield this result if the mean pressure difference ratio is given by the following expression:

$$\frac{p^0 - \bar{p}_w}{p^0 - p_s} = \left[\frac{\pi^2}{4}\kappa - 1\right]\left[\frac{\kappa}{\kappa - 1}\right] \tag{28}$$

Next a similar expression can be obtained from the potential flow theory by first inverting equation (17) to obtain an expression for α in terms of the contraction coefficient. Equation (1) can be substituted into the resulting relation and upon comparison to equation (27), agreement will result if the mean pressure difference ratio is given by:

$$\frac{p^0 - \bar{p}_w}{p^0 - p_s} = \left[\frac{\pi^2 \kappa}{\pi^2 - 4} - 1\right]\left[\frac{\kappa}{\kappa - 1}\right] \tag{29}$$

Equations (28) and (29) are quite similar and it is interesting to note that both are functionally dependent upon the upstream width ratio, κ, and that both predict the mean pressure to be the stagnation pressure when κ is zero. Next we turn our attention to developing an alternative representation for the pressure distribution, one which presents the distribution explicitly rather than as a mean.

Wall Pressure Distribution. The potential surface construct eases the representation of the orifice plane pressure distribution because it provides a means for conceptualizing the pressure "discontinuity" which exists at the orifice lip. As shown in Fig. 5, the fluid streaming along the wall passes from the pressure p_s, at the juncture of the lip and "surface," to the downstream pressure, p_d, via a sudden expansion. The wall pressure distribution upstream of the orifice lip is based on the N-S equations in the following manner. Referring to Fig. 1, for a given streamtube of width $d\theta$, the flow tube cross-sectional area must vary in proportion to r for the two-dimensional case (by analogy, in proportion to y for $\Phi = \pi/2$). Flow continuity requires that:

$$\frac{U}{U_s} = \frac{r_s}{r} \tag{30}$$

and substituting into the integral form of equation (5) with $\mu = 0$ yields:

$$p_w = \frac{\rho U_s^2}{2}\left(\frac{r_s}{r}\right)^2 + C_i \tag{31}$$

At the lip, for $\Phi = \pi/2$; $r = r_s = y_0 = a$; $p_w = p_s$; and thus

$$p_s = \frac{\rho U_s^2}{2} + C_i \tag{32}$$

By analogy to the Bernoulli equation used earlier, it follows that the integration constant C_i is identical to the stagnation pressure p^0. Using this fact and rearranging equation (31), one can obtain the following expression for the pressure distribution:

$$\frac{p^0 - p_w}{p^0 - p_s} = \left(\frac{a}{y}\right)^2 \tag{33}$$

One can also show that if equation (33) is used in the integral for the wall pressure force in an axial force balance on the upstream control volume for $\kappa = 0$, that the trivial result $0 = 0$ is obtained. This meaningless identity can be avoided by considering the finite geometry situation (i.e., $\kappa \neq 0$), and then the orifice in an infinite plane can be treated as a limiting condition. Further, equations (28) and (29) indicate that a geometric variable should be found in the pressure distribution equation. The satisfaction of these requirements is accomplished by the introduction of a wall pressure distribution postulate.

Various inviscid fluid-dynamic theories indicate that a stagnation pressure condition is reached at the apex of a right angle turn [8]. It is hypothesized here that such a stagnation condition occurs in orifice flow at the juncture of the orifice plane and the upstream conduit as shown in Fig. 5. It is further conjectured that the pressure monotonically decreases from this value to the lip pressure. A formal derivation of an equation possessing these attributes is not attempted here; rather equation (33) is modified to yield these characteristics through the inclusion of κ terms, in a way suggested by equations (28), (29) and (33):

$$\frac{p^0 - p_w}{p^0 - p_s} = \left[\left(\frac{a}{y}\right)^2 - \kappa^2\right]\left[\frac{1}{1 - \kappa^2}\right] \tag{34}$$

This postulated function retains the exponential pressure distribution characteristic while satisfying the boundary conditions at $y = a$ and $y = b$. To re-emphasize, this postulated function must be considered a first approximation to an exact potential flow (nonviscous) solution, presumably nonexistent at this time. As a consequence, the use of equation (34) can only be justified by the fact that meaningful results are obtained when it is used in the control volume force balance.

The derivation of the upstream control volume force balance equation is next repeated using an integral for the orifice wall pressure force contribution:

$$\rho U_u^2 b + p_u b - \int_a^b p_w dy - p_s a - \rho U_s^2 a = 0 \tag{35}$$

The postulated pressure distribution relation, equation (34), can be utilized in equation (35) if appropriate algebraic manipulations are performed. Performing these manipulations and nondimensionalizing the resultant equation produces:

$$\left(\frac{U_u}{U_s}\right)^2 + \frac{1}{b}\int_a^b \frac{p^0 - p_w}{p^0 - p_s}\, dy - \kappa = 0 \tag{36}$$

Equation (36) is now of the form that allows the substitution of equation (34). Making this substitution and performing the integration results in the following equation:

$$\left(\frac{U_u}{U_s}\right)^2 \frac{1}{\kappa} = 1 + \frac{1-2\kappa+\kappa^2}{1-\kappa} \tag{37}$$

Substituting equation (23) into equation (37) and solving for the "surface" area ratio, α, yields:

$$\alpha^2 = \frac{2}{1+\kappa} \tag{38}$$

Equation (38) is remarkably simple and obviously satisfies the constraint of no contraction at $\kappa = 1$. Moreover, at $\kappa = 0$, $\alpha^2 = 2$. The corresponding value for the contraction coefficient, C_c from equation (17), is 0.5858. These results are recapitulated in Table 1 which shows the similarities between the three theoretical approaches.

Like the classic potential flow theory result, the elliptical theory shows the contraction coefficient to be independent of fluid-dynamic quantities (e.g., pressure ratio). Unlike the classical theory, however, it shows the coefficient to be dependent on the geometry.

Axisymmetric Orifice Geometry

Equations (18) and (27) are valid for the axisymmetric orifice geometry as well as the two dimensional geometry. Differences arise in the representation for the pressure distribution and hence the area ratio for the potential "surface." If, in the axisymmetric case, it is presumed the surface is a spherical sector, then it can be shown that the area ratio is given by:

$$\alpha = \frac{2}{\sin^2\Phi} - \frac{2}{\sin\Phi\tan\Phi} \tag{39}$$

Interestingly enough, equation (39) when substituted into (18) yields the same value for the contraction coefficient at $\Phi = 0$ and $\Phi = \pi$ as does the two-dimensional equation; namely, 1.0 and 0.5, respectively. However, at $\Phi = \pi/2$, a value of 0.5359 is obtained which is not only different from the two-dimensional theoretical value, but compares even less well with experimental values.

Unfortunately, there does not appear to have been a conformal transformation theory developed for the axisymmetric orifice with which to compare. However it is possible to develop an analogous elliptical theory using a similar pressure distribution postulate. To do this we return to Fig. 2 and the simplified N-S equations.

The differential surface area of a spherical surface sector annulus is given by:

$$dA = 2\pi r^2 d\theta \tag{40}$$

which, by analogy to the development used previously, results in the following expression for the pressure difference ratio:

$$\frac{p^0 - p_w}{p^0 - p_s} = \left(\frac{r_s}{r}\right)^4 \tag{41}$$

It also can be shown that the use of equation (41) in the integral term of the upstream control volume force balance equation for the orifice in a infinite plane results in the same trivial identity, $0 = 0$, so that once again use must be made of a finite upstream geometry. Presuming the existence of the corner stagnation pressure, the analogous expression for the postulated pressure distribution is:

$$\frac{p^0 - p_w}{p^0 - p_s} = \left[\left(\frac{r_0}{r}\right)^4 - \beta^4\right]\left[\frac{1}{1-\beta^4}\right] \tag{42}$$

Using this relation and following a development parallel to the two-dimensional analysis, it can be shown that the following equation is obtained:

Table 1 Comparison of two-dimensional orifice theories infinite orifice plane-$\kappa = 0$

	"Surface" area ratio	Contraction coefficient
Potential flow theory	$\alpha^2 = \frac{\pi^2}{\pi^2 - 4} = 1.6815$	0.611
Circular arc theory	$\alpha^2 = \frac{\pi^2}{4} = 2.467$	0.5646
Elliptical theory	$\alpha^2 = \frac{2}{1+\kappa} = 2(@\kappa = 0)$	0.5858

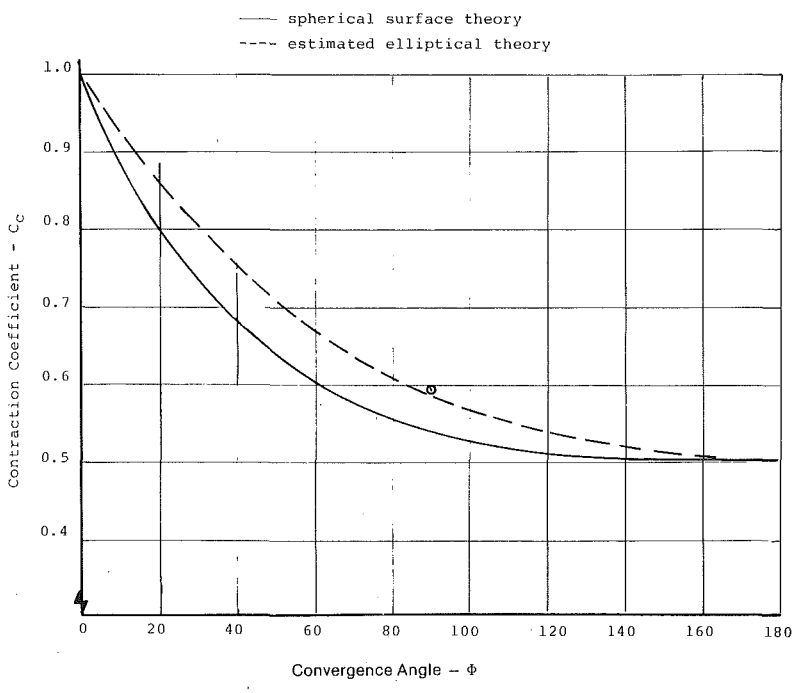

Fig. 6 Inviscid axisymmetric flow contraction coefficient

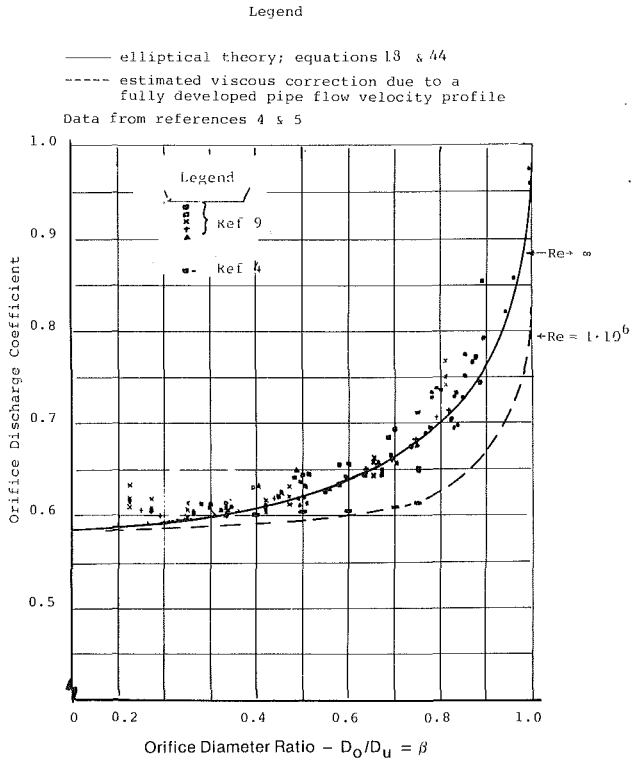

Fig. 7 Comparison of axisymmetic orifice discharge coefficient data with inviscid elliptical contraction coefficient theory

$$\left(\frac{U_u}{U_s}\right)^2 \frac{1}{\beta^2} = 1 + \frac{1-2\beta^2+\beta^4}{1-\beta^4} \tag{43}$$

Substituting the velocity ratio expression derived from the flow continuity equation, equation (23), with $\gamma=\beta^2$; and solving for the surface area ratio results in the following expression:

$$\alpha^2 = \frac{2}{1+\beta^2} \tag{44}$$

which is of the same algebraic form as the equation for the two-dimensional orifice geometry; and more importantly, at $\beta=0$ yields the same value for the area ratio, α. In other words, this theory yields the same value for the contraction coefficient for the orifice in an infinite plane for both the two-dimensional and axisymmetric geometries, even though the equations are different. This value, $C_c=0.5858$ is in excellent agreement with published contraction coefficient values determined by numerical techniques for the circular orifice [9]. It also agrees very well with extrapolated experimental orifice discharge coefficient data [10]. This theory shows that for the same values for the diameter and width ratios, β and κ respectively, different contraction coefficient values will result except at the limits 0 and 1. That is, analgous geometries in axisymmetric and two-dimensional orifice flows do not have, in general, the same contraction coefficient. On the basis of area ratio, however, the contraction coefficient values are identical.

Comparison With Orifice Data

It must be recognized at the outset that experimental data do not exist with which the present inviscid orifice contraction theory can be compared directly since all such data currently available reflect viscous influences to some extent. There is no known method for separating the viscous effects from contraction effects. Viscous influences can only be minimized by choosing discharge coefficient data which have been obtained at the highest possible Reynolds number.

The comparison is done two ways – first from the standpoint of a variation in the convergence angle, Φ, for an unbounded diameter ratio (e.g., $\beta=0$) and for a variation in the diameter ratio, β, for the flat plate orifice (e.g., $\Phi=\pi/2$).

Using equations (18) and (39), a characteristic curve can be constructed which displays the contraction coefficient as a function of the convergence angle, Φ. This characteristic curve is presented in Fig. 6 as the solid line. This equation set and the resultant curve are for the spherical sector theorem; the only one developed with sufficient generality for this display. The dashed curve on the figure is the *expected* characteristic for the elliptical "surface" theory once that theory is fully developed. The dashed curve passes through a computed data point at the only convergence angle for which a computation can be made – at $\Phi=\pi/2$. The dashed curve connects this point to the known limiting conditions. A representative experimental data point is also shown which is in excellent agreement with the dashed curve [4].

Figure 7 presents the variation of the contraction coefficient as a function of the orifice diameter ratio, β, using the elliptical theorem – equations (18) and (44). A comparison with representative orifice discharge coefficient data is also presented in the figure. The solid curve gives the theoretical contraction coefficient variation. Interestingly enough, the agreement is excellent between the theory and rather old orifice data, presumably obtained without due regard for upstream influences [10]. On the other hand, comparison with more recent, high Reynolds number, orifice discharge coefficient data, taken under experimental conditions where the upstream flow conditions were fully developed, is not as good (the lower valued bar symbols on the figure) [4]. For β values less than 0.4, the agreement with the fully developed flow data is excellent, however, a gradually increasing disparity is evident for β values greater than 0.4. Since the contraction must be zero (e.g., $C_c=1.0$) at the upper limit, $\beta=1$, the low experimental values at the higher β conditions must reflect viscous effects on the discharge coefficient – that is, profile effects. It can be shown theoretically that the profile coefficient for fully developed pipe flow is about 0.85 at high Reynolds numbers ($\mathrm{Re}\simeq 1.10^6$) [11]. The dashed curve in Fig. 7 joins this value with the predicted contraction coefficient values at the lower β ratios to show that a much better prediction of the orifice discharge coefficient would be obtained with a theory that combines both effects simultaneously. One could also expect the occurrence of second order viscous effects on the contraction coefficient itself at lower Reynolds numbers. Either this viscous effect, or the lack of long entrance sections upstream of the orifice could account for the agreement between the theory and the older data at the higher β values. Theoretical treatment of these velocity profile effects is in progress.

Comparison With Empirical Equations

There are several strictly empirical equations for predicting the discharge coefficient of flat plate orifices at relatively high Reynolds numbers. A fairly recent paper by Miller summarizes the agreement between these equations and applicable data [12]. These equations are currently undergoing review and recorrelation by a number of organizations. It is possible to compare them to the inviscid elliptical theory by dropping all Reynolds number containing terms. Further the elliptical theory shows that the inviscid contraction coefficient, and hence the inviscid discharge coefficient, is independent of all geometric factors save the upstream diameter ratio. Logically, it must also be independent of instrumentation location used for the determination of the inviscid discharge velocity (which in reality is the purpose of the Δp term in the orifice equation). Accordingly these types of terms have also been arbitrarily dropped from the empirical equations. With these modifications, the Stolz equations is:

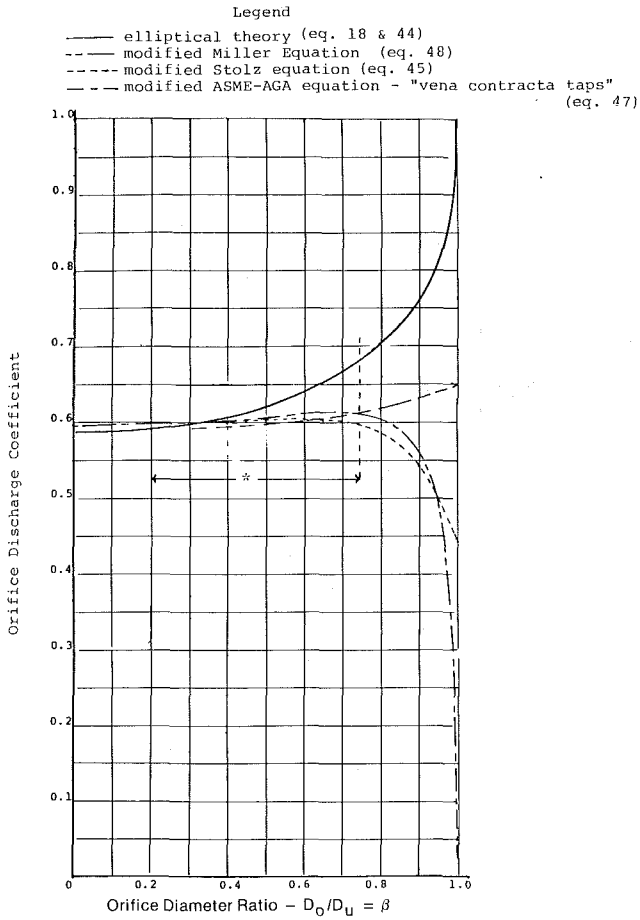

Fig. 8 Comparison of elliptical theory with modified empirical formulas for discharge coefficient as Re→∞.* Stated range applicability for empirical equations

$$C = 0.5959 + 0.0312\beta^2 - 0.184\beta^8 \quad \mathrm{Re}\to\infty \tag{45}$$

range of applicability $.15 < \beta < .75$

All terms in the ASME-AGA "flange tap" equation for the orifice discharge coefficient contain dimensionally dependent terms and hence this equation is too flawed for this comparison. However, the ASME-AGA "1-D, 1/2-D" and "vena-contracta" equations for the orifice discharge coefficient can be modified to yield:

$$\left.\begin{aligned} C &= [0.6014 + 0.3760(\beta^4 + 1.5\beta^{16})](1-\beta^4)^{1/2} \\ &\quad \text{"1 - D, ½ - D taps"} \end{aligned}\right\} \mathrm{Re}\to\infty \tag{46}$$

$$\left.\begin{aligned} C &= [0.5992 + 0.4242(\beta^4 + 1.25\beta^{16})](1-\beta^4)^{1/2} \\ &\quad \text{"vena contracta taps"} \\ &\quad \text{range of applicability } .15 < \beta < .75 \end{aligned}\right\} \tag{47}$$

Likewise, the Miller equation can be modified by dropping the dimensionally dependent terms to give:

$$C = 0.5812 + 0.0933\beta - 0.1929\beta^2 + 0.1641\beta^3 \quad \mathrm{Re}\to\infty \tag{48}$$

range of applicability $.15 < \beta < .75$

These modified empirical equations are compared to the elliptical theory contraction coefficient prediction in Fig. 8. Over the range of stated applicability, the empirical equations agree with each other quite well, but depart from the theoretical equation when β is greater than 0.4. This departure is probably a consequence of the fact that the empirical equations do not account for the demise of profile effects as $\mathrm{Re}\to\infty$.

Outside the stated range of applicability the empirical equations and the theory agree quite well for β less than 0.2. In fact the Miller equation and the theory agree to two significant figures (0.5858 versus 0.5812) at $\beta = 0$. However for β values greater than 0.7, the equations diverge from the theory and from each other as well. Only the Miller equation tends to the theoretically correct value of unity at $\beta = 1$. The ASME-AGA equation is the furthest off at a value of 0. This result has apparently come about from a misunderstanding of the $(1-\beta^4)^{1/2}$ term which appears in the inviscid flow theoretical orifice equation. It is not necessary for the discharge coefficient to go to zero as the diameter ratio goes to unity to keep the predicted flow rate finite since, for viscid flow, the pressure drop term, Δp, goes to zero faster than the $(1-\beta^4)^{1/2}$ term. A detailed discussion of this misunderstanding and of the theoretical difficulty which exists with the appearance of dimensional and instrumentational factors in the empirical equations, is outside the scope of this paper.

Conclusion

This paper has presented the development of a theory for predicting the orifice contraction coefficient as a function of the upstream area ratio. It also sets the frame work for introducing the effect of the convergence angle on the contraction coefficient. At present, the theory has been developed only for incompressible, inviscid flow for concentric circular and two dimensional orifices. The theory shows that the same contraction coefficient values are obtained for axisymmetric and two-dimensional orifice flows at the geometry limits of unity and zero, but not elsewhere (when the contraction coefficient is calculated as a function of the diameter ratio or the width ratio). The calculated value of 0.5858 for the contraction coefficient at a diameter ratio of zero agrees with extrapolated experimental data and with numerical calculations as well. Development of a theory for the profile coefficient and expansion of the contraction coefficient theory to include Reynolds number effects and density changes would provide the means for predicting the orifice discharge coefficient over a wide range of conditions. Work in this direction is in progress.

Acknowledgment

This work has been supported solely by InterNorth, Inc., Research Division.

References

1 Grose, R. D., "Orifice Flow at Low Reynolds Number," *Journal of Pipelines*, Vol. 3, 1983, pp. 207–214.

2 Streeter, V. L., *Fluid Mechanics*, 3rd Edition, McGraw-Hill, 1962.

3 Milne-Thompson, L. M., *Theoretical Hydrodynamics*, 3rd Edition, McMillan Co., 1957.

4 The American Society of Mechanical Engineers, *Fluid Meters—Their Theory and Application*, 6th Edition, 1971.

5 Flugge, S., "Encyclopedia of Physics," Vol. 9, *Fluid Dynamics III*, Springer-Verlag, 1960.

6 Benedict, R. P., "Generalized Contraction Coefficient of an Orifice for Subsonic and Supercritical Flows," ASME *Journal of Basic Engineering*, June 1971, p. 99.

7 *Theoretical Hydrodynamics*, p. 299, op. cit.

8 Goldstein, S., *Modern Developments in Fluid Dynamics*, Vols. 1 and 2, Dover Publishing Co., 1965.

9 Encyclopedia of Physics, op. cit., pp. 424–425.

10 Encyclopedia of Physics, op. cit., pp. 318–319.

11 Schlichting, H., *Boundary-Layer Theory*, McGraw-Hill, 6th Edition, 1968.

12 Miller, R. W., "The Stolz and the ASME-AGA Orifice Equations Compared to Laboratory Data," ASME JOURNAL OF FLUIDS ENGINEERING, Vol. 101, Sept. 1979, p. 483.

Calculated Turbulent-Flow Meter Factors for Nondiametral Paths Used in Ultrasonic Flowmeters

A. M. Lynnworth

L. C. Lynnworth

Panametrics, Inc.,
Waltham, Mass. 02254

In applying the ultrasonic contrapropagation method to the measurement of flow in highly attenuating fluids, or to fluids in conduits having only limited access, it is sometimes necessary to interrogate along a path other than the conventional tilted diameter or midradius chordal paths. The meter factor K, which relates the path average to the area-averaged flow velocity, is derived from Nikuradse profiles for several new paths. The results enable one to locate transducers so that for the chosen type of path, K will be (a) minimally dependent on Re, and/or (b) approximately equal to unity, or (c) represented by a simple function of Re. For smooth-wall steady flow conditions, the error in the calculated K's is estimated as ±2 percent ± the effect due to the disturbance of Nikuradse profiles by the transducers.

1 Introduction

The ultrasonic contrapropagation method of measuring the flow velocity of liquids or gases is based on the difference in transit time upstream versus downstream [1, 2]. The velocity calculated from the transit times t_1 and t_2 is the harmonic mean velocity averaged over the interrogation path. For flow velocities small compared to the sound speed, the path-averaged flow velocity is:

$$u_p = c^2 \Delta t / 2L \tag{1}$$

where c = sound speed (assumed constant over the path, in the present work), $\Delta t = t_2 - t_1$, and L = axial projection of the interrogation path in the flowing fluid Ordinarily the path is along a tilted diameter.

The path average is related to the area-averaged flow velocity $\bar{u}$ by the meter factor K:

$$K = \bar{u}/u_p \tag{2}$$

Consider conventional interrogation of Newtonian fluid in a smooth-wall round pipe, along a tilted diameter path. If the beam diameter d is small compared to the conduit inside diameter D, $K = 0.750$ for laminar flow and

$$K = 1/(1.12 - 0.011 \log \mathrm{Re}) \tag{3}$$

for turbulent steady flow, where Re is the Reynolds number [3].

In the past, to avoid sensitivity to flow profile, paths other than the tilted diameter have been suggested or used. For example, in the four-chord Gaussian quadrature method, paths are located in planes having normalized distances from the axis $X_k = \pm 0.8611$ and ± 0.3399 [4, 5]. Paths at or near the midradius chord [6, 7] are useful if the profile is known to be axisymmetric.

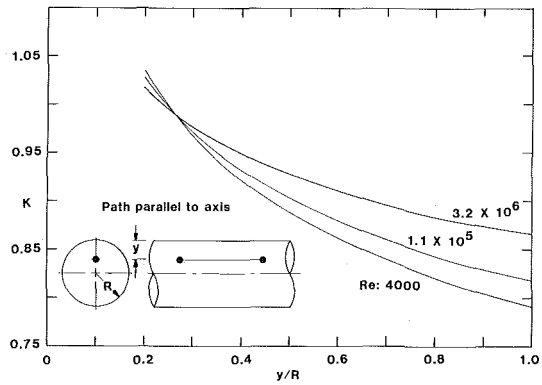

Fig. 1 Meter factor K versus normalized distance from wall y/R, for ultrasonic interrogation path parallel to axis, for Reynolds numbers Re = 4000, 1.1 × 10^5 and 3.2 × 10^6

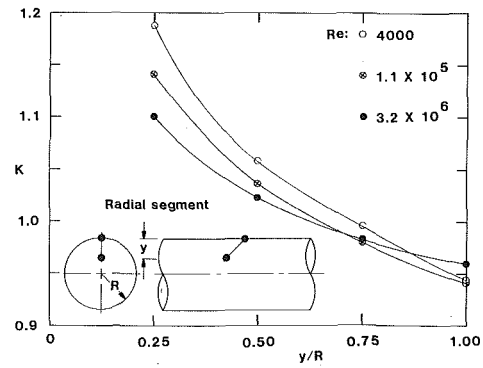

Fig. 2 Meter factor K versus normalized distance from wall y/R at which the in-the-flowstream transducer is located, for ultrasonic interrogation path along a tilted radial segment from wall to y, for Re as in Fig. 1

Contributed by the Fluids Engineering Division for publication in the JOURNAL OF FLUIDS ENGINEERING. Manuscript received by the Fluids Engineering Division, November 28, 1983.

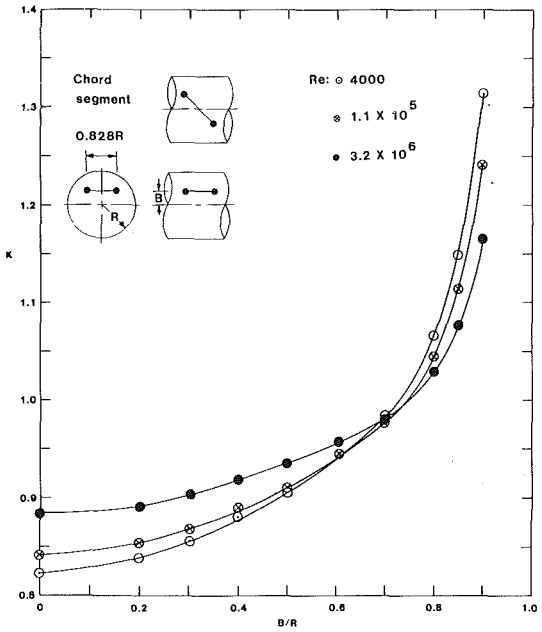

Fig. 3 Meter factor K for symmetrical chord segment of projected length 0.828R representing projection of ultrasonic interrogation path that is skewed with respect to pipe axis, and located in a plane at the normalized distance B/R from the axis, for Re as in Fig. 1

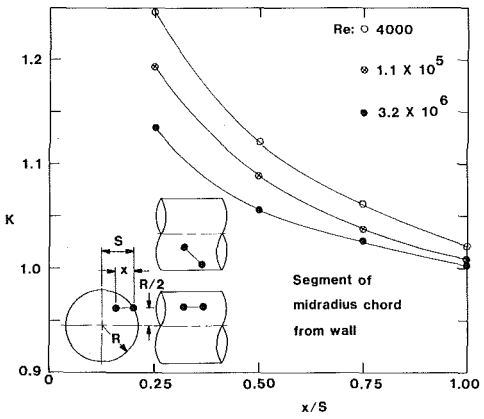

Fig. 4 Meter factor K for ultrasonic interrogation path in midradius plane, along segment of midradius chord, with path skewed to pipe axis, and of projected length x, for Re as in Fig. 1. S = 0.866R, which is half the length of one leg of the projected inscribed equilateral triangle formed by three midradius chords.

The present calculations are motivated by the need to predict K for turbulent profiles, when fluid attenuation, phase (or cycle) ambiguity or restricted access lead one to consider special paths which can be substantially shorter than the conventional tilted diameter path. The insets in Figs. 1–4 define the end points of four special paths. Figure 5 includes perspective views which make it easier to visualize how such special paths are utilized in practical applications, for example, in refinery flare stack installations [11].

2 Method of Calculation

In principle, the calculation of K would seem fairly straightforward, since the normalized velocity is usually represented by a simple power law, $u/U_0 = (y/R)^{1/n}$, where U_0 = velocity on axis, u = velocity at the distance y from the wall, R = pipe radius, and $6 \leq n \leq 10$ for $4000 \leq \mathrm{Re} \leq 3.24 \times 10^6$ [8]. For points at or near the wall, however, this power law is inadequate, as previous writers have pointed out, and as is evident from the profile data plots given in Nikuradse's

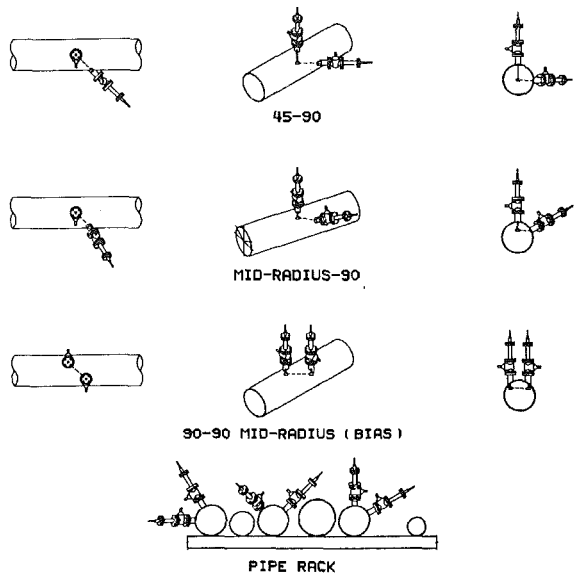

Fig. 5 Practical implementations of some of the special paths of the present work. Illustration courtesy Exxon Company USA, Baytown, Texas [11].

1932 paper [9] or in more readily available translated reproductions [8].

For points at or very near the wall, and some other points, we found that a fifth degree polynomial [10] provides a better representation of Nikuradse's data [9] than the power law. Tables 1–3 list normalized velocities as a function of y/R for Re = 4000, 1.05×10^5, and 3.24×10^6, respectively. In Tables 1–3, the N column lists normalized values of the velocities measured by Nikuradse. The PN column lists the values generated by the fifth degree polynomial at the particular y/R (polynomial coefficients are listed in Table 4), and the PL column lists the power law values. At each y/R, the PN or PL value closest to Nikuradse's is marked with an asterisk (*); this information is required as explained next.

In order to find the average velocity over each given path, (other than paths parallel to the axis, Fig. 1) y/R was first calculated for eleven equally-spaced points along the path. A normalized velocity was then calculated at each y/R. If the y/R value was one used by Nikuradse, for example, y/R = 0.07, then the velocity value in the N column was chosen. Otherwise, either the PN or PL equation was used, depending on which yielded a velocity closest to Nikuradse's data at the nearest y/R that he used. For example, to find the velocity for y/R = 0.076 when Re = 4000 (Table 1), we chose, according to the above criterion, the power law.

For Fig. 1, the normalized velocities calculated for Re = 4000, 1.05×10^5, and 3.24×10^6 were converted to K using

$$K = (\bar{u}/U_0)/(u_p/U_0) = \bar{u}/u_p \tag{4}$$

In this case (paths parallel to axis) we used only the PL, not the PN, to determine $\bar{u}/U_0$ [8]:

$$\bar{u}/U_0 = 2n^2/(n+1)(2n+1) \tag{5}$$

Using this equation, the ratio of mean to maximum velocity was determined for the three values of Re we use as examples, and the numerial results appear in Table 5 next to the K = 1.0000 entries.

The choice of the power law (PL) to represent the Nikuradse profile is accurate enough to explain the calculation of K for paths parallel to the pipe axis. Even though a polynomial (PN) can fit Nikuradse's data better than the PL near the wall, this advantage does not appear important in this particular example, for the following

reason. In tests in 250 mm diameter pipe with 19 mm diameter transducers spaced about 300 mm apart (see below) it was found that the dominant error in calculating K for paths parallel to the axis was due to perturbation of the profile by the transducers themselves. Furthermore, the potential advantage of the *PN* over the *PL* is right near the wall. Generally, this would not be a wise location because of the profile gradient; the influence of wall roughness on the actual profile, in practical piping situations; and the somewhat unpredictable modulation of the sound beam by reflections from the pipe wall.

For the other paths considered in this paper, Figs. 2–4, depending on Re and y/R, the *PN* offers some slight advantage in calculating K accurately. This can be seen in Tables 1–3 by comparing *PL* and *PN* values with Nikuradse's data. The asterisked *PN* values are typically about 1 to 2 percent closer to Nikuradse's data than the corresponding nonasterisked *PL* values. Near the wall, the *PN* advantage is more obvious. Note, however, that asterisked *PL* values are closer to Nikuradse's data than the corresponding nonasterisked *PN* values.

The question of how closely Nikuradse's smooth-wall steady flow data represent actual profiles (rough walls and/or unsteady flow) is not treated here.

Table 1 Comparison of *N*, *PN*, and *PL* for Re = 4000

y/R	N	PN	PL
0.00	0.297	0.368*	0.000
.01	.411	.416*	.464
.02	.514	.461	.521*
.04	.584	.539	.585*
.07	.652	.630	.642*
.10	.690	.697*	.681
.15	.737	.767	.729*
.20	.774	.803	.765*
.30	.831	.830*	.818
.40	.874	.852	.858*
.50	.906	.891	.891*
.60	.932	.938*	.918
.70	.954	.973	.942*
.80	.975	.981*	.963
.90	.990	.975	.983*
.96	.997	.987	.993*
.98	.999	.998*	.997*
1.00	1.000	1.014	1.000*

*Asterisks explained in text.

Table 2 Comparison of *N*, *PN*, and *PL* for Re = 1.05×10^5

y/R	N	PN	PL
0.00	0.423	0.482*	0.000
.01	.535	.520*	.518
.02	.581	.555	.572*
.04	.649	.616	.631*
.07	.703	.688*	.684
.10	.739	.742*	.720
.15	.778	.800	.763*
.20	.809	.831	.795*
.30	.861	.859*	.842
.40	.898	.882*	.877
.50	.925	.915*	.906
.60	.950	.953*	.930
.70	.967	.981*	.950
.80	.981	.987*	.969
.90	.994	.982	.985*
.96	.998	.990	.994*
.98	.999	.998*	.997
1.00	1.000	1.010	1.000*

3 Calculated Results and Intepretations

Graphs of K versus a path geometry parameter for the four types of paths are given in Figs. 1–4. Of particular interest are paths for which K nearly equals unity, and/or where K is nearly independent of Re. Regarding practical implementations, one also prefers paths for which the transducer ports can be fabricated safely and easily; paths for which K is substantially independent of the particular transducer; and paths which do not subject the transducer holder to excessive stress, nor the transducer to excessive wear.

Comparing paths parallel to the axis (Fig. 1 and Table 5) one finds, as expected, that $K \approx 1$ at $y/R \approx 0.24$. Here, K is nearly independent of Re for fully developed turbulent flows. The three values for y/R in Table 5 that yield $K = 1.0000$ are obtained by equating $(y/R)^{1/n}$ to the right-hand side of equation (5), for $n = 6$, 7, and 10. The entries for $y/R = 0.2929$ are included because at that particular y/R, if the flow were laminar (parabolic profile) the local velocity u_p would equal the area-averaged velocity $\bar{u}$. Conversely, it may be worth reiterating a point made in [1], p. 445, dealing with the incorrect use of a "turbulent K" when in fact the flow is laminar. Consider, for example, the location $y/R = 0.24$. (Again, this location is preferred for turbulent profiles because here, $K \approx 1$ with relative immunity to Re.) If the flow profile were parabolic, but one inadvertently retained $K = 1$, an error of nearly 15 percent occurs ($u_p/\bar{u} = 0.8448$). The theoretically correct value for K is 1.1837 in this laminar flow situation.

(It may be mentioned that the proper, i.e., theoretical or calibrated value for K, can in fact be introduced into the instrument's flow velocity algorithm if the flowmeter can compute a reasonable estimate for Re after each interrogation based on u_p and other site parameters such as pipe diameter and kinematic viscosity [12]. The relative insensitivity of K to Re shown in Figs. 1–4, for preferred path locations, enables one to calculate how tolerant one may be of errors or uncertainties in Re, for an allowable error or uncertainty in K.)

Paths parallel to the axis are the easiest of the present cases with respect to calculating K. Air flow tests conducted in our

Table 3 Comparison of *N*, *PN*, and *PL* for Re = 3.24×10^6

y/R	N	PN	PL
0.00	0.546	0.599*	0.000
.01	.649	.630	.631*
.02	.683	.658	.676*
.04	.732	.708	.725*
.07	.774	.767*	.766
.10	.806	.810*	.794
.15	.841	.856	.827*
.20	.866	.881	.851*
.30	.901	.901*	.887
.40	.928	.916*	.912
.50	.948	.940*	.933
.60	.965	.968*	.950
.70	.978	.989*	.965
.80	.989	.992*	.978
.90	.996	.987	.990*
.96	.999	.993	.996*
.98	.999	.999*	.998
1.00	1.000	1.008	1.000*

Table 4 List of rounded-off coefficients for fifth degree polynomial of the form $Y = C_0 + C_1X^1 + C_2X^2 + C_3X^3 + C_4X^4 + C_5X^5$

Re	Co	C_1	C_2	C_3	C_4	C_5
4000	0.3675	5.1063	−22.4380	47.4210	−45.6929	16.2502
1.05×10^5	0.4818	3.9727	−16.9802	35.6317	−34.2899	12.1942
3.24×10^6	0.5989	3.2324	−13.8650	28.8959	−27.6228	9.7684

Table 5 Normalized velocities and K's calculated from power law $u/U_0 = (y/R)^{1/n}$, and equation (4), for paths parallel to axis

Re	4000		1.05×10^5		3.24×10^6	
n	6		7		10	
y/R	u_p/U_0	K	u_p/U_0	K	u_p/U_0	K
0	0	∞	0	∞	0	∞
.2	.7647	1.0347	.7946	1.0278	.8513	1.0170
.2929	.8149	.9706	.8391	.9733	.8814	.9789
.2453	.7912	1.0000	.8181	.9983	.8689	.9964
.2423	.7896	1.0021	.8167	1.0000	.8678	.9977
.2367	.7865	1.0060	.8140	1.0034	.8658	1.0000
.4	.8584	.9217	.8773	.9309	.9124	.9489
.6	.9184	.8615	.9296	.8785	.9502	.9112
.8	.9635	.8212	.9686	.8432	.9779	.8853
.9	.9826	.8052	.9851	.8291	.9895	.8750
1.0	1.0000	.7912	1.0000	.8167	1.0000	.8658

Table 6 *Comparison of K calculated in present work for tilted radius versus K for tilted diameter calculated from equation (3) [3]*

Re	K, tilted radius, present work	K, tilted diameter, equation (3)	Difference, Percent
4000	0.944	0.926	1.9
1.05×10^5	0.941	0.940	0.1
3.24×10^6	0.960	0.955	0.5

laboratory by D. R. Wallace, however, showed that for 19 mm diameter transducer housings installed on the axis of a 250 mm diameter pipe, and spaced about 300 mm apart, the ultrasonically measured flow was linearly related to the actual flow but was not higher than the area-average flow (as predicted by the present method of calculating K, which neglects transducer effects on the profile) but in fact was substantially lower than the area-average. This demonstrated that the transducers behaved as significant obstacles near the axis, and motivated the investigation of paths skewed to the axis, or otherwise oriented so that blocking by the transducers would not significantly affect the average flow between the transducers. Air flow calibration tests subsequently conducted in ~ 200 and 400 mm diameter pipes have shown that small transducers installed in the flowing fluid, but at one end of a path oblique to the flow cause much less perturbation to the profile in the interrogated path than if the transducers were located at the ends of a path which is parallel to the flow.

On the other hand, the well-established axial interrogation of paths which are very long compared to the transducer diameter, as in the so-called offset style flowcell [1, 2] indicates that paths parallel to the axis can indeed yield a K within about 2 percent of the value predicted theoretically, depending on how the profile is sampled. Better results may be expected, for example, when the entire cross section is interrogated, rather than when only part of the cross section is interrogated.

The present results enable one to locate transducers so that for the chosen type of path, K will be (*a*) minimally dependent on Re, and/or (*b*) approximately equal to unity, or (*c*) represented by a simple function of Re. For pipes in which the profile is equivalent to that found in [9], and for sound beams of diameter d sufficiently small compared to the pipe's inside diameter $2R$, the error in the present calculated K's is estimated as ± 2 percent ± the effect due to the disturbance of the profile by the transducers. (This error estimate is based on comparing independently-calculated K's, as discussed in the paragraph below.) The PN coefficients and normalized velocity comparisons may be useful in calculating K for paths other than those shown in Figs. 1-4.

Referring now to Fig. 2, the radial segment yields $K = 1 \pm 0.02$ for paths from the wall to about 63 to 75 percent in towards the axis. As a check on Fig. 2, K's at $y/R = 1$ (tilted full radius) are within 2 percent of the values calculated by equation (3) for the conventional tilted diameter. See Table 6.

In Fig. 3, for a hammock-like symmetrical chord segment of end-view-projected length = 0.828R, $K \approx 1$ with rather little dependence on Re for $B/R = 0.7$. K's dependence on Re is minimal for B/R corresponding to where the curves intersect. As a check on Fig. 3, for $B = 0$, K's are less than those given by equation (3), which makes sense since the segment gives inadequate weight to be lower-velocity contributions near the wall. K increases as B increases because, as B increases, the chord segment samples more lower-velocity contributions than higher-velocity contributions.

One particularly convenient and practical location for the chord segment of projected length 0.828R is at $B/R = 0.5$. At this elevation the chord lies in the midradius plane; K is about 0.92; and K varies only about ± 1.5 percent over the plotted range of Re. Note that for this midradius chord segment K is about 8 percent less than unity, whereas if the segment reached from wall to wall in the midradius plane, the "turbulent" $K = 0.9961$, according to [1], p. 495. Again, for the midradius chord segment, K is smaller than for the full midradius chord because the segment preferentially weights the higher velocity contributions. In fact, for any B/R in Fig. 3,

$$K_{\text{chord segment}} < K_{\text{full chord}} \tag{6}$$

Regarding practical applications, the geometry of Fig. 3 is utilized in one refinery flare line in a pipe of approximately 750 mm diameter, with $B/R = 0.5$, and where the distance between the radiating faces of the two transducers, measured along the 45 deg skewed path, is 400 mm (reference [11], Fig. 10, upper right).

Turning now to Fig. 4, K approaches 1, with lessening dependence on Re, as the midradius segment approaches the semichord length ($x/S \rightarrow 1$), as expected, based on analyses in [6] and [7].

In closing, it may be of interest to offer a general remark, namely, in Figs. 1-4, the calculated curves exhibit less curvature as Re increases, and as the terminus or path location moves away from the wall. In other words, the flatter the profile, the less K depends on the terminus or location of the path. As an extreme example, for plug flow (perfectly uniform flat profile), $K = 1$ independent of the portion of the flow that is sampled.

Practical applications of the present special paths are illustrated and discussed in [11] and [12], with respect to ultrasonically measuring gas flow in flare lines in a

petrochemical refinery. Examples of the transducers used in flare gas and some other applications appear in [12] and [13]. Practical counterparts of the paths symbolized by the insets in Figs. 2–4 are given in Fig. 5.

References

1 Lynnworth, L. C., "Ultrasonic Flowmeters," Chapter 5, in: Mason, W. P. and Thurston, R. N., *Physical Acoustics*, Vol. 14, 1979, pp. 407–525, Academic Press, NY; "Ultrasonic Flowmeters, Part 1," *Trans Inst. MC*, Vol. 3, No. 4, 1981, pp. 217–223; "Ultrasonic Flowmeters, Part 2," Vol. 4, No. 1, 1982, pp. 2–24.

2 Sanderson, M. L., and Hemp, J., "Ultrasonic Flowmeters — A Review of the State of the Art," in *Proc. BHRA International Conference Adv. in Flow Measurement Techniques*, 1981, pp. 157–178.

3 Kivilis, S. S., and Reshetnikov, V. A., Izmerit. Tekhn. No. 3, 1965, pp. 52–54. Equation (3) is derived in this work, based on Nikuradse's data in [9].

4 Knapp, C., "Geschwindigkeits- und Mengenmessung strömender Flussigkeiten mit Ultraschall," VDI-Bericht, No. 86, 1964, pp. 65–70.

5 Malone, J. T., and Whirlow, D. K., "Fluid Flow Measurement System," U.S. patent 3,564,912, Feb. 23, 1971.

6 Baker, R. C., and Thompson, E. J., "A Two Beam Ultrasonic Phase-Shift Flowmeter," *Proc. Conf. Fluid Flow Measurement Mid 1970s*, Apr. 1975; "Measurement of Fluid Flow," U.S. patent 4,078,428, Mar. 14, 1978.

7 Lynnworth, L. C., "Ultrasonic Measuring System for Differing Flow Conditions," U.S. patent 4,103,551, Aug. 1, 1978.

8 Schlichting, H., *Boundary Layer Theory*, 6th Edition, McGraw-Hill, New York, 1968.

9 Nikuradse, J., "Gesetzmässigkeiten der turbulenten Strömung in Glatten Rohren," (Laws of Turbulent Flow in Smooth Pipes), VDI-Forschungsheft 356, Ausgabe (Edition) B, Vol. 3, Sept./Oct. 1932, pp. 1–36.

10 Rugg, T., and Feldman, P., 32 BASIC Programs for the Pet Computer, Dilithium Press, Beaverton, OR, 1979.

11 Smalling, J. W., Braswell, L. D., Lynnworth, L. C., and Wallace, D. R., "Flare Gas Ultrasonic Flowmeter," pp. 27–38 in: *Proc. Instrumentation Symposium for the Process Industries*, Texas A&M University, College Station, TX, Jan. 1984; available from Instrument Society of America (ISA), Research Triangle Park, N. C. 27709.

12 Lynnworth, L. C., pp. 231–238 in: "Special Ultrasonic Flowmeter Applications," *Proc. 30th International Instrumentation Symposium*, Denver, ISA, May 1984.

13 Lynnworth, L. C., Patch, D. R., and Mellish, W. C., "Impedance-Matched Metallurgically-Sealed Transducers," *IEEE Trans. Sonics and Ultrasonics SU-31*, Vol. 2, Mar. 1984, pp. 101–104.

A Numerical Method for Solving Momentum Equations in Generalized Coordinates (Its Application to Three-Dimensional Separated Flows)

A. Nakayama
Department of Mechanical Engineering,
Shizuoka University,
Hamamatsu, 432 Japan

A finite difference calculation procedure has been developed for the calculations of the three-dimensional fully elliptic flows over irregular boundaries. A simple control volume analysis is introduced to reformulate the momentum equations in the generalized velocity and coordinate system, without resorting to any extensive tensor calculus. The finite difference equations are obtained by discretizing the conservation equations in this generalized system. For a practical application of the present finite difference calculation scheme, calculations are carried out on the three-dimensional separated flow in a converging-diverging rectangular duct. The calculation results reveal an extremely complex nature of the three-dimensional separated flow.

Introduction

The complexity of the problem in numerical calculations often stems from the treatment of curved wall boundaries. It is possible to employ Cartesian or cylindrical polar meshes even for the irregular boundaries. However, one must also accept the penalties such as inefficient distributions of mesh points and the extensive interpolative calculations so as to satisfy the required boundary conditions. Moreover, a considerable number of the mesh points will be wasted since the points external to the flow field do not participate in the calculations in any meaningful manner.

To overcome this problem, coordinate transformations have been widely used to solve a number of complex flow problems e.g. [1-4]. Most of these numerical calculation procedures, however, restrict themselves to certain conditions such as the two-dimensional configuration and the conformity of geometry to a certain functional form. It is quite often that the source program requires considerable modifications each time for a slight change in the geometrical configuration.

The present paper introduces a general finite difference procedure for the three-dimensional elliptic flows over irregular boundaries. The momentum equations are reformulated into arbitrary velocity and coordinate systems by means of a simple control volume analysis without resorting to any extensive tensor calculus. The resulting conservation equations in the generalized system are integrated within a finite volume element to obtain the general finite difference forms. It will be shown that, when the coordinate transformation is introduced in this generalized manner, it is possible to formulate the finite difference equations so universal that a single computer code may be used for any type of coordinate transformation simply by specifying the coordinate base vectors appropriate to a given geometrical configuration.

For the illustrative purpose, the finite difference calculations are performed on the separated flow through a converging-diverging rectangular duct. The calculation results presented here reveal an extremely complex nature of the three-dimensional fully elliptic flow.

Momentum Equations in Generalized Coordinate System

Figure 1 depicts a transformed domain (ξ, η, ζ) and its corresponding physical domain (x, y, z). Gradient of a general scalar ϕ may be written in either of the coordinate systems as

$$\nabla\phi = \bar{i}\phi_x + \bar{j}\phi_y + \bar{k}\phi_z = \bar{d}^1\phi_\xi + + \bar{d}^2\phi_\eta + \bar{d}^3\phi_\zeta \qquad (1a)$$

where

$$\bar{d}^1 = (\bar{r}_\eta x \bar{r}_\zeta)/\mathrm{J}, \bar{d}^2 = (\bar{r}_\zeta x \bar{r}_\xi)/\mathrm{J}, \bar{d}^3 = (\bar{r}_\xi x \bar{r}_\eta)/J \qquad (1b)$$

$$\bar{r} = \bar{i}x + \bar{j}y + \bar{k}z \text{ and } \mathrm{J} = \bar{r}_\xi \cdot (\bar{r}_\eta x \bar{r}_\zeta) \qquad (1c)$$

The bar indicates vector quantities such as $\bar{r}$ for the position vector. The subscripts x, y, z, ξ, η, and ζ denote their partial derivatives, and $\bar{i}$, $\bar{j}$, and $\bar{k}$ are the unit vectors in the Cartesian coordinates (x, y, z).

Referring to Fig. 1, $(\mathrm{J}\bar{d}^1\Delta\eta\Delta\zeta)$ may be identified as the vector element of the area in the physical domain, which

Contributed by the Fluids Engineering Division for publication in the JOURNAL OF FLUIDS ENGINEERING. Manuscript received by the Fluids Engineering Division, March 15, 1982.

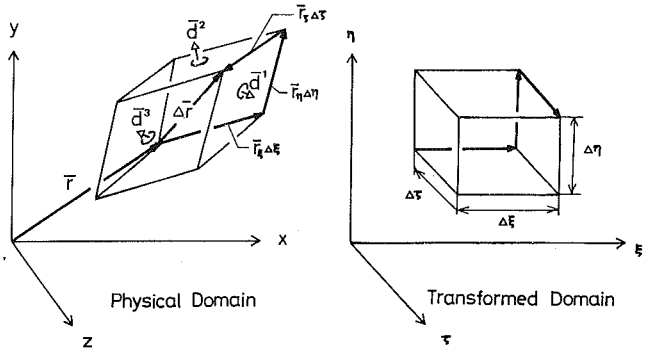

Fig. 1 Physical domain and transformed domain

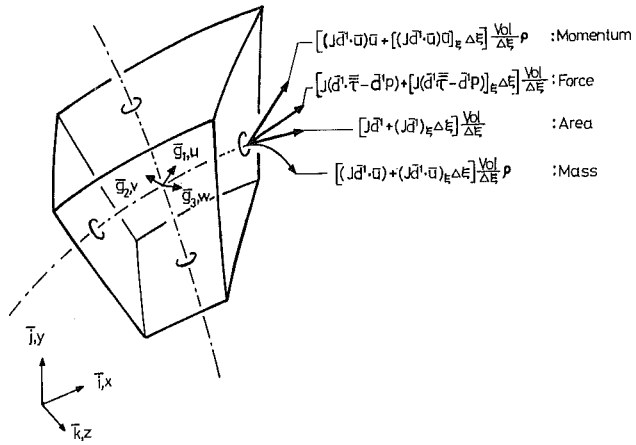

Fig. 2 Momentum balance on a volume element

corresponds to the area $(\Delta\eta\Delta\zeta)$ in the transformed domain. Correspondingly, similar geometrical relationships are valid for $\bar{d}^2$ and $\bar{d}^3$.

From the preceding geometrical consideration, one may draw Fig. 2 where the mass and momentum balances on an element $\text{Vol} \equiv \Delta\xi\Delta\eta\Delta\zeta$ are indicated in a generalized coordinate system. Referring to this figure, the momentum balance relationship may be found to be

$$\frac{\partial}{\partial x^i} \text{J}[(\bar{d}^i \cdot \bar{u})\bar{u} - \bar{d}^i \bar{\bar{\tau}}/\rho + \bar{d}^i p/\rho] = \bar{0} \tag{2}$$

where the generalized coordinates ξ, η, and ζ are renamed, respectively, by x^i $(i=1, 2, 3)$, and the usual summation convention is adopted for a repeated index in the expression. As explicitly indicated by the equation (1*b*), the vectors $\bar{d}^i$ are the contravariant base vectors such that

$$\bar{d}^i \cdot \bar{d}_j = \delta^i_j\text{: Kronecker delta} \tag{3a}$$

where

$$\bar{d}_i = \frac{\partial}{\partial x^i}\bar{r}\text{: i.e., } \bar{r}_\xi, \bar{r}_\eta,$$

$$\text{and } \bar{r}_\zeta \text{ for } i=1, 2, \text{ and } 3 \tag{3b}$$

Moreover, $\bar{\bar{\tau}}$ denotes the stress while the pressure and density are indicated by p and ρ, respectively.

For the numerical computation, one must decompose the vector equation (2) into the scalar form. However, there is no need to restrict it to the conventional contravariant representation. Another set of base vectors $\bar{g}_i$, independent of the covariant base vectors $\bar{d}_i$, may be introduced for the decomposition of $\bar{u}$ and $\bar{\bar{\tau}}$. Such a general procedure for the derivation of the conservation equations in the generalized velocity and coordinate systems is described in Appendix A. For the flows in ducts of arbitrary cross-section, it turns out to be convenient to retain the Cartesian velocity frame even using the transformed coordinates appropriate to a given duct geometry. The momentum equation for this case as described in Appendix A is given by

$$\frac{\partial}{\partial x^i}\text{J}\left(d^i_j u^j u^h - \nu_{\text{eff}} G^{ij}\frac{\partial u^h}{\partial x^j}\right)$$

$$= -\frac{\text{J}}{\rho} d^i_h \frac{\partial p}{\partial x^i} + \frac{\partial}{\partial x^i}\text{J}d^i_j d^k_h \frac{\partial u^j}{\partial x^k} \tag{4a}$$

where

$$d^i_j \equiv \bar{d}^i \cdot \bar{e}_j \text{ and } \nu_{\text{eff}} = \nu + \nu_t \tag{4b,c}$$

$\bar{e}_j$ is the Cartesian unit vectors while G^{ij} is the metric tensor as defined by equation (A11) in Appendix A. The effective viscosity (ν_{eff}) formulation as described in equation (A5) is adopted for the stress components where ν is the laminar kinematic viscosity while ν_t is its turbulent counterpart which should be set to zero for the laminar flow case (The sub- and super- indices used here should not be confused with those in the general tensors).

Finite Difference Form

It is interesting to note that, when u^h (for a particular h) is regarded as a general scalar ϕ, the left-hand side of equation (4*a*) appears to be identical to the transformed form of $J\nabla\cdot(\bar{u}\phi - \nu_{\text{eff}}\nabla\phi)$, namely, the convection and diffusion rates of the general scalar ϕ. Thus, upon setting the right-hand side of equation (4*a*) to the source term so, one may write the general conservation form as

$$\frac{\partial}{\partial x^i}\text{J}\left(d^i_j u^j \phi - \nu_{\text{eff}} G^{ij}\frac{\partial \phi}{\partial x^j}\right) = so \tag{5a}$$

The effective diffusion coefficient ν_{eff} and the source term so to be substituted into the above general equation are listed below for the continuity, momentum, and energy equations.

For the continuity equation:

$$\phi = 1,\ \nu_{\text{eff}} = 0,\ so = 0 \tag{5b}$$

For the momentum equations $(h=1, 2, 3)$:

$\phi = u^h$, $\nu_{\text{eff}} = \nu + \nu_t$,

$$so = -\frac{\text{J}}{\rho} d^i_h \frac{\partial p}{\partial x^i} + \frac{\partial}{\partial x^i}\text{J}d^i_h \frac{\partial u^j}{\partial x^k} \tag{5c}$$

For the energy equation:

$$\phi = T,\ \nu_{\text{eff}} = \nu/\sigma + \nu_t/\sigma_t,\ so = 0 \tag{5d}$$

where T is the temperature while σ and σ_t are the laminar and turbulent Prandtl numbers. For the turbulent flow calculations, the turbulence model equations may be added to

Nomenclature

$\bar{d}_i$ = covariant base vectors
$\bar{d}^i$ = contravariant base vectors
$\bar{e}_i$ = Cartesian unit vectors
$\bar{g}_i$ = velocity base vectors
$\bar{g}^i$ = recriprocal vectors of $\bar{g}_i$
J = Jacobian of transformation
p = pressure
$\bar{r}$ = position vector
$\bar{u}$ = velocity vector
x^i = generalized coordinates
δ^i_j = Kronecker delta
ν = kinematic viscosity
ρ = density
τ = stress

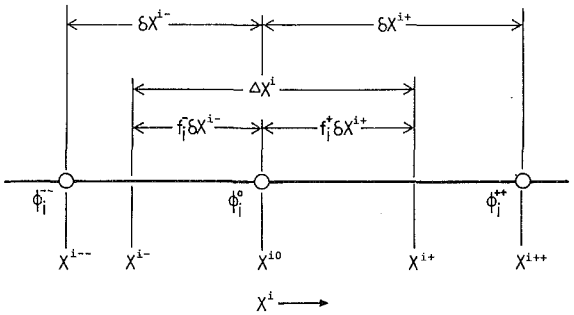

Fig. 3 Grid nomenclature for discretization

the governing equations in a similar fashion without any difficulties.

Since all governing equations are expressed by a single expression given by the general equation (5), the discretization can be carried out once for all governing equations following the procedure employed in the innovative work on the three-dimensional parabolic flow by Patankar and Spalding [5]. For this purpose, the general equation (5) is rewritten as follows:

$$\frac{\partial}{\partial x^i} J\left(d_j^i u^j \phi - \nu_{\text{eff}} |\bar{d}^i|^2 \frac{\partial \phi}{\partial x^i}\right) = s^0(\phi) + so(\phi) \tag{6a}$$

where

$$s^0(\phi) = \frac{\partial}{\partial x^i} J \nu_{\text{eff}} [G^{ij} - |\bar{d}^i|^2 \delta_j^i] \frac{\partial \phi}{\partial x^j} \tag{6b}$$

In the above equations, the index associated with the absolute value $|\bar{d}_i|$ is to be excluded from the summation rule. Hence, $|\bar{d}_i|^2 = \bar{d}^i \cdot \bar{d}^i$ for a particular i (no summation on i). Only the diagonal components of the metric tensor G^{ij} are retained in the left-hand side of the equation (6*a*). Its counterpart s^0 in the right-hand side accounts for the nonorthogonality since it obviously vanishes for the orthogonal set of $\bar{d}^i$.

The finite difference equation is reduced by integrating the general equation (6*a*) within a finite volume element of $\text{Vol} \equiv \Delta x^1 \Delta x^2 \Delta x^3$. The details of this discretization procedure has been already given by Patankar and Spalding [5] for the three-dimensional parabolic flow. Since its extension to the fully elliptic form is rather straight forward even in this transformed coordinates, only the final form of the difference equation is given below:

$$(A_i^+ + A_i^-)\phi_i^0 = A_i^+ \phi_i^{++} + A_i^- \phi_i^{--} + SO \tag{7a}$$

where

$$SO = (s^0 + so)|_{x^{i0}} \text{ Vol} \tag{7b}$$

$$A_i^+ = -f_i^+ CO_i^+ + DI_i^+ \tag{7c}$$

$$A_i^- = f_i^- CO_i^- + DI_i^- \tag{7d}$$

no summation on i

$$CO_i^{(\,)} \equiv J d_j^i u^j (\text{Vol}/\Delta x^i)|_{x i(\,)} \tag{7e}$$

and

$$DI_i^{(\,)} \equiv (J \nu_{\text{eff}} |\bar{d}^i|^2 / \delta x^i)(\text{Vol}/\Delta x^i)|_{x i(\,)} \tag{7f}$$

The locations of $\phi(\phi_i^{++}, \phi_i^{--}, \phi_i^0)$, the interpolation factors (f_i^+, f_i^-) and the internodal distances $(\Delta x^i, \delta x^{i+}, \delta x^{i-})$ are shown for a particular general coordinate x^i in Fig. 3. In the above equations, the subscript i such as in ϕ_i and A_i indicates that the quantities are to be defined along this particular x^i-coordinate, while the superscripts such as 0, +, and − refer to the relative locations (along x^i) where the quantities are evaluated. Furthermore, the summation rule is effective in the finite difference equation (7*a*) while the rule does not apply in the equations (7*c*−*f*) (again, the present short-hand notation should not be confused with the tensor notation since ϕ_i, A_i etc. are all "scalar" quantities). The resulting finite difference equation (7*a*) gives an algebraic equation for the scalar $\phi^0 (\equiv \phi_1^0 = \phi_2^0 = \phi_3^0)$ in terms of the values at six neighboring nodes. Thus, if the pressure field is given, the finite difference equation (7*a*) can be written for each variable at each node. This procedure, then, yields a closed set of algebraic equations, which can be solved by any standard iterative scheme such as the tridiagonal matrix algorithm. However, the velocity field thus obtained usually does not satisfy the continuity equation, since the pressure field assumed beforehand does not represent the true pressure field. Therefore these pressure and velocity fields must be subsequently adjusted to satisfy the continuity principle.

For the correction on the pressure and velocity fields, Patankar and Spalding [5] formulated the "pressure correction equation" equivalent to the Poisson's equation for the pressure field by substituting an abbreviated momentum balance relationship into the continuity equation. This pressure correction equation can be solved most effectively using the so-called "staggered" grid system, in which the velocities are defined midway between the pressure nodes. The present formulation of the pressure correction equation is in essence identical to the one developed by Patankar and Spalding for the three-dimensional parabolic flow. The details of the formulation for the three-dimensional fully elliptic flow of the present concern are given in Appendix B for the generalized coordinate system. The final expression of the pressure correction equation (B14) takes the same form as the general finite difference equation (7*a*).

Numerical Solution Procedure

The resulting closed set of the finite difference expressions is universal in the sense that it can be used for any coordinate systems simply by spatially specifying the coordinate base vectors ($\bar{d}_i$ or $\bar{d}^i$) appropriate to a given flow configuration. This input procedure for the base vectors can be carried out either analytically or digitally.

For the flows in ducts of variable cross-section, a family of grid systems may be conveniently specified analytically as

$$\bar{r} = x^1 \bar{e}_1 + Y_{tb} x^2 \bar{e}_2 + x^3 \bar{e}_3 \tag{8}$$

where Y_{tb} is the vertical distance between the upper wall boundary and the horizontal plane of symmetry so that x^2 varies from zero to unity. Subsequently, the equation (8) specifies d_j^i as

$$d_j^i = \begin{matrix} \\ i \downarrow \end{matrix} \begin{matrix} j \longrightarrow \\ \end{matrix} \begin{bmatrix} 1 & 0, & 0 \\ -x^2 \dfrac{\partial}{\partial x^1} \ln Y_{tb}, & 1/Y_{tb}, & -x^2 \dfrac{\partial}{\partial x^3} \ln Y_{tb} \\ 0, & 0, & 1 \end{bmatrix} \tag{9}$$

Once the duct geometry is given in terms of $Y_{tb}(x^1, x^3)$, all coefficients and source terms needed for the finite difference equations can be specified by substituting the equation (9) into the corresponding equations. The function Y_{tb} of the converging-diverging duct for the test calculations is described by

$$Y_{tb}/L_{\text{ref}} = 1 - \frac{1}{2} \exp[-(2x^1/L_{\text{ref}})^2] \tag{10}$$

The reference length L_{ref} is a half of the duct width while the reference velocity u_{ref} is taken as the uniform velocity at the inlet of $x^1 = -5L_{\text{ref}}$. The laminar flow calculations (without solving the energy equation) have been made at Reynolds number $u_{\text{ref}} L_{\text{ref}}/\nu = 50$, for a quadrant of the duct over the axial distance of $32\,L_{\text{ref}}$, with a highly nonuniform grid layout $(30 \times 9 \times 9)$. At the outlet, the zero gradient conditions are imposed for all variables except the pressure. It has been confirmed that the solution is not affected by shifting the outlet boundary farther downstream.

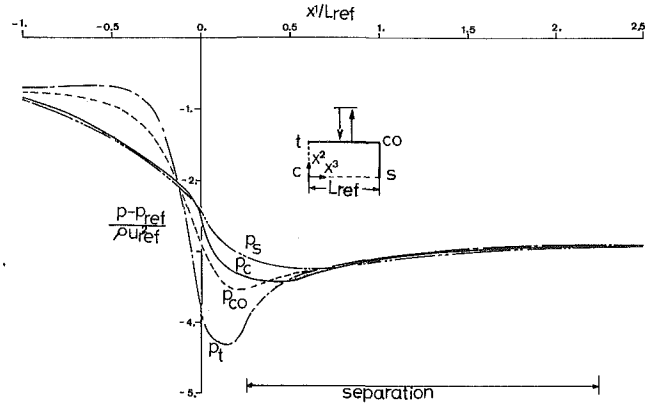

Fig. 4 Axial variation of pressure

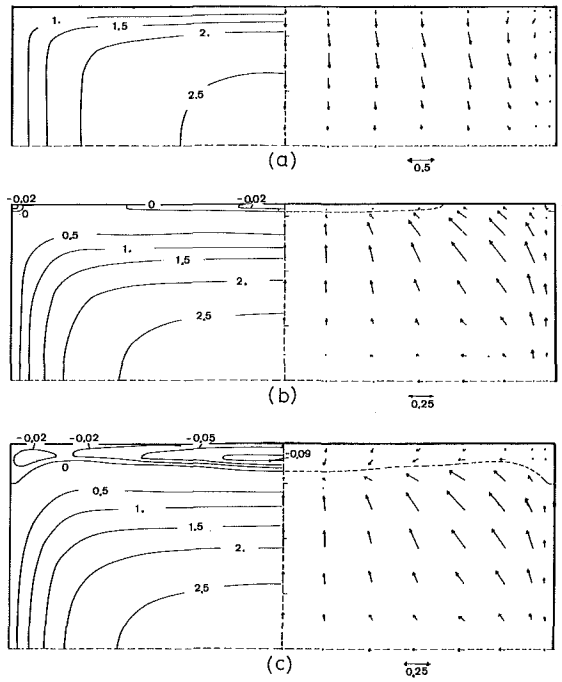

Fig. 5 Development of axial and crossflow velocity components (all values normalized by u_{ref}) (a) $x^1/L_{ref} = -0.05$ (b) $x^1/L_{ref} = 0.29$ (c) $x^1/L_{ref} = 0.41$

Calculations start with solving three momentum equations. Then, the resulting velocity field and the pressure field are corrected by solving the pressure correction equation, and the sequence is repeated till the solution converges. The requirement for the convergence has been taken as satisfied when the maximum change in each variable during an iteration becomes less than a prescribed value, 10^{-5}. The computational time required for this case is approximately 14 minutes on the CDC CYBER 175 computer system.

Prior to the calculations on the converging-diverging duct, the preliminary calculations were also carried out on various duct geometries such as the square duct, the triangular duct and the constricted circular duct. Some of these results were examined against the exact solutions (fully developed flows), and others against numerical solutions. The agreement of the present solutions with these available solutions has turned out to be excellent. Neither of the non-orthogonality of the coordinates nor the nonuniform grid spacing affected the solutions. Thus the accuracy of the present finite difference solution procedure has been thoroughly checked.

Calculation Results

The calculation results obtained for the converging-diverging rectangular duct are discussed below. The axial variation of the pressure field is shown in Fig. 4 where the pressure at the inlet is taken as the reference pressure p_{ref}. It is seen that the pressure field in the expansion region exhibits high and low pressures at the side wall (p_s) and top wall (p_t) bisector points, respectively.

The velocity field is plotted at the three selected axial stations in Figs. 5 in terms of the axial velocity contours (in the left-hand side) and the cross flow vectors (in the right-hand side). As the flow passes through the throat, the cross flow vectors pointing originally at the horizontal plane of symmetry (Fig. 5(*a*)), change the direction toward the top wall bisector point, conforming to the pressure field prevailing through the expansion region. The on-set of the separation is shown in Fig. 5(*b*) where two distinct reverse primary flow regions are observed near the corner and the top wall bisector point. By the time the flow reaches the station at $x = 0.41\ L_{ref}$ (Fig. 5(*c*)), two regions coalesce to form one big reverse flow region, and the secondary flow currents are continuously drawn into this reverse flow region. The separated flow region expands further downstream, changing its location of the maximum reverse flow velocity from near the top wall bisector point toward the corner, and the flow finally reattaches around $x = 2.2\ L_{ref}$.

Concluding Remarks

A general finite difference calculation procedure has been developed for the prediction of the three-dimensional fully elliptic flows. The conservation equations are reformulated into the generalized velocity and coordinate systems using a simple control volume analysis which unhooks the velocity base vectors from the coordinate (covariant) base vectors. Although the Cartesian unit vectors are chosen for the velocity base vectors in the present study of the three-dimensional duct flows, there are no special difficulties in generalizing the present calculation method with variable velocity base vectors upon discretizing the equation (A4) in Appendix A instead of equation (5).

References

1 Thom, A., and Apelt, C. J., *Field Computation in Engineering and Physics*, D. Van Nostrand Co., London, 1961.

2 Lee, J. S., and Fung, Y. C., "Flow in Locally Constricted Tubes at Low Reynolds Number," ASME *Journal of Applied Mechanics*, Mar. 1970, pp. 9-16.

3 Chow, W. L., Bober, L. J., and Anderson, B. H., "Numerical Calculation of Transonic Boattail Flow," NASA TN D-7984, 1975.

4 Nakayama, A., and Chow, W. L., "Calculation of Transonic Boattail Flow at Small Angle of Attack," ME-TN-395-6, Dept. of Mech. and Industrial Eng., University of Illinois at U-C, Rept. prepared for the Research Grant NASA NGL 14-005-140, 1979.

5 Patankar, S. V., and Spalding, D. B., "A Calculation Procedure for Heat, Mass and Momentum Transfer in Three-Dimensional Parabolic Flows," *Int. J. Heat Mass Transfer*, Vol. 15, 1972.

6 Gal-Chen, T., and Somerville, R. C. J., "On the Use of a Coordinate Transformation for the Solution of the Navier-Stokes Equations," *J. Computational Phys.*, Vol. 17, 1975.

7 Warsi, Z. U. A., "Conservation Form of the Navier-Stokes Equations in General Nonsteady Coordinates," *AIAA Journal*, Vol. 19, No. 2, Feb. 1981, pp. 240-242.

8 Nakayama, A., "Three-Dimensional Flow within Conduits of Arbitrary Geometrical Configurations," Ph.D. thesis, University of Illinois at U-C, Apr. 1981.

9 Nakayama, A., Chow, W. L., and Sharma, D., Summary of Methods submitted to the 1980-81-HTTM-Stanford Conference on Complex Turbulent Flows, Sept., 1981.

APPENDIX A

Derivation of Momentum Equations in General Coordinates

The velocity $\bar{u}$ and the stress $\bar{\bar{\tau}}$ may be decomposed by an arbitrary set of vectors $\bar{g}_i$ as

$$\bar{u}=\tilde{g}_i u^i \quad \text{and} \quad \bar{\bar{\tau}}=(\tilde{g}_i,\tilde{g}_j)\tau^{ij} \tag{A1,2}$$

where the dyadic operation (,) is used for the stress. The present approach may be found to be quite different from a general-tensor approach in the sense that the velocity base vectors $\tilde{g}_i$ are arbitrary and "unhooked" from the coordinate (covariant) base vectors $\bar{d}_i$ (Note, u^i and τ^{ij} are no longer the contravariant tensors since $\tilde{g}_i \equiv \bar{d}_i$ in general.) The momentum equation (2) may now be decomposed by the reciprocal vectors $\tilde{g}^i$ defined as

$$\tilde{g}^i \cdot \tilde{g}_j = \delta^i_j \tag{A3}$$

The scalar product operation between the vector momentum equation (2) and the vectors $\tilde{g}^h$ yields the following scalar form of the momentum equation in the generalized velocity and coordinate systems:

$$\frac{\partial}{\partial x^i} \mathrm{J} D^i_j (u^j u^h - \tau^{jh}/\rho) + \gamma^h_{ik} \mathrm{J} D^i_j (u^j u^k - \tau^{jk}/\rho)$$

$$= -\frac{\mathrm{J}}{\rho} D^{ih} \frac{\partial p}{\partial x^i} \tag{A4}$$

where

$$\tau^{jk}/\rho\nu_{\text{eff}} = \epsilon^{jk} + \epsilon^{kj} \tag{A5}$$

$$\epsilon^{jk} = D^{lj}\left(\frac{\partial u^k}{\partial x^l} + \gamma^k_{lm} u^m\right) \tag{A6}$$

$$D^i_j \equiv \bar{d}^i \cdot \tilde{g}_j, \quad D^{ij} \equiv \bar{d}^i \cdot \tilde{g}^j \quad \text{and} \quad \gamma^k_{ij} \equiv \tilde{g}^k \cdot \frac{\partial}{\partial x^i} \tilde{g}_j \tag{A7,8,9}$$

The general equation (A4) may be appreciated by actually specifying $\tilde{g}_i$. The contravariant representation of the momentum equations, for example, may readily be obtained by setting $\tilde{g}_i = \bar{d}_i$, which yields

$$D^i_j = \delta^i_j, \quad D^{ij} = G^{ij} \equiv \bar{d}^i \cdot \bar{d}^j$$

and

$$\gamma^k_{ij} = \Gamma^k_{ij} \equiv \bar{d}^k \cdot \frac{\partial}{\partial x^i} \bar{d}_j \tag{A10, 11, 12}$$

Naturally, D^{ij} and γ^k_{ij} for this case have reduced to the contravariant components of the metric tensor G^{ij} and the Christoffel symbols of the second kind Γ^k_{ij}, respectively. The substitution of the above relations into equation (A4) leads to the expression identical to the one derived through a general tensor analysis by Gal-Chen and Somerville [6] and Warsi [7].

For the duct flows of the present concern, the velocity base vectors $\tilde{g}_i$ may be unhooked from the covariant base vectors $\bar{d}_i$. The transformation in the text has been carried out by setting $\tilde{g}_i$ in equation (A4) to the Cartesian unit vectors. The resulting equation (4*a*) in the text may be found to be identical to the one obtained by the authors [8, 9].

APPENDIX B

Derivation of Pressure Correction Equation

Upon setting $\phi = u^h$ $(h = 1,2,3)$ in equation (7*a*) in the text, three momentum equations may be written collectively as

$$(A_i^+ + A_i^-)\,(u^h)^0_i = A_i^+\,(u^h)^{++}_i + A_i^-\,(u^h)^{--}_i + SO + b_{hi}\,(p_i^- - p_i^+) \tag{B1}$$

where

$$b_{hi} \equiv \frac{\mathrm{J}}{\rho} d^i_h (\mathrm{Vol}/\Delta x^i)\,|_{x^{i0}} \quad \text{(no summation on } i\text{)} \tag{B2}$$

Here, the pressure term is treated separately from the momentum source SO. The pressure p and velocity u^h may be decomposed into the estimated value ($\overset{*}{p}$ and $\overset{*}{u}{}^h$) and its correction ($\acute{p}$ and $\acute{u}^h$) as

$$P = \overset{*}{\mathrm{p}} + \acute{p} \quad \text{and} \quad u^h = \overset{*}{u}{}^h + \acute{u}^h \tag{B3,4}$$

The substitution of the above equations into equation (B1) yields

$$(\acute{u}^h)^0 = B_h\,(\acute{P}_h^- - \acute{p}_h^+) \tag{B5}$$

where

$$B_h \frac{b_{hh}}{(1-\acute{\alpha}_h)\sum_i (A_i^+ + A_i^-)} \quad \text{(no summation on } h\text{)} \tag{B6}$$

and

$$\acute{\alpha}_h \equiv \frac{A_i^+\,(\acute{u}^h)_i^{++} + A_i^-\,(\acute{u}^h)_i^{--} + \acute{SO} + \sum_i^{i\neq h} b_{hi}\,(\acute{p}_i^- - \acute{p}_i^+)}{(\acute{u}^h)^0_i (A_i^+ + A_i^-)} \tag{B7}$$

The summation

$$\sum_{i=1}^{3}$$

is to be denoted simply by

$$\sum_i$$

while

$$\sum_i^{i\neq h}$$

indicates the summation over the two values of the repeated index i whose value is different from that of h. Equation (B5) is formulated so that each velocity correction $\acute{u}^h$ at x^{h0} is to be affected directly by the pressure correction $\acute{p}$ at x^{h+} and x^{h-}.

For the continuity equation, the finite difference equation (7*a*) reduces to

$$\sum_i (CO_i^+ - CO_i^-) = 0 \tag{B8}$$

or

$$\sum_i \sum_j (co^i_{ij} - co^{\bar{i}}_{\bar{i}j}) = 0 \tag{B9}$$

where

$$co_{ij} \equiv \mathrm{J} d^i_j u^j (\mathrm{Vol}/\Delta x^i) \quad \text{(no summation on } i \text{ nor } j\text{)} \tag{B10}$$

i.e.

$$CO_i = \sum_j co_{ij} \tag{B11}$$

Again, decomposing CO_i into the estimated value $\overset{*}{CO}_i$ and its correction $\acute{CO}_i$, the continuity equation (B8) may readily be rewritten as

$$\sum_i (\acute{co}^+_{ii} - \acute{co}^-_{\bar{i}\bar{i}}) = -\sum_i (\acute{CO}_i^+ - \overset{*}{CO}_i^-) - \acute{\beta} \tag{B12}$$

where

$$\acute{\beta} \equiv \sum_i^{i\neq j} \sum_j (\acute{co}^+_{ij} - \acute{co}^-_{\bar{i}\bar{j}}) \tag{B13}$$

Upon noting the locations of the pressure nodes relative to those of the velocities in the staggered grid system, the substitution of the equation (B5) into the left-hand side of the continuity equation (B12) leads to the following pressure

correction equation in the form identical to that of the general finite difference equation (7*a*) in the text:

$$(A_i^+ + A_i^-)\acute{p}_i^0 = A_i^+ \acute{p}_i^{++} + A_i^- \acute{p}_i^{--} + SO \tag{B14}$$

where

$$SO = -\sum_i (\overset{*}{C}O_i^+ - \overset{*}{C}O_i^-) - \acute{\beta} \tag{B15}$$

and

$$A_i^{(\,)} = \mathrm{J}d_i^i B_i (\mathrm{Vol}/\Delta x^i)\,|_{x^{i(\,)}}$$

(no summation on i) (B16)

Thus, the pressure correction equation (B14) may be solved in the same manner as for the other governing equations. Subsequently, the velocity and pressure fields can be corrected using equations (B3,4) and (B5). The coefficient needed in the pressure correction equation must be evaluated from the current information available during the course of the iteration. With this view, the correction coefficients $\acute{\alpha}_h$ and $\acute{\beta}$ may well be set to zero since this remains to be a good estimation during the course of the iteration, and obviously becomes the exact condition as the solution converges, namely, $\acute{p} \to 0$ and $\acute{u}^h \to 0$. A similar practice has been adopted also by Patankar and Spalding [5].

Acknowledgment

The author would like to express his sincere thanks to Professor W. L. Chow for his interest and many helpful discussions on this study. A part of the present study has been carried qut at University of Illinois at Urbana-Champaign.

Khosrow Nourmohammadi
Nuclear Engineering Program.
Present Address: Tehran, Iran

P. K. Hopke
Institute for Environmental Studies,
Nuclear Engineering Program, and
Department of Civil Engineering.

J. J. Stukel
Department of Civil Engineering, and
Department of Mechanical Engineering.

University of Illinois,
Urbana, Ill. 61801

Turbulent Air Flow Over Rough Surfaces
II. Turbulent Flow Parameters

The objective of the present study was to examine experimentally the turbulent flow structure in a repeated rib geometry rough wall surface as a function of the ratio of the roughness height to the pipe diameter (K/D), the ratio of the spacing between the elements to the roughness height (P/K), the axial position within a rib cycle, and the Reynolds number. For small P/K values, the turbulent intensities and Reynolds shear stress variations were similar to those found for smooth wall pipe flow. Unique relationships for the u' and v' were found that were valid in the outer layer of the flow for all axial positions and all values of P/K and K/D.

Introduction

In flow experiments in which repeated rib roughness configurations were used, the geometrical parameter used to describe the roughness patterns is the ratio of the spacing between the elements, P, to the spacing between the elements, K (P/K). Morris [1] has categorized this flow into three regimes: quasi-smooth (low P/K, $P/K<7$), hyperturbulent or wake interference (medium P/K, $7 < P/K<16$), and isolated-roughness-element (high P/K, $P/K>16$) flow regimes. The flow was further separated into an outer and an inner flow region. The outer region is defined as that flow region unaffected by the presence of the roughness elements whereas the effects of the roughness elements on the fluid flow properties are confined in the inner layer.

In the quasi-smooth flow regime, the outer layer is large in comparison with the inner layer. Therefore, the turbulence profiles in the outer layer are expected to be similar to those found for smooth walls. There are several sand-roughened pipe turbulence flow measurements that demonstrate this fact. Robertson et al. [2–4] noted that for these types of surfaces, the turbulence parameters in the outer flow region of the rough wall are essentially the same as the smooth pipe when normalized with the shear velocity, U_s. Goma and Gelhar [5] and Chen and Roberson [6], using discrete roughness elements in pipes, reached the same conclusion.

For the isolated-roughness-element and hyperturbulent flow regimes, the outer layer is expected to behave in the same manner. There is little data available for the inner layer of repeated-rib rough wall geometries and of those available, they are for developing flow from smooth to rough wall surfaces [7–11]. As the wall is approached in the inner layer, the surface roughness produces a very sharp rise in the turbulence parameters. Downstream of the element, this effect is reduced and smaller increases in the turbulence parameters are observed. The inner layer thickness also experiences a periodic variation between roughness elements for these two flow regimes.

Rough wall pipe eddy diffusivity data are limited. Two types of small and large sand-roughness pipes were examined by Powe [12]. In both cases, the variation of the eddy diffusivity parameter, ϵ/U_sR, for the rough and smooth walls were similar. Liu [13], in a study of a flat plate roughened with transverse square bars, obtained the same ϵ/U_sR versus Y/δ_1 values for rough wall element P/K values of 2, 4, and 12 as for a smooth wall. δ_i is the boundary layer thickness of the wall roughess. No detailed eddy diffusivity data are available in the literature on a repeated rib pipe geometry.

This study examined experimentally the axial and radial variations of u', v', $\overline{uv}$, and ϵ for turbulent flow over a repeated rib rough wall. The roughness configurations were changed so that a wide range of rough wall flow regimes could be studied.

Experimental Facility

Two circular duct configurations were utilized to conduct the experimental measurements. In both systems, air was filtered at the bell-shaped inlet to the duct system by a HEPA filter to produce particle-free air. The maximum attainable Reynolds number, based on the hydraulic diameter, in the smalll and large diameter systems was 150,000 and 170,000, respectively.

The small diameter system was constructed from 0.35 cm thick wall, 10.17, cm O.D. stainless steel pipe. The total length of the system was 8.53 m. The configuration was constructed of a series of 0.91 m and 0.45 m pipe sections that were connected with vacuum "O"-ring flanges. When in place, the effective roughness height (K) of the small system was 0.635 cm. The tolerance between the spacer rings and the pipe was 0.051 cm. The distance, R, from the center of the pipe to the spacer surface was 4.4175 cm. The various P/K

Contributed by the Fluids Engineering Division for publication in the JOURNAL OF FLUIDS ENGINEERING. Manuscript received by the Fluids Engineering Division, November 8, 1982.

Table 1 Axial location of measurement stations (X/K values)

	X/K Station			
P/K	$X1$	$X2$	$X3$	$X4$
Small Pipe System		$K = 0.635$ cm		$R = 4.4175$ cm
2	0.5			
5	−1.5	1	3.5	
7	1	3	5.5	1
10	−1.5	1	5	8.5
13	−1.5	1	5	11.8
16	−1.5	1	8	14.5
19	−1.5	1	8	17.5
22	−1.5	1	11	20.5
25	−1.5	1	11	22.5
Large Pipe System		$K = 0.954$ cm		$R = 9.5275$ cm
2	0.5			
13	−1.5	1	5	11.5
24	−1.5	1	11	22.5

geometries used in the small system were 2, 5, 7, 10, 13, 19, 22, and 25.

The second pipe system, the large pipe system, was constructed from 0.305 cm thick wall, 20.3 cm O.D. stainless steel. The total length of this system was 13.41 m. Custom 0.305 cm thick aluminum angle iron was bent into rings that gave roughness elements 1.27 cm wide and 1.27 cm high. When in place, the effective roughness height (K) was 0.954 cm. The value of R for the large system was 9.5275 cm.

In order to obtain a fully developed profile as rapidly as possible, roughness elements ($P/K = 2$) were placed upstream of the test section. Seventy and seventy-five diameters were sufficient for the small and large pipe systems, respectively, to achieve a fully developed flow condition. The positions of the four axial measurement locations are given in Table 1. The first region, $X1$, is directly behind the step ($X/K = -1.5$). The second region, $X2$, is defined by the recirculation region ($0 < X/K < 5$) and the third region, $X3$, extends from the reattachment point downstream of the element to the vicinity of the donwstream element. It should be noted that the $X1$ and $X4$ locations were measurement points at the same relative positions with respect to the upstream side of the roughness element for the ith and $i+1$th cycles. The velocity and turbulence measurements were made for three Reynolds numbers at each measurement.

For static pressure measurements, two static pressure tubes were placed at the center of pipe to minimize the influence of velocity fluctuations. Hot-film or hot-wire anemometry techniques were used to measure the turbulent mean flow characteristics.

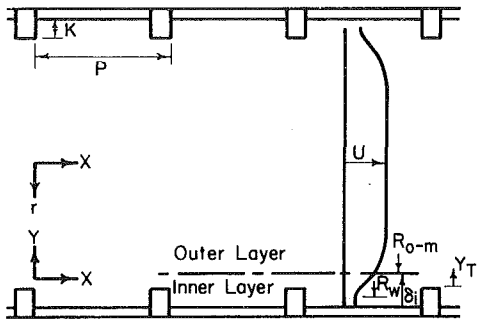

Fig. 1 Schematic diagram of experimental repeated rib configuration

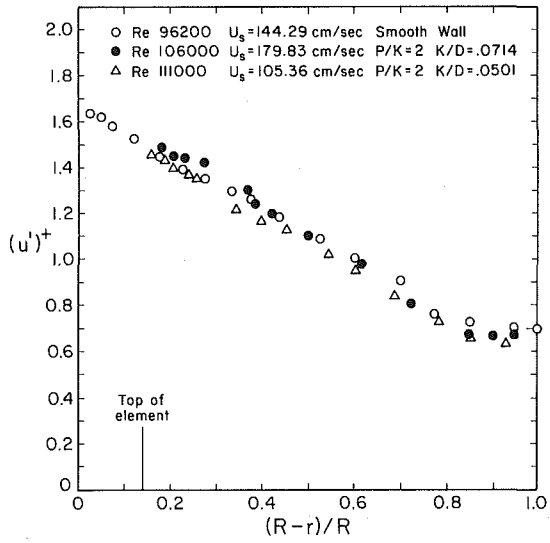

Fig. 2 Fluctuating axial velocity components in rough wall pipe at $P/K = 2$ for K/D values of 0.0714 and 0.0938. The uncertainty in the values of $(u')^+$ are ± 16 percent.

Experimental Results and Discussion

Detailed measurements were made of the variation of u', v', and $\overline{uv}$ for a large number of repeated rib configurations. The shear velocity, U_s, was determined from friction factor data in the conventional manner. Rib spacing to element height, P/K, values of 2, 5, 7, 10, 13, 16, 19, 22, and 25 for the small pipe system ($K/D = 0.0714$) and P/K values of 2, 13, and 24 for the large pipe system ($K/D = 0.0938$) were examined. This paper summarizes the results of these experiments and presents some typical results.

Outer Layer Results. In the quasi-smooth flow regime, the

Nomenclature

P = length of one cycle of repeated rib geometry
K = height of the roughness element
U_s = shear velocity
ϵ = turbulent fluid eddy diffusivity
R = smooth pipe radius or the inner spacing radius measured
Y = distance measured from inner spacing toward the center of pipe
δ_i = inner layer thickness
u' = fluctuating axial velocity component
v' = fluctuating radial velocity component
$\overline{uv}$ = Reynolds shear stress component
$X1$ = measurement location at axial distance of $X/K = -1.5$.
$X2$ = measurement location at axial distance of $X/K = 1$
$X3$ = measurement location approximately midway between the roughness elements. Exact location depends on P/K value.
X = axial distance measured from downstream of the roughness element
D = pipe diameter, $2R$
γ = intercept of eddy diffusivity near the wall at station $X3$
β = slope of eddy diffusivity near the wall at station $X3$
R_{om} = radial location of the mean outer layer

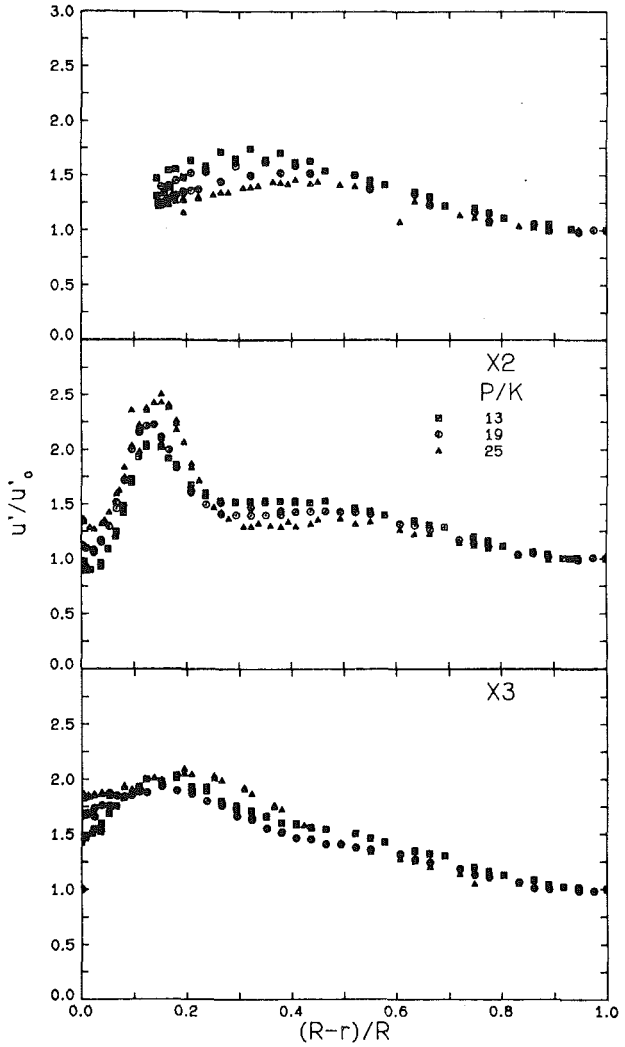

Fig. 3 Fluctuating axial velocity components in rough wall pipe at P/K = 13, 19, and 25 in the small pipe system and measurement positions X1, X2, and X3. For P/K = 13, Re = 98,100, u_0 = 2243 cm/s, u_s = 256.8 cm/s. For P/K = 19, Re = 98,800, u_0 = 2300 cm/s, u_s = 239.6 cm/s, and for P/K = 25, Re = 93,200, u_0 = 2149, cm/s, u_s = 229.9 cm/s. The uncertainty in the u/u'_0 values is ± 25 percent.

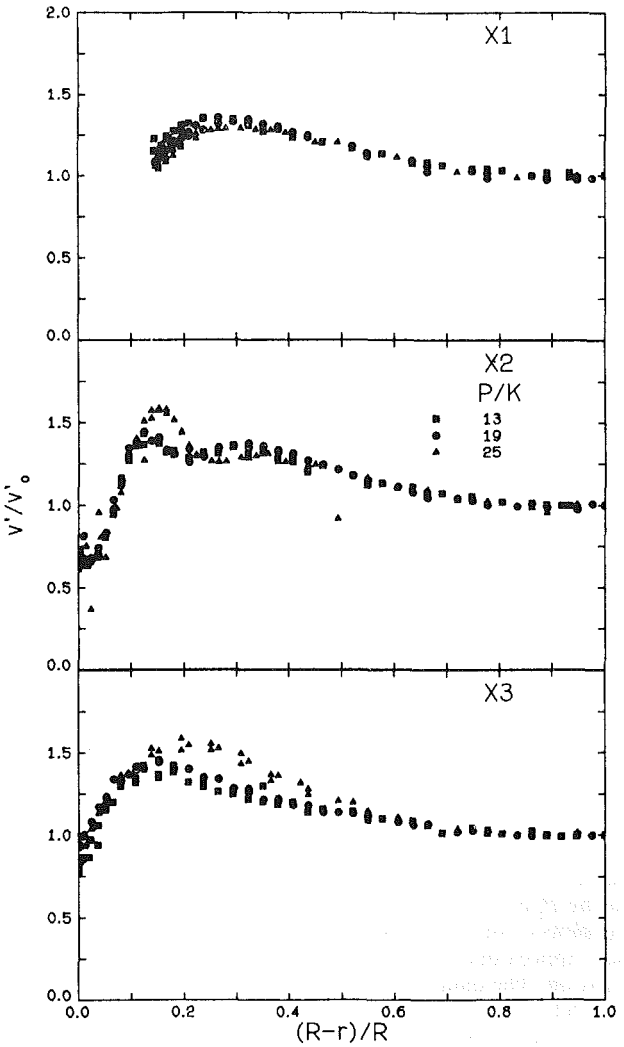

Fig. 4 Fluctuating radial velocity components in wall pipe at P/K = 13, 19, and 25 in the small pipe system and measurement positions X1, X2, and X3. For P/K = 13, Re = 98,100, u_0 = 2243 cm/s, u_s = 256.8 cm/s. For P/K = 19, Re = 98,800, u_0 = 2300 cm/s, u_s = 239.6 cm/s, and for P/K = 25, Re = 93,200, u_0 = 2149, cm/s, u_s = 229.9 cm/s. The uncertainty in the v/v'_0 values is ± 15 percent.

outer layer extends from the pipe center to the top of the elements. For P/K values of 2 and 5 in the small pipe system and P/K of 2 in the large pipe system, the axial fluctuating velocity, u'/U_s, and the Reynolds shear stress, $\overline{uv}/U_s^2$, were approximately the same in the outer layer as that for smooth wall flow. The radial fluctuating velocity component profiles in the small pipe system had a smaller slope than the smooth wall profile. The ratio v'/U_s increased linearly from a value of 0.459 ± 0.003 in the center to 0.577 ± 0.033 in the vicinity of top of the elements. In the larger pipe system, v'/U_s values were essentially the same as the smooth pipe data. Figure 2 gives typical results for the axial fluctuating velocity. This result agrees with Robertson et al. [2] and Chen and Roberson [6], Where they observed that the rough wall turbulence parameters for discrete wall roughness elements when normalized with U_s are approximately the same as the smooth wall measurements in the outer region.

For the hyperturbulent and isolated-roughness-element flow regime the shear velocity was not the best characteristic velocity for the fluctuating velocities. Normalization utilizing the fluctuating velocities at the center of the pipe gave the best results.

Figures 3 and 4 show the axial and radial fluctuating velocities at three axial positions ($X1$, $X2$, $X3$) for geometries with P/K values of 13, 19, and 25 for the small pipe system. These results are typical for all geometries in these flow regimes. The expressions

$$\frac{u'}{u'_0} = 1.54\frac{r}{R} + 1.0 \quad (7) \qquad \frac{R_{om}}{R} \le \frac{r}{B} < 1$$

and

$$\frac{v'}{v'_0} = 0.381\frac{r}{R} + 1.0 \quad (8) \qquad \frac{R_{om}}{R} \le \frac{r}{B} < 1$$

were found to be valid in the outer layer of the flow for the $X2$ and $X3$ axial positions for all geometries in both the large and small diameter pipe systems, and for Reynolds numbers ranging from 95,000 to 150,000 for all P/K values, and for K/D between 0.0174 and 0.0938. The outer layer distances, R_{om}, for the various geometries are given in Table 2. The square of the shear velocity, U_s, was the best normalization parameter for the Reynolds shear stress for all stations and geometries.

Inner Layer Results. Turbulence measurements in the inner layer were more complex for the hyperturbulent and isolated

Table 2 Mean outer layer thickness, R_{om}

P/K	Stations X2	X3
Small Pipe System		
7	0.85*	0.85*
10	0.85	0.90
13	0.79	0.92
16	0.82	0.91
19	0.65	0.93
22	0.76	0.91
25	0.61	0.91
Large Pipe System		
13	0.84	0.94
24	0.84	0.91

*Uncertainties in these values are ± 0.03

roughness configurations. Figures 3 and 4 also give typical results for each of three axial positions in these regimes.

At the first position ($X1$), the axial fluctuating velocity components u'/u'_0, and v'/v'_0 were similar for all geometries. Apparently the presence of the step was the dominating feature of the region and the flow did not distinguish between regimes. At the second position ($X2$), all the turbulence parameters increased sharply in the vicinity of the roughness element. The rate of increase varied little with geometry when the fluctuating velocities were normalized with their corresponding center of pipe values. This rate of increase was a more pronounced function of P/K, however, when these parameters were normalized with the center of pipe mean axial velocity. The turbulence parameters for P/K of 7 and 10 in the small pipe system showed negligible peaks caused by the presence of the step. These profiles were similar to the P/K of 5 geometry of quasi-smooth flow regime. All the plots of the turbulence velocities at the third position ($X3$) had approximately the same shape regardless of the axial position. The data suggest that the turbulence flow quantities beyond the attachment point reached a quasi-equilibrium state and did not change until the flow encountered the next step.

The variation of the shear stress at each of the three positions is given in Fig. 5. At position 1 ($X1$), it is seen that for P/K of 5, the shear stress distribution is linear until the top of the element is reached. As the spacing between the roughness elements is increased (higher P/K values), the effect of the step becomes more pronounced. For P/K values greater than 10, the effect of the element on the shear stress extends into the flow to $(R-r)/R$ values ranging between 0.3 and 0.35. The shear stress variation at position 2 ($X2$) characterized by a decrease as the element is approached followed by a sharp increase in the stress at the top of the element. The effect of the element on the flow extends to $(R-r)/R$ values of 0.4 to 0.45. Position 3 ($X3$) data gives insight into the variation of the shear stress with distance downstream of the element. It is seen that for $X/K=11$, the shear stress "overshoots" the linear distribution expected for rough wall flow. Siuru and Logan [9] reported similar "overshoot" results. Data at position 3 ($X3$) represent flow conditions near the midpoint between the elements for each configuration. As can be seen from the figure, the "overshoot" does not occur for P/K values less than 19. Figures 3, 4, and 5 also confirm the periodic nature of the flow in the inner layer as reported by Siuru and Logan [9] for P/K values greater than 5(7?).

Turbulent Eddy Diffusivity. The Boussinesq definition of the eddy diffusivity was used. In the quasi-smooth flow regime, the eddy diffusivities were distinctly different from other flow regimes. Figure 6 shows the eddy diffusivities for P/K of 2 in the small pipe system and in the large pipe system, respectively. In general, the eddy diffusivity in this flow

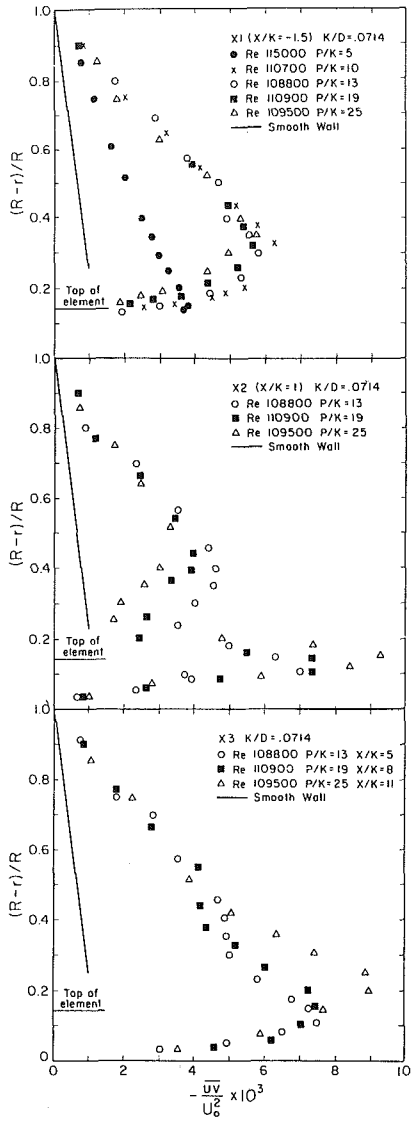

Fig. 5 Rough wall shear stress distribution at measurement positions $X1$, $X2$, and $X3$. The uncertainty in the $-uv/u_0^2$ values range from ± 20 percent for the smaller values to ± 2 percent for the largest values.

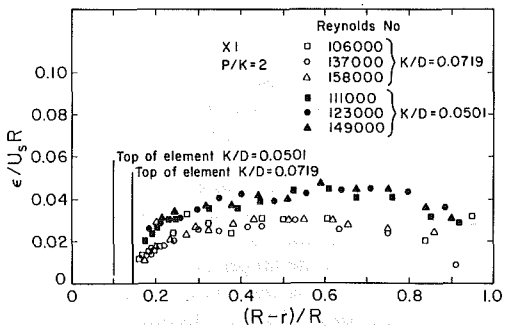

Fig. 6 Turbulent eddy diffusivity in the quasi-smooth flow regime for P/K = 2 in the small and large system. The uncertainty in the $/U_S\ R$ values range from ± 13 percent at $(R-r)/R$ = 0.866 to ± 7 percent at $(R-r)R$ = 0.326 to ± 10 percent at $(R-r)/R$ = 0.164.

regime increased from a small value near top of the element to a nearly constant value in the region of the pipe center.

In the isolated-roughness-element and hyperturbulent flow regimes, the turbulent eddy diffusivities distributions were clearly different from those in the quasi-smooth regime. Measurements of turbulent eddy diffusivities were made for

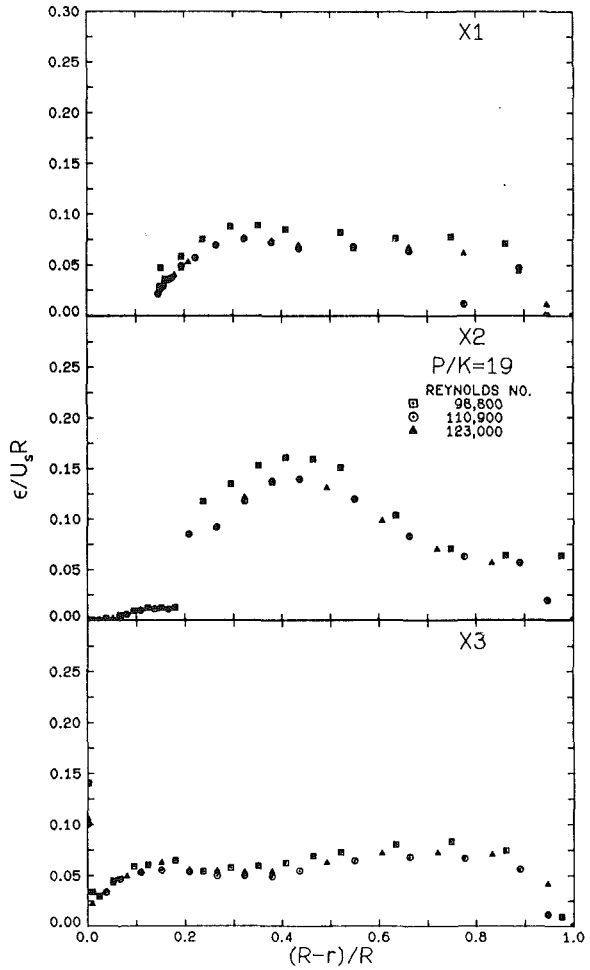

Fig. 7 Turbulent eddy diffusivity in the isolated-roughness-element regime for $P/K = 19$ in the small pipe system. The uncertainty in the $/U_s$ R values range from ± 20 percent at $(R-r)/R = 0.890$ to ± 6 percent at $(R-r)R = 0.351$ to ± 15 percent at $(R-r)/R = 0.152$.

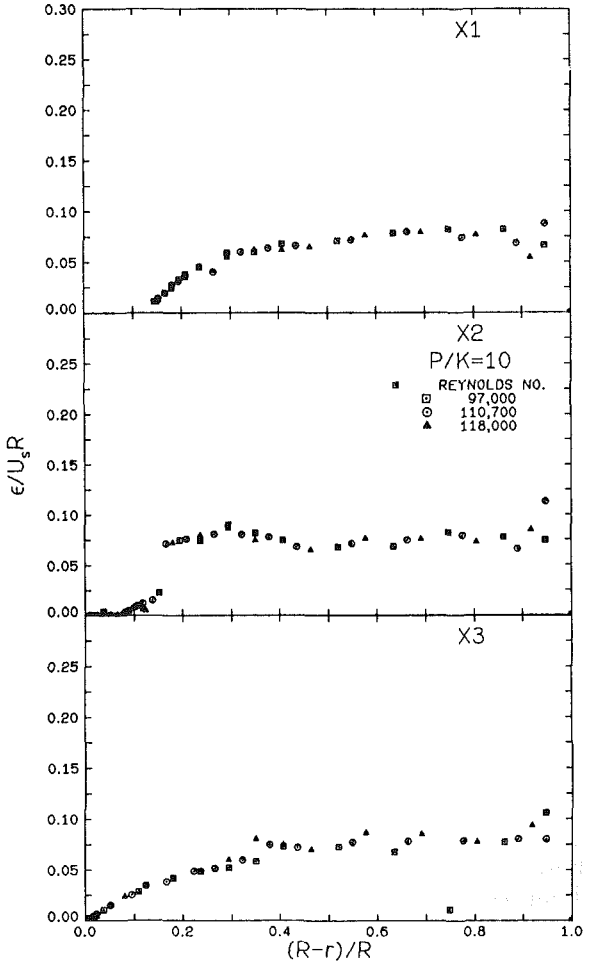

Fig. 8 Turbulent eddy diffusivity in the hyperturbulent flow regime for $P/K = 10$ in the small pipe system. The uncertainty in the $/U_s$ R values range from ± 18 percent at $(R-r)/R = 0.890$ to ± 8 percent at $(R-r)R = 0.322$ to ± 11 percent at $(R-r)R = 0.103$.

P/K values of 7, 10, 13, 19, 22, and 25. Figures 7 and 8 show the results for $P/K = 19$ and 10. As can be seen from the figures, values of the eddy diffusivities are given for three stations and flow rates.

At the first axial position ($X1$) of the isolated-roughness-element flow regime ($P/K = 19$), the eddy diffusivity decreased from a relatively constant value in the outer layer as the step was approached. At the second axial position, the eddy diffusivity was essentially constant in the outer layer. As the wall was approached, the presence of the roughness element caused an increase of the eddy diffusivity where this increase was a function of geometry. A rapid change in the value of the diffusivity was observed near the top of the element. This rapid variation was due to two effects: the large velocity gradient and the increase in the Reynolds shear in the vicinity of the element. The velocity graduate variation was the more dominant of the two effects. In the large pipe system, similar behavior with much lower amplitude was observed for P/K of 24. At the third axial position ($X3$), the eddy diffusivity increased from a very small value (nearly zero) at the wall to a constant value near the center of pipe. For the isolated-roughness-element flow regime, the rise of the ϵ^+ near the wall can be approximated by

$$\epsilon^+ = \beta(R-r)/R + \gamma \tag{12}$$

The slope, β, varies from 0.286 ± 0.011 to 0.407 ± 0.019 and the intercept, γ, varies from 0.013 ± 0.001 to 0.029 ± 0.006 in the isolated-roughness-element flow regime. Table 3 gives the values of these slopes and intercepts for geometries of $P/K > 7$ in the small pipe system and greater than P/K of 13 in the large pipe system.

Table 3 Eddy diffusivity near the wall at station $X3$

$$\epsilon = \beta\left(\frac{R-r}{R}\right) + \gamma$$

P/K	γ	β
Small Pipe System		
7	0.005 ± 0.001	0.093 ± 0.010
10	0.000 ± 0.001	0.267 ± 0.015
13	0.000 ± 0.001	0.272 ± 0.015
16	0.028 ± 0.002	0.433 ± 0.040
19	0.029 ± 0.006	0.286 ± 0.111
22	0.013 ± 0.001	0.407 ± 0.019
25	0.015 ± 0.001	0.388 ± 0.017
Large Pipe System		
13	0.001 ± 0.001	0.310 ± 0.019
24	0.012 ± 0.003	0.160 ± 0.043

The eddy diffusivity distribution in the hyperturbulent flow region ($P/K = 10$) was quite similar to that formed in the isolated isolated-roughness element case. The variation of ϵ^+ for P/K of 10 was much less pronounced in the vicinity of the element ($X2$) than that for P/K of 19. Also the increase in magnitude of ϵ^+ in the third axial region ($X3$) was smaller. The slope and intercepts of equation (12) are given in Table 3.

Conclusions

1. For the quasi-smooth regime, the values of u'/u_s, v'/u_s, and $\overline{uv}/u_s^2$ were essentially the same as those for smooth wall pipe flow for all axial stations.

2. The expressions

$$\frac{u'}{u_0'} = 1.54\frac{r}{R} + 1.0 \qquad \frac{R_{om}}{R} \leq \frac{r}{R} \leq 1$$

$$\frac{v'}{v_0'} = 0.381\frac{r}{R} + 1.0 \qquad \frac{R_{om}}{R} \leq \frac{r}{R} \leq 1$$

were found to be valid in the outer layer of the flow for the $X1$ and $X2$ axial position, all geometries in both the large and small diameter pipe systems, and Reynolds numbers ranging from 95,000 to 150,000.

3. The Reynolds stress distribution is linear in the outer layer for all flow configurations.

Acknowledgments

This work was conducted under contract H0292032 from the U.S. Bureau of Mines. The authors would like to thank Drs. B. G. Jones, R. J. Adrian, J. M. Robertson, J. S. Walker, and T. J. Hanratty for their discussion of results and interpretation with one of the authors (K.N.). We would also like to thank Dr. K. Leong, and Mr. A. Hubbard for their assistance in performing the experiments.

References

1 Morris, H. M., "A New Concept of Flow in Rough Conduits," Ph.D. dissertation, University of Minnesota, 1950.

2 Robertson, J. M., Martin, J. D., and Burkhurt, T. H., "Turbulent Flow in Rough Pipes," *Industrial and Engineering Chemistry Fundamentals*, Vol. 7, 1963, pp. 253-265.

3 Robertson, J. M., Burkhurt, T. H., and Martin, J. D., "Study of Turbulent Flow in Rough Pipes," University of Illinois, Theoretical and Applied Mechanics Report No. 279, Urbana, 1965.

4 Robertson, J. M., and Martin, J. D., "Turbulence Structure Near Rough Surface," *AIAA Journal*, Vol. 4, 1966, pp. 2242-2245.

5 Goma, R. J., and Gelhar, L. W., "Turbulent Pipe Flow With Rough and Porous Walls," Department of Civil Engineering, Massachusetts Institute of Technology, Hydrodynamic Laboratory Report No. 109, Cambridge, 1968.

6 Chen, C. K., and Roberson, J. A., "Turbulence in Wakes of Roughness Elements," *Journal of Hydraulic Division*, Vol. 100, 1974, pp. 53-67.

7 Islam, O., and Logan, E., "Channel Flow Over Smooth-to-Rough Surface Discontinuity With Zero Pressure Gradient," ASME JOURNAL OF FLUIDS ENGINEERING, Dec. 1976, pp. 626-634.

8 Antonia, R. A., and Luxton, R. E., "The Response of a Turbulent Boundary Layer to a Step in Surface in Surface Roughness, Part-1, Smooth to Rough," *Journal of Fluid Mechanics*, Vol. 48, 1971, pp. 721-761.

9 Siuru, W. D., and Logan, E., Jr., "Response of a Turbulent Pipe Flow to a Change in Roughness," ASME JOURNAL OF FLUIDS ENGINEERING, Vol. 99, 1977, pp. 548-555.

10 Siuru, W. D., "Response of a Turbulent Pipe Flow to a Change in Surface Roughness," Ph.D. dissertation, Arizona State University, 1975.

11 Antonia, R. A., and Luxton, R. E., "The Response of a Turbulent Boundary to an Upstanding Step Change in Surface Roughness," ASME *Journal of Basic Engineering*, Vol. 93, 1971, pp. 22-34.

12 Powe, R. E., "Turbulent Structure in Smooth and Rough Pipes," Ph.D. dissertation, Montana State University, 1970.

13 Liu, C. K., "An Experimental Study of Turbulent Boundary Layer on Rough Walls," Ph.D. dissertation, Stanford University, 1966.

Vortex Shedding in a Linear Shear Flow From a Vibrating Marine Cable With Attached Bluff Bodies

R. D. Peltzer
Naval Research Laboratory,
Washington, D.C. 20375

D. M. Rooney
Engineering Sciences Department,
Hofstra University,
Hempstead, N.Y. 11550

The present study examines the vortex street wake behavior of a flexible, helically wound, high aspect ratio marine cable in a linear shear flow. Particular attention is paid to the lock-on phenomena associated with uniform and sheared flow past the cable when it is forced to vibrate in the first mode, normal to the flow. An analysis is given of the effects on the vortex shedding and synchronization phenomena that are generated by placing distributions of spherical bluff body shapes along the span of the cable in uniform and sheared flow. The latter geometry is representative of a number of cable system deployments and has special consequencies for strumming in a shear flow. The effectiveness of these attached spheres as strumming-suppression devices is evaluated. Synchronized vibration and/or the presence of the bluff bodies significantly affected the spanwise character of the near wake cellular vortex shedding structure. The spanwise extent of the resonant, vortex-excited oscillations was significantly extended by the presence of the spheres along the cable span. This finding was particularly significant because it meant that the undesirable effects that accompanied synchronization would be extended over a longer portion of the cable span.

Introduction

Mooring systems and risers of offshore drilling and production platforms, cable networks used to support marker buoys, and towed cable arrays are all examples of long flexible, cylindrically shaped bodies. When they are towed through the water, or exposed to waves and currents, vortices are shed as the flow separates alternately from opposite sides of these high aspect ratio bodies. If these vortices are shed at a frequency close to one of the natural frequencies of the structural system, the shedding can lock-on to (synchronize with) the natural frequency if the damping is sufficiently small. This phenomenon, commonly referred to as cable-strumming, is characterized by large amplitude cross flow oscillations, increased stresses, amplified acoustic flow noise, amplified hydrodynamic forces and increased fatigue and damage to the entire system.

Further complicating the situation is the occurrence of vertical velocity gradients or sheared current profiles that are typically found in the oceans. The vortex shedding frequency along the span of a vertical or inclined cable then also varies with depth. Synchronization or strumming and its related phenomena may occur over part or all of the cable.

The present study examines the near wake behavior of a flexible, helically wound, high aspect ratio marine cable in a linear shear flow. Particular attention is paid to the lock-on phenomena associated with uniform and sheared flow past the cable when it is forced to vibrate in the first mode, normal to the flow. An analysis is given of the effects on the vortex shedding and synchronization phenomena that are generated by the noncircular helical cross section and by the placement of distributions of spherical bluff body shapes along the span of the cable in uniform and sheared flow. The effectiveness of these spheres as strumming-suppression devices is evaluated in light of this analysis.

The spheres were 1.5 in. (3.81 cm) diameter ping pong balls. They were chosen because their negligible mass did not affect significantly the vibration amplitude and frequency. Since the spheres were massless, their effects on the synchronized vortex shedding would be due solely to changes in the near wake flow created by their presence.

Background

Since the cable system employed in the present tests was too highly damped to be self-excited in an air flow, forced excitation was used to simulate the self-excited resonant wake conditions in order to study the lock-on induced changes in the cable wake. The validity of this approach has been examined by Griffin [2] who found that changes in the near wake that accompany resonant vortex excited oscillations were reproducible from forced, externally-excited oscillations when the experimental conditions were carefully duplicated. This method also had the advantage that the amplitude of vibration, and the natural frequency and mode shape, could be varied independently.

Observations of, and measurements of wake velocity profiles, wake spectra, and flow visualization studies led Ramberg and Griffin [9–11] to define three distinct flow regimes along the vibrating cable span in a uniform flow. The

Contributed by the Fluids Engineering Division of THE AMERICAN SOCIETY OF MECHANICAL ENGINEERS and presented at the Fluids Engineering Conference, Houston, Texas, June 20–22, 1983. Manuscript received by the Fluids Engineering Division, February 11, 1983.

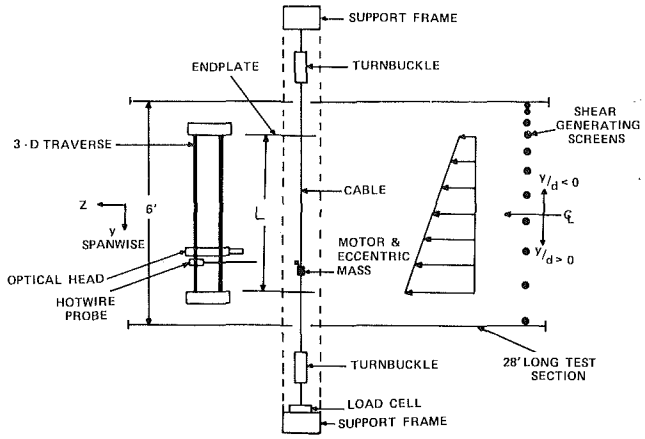

Fig. 1 Wind tunnel test section and cable model (top view)

first region was the flow in the immediate vicinity of a cable node which closely resembled that past a stationary body. A transition region was identified which was adjacent to the cable node region and which extended to the cable antinode region where the vortex shedding had locked-on to the cable vibration. The third region occurred in the vicinity of the cable antinode where the vortex shedding was highly correlated along the span and the power spectra contained a sharp peak at the synchronization frequency. The spanwise extent of this region could be closely approximated by the lock-on regions previously found for rigid cylinders [4, 13].

Results dealing with the wake flow behind a stationary bluff body in a linear shear flow have been published by Peltzer and Rooney [7], Woo et al. [14], Mair and Stansby [5], Stansby [13] and Maull and Young [6]. Linear shear flows are characterized by the nondimensional shear parameter $\beta = d/U_c(dU/dy)$. Both Maull and Young, and Mair and Stansby have examined the effect of a sheared flow on the spanwise distribution of the vortex shedding frequency for small aspect ratio bluff bodies ($L/d < 20$). They found that a number of coherent cells of constant shedding frequency were present along the span of their models for Reynolds numbers less than 2.0×10^4. Flow visualization photographs taken by Maull and Young indicated that the cells were separated by cross-stream vortices aligned with the free stream direction. Both Woo et al. and Peltzer [7] have shown that the length of the discrete cells in a sheared flow varied inversely with the shear parameter β. For high aspect ratio cylinders ($L/d > 27$), Woo's results showed that some type of cellular vortex structure could exist in the wake of a cylinder up to Reynolds numbers of approximately 10^4.

The work by Stansby represented the only previous experimental study dealing with the wake properties behind a vibrating rigid cylinder in a sheared flow. The vortex shedding frequency locked-on to the cylinder vibration frequency, as well as to subharmonics of it, over a portion of the cylinder span. The balance of the cells that were not "captured" became very stable at other frequencies i.e., the spanwise shedding structure became very well defined.

Woo et al. [14] studied the vortex wakes of oscillating cables in a linear shear flow. They found that the body oscillations induced vortices which were in perfect synchronization with the body motion, and that the strength of these vortices was amplified. The unforced cells adjacent to the lock-on region were again stabilized, and the frequency of the shedding in these cells was forced away from that value corresponding to the stationary cable shedding frequency (in a sheared flow).

Efforts have been made [3] to reduce cable strumming by attaching strumming-suppression devices that alter the formation of vortices by changing the near wake flow about the cable, to the cable. These devices suppress the strumming by breaking down the vortex shedding coherence, and/or by increasing the vortex formation length (delaying the vortex formation), and/or by increasing the viscous damping characteristics of the cable. An excellent summary of strumming suppression devices and their effectiveness is also given in reference [3].

The results that are presented in this paper are part of a wider-ranging study [8] which also dealt with the effects that forced vibration and the helically-wound cross section have on the vortex formation length, shedding frequency, vortex strength, reduced velocity and wake width in uniform flow. The mean Strouhal number of the nonvibrating cable was constant throughout the Reynolds number range 2.0×10^3 to 4.0×10^4 at the value St = 0.192. The helical cross section of the cable lengthened the vortex formation region by as much as thirty-three percent when compared to circular cross section cable values. The synchronized vibration caused significant changes in the near wake development in uniform flow. As the vibration amplitude along the span of the cable increased locally, the formation length increased and the vortex strength, shedding frequency and Strouhal numbers decreased.

The Wind Tunnel and Measuring Systems

The present experiments were conducted in the 8.5m long, 1.8m square test section of the VPI&SU subsonic stability wind tunnel. An upstream velocity shear was generated in the tunnel by a series of six wire screens, incorporating vertical rods in a nonuniform cross-tunnel distribution. The screens could be arranged in any combination to produce a variety of free-stream shear levels, $\beta = d/U_c(dU/dy)$. An electronically controlled three-dimensional traverse was available to transport the measuring instruments in the vertical (x), spanwise (y), or streamwise (z) directions. Figure 1 shows a diagram of the wind tunnel test section including the cable model.

The cable that was used in the tests is constructed of seven strands of Kevlar synthetic fiber rope, wound around each other helically, and wrapped with a polyurethane jacket. The noncircular cross section has a 1.143 cm measured mean diameter over the jacket. The aspect ratio of the cable, which was securely pinned at the endplates, was $L/d = 107$. The cable tension was adjusted with the turnbuckles and measured by a Strainsert Universal Flat Load Cell. The small dc motor with an eccentrically located mass was attached to the cable in order to excite the lower vibration modes by varying the motor speed and cable tension. The cable mode shape,

Nomenclature

a = local vibration amplitude
a_{max} = vibration amplitude at an antinode
d = general bluff body diameter
d_s = sphere diameter
f_{csv} = vortex shedding frequency from a vibrating cable
L = bluff body length
Re_c = $(U_c d/\nu)$; center-span Reynolds number
St_c = $(f_{csv} d/U_c)$; center-span Strouhal number
f_{ssv} = vortex shedding frequency from a vibrating cable
f_{cv} = cable vibration frequency
U_c = velocity at wind tunnel centerspan
y/d = nondimensional spanwise location
β = $d/U_c(dU/dy)$; shear parameter

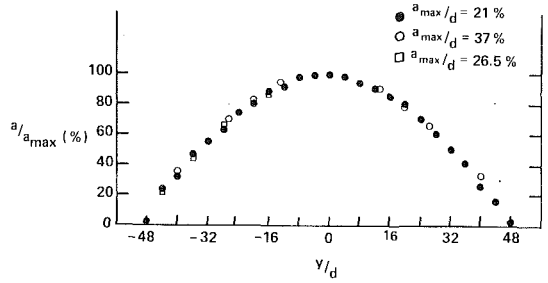

Fig. 2 Cable mode shape (first mode)

vibration amplitude, and frequency were obtained using a Physitech Electro-Optical Auto-Collimator Tracking Unit. The optical head was mounted on the traverse downstream of the cable, and focused on the top edge of the cable which had an incandescent light source placed upstream of it to give a clear edge for tacking. Details of the cable vibration measuring procedure are given by Peltzer [8].

To examine the vortex shedding characteristics in the near wake of the cable, a straight hot wire probe was attached to the traverse and positioned in the cable wake at a position where the strongest vortex shedding occurred (x/d = 0.92, z/d = 3.5). The probe was connected to a TSI Model 1050 Constant Temperature Anemometer module. The output signal from the anemometer was also band-pass filtered and sent to the ZTL FFT processor.

The experiment was designed to measure the flow properties in the near wake of a flexible cable forced to vibrate in the first mode. The nondimensional first mode shape is shown in Fig. 2. The absolute value of a/a_{max} was plotted against the spanwise location (y/d) along the cable. The mode shape was invariant with peak to peak vibration amplitude, a_{max}/d. The measured values of the vibration amplitude (a) along the span of the cable were accurate to within ±4 percent, which was the overall accuracy of the Physitech/rms meter measuring arrangement.

Results and Discussion

The spanwise power-spectral data are plotted here as Strouhal numbers based on the centerline velocity, $St_c = f_{csv}d/U_c$, versus the spanwise position, y/d. The data were presented in this manner to elucidate the spanwise cellular structure of the shedding frequency, whenever it existed. A single closed circle on these plots represents a narrow band shedding frequency peak on the power spectra. A closed circle connected to a bar represents a high energy narrow band shedding peak with a lower energy wide band to either side of the peak, and a bar represents a wide, broad-banded peak with no dominant high energy shedding peak present. The Strouhal numbers in the plots are accurate to within ±2.0 percent.

The Stationary Bare Cable. The Strouhal numbers in the near wake of the stationary cable at $Re_c = 2.96 \times 10^3$, are plotted in Fig. 3. A definite spanwise cellular structure was evident, where the frequency peaks within each of these cells were generally sharp and narrow-banded. At the boundaries between some cells, the spectra were broad-banded with no dominant shedding frequency or they exhibited the two distinct frequencies associated with the individual cells. The fluctuating cell boundaries, when averaged twenty times during the two minute data record, allowed the contribution from both cells to be included in the spectral average. Depending on how rapidly the cell boundaries were fluctuating, the power spectrum was either broad-banded or showed the two distinct frequency peaks. Not including end cells, there were ten cells of constant Strouhal number along the cable span, ranging in length from eight to eighteen

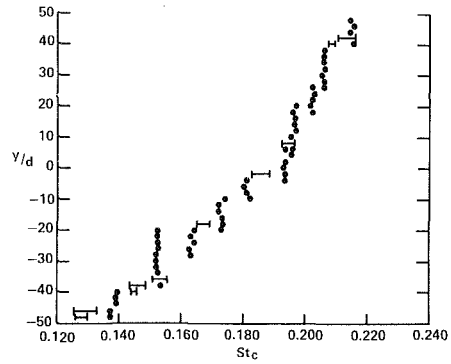

Fig. 3 Spanwise Strouhal number variation, $Re_c = 2.96 \times 10^3$, no vibration, no spheres, $\beta = 0.0053$

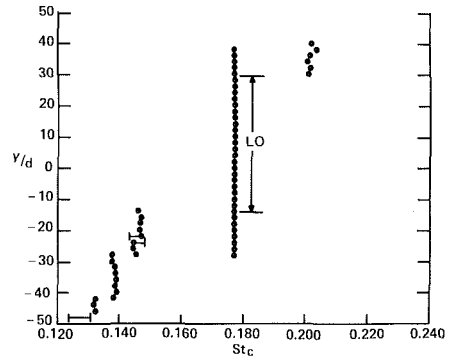

Fig. 4 Spanwise Strouhal number variation, $Re_c = 2.96 \times 10^3$, no spheres, a_{max}/d = 29.1 percent, $\beta = 0.0053$

diameters. The average length of these cells was eleven diameters.

The Vibrating Bare Cable. The Strouhal numbers corresponding to the vibrating cable spectra, with a_{max}/d = 0.291 and $Re_c = 2.96 \times 10^3$, are shown in Fig. 4. The already complicated cellular structure of the vortex shedding along the cable in a sheared flow (Fig. 3) is further complicated by the synchronized vibration and the local changes in the formation length, vortex strength, vortex shedding frequency and Strouhal number that accompany the local vibration amplitude variation along the span of the flexible cable. A definite spanwise cellular structure in the shedding frequency was present along the cable. The spanwise power spectra in the synchronization region, centered near the cable antinode between $y/d = -14.0$ and $y/d = 30.0$ contained a sharp, high energy peak at the synchronization frequency. The length of this region is dependent upon the vibration amplitude, as well as the shear parameter β and the natural frequency. In the locked-on region, the fluctuating lift force created by the alternately shed vortices is in phase with the oscillatory velocity of the cable. The resonant amplitude dies out completely when the two frequencies can no longer act in unison. The vortex shedding frequency then jumps to a value close to that governed by the usual Strouhal relationship [12].

The forty-four diameter length of the locked-on cell was greater than the thirty-eight diameter length associated with the vibration amplitude, $a_{max}/d = 0.233$, $Re_c = 2.6 \times 10^3$, since the length of the locked-on region increased with vibration amplitude. This increase has been documented by Koopmann [4], Stansby [12], and Peltzer [8]. The average length of the unforced cells adjacent to the locked-on region was fourteen diameters, nearly equivalent to the 13.5 diameter length associated with the vibrating cable results at a_{max}/d = 0.233, and significantly larger than the average length of eleven diameters found along the nonvibrating cable span.

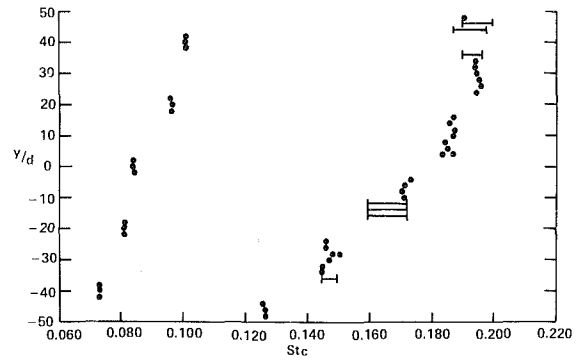

Fig. 5 Spanwise Strouhal number variation, $Re_c = 2.96 \times 10^3$, five spheres, no vibration, $\beta = 0.0053$

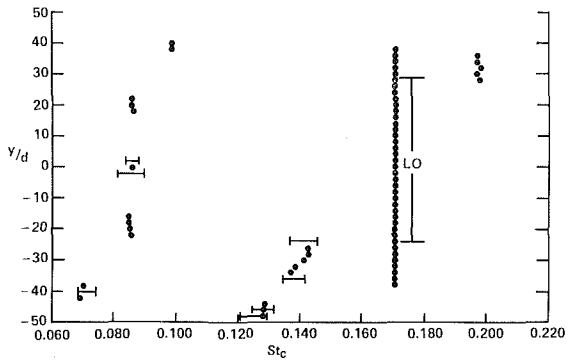

Fig. 6 Spanwise Strouhal number variation, $Re_c = 2.96 \times 10^3$, five spheres, $a_{max}/d = 23.3$ percent, $\beta = 0.0053$

The boundaries between cells were marked by discontinuous spatial jumps in Strouhal number. In both the vibrating cable results, the synchronized vibrations stabilized the general cellular structure and eliminated the fluctuating boundary effects. Stansby [13] and Woo et al. [14] also noted this stabilization.

The Strouhal numbers of the cells adjacent to the locked-on region were nearly equivalent to the stationary cable values. The shedding in these adjacent cells was intermittent between forced and unforced, characteristic of the transition region observed by Ramberg and Griffin [9–11] along the span of their vibrating, flexible cable in a uniform flow. This result was consistent with one of the observations listed by Sarpkaya [12] in his summary of the primary consequences of synchronized shedding. He noted that at the end of the lock-on range the vortex shedding frequency jumped to a value governed by the Strouhal relationship.

The Stationary Cable, Five Spheres. The Strouhal numbers along the stationary cable with five spheres at spanwise locations $y/d = -40, -20, 0, 20, 40$ are shown in Fig. 5. The Strouhal number (shedding frequency) of the spheres, based on the centerline velocity, increased proportionally to the velocity across the span. The sphere vortex wakes significantly influenced the cable vortex wake for six cable diameters, i.e., ± three diameters from the center of the spheres. Between the shedding cells downstream of the spheres, the cable shedding frequency peaks on the power spectra were generally more broad-banded than the narrow-banded high energy peaks that were characteristic of the bare cable spectra. The highly three-dimensional turbulent wakes of the spheres disrupted the cellular shedding pattern normally present in the bare cable wake and broadened the shedding peaks with the increased turbulent energy they imparted to the cable wake. Not including the two end cells, four cable shedding frequency cells with an average length of fourteen diameters, separated by five sphere shedding cells with an average length of six diameters, were located along the entire cable span.

The cable shedding frequencies between the spheres were generally forced into discrete cells, the exception being the cell centered around $y/d = -10$. The spheres act like individual endplates, splitting the high aspect ratio cable into six small aspect ratio segments. It has been established [5] that for a constant shear level the number and length of discrete cells present in the wake of cylinders with aspect ratios less than twenty is dependent upon the aspect ratio and the type of end effects present. The average length of the cells along the span of the cable with no spheres was eleven diameters. The shedding between the spheres was forced into single discrete cells, fourteen diameters long, by the combination of small aspect ratio effects and the added turbulence contributed by the spherical endplates.

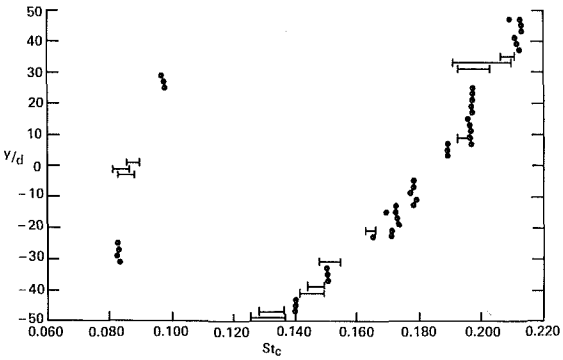

Fig. 7 Spanwise Strouhal number variation, $Re_c = 2.96 \times 10^3$, three spheres, no vibration, $\beta = 0.0053$

The Vibrating Cable, Five Spheres. The cable with the five spheres attached was vibrated in the first mode ($a_{max}/d = 0.233$). The spanwise Strouhal numbers are shown in Fig. 6. The cable vortex shedding frequency power spectra in the regions separated by the spheres were again slightly broad-banded. The three central spheres ($y/d = -20, 0, 20$) locked on to a submultiple of the cable vibration, $f_{ssv}/f_{cv} = 1/2$. The presence of the spheres had a significant effect on the length of the lock-on region. The lock-on region extended from $y/d = -24.0$ to $y/d = 29.0$ (fifty-three diameters), compared to forty-four diameters on the bare vibrating cable with $a_{max}/d = 0.291$, and thirty-eight diameters on the bare vibrating cable with $a_{max}/d = 0.233$.

It was shown in Fig. 4 that the shedding was locked on to the vibration between $y/d = 0.0$ and $y/d = -14.0$, and was intermittent between forced and unforced in the region between $y/d = -14.0$ and $y/d = -28.0$ along the span of the vibrating cable with no spheres attached. The spheres enclosing the small aspect ratio segment of the cable, $y/d = 0.0$ to $y/d = -20.0$, were locked on to a submultiple of the vibration frequency. This together with the singular cell pattern forced between the spheres enforced the already present, highly correlated, synchronized shedding, thereby eliminating the intermittent shedding and extending the lock-on region for ten more diameters. Again, the unforced cells adjacent to the locked-on region were intermittent between forced and unforced shedding and the Strouhal numbers were nearly equal to those found in stationary flow. The extension of the length of this locked-on region by as much as forty percent was very significant because it meant that the undesirable effects that accompany synchronization (i.e., large amplitude oscillations, increased drag and fluctuating lift forces, highly correlated shedding, etc.) extended over a longer portion of the cable span. The spheres were ineffective in acting as strumming-suppression devices. The increased vortex shedding coherence created by their presence actually reinforced the strumming.

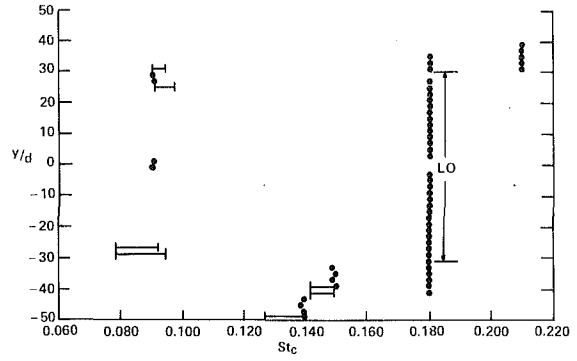

Fig. 8 Spanwise Strouhal number variation, $Re_c = 2.96 \times 10^3$, three spheres, $a_{max}/d = 23.5$ percent, $\beta = 0.0053$

The Stationary Cable, Three Spheres. The number of spheres attached to the cable was then reduced to three, and the spacing between them increased to twenty-eight diameters. The resulting spanwise Strouhal number distribution for flow past the stationary cable at $Re_c = 2.96 \times 10^3$ is shown in Fig. 7. Those cable shedding frequency peaks not directly in the regions adjacent to the spheres were narrow-banded like those associated with the bare stationary cable frequency peaks. The frequency peaks in the cable wake regions adjacent to the spheres were again more broad-banded because of the influence of the three-dimensional turbulent wakes of the spheres. These three-dimensional turbulent wakes were no longer able to exert influence over the entire spanwise distance between the spheres. The cable vortex shedding frequencies were not forced into discrete cells between the spheres as they had been when the spacing was twenty diameters. Across the cable span there were seven or eight cells of constant vortex shedding frequency, ranging in length from four to eighteen diameters, plus the three cells representing the sphere vortex shedding frequencies.

At the shear level of $\beta = 0.0053$, twenty diameters was the maximum spacing that forced the cable shedding frequencies between the spheres into discrete cells. Generally, the maximum spacing that forced the vortex shedding frequency between these discrete bluff body shapes into identifiable cells of constant frequency depended on the shear level β, the geometry of the discrete bluff body and the body to which it was attached, the flow Reynolds number, and the stability of the flow itself.

The Vibrating Cable, Three Spheres. The cable with the three spheres was vibrated ($a_{max}/d = 0.235$) in the first mode at a Reynolds number of 2.96×10^3. The Strouhal number plot is shown in Fig. 8. The vortex shedding was locked on to the vibration over the entire spanwise region bounded by the spheres, $-31.0 \leq y/d \leq 30.0$ (sixty-one diameters)). The three spheres were all locked on to a submultiple of the cable vibration frequency, $f_{ssv}/f_{cv} = 1/2$.

The sphere lock-on enforced the highly correlated, synchronized shedding that was already present in the twenty-eight diameter segment between $y/d = 0.0$ and $y/d = -28.0$. Again, the synchronized shedding was strengthened enough such that the intermittent shedding was eliminated and the lock-on region was extended. Again the spheres were ineffective in acting as strumming-suppression devices. Their presence enforced the synchronized shedding. The unforced cells adjacent to the lock-on region were intermittent between forced and unforced shedding and the Strouhal numbers were nearly equivalent to those in unforced shedding. The sixty-one diameter locked-on region was fifteen percent longer than the fifty-three diameter locked-on region in the five sphere test, thirty-nine percent longer than the forty-four diameter locked-on range corresponding to the bare vibrating cable ($a_{max}/d = 0.291$), and sixty-one percent longer than the thirty-eight diameter range found on the bare cable which was vibrated at a comparable amplitude, $a_{max}/d = 0.233$. The spanwise distance between the spheres had a very significant effect on the length of the locked-on region. The spanwise extent of resonant, vortex-excited oscillations approached the half-wavelength of the marine cable in the present study.

Summary

The principal results of the present study concerning the individual and combined effects of vibration, shear and attached spheres on the vortex shedding in the near wake of a marine cable can be summarized as follows.

A small amount of linear shear in the upstream velocity profile initiated a strong cellular vortex shedding structure in the wake of the helical cross-section cable at the Reynolds number considered. The spanwise cellular structure of the vortex shedding was stabilized significantly by the vibration, and the unlocked cells on the vibrating cable were longer than the cells along the span of the stationary cable. The length of the locked-on region in sheared flow was vibration-amplitude dependent. The presence of and spanwise distance separating the spherical bluff bodies along the span of the high aspect ratio cable had a significant effect on the spanwise character of the vortex shedding structure in the near wake of the stationary and synchronized vibrating cable in a shear flow.

For flow past both the stationary and the vibrating cable with the attached spheres, the spheres acted as endplates, splitting the high aspect ratio cable into smaller aspect ratio segments. The character of the spanwise cellular vortex shedding structure was dependent upon the length of these smaller segments. The spanwise extent of the resonant, vortex excited oscillations was significantly extended by the presence of the spheres. The magnitude of this extension was also dependent upon the length of the segments between the spheres. This finding was particularly significant because it meant that the undesirable effects that accompanied synchronization would be extended over a longer portion of the cable span, up to one-half a wavelength. The spheres did not act as strumming suppression devices. The vortex shedding coherence created by their presence did not reduce the cable strumming.

Acknowledgments

The experiments were carried out at the Virginia Polytechnic Institute and State University under a contract from the Naval Civil Engineering Laboratory.

References

1 Davies, M. E., "The Effects of Turbulent Shear Flow on the Critical Reynolds Number of a Circular Cylinder," National Physics Laboratory (U.K.) NPL Report MarSci R 151, Jan. 1976.

2 Griffin, O. M., "Flow Near Self-Excited and Forced Vibrating Circular Cylinders," ASME *Journal of Engineering for Industry*, Vol. 94, May 1972, pp. 539-548.

3 Kline, J., Brisbane, A., and Fitzgerald, E., "A Study of Cable Strumming Suppression," Final report on contract N68305-78-C-0049 for the Naval Civil Engineering Laboratory, MAR Incorporated, Apr. 1981, 107 pp.

4 Koopmann, G. H., "The Vortex Wakes of Vibrating Cylinders at Low Reynolds Numbers," *JFM*, Vol. 28, Part 3, 1967, pp. 501-512.

5 Mair, W. A., and Stansby, P. K., "Vortex Wakes of Bluff Cylinders in a Shear Flow," *SIAM Journal of Applied Mathematics*, Vol. 28, 1975, pp. 519-540.

6 Maull, D. J., and Young, R. A., "Vortex Shedding From Bluff Bodies in a Shear Flow," *JFM*, Vol. 60, 1973, Part 2, pp. 401-409.

7 Peltzer, R. D., and Rooney, D. M., "Wake Characteristics of High Aspect Ratio Cylinders in Subcritical Spanwise Sheared Flows," ASME Paper 81-WA/FE-10, Nov. 1981.

8 Peltzer, R. D., "Vortex Shedding From a Vibrating Cable With Attached Spherical Bodies in a Linear Shear Flow," Ph.D. thesis, VPI&SU, Apr. 1982.
9 Ramberg, S. E., and Griffin, O. M., "Vortex Formation in the Wake of a Vibrating, Flexible Cable," ASME JOURNAL OF FLUIDS ENGINEERING, Dec. 1974, pp. 317-322.
10 Ramberg, S. E., and Griffin, O. M., "The Effects of Vortex Coherence, Spacing and Circulation on the Flow-Induced Forces on Vibrating Cables and Bluff Structures," Naval Research Laboratory Report 7945, Jan. 1976, 32 pp.
11 Ramberg, S. E., and Griffin, O. M., "Velocity Correlation and Vortex Spacing in the Wake of a Vibrating Cable," ASME JOURNAL OF FLUIDS ENGINEERING, Vol. 98, Mar. 1976, pp. 10-18.
12 Sarpkaya, T., "Vortex-Induced Oscillations; A Selective Review," ASME *Journal of Applied Mechanics*, Vol. 46, June 1979, pp. 241-258.
13 Stansby, P. K., "The Locking-on of Vortex Shedding Due to the Cross Stream Vibration of Circular Cylinders in Uniform and Shear Flows," *JFM*, Vol. 74, Part 4, 1976, pp. 641-665.
14 Woo, H. G. C., Cermak, J. E., and Peterka, J. A., "Experiments on Vortex Shedding From Stationary and Oscillating Cables in a Linear Shear Flow," Final report on contract N68305-78-C0055 for the Naval Civil Engineering Laboratory, Colorado State University, July 1981, 223 pp.
15 Zdravkovich, M. M., "Modification of Vortex Shedding in the Synchronization Range," ASME Paper 81-WA/FE-25, Nov. 1981.

Jean-Nicolas Favre
Research Engineer.

I. L. Ryhming
Professor.

Fluid Mechanics Laboratory,
Swiss Federal Institute of Technology,
Lausanne, Switzerland

On Liquid Film Pressure Sealing

The dynamics of the thin film established, by oil injection, on the inside wall of the casing in certain rotary compressors are analyzed both experimentally and theoretically. The film may provide an effective pressure seal to prevent leakage of air from one side of a rotor lobe to the other. It is found that Reynolds' bearing theory, corrected for Reynolds number and surface tension effects, gives reasonable results for the film thickness needed to sustain typical operational pressure differences in the machine. The theoretical predictions have been verified experimentally in a series of tests performed in a specially designed apparatus.

1 Introduction

To improve the performance of certain screw compressors a common technique is to inject oil into the machine in order to prevent leakage of compressed air in the fine tolerance passages between rotor lobe edges and the casing, or in the interaction zones between the intermeshing rotors.

Because of the rotation of the rotors the injected oil forms a thin film primarily on the walls of the casing due to centrifugal forces. Under conditions of correctly injected amounts of oil the rotor lobes will squeeze the film through the smallest gap width between the lobes and the casing wall, thereby forming an effective seal preventing the loss of air pressure from one side of the lobe to the other. The film resists the squeeze through motion by viscous forces which are low due to the small areas of contact between lobe edge and film. If, however, the film is too thick, the top layer of the film cannot be squeezed through by the lobe. A free surface wave will then be formed in front of the lobe, causing a much increased drag force compared to the viscous forces, Hence, it is important to assess an allowable range of film thicknesses as a function of appropriate parameters for the proper functioning of the machine.

To do this, an experimental and theoretical study has been undertaken. In the theoretical part the film motion has been calculated by Reynolds' theory, but corrected for Reynolds number and surface tension effects. To verify the theoretical results a test apparatus has been built and a series of experiments performed. The experimental results support by and large the theoretical predictions.

2 The Film-Lobe Interaction

The gap size between the lobe edge and casing is of the order of $0.1-0.15$ mm. Hence all other dimensions of the machine such as the rotor radius are large. This justifies a two-dimensional approach to the squeeze film problem with the flat wall moving with the velocity V_n past the lobe edge, see Fig. 1. The pressure difference $p_2 - p_1$ (where $p_2 > p_1$) over the lobe acts in the same (compressor) or opposite (expander) direction.

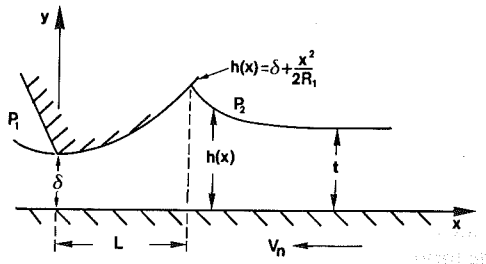

Fig. 1 Flow situation in lobe fixed coordinates showing detached flow at the lobe edge, upstream film thickness t, and upstream flow attachment at x = L

By neglecting inertial effects the motion of the film shown in Fig. 1 is assumed to be governed by Reynolds'[1] equation, i.e.,

$$\frac{d}{dx}\left(\frac{h^3}{\mu}\frac{dp}{dx}\right) = -6V_n\frac{dh}{dx} \tag{1}$$

The viscous flow (dynamic coefficient of viscosity μ(kg/ms)) driven by the pressure gradient dp/dx and the wall velocity V_n, cause a certain flow rate through the minimum gap height $h(0) = \delta$. The question is how this flow rate is related to the pressure difference $p_2 - p_1$ and the film thickness t advancing with uniform velocity V_n toward the lobe on the far upstream side.

The justification for using equation (1) to study the flow in the relatively short interaction zone is, as we shall see, that the results of equation (1), properly corrected for Reynolds number effects, do correspond well with the observed behavior of the flow.

To analyze the problem a lobe profile is selected represented by a parabola with a radius of curvature equal to R_1, i.e., the local film thickness is

$$h(x) = \delta + \frac{x^2}{2R_1} \tag{2}$$

or, expressed in nondimensional form,

$$\eta = 1 + \epsilon\xi^2, \text{ where } \eta = \frac{h}{\delta}, \ \xi = \frac{x}{\delta}, \text{ and } \epsilon = \frac{\delta}{2R_1} \tag{3}$$

Contributed by the Fluids Engineering Division for publication in the JOURNAL OF FLUIDS ENGINEERING. Manuscript received by the Fluids Engineering Division, June 6, 1983.

[1] Pinkus, O., and Sternlicht, B., *Theory of Hydrodynamic Lubrication*, McGraw-Hill, New York, 1961.

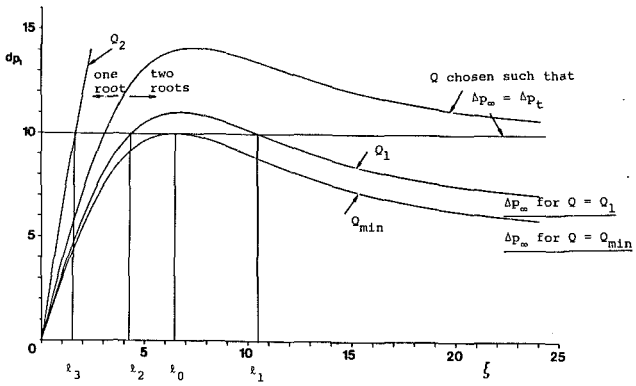

Fig. 2 Four solutions l_0, l_1, l_2, and l_3 evaluated from three different Δp curves corresponding to $Q = Q_{min}$, Q_1, and Q_2. Data chosen $\Delta p_t = 10$, $\epsilon = 0.0119$.

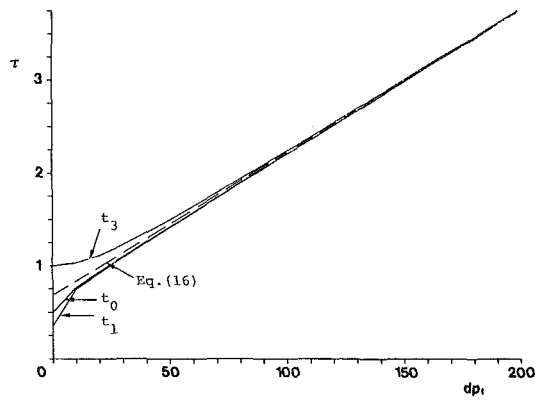

Fig. 3 Thickness τ of the film upstream of lobe edge according to the different solutions for l, and compared with asymptotic result; $\epsilon = 0.0119$

To solve equation (1) boundary conditions are necessary. With the assumption of flow separation at the edge $\xi = 0$, the pressure at the location $\xi = 0$ is known and equal to p_1. Reynolds' equation describes a boundary layer type of flow and hence variations in pressure over the thickness η of the film can be neglected in comparison with the pressure variation in the streamwise direction. The pressure p_2 acts on the lobe front flank and on the surface of the film, but the location $l = L/\delta$ where the film attaches to the lobe front flank is not known. The correct boundary condition is then

$$p(\xi = l) = p_2 \tag{4}$$

The Reynolds equation (1) integrated by using equation (2) takes the form

$$\Delta p(\xi) = \frac{p(\xi) - p_1}{\frac{\mu V_n}{\delta}} = -3\left[\frac{\xi}{1+\epsilon\xi^2} + \frac{1}{\sqrt{\epsilon}}\tan^{-1}(\xi\sqrt{\epsilon})\right]$$

$$+ \frac{C_1}{4\delta V_n}\left[\frac{\xi}{(1+\epsilon\xi^2)^2} + \frac{3}{2}\cdot\frac{\xi}{1+\epsilon\xi^2} + \frac{3}{2\sqrt{\epsilon}}\tan^{-1}(\xi\sqrt{\epsilon})\right] \tag{5}$$

where $\Delta p(\xi)$ is the dimensionless pressure increase along the lobe surface with respect to the parameter $\mu V_n/\delta$ and where C_1 is an integration constant. At

$$\xi = l,\ \Delta p(l) = \Delta p_t = \frac{p_2 - p_1}{\frac{\mu V_n}{\delta}}$$

or the total nondimensional pressure difference over the lobe the film has to sustain is Δp_t. In equation (5) two unknowns, C_1 and l, are involved which must both be found in order to have a fully determined solution. We have

$$\eta_l = 1 + \epsilon l^2 \tag{6}$$

and it is clear that $\eta_l > 1$ for a proper functioning of the film. The constant C_1 is related to the flow rate in the layer per unit edge length. From Reynolds' theory the velocity profile is given by the expression[2]

$$U = \frac{u(y)}{V_n} = -\left(1 - \frac{y}{h}\right)\left[\frac{1}{2}\left(\frac{C_1}{hV_n} - 6\right)\frac{y}{h} + 1\right] \tag{7}$$

and the pressure gradient is obtained as

$$\frac{dp}{dx} = -6\mu\frac{V_n}{h^2} + \frac{C_1\mu}{h^3} \tag{8}$$

[2]Idem footnote 1.

The flow rate in the x direction per unit lobe edge distance is thus

$$Q = -\int_0^h u(y)\,dy = \frac{C_1}{12} = V_n t \tag{9}$$

Hence, the pressure gradient according to (8) depends on the parameter Q. Therefore, a whole range of Q values for the same value of Δp_t can be found, representing different flow patterns through the channel. This situation comes about because the $\Delta p(\xi)$ function attains a maximum value at the location

$$h = h_0 = \frac{C_1}{6V_n} = \frac{2Q}{V_n} \tag{10}$$

Hence, by making the corresponding maximum value of $\Delta p(\xi)$ equal to Δp_t at the location $\xi = l_0$ we have established a lower limit for Q needed to sustain the total pressure difference over the layer, see Fig. 2. Hence, by substituting (10) into (5) and puting $\xi = l_0$ we obtain a transcendental equation determining l_0 or η_{l_0} fixing the lowest possible flow rate through the layer

$$Q_{min} = \tfrac{1}{2}\eta_{l_0}\delta V_n = t_0 V_n \tag{11}$$

By a slight increase in the $Q_{\min}$ value according to (11), the $\Delta p(\xi)$ curve is shifted upwards from the $Q_{\min}$ distribution, and the Δp_t = constant line may then intersect the new curve characterized by $Q = Q_1$ at two locations which we label l_1 and l_2 respectively, see Fig. 2. However, the range of Q for which two solutions can be found is limited. This depends on the fact that the $\Delta p(\xi)$ function attains an asymptotic value for large ξ values, i.e.,

$$\Delta p(\xi) \underset{\xi\to\infty}{=} \Delta p_\infty = -\frac{3\pi}{2\sqrt{\epsilon}} + \frac{C_1}{4\delta V_n}\cdot\frac{3\pi}{4\sqrt{\epsilon}} \tag{12}$$

Hence, if Q is increased beyond the limiting value corresponding to $\Delta p_\infty = \Delta p_t$ only one intersection l_3 between the line Δp_t = constant and the $\Delta p(\xi)$ curve characterized by $Q = Q_2$ can be found, see Fig. 2.

At the attachment point $l = l_0$ the velocity profile is linear, which follows from the concurrence of Δp_t with the $\Delta p(\xi)$ curve maximum.

The flow configuration for $l > l_0$ means velocity profiles that become concave with respect to the linear profile. A position is first attained where

$$\frac{dU}{d\left(\frac{y}{h}\right)} = 0 \qquad \text{for } y = h \tag{13}$$

This condition is tantamount to no wall friction at $l = l_1$ if Q

$> Q_1$. In other words, $l = l_1$ corresponds to a film thickness upstream which is determined from the condition (3) giving

$$\frac{t_1}{\delta} = \frac{1}{3}\eta_{l_1} \tag{14}$$

If $Q > Q_1$, $t > t_1$ and the top part of the layer is deflected upstream, provided we obtain a solution branch characterized by the condition $l > l_0$. Several other types of flow are found on the branch of solutions characterized by $l < l_0$. The first solution of this branch is $l = l_2$, which corresponds to another attachment point only for the flow obtained with $Q = Q_1$. Hence, the far upstream flow film thickness is again given by (14) and the velocity profile at $l = l_2$ is convex with respect to the linear profile.

Yet another solution of this branch $l < l_0$ can be envisaged corresponding to $Q_2 > Q_1 > Q_{\min}$ and is designated l_3. At this entrance location the film thickness $t_3\ \delta^{-1}$ far upstream is exactly equal to η_{l_3}. Even higher flow rates $Q_m > Q_2$ would correspond to $l > \eta_{l_m}$ hence to $t > \delta$ as $\Delta p_t \to 0$ which is not possible. Hence, the maximum flow rate in the layer is given by $Q = Q_2$.

However, it is not possible to draw a precise conclusion from our simple theory which one of our two dynamically possible solution branches $l > l_0$ or $l < l_0$ will be the only possible one under a given set of conditions. This has to do with surface tension phenomena. In fact, the condition for a stable attachment point is given by the condition[3]

$$\frac{d}{dx}\left(\frac{\gamma}{R} + p_{\text{liq}} - p_{\text{air}}\right) < 0 \tag{15}$$

where d/dx is the streamwise derivative, R is the radius of curvature of the free film surface, and γ the surface tension. In our problem an attachment point of the l_1 type will be structurally unstable since p_{air} is constant and the streamwise derivative of the pressure and the inverse radius of curvature of the free film surface are both positive. Hence we can conclude from a simple stability argument that the solution branch cannot materialize.

For small values of Q, i.e., small values of Δp_t the change in film thickness t predicted by all four solutions differs considerably. However, for large values of Δp_t all four solutions become essentially the same with only a few percent difference, see Fig. 3. This has to do with the fact that $\Delta p_\infty \to \Delta p_t$ as Δp_t becomes large. An asymptotic formula for the film thickness can then be provided which becomes

$$\tau = \frac{t}{\delta} = \frac{4}{9\pi}\Delta p_t \sqrt{\epsilon} + \frac{2}{3} \tag{16}$$

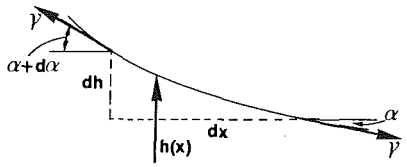

Fig. 4 Free surface film element for establishing force balance

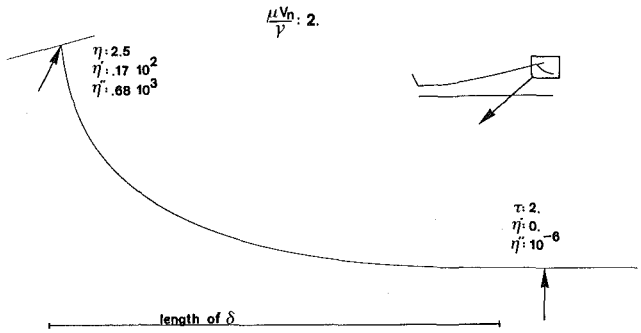

Fig. 5 Integrating free surface shape; $\tau = 2$ and $\mu V_n/\gamma = 2$

3 The Free Film Development

Upstream of the attachment point the velocity profile in the liquid layer is distorted from a parallel to a parabolic shape, see Fig. 1, with zero velocity at the attachment point. Since the Reynolds theory provides parabolic velocity profiles, we can write for the velocity distribution upstream of the attachment point

$$\frac{u}{V_n} = -1 - \left[3\left(1 - 2\frac{t}{h_L}\right)\left(\frac{y}{h}\right)^2 - 4\left(1 - \frac{3t}{2h_L}\right)\frac{y}{h}\right] f\left(\frac{x}{\delta}\right) \tag{17}$$

where the function f allows for the film surface to change its velocity continuously from zero to $-V_n$, i.e.,

$$f \to 1 \text{ as } x \to L$$

$$f \to 0 \text{ as } x \to \infty, \text{ and } u = -V_n$$

Furthermore, $h_L = h(x = L)$, see Fig. 1. To determine the

[3] Savage, M. D., "Cavitation in Lubrication. Part I. On Boundary Conditions and Cavity-Fluid Interface," *Journal of Fluid Mechanics*, Vol. 80, Part 4, 1977.

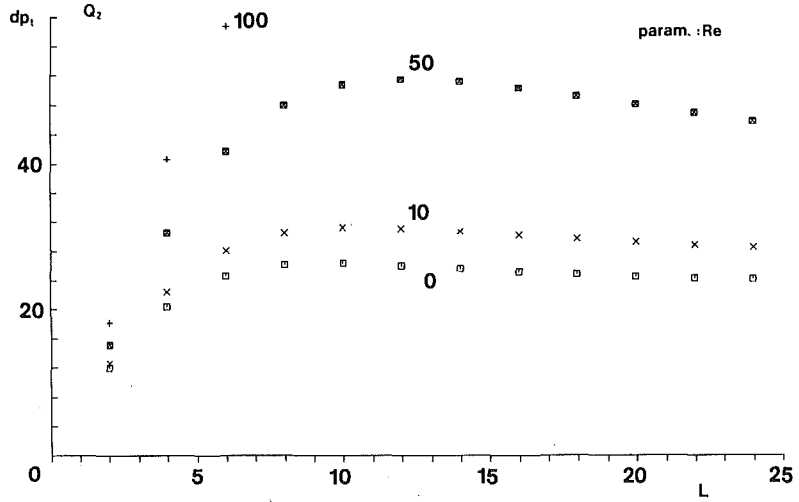

Fig. 6 Influence of Reynolds number on the Δp curve; Q_2 as in Fig. 2

function f, equation (9) provides first a relation between f and h, i.e.,

$$f(\xi) = \frac{1-\tau\eta^{-1}}{1-\tau\eta_l^{-1}}, \quad \tau = \frac{t}{\delta} \tag{18}$$

Next, the momentum balance in the x direction of a small liquid element is considered, see Fig. 4. We observe that the pressure is constant along the free surface and also across the layer (first order analysis). Furthermore, the inertia terms likewise give contributions of the second order only. Hence, the surface tension force will be balanced only by the viscous forces, i.e.,

$$\gamma \sin\alpha d\alpha - \mu \frac{\partial u}{\partial y}\bigg|_h dx = 0 \tag{19}$$

where

$$\tan\alpha = \frac{dh}{dx} \tag{20}$$

By making use of equations (17), (18), and (20), equation (19) takes the form

$$\eta'' = \frac{\mu V_n}{\gamma} \cdot \frac{2(3\tau-\eta_l)}{\eta_l-\tau} \cdot \frac{(\tau-\eta)\,(1+\eta'^2)^{3/2}}{\eta^2\eta'} \tag{21}$$

This equation can be solved by numerical integration proceeding in the negative ξ direction by using e.g., the Runge-Kutta method, for which initial values are needed. These are given as follows: at an arbitrary large value of ξ, $\eta = \tau$, $\eta' = 0$ and η'' is small. Actually, integration runs with $\eta'' = 10^{-2}$, 10^{-4} and 10^{-6} have shown that the initial value of η'' has a negligible influence provided the parameter $\mu V_n/\gamma < 1$. In this case the adjustment region is long in comparison with the film thickness and η'_l is also small. However, for large values of $\eta V_n/\gamma$ the adjustment region is short or of the order of the film thickness and hence η'_l is large. The numerical integration is performed for different parameter values of $\tau\eta_l^{-1}$ and $\mu V_n/\gamma$. The result of such and integration is shown in Fig. 5.

4 Influence of Reynolds Number

In Reynolds' theory the inertia terms are neglected. Hence, Reynolds' theory is applicable for example in bearing problems where the Reynolds number based on the smallest gap height is of the order of 10^{-1} or less. However, in the sealing problem of interest here the Reynolds number based on the gap height is much larger, of the order of 10-400, and will thus have a considerable influence. Therefore, Reynolds' theory needs to be corrected for Reynolds number effects in the present application.

By following the standard procedure in the literature (c.f. footnote 1) the effect of the inertia terms will be calculated by iteration. Hence, using the continuity equation the y component of the velocity vector can be computed from the known u distribution. We obtain

$$v = V_n h' \left(\frac{y}{h}\right)^2 \left[1-\frac{y}{h}\right]\left(2-6\frac{t}{h}\right) \tag{22}$$

where the boundary conditions $v(x, 0) = v(x, h) = 0$ have been observed. Next, a new u distribution can be obtained from the momentum equation in which the inertia terms are calculated using equations (7) and (22). This gives a lengthy expression for u as a function of h and y. To find the correction for the pressure gradient the corrected u distribution is substituted into equation (9) with the result that the correction term in dp/dx takes the form

$$\left(\frac{dp}{dx}\right)_{\text{corr}} = 6\rho \frac{V_n^2 h'}{h}\left[-\frac{1}{42}-\frac{1}{70}\frac{t}{h}+\frac{9}{35}\left(\frac{t}{h}\right)^2\right] \tag{23}$$

which should be added to the right-hand side of equation (8). Finally, to obtain the correction to $\Delta p(l)$, integration with respect to x up to the limit l gives the following correction term to Δp

$$(\Delta p)_{\text{corr}} = \text{Re}\left[-\frac{1}{7}\ln\eta_l + \frac{3}{35}\tau(9\tau-1)(1-\eta_l^{-1})\right] \tag{24}$$

where Re is the Reynolds number defined by

$$\text{Re} = \frac{V_n \delta}{\nu} \tag{25}$$

The Re influence on a typical pressure distribution is shown in Fig. 6. As a general result the interaction length for given Δp_l decreases with an increasing Reynolds number. The velocity distribution in the layer is also changed and the resulting profiles in the layer for different Reynolds numbers are shown in Fig. 7. It follows that τ as a function of Δp_l is also reduced with an increasing Reynolds number, see Fig. 8. The results shown indicate that large deviations occur as soon as Re is of the order of 10-50 between the iterated solutions and the solutions obtained from Reynolds' theory. For this reason, the iterated solutions at large Re are at best qualitative in nature.

5 Test Apparatus

In order to simulate Δp_l numbers in the 10-100 range as well as Re numbers in the 10-600 range a testbed has been designed in which the lobe surfaces are at rest and the casing/end walls are rotating. This has the great advantage of simplifying the observation and measurement of the flow phenomena. In addition, a positive pressure difference on either side of the lobe surfaces can be created thus permitting

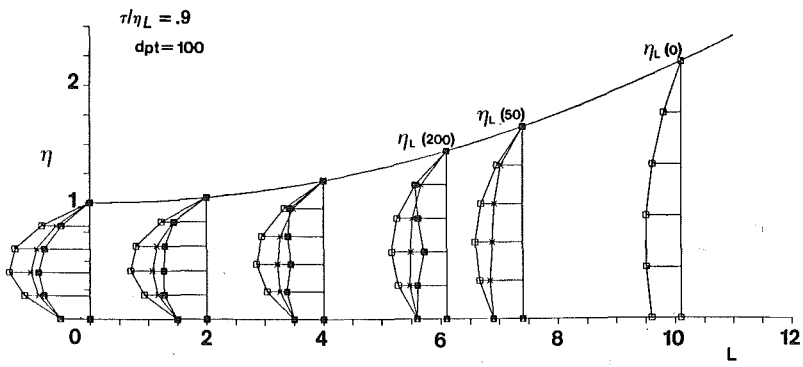

Fig. 7 Influence of Reynolds number on the interaction zone length and on velocity profiles in the layer; $\tau/\eta_L = 0.9$ and $\Delta p_t = 100$

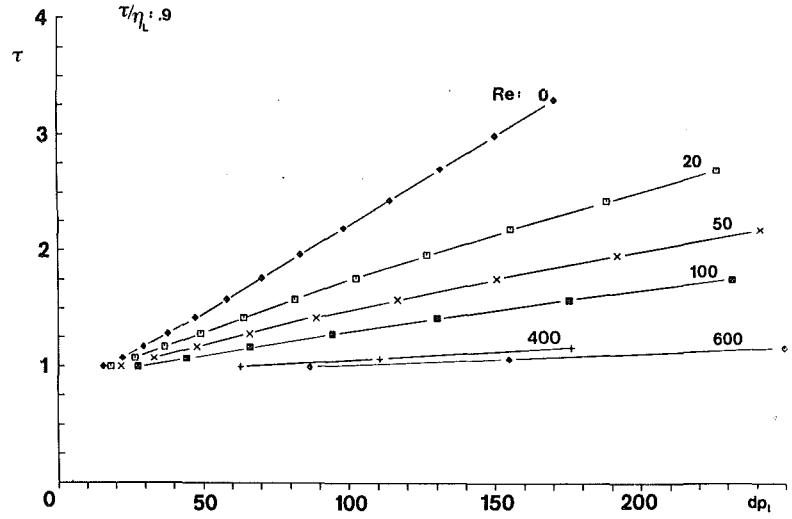

Fig. 8 Calculated influence of Reynolds number on τ as a function of Δp_t

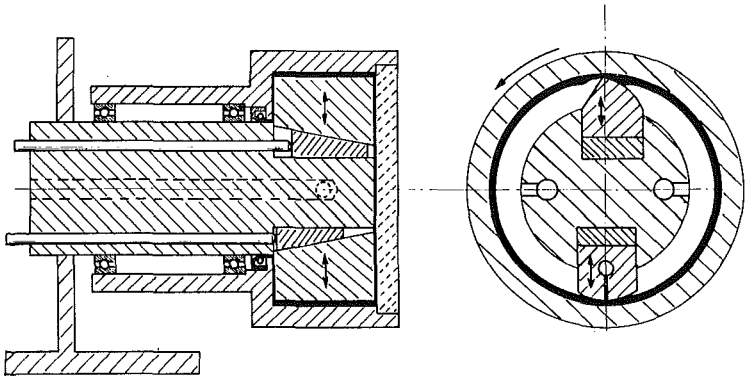

Fig. 9 Test apparatus design concept

the verification and study of the sealing effect. The various needs for adjustments of gap size as well as chamber and lobe geometry are easily accommodated in such a design.

The design concept is shown in Fig. 9. The machine consists of a partially transparent drum rotating around a stationary central core which includes the simulated lobe tip, a regulation head and the various fluid feeding channels. The lobe tip and the regulation head are radially adjustable through axially moving wedges and delimit two semicylindrical chambers with different gas pressures. In normal conditions one chamber is maintained at atmospheric pressure while the other is fed with compressed air. The liquid is injected through the regulation head.

The clearance between the rotor and both the tested lobe tip and regulating head can be adjusted while the rotor is rotating.

The rotating drum includes two parts: an external brass container with window-type openings and an inner cylinder which is either a transparent plexiglass cylinder to allow for radial observation of the tested zone, or a solid cylinder for greater radial accuracy under asymmetrical pressures. Visualization is also possible through the transparent front window which rotates with the drum.

A d-c electric motor drives the rotating parts via rubber belts allowing the speed of rotation to be set at any low value.

6 Test Procedure and Results

Tests have been run with two different kinds of liquid, light machine oil ($\mu \simeq 0.05$ kg/ms) and a mixture of water and glycerine ($\mu \simeq 0.01$ kg/ms. By changing the liquid viscosity the testing at two different Reynolds number regimes, $18 < \mathrm{Re} < 77$ and $375 < \mathrm{Re} < 645$ was made possible. During the running of the tests the temperature evolution of the liquid was continuously checked for a correct determination of μ. Maximum temperature increase was limited to 1.5°C allowing the μ value to be determined within a 10 percent accuracy limit.

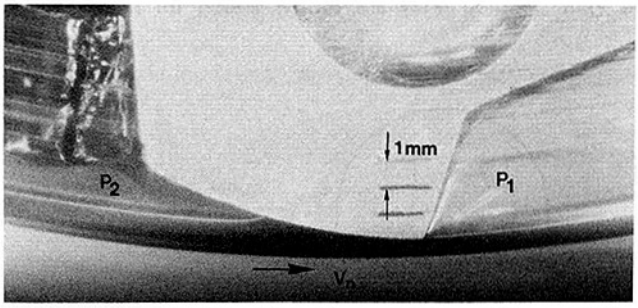

Fig. 10 Photograph of the interaction zone; flow conditions as in Fig. 5

The minimum speed V_n of the drum was found to be about 1.4 m/s. At even lower speeds film inhomogeneities upstream of the interaction zone were observed. The drum speed was recorded by a magnetic rpm counter, minimum rpm used ~ 200, which corresponds to a centrifugal acceleration of 28 m/s^2 of the film. Although various gap sizes could be accommodated in the machine a value of $\delta = 0.65$ mm was chosen and judged sufficient for macrophotography of the interaction zone.

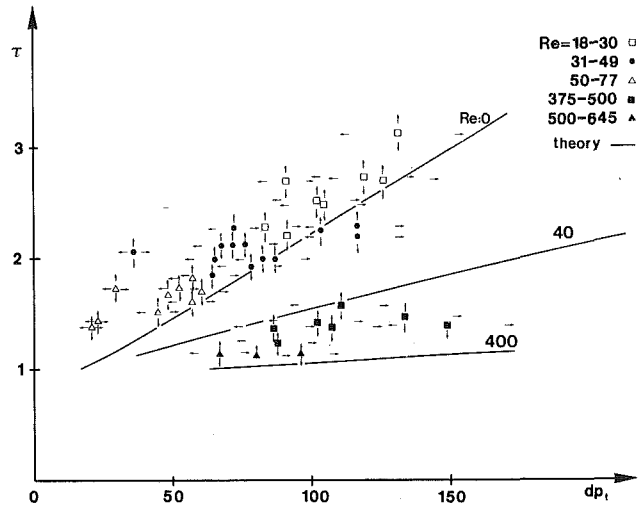

Fig. 11 Measured influence of Reynolds number on τ as a function of Δp_t. Conditions are the same as in Fig. 8.

The pressure in the two chambers was recorded by a Betz-type Hg manometer.

The required film thickness for complete sealing at a given Δp_t value was obtained in the following way. The machine was first prepared to simulate a certain Re number domain. Then the liquid film generated by fluid injection through the regulation head would seal off the two pressurized chambers, allowing for application of a desired pressure difference. Normally the film slowly reduced its thickness by fluid leakage through the low-pressure air tube. At some moment the film thickness would have been diminished to such an extent that film beakdown would have occurred. To measure the film thickness a series of photos of the film interaction zone was taken at the moment that stable conditions were observed. An example of such a photo is provided in Fig. 10.

The results of the measurements are shown in Fig. 11 for the two Reynolds number domains and for Δp_t values up to 150. Conservative error estimates on every measured point are indicated by small arrows. The agreement between theory and experiment is demonstrated indicating much reduced film thicknesses in the higher Re domain, as shown in Fig. 8.

On the Stability of Vortex Motions in Compressible Stratified Fluids

Y. T. Fung
Fluid Dynamics Branch,
Marine Technology Division,
Naval Research Laboratory,
Washington, D.C. 20375

Necessary conditions for the stability of a general class of compressible vortex flows are obtained using the method of generalized progressing wave expansion. The vortex motion and the density are assumed to vary in both the radial and axial directions. These conditions, representing a generalized state of statically stable distribution for the steady flow, require that the flow be stable in the centrifugal force field created by the rotation of the fluids, in the gravitational force field arisen from the density variation, and in the pressure field constraining the variation of density and forces in both the radial and axial directions. These results also suggest the likely behavior of Richardson criteria for stability of the flow yet to be derived.

Introduction

Vortex shedding behind an axisymmetric body submerged in stratified fluids has been puzzling many researchers because of the intrinsic vortex pattern developed in the late wake [1]. When an axisymmetric body is towed through a stratified fluid at a particular Reynolds number, vortices are first shed three dimensionally. However, the gravitational effects soon inhibit the vertical motion. The resultant vortex structure is vertically oriented and resembles the two-dimensional Kármán vortex street behind a bluff body if observed from the gravitational direction. Such inhibition can qualitatively be viewed by examining the motion of fluid particles in the gravitational force field. When a sphere is towed through a stratified fluid, the fluid particles in four locations are of particular interest. Figures 1(*a*) and 1(*b*), respectively, show the top view and side view of the sphere and of the four fluid particles A, B, C, and D being considered. Since the fluid is stably stratified in the vertical direction, the densities of particles A and B are equal while the density of particle C is lighter than that of particle D. To create a rotational motion at the onset of shedding means that either particles A and B or particles C and D have to interchange their positions. The interchange of particles A and B requires no work done in the gravitational force field. The interchange of particles C and D, however, requires a work done equal to the increase of the potential energy at the new location. Accordingly, nature will take an easy way. With the vertical motion suppressed by the gravitational forces, the resultant vortex motion will be confined in a relatively two-dimensional motion reminiscent of the Kármán vortex street behind an infinitively long cylinder when viewed in the vertical direction.

To understand the behavior of such vortex motions, we need to consider mathematically flow profiles of a more general nature to describe this kind of flow patterns. In the present investigation, we consider a general class of compressible vortex flows with their steady state distributions depending on the radial and axial coordinate. All dissipation effects are disregarded. Necessary conditions for stability of the flows are derived by using the method of generalized progressing wave expansion as the one used by Eckhoff and Storesletter [2]. These conditions can be interpreted by a kinetic energy approach similar to the one used by Rayleigh [3] and by a work done approach based on the movement of fluid particles in the centrifugal and gravitational force fields. A constraint relation, required to satisfy the pressure balance condition at all points within the flow domain, may be

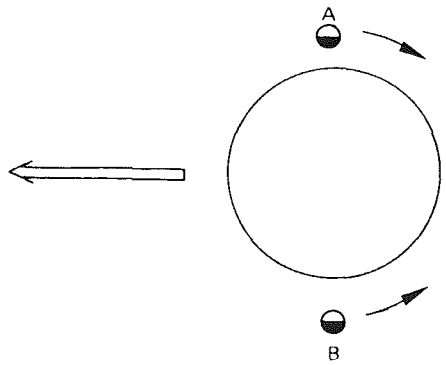

Fig. 1(*a*) Top view of a sphere towed in a stably stratified fluid

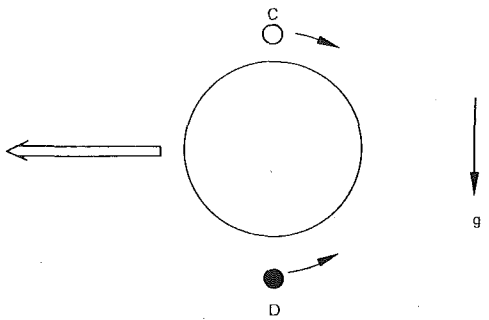

Fig. 1(*b*) Side view of a sphere towed in a stably stratified fluid

Contributed by the Fluids Engineering Division and presented at the Winter Annual Meeting, New Orleans, La., December 9–14, 1984, of The American Society of Mechanical Engineers. Manuscript received by the Fluids Engineering Division, July 27, 1983. Paper No. 84-WA/FE-4.

responsible for the variation or redistribution of the density and for the special vortex pattern developed in the stratified late wake behind a towed sphere [4].

Governing Equations

Consider an isentropic vortex motion having the axis of symmetry aligned with the z-axis of a cylindrical coordinate (r, θ, z) and with the direction of gravity. The fluid, rotating at an angular velocity $\Omega(r,z)$ and having a density $\rho_0(r,z)$, is assumed to be compressible but inviscid. To satisfy the pressure balance condition anywhere within the flow regime, the constraint equation is

$$\frac{\partial}{\partial z}(\rho_0 r\Omega^2)+\frac{\partial}{\partial r}(\rho_0 g)=0. \tag{1}$$

The perturbations of velocity in r, θ, and z directions are, respectively, $\hat{u}$, $\hat{v}$ and $\hat{w}$ while the perturbations of the density and pressure are, respectively, $\hat{\rho}$ and $\hat{p}$. Using the transformation

$$\hat{p}=\frac{\rho_0}{c_0}(\rho+p)$$
$$\hat{p}=c_0\rho_0 p, \tag{2}$$

where c_0 is the velocity of sound, we construct a symmetric hyperbolic system for the present flow subject to small perturbations as follows:

$$\left\{\frac{\partial}{\partial t}+\mathbf{A}_1\frac{\partial}{\partial r}+\mathbf{A}_2\frac{\partial}{\partial \theta}+\mathbf{A}_3\frac{\partial}{\partial z}+\mathbf{B}\right\}\begin{pmatrix}\hat{u}\\ \hat{v}\\ \hat{w}\\ \rho\\ p\end{pmatrix}=0 \tag{3}$$

where

$$\mathbf{A}_1=\begin{pmatrix}0&0&0&0&c_0\\0&0&0&0&0\\0&0&0&0&0\\0&0&0&0&0\\c_0&0&0&0&0\end{pmatrix}\quad \mathbf{A}_2=\begin{pmatrix}\Omega&0&0&0&0\\0&\Omega&0&0&c_0/r\\0&0&\Omega&0&0\\0&0&0&\Omega&0\\0&c_0/r&0&0&\Omega\end{pmatrix}$$

$$\mathbf{A}_3=\begin{pmatrix}0&0&0&0&0\\0&0&0&0&0\\0&0&0&0&c_0\\0&0&0&0&0\\0&0&c_0&0&0\end{pmatrix}$$

$$\mathbf{B}=\begin{pmatrix}0&-2\Omega&0&-\frac{r\Omega^2}{c_0}&\frac{1}{\rho_0}\frac{\partial}{\partial r}(c_0\rho_0)-\frac{r\Omega^2}{c_0}\\ r\frac{\partial\Omega}{\partial r}+2\Omega&0&r\frac{\partial\Omega}{\partial z}&0&0\\ 0&0&0&\frac{g}{c_0}&\frac{1}{\rho_0}\frac{\partial}{\partial r}(c_0\rho_0)+\frac{g}{c_0}\\ \frac{c_0}{\rho_0}\frac{\partial\rho_0}{\partial r}-\frac{r\Omega^2}{c_0}&0&\frac{c_0}{\rho_0}\frac{\partial\rho_0}{\partial z}+\frac{g}{c_0}&0&0\\ \frac{c_0}{r}+\frac{r\Omega^2}{c_0}&0&-\frac{g}{c_0}&0&0\end{pmatrix}$$

Following the method of generalized progressing wave expansion used by Eckhoff and Storesletten [2], we obtain the characteristic equation

$$\det|\xi_1\mathbf{A}_1+\xi_2\mathbf{A}_2+\xi_3\mathbf{A}_3-\lambda\mathbf{I}|=0. \tag{4}$$

The characteristic roots of the determinant are given by

$$\lambda_1=\Omega\xi_2$$
$$\lambda_2=\Omega\xi_2+c_0\eta \tag{5}$$
$$\lambda_3=\Omega\xi_2-c_0\eta.$$

Here ξ_j are components for the orthogonal eigenvectors associated with the eigenvalue λ_j and

$$\eta=(\xi_1^2+\xi_2^2/r^2+\xi_3^2)^{1/2} \tag{6}$$

The eigenvalues λ_2 and λ_3 correspond to acoustic solutions and will not be discussed any further. The eigenvalue λ_1, a triple root, corresponds to gravity waves and is the main concern in this paper. The corresponding ray equations for gravity waves are

$$\frac{dr}{dt}=\frac{\partial\lambda_1}{\partial\xi_1}=0\qquad \frac{d\xi_1}{dt}=-\frac{\partial\lambda_1}{\partial r}=-\frac{\partial\Omega}{\partial r}\xi_2$$
$$\frac{d\theta}{dt}=\frac{\partial\lambda_1}{\partial\xi_2}=\Omega\qquad \frac{d\xi_2}{dt}=-\frac{\partial\lambda_2}{\partial\theta}=0 \tag{7}$$
$$\frac{dz}{dt}=\frac{\partial\lambda_1}{\partial\xi_3}=0\qquad \frac{d\xi_3}{dt}=-\frac{\partial\lambda_3}{\partial z}=-\frac{\partial\Omega}{\partial z}\xi_3$$

with the solutions to these ray equations given by

$$\xi_1=\xi_{10}-\xi_{20}\frac{\partial\Omega}{\partial r}\Big|_{r_0,z_0}t$$
$$r=r_0$$
$$\theta=\theta_0+\Omega(r_0,z_0)t\qquad \xi_2=\xi_{20} \tag{8}$$
$$z=z_0$$
$$\xi_3=\xi_{30}-\xi_{20}\frac{\partial\Omega}{\partial z}\Big|_{r_0,z_0}t$$

where r_0, θ_0, z_0 and ξ_{k0} $(k=1,2,3)$ stand for the initial values at $t=0$. The amplitude of the leading term of the generalized

Nomenclature

c_0 = velocity of sound
F = Froude number
g = gravitational constant
N_r, N_z = Brunt-Värsälä frequencies
$\hat{p}$ = pressure perturbation
Q_1, Q_2 = locations of fluid particles
r = radial coordination
$\mathbf{r}_1, \mathbf{r}_2, \mathbf{r}_3$ = eigenvectors
t = time
$\hat{u}$ = velocity perturbation in the radial direction
$\hat{v}$ = velocity perturbation in the azimuthal direction
v_0 = tangential velocity
$\hat{w}$ = velocity perturbation in the axial direction
W_1, W_2 = work done by fluid particles in force fields
z = axial coordinate
θ = azimuthal coordinate
$\lambda_1, \lambda_2, \lambda_3$ = characteristic roots
ξ_1, ξ_2, ξ_3 = components of eigenvectors
$\rho_0(r,z)$ = density of the fluid
$\sigma_1, \sigma_2, \sigma_3$ = scalar function
$\Omega(r,z)$ = angular velocity

progressing wave expansion for the gravity waves is described by

$$L=\sum_{k=1}^{3}\sigma_k \mathbf{r}_k \tag{9}$$

where σ_k are scalar functions to be used as dependent variables in the transport equations, and r_k are orthonormal eigenvectors defined by

$$\mathbf{r}_l \cdot \mathbf{A}_k \mathbf{r}_m = \begin{cases} 0 & \text{for } l \neq m \\ \dfrac{\partial \lambda_1}{\partial \xi_k} & \text{for } l=m \end{cases} \qquad k=1,2,3. \tag{10}$$

The eigenvectors are selected such that

$$\begin{aligned} \mathbf{r}_1 &= \{\xi_2/r \quad \xi_3 \quad 0 \quad \xi_1 \quad 0\}/\eta \\ \mathbf{r}_2 &= \{0 \quad \xi_1 \quad -\xi_2/r \quad -\xi_3 \quad 0\}/\eta. \\ \mathbf{r}_3 &= \{-\xi_1 \quad 0 \quad -\xi_3 \quad \xi_2/r \quad 0\}/\eta \end{aligned} \tag{11}$$

The transport equations for the flow under consideration are given by

$$\frac{d\sigma_j}{dt} = -\sum_{k=1}^{3} \mathbf{r}_j \cdot \left\{ \left(\mathbf{A}_1 \frac{\partial \mathbf{r}_k}{\partial r} + B\mathbf{r}_k \right) \right\} - \left\{ \left(\frac{\partial \lambda_1}{\partial r} \frac{\partial \mathbf{r}_k}{\partial \xi_1} + \frac{\partial \lambda_1}{\partial z} \frac{\partial \mathbf{r}_k}{\partial \xi_3} \right) \right\}_{j=1,2,3} \sigma_k \tag{12}$$

or

$$\frac{d\sigma}{dt} = \mathbf{A}(t)\,\sigma. \tag{13}$$

Here $\sigma = \{\sigma_1, \sigma_2, \sigma_3\}$ and $\mathbf{A}(t)$ is a time dependent matrix with its elements described by

$$A_{jk} = a_{jk}/\eta^2. \tag{14}$$

Here also

$$a_{11} = -\left(F_r - \frac{r\Omega^2}{c_0}\right)\xi_1 \frac{\xi_2}{r} - D_*(r\Omega)\frac{\xi_2}{r}\xi_3$$

$$a_{12} = \left[F_z + 2\Omega - \frac{\partial}{\partial z}(r\Omega)\right]\xi_1 \frac{\xi_2}{r} + \left[-\frac{r\Omega^2}{c_0} + \frac{\partial}{\partial z}(r\Omega) + D_*(r\Omega)\right]\frac{\xi_2}{r}\xi_3$$

$$a_{13} = F_r \xi_1^2 - \left[D_*(r\Omega) - \frac{r\Omega^2}{c_0}\right]\frac{\xi_2^2}{r^2} + \frac{\partial}{\partial z}(r\Omega)\xi_3^2 + [F_z + D^*(r\Omega)]\xi_1 \xi_3$$

$$a_{21} = -\left[D^*(r\Omega) - \frac{\partial}{\partial z}(r\Omega) - \frac{g}{c_0}\right]\xi_1 \frac{\xi_2}{r} + [F_r - D_*(r\Omega)]\frac{\xi_2}{r}\xi_3$$

$$a_{22} = \frac{\partial}{\partial z}(r\Omega)\xi_1 \frac{\xi_2}{r} - \left(F_z + \frac{g}{c_0}\right)\frac{\xi_2}{r}\xi_3$$

$$a_{23} = D^*(r\Omega)\xi_1^2 + \left[\frac{\partial}{\partial z}(r\Omega) + \frac{g}{c_0}\right]\frac{\xi_2^2}{r^2} - F_z \xi_3^2 - \left[F_r - \frac{\partial}{\partial z}(r\Omega)\right]\xi_1 \xi_3$$

$$a_{31} = -\frac{r\Omega^2}{c_0}\xi_1^2 - [F_r - D_*(r\Omega)]\frac{\xi_2^2}{r^2} - \left(2\Omega - \frac{g}{c_0}\right)\xi_1 \xi_3$$

$$a_{32} = -2\Omega\xi_1^2 + \left[F_z - \frac{\partial}{\partial z}(r\Omega)\right]\frac{\xi_2^2}{r^2} - \frac{g}{c_0}\xi_3^2 + \frac{r\Omega^2}{c_0}\xi_1 \xi_3$$

$$a_{33} = \left(F_r - \frac{r\Omega^2}{c_0}\right)\xi_1 \frac{\xi_2}{r} + \left(F_z + \frac{g}{c_o}\right)\frac{\xi_2}{r}\xi_3$$

where

$$D^* = \frac{\partial}{\partial r} = \frac{1}{r}, \quad D_* = \frac{\partial}{\partial r} - \frac{1}{r}, \quad F_r = \frac{c_0}{\rho_0}\frac{\partial \rho_0}{\partial r} - \frac{r\Omega^2}{c_0}$$

and

$$F_z = \frac{c_0}{\rho_0}\frac{\partial \rho_0}{\partial z} + \frac{g}{c_0}.$$

The transport equations are valid along the rays described by equations (8). The stability characteristics of the flow governed by partial differential equations (3) are now equivalent to those of ordinary differential equations (13) evaluated along the rays.

Stability Characteristics

The system described by the transport equation (13) is, in general, nonautonomous. A stable asymptotic behavior for large t will be required in order to have stability for the system. For $t \to \infty$, the non-vanishing elements of matrix $\mathbf{A}$ are

$$\begin{aligned} a_{13} &= \left\{F_r x^2 + [F_z + D^*(r\Omega)]xy + \frac{\partial}{\partial z}(r\Omega)y^2\right\}/\Delta \\ a_{23} &= \left\{D^*(r\Omega)x^2 - \left[F_r - \frac{\partial}{\partial z}(r\Omega)\right]xy - F_z y^2\right\}/\Delta \\ a_{31} &= \left\{-\frac{r\Omega^2}{c_0}x^2 - \left(2\Omega - \frac{g}{c_0}\right)xy\right\}/\Delta \\ a_{32} &= \left\{-2\Omega x^2 + \frac{r\Omega^2}{c_0}xy - \frac{g}{c_0}y^2\right\}/\Delta \end{aligned} \tag{15}$$

where

$$x = \frac{\partial \Omega}{\partial r}, \quad y = \frac{\partial \Omega}{\partial z} \quad \text{and} \quad \Delta = x^2 + y^2.$$

The characteristic equation for the eigenvalue λ of the non-autonomous system is

$$\lambda(\lambda^2 + \Psi/\Delta) = 0 \tag{16}$$

where

$$\Psi = \left\{F_r \frac{r\Omega^2}{c_0} + 2\Omega D^*(r\Omega)\right\}x^2 - \left\{F_r \frac{g}{c_0} - F_z \frac{r\Omega^2}{c_0} - 2\Omega \frac{\partial}{\partial z}(r\Omega)\right\}xy - F_z \frac{g}{c_0}y^2. \tag{17}$$

In order that the system with the elements described by equations (15) shall be stable, it is necessary that all the characteristic roots in equation (16) have nonpositive real parts, i.e.,

$$\Psi \geq 0. \tag{18}$$

Equation (18) will be satisfied if

$$F_r \frac{r\Omega^2}{c_0} + \phi - F_z \frac{g}{c_0} \geq 0 \tag{19a}$$

and

$$-F_z \frac{g}{c_0}\left[F_r \frac{r\Omega^2}{c_0} + \phi\right] \geq \left(F_r \frac{g}{c_0}\right)^2. \tag{19b}$$

Here $\phi = 2\Omega D^*(r\Omega)$ reduces to the Rayleigh discriminant if the azimuthal velocity is radius-dependent only. Since the right-hand side of equation (19b) is always positive, conditions (19) require

$$\Phi - \left(\frac{r\Omega^2}{c_0}\right)^2 \geq 0 \tag{20a}$$

$$-\left[\frac{g}{\rho_0}\frac{\partial \rho_0}{\partial z} + \left(\frac{g}{c_0}\right)^2\right] \geq 0 \tag{20b}$$

and

$$-\left[\frac{g}{\rho_0}\frac{\partial \rho_0}{\partial z} + \left(\frac{g}{c_0}\right)^2\right]\left[\Phi - \left(\frac{r\Omega^2}{c_0}\right)^2\right] \geq \left(\frac{g}{r\Omega^2}\right)^2\left[\frac{r\Omega^2}{\rho_0}\frac{\partial \rho_0}{\partial r} - \left(\frac{r\Omega^2}{c_0}\right)^2\right]^2. \tag{20c}$$

Here

$$\Phi = \frac{r\Omega^2}{\rho_0}\frac{\partial \rho_0}{\partial r} + \phi = \frac{\partial}{\partial r}(\rho_0 r^4 \Omega^2)/\rho_0 r^3$$

reduces to the Rayleigh-Synge discriminant if the flow quantities are dependent only on the radius. It represents the variations of centrifugal forces that arise from the variation of density and that result from the conservation of circulation in the radial direction.

For uniform rotation, no criteria can be observed since equation (18) will become trivial. In this case, system (13) becomes autonomous, since $\partial\Omega/\partial r = \partial\Omega/\partial z = 0$, and the ray equations (8) for autonomy reduce to

$$\xi_k = \xi_{k0} \quad k = 1, 2, 3 \tag{21}$$

The eigenvalues λ of system (13) are now governed by the equation

$$\lambda[\lambda^2 + \psi/(\xi_{10}^2 + \xi_{20}^2 + \xi_{30}^2)] = 0 \tag{22}$$

where

$$\psi = \left(F_r \frac{r\Omega^2}{c_0} + 4\Omega^2\right)\xi_{10}^2 - \left(F_r \frac{g}{c_0} - F_z \frac{r\Omega^2}{c_0}\right)\xi_{10}\xi_{30} - F_z \frac{g}{c_0}\xi_{30}^2 + \left(F_r \frac{r\Omega^2}{c_0} - F_z \frac{g}{c_0}\right)\left(\frac{\xi_{20}}{r}\right)^2.$$

To have system (13) be autonomous and stable, it is required that the eigenvalues have nonpositive real parts, i.e.,

$$\psi \geq 0. \tag{23}$$

Since ξ_{10}, ξ_{20}, and ξ_{30} are independent components of the orthonormal eigenvectors, stability of the system of equations (13) for autonomy therefore requires that

$$\frac{r\Omega^2}{\rho_0}\frac{\partial \rho_0}{\partial r} - \left(\frac{r\Omega^2}{c_0}\right)^2 \geq 0 \tag{24a}$$

$$-\left[\frac{g}{\rho_0}\frac{\partial \rho_0}{\partial z} + \left(\frac{g}{c_0}\right)^2\right] \geq 0. \tag{24b}$$

Equations (20) and (24) represent the stability conditions of the system in equations (13) for both nonautonomous and autonomous cases, respectively. The stability characteristics of the flow governed by the partial differential equation (3) are equivalent to those of the system governed by the ordinary differential equation (13) evaluated along the rays. Therefore, one can conclude that the necessary conditions for stability of the compressible stratified flows under consideration require the inequalities

$$N_r^2 + \phi \geq 0 \tag{25a}$$

$$N_z^2 \geq 0 \tag{25b}$$

$$(N_r^2 + \phi)N_z^2 \geq N_r^4/F^2 \tag{25c}$$

to be satisfied anywhere within the flow regime. Here the Brunt-Värsälä frequencies are defined as

$$N_r^2 = \frac{r\Omega^2}{\rho_0}\frac{\partial \rho_0}{\partial r} - \left(\frac{r\Omega^2}{c_0}\right)^2 \tag{26a}$$

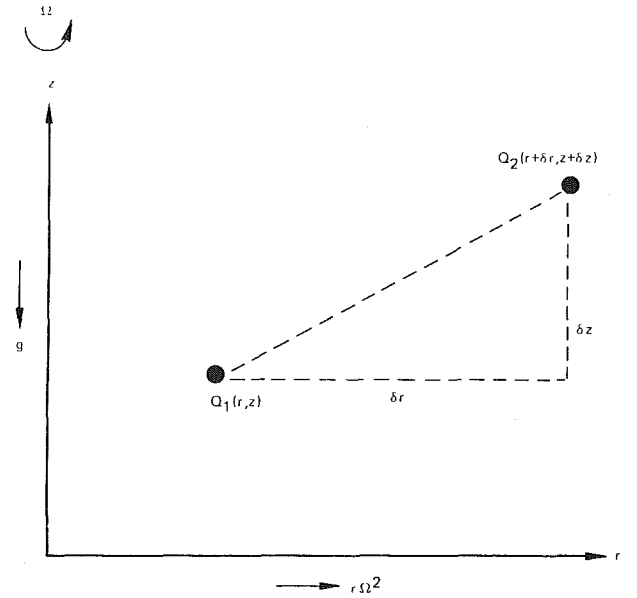

Fig. 2 Coordinate of the fluid particles in the centrifugal and gravitational force fields

$$N_z^2 = -\frac{g}{\rho_0}\frac{\partial \rho_0}{\partial z} - \left(\frac{g}{c_0}\right)^2 \tag{26b}$$

to, respectively, represent the density variations along the radial and gravitational force fields. The Froude number is defined as

$$F = \frac{r\Omega^2}{g} \tag{27}$$

to represent the ratio between the centrifugal and gravitational forces. Equation (25*a*) will be replaced by $N_r^2 \geq 0$ for uniformly rotating flows. It is worth mentioning that equations (25) actually do not represent three independent conditions. Condition (25*c*) implies that either one of the two conditions in (25*a*) and (25*b*) must be automatically satisfied if the other one is satisfied. This behavior as well as the physical mechanism behind the three conditions will be explained in the following section.

Interpretation of the Results

The necessary conditions for stability previously derived can be explained by a kinetic energy approach similar to the one used by Rayleigh [3] and by a work done approach based on the movement of fluid particles in the centrifugal and gravitational force fields. For simplicity, compressibility effects will be ignored.

Consider two fluid particles originally located at Q_1 and Q_2 within the flow regime in the r-z plane as illustrated in Fig. 2. The particle at Q_1 has a density ρ_0 and a velocity v_0 while the particle at Q_2 has a density $\rho_0 + \delta\rho_0$ and a velocity $v_0 + \delta v_0$. Here $v_0 = r\Omega$ and

$$\delta = \delta r \frac{\partial}{\partial r} + \delta z \frac{\partial}{\partial z}.$$

First we use the energy approach by considering the variation of the total energy as a result of a perturbation to the system. In the steady-state, the kinetic and potential energy of the two particles are given by

$$\text{K.E.} \quad \frac{1}{2}\{\rho_0 v_0^2 + (\rho_0 + \delta\rho_0)(v_0 + \delta v_0)^2\}$$

and (28)

$$\text{P.E.} \quad \rho_0 g z + (\rho_0 + \delta\rho_0) g (z + \delta z).$$

When the two particles interchange their positions, the kinetic and the potential energy of the perturbed system are

$$\text{K.E.}\quad \frac{1}{2}\left\{\rho_0\left[\frac{rv_0}{r+\delta r}\right]^2 + (\rho_0+\delta\rho_0)\left[\frac{(r+\delta r)(v_0+\delta v_0)}{r}\right]^2\right\}$$

and

$$\text{P.E.}\quad \rho_0 g(z+\delta z)+(\rho_0+\delta\rho_0)gz. \tag{29}$$

Here the conservation of circulation has been applied to the resultant kinetic energy in (29). If the perturbation is small, the stability of the system requires

$$\Phi(\delta r)^2-\left[\frac{g}{\rho_0}\frac{\partial\rho_0}{\partial r}-\frac{1}{\rho_0}\frac{\partial}{\partial z}(\rho_0 r\Omega^2)\right](\delta r)(\delta z) - \frac{g}{\rho_0}\frac{\partial\rho_0}{\partial z}(\delta z)^2\geq 0 \tag{30}$$

everywhere within the flow domain.

An alternative approach to observe the stability characteristics of the system is to examine the work done by the two particles in the centrifugal and gravitational force fields. When the two particles interchange their positions, the work done by the particle originally located at Q_1 is

$$W_1=-\frac{\rho_0}{2}\left\{\frac{v_0^2}{r}+\frac{(rv_0)^2}{(r+\delta r)^3}\right\}\delta r+\rho_0 g\delta z \tag{31}$$

while the work done by the particle originally located at Q_2 is

$$W_2=\frac{\rho_0+\delta\rho_0}{2}\left\{\frac{(v_0+\delta v_0)^2}{(r+\delta r)} + \frac{[(r+\delta r)(v_0+\delta v_0)]^2}{r^3}\right\}\delta r-(\rho_0+\delta\rho_0)g\delta z. \tag{32}$$

Condition (30) can be reached following the argument that the stability of the system requires the leading terms of the total work done by the interchange of the two particles to be non-negative, i.e.,

$$W_1+W_2=\frac{1}{r^3}\delta[\rho_0 r^2 v_0^2]\delta r+\delta(\rho_0 g)\delta z\geq 0. \tag{33}$$

The physical meaning of the necessary condition for stability derived by the method of generalized progressing wave expansion can be seen immediately if one compares equation (18) with equation (30) or (33). Equation (18) for incompressible fluids reduces to

$$\Phi\left(\frac{\partial\Omega}{\partial r}\right)^2-\left[\frac{g}{\rho_0}\frac{\partial\rho_0}{\partial r}-\frac{1}{\rho_0}\frac{\partial}{\partial z}(\rho_0 r\Omega^2)\right]\left(\frac{\partial\Omega}{\partial r}\right)\left(\frac{\partial\Omega}{\partial z}\right) - \left[\frac{g}{\rho_0}\frac{\partial\rho_0}{\partial z}\right]\left(\frac{\partial\Omega}{\partial z}\right)^2\geq 0. \tag{34}$$

Equations (30) and (34) are identical if one matches $\partial\Omega/\partial r$ with δr and $\partial\Omega/\partial z$ with δz. If the variation in the axial direction is restrained, equations (30) and (34) reduce to the well-known Rayleigh-Synge criterion [5], which is a requirement for centrifugal stability. Also it can be easily shown, by the same integral method used by Fung [6], that the first term in equations (30) or (34) is in fact a differential representation of a stable centrifugal force field. This mechanism is reflected in equation (25*a*) saying that the steady state of the flow should be stable in the radial direction. Two parts are involved in this first term. The first part is the variation of density in the centrifugal force field. The second part is the Rayleigh discriminant representing a variation of the centrifugal balance constrained by the conservation of circulation.

If the variation in the radial direction is suppressed, equations (30) and (34) reduce to a condition representing the variation of density in the gravitational force field. This mechanism is reflected in (25*b*) saying that the steady state of density should be statically stable in the axial direction.

The second term in equations (30) and (34) represents the cross correlation between the radial and axial variations of the density in the centrifugal and gravitational force fields. This variation is reflected in condition (25*c*) with a mechanism to be immediately revealed. For incompressible flows, equation (25*c*) reduces to

$$-\left(\frac{\Phi}{\dfrac{r\Omega^2}{\rho_0}\dfrac{\partial\rho_0}{\partial r}}\right)\frac{\dfrac{\partial\rho_0}{\partial z}}{\dfrac{\partial\rho_0}{\partial r}}\geq\frac{1}{F}, \tag{35}$$

which represents a requirement for stability imposed on the density variations in the radial and axial directions. For fixed values of the Froude number, the density variation in the radial direction, as compared to that in the axial direction, plays an opposite role in flow stability. While large density gradients (negative) in the axial direction stabilize the flow as in the case of two dimensional stratified fluids in a gravitational force field, large density gradients (positive) in the radial direction destabilize the flow. This is opposite to the role played by density gradients in radius-dependent rotating flows, and seems to be implausible at the first look. However, this is also an interesting point that reveals the physical mechanism carried by equations (25*c*) and (35). For potential flows, both equations (1) and (35) reduce to

$$-\frac{\partial\rho_0}{\partial r}\Big/\frac{\partial\rho_0}{\partial z}=F=\frac{r\Omega^2}{g} \tag{36}$$

saying that the ratio between the density gradient in the radial direction and that in the axial direction should be compatible with the ratio between the centrifugal force field and the gravitational force field. And it is also the constraint condition for the pressure balance requires that large density gradients (positive) in the radial direction result in large negative density gradients in the axial direction for a fixed Froude number.

The arguments just presented for the physical mechanisms of the necessary conditions allows us to conclude that equations (25) represent a generalized state of statically stable profiles for the steady flow. To secure stability for the basic flow, it is necessary that the steady-state distribution satisfy (*a*) the radial force balance condition, (*b*) the axial force balance condition, and (*c*) a pressure balance condition constraining the variations of density in both the centrifugal and gravitational force fields. As a result of the third constraint, equations (25) do not represent three independent conditions. Either one of the two conditions in (25*a*) and (25*b*) will have to be automatically satisfied if the other condition and equation (25*c*) are fulfilled.

Conclusions and Discussions

Necessary conditions of stability for an isentropic compressible vortex flow, with the density being stratified in both the radial and axial directions, have been derived using the method of generalized progressing wave expansion. This method transforms a set of partial differential equations into a set of ordinary differential equations with equivalent stability characteristics evaluated along the rays, thus, provides one with a powerful tool to attack a class of steady flows with more than one independent variable. The necessary conditions derived here represent a generalized state of statically stable distribution for the steady flow. They require

the flow to satisfy the centrifugal force balance condition, the gravitational force balance condition, and the pressure balance condition restraining the variation of densities and forces in both force fields.

We have not been successful in obtaining a sufficient condition for stability. However, the necessary conditions derived suggest that a sufficiency condition for flows with the steady distributions varying in both the radial and axial directions should satisfy three criteria: (*a*) one in the radial direction [7, 8], (*b*) one in the vertical direction (the classical Richardson criterion for 2*D* parallel flows), and (*c*) one constrained by the pressure relation for the variation of the density and for the balance of the two force fields [4].

An understanding of the stability criteria for the flow under consideration is essential to the vortex motion in the late wake behind a towed axisymmetric body. The existence of the vertically oriented vortex structure far downstream of the wake implies that the vortex motion satisfies some Richardson criteria [4]. The stability criteria, if derived, will provide us with an insight into the flow characteristics that may be used to predict the evolution and breakdown of the vertically oriented vortex motion.

References

1 Pao, H.-P., and Kao, T. W., "Vortex Structure in the Wakes of a Sphere," *Physics of Fluids*, Vol. 20, 1977, pp. 187–191.

2 Eckhoff, K. S., and Storesletten, L., "A Note on the Stability of Steady Inviscid Helical Gas Flows," *Journal of Fluid Mechanics*, Vol. 89, 1978, pp. 401–411.

3 Rayleigh, J. W. S., "On the Dynamics of Revolving Fluids," *Proceedings of Royal Society of London*, Series A, Vol. 93, 1916, pp. 148–154.

4 Fung, Y. T., "On the Stability of Vortex Motions in Compressible Stratified Fluids," NRL Memorandum Report 4571, 1981.

5 Synge, J. L., "The Stability of Heterogeneous Liquids," *Transactions of Royal Society of Canada*, Series III, XXVII, 1933, pp. 1–18.

6 Fung, Y. T., "Stability Characteristics for Flows of the Vortex Sheet Type," *Journal of Fluid Mechanics*, Vol. 136, 1983, pp. 201–217.

7 Fung, Y. T., and Kurzweg, U. H., "Stability of Swirling Flows with Radius-Dependent Density," *Journal of Fluid Mechanics*, Vol. 72, 1975, pp. 243–255.

8 Lalas, D. P., "The 'Richardson' Criterion for Compressible Swirling Flows," *Journal of Fluid Mechanics*, Vol. 69, 1975, pp. 65–72.

A. J. Paullay
Department of Mathematics and Computer Science,
Bronx Community College,
City University of New York,
Bronx, N.Y.

R. E. Melnik

A. Rubel

S. Rudman

M. J. Siclari

Research and Development Center,
Grumman Aerospace Corporation,
Bethpage, N.Y. 11714

Similarity Solutions for Plane and Radial Jets Using a k-ε Turbulence Model

When the eddy viscosity is defined by the standard k-ε turbulence model, the equations governing self-similar incompressible plane and radial jets have a solution that is not analytic at the jet edge. A transformation that stretches the similarity variable simplifies the defining set of ordinary differential equations and makes them amenable to efficient numerical integration. Highly resolved solutions for the velocity, turbulent kinetic energy and dissipation rate profiles are tabulated and entrainment, velocity decay rate and growth rate are determined. The growth rate differs by 6 percent from a parabolic marching asymptotic solution to the full partial differential equations.

Introduction

Self similar descriptions of turbulent incompressible jets issuing into stagnant surroundings belong to an established class of fluid dynamics problems. Simple Prandtl mixing length models for the turbulent shear stress have been used to produce Goertler or Tollmien type solutions when the eddy viscosity is independent of, or dependent upon, the lateral coordinate, respectively [1]. Goertler's solutions are infinite in lateral extent while Tollmien's solutions possess a finite lateral edge but predict a vanishing eddy viscosity at the symmetry location. Recent applications of two-equation turbulence models to the jet problem [2–5] have produced more realistic solutions with a non-vanishing eddy viscosity at the symmetry location as well as a finite lateral edge.

Although Rodi [3] set down the conditions governing self-similarity, using the two-equation model, the parabolic partial differential equations are generally employed and far field solutions are approached using numerical marching procedures. These techniques introduce a degree of inaccuracy that must be separated from faults due to turbulence modeling [6]. Hence, it is desirable to cast the governing equations into similarity form and solve them directly thereby establishing a standard for comparison.

In this work the most commonly used of the two-equation models, the k-ϵ model [7], is employed to formulate the plane and radial jet problems in similarity variables. Plane and radial jets are chosen since they both appear to be adequately described with the same set of model constants. No attempt is made here to evaluate the $k-\epsilon$ model's performance with respect to experimental data.

Contributed by the Fluids Engineering Division and presented at the Winter Annual Meeting, New Orleans, La., December 9-14, 1984 of THE AMERICAN SOCIETY OF MECHANICAL ENGINEERS. Manuscript received by the Fluids Engineering Division, June 27, 1982. Paper No. 84-WA/FE-3.

An analysis of the set of governing ordinary differential equations reveals them to be singular at the jet edge. Such behavior was used [4] to generate k-kL model constants; however, shooting techniques that were difficult to implement [5] were required to solve the equation set. A transformation is presented herein that removes the finite edge to infinity and decouples the equation system rendering it amenable to efficient numerical solution. Detailed results are tabulated which can be used to assess the accuracy of alternate numerical approaches to the far field solution.

Formulation and Analysis

The high Reynolds number, thin shear layer equations governing the turbulent incompressible jet are

continuity

$$\frac{\partial}{\partial x}(ux^j) + \frac{\partial}{\partial y}(vx^j) = 0 \quad \begin{matrix} j=0, \text{ plane jet} \\ j=1, \text{ radial jet} \end{matrix} \tag{1}$$

momentum

$$u\frac{\partial u}{\partial x} + v\frac{\partial u}{\partial y} = \frac{\partial}{\partial y}\left(\nu_T \frac{\partial u}{\partial y}\right) \tag{2}$$

turbulent kinetic energy

$$u\frac{\partial k}{\partial x} + v\frac{\partial k}{\partial y} = \frac{1}{\sigma_k}\frac{\partial}{\partial y}\left(\nu_T \frac{\partial k}{\partial y}\right) + \mathrm{P} - \epsilon \tag{3}$$

turbulent dissipation

$$u\frac{\partial \epsilon}{\partial x} + v\frac{\partial \epsilon}{\partial y} = \frac{1}{\sigma_\epsilon}\frac{\partial}{\partial y}\left(\nu_T \frac{\partial \epsilon}{\partial y}\right) + \frac{\epsilon}{k}(C_{\epsilon 1}P - C_{\epsilon 2}\epsilon) \tag{4}$$

Here u and v are the velocities in the streamwise, x, and lateral, y, directions, respectively. The turbulent kinetic energy is denoted by k, its dissipation rate by ϵ and its rate of production by P, where

$$P = \nu_T \left(\frac{\partial u}{\partial y} \right)^2 .$$

The eddy viscosity, ν_T, is defined by

$$\nu_T = C_\mu \frac{k^2}{\epsilon}$$

Boundary conditions for equations (1)–(4) are

$$\text{symmetry plane, } y=0: \quad \frac{\partial u}{\partial y} = \frac{\partial k}{\partial y} = \frac{\partial \epsilon}{\partial y} = v = 0 \qquad (5a,b,c,d)$$

$$\text{jet edge, } y = y_e: \quad u = k = \epsilon = 0. \qquad (6a,b,c)$$

The only initial condition of consequence for the far field solution is the momentum flux constraint from the integration of equation (2) across the jet,

$$\frac{dJ}{dx} = 0, \quad J = 2x^j \int_0^{y_e} u^2 dy. \qquad (7)$$

Here J is the kinematic momentum flux per unit width for the plane jet, per radian for the radial jet. Model constants [7] complete the specification of the problem,

$$C_\mu = 0.09, C_{\epsilon 1} = 1.44, C_{\epsilon 2} = 1.92, \sigma_k = 1, \sigma_\epsilon = 1.3.$$

It is advantageous to define a stream function, ψ, where

$$\frac{\partial \psi}{\partial y} = u x^j, \quad \frac{\partial \psi}{\partial x} = -v x^j \qquad (8a,b)$$

and equation (1) is then identically satisfied.

Let the similarity variable be

$$\eta = \frac{y}{C_\mu^{1/2} x} \qquad (9)$$

and choose the dimensionless stream function, $F(\eta)$, so that

$$\psi(x,\eta) = C_\mu^{1/2} u_0(x) x^{j+1} F(\eta) \qquad (10)$$

The lateral distributions of velocity are evaluated from equations (7–10)

$$\frac{u}{u_0} = F'(\eta), \quad \frac{v}{C_\mu^{1/2} u_0} = \eta F'(\eta) - 2^{j-1} F(\eta) \qquad (11a,b)$$

where the primes indicate derivatives with respect to η. The centerline velocity distribution, u_0 (x), can be determined from equation (7), written in form

$$\frac{J}{u_0^2 x^{j+1}} = 2 C_\mu^{1/2} \int_0^{\eta_e} F'^2(\eta) d\eta \qquad (12)$$

When the turbulent kinetic energy and dissipation functions are expressed as

$$\frac{k}{u_0^2} = G(\eta), \quad \frac{\epsilon x}{u_0^3} = H(\eta) \qquad (13a,b)$$

then equation (2) is easily placed in similarity form,

$$2^{j-1}(F'^2 + FF'') + \left(\frac{G^2}{H} F'' \right)' = 0. \qquad (14)$$

Equation (14) may be integrated once yielding

$$2^{j-1} FF' + \frac{G^2}{H} F'' = 0 \qquad (15)$$

where symmetry plane boundary conditions require that the constant of integration vanishes.

The similarity form for equations (3) and (4) is achieved in a like manner, viz.

$$2^j F'G + 2^{j-1} FG' + \frac{1}{\sigma_k} \left(\frac{G^2}{H} G' \right)' + \frac{G^2}{H} F''^2 - H = 0 \qquad (16)$$

$$\frac{1}{2}(5+3j) F'H + 2^{j-1} FH' + \frac{1}{\sigma_\epsilon} \left(\frac{G^2}{H} H' \right)' + C_{\epsilon 1} G F''^2 - C_{\epsilon 2} \frac{H^2}{G} = 0 \qquad (17)$$

To apply the boundary conditions (5), (6) to equations (15)–(17) recall that equation (5a) is already satisfied by equation (15) and that the scaling implied by equation (11a) must be fulfilled. Thus,

$$\text{symmetry plane: } F(0) = G'(0) = H'(0) = 0, F'(0) = 1 \qquad (18a,b,c,d)$$

$$\text{jet edge: } G(\eta_e) = H(\eta_e) = 0 \qquad (19a,b)$$

It is to be noted that the similarity profile shapes are independent of the model constant, C_μ. The requirement that $F'(\eta_e) = 0$ (equation 6(a)) is met as a consequence of equations (15) and (19) and does not demand the imposition of a boundary condition. In addition, the value of η_e is unknown and must be determined during the course of the solution. Equations (15)–(17), with boundary conditions equations (18) and (19), form a highly nonlinear two-point boundary value problem which must be solved numerically. The solution of this problem is further complicated by the appearance of a singularity at the jet edge which is caused by the vanishing of the turbulent kinetic energy and its dissipation rate. As a consequence it will be shown that the eddy viscosity also vanishes at the jet edge.

The structure of the edge singularity is deduced as follows. Define the distance from the jet edge as

Nomenclature

a,b,c = exponents (equation (20))
A,B,C = coefficients (equation (20))
$C_{\mu,\epsilon 1,\epsilon 2}$ = constants in turbulence model
F = stream function similarity variable
G = turbulent kinetic energy similarity variable
H = dissipation rate similarity variable
j = index; plane jet (j = 0), radial jet (j = 1)
J = kinematic jet momentum flux per width, per radian
k = turbulent kinetic energy = $\frac{1}{2}\left(\overline{u'^2} + \overline{v'^2} + \overline{w'^2}\right)$
l_T = turbulent length scale
P = production of k
u = streamwise mean velocity
U = streamwise mean velocity similarity variable
v = lateral mean velocity
x = streamwise coordinate
y = lateral coordinate
ϵ = dissipation rate of k
η = similarity coordinate = $C_\mu^{-1/2} y/x$
λ = distance from the jet edge = $\eta_e - \eta$
ν_T = turbulent eddy viscosity
ξ = transformed similarity coordinate
$\sigma_{k,\epsilon}$ = diffusion constants in k, ϵ equations
τ = turbulent shear stress = $-\overline{u'v'}$
ψ = stream function

Subscripts

e = jet edge
0 = symmetry plane
$1/2$ = velocity half-width
$*$ = edge of computational domain

$$\lambda = \eta_e - \eta$$

and assume that, to leading order in λ, the dependent variables can be represented by

$$F = F_e - A\lambda^a, G = B\lambda^b, \quad H = C\lambda^c; \lambda \to 0 \qquad (20a,b,c)$$

where F_e is the edge value of the stream function and each of the coefficients and exponents is required to be positive. Also, for the streamwise velocity to exhibit the proper decay, $a > 1$.

For this behavior to be consistent with the momentum balance (equation (15)) requires that

$$-2^{j-1}AaF_e\lambda^{a-1} + \frac{B^2}{C}Aa(a-1)\lambda^{2b-c+a-2} = 0.$$

Matching coefficients and exponents reveals

$$(a-1)\frac{B^2}{C} = 2^{j-1}F_e, \quad 2b - c - 1 = 0. \qquad (21a,b)$$

Satisfaction of the turbulent kinetic energy balance (equation (16)) dictates that

$$2^j ABa\lambda^{a+b-1} + \frac{B^3 b}{C}\left(\frac{b}{\sigma_k} - a + 1\right)\lambda^{b-1} + \frac{A^2B^2}{C}a^2(a-1)^2\lambda^{2a-3} - C\lambda^{2b-1} = 0$$

where use has been made of equation (21a,b). Two leading order exponent possibilities exist, viz.

(I) $b = 2(a-1)$
(II) $b < 2(a-1)$.

Possibility (I) is unworkable since it produces an inconsistent coefficient balance. That is,

$$\frac{B^3}{C}b^2\left(\frac{1}{\sigma_k} - \frac{1}{2}\right) + \frac{A^2B^2}{C}a^2(a-1)^2 = 0$$

where both terms are positive. Possibility (II) is acceptable and the coefficient balance yields

$$b = \sigma_k(a-1) \qquad (22)$$

Finally, the dissipation balance (equation (17)) along with the relationships of equation (21a,b) and (22) necessitate that

$$\frac{1}{2}(5+3j)aAC\lambda^{2(b-1)+a} + \frac{cB^2}{\sigma_\epsilon}\left[\left(2 - \frac{\sigma_\epsilon}{\sigma_k}\right)b - 1\right]\lambda^{2(b-1)} + C_{\epsilon 1}BA^2a^2(a-1)^2\lambda^{2[b(1/\sigma_k+1/2)-1]} - C_{\epsilon 2}\frac{C^2}{B}\lambda^{3b-2} = 0$$

where, by inspection, the second term is of leading order and its vanishing coefficient determines the value of b. This, and equation (21b), (22) give

$$a - 1 = \frac{1}{2\sigma_k - \sigma_\epsilon}, b = \frac{\sigma_k}{2\sigma_k - \sigma_\epsilon}, c = \frac{\sigma_\epsilon}{2\sigma_k - \sigma_\epsilon} \qquad (23a,b,c)$$

so that equation (21a) becomes

$$\frac{G^2}{H} = 2^{j-1}(2\sigma_k - \sigma_\epsilon)F_e\lambda, \quad \lambda \to 0 \qquad (24)$$

This analysis of the standard k-ϵ model in the vicinity of the jet edge shows that diffusion of k and ϵ toward the edge is in balance with advection toward the jet interior due to the entrainment velocity. In addition, equation (23a) assures that the streamwise velocity vanishes as the edge is approached. Equation (24) predicts that the eddy viscosity increases linearly with distance from the edge, its slope given in terms of the edge value of the dimensionless stream function. In contrast to k-kL models [2]-[4], which incorporate a finite turbulent length scale at the jet edge, the k-ϵ model [7] causes this scale to decay with the 2/7 power of λ, i.e.,

$$l_T = C_\mu^{3/4}k^{3/2}/\epsilon \sim \lambda^{(3a/2-\sigma_\epsilon)/(2\sigma_k-\sigma_\epsilon)}, \lambda \to 0.$$

Other consequences of the model are also of interest. The velocity, u, is given by

$$\frac{u}{u_0} = aA\lambda^{1/(2\sigma_k-\sigma_\epsilon)}. \qquad (25)$$

The dimensionless shear stress is defined by

$$\frac{\overline{u'v'}}{u_0^2} = -C_\mu^{1/2}\frac{G^2}{H}F'' \qquad (26a)$$

and it must exhibit the same edge behavior as the streamwise velocity (equation (15)). Furthermore, the turbulent shear stress to kinetic energy ratio is

$$\frac{\overline{u'v'}}{k} \sim \lambda^{(1-\sigma_k)/(2\sigma_k-\sigma_\epsilon)}, \lambda \to 0 \qquad (26b)$$

which reduces to a constant for the model value of $\sigma_k = 1$.

Method of Solution

The three second order ordinary differential equations (equations (15-17)) and their boundary conditions (equations (18), (19)) are not in a form particularly amenable to numerical solution. Both boundary conditions on the stream function of equation (15) are applied at $\eta = 0$. This suggests that a better arrangement can be found in terms of two first order equations via the introduction of a new dependent variable, U, so that

$$U = F' \qquad (27)$$

and

$$2^{j-1}FU + \frac{G^2}{H}U' = 0 \qquad (28)$$

In addition, the two point boundary value problems for G and H (equations (16), (17)) are highly coupled, nonlinear and difficult to implement because the jet edge location is unknown a priori. Fortunately, a simple transformation of the independent variable, viz. $\eta = \eta(\xi)$ where

$$\frac{d\eta}{d\xi} = \frac{G^2}{H}, \quad \eta = \int_0^\xi \frac{G^2}{H}d\xi \qquad (29a,b)$$

eliminates much of these difficulties. Note that, as defined, $\xi = 0$ is the symmetry plane, $\eta = 0$. If the transformation is applied to equations (27), (28), (16), and (17) the result is

$$\frac{G^2U}{H} = F_\xi \qquad (30)$$

$$2^{j-1}FU + U_\xi = 0 \qquad (31)$$

$$2^jF_\xi G + 2^{j-1}FG_\xi + \frac{1}{\sigma_k}G_{\xi\xi} + 4^{j-1}F^2U^2 - G^2 = 0 \qquad (32)$$

$$\frac{1}{2}(5+3j)F_\xi H + 2^{j-1}FH_\xi + \frac{1}{\sigma_\epsilon}H_{\xi\xi} + \frac{H}{G}(4^{j-1}C_{\epsilon 1}F^2U^2 - C_{\epsilon 2}G^2) = 0 \qquad (33)$$

where the subscript, ξ, indicates differentiation with respect to ξ. Of particular note is that the transformation has uncoupled the turbulent kinetic energy, equation (32), from the dissipation rate, equation (33), and virtually removed the nonlinearities. Equations (30), and (31) can be integrated using the boundary conditions (equation 18a,d) to produce

$$F(\xi) = \int_0^\xi \frac{G^2}{H}Ud\xi \qquad (34)$$

$$U(\xi) = \exp\left(-\int_0^\xi 2^{j-1}Fd\xi\right), \qquad (35)$$

and along with equations (32) and (33) they comprise the system to be solved numerically.

Because the lateral dependence of the eddy viscosity is embodied in the coordinate transformation the equations formulated in the ξ variable take on a constant eddy viscosity appearance. In fact, the jet edge has been transformed to infinity. This is demonstrated by substituting equation (24) into equation (29*a*) to obtain

$$\frac{d\xi}{d\eta} \rightarrow \frac{1}{2^{j-1}(2\sigma_k - \sigma_\epsilon)F_e(\eta_e - \eta)}, \eta \rightarrow \eta_e$$

Integration yields

$$\xi = -\frac{1}{2^{j-1}(2\sigma_k - \sigma_\epsilon)F_e} \ln \lambda + \text{constant}, \lambda \rightarrow 0 \tag{36}$$

so that $\xi \rightarrow \infty$ for $\eta \rightarrow \eta_e$. Using this result in equation (29*b*) gives

$$\eta_e = \int_0^\infty \frac{G^2}{H}\, d\xi \tag{37}$$

which provides an explicit expression for the location of the edge of the shear layer. Using equation (36) for $\xi(\lambda)$ along with equation (20*b*,*c*) and equation (23*b*,*c*) establishes the asymptotic boundary conditions on $G(\xi)$, $H(\xi)$ as the jet edge is approached. Namely,

$$G(\xi) = G(\xi_*)\exp[2^{j-1}\sigma_k F_e(\xi_* - \xi)], \xi \rightarrow \infty \tag{38a}$$

$$H(\xi) = H(\xi_*)\exp[2^{j-1}\sigma_\epsilon F_e(\xi_* - \xi)], \xi \rightarrow \infty \tag{38b}$$

where ξ_* is an arbitrary constant. These asymptotic forms can also be found directly from the transformed equation (30)–(33).

A numerical solution is sought to equations (32)–(35) in the domain $0 \le \xi \le \xi_*$ where ξ_* is chosen large enough so that equations (38) are applicable for $\xi > \xi_*$. (Numerical experiments determined that $\xi_* \simeq 46/2^j$ places η_* within 1 percent of the jet boundary, well into the asymptotic edge region.) The second order finite-difference representation of equations (32)–(33) is formed by replacing all derivatives by their three point central differenced counterparts using a uniform mesh. At the symmetry plane ($\xi = 0$) a reflecting boundary condition is invoked and at the outer edge of the domain $G(\xi_*)$ and $H(\xi_*)$ are related to their corresponding values at the neighboring interior point by equation (38). A tridiagonal solver is used to find the $G(\xi)$, $H(\xi)$ distributions and $F(\xi)$, $U(\xi)$ are found from equations (34) and (35) by quadrature. This cycle is repeated until the residuals of the difference equations for G and H are less than 10^{-11} at every point. Generally, this tolerance required less than 100 iterations independent of the number of grid points.

The numerical solution may be continued analytically into the domain $\xi > \xi_*$. For example, recasting equation (29*b*) gives

$$\eta(\xi) = \int_0^{\xi_*} \frac{G^2}{H}\, d\xi + \int_{\xi_*}^{\xi} \frac{G^2}{H}\, d\xi,$$

and, with the use of equation (38) this may be expressed as

$$\eta(\xi) = \eta(\xi_*) + \frac{G^2(\xi_*)/H(\xi_*)}{2^{j-1}F_e(2\sigma_k - \sigma_\epsilon)}\{1 - \exp[2^{j-1}F_e(2\sigma_k - \sigma_\epsilon)(\xi_* - \xi)]\}. \tag{39}$$
$$\xi \ge \xi_*$$

In a like manner, the velocity may be evaluated from equation (35), viz

$$U(\xi) = U(\xi_*)\exp[2^{j-1}F_e(\xi_* - \xi)] \tag{40}$$
$$\xi \ge \xi_*$$

and the stream function from equation (34),

$$F(\xi) = F(\xi_*) + \frac{G^2(\xi_*)U(\xi_*)/H(\xi_*)}{2^{j-1}F_e(2\sigma_k - \sigma_\epsilon + 1)}\{1 - \exp[2^{j-1}F_e(2\sigma_k - \sigma_\epsilon + 1)(\xi_* - \xi)]\} \tag{41}$$
$$\xi \ge \xi_*$$

Table 1 Plane jet similarity solution

ξ	η	F	U	G	H
0.0	0.0	0.0	1.00000	0.06567	0.11647
0.55160	0.02014	0.02042	0.99719	0.06596	0.11723
1.10321	0.04097	0.04081	0.98880	0.06678	0.11945
1.65481	0.06166	0.06114	0.97500	0.06808	0.12290
2.15135	0.08048	0.07934	0.95814	0.06954	0.12677
2.70286	0.10168	0.09941	0.93481	0.07138	0.13151
3.19930	0.12106	0.11729	0.91000	0.07308	0.13577
3.69574	0.14075	0.13493	0.88195	0.07470	0.13965
4.19218	0.16074	0.15226	0.85106	0.07613	0.14279
4.68863	0.18104	0.16920	0.81776	0.07725	0.14492
5.18507	0.20162	0.18567	0.78252	0.07799	0.14580
5.62635	0.22012	0.19985	0.74993	0.07827	0.14544
6.12280	0.24113	0.21521	0.71227	0.07812	0.14368
6.61924	0.26228	0.22987	0.67398	0.07747	0.14055
7.06052	0.28114	0.24226	0.63977	0.07648	0.13668
7.50180	0.30002	0.25402	0.60567	0.07511	0.13192
7.99825	0.32121	0.26645	0.56778	0.07315	0.12566
8.49469	0.34228	0.27802	0.53067	0.07082	0.11867
8.93597	0.36084	0.28757	0.49856	0.06847	0.11201
9.43241	0.38148	0.29750	0.46363	0.06558	0.10422
9.92886	0.40179	0.30657	0.43014	0.06249	0.09631
10.42530	0.42171	0.31482	0.39821	0.05926	0.08844
10.92174	0.44119	0.32228	0.36793	0.05595	0.08076
11.41819	0.46019	0.32900	0.33935	0.05262	0.07338
11.96979	0.48066	0.33564	0.30963	0.04894	0.06562
12.52139	0.50044	0.34149	0.28202	0.04534	0.05841
13.12816	0.52134	0.34709	0.25404	0.04151	0.05115
13.73492	0.54131	0.35190	0.22848	0.03786	0.04461
14.34168	0.56033	0.35603	0.20521	0.03443	0.03877
15.05877	0.58158	0.36012	0.18048	0.03065	0.03274
15.72069	0.60001	0.36326	0.16012	0.02746	0.02793
16.49294	0.62011	0.36626	0.13908	0.02408	0.02314
17.37550	0.64126	0.36898	0.11825	0.02065	0.01852
18.25807	0.66056	0.37109	0.10043	0.01766	0.01495
19.25095	0.68018	0.37290	0.08350	0.01478	0.01168
20.40932	0.70048	0.37442	0.06725	0.01197	0.00874
21.73317	0.72059	0.37562	0.05246	0.00939	0.00628
23.27756	0.74037	0.37653	0.03924	0.00705	0.00427
25.20827	0.76038	0.37719	0.02727	0.00492	0.00264
27.74564	0.78030	0.37763	0.01689	0.00305	0.00140
31.49654	0.80009	0.37788	0.00832	0.00151	0.00055
39.21899	0.82001	0.37797	0.00193	0.00035	0.00008
∞	0.83127	0.37798	0.0	0.0	0.0

Table 2 Radial jet similarity solution

ξ	η	F	U	G	H
0.0	0.0	0.0	1.00000	0.15594	0.35967
0.31735	0.02146	0.02143	0.99660	0.15610	0.36034
0.60586	0.04097	0.04080	0.98769	0.15650	0.36198
0.89436	0.06050	0.05996	0.97343	0.15704	0.36430
1.18286	0.08003	0.07879	0.95413	0.15762	0.36682
1.50021	0.10153	0.09903	0.92757	0.15812	0.36913
1.78872	0.12106	0.11688	0.89912	0.15828	0.37017
2.07722	0.14057	0.13411	0.86713	0.15801	0.36960
2.36572	0.16003	0.15065	0.83222	0.15718	0.36695
2.68307	0.18134	0.16795	0.79118	0.15549	0.36125
2.97158	0.20058	0.18280	0.75213	0.15319	0.35337
3.28893	0.22154	0.19810	0.70799	0.14979	0.34177
3.57743	0.24036	0.21104	0.66740	0.14594	0.32876
3.89478	0.26074	0.22419	0.62285	0.14093	0.31212
4.21214	0.28072	0.23620	0.57895	0.13521	0.29356
4.52949	0.30024	0.24709	0.53620	0.12893	0.27367
4.87569	0.32095	0.25772	0.49131	0.12159	0.25112
5.22189	0.34099	0.26714	0.44863	0.11393	0.22839
5.56810	0.36029	0.27541	0.40840	0.10612	0.20606
5.94315	0.38032	0.28318	0.36777	0.09768	0.18286
6.34705	0.40084	0.29031	0.32754	0.08878	0.15952
6.75096	0.42023	0.29631	0.29094	0.08025	0.13819
7.21256	0.44101	0.30196	0.25340	0.07109	0.11646
7.67417	0.46031	0.30652	0.22019	0.06265	0.09755
8.19347	0.48030	0.31060	0.18758	0.05407	0.07948
8.77048	0.50046	0.31406	0.15664	0.04547	0.06296
9.40518	0.52028	0.31688	0.12821	0.03776	0.04850
10.12644	0.54006	0.31916	0.10193	0.03027	0.03592
10.99194	0.56032	0.32097	0.07726	0.02312	0.02497
12.03055	0.58031	0.32229	0.05532	0.01665	0.01610
13.35766	0.60021	0.32319	0.03604	0.01091	0.00918
15.23293	0.62014	0.32374	0.01965	0.00597	0.00415
18.49301	0.64004	0.32400	0.00683	0.00208	0.00105
∞	0.65834	0.32405	0.0	0.0	0.0

The edge values, $\eta_e = \eta(\infty)$ and $F_e = F(\infty)$ are evaluated from equations (39) and (41), respectively.

Results and Discussion

The similar solutions tabulated for the plane jet (Table 1) and the radial jet (Table 2) are highly mesh resolved and considered to be "exact" to four decimal places. These computations used 801 ponts across the jet, equally spaced in the ξ coordinate, and required 10–13 CPU seconds on the IBM-3033. Approximately 80 percent of the grid points fall beyond the velocity half-width location. A mesh width study revealed that reasonable accuracy can be attained with far fewer points. In fact, calculations with 41 points produced

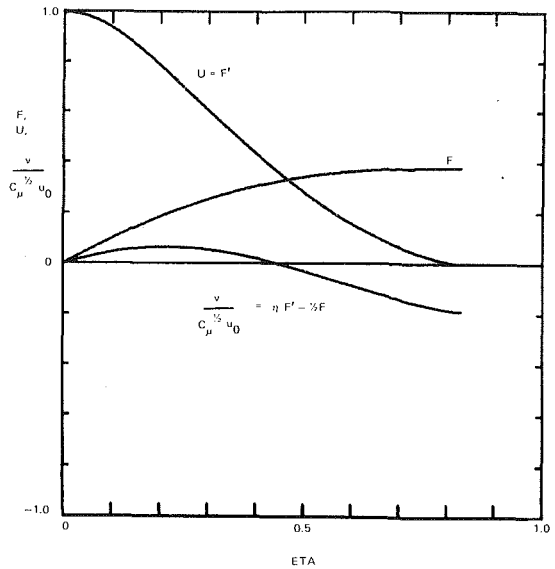

Fig. 1 Plane jet similar solution, mean properties. Stream function, streamwise velocity and lateral velocity profiles.

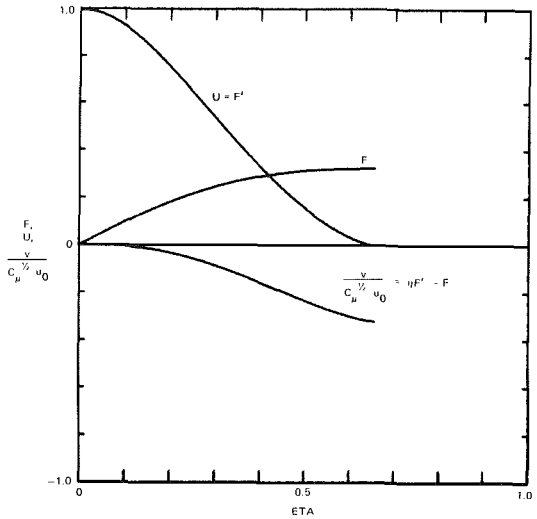

Fig. 2 Radial jet similar solution, mean properties. Stream function, streamwise velocity and lateral velocity profiles.

local symmetry plane and jet edge results with less than 1 percent deviation from the 801 point solution. Global features of these solutions (e.g., growth rate) showed even less deviation ($\simeq 0.1$ percent). The centerline velocity decay rate (equation (12)) as well as the half-width growth rate (see (equation (9)) and the entrainment velocity (see Eq 11b) predicted by the present computations are given in Table 3.

These results represent a standard by which the calculations utilizing parabolic-type marching schemes can be judged on their approach to far field similarity. It is not the purpose of this work to evaluate the performance of the standard k-ϵ model with respect to the body of experimental data. Nevertheless, it is worth noting that the overall features predicted in Table 3 are consistent with plane jet [8] and radial jet [9] data. The plane jet growth rate calculated by Ljuboja and Rodi [10] with the identical turbulence model as used here is 0.114. This exceeds the present result by 6 percent.

The Goertler and Tollmien type similarity solutions, based upon Prandtl mixing length concepts, produce identical streamwise velocity profiles for the plane and radial jets [1]. It can be proven, and the velocity profiles of Figs. 1 and 2 show, that this is not the case for the k-ϵ model. The ratio of the jet edge width to the velocity half-width, $\eta_e/\eta_{1/2}$ is determined to be 2.309 for the plane jet and 2.077 for the radial jet.

Table 3 Overall features of the similar solutions

	Velocity Decay Rate $J/(u_0^2 x^{j+1})$	Growth Rate $y_{1/2}/x$	Entrainment $-v_e/u_o$
Plane Jet	0.1595	0.1080	0.0567
Radial Jet	0.1412	0.0951	0.0972

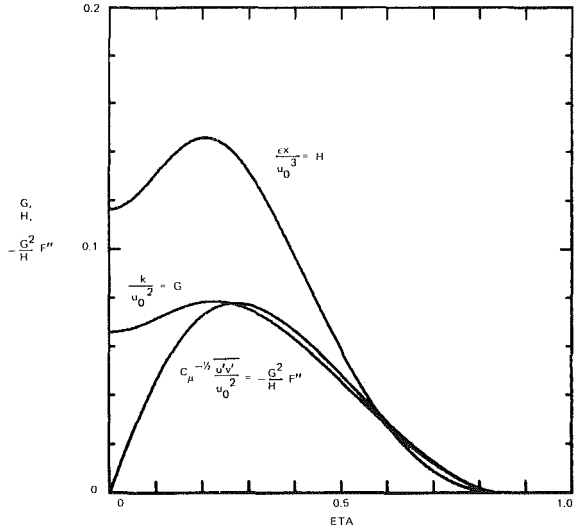

Fig. 3 Plane jet similar solution, turbulence properties. Shear stress, kinetic energy, and dissipation profiles.

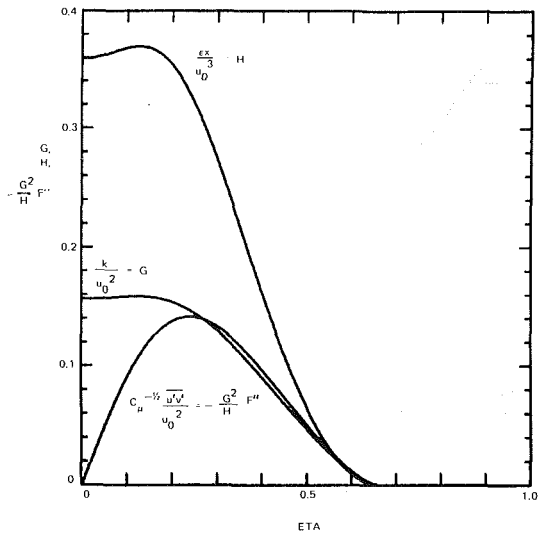

Fig. 4 Radial jet similar solution, turbulence properties. Shear stress, kinetic energy, and dissipation profiles.

Calculations by Rodi and Spalding [2] with a $(k-kL)$ model produced edge width to velocity half-width ratios about 10 percent greater than those given here. Such computations have consistently predicted radial jet growth rates larger than plane jet growth rates [3], a trend opposite to that noted in Table 3.

The lateral distribution of turbulence properties (Figs. 3 and 4) are much like those given by Rodi [3]. To be noted are slight minimums in the turbulent kinetic energy and dissipation functions at the radial jet symmetry plane. These features were found by Rodi and Spalding [2] but not by Rodi [3].

The level of the turbulent shear stress in the radial jet is about twice that occurring in the plane jet. This is a consequence of the factor 2^{j-1} appearing in equation (15) and has been pointed out by several researchers. That the turbulent kinetic energy levels are also in this proportion follows from observing that the profiles $G(\eta)$ and $G^2 F''(\eta)/H(\eta)$ are nearly

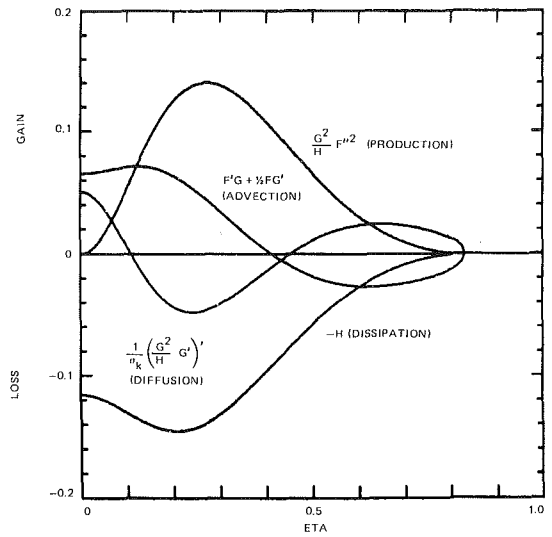

Fig. 5 Plane jet similar solution; turbulent energy balance as a function of lateral position

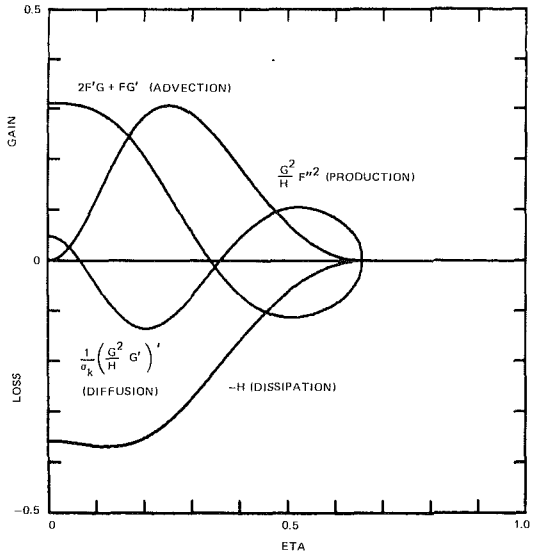

Fig. 6 Radial jet similar solution; turbulent energy balance as a function of lateral position

coincident beyond the location of maximum shear. The balance of turbulent kinetic energy equation terms (Figs. 5 and 6) shows that the maximum shear point occurs approximately where production and dissipation are dominant. In such an equilibrium region equations (16) and (26*a*) yield

$$\left(\frac{\overline{u'v'}}{k}\right)_{k\text{-equilibrium}} = -C_\mu^{1/2}\frac{GF''}{H} = C_\mu^{1/2}. \tag{42}$$

Previously, it was shown (equation (26*b*)) that in the vicinity of the jet edge the shear stress to kinetic energy ratio is constant for $\sigma_k = 1$. Therefore, the equilibrium region fixes the value of this ratio (equation (42)) and the constraints of the energy balance in the edge region act to maintain the relationship throughout the outer region of the jet.

The modeled balance given by the turbulent dissipation equation (Figs. 7 and 8) shows enhanced effects due to convection near the radial jet symmetry plane vis a vis the plane jet. This effect is also apparent in the turbulent kinetic energy balance but not to the extent shown by Rodi [3] or Rodi and Spalding [2] with their *k-kL* model computations. The production and destruction of the dissipation function are in near balance at the same location as the turbulent kinetic energy near-equilibrium region. Such a balance for dissipation requires

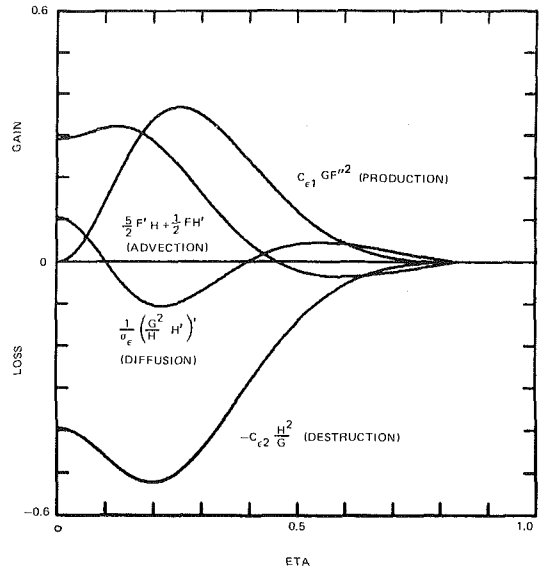

Fig. 7 Plane jet similar solution; dissipation function balance versus lateral position

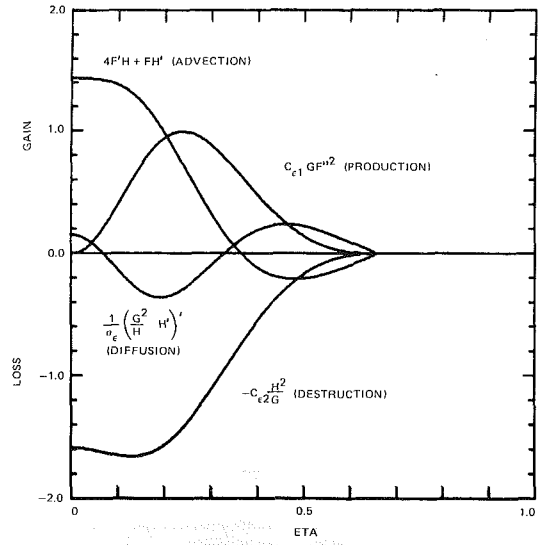

Fig. 8 Radial jet similar solution; dissipation function balance versus lateral position

$$\left(\frac{\overline{u'v'}}{k}\right)_{\epsilon\text{-equilibrium}} = -C_\mu^{1/2}\frac{GF''}{H} = \left(\frac{C_\mu C_{\epsilon 2}}{C_{\epsilon 1}}\right)^{1/2} \tag{43}$$

which implies a 15 percent excess over the ratio of equation (42). The modeling of the dissipation equation (e.g., Rodi [11]) is responsible for the slight excess in turbulent shear with respect to turbulent kinetic energy depicted in Figs. 3 and 4.

The edge regions of Figs. 5–8 are consistent with the analysis given here showing that, in this neighborhood, diffusion and convection (i.e., entrainment) effects are in balance. The rapid variation of the balancing terms as the edge is approached, and the fact that the location of the edge is not known a priori, serve to magnify the difficulty of obtaining numerical solutions using η as the independent variable.

Concluding Remarks

The far field similarity equations for plane and radial jets subject to the standard k-ϵ turbulence model has been presented. The nature of the solutions has been elucidated in the vicinity of the boundary separating the jets from their stagnant surroundings. This analysis was shown to be

necessary in order to achieve the numerical solutions to the governing equations and should prove helpful to other investigators.

A coordinate transformation has been given that accounts for the lateral distribution of eddy viscosity by a stretching of the similarity variable. This method yields a simplified set of governing equations amenable to efficient computational solution. The technique is applicable to other related problems.

It is hoped that the detailed solutions tabulated here can serve as a guide by which the accuracy of parabolic type marching schemes can be assessed to have achieved self-similarity. For example, Ljuboja and Rodi calculated a plane jet growth rate 6 percent in excess of the present calculations using the identical turbulence model. The separation of such numerical inaccuracy from model shortcomings remains an important concern of modelers. Similarity solutions for other turbulence models currently in use can help to eliminate some of these numerical uncertainties.

Acknowledgement

This research has been supported by the Office of Naval Research.

References

1 Rajaratnam, N., *Turbulent Jets*, Elsevier, Amsterdam, 1976.

2 Rodi, W., and Spalding, D. B., "A Two-Parameter Model of Turbulence and Its Application to Free Jets," *Würme und Stoffübertragung*, Vol. 3, 1970, pp. 85–95.

3 Rodi, W., "The Prediction of Free Turbulent Boundary Layers by Use of a Two-Equation Model of Turbulence," PhD thesis, Univ of London, 1972.

4 Vollmers, H., and Rotta, J. C., "Similar Solutions of the Mean Velocity, Turbulent Energy and Length Scale Equation," *AIAA J*, Vol. 15, 1977, pp. 714–720.

5 Rotta, J. C., and Vollmers, H., "Aehniche Lösungen der Differentialgleichungen für gemittelte Geschwindigkeiten," Turbulenzenergie und Turbulenzlänge, DLF-FB 76–24, 1976.

6 Launder, B. E., and Morse, A., "Numerical Prediction of Axisymmetric Free Shear Flows with Reynolds Stress Closure," *Turbulent Shear Flows*, Vol. I, (ed. F. Durst et al.), Springer-Verlag, Berlin, 1979, pp. 279–294.

7 Launder, B. E., and Spalding, D. B., "The Numerical Computation of Turbulent Flows," *Comp Meth in Appl Mech and Engng*, Vol. 3, 1974, pp. 269–289.

8 Everitt, K. W., and Robins, A. B., "The Development and Structure of Turbulent Plane Jets," *J Fluid Mech*, Vol. 88, 1978, pp. 563–583.

9 Tanaka, T., and Tanaka, E., "Experimental Study of a Radial Turbulent Jet," *Bull. of the JSME*, Vol. 19, 1976, pp. 792–799.

10 Ljuboja, M., and Rodi, W., "Calculations of Turbulent Wall Jets with an Algebraic Reynolds Stress Model," ASME JOURNAL OF FLUIDS ENGINEERING, Vol. 102, 1980, pp. 350–356.

11 Rodi, W., Examples of Turbulence Models for Incompressible Flows," *AIAA J*, Vol. 20, 1982, pp. 872–879.

Near Wake Properties of a Strumming Marine Cable: An Experimental Study

R. D. Peltzer
Naval Research Laboratory,
Washington, D.C. 20375

D. M. Rooney
Engineering Sciences Dept.,
Hofstra University,
Hempstead, NY 11550

Resonant flow-induced oscillations of a flexible cable can occur when the damping of the cable system is sufficiently small. The changes in the flow field that occur in the near wake of the cable during these resonant oscillations are closely related to the changes in the fluid forces that accompany these oscillations. The present wind tunnel experiments were undertaken to examine the effects that forced synchronized vibration and the helically-wound cross section of the cable have on near wake vortex shedding-related parameters; specifically the shedding frequency, vortex formation length L_f, reduced velocity U_r, vortex strength and the wake width L_w. The range of flow speeds over which the vortex shedding was locked on to the vibration frequency varied directly with the vibration amplitude. The helical cross section and the synchronized vibration caused significant changes in the near wake development that could be directly related to the increase in hydrodynamic forces associated with unforced synchronized vibration.

Introduction

Marine cables are often integral parts of a complex structural system. When fluid flows uniformly past, or when these high aspect ratio bluff bodies are exposed to waves and nonuniform current flows, vortices are shed as the flow separates alternately from opposite sides of the body. When the shedding frequency is close to one of the natural frequencies (or sometimes a multiple thereof) of the cable system, intensified large amplitude cross flow oscillations can occur if the structural damping is sufficiently small. Strumming, or lock-on is also characterized by increased stresses, hydrodynamic forces, fatigue, and ultimately it reduces the overall life of the structure and its components.

Numerous references to vortex shedding-related structural problems in the literature attest to the fact that substantial research into vortex related synchronization phenomena must be performed and analyzed. The present wind tunnel experiments were undertaken to examine the effects that forced synchronized vibration and the helically-wound noncircular cross section of the marine cable have on the near wake vortex shedding-related parameters; specifically the shedding frequency, vortex formation length, and the wake width. The results that are presented in this paper are part of a wider-ranging study dealing with vortex shedding from a vibrating cable in a linear shear flow [14].

Background

The cable system employed in the present study was too highly damped to be self-excited in an air flow. Forced excitation was used to simulate the self-excited resonant wake conditions in order to study the lock-on induced changes in the cable wake. The validity of this approach has been examined by Griffin [5] who found that changes in the near wake that accompany resonant vortex excited oscillations were reproducible from forced, externally-excited oscillations when the experimental conditions were carefuly duplicated.

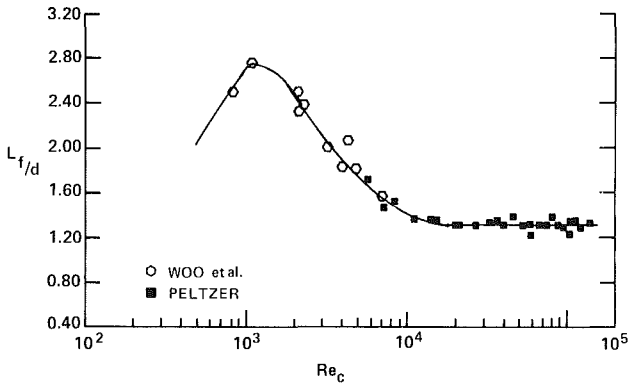

Fig. 1 Vortex formation lengths for circular cylinders in uniform and linear shear flows

The vortex formation length (L_f) is a measure of the downstream extent of the vortex formation region in the cylinder wake, and is generally defined as the distance between the cylinder center axis and the first downstream appearance of the fully formed periodic vortex street. The measurement criterion that was used in the present study to define the location of the formation length was the rms maximum of the second harmonic of the fluctuating velocity on the axis of the wake. This criterion was used in most previous studies [1, 4, 12, 14, 21].

Contributed by the Fluids Engineering Division and presented at the Winter Annual Meeting, New Orleans, La., December 9-14, 1984, of THE AMERICAN SOCIETY OF MECHANICAL ENGINEERS. Manuscript received by the Fluids Engineering Division, November 1, 1983. Paper No. 84-WA/FE-9.

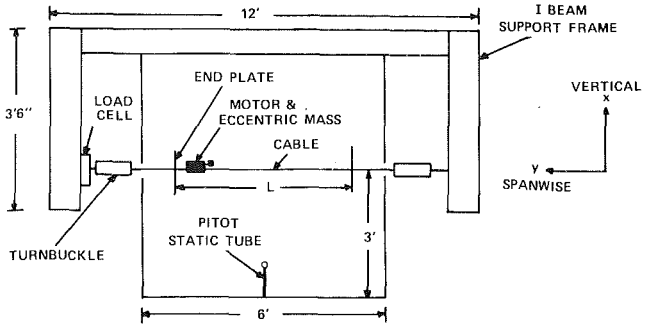

Fig. 2 Wind tunnel test section and cable model (streamwise view)

Figure 1 shows a summary of two experimental studies [14, 21] dealing with the measurement of the formation length in the Reynolds number range 8.0×10^2 to 1.6×10^5. Woo et al. measured the formation length at the centers of five high aspect ratio brass tubes in various low and moderate linearly sheared flows. The formation length values were not significantly affected by the sheared flows. There is not much scatter in the data of Woo et al. and Peltzer which fall on the solid curve, as both were careful to minimize end effects. At a Reynolds number of 1.0×10^3, the formation length, L_f/d is 2.8. As the Reynolds number increases, L_f/d decreases until it becomes constant at a value $L_f/d = 1.32$ when the Reynolds number reaches 1.0×10^4, and it remains constant until Re = 1.6×10^5.

Studies dealing with changes induced in the near wake of a rigid cylinder by self-excited or forced motion of the body were conducted by Koopmann [11], Griffin et al. [4, 5, 8, 9, 10], Davies [3], Stansby [20], Sarpkaya [18], and Zdravkovich [22], among others. Koopmann found that the frequency range over which lock-on occurred increased as the amplitude of cylinder vibration increased. The correlation length, defined as the spanwise distance along the cylinder span over which the vortex shedding is in phase, increased rapidly as a/d increased. Griffin et al. found that the length of the vortex formation region decreased when the cylinder vibration amplitude (a/d) and cylinder vibration frequency (f_{cv}/f_{csv}) ratio were increased while the cylinder and vortex shedding frequencies were lock-on. The vortex strength, vorticity generation, and the wake width increased as the cylinder vibration amplitude was increased.

Zdravkovich summarizes three major reasons why the vortex shedding behind a synchronized oscillating cylinder is stronger and more regular than that found behind a stationary one:

1). The formation length decreases and the fluctuating and time averaged forces are magnified.

2). The spanwise correlation of the vortex formation and shedding are enhanced remarkably by the cyclic oscillations.

3). Since the synchronization frequency remains constant over a range of flow velocities, there is a constant period of time available for the formation. More vorticity is generated with increased velocity within and along the synchronization range and the vortices become stronger.

By vibrating small aspect ratio ($L/d = 16$, 20) circular cylinders in a uniform flow, Stansby developed empirical formulas to predict the frequency boundaries of the lock-on region as a function of vibration amplitude in the Reynolds number range 3.6×10^3 to 9.2×10^3. He found that the vortex shedding locked on to submultiples, $f_{cv}/f_{csv} = 2$, 3 of the cylinder vibration. At the upper and lower boundaries of locking-on, the regular unforced vortex shedding frequency was intermittent with the locked-on shedding frequency.

Studies dealing with synchronization phenomena in the near wakes of vibrating flexible cylinders in uniform flow have been performed by Ramberg and Griffin [15-17]. With hot-wire anemometry measurements they studied the vortex wake of a synchronized forced vibrating cable in uniform flow for Reynolds numbers between 230 and 1300. There it was found that spanwise variation of the vortex formation length was determined by the local amplitude (a/d) variation. As a/d increased, L_f/d decreased. An inverse relation was found between the local formation length and vortex strength, which was consistent with Davies' and Zdravkovich's observations.

Experimental Apparatus and Methods

The present experiments were conducted in the 8.5 m long, 1.8 m square test section of the VPI&SU subsonic stability wind tunnel. An electronically controlled three-dimensional traverse was available to transport the measuring instruments in the vertical (x), spanwise (y), or streamwise (z) directions. Figure 2 shows a diagram of the wind tunnel test section including the cable model.

The cable that was used in the tests was constructed of seven strands of Kevlar synthetic fiber rope, wound around each other helically, and wrapped with a polyurethane jacket. The noncircular cross section had a 1.143 cm measured mean diameter over the jacket. The aspect ratio of the cable was $L/d = 107$. The cable tension was adjusted with the turnbuckles and measured using a Strainsert universal flat load cell. The small dc motor with an eccentrically located mass was attached to the cable in order to excite the lower vibration modes by varying the motor speed and cable tension. The cable mode shape, vibration amplitude and frequency were obtained using a Physitech electro-optical auto-collimator tracking unit. The optical head was mounted on the traverse downstream of the cable, and focused on the top edge of the cable which had an incandescent light source placed upstream to give a clear edge for tracking the motion of the cable. Details of the cable vibration measuring procedure are given by Peltzer [14].

To examine the vortex shedding characteristics in the near wake of the cable, a straight hot-wire probe was attached to the traverse and positioned in the cable wake where the strongest vortex shedding occurred ($x/d = 0.92$, $z/d = 3.5$). The probe was connected to a TSI model 1050 constant temperature anemometer. The output signal from the anemometer was band-pass filtered and sent to a ZTL FFT processor.

Previous investigators [11, 20, 21] had not established uniform criteria that could be used to determine when the

Nomenclature

a = local vibration amplitude
a_{csv} = amplitude of vortex shedding frequency peak on power spectrum
a_{cv} = amplitude of cable vibration frequency peak on power spectrum
d = cable diameter
f_{cs} = vortex shedding frequency from a stationary cable
f_{csv} = vortex shedding frequency from a vibrating cable
f_{cv} = cable vibration frequency
L = cable length
L_f = vortex formation length
L_w = wake width
Re = (Ud/ν) Reynolds number
St = $(f_{csv}, f_{cs})\ d/U$ Strouhal number
U_r = $(U/f_{cv}d)$ reduced velocity
U_r^* = $(U/f_{csv}d)$ critical reduced velocity
y = spanwise location

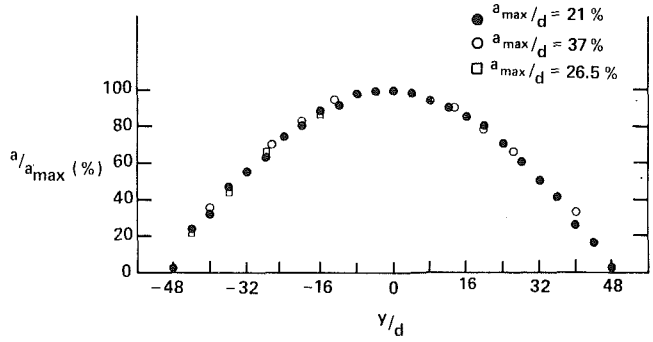

Fig. 3 Cable mode shape

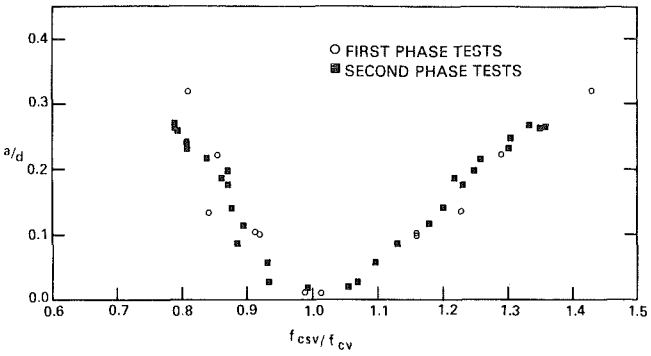

Fig. 4 Cable lock-on regions as a function of vibration amplitude

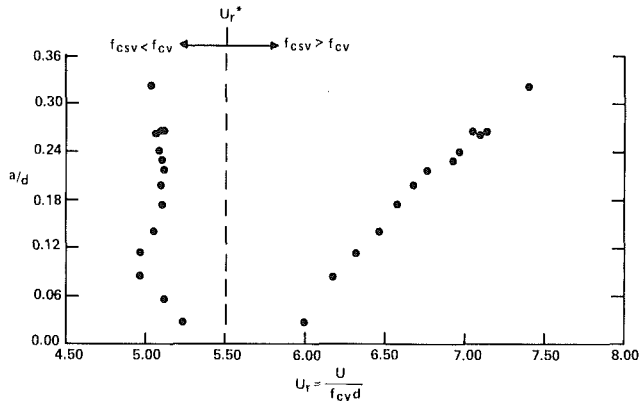

Fig. 5 Reduced velocity at the boundaries of the lock-on region for the vibrating cable as a function of the vibration amplitude

vortex shedding initially locked on to the cable vibration. Preliminary observations of power spectra of the hot-wire signal were used to help establish the criteria that would determine when the vortex shedding frequency from the cable (f_{csv}) locked on to the forced vibration frequency of the cable (f_{cv}). When the amplitude ratio of the vibration and vortex shedding peaks was equal to 20 ($a_{cv}/a_{csv} = 20$), the ratio, f_{csv}/f_{cv}, became equal to a constant and the vortex shedding was considered locked on to the forced cable vibration. The reasons for choosing this criteria are the following. When the ratio, a_{cv}/a_{csv}, was equal to 20, this typically corresponded to the Reynolds number (flow velocity) where the frequency ratio, f_{csv}/f_{cv}, initially became equal to a constant even though a_{cv}/a_{csv} still varied with changes in the flow velocity. For values of a_{cv}/a_{csv} less than 20, the vortex shedding was intermittent between forced and unforced, evidenced by the changing ratio f_{csv}/f_{cv}. The intermittent shedding ceased when the amplitude ratio was greater than 20, and only forced shedding remained.

The present investigations were performed in two phases separated by three months time; a preliminary first phase where some experimental data were obtained while the measurement techniques were established, and the primary second phase where the majority of the data was obtained. Unless otherwise noted, the results presented in this paper were obtained during the primary phase of the investigation.

Results and Discussion

The experiment was designed to measure the flow properties in the near wake of a flexible cable forced to vibrate in the first mode. The nondimensional first mode shape is shown in Fig. 3. The absolute value of a/a_{max}, is plotted against the spanwise location (y/d) along the cable. The mode shape was invariant with peak-to-peak vibration amplitude ratio, a_{max}/d. The measured values of the vibration amplitude (a) were accurate to within ±4 percent for the second phase tests and ±10 percent for the first phase tests.

The frequency boundaries of the synchronization or lock-on region were measured for vibration amplitudes ranging from 0.02 to 0.32 along the span of the cable. The lower boundary of the lock-on region is defined as the initial velocity where the frequency ratio, f_{csv}/f_{cv}, becomes equal to a constant (less than 1.0) and the ratio a_{cv}/a_{csv} is equal to 20. The upper boundary of the lock-on region is defined as that initial velocity where f_{csv}/f_{cv} becomes equal to a constant (greater than 1.0) and the ratio, a_{cv}/a_{csv}, is equal to 20. The significant results are presented in the next four figures.

The frequency boundaries of the cable lock-on regions are plotted in Fig. 4 as a function of increasing forced cable vibration amplitude. The numerical values of the frequencies defining the boundaries of the lock-on region could be measured accurately to within ±1.5 percent. The individual frequency ranges that were measured at specific a/d locations along the span of the vibrating cable were not influenced by changing the maximum value of the vibration amplitude at the antinodes.

The frequency range over which the vortex shedding locked on to the cable vibration increased proportionally with the vibration amplitude, a finding consistent with Koopmann's [11] and Stansby's [20] results. The absolute value of (f_{csv}/f_{cv} − 1.0) at the upper boundary was measurably larger than the corresponding value at the lower boundary. The shedding remained locked on to the cable vibration over a significantly wider frequency range at the upper boundary a finding which is consistent with unforced lock-on behavior.

The lock-on phenomena can be further examined by plotting the reduced velocity, $U_r = U/f_{cv}d$, at the boundaries of the lock-on region versus the vibration amplitude. U_r is the critical reduced velocity ($f_{csv} = f_{cv}$), where so called perfect synchronization occurs [18]. In order for a cable to be naturally excited into strumming, the reduced velocity must be nearly equal to the critical reduced velocity such that the frequency of the vortices that are shed from the cable is nearly equal to an excitable natural frequency of vibration ($f_{csv}/f_{cv} = 1.0$).

The present results are shown in Fig. 5. Perfect synchronization occurred at the critical reduced velocity value $U_r^* = 5.50 \pm 0.22$. The corresponding Reynolds number was $Re = 2.93 \times 10^3$. The cable vortex shedding locked on to the forced vibration frequency at a constant reduced velocity $U_r = 5.10 \pm 0.15$. This value of U_r at the lower boundary of the lock-on region was 7.3 percent less than U_r^*. The reduced velocity at which lock-on occurs is not a function of the vibration amplitude and is nearly equal to the critical reduced velocity as it should be in order to correctly simulate unforced cable strumming by forced excitation. The upper boundary of the lock-on region increased linearly with a/d. Larger

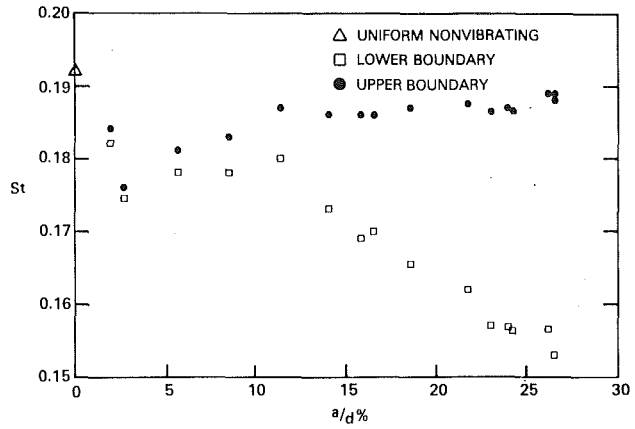

Fig. 6 Variation of the Strouhal number as a function of vibration amplitude at the boundaries of the lock-on region

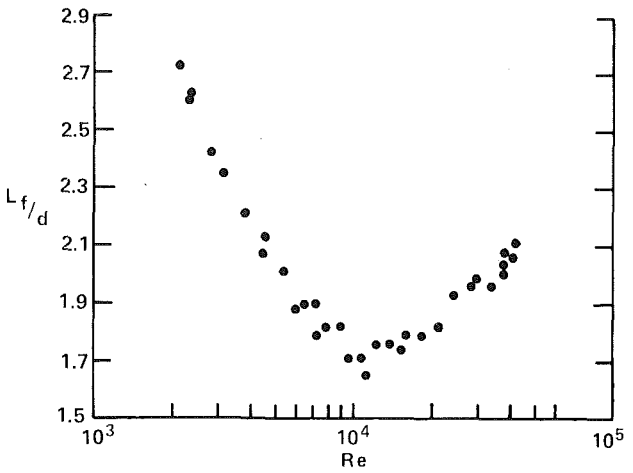

Fig. 8 Variation of the formation length as a function of increasing Reynolds number, $a/d = 0.0$

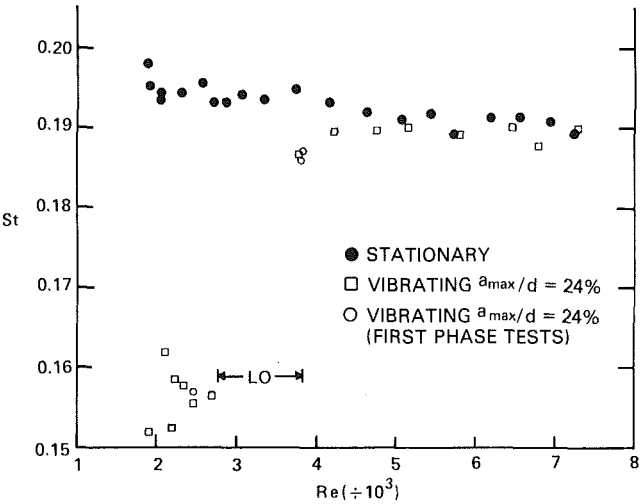

Fig. 7 Variation of the centerline Strouhal number as a function of Reynolds number of a stationary and vibrating cable

vibration amplitudes sustain lock-on over a wider Reynolds number range. Griffin [3] notes in his summary report that the Reynolds number range over which resonant vortex excited oscillations occur is directly proportional to the vibration amplitude.

A combined analysis of Figs. 4 and 5 reveals that the frequency at which the vortex shedding initially locked on to the forced cable vibration frequency was the chief variable that was changing with amplitude. The Strouhal numbers at the upper and lower boundaries of the lock-on region are plotted as a function of increasing vibration amplitude a/d in Fig. 6 to examine how the frequency changed. For vibration amplitudes below 11 percent, the data exhibited no substantial change, a result consistent with both Griffin's [4] and Koopmann's [11] observations pertaining to vibration amplitude-related changes. They both noted that for forced vibration amplitudes less than 10 percent, no measurable increases in the correlation or coherence of the vortex shedding along the cylinder span could be observed, and that above 10 percent there was a measurable increase in the correlation or coherence of the shedding.

For amplitudes greater than 11 percent the Strouhal numbers defining the lower boundary of the lock-on region decreased linearly with increasing a/d. This reduction in Strouhal number with increasing a/d has been observed by Woo et al. [21] in their experimental studies and by Sarpkaya et al. [18, 19] in their numerical analyses. In the background section, it was noted that in the synchronization region, L_f varied inversely with a/d [2, 4, 5], the vortex strength increased as L_f decreased [2, 8, 9] and there was a constant period of time available for the vortices to form. In the present experiments the vortices were shed at a lower Strouhal number because of the increased vortex strength. The vortex strength was increased because each growing vortex was fed circulation over a longer constant period of time. Davies [3] found that there was a thirty-five percent increase in the strength of the vortices shed from a D-shaped cylinder undergoing forced synchronized oscillations. Sarpkaya and Shoaff [19] numerically showed that as the strength of the vortices in the near wake of a vibrating cylinder was increased, the Strouhal number decreased proportionally.

At the upper lock-on limit, the Strouhal number jumped to a constant value (independent of a/d) slightly less (2.5 percent) than that found in uniform flow about a stationary cable (St = 0.192). This result was consistent with one of the observations listed by Sarpkaya [18] in his summary of the primary consequences of synchronized shedding. He stated that at the end of the lock-on range the vortex shedding frequency jumped to a value governed by the Strouhal relationship.

A plot of the centerline Strouhal number variation with Reynolds number in the near wake of a stationary and vibrating cable is presented in Fig. 7 to examine the range of Reynolds numbers over which the vibration had significant influence on the Strouhal number. The stationary Strouhal numbers increased by 2.5 percent over the Reynolds number range examined. Adjacent to the lower Reynolds number boundary of the lock-on region ($Re < 2.75 \times 10^3$), the Strouhal numbers associated with the vibrating cable were centered around a constant value of $St = 0.157 \pm 0.05$. It will be shown later that the formation length was substantially reduced in this region also. The vortices were shed at a lower Strouhal number because of the increased vortex strength accompaning the decrease in L_f. It has been noted [18] that in the regions adjacent to the lock-on region the vortex shedding was intermittent between forced and unforced. The intermittency will also contribute to the increase in vortex strength, thereby lowering the Strouhal number. At the upper Reynolds number boundary of the lock-on region ($Re > 3.85 \times 10^3$), the Strouhal number jumped to within 3.6 percent of the non-vibrating Strouhal number, a result that was consistent with those found in Fig. 6 and Sarpkaya's [18] summary. The Strouhal number was slightly less than the unforced value because the intermittency between forced and unforced shedding probably caused the vortices to be slightly

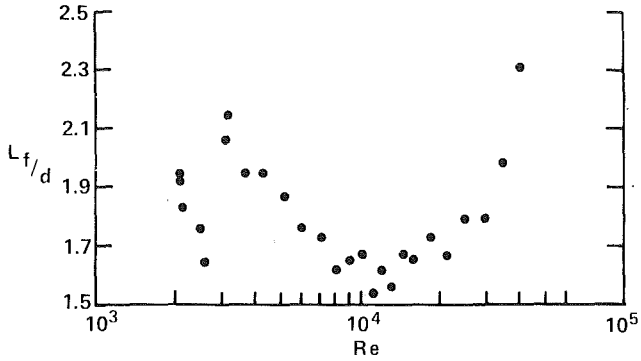

Fig. 9 Variation of the formation length as a function of increasing Reynolds number, a/d = 0.099

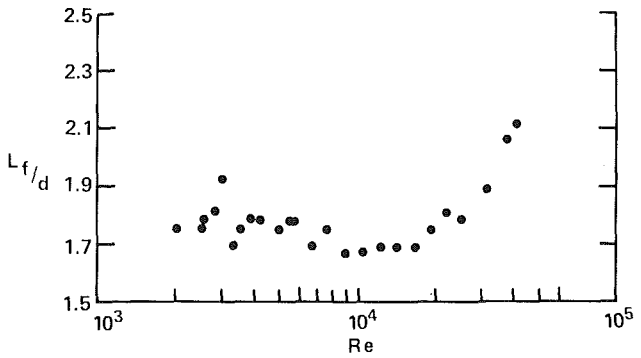

Fig. 10 Variation of the formation length as a function of increasing Reynolds number, a/d = 0.255

stronger and the Strouhal number slightly smaller. The formation lengths in this adjacent region were also measurably less than those behind the stationary cable, another indication that the vortices were stronger. At still higher Reynolds numbers, the vibrating and stationary curves merged, and the vibration no longer had an appreciable influence on the vortex strength, formation length and shedding frequency.

The variation of the vortex formation length values in the Reynolds number range, $1.8 \times 10^3 \leq \mathrm{Re} \leq 4.2 \times 10^4$, was studied using five different vibration amplitudes; a/d = 0.0, 0.099, 0.13, 0.176 and 0.255. Figures 8–10 present the results obtained at a/d = 0.0, 0.99, and 0.255. Most of the experimentally measured values of the formation length were reproducible to within ±4.0 percent with a few extreme values differing by 8.0 percent. Changes in the formation lengths that can be related to increasing Reynolds number, vibration amplitude variations, and synchronization will be discussed presently.

The formation length values in the near wake of the stationary cable are plotted in Fig. 8. The formation length was highly Reynolds number dependent. Measurable differences in the shape of the curve and magnitudes of the values were evident when these near wake cable results were compared with the smooth circular cylinder results (Fig. 1). These differences were the result of the changes in the near wake created by the helically wound cross section of the cable. Between Reynolds numbers 2.0×10^3 and 1.0×10^4, the cylinder and cable L_f curves exhibited a decrease in L_f with increasing Reynolds number. The cable values were larger, 14 percent at 2.0×10^3 and 33 percent at 1.0×10^4 on both curves, with L_f = 1.32 behind the cylinder and L_f/d = 1.75 behind the cable. The smooth cylinder values then remained constant with Reynolds number out to $\mathrm{Re} = 1.5 \times 10^5$ while the cable values increased with Reynolds number such that at $\mathrm{Re} = 4.1 \times 10^4$, the formation length was L_f/d = 2.10. The helical cross section of the cable lengthened the vortex formation region.

The major similarities and/or differences that were observed when the four sets of vibrating-cable formation length results were compared with the stationary cable results are discussed below.

At Reynolds numbers below the synchronization region centered around $\mathrm{Re} = 2.93 \times 10^3$, the vibrating cable formation lengths were significantly less than the stationary cable values. This vibration amplitude dependent reduction was as expected, based on the analysis of the results presented in Figs. 6 and 7. The strength of the vortices was increased which suggested that the formation length decreased correspondingly. At the two lowest vibration amplitudes, a/d = 0.099 (Fig. 9) and 0.13 the Reynolds number-related decrease in L_f was preserved, although the vibrating cable values were significantly smaller than the stationary ones. At the two highest vibration amplitudes, a/d = 0.176 and 0.255 (Fig. 10), the Reynolds number decrease was obscured by the larger vibration-induced changes, which made L_f relatively constant before the lock-on region.

The minimum formation length value, L_f/d = 1.70, and the Reynolds number around which it was centered, $\mathrm{Re} = 1.0 \times 10^4$, were not significantly influenced by the addition of vibration. The five sets of results all overlayed each other with minimal data scatter for Reynolds numbers greater than 1.0×10^4, signifying that the vibration had minimal influence on the near wake shedding properties beyond this point.

When the four sets of vibrating cable formation length results are compared, a significant synchronization related phenomenon can be observed. A sudden increase in L_f/d occurs during perfect synchronization, at $\mathrm{Re} = 2.93 \times 10^3$ and $U_r^* = 5.50$. The maximum value L_f/d approached during synchronization was inversely proportional to the amplitude a/d, a result consistent with previous observations where L_f/d decreased with increasing a/d [15, 16, 21, 22].

Griffin [6] has shown that the base pressure and wake width behaved similarly to the present L_f/d data in the perfect synchronization region. The values were strongly affected during synchronization and returned to stationary values shortly thereafter. Other authors have noted a sudden increase in spanwise correlation of the phase of the shedding [8], fluctuation lift and steady drag forces [22], wake width [20], and phase angle between the cylinder displacement and maximum rms pressure on that side [22]. The sudden increase in the vortex formation length during synchronized vibration is directly related to the increase in hydrodynamic forces that occurs during lock-on. In the background section of this paper, the two modes of synchronized vortex shedding observed by Zdravkovich were described. The vortices in the upper synchronization range ($f_{csv}/f_{cv} > 1.0$) were shed when the cylinder was near its maximum amplitude on that same side of the wake, whereas in the lower synchronization region, the vortices formed on one side of the cylinder and were shed when the cylinder was close to its maximum amplitude position on the opposite side. The longer formation length in the upper synchronization region was a direct result of the increased stability of the shedding.

Summary

A summary of the significant results pertaining to the effects of vibration on the vortex shedding in the near wake of a marine cable is as follows:

Locked-on vortex shedding in the near wake of a forced vibrating marine cable behaved similarly to that exhibited in the near wake of a circular cross section cable undergoing natural synchronization. The frequency range over which the vortex shedding locked on to the cable vibration increased proportionally with the amplitude of vibration.

At the lower boundary of the locked-on region, the Strouhal numbers and vortex formation lengths varied inversely with the vibration amplitude a/d, while the vortex strengths varied in direct proportion to a/d. The reduced velocity was independent of a/d. At the upper boundary the vortex strengths, Strouhal numbers, and formation lengths in the vibrating cable wake were virtually amplitude independent and nearly equaled those values measured in the wake of a non-vibrating marine cable. The reduced velocity increased linearly with a/d.

Perfect synchronization occurred when the critical reduced velocity was $U_r^* = 5.50$, and was accompanied by a sudden increase in the vortex formation length. This increase is directly related to the increase in hydrodynamic forces associated with unforced synchronized vibration. Shortly after the end of synchronization the L_f values returned to stationary values. Other authors had found that the base pressure, wake width, spanwise vortex shedding phase correlation, and fluctuating lift and steady drag were also strongly influenced during perfect synchronization and returned to stationary values thereafter.

Acknowledgments

The experiments were conducted at the Virginia Polytechnic Institute & State University under the sponsorship of the Naval Civil Engineering Laboratory, Port Hueneme, CA. Dr. Owen Griffin of the Naval Research Laboratory was the Technical Monitor for this project.

References

1 Bloor, M. S., and Gerrad, J. H., "Measurements on Turbulent Vortices in a Cylinder Wake," *Royal Society of London Proceedings*, Vol. 294, 1966, pp. 319–342.

2 Davies, M. E., "A Comparison of the Wake Structure of a Stationary and Oscillating Bluff Body, Using a Conditional Averaging Technique," *JFM*, Vol. 75, Part 2, 1976, pp. 209–231.

3 Davies, M. E., "The Effects of Turbulent Shear Flow on the Critical Reynolds Number of a Circular Cylinder," National Physics Laboratory (U.K.) NPL Report, Mar. Sci. R 151, Jan. 1976.

4 Griffin, O. M., "The Unsteady Wake of an Oscillating Cylinder at Low Reynolds Numbers," ASME *Journal of Applied Mechanics*, paper no. 71-APM-33, Dec. 1971, pp. 729–738.

5 Griffin, O. M., "Flow Near Self-Excited and Forced Vibrating Circular Cylinders," ASME *Journal of Engineering for Industry*, Vol. 94, May 1972, pp. 539–548.

6 Griffin, O. M., "Universal Similarity in the Wakes of Stationary and Vibrating Bluff Structures," ASME JOURNAL OF FLUIDS ENGINEERING, Vol. 103, Mar. 1981, pp. 52–58.

7 Griffin, O. M., Ramberg, S. E., Skop, R. A., Meggitt, D. J., and Sergev, S. S., "The Strumming Vibrations of Marine Cables: State of the Art," Naval Civil Engineering Laboratory Technical Note, TN no. N-1608, May 1981.

8 Griffin, O. M., Ramberg, S. E., "The Vortex-Street Wakes of Vibrating Cylinders," *JFM*, Vol. 66, Part 3, 1974, pp. 553–576.

9 Griffin, O. M., and Ramberg, S. E., "On Vortex Strength and Drag in Bluff Body Wakes," *JFM*, Vol. 69, Part 4, 1975, pp. 721–728.

10 Griffin, O. M., and Votaw, C. W., "The Vortex Street in the Wake of a Vibrating Cylinder," *JFM*, Vol. 51, Part 1, 1972, pp. 31–48.

11 Koopmann, G. H., "The Vortex Wakes of Vibrating Cylinders at Low Reynolds Numbers," *JFM*, Vol. 28, Part 3, 1967, pp. 501–512.

12 Peltzer, R. D., and Rooney, D. M., "Wake Characteristics of High Aspect Ratio Cylinders in Subcritical Spanwise Sheared Flows," ASME Publication 81-WA/FE-10, Nov. 1981.

13 Peltzer, R. D., "The Effect of Upstream Shear and Surface Roughness on the Vortex Shedding Patterns and Pressure Distributions Around a Circular Cylinder in Transitional Reynolds Number Flows," M.S. thesis, VPI&SU, Apr. 1980, 176 pp.

14 Peltzer, R. D., "Vortex Shedding From a Vibrating Cable with Attached Spherical Bodies in a Linear Shear Flow, Ph.D. thesis, VPI&SU, Aug. 1982.

15 Ramberg, S. E., and Griffin, O. M., "Vortex Formation in the Wake of a Vibrating, Flexible Cable," ASME JOURNAL OF FLUIDS ENGINEERING, Dec. 1974, pp. 317–322.

16 Ramberg, S. E., and Griffin, O. M., "The Effects of Vortex Coherence, Spacing and Circulation on the Flow-Induced Forces on Vibrating Cables and Bluff Structures," NRL Report 7945, Jan. 1976, 32 pp.

17 Ramberg, S. E., and Griffin, O. M., "Velocity Correlation and Vortex Spacing in the Wake of a Vibrating Cable," ASME JOURNAL OF FLUIDS ENGINEERING, Vol. 98, Mar. 1976, pp. 10–18.

18 Sarpkaya, T., "Vortex-Induced Oscillations; A Selective Review," ASME *Journal of Applied Mechancis*, Vol. 46, June 1979, pp. 241–258.

19 Sarpkaya, T., and Shoaff, R. L., "A Discrete-Vortex Analysis of Flow About Stationary and Transversely Oscillating Circuit Cylinders," Naval Postgraduate School Report NPS-69SL79011, Jan. 1979, 166 pp.

20 Stansby, P. K., "The Locking-on of Vortex Shedding Due to the Cross Stream Vibration of Circular Cylinders in Uniform and Shear Flows," *JFM*, Vol. 74, Part 4, 1976, pp. 641–665.

21 Woo, H. G. C., Cermak, J. E., and Peterka, J. A., "Experiments on Vortex Shedding from Stationary and Oscillating Cables in a Linear Shear Flow," Final report on contract N68305-78-C-0055 for the Naval Civil Engineering Laboratory, Colorado State University, July 1981, 233 pp.

22 Zdravkovich, M. M., "Modification of Vortex Shedding in the Synchronization Range," ASME JOURNAL OF FLUIDS ENGINEERING, Vol. 104, No. 4, Dec. 1982.

Transient Starting Flow in a Cylinder With Counter-Rotating Endwall Disks

Jae Min Hyun
Department of Mechanical Engineering,
Clarkson College of Technology,
Potsdam, NY 13676
Mem. ASME

Spin-up from rest in a cylinder with top and bottom endwall disks rotating in opposite directions (Ω_T and Ω_B are the respective rotation rate, but $S[\equiv\Omega_T/\Omega_B]<0$) is investigated. The sidewall is fixed to the faster-rotating disk. A finite-difference numerical model is adopted to integrate the unsteady Navier-Stokes equations. We consider a cylinder of aspect ratio $0(1)$ and minute Ekman numbers. Numerical solutions are presented to show the transient azimuthal flow structures, axial vorticity profiles, and meridional flow patterns. An azimuthal velocity front, which separates the rotating from the nonrotating fluid, propagates radially inward from the sidewall. The appearance of the front is similar to the front propagation in spin-up in a rigid cylinder. As S decreases from zero, the direction of rotation in the bulk of the interior fluid becomes the same as that of the faster-rotating disk. The azimuthal velocities are still vertically uniform in the bulk of the interior. The scaled time to reach the steady state decreases. The angular velocities of the interior fluid near the central axis become very small. Under counter-rotation, the meridional circulation forms a two-cell structure. A stagnation point appears on the slower-rotating disk. During spin-up, the stagnation point moves from the sidewall to its steady-state position. As counter-rotation increases, the radial distance traveled by the stagnation point decreases.

1 Introduction

The transient process of adjustment of a contained fluid initially at rest to the impulsively-started spinning container has been termed "spin-up from rest" [1, 2]. Knowledge of this internal flow is needed in various applications [3–5], e.g., spin-stabilized liquid-filled projectiles and rockets, rotating fluid machinery, chemical mixers, etc. We confine attention to cylindrical containers of aspect ratio $h/a\sim 0(1)$ and we consider situations in which the Ekman number $E\equiv\nu/\Omega h^2$ is minute, where a is the radius of the cylinder, h the height, ν the kinematic viscosity of the fluid, Ω the rotation rate of the container.

The basic analytical model for impulsive spin-up from rest in a rigid cylinder was developed by Wedemeyer [6]. It has been established that the most important process controlling spin-up is the weak meridional circulation driven by Ekman layers on the endwall disks [6, 7]. The azimuthal flows in the interior are divided into two regions by a moving front, which propagates from the cylinder sidewall to the central axis. The nonlinear properties associated with the front propagation were analyzed by several authors [8–11]. The overall fluid adjustment in the interior is substantially accomplished in the spin-up time scale $0(E^{-1/2}\Omega^{-1})$. Spin-up from rest in a rigid cylinder has since been investigated extensively.

The flow in a differentially-rotating cylinder, i.e., the top endwall disk rotates at Ω_T, the bottom disk at Ω_B, and the sidewall at Ω_S, exhibits some qualitative differences from the flow in a rigid cylinder. The final steady-state in a differentially-rotating container is not a solid-body rotation; there is a vertical motion in the interior sustained by the Ekman suction (blowing) at the faster (slower) rotating disk. Accordingly, the transient motion, which occurs between the initial impulse and the final state, shows features distinguishable from spin-up flows in a rigid cylinder. The ratio of the rotation rates of the endwall disks, $S=\Omega_T/\Omega_B$, emerges as a key parameter. For the special cases when one disk is stationary ($S=0.0$), numerical investigations were conducted for steady flow [12], and for both steady and unsteady flow [13]. Recently, reference [14] presented numerical solutions for the spin-up from rest for the parameter range of $0.0<S\leq 1.0$. It was demonstrated that as the steady state is approached, the interior core fluid rotates at a constant angular velocity which takes a value intermediate between Ω_T and Ω_B. The transient flows are no longer antisymmetric about the cylinder middepth as S deviates from unity [15]. These features are in qualitative agreement with the predictions of the analytical model of [16], which is a direct extension of Wedemeyer's model [6].

The steady flow of an incompressible fluid confined between two disks rotating in opposite directions, $S[\equiv\Omega_T/\Omega_B]<0$, has been the subject of some uncertainty (see [17], [18], and the papers cited in reference [19]). Dijkstra and Heijst [19] recently studied both numerically and ex-

Contributed by the Fluids Engineering Division for publication in the JOURNAL OF FLUIDS ENGINEERING. Manuscript received by the Fluids Engineering Division, February 20, 1984.

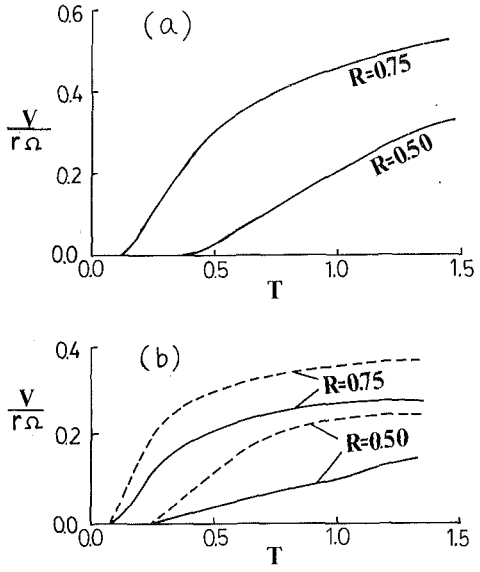

Fig. 1 Plots of scaled angular velocity $v/r\Omega$ versus scaled time T at two radial locations, $R=0.50$ and $R=0.75$, along middepth $Z=0.5$. (*a*) for case C2 ($E=4.34\times10^{-4}$, $S=0.0$); (*b*) solid lines are for case C4 ($E=4.34\times10^{-4}$, $S=-0.83$), and broken lines are for case C5 ($E=1.0\times10^{-3}$, $S=-0.83$).

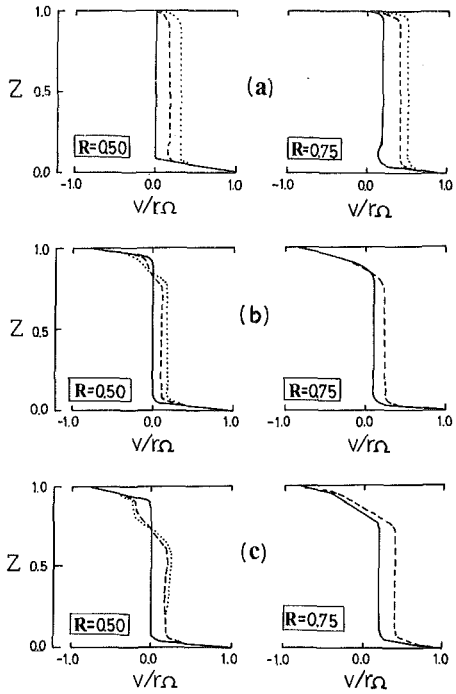

Fig. 2 Vertical profiles of $v/r\Omega$ at $R=0.50$ and $R=0.75$. Scaled times are ____, $T=0.29$; _ _ _ _, $T=0.75$; . . . . . , $T=1.40$. (*a*) for case C2, (*b*) for case C4, (*c*) for case C5. For plots in Figs. (*b*) and (*c*), the curves for $T=0.75$ and for $T=1.40$ overlap within graphical resolution.

perimentally the steady flow between two finite, counter-rotating disks enclosed by a cylinder. They considered a cylinder of low aspect ratio ($\delta[\equiv h/a]=0.07$) and the smallest Ekman number used was $E[\equiv \nu/\Omega h^2]=0.001$, where Ω is the larger value of $|\Omega_T|$ and $|\Omega_B|$. They reported that owing to the presence of the sidewall the physically realizable flows are unique for the parameter range covered. Most significantly, they showed that a stagnation point appears in the meridional flow field at the slower-rotating disk under moderate and strong counter-rotation. It was also found that for strong counter-rotation a sizable portion of interior fluid at small radii does not rotate or has a very small rotation rate. Although the parameter range of [19] is restricted, [19] provides definitive information vital to a proper understanding of the steady flow between two counter-rotating disks.

We propose in this paper to examine the transient flows occurring in spin-up from rest in a cylinder with counter-rotating endwall disks. As was done in [19], the sidewall of the cylinder is fixed to the bottom disk, i.e., $\Omega_S=\Omega_B$. The purpose of this study is to gain knowledge on the transient process whereby the steady flow between counter-rotating disks is built up from the initial state of rest. In much the same way as in [12–14], we acquired comprehensive flow data by numerically integrating the unsteady Navier-Stokes equations. The main thrust of this paper is to present the details of (1) transient azimuthal flow structures, and (2) the patterns of the meridional circulation, especially the transient behavior of the stagnation point [19]. This paper reports only the representative and physically illuminating results of the flow computations.

2 Formulation

The governing equations are the unsteady, axisymmetric, incompressible Navier-Stokes equations. Written in cylindrical coordinates (r, θ, z) with respective velocity components (u, v, w), those equations are standard and will not be repeated here (see, e.g., equation (1) of reference [13]).

The initial conditions for the fluid are

$$u=v=w=0 \text{ at } t=0, \tag{1}$$

and the boundary conditions are

$$u=w=0,\ v=r\Omega_T \text{ at } z=h, \tag{2}$$

$$u=w=0,\ v=r\Omega_B \text{ at } z=0, \tag{3}$$

$$u=w=0,\ v=a\Omega_B \text{ at } r=a. \tag{4}$$

To satisfy numerical stability requirements, the boundary conditions at the central axis are applied at a small, but finite radius $r=r_i$. Thus, we have [20]

$$u=v=0,\ \partial w/\partial r=0 \text{ at } r=r_i. \tag{5}$$

We employed the finite-difference techniques to solve this system of equations. The details of the numerical model adopted, including the finite-differencing schemes, were given in [20]. The reader is referred to [14] and [20] for a description of the actual implementation of the numerical model for the spin-up problems.

3 Results and Discussion

Computations were performed for the following five sets of experimental parameters (rotation rates in rad/s):

C1, $E=4.34\times10^{-4}$, $\Omega_T=0.211$, $\Omega_B=0.211$, $S=1.0$;
C2, $E=4.34\times10^{-4}$, $\Omega_T=0.0$, $\Omega_B=0.211$, $S=0.0$;
C3, $E=4.34\times10^{-4}$, $\Omega_T=-0.063$, $\Omega_B=0.211$, $S=-0.3$;
C4, $E=4.34\times10^{-4}$, $\Omega_T=-0.175$, $\Omega_B=0.211$, $S=-0.83$;
C5, $E=1.00\times10^{-3}$, $\Omega_T=-0.082$, $\Omega_B=0.099$, $S=-0.83$.

The dimension of the cylinder used was $a=10.14$ cm, $h=10.05$ cm. The fluid was water with $\nu=9.3\times10^{-3}$ cm^2/s except for case C5 for which $\nu=1.0\times10^{-2}$ cm^2/s. These values were chosen from the laboratory experiments of Hyun et al. [10] for the spin-up in a rigid cylinder. Note that the cylinder aspect ratio h/a is about unity.

The results of the computations are given in Figs. 1–7. Since $|\Omega_B|>|\Omega_T|$ in the present calculations, the value of Ω in the figures is the same as Ω_B. The nondimensional quantities are defined as $R=r/a$, $Z=z/h$, $T=E^{1/2}\Omega t$.

(*a*) **Azimuthal Flows.** Figure 1 displays the temporal variation of the azimuthal flows, plotted as scaled non-

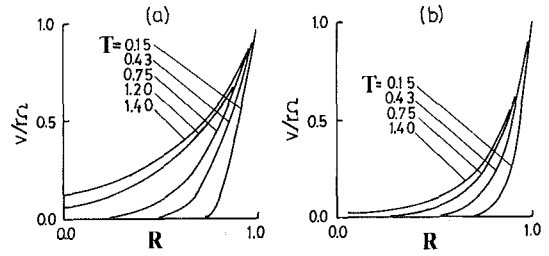

Fig. 3 Radial profiles of $v/r\Omega$ along $Z = 0.5$. (*a*) for case C2, and (*b*) for case C4. In Fig. (*b*), the curves for $T = 1.20$ and for $T = 1.40$ overlap.

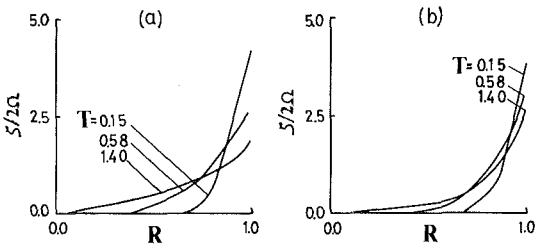

Fig. 4 Radial profiles of the axial vorticity ζ along $Z = 0.5$. (*a*) for case C2, and (*b*) for case C4.

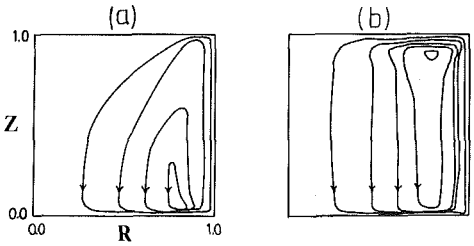

Fig. 5 Plots of the meridional stream function ψ for case C2. (*a*) at $T = 0.30$. $\psi_{max} = 0.97$, $\psi_{min} = 0.0$, $\Delta\psi = 0.2$; (*b*) at $T = 1.40$. $\psi_{max} = 0.78$, $\psi_{min} = 0.0$, $\Delta\psi = 0.15$. Values of ψ are normalized by $\frac{1}{2}\, E^{1/2}\, \Omega a^2 h$. $\Delta\psi$ denotes the contour increment.

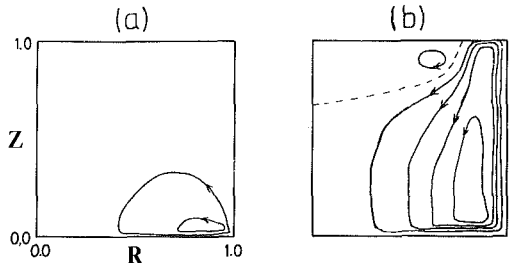

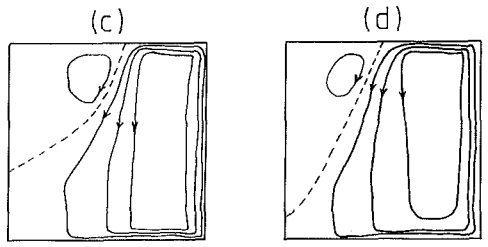

Fig. 6 Plots of ψ for case C3. (*a*) at $T = 0.014$. $\psi_{max} = 0.44$, $\psi_{min} = -0.06$, $\Delta\psi = 0.2$; (*b*) at $T = 0.30$. $\psi_{max} = 1.00$, $\psi_{min} = -0.29$, $\Delta\psi = 0.2$; (*c*) at $T = 0.82$. $\psi_{max} = 0.85$, $\psi_{min} = -0.18$, $\Delta\psi = 0.2$; (*d*) at $T = 1.40$. $\psi_{max} = 0.84$, $\psi_{min} = -0.13$, $\Delta\psi = 0.2$. Broken lines denote $\psi = 0.0$.

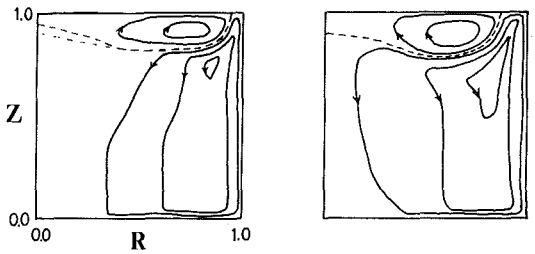

Fig. 7 Plots of ψ for case C4. (*a*) at $T = 0.30$. $\psi_{max} = 1.05$, $\psi_{min} = -0.86$, $\Delta\psi = 0.4$; (*b*) at $T = 1.40$. $\psi_{max} = 1.20$, $\psi_{min} = -0.83$, $\Delta\psi = 0.4$.

dimensional angular velocity $v/r\Omega$ versus scaled time T, at two radial locations along middepth $Z = 0.5$. Figure 1(*a*) shows the results for the case when the top disk is stationary ($S = 0.0$), and Fig. 1(*b*) for the case of counter-rotating disks ($S = -0.83$). Plots depicting the spin-up in a rigid cylinder ($S = 1.0$) were presented previously (see, e.g., Fig. 1 of [10], Fig. 1 of [14]). Figures 1(*a*) and 1(*b*) clearly demonstrate the presence of the front. Ahead of the front, the fluid remains nonrotating, and only after the passage of the front the fluid begins to rotate.

Note that Fig. 1(*a*) for S = 0.0, and the solid curves in Fig. 1(*b*) for $S = -0.83$, and Fig. 1 of [14] for $S = 1.0$ all have the same value for the Ekman number. Comparisons of these figures reveal that the scaled angular velocity at a given location and at a given time decreases as S decreases from unity. For instance, at $R = 0.5$, $Z = 0.5$, and at $T = 0.93$, the value of $v/r\Omega$ is approximately 0.63 for $S = 1.0$, 0.20 for $S = 0.0$, and 0.10 for $S = -0.83$, respectively.

Figure 1(*b*) shows that the angular velocity at a given point increases as the Ekman number increases. This is attributed to the increased influence of viscous diffusion effects as E increases. A similar finding regarding the effect of E was obtained for the case of a rigid cylinder ([10], [11], [14]).

The vertical structures of the transient azimuthal flows are illustrated in Fig. 2. It is important to recognize that for all values of S, the azimuthal flows are, to a high degree of accuracy, uniform in the vertical direction in the bulk of the interior. The structure of the bottom boundary layer remains substantially unchanged as S decreases from zero.

Figure 2(*a*) for $S = 0.0$ demonstrates that at the radial location $R = 0.50$, the value of $v/r\Omega$ in the interior at large times (see the curve for $T = 1.40$) approaching the steady state is approximately 0.33. We note that the theoretical similarity solution for steady flows between two infinite disks for $S = 0.0$ in the limit $E \to 0$ yields $v/r\Omega = 0.313$ in the interior core region ([17], [19]); the present calculations at large times are in qualitative agreement with the similarity solutions. We expect that, due to the presence of the rotating sidewall, the angular velocity of the fluid confined in a finite cylinder tends to be larger than the prediction of the similarity solutions for infinite disks; obviously, the similarity solutions become less accurate at large radii (see the plots for $R = 0.75$ in Fig. 2(*a*)).

Figures 2(*b*) and 2(*c*) show the angular velocity profiles for strong counter-rotation of the disks ($S = -0.83$). It is important to observe that the azimuthal flows are still vertically uniform in the main body of the interior. This is in contrast to the steady flow profiles depicted in [19]. Figure 12 of [19] shows that under strong counter-rotation ($S = -0.825$) the steady-state azimuthal velocity varies continuously with height from the bottom to the top disk. We note two factors for this apparent discrepancy. Figure 12 of [19] used $E = 0.01$, which is an order of magnitude larger than the value of E used in the present computations. Therefore, for the flows in Fig. 12 of [19], the influence of viscous diffusion from the disks would penetrate to a larger distance into the main body of fluid. In addition, we recall that the aspect ratio in [19] is very small ($\delta = 0.07$), whereas $\delta \sim 1$ for the present computations. Because of the above two reasons, the viscous diffusive effects

permeate over much of the flow field considered in [19], producing an azimuthal velocity profile which varies continuously with height. On the other hand, for the present computations, a substantial portion of the flow field outside the disk boundary layers is essentially inviscid; therefore, the azimuthal velocity is vertically uniform in that inviscid region, as is demonstrated in Fig. 2(*b*) and Fig. 2(*c*).

Inspection of Fig. 2(*a*) and Fig. 2(*b*) indicates that, as S decreases from zero, the region near the top disk in which the azimuthal velocity varies with height widens, and the angular velocities in the bulk of interior decrease. Furthermore, the scaled time to reach the steady state decreases under strong counter-rotation.

Comparisons of Fig. 2(*b*) and Fig. 2(*c*) reveal the effect of the Ekman number. As the Ekman number increases, the overall spin-up process is facilitated due to the increased influence of viscous diffusion. It is also to be noted that, as E increases, the influence of the top disk penetrates deeper into the fluid and, consequently, the region in which the fluid rotates in the same direction as the top disk widens.

Figure 3 displays the radial profiles of the transient angular velocities along middepth $Z=0.5$. The radially propagating velocity front is clearly discernible in Fig. 3. It is shown that the front takes $T\sim 1$ to reach the central axis. Figure 3(*a*) for $S=0.0$ indicates that at $T=1.40$, which is the largest time for which the present computations were made, the azimuthal flows are still evolving slowly with time. Under counter-rotation (see Fig. 3(*b*) for $S=-0.83$), the steady state is achieved over a shorter perioed of time than for $S=0.0$. As was stated earlier, the angular velocities are very small in the core region away from the sidewall during the entire spin-up process under strong counter-rotation.

The radial gradients of the azimuthal flows are described by the axial vorticity, $\zeta=(1/r)[(\partial/\partial r)(rv)]$, as shown in Fig. 4. The vorticity is zero ahead of the front, and behind the front ζ varies continuously from zero to the maximum value at the sidewall. The values of nonzero ζ are large at early times. This points to the existence of large flow gradients caused by vigorous spin-up flows concentrated behind the front [21]. As time progresses, the spin-up flows are less concentrated and the vorticity behind the front weakens accordingly. As was seen in Fig. 3(*b*), under strong counter-rotation, the angular velocity varies radially from very small values in the central core region to unity at the sidewall. Therefore, the intensification of the radial flow gradients, which are represented by the ζ-distribution, is more pronounced in the region near the sidewall, as S decreases from zero. Figure 4(*b*) for $S=-0.83$ exemplifies this argument.

(*b*) Meridional Flows. In order to illustrate the meridional flows, we introduce the meridional stream function ψ, which is defined as $u=(1/r)(\partial\psi/\partial z)$, $w=-(1/r)(\partial\psi/\partial r)$. In the ensuring figures, positive values of ψ imply counter-clockwise circulation.

Figure 5 shows the ψ-plots for $S=0.0$. Since the top disk is stationary, the bottom disk dominates the flow field. The general patterns of the meridional circulation can be depicted as follows. The fluid is sucked into the bottom boundary layer over much of the length of the bottom disk. The return circuit is in the sidwall boundary layer, whose thickness is scaled by $0(E^{1/4}h)$. The top boundary layer expells the fluid into the interior region, thus completing the circulation. Only counter-clockwise circulation appears in the meridional plane, a flow pattern referred to as the one-cell structure [19]. At early times (see Fig. 5(*a*) for $T=0.30$), the meridional flows are vigorous and, consequently, the spin-up proceeds at a fast rate. The meridional circulation is concentrated in the region near the bottom disk and near the sidewall. This meridional circulation has not fully affected the region near the top disk and near the central axis. At large times (see Fig. 5(*b*) for $T=1.40$), the flows have approached the steady state. In the interior, there is an almost uniform vertical flows sustained by the Ekman suction (blowing) at the faster (slower) rotating disk.

As S decreases below zero, several qualitatively distinctive features are seen. Figure 6 shows the ψ-plots for moderate counter-rotation ($S=-0.3$). Since $|\Omega_B|>|\Omega_T|$, the interior flows are controlled by the bottom disk. At very early times (see Fig. 6(*a*) for $T=0.014$), the counter-clockwise circulation begins to form near the lower right corner in the meridional plane. At early times (see Fig. 6(*b*) for $T=0.30$), the counter-clockwise circulation has grown and reaches up to the top disk. We note that a weak clockwise ciculation has appeared near the top because of the rotation rate of the top disk. Thus, the meridional flows form a two-cell structure. A stagnation line, along which $\psi=0$, separates the two cells. The point where the stagnation line meets the top disk was termed the stagnation point [19]. At intermediate times (see Fig. 6(*c*) for $T=0.82$), the stagnation point has moved toward the central axis. At large times approaching the steady state (see Fig. 6(*d*) for $T=1.40$), the stagnation point has advanced further toward the central axis (approximately at $R=0.5$).

Under strong counter-rotation, the qualitative patterns of the meridional flows are similar to those for Fig. 6. Figure 7 shows the ψ-plots for $S=-0.83$. Although $|\Omega_B|$ is only slightly larger than $|\Omega_T|$, the meridional flows in the bulk of the interior are dominated by the faster-rotating disk. The clockwise circulation near the top disk occupies a small region, but it is stronger than for moderate counter-rotation (compare the magnitudes of $\psi_{\max}$ and $\psi_{\min}$ of Fig. 6 and Fig. 7). The presence of the stagnation line is apparent in Fig. 7. However, under strong counter-rotation, the stagnation point travels a smaller radial distance from the sidewall during the spin-up process than under moderate counter-rotation.

In summary, Figs. 6 and 7 demonstrate that counter-rotation of the disks creates the stagnation point on the slower-rotating disk. During the spin-up process, the stagnation point moves radially inward from the sidewall to the steady-state position. As the strength of counter-rotation increases, the steady-state stagnation point is located further away from the central axis. This behavior of the steady-state stagnation with increasing counter-rotation was pointed out by [19], who made numerical computations and experimental measurements of the steady flows.

4 Conclusion

The transient azimuthal flows are vertically uniform in the bulk of the interior even under strong counter-rotation of the disks. This is due to the very small values of the Ekman numbers used and the cylinder aspect ratio $\delta\sim 1$. Similarly to the case of a rigid cylinder, the azimuthal velocity front propagates radially inward from the sidewall. The time scale characterizing the overall spin-up adjustment is $E^{-1/2}\Omega^{-1}$. As S decreases below zero, the following features are noted: the angular velocities in the interior region away from the sidewall become very small; the region near the slower-rotating disk in which the azimuthal flows vary rapidly with height widens; and the scaled time to reach the steady state decreases. The spin-up process tends to be facilitated as E increases. The axial vorticity behind the front increases under counter-rotation, pointing to large radial flow gradients.

When $S=0.0$, the meridional flows form a one-cell structure. Under counter-rotation, the meridional flows show a two-cell structure; the stagnation line, $\psi=0$, separates the two cells. As spin-up proceeds, the stagnation point on the slower-rotating disk moves radially inward from the sidewall to the steady-state position. As counter-rotation increases, the radial distance traveled by the stagnation point during spin-up decreases.

References

1 Greenspan, H. P., *The Theory of Rotating Fluids*, Cambridge University Press, Cambridge, England, 1968, p. 327.

2 Benton, E. R. and Clark, A., "Spin-Up," *Annual Review of Fluid Mechanics*, Vol. 6, 1974, pp. 257–280.

3 Goller, H., and Ranov, T., "Unsteady Rotating Flow in a Cylinder with a Free Surface," ASME *Journal of Basic Engineering*, Vol. 90, 1968, pp. 445–454.

4 Kitchens, C. W. Jr., "Navier-Stokes Solutions for Spin-up in a Filled Cylinder," *AIAA Journal*, Vol. 18, Aug. 1980, pp. 929–934.

5 Kitchens, C. W. Jr., Gerber, N., and Sedney, R., "Spin Decay of Liquid-Filled Projectiles," *Journal of Spacecraft and Rockets*, Vol. 15, Nov.–Dec. 1978, pp. 348–354.

6 Wedemeyer, E. H., "The Unsteady Flow within a Spinning Cylinder," *Journal of Fluids Mechanics*, Vol. 20, 1964, pp. 383–399.

7 Greenspan, H. P., and Howard, L. N., "On a Time-Dependent Motion of a Rotating Fluid," *Journal of Fluid Mechanics*, Vol. 17, 1963, pp. 385–404.

8 Venezian, G., "Spin-up of a Contained Fluid," *Topics in Ocean Engineering*, Vol. 1, 1969, pp. 212–223.

9 Weidman, P. D., "On the Spin-up and Spin-down of a Rotating Fluid, Pt. 1, Extending the Wedemeyer Model," *Journal of Fluid Mechanics*, Vol. 77, 1976, pp. 685–708.

10 Hyun, J. M., Leslie, F., Fowlis, W. W., and Warn-Varnas, A., "Numerical Solutions for Spin-up from Rest in a Cylinder," *Journal of Fluid Mechanics*, Vol. 127, 1983, pp. 263–281.

11 Watkins, W. B. and Hussey, R. B., "Spin-up from Rest in a Cylinder," *The Physics of Fluids*, Vol. 20, 1977, pp. 1596–1604.

12 Pao, H.-P., "A Numerical Computation of a Confined Rotating Flow," ASME *Journal of Applied Mechanics*, Vol. 37, 1970, pp. 480–487.

13 Bertela, M. and Gori, F., "Laminar Flow in a Cylinder Container with a Rotating Cover," ASME JOURNAL OF FLUIDS ENGINEERING, Vol. 104, 1982, pp. 31–39.

14 Hyun, J. M., "Spin-up from Rest in a Differentially Rotating Cylinder," *AIAA Journal*, Vol. 21, 1983, pp. 1278–1282.

15 Pearson, C. E., "A Computational Method for Viscous Flow Problems," *Journal of Fluid Mechanics*, Vol. 21, 1965, pp. 611–622.

16 Venezian, G., "Nonlinear Spin-up," *Topics in Ocean Engineering*, Vol. 2, 1970, pp. 87–96.

17 Batchelor, G. K., "Note on a Class of Solutions of the Navier-Stokes Equations Representing Steady Rotationally-Symmetric Flow," *Quarterly Journal of Mechanics and Applied Mathematics*, Vol. 4, 1951, pp. 29–41.

18 Stewartson, K., "On the Flow between Two Rotating Coaxial Disks," *Proceedings of Cambridge Philosophical Society*, Vol. 49, 1953, pp. 331–341.

19 Dijkstra, D. and Van Heijst, G. J. F., "The Flow between Two Finite Rotating Disks Enclosed by a Cylinder," *Journal of Fluid Mechanics*, Vol. 128, 1983, pp. 123–154.

20 Warn-Varnas, A., Fowlis, W. W., Piacsek, S., and Lee, S. M., "Numerical Solutions and Laser Doppler Measurements of Spin-up," *Journal of Fluid Mechanics*, Vol. 85, 1978, pp. 609–639.

21 Benton, E. R., "Vorticity Dynamics in Spin-up from Rest," *The Physics of Fluids*, Vol. 22, 1979, pp. 1250–1251.

M. A. I. El-Shaarawi
Associate Professor.

M. F. El-Refaie
Professor.

S. A. El-Bedeawi
Assistant Lecturer.

Department of Mechanical Engineering,
Alazhar University,
Nasr City, Cairo, Egypt

Numerical Solution of Laminar Boundary Layer Flow About a Rotating Sphere in an Axial Stream

A finite-difference scheme is developed for solving the boundary layer equations governing the laminar flow about a rotating sphere which is subjected to a uniform stream in the direction of the axis of rotation. Numerical results are presented for the meridional and azimuthal velocities and for the wall-shear-stress components. Also, the angle at which the meridional velocity gradient normal to the wall vanishes is given at values of the parameter Ta/Re^2 ranged from zero (the stationary sphere case) to 10000. As compared with the momentum integral technique of Schlichting [8], the present scheme succeeded in obtaining solutions for very considerably larger values of the parameter Ta/Re^2.

Introduction

The flow on a body of revolution spinning about its axis, which is parallel to a stream, is of importance in many engineering applications. Examples of such applications are the ballistics of projectiles with spin and the flow on the hub of an axial turbomachine. The present paper deals with a special case of this problem; namely, the flow around a sphere rotating about its axis and simultaneously subjected to a stream in the direction of the axis of rotation.

The limiting case which is a fixed sphere in a stream of air has been theoretically investigated by Tomotika [1], Tomotika and Imai [2], Frössling [3], Scholkemeier [4], Rott and Crabtree [5], Smith and Clutter [6], Sheridan [7], and Schlichting [8]. In all these investigations [1-8] the boundary layer simplifications were considered but, however, several methods were utilized for obtaining the solutions. Momentum integral techniques were used by [1, 2, 5 and 8], series solutions were considered by [3 and 4], and combined finite-difference-integral methods were utilized by [6 and 7].

On the other hand, limited publications are available for the case of a rotating sphere in an axial stream. Luthander and Rydberg [9] considered the air drag on a rotating sphere which is subjected to a flow in the direction of the axis of rotation. Their results showed a considerable increase in the drag with the ratio of the circumferential velocity to the free-stream velocity (V_m/U_∞). Burgers [10] gave a few general formulations for the same case. Similar results were obtained by Schlichting [8] who investigated the laminar flow about a rotating body of revolution in an axial air-stream by using a momentum integral technique. Also, Parr [16] investigated the boundary layer flow on a spinning body of revolution. For the special case of a rotating sphere in an air-stream, Schlichting [8] obtained the separation point, the drag, and the resisting moment for some values of the spin parameter V_m/U_∞. The effect of rotary motion on the position of the line of laminar separation on a sphere has also been computed by Hoskin [11]. Both Schlichting [8] and Hoskin [11] found that the separation point of the laminar boundary layer is advanced at the rear hemisphere by the effect of rotational motion.

In order to augment the information available on the methods of solving the boundary layer equations governing the case under consideration, a finite-difference scheme has been developed and numerical results of this scheme are presented here. Also, additional data to those available in the literature concerning the flow details are given.

Governing Equations and Boundary Conditions

We consider the steady laminar flow of an incompressible Newtonian fluid with constant physical properties in the region outside a sphere which is rotating with constant angular velocity about a diameter parallel to the flow direction. The flow is assumed to be rotationally symmetric about the axis of rotation. Let x, y, z be a rectangular curvilinear fixed coordinate system as shown in Fig. 1. The x-axis is measured along a meridional section, the y-axis is along a circular cross section of the sphere by a plane perpendicular to the axis of rotation, and the z-axis is at right angles to the tangential xy-plane.

Under the above mentioned assumptions and in the absence of of body forces, the boundary layer equations for the problem at hand, as given by Schlichting [8], are:

Continuity equation:

$$\frac{\partial u}{\partial x} + \frac{u}{r}\frac{dr}{dx} + \frac{\partial w}{\partial z} + \frac{2w}{z+a} = 0 \qquad (1)$$

Contributed by the Fluids Engineering Division for publication in the JOURNAL OF FLUIDS ENGINEERING. Manuscript received by the Fluids Engineering Division, March 13, 1984.

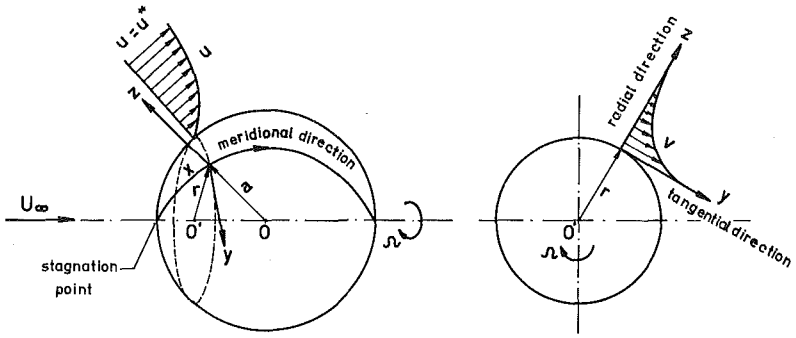

Fig. 1 Coordinate system

x-momentum equation:

$$u\frac{\partial u}{\partial x}-\frac{v^2}{r}\frac{dr}{dx}+w\frac{\partial u}{\partial z}=U_0^*\frac{du^*_0}{dx}+\nu\frac{\partial^2 u}{\partial z^2} \tag{2}$$

y-momentum equation:

$$u\frac{\partial v}{\partial x}+\frac{uv}{r}\frac{dr}{dx}+w\frac{\partial v}{\partial z}=\nu\frac{\partial^2 v}{\partial z^2} \tag{3}$$

Equations (1) through (3) are subject to the following boundary conditions:

$$\left.\begin{array}{l}\text{at } z=0 \text{ (sphere surface) and } x>0,\\ \quad u=w=0 \text{ and } v=v_0,\\ \text{at } z=0 \text{ and } x=0\ u=v=w=0\\ \quad \text{(stagnation point)},\\ \text{at } z\geq\delta \text{ and } x>0,\ u=u^*,\ v=0,\\ \quad \text{and}\\ \text{at } x=0,\ z>0\ w=w^* \text{ and } v=u=0.\end{array}\right\} \tag{4}$$

It is noteworthy that the foregoing boundary conditions take into consideration that far away from the surface of the sphere (i.e., $z\geq\delta$) the flow is of a two dimensional potential type. The two velocity components for such a two dimensional potential flow are [12]:

$$u^*=U_\infty\left[1+\frac{a^3}{2(a+z)^3}\right]\sin\theta,$$

$$w^*=-U_\infty\left[1+\frac{a^3}{(a+z)^3}\right]\cos\theta,$$

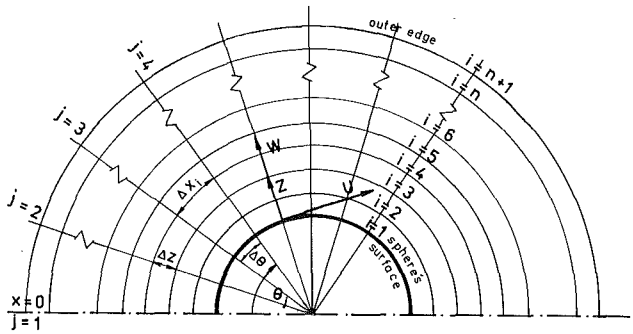

Fig. 2 Numerical grid

and hence $u_0^*=\frac{3}{2}U_\infty\sin\theta$.

Introducing the dimensionless parameters given in the nomenclature, equations (1-3) and the boundary conditions (4) become:

$$\frac{\partial U}{\partial X}+\frac{U}{R}\frac{dR}{dX}+\frac{\mathrm{Re}}{2}\frac{\partial W}{\partial Z}+\mathrm{Re}\frac{W}{1+Z}=0 \tag{5}$$

$$U\frac{\partial U}{\partial X}-\left(\frac{\mathrm{Ta}}{\mathrm{Re}^2}\right)\frac{V^2}{R}\frac{dR}{dX}+\frac{\mathrm{Re}}{2}W\frac{\partial U}{\partial Z}=U_0^*\frac{dU_0^*}{dX}+\frac{\partial^2 U}{\partial Z^2} \tag{6}$$

$$U\frac{\partial V}{\partial X}+\frac{UV}{R}\frac{dR}{dX}+\frac{\mathrm{Re}}{2}W\frac{\partial V}{\partial Z}=\frac{\partial^2 V}{\partial Z^2} \tag{7}$$

Nomenclature

a = sphere radius
C_M = dimensionless torque coefficient, $2M/\rho\Omega^2 a^5$
C_D = dimensionless drag coefficient, $2D/\pi\rho U_\infty^2 a^2$
D = frictional drag
m = number of steps of the numerical mesh network in the X-direction
M = torque
n = number of steps of the numerical mesh network in the Z-direction
r = radius of a circular cross section of the sphere by a plane perpendicular to the main stream direction
R = dimensionless radius of a circular cross section of a sphere by a plane perpendicular to the main stream direction, $\frac{2r}{a\mathrm{Re}}$
Re = Reynolds number, $2U_\infty a/\nu$
t_x = wall shear stress in meridional direction, $\mu\frac{\partial u}{\partial z}\Big|_0$
t_y = wall shear stress in azimuthal direction, $\mu\frac{\partial v}{\partial z}\Big|_0$
T_x = dimensionless wall shear stress in meridional direction, $\frac{t_x\sqrt{\mathrm{Re}/2}}{\rho U_\infty^2}$
T_y = dimensionless wall shear stress in azimuthal direction, $\frac{t_y\sqrt{\mathrm{Re}/2}}{U_\infty^2}$
Ta = Taylor number, $\frac{4\Omega^2 a^4}{\nu^2}$
u = meridional (x-direction) component of velocity
U = dimensionless meridional component of velocity, u/U_∞

$$\left.\begin{aligned}
&\text{at } Z=0 \text{ and } X>0,\ U=W=0\\
&\quad \text{and } V=\frac{\mathrm{Re}}{2}R,\\
&\text{at } Z=0 \text{ and } X=0,\ U=V=W=0,\\
&\text{at } Z\geq\delta^* \text{ and } X>0,\ U=U^*\\
&\quad =\left[1+\frac{1}{2(1+Z)^3}\right]\sin\theta,\ V=0, \text{ and}\\
&\text{at } X=0 \text{ (i.e., } \theta=0) \text{ and } Z>0,\ W=W^*\\
&\quad =-\left[1-\frac{1}{(1+Z)^3}\right] \text{ and } V=U=0
\end{aligned}\right\} \quad (8)$$

The parameter $\mathrm{Ta}/\mathrm{Re}^2$, which appears in equation (6), has a physically significant meaning in that it represents the ratio between the centrifugal and inertia forces.

Finite-Difference Representation of the Governing Equations and Method of Solution

The numerical analysis and the method of solution which will be used here can be considered as an indirect extension of the original work of Rouleau and Osterle [13] to include the case of rotating boundaries, and the work of El-Shaarawi and Sarhan [14] to include the case of unconfined flows.

Figure 2 shows the numerical grid where the independent variables are computed at the intersections of the grid lines and (i, j) is a typical mesh point. Mesh points are numbered consecutively with the i progressing in the radial direction with $i = 1, 2, 3, \ldots, n+1$ from the sphere surface, and the j progressing in the meridional direction with $j = 1, 2, 3, \ldots, m+1$ from the stagnation point. At each meridional station j, the number of radial increments n should be chosen so that the uppermost point $(i=n+1)$ lies in essentially undisturbed fluid.

Replacing the derivatives by the appropriate finite-difference representations [13-14], equations (5-7) and the boundary conditions (8) can be written in the following forms:

$$\frac{U_{i+1,j+1}+U_{i,j+1}-U_{i+1,j}-U_{i,j}}{2\Delta X_{i+\frac{1}{2}}}+\frac{(U_{i+1,j+1}+U_{i,j+1})\mathrm{Re}}{4[1+Z_{i+\frac{1}{2}}]}\cot(j\cdot\Delta\theta)$$

$$+\frac{\mathrm{Re}}{2}\frac{W_{i+1,j+1}-W_{i,j+1}}{\Delta Z}+\frac{\mathrm{Re}(W_{i+1,j+1}+W_{i,j+1})}{2[1+z_{i+\frac{1}{2}}]}=0 \quad (9)$$

$$U_{i,j}\frac{U_{i,j+1}-U_{i,j}}{\Delta X_i}-\left(\frac{\mathrm{Ta}}{\mathrm{Re}}\right)\frac{V_{i,j}V_{i,j+1}}{2[1+(i-1)\Delta Z]}\cdot\cot(j\cdot\Delta\theta)+W_{i,j}\frac{\mathrm{Re}}{2}$$

$$\frac{U_{i+1,j+1}-U_{i-1,j+1}}{2\Delta Z}=\frac{3}{2}\sin(j\cdot\Delta\theta)\cdot\tfrac{3}{4}\mathrm{Re}\cos(j\cdot\Delta\theta)+\frac{U_{i+1,j+1}-2U_{i,j+1}+U_{i-1,j+1}}{(\Delta Z)^2}, \quad (10)$$

$$U_{i,j}\frac{V_{i,j+1}-V_{i,j}}{\Delta X_i}+\frac{\mathrm{Re}}{4}U_{i,j}\frac{V_{i,j+1}+V_{i,j}}{1+(i-1)\Delta Z}\cot(j-\tfrac{1}{2})\Delta\theta+W_{i,j}\frac{V_{i+1,j+1}+V_{i+1,j}-V_{i-1,j}-V_{i-1,j+1}}{4\Delta Z}\frac{\mathrm{Re}}{2}$$

$$=\frac{V_{i+1,j+1}+V_{i+1,j}-2V_{i,j+1}-2V_{i,j}+V_{i-1,j+1}+V_{i-1,j}}{2(\Delta Z)^2} \quad (11)$$

$$\left.\begin{aligned}
&\text{at } Z=0 \text{ i.e., } i=1 \text{ and } X>0 \text{ i.e., } j>1,\\
&\quad U_{1,j}=W_{1,j}=0,\ V_{1,j}=\sin[(j-1)\Delta\theta]\\
&\text{at } Z=0 \text{ i.e., } i=1 \text{ and } x=0 \text{ i.e., } j=1,\\
&\quad U_{1,1}=V_{1,1}=W_{1,1}=0,\\
&\text{at } Z\geq\delta^* \text{ and } X>0 \text{ i.e., } i=n+1 \text{ and } J>1,\\
&\quad U_{n+1,j}=\left[1+\frac{1}{2(1+n\Delta Z)^3}\right]\sin[(j-1)\Delta\theta],\\
&\quad V_{n+1,j}=0,\\
&\text{at } X=0 \text{ and } Z>0 \text{ i.e., } j=1 \text{ and } i>1,\\
&\quad W_{i,1}=\frac{1}{(1+(i-1)\Delta Z)^3}-1,\\
&\quad \text{and } V_{i,1}=U_{i,1}=0
\end{aligned}\right\} \quad (12)$$

It should be noted that the variables with subscript $j+1$, in the finite-difference equations (9)-(11) represent the unknowns and those with subscript j are knowns. Also, applying the numerical stability theories summarized in [17] shows that finite-difference equations (9-11) are consistent

Nomenclature (cont.)

u^* = potential velocity component in the x-direction
U^* = dimensionless potential velocity component in the x-direction, u^*/U_∞
U_∞ = free stream velocity
v = azimuthal (y-direction) component of velocity at any point
V = dimensionless azimuthal velocity component at any point, $v/\Omega a$
v_0 = circumferential velocity at a point on the sphere surface, Ωr
V_0 = dimensionless azimuthal velocity component at a point on the sphere surface, r/a
v_m = maximum circumferential velocity, Ωa
w = radial (Z-direction) velocity component
W = dimensionless radial velocity component, w/U_∞
w^* = radial velocity component for potential flow
W^* = dimensionless radial (z-direction) velocity component for potential flow, w^*/U_∞
x = distance along the circular generator of the sphere's surface measured from the stagnation point
X = dimensionless meridional distance along the surface measured from the stagnation point, $2x/\mathrm{Re}a$
y = distance measured along a circular cross section of the sphere by a plane perpendicular to the axis of rotation
z = distance from the surface measured along the normal to the wall in the radial direction
Z = dimensionless distance perpendicular to the wall in the radial direction, z/a
θ = center angle measured from the axis of rotation
Ω = angular velocity of the sphere
μ = dynamic viscosity of fluid
ν = kinematic viscosity of fluid
δ = meridional boundary layer thickness
δ^* = dimensionless meridional boundary layer thickness, δ/a

Subscripts

0 = on the sphere surface
s = at separation point

with the boundary layer equations (5–7) and are stable as long as U is non-negative.

The foregoing finite-difference equations are linearized by assuming that, where the product of two unknowns (with subscript $j+1$) occurs, one of them is given approximately by its value at the previous meridional step (with subscript j). This is done so as to enable the equations to be numerically solved in the following manner.

The numerical solution of these equations is obtained by first selecting values of Re and Ta/Re^2. Then starting with $j=1$ (stagnation line) and applying equation (11) for $i = 2, 3, \ldots, n$, we get $(n-1)$ simultaneous linear equations in $(n-1)$ unknowns at the second meridional station ($V_{2,2}, V_{3,2}, \ldots, V_{n,2}$). Solving these simultaneous linear algebraic equations by any kind of matrix inversion techniques (Thomas' method [15] was used in our program), we obtain the unknown values of V's at all points of the second meridional station. Similarly, using the computed values of V's and applying (10) with $i = 2, 3, \ldots, n$, we obtain the unknown values of U's at the second meridional station ($j=2$). Using the computed values of U's and applying (9) with $i = 1, 2, 3, \ldots, n$, the values of W's at the grid points of the second meridional station are obtained. Repeating this procedure, we can advance, step by step, along the sphere surface until the separation point (at which $\partial U/\partial Z|_0 = 0$) is reached.

For the selection of n at each meridional station (j) an iterative type method is used. In this method the criterion of solution is the asymptotic matching between the computed meridional velocity distribution U and the corresponding theoretical potential distribution U^* within an arbitrarily

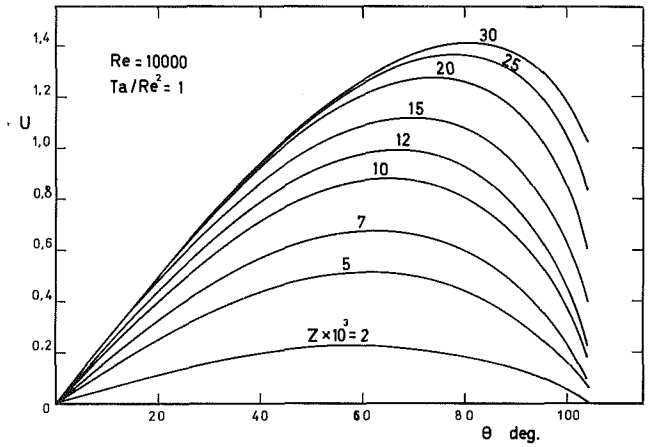

Fig. 3(a) Meridional velocity development for $Ta/Re^2 = 1$

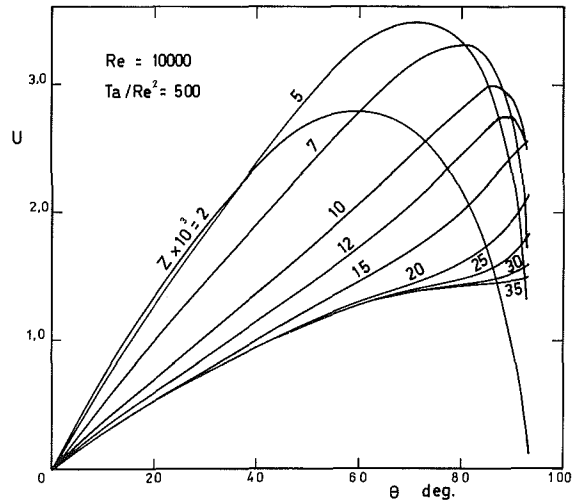

Fig. 3(b) Meridional velocity development for $Ta/Re^2 = 500$

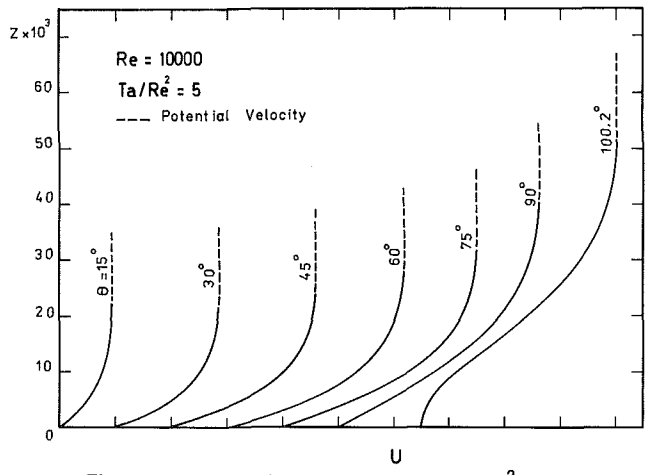

Fig. 3(c) Meridional velocity profiles for $Ta/Re^2 = 5$

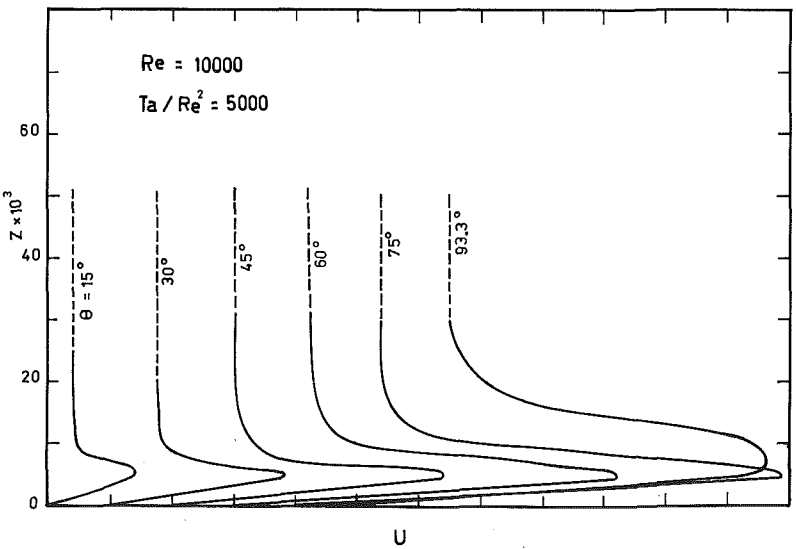

Fig. 3(d) Meridional velocity profiles for $Ta/Re^2 = 5000$

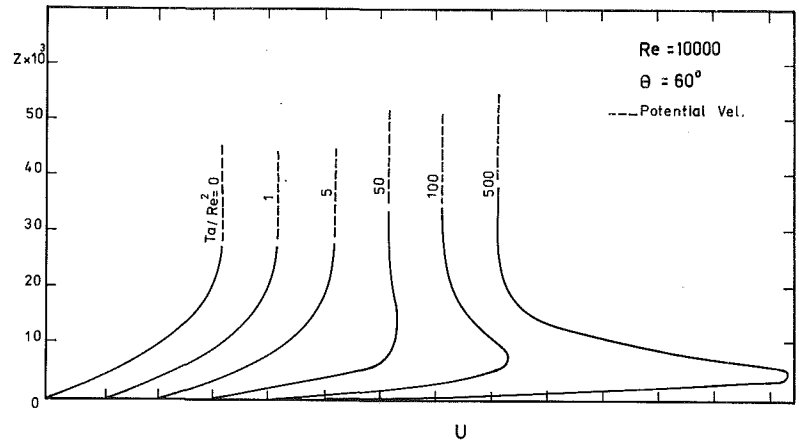

Fig. 4 Effect of the parameter Ta/Re^2 on meridional velocity profiles at $\theta = 60$ deg

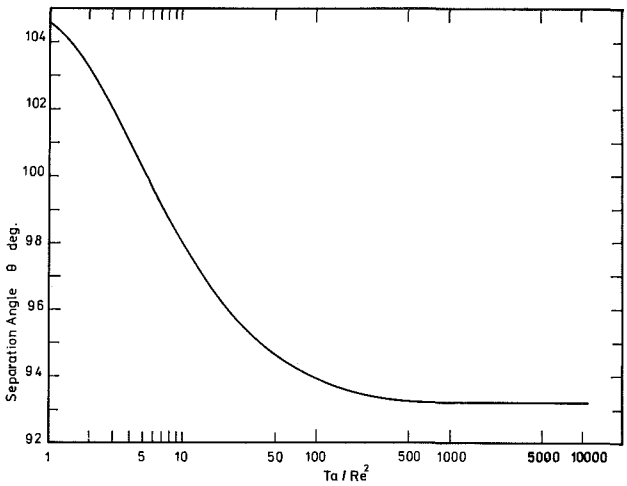

Fig. 5 Separation angle against Ta/Re^2 for Re = 10000

accepted accuracy of at least 0.005. In other words, the value of n should be large enough so that the computed meridional velocity distribution U is close in tangent at the uppermost point $(n+1)$, within the arbitrarily chosen accuracy, to the potential distribution U^*. Thus the value of n depends on the accuracy desired and the selection of n is more or less of a trial process. For a given value of n, once the computations have been carried out for the U's and the asymptotic matching was not attained, the value of n could be increased, the computations again performed and the computed U's accepted if the asymptotic matching criterion is satisfied.

Results and Conclusions

The numerical calculations were carried out for Reynold's number of 10000, and for the spin parameter Ta/Re^2 ranging from zero, the case of a stationary sphere, to 10000. It is known that large gradients exist near the stagnation point and also near the separation point (at which $\partial U/\partial z|_0 = 0$). Therefore, near these two points the step sizes in the meridional and radial directions were chosen to give $\Delta\theta = 0.1$ deg and $\Delta Z \leq 0.0005$, respectively. However, far downstream of the stagnation point and upstream of the separation point the step size in the meridional direction was usually chosen to give $\Delta\theta = 1$ deg, while that in the radial direction (Δz) was 0.001. In all the computer runs the initial value of n (i.e., value of n at $j = 1$) was chosen equal to at least 20 increments. During computation the asymptotic matching criterion was checked at each meridional station (j) and the value of n was increased if necessary until n attains its final maximum value

Table 1 Comparison between the results of Schlichting [8] and those of the present analysis for the dimensionless torque coefficient and the separation angle

Ta/Re^2	C_M		θ_S, degree	
	Present analysis	Schlichting	Present analysis	Schlichting
0	0	–	107.0	108.2
0.0625	0.513	0.517	106.5	108.0
0.2500	0.257	0.256	106.2	107.3
0.5625	0.170	0.170	105.4	106.2
1.000	0.126	0.127	104.5	104.9
1.4884	0.104	0.103	104.0	103.5

at the separation point. For example, this final value of n reached 42, 52, and 64 for $Ta/Re^2 = 10000$, 5, and 0, respectively. Due to space limitation, only a sample of the results will be given here for the purpose of illustration.

Development of the Meridional Velocity Component

Figures 3(*a*)–3(*b*) represent the developing meridional velocity distribution U corresponding to values of the parameter $Ta/Re^2 = 1$ and 500, respectively. In each figure, curves corresponding to some selected values of the dimensionless radial distance from the wall (Z) are drawn. Sufficient values of this radial distance were selected so that accurate reconstruction of velocity profiles, similar to those presented in Figs. 3(*c*)–3(*d*), could, if desired, be carried out by cross plotting. Examples of the developing meridional velocity profiles are presented in Figs. 3(*c*)–3(*d*), each of which corresponds to a specific value of the parameter Ta/Re^2. It is clear from these figures that the radial distance from the sphere's wall (Z) required for attaining the matching between the computed velocity profile and the corresponding potential velocity profile increases with the meridional distance X (i.e., θ). This means that the required number of radial increments n increases with j and implies that the thickness of the meridional boundary layer formed on the wall increases with the meridional distance.

On the other hand, it is clear, from the aforementioned figures, that the parameter Ta/Re^2 has significant effects on the developing meridional velocity profiles. In order to show such effects more clearly, the meridional velocity profiles are redrawn in Fig. 4 at a selected meridional position (i.e., a selected value of θ) for various chosen values of the parameter Ta/Re^2. It is evident that, at a given meridional position, as values of the parameter Ta/Re^2 increase, the effect of the rotating wall on the meridional velocity profile becomes increasingly significant. At high values of Ta/Re^2 the fluid

accelerates within the boundary layer as if there were blowing from the sphere's wall. Such a phenomenon may be attributed to the fact that the higher the value of Ta/Re^2 the greater is the centrifugal force and hence the more is the fluid transported by centrifugal action from regions close to the rotating wall to adjacent regions, thus causing the acceleration of the fluid within the boundary layer.

Finally, it is important to know the effect of the rotary motion on the position of the point of laminar separation at which $\partial U/\partial Z|_0 = 0$ [8]. For the chosen Re = 10000, Fig. 5 gives the position of the separation point (θ_s) as a function of the spin parameter Ta/Re^2. From this figure it can be seen that, over the investigated range of $0 \leq Ta/Re^2 \leq 10000$ the separation point always lies behind the equatorial plane ($\theta >$ 90 deg) and shifts forward as the value of the parameter Ta/Re^2 increases. This conclusion agrees with the conclusion of Schlichting [8] that the displacement of the separation point is due to the effect of centrifugal forces which, behind the equatorial plane, have the effect of an additional pressure increase in flow direction and therefore cause the separation point to shift forward. In Table 1, the only tabulated results in [8] for θ_s are compared with the corresponding results of the present analysis at same values of Ta/Re^2. It is clear from this table that θ_s values of the present analysis agree, within less than 1.5 percent, with those of Schlichting [8]. However, it may be worth mentioning here that the calculation method of Schlichting [8] fails for values of $V_m/U_\infty > 1.22$ (i.e., for values of $Ta/Re^2 > 1.4884$); the present method has succeeded in obtaining solutions for very considerably larger values of Ta/Re^2 as can be seen from the present results.

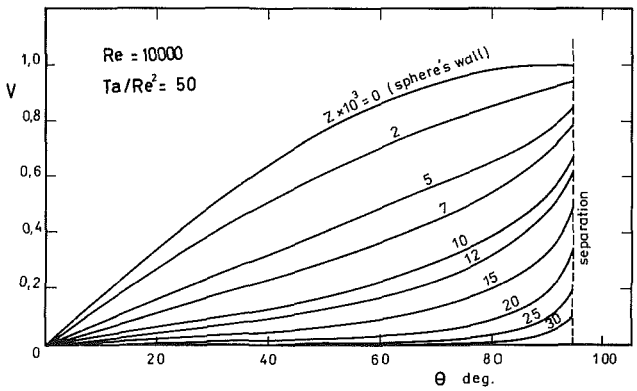

Fig. 6(*a*) Azimuthal velocity development for $Ta/Re^2 = 50$

Development of the Azimuthal Velocity Component

Figure 6(*a*) represents the developing velocity distribution V corresponding to a value of Re = 10000 for a chosen value of $Ta/Re^2 = 50$. Again, curves corresponding to some selected values of the dimensionless radial distance Z are drawn in this

Table 2 Effect of Ta/Re^2 on the resisting moment, frictional drag, and separation angle, Re = 10000

Ta/Re^2	C_M	C_D	θ_S, degree
0	0	0.06716	107.0
1	0.12583	0.07013	104.5
5	0.05689	0.08277	100.2
36	0.02365	0.17326	95.1
50	0.02069	0.21090	94.4
100	0.01663	0.31846	94.0
500	0.01026	0.92407	93.3
5000	0.00548	4.32150	93.3
10000	0.00460	6.56464	93.3

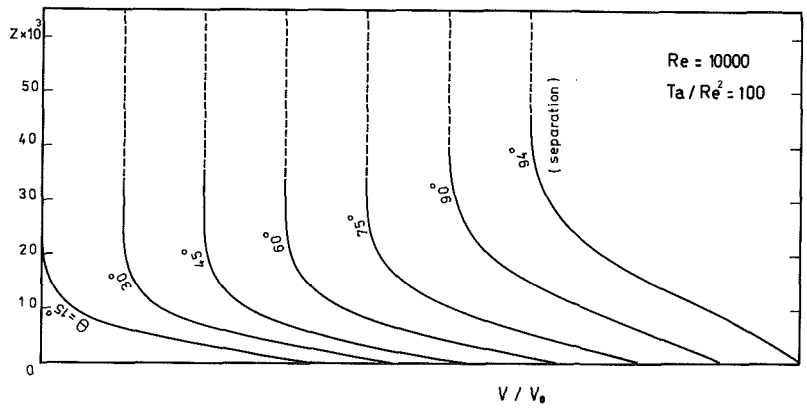

Fig. 6(*b*) Azimuthal velocity profiles for $Ta/Re^2 = 100$

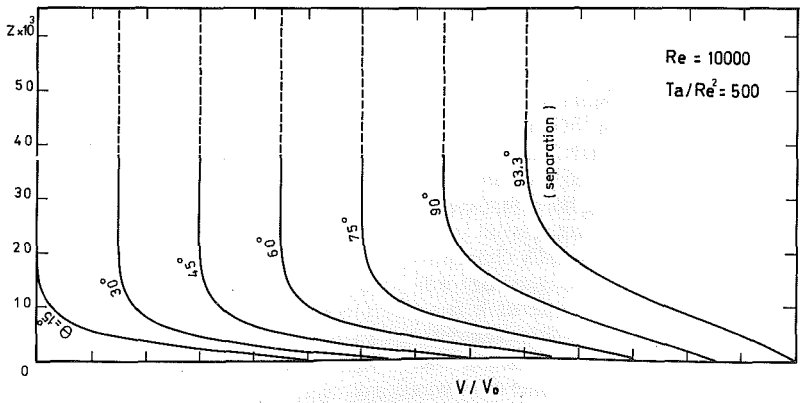

Fig. 6(c) Azimuthal velocity profiles for $Ta/Re^2 = 500$

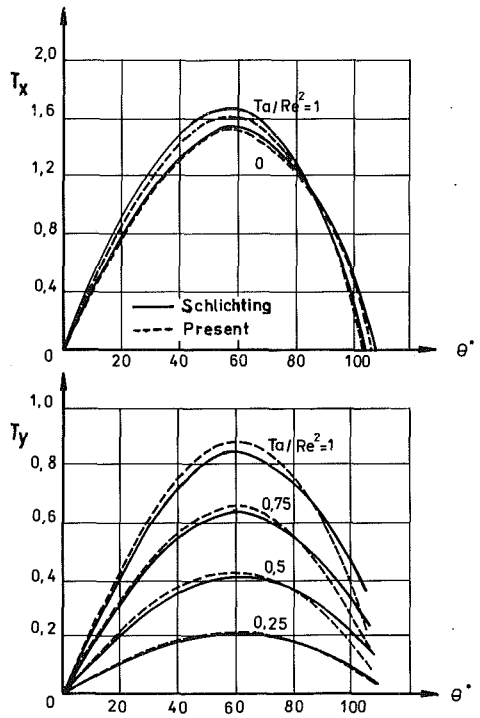

Fig. 7 Comparison between the present results and those of [8] for the wall shear stress components T_x and T_y

figure. It is noticeable that these curves intersect the θ axis at different points, where the points of intersection with high values of θ correspond to the curves of higher values of Z. This, of course, is due to the fact that, near the stagnation point, only fluid in the vicinity of the rotating wall acquires a tangential velocity component and fluid far away from the rotating wall (i.e., outside the developing azimuthal boundary layer) will only move downstream until tangential momentum can be diffused into it due to the viscosity of the fluid and transported to it by means of radial velocity component and centrifugal action. In Figs. 6(*b*) and 6(*c*), azimuthal velocity profiles are drawn for $Ta/Re^2 = 100$ and 500, respectively; all profiles start with a value of $V/V_0 = 1$ at the rotating wall (i.e., $Z = 0$) and end with zero in the undisturbed fluid region. Velocity profiles similar to those presented in Figs. 6(*b*) and 6(*c*) could be obtained by cross plotting in Fig. 6(*a*). From these figures one can see how the circumferential boundary layer develops. Also, a careful examination of Figs. 6(*b*) and 6(*c*) indicates that the azimuthal boundary layer thickness decreases by increasing the rotation of the sphere (i.e., increasing the value of the parameter Ta/Re^2). By analogy with a one dimensional fluid flow past a flat plate, this might be expected, since in that case, the boundary layer thickness is known to be decreased by increasing the fluid velocity in the longitudinal direction of the plate and therefore one may expect a similar effect on the azimuthal boundary layer thickness i.e., keeping the Reynolds number constant and increasing the sphere rotation would decrease the azimuthal boundary layer thickness.

Wall Shear Stress in Meridional and Azimuthal Directions, Frictional Drag and Resisting Moment

Over the range of $0 \leq Ta/Re^2 \leq 1$, Fig. 7 compares the present results for the dimensionless wall shear stresses T_x and T_y with the corresponding results of Schlichting [8]. It is clear from this figure that the results of the present analysis agree, within less than 5 percent, with those of reference [8]. However, to augment the information presently available in

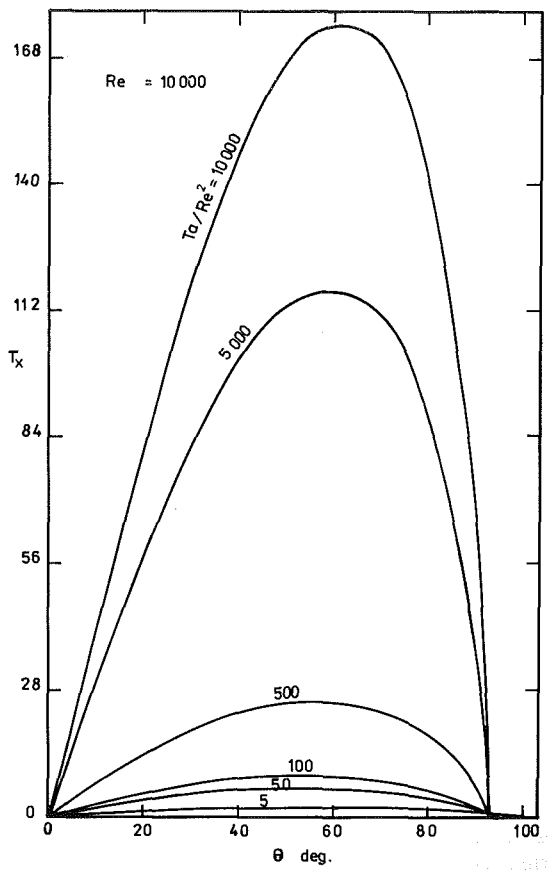

Fig. 8(*a*) Dimensionless meridional wall shear stress against meridional distance for various values of Ta/Re^2

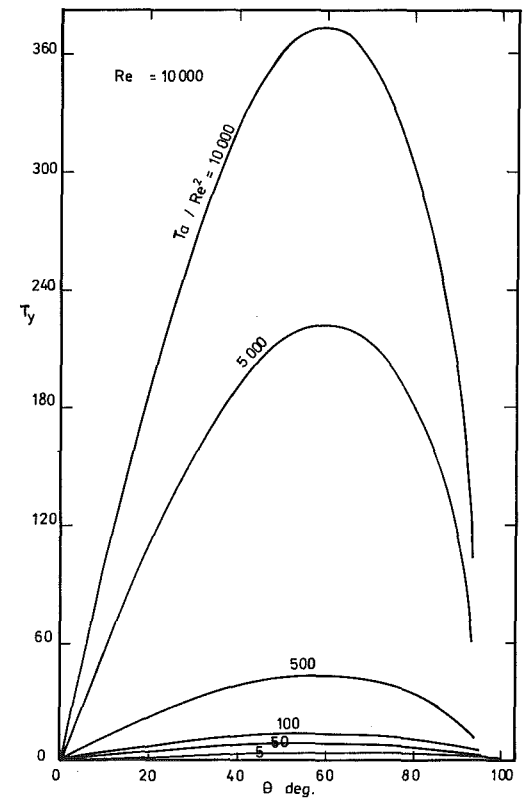

Fig. 8(*b*) Dimensionless azimuthal wall shear stress against meridional distance for various values of Ta/Re^2

the literature, Figs. 8(*a*) and 8(*b*) give the variation of T_x and T_y, respectively, with the meridional distance (i.e., θ) over a wide range of the parameter Ta/Re^2.

The frictional drag D may be determined by using the following equation,

$$D = \int_0^{\bar{x}_S} 2\pi r t_x d\bar{x},$$

where $\bar{x}$ is the coordinate measured along the axis of rotation. Using this equation, the dimensionless drag coefficient C_D has been computed and is given as a function of the parameter Ta/Re^2 in Table 2. As can be seen from this table, the rotation causes a considerable increase in the frictional drag.

Similarly, the resisting moment of a rotating sphere may be obtained from the following expression:

$$M = -2\pi \int_0^{x_S} r^2 t_y dx.$$

Using this expression, the dimensionless torque coefficient C_M has been computed and is given for various values of Ta/Re^2 in Table 2. Also, Table 1 gives a comparison between the present results for C_M and those of Schlichting [8] over the narrow range of Ta/Re^2 for which Schlichting's solution technique is valid. The results of the present analysis for C_M are in excellent agreement with those of [8] in this narrow range of Ta/Re^2.

Scaling the Present Results for Other Values of Re

Even though the computations were all done at one Reynolds number, viz. 10000, the results presented in this paper could be scaled for other values of Re. Since the two coefficients C_M and C_D are of particular interest to the engineer, the following paragraph explains how these two important coefficients could be scaled for other values of Re.

It is shown in [8] that C_M is in first approximation proportional to $\sqrt{Re^2/Ta}$ and inversely proportional to $\sqrt{Re}$. Thus, for a given Ta/Re^2, the value of $C_M\sqrt{Re}$ is approximately constant regardless of the value of Re. Similarly, for a given Ta/Re^2, the scaled frictional drag coefficient $C_D\sqrt{Re}$ could be considered approximately constant in the Reynolds number range over which the laminar boundary layer theory is valid. Both values of $C_M\sqrt{Re}$ and $C_D\sqrt{Re}$ can easily be calculated for various values of Ta/Re^2 from Table 2.

Acknowledgment

The financial support of Alazhar University, which allowed us to carry out this investigation on the ICL (DME GEORGE3) computer of Cairo University, is gratefully acknowledged.

References

1 Tomotika, S., "Laminar Boundary Layer on the Surface of a Sphere in a Uniform Stream," Aeronautical Research Committee (A.R.C.) Reports and Memoranda No. 1678, London, 1935.

2 Tomotika, S., and Imai, I., "On the Transition from Laminar to Turbulent Flow in the Boundary Layer of a Sphere," Tokyo Imp. Univ. Aeronaut. Res. Inst. Rep., 13, 1938, pp. 389–423.

3 Frössling, N., "Evaporation, Heat Transfer, and Velocity Distribution in Two Dimensional and Rotationally Symmetrical Laminar Boundary Layer Flow," NACA, TM 1432, 1940.

4 Scholkemeier, F. W., "Losung der Prandtschen Grenzschicht differential gleichungen mit Hilfe Von Potenzreihentwicklungen," *Arch. Math. Karlsruhe*, Vol. 1, 1949, pp. 270–277.

5 Rott, N., and Crabtree, L. F., "Simplified Laminar Boundary Layer Calculations for Bodies of Revolution and for Yawed Wings," *J. Aeronaut. Sci.*, Vol. 19, 1952, pp. 553–565.

6 Smith, A. M. O., and Clutter, D. W., "Solution of the Incompressible Laminar Boundary Layer Equations," *AIAAJ.*, Vol. 1, No. 9, 1963, pp. 2063–2071.

7 Sheridan, R. E., "Laminar Boundary Layers on Bodies of Revolution: Computer Programs and Vorticity Budgets," Pa. State Univ. Ordnance Res. Lab. Tech. Mem. 502-2421-19, 1968.

8 Schlichting, H., "Laminar Flow about a Rotating Body of Revolution in an Axial Airstream," NACA TM 1415, 1953.

9 Luthander, S., and Rydberg, A., *Phys. Z.*, Vol. 36, 1935, p. 552.

10 Burgers, J. M., Kon Akad. Von Wetenschappen, Amsterdam, 45, 1941, p. 13.

11 Hoskin, N. E., "The Laminar Boundary Layer on a Rotating Sphere," Fifty Years of Boundary Layer Research, Braunschweig, 1955, pp. 127–131.

12 Milne-Thomson, L. M., *Theoretical Hydrodynamics*, Fifth ed., Macmillan & Co., London, 1968, pp. 488–489.

13 Rouleau, W. T., and Osterle, J. F., "The Application of Finite-Difference Methods to Boundary-Layer Type Flows," *J. Aeronautical Sci.*, Vol. 22, 1955, pp. 249–254.

14 El-Shaarawi, M. A. I., and Sarhan, A., "Developing Laminar Free Convection in an Open Ended Vertical Annulus with a Rotating Inner Cylinder," ASME *Journal of Heat Transfer*, Vol. 103, No. 3, Aug. 1981, pp. 552–558.

15 Lapidus, L., *Digital Computation for Chemical Engineers*, McGraw-Hill, 1962, pp. 254–255.

16 Parr, O., "Flow in the Three-Dimensional Boundary Layer on a Spinning Body of Revolution," *AIAA Journal*, Vol. 2, No. 2, Feb. 1964, pp. 361–363.

17 Carnahan, B., Luther, H. A., and Wilkes, J. O., *Applied Numerical Methods*, Wiley, 1969, p. 450.

Radial and Axial Variations in Transient Pressure Waves Transmitted Through Liquid Transmission Lines

A. K. Mitra*
Research Associate.
Mem. ASME

W. T. Rouleau
Professor.
Mem. ASME

Department of Mechanical Engineering,
Carnegie-Mellon University,
Pittsburgh, Pa. 15213

An implicit factorization method has been developed for solving numerically the complete two-dimensional Navier-Stokes and continuity equations for pressure transients in a slightly compressible viscous liquid contained in a rigid pipe. Two problems have been analyzed: (1) The stopping of a steady Poiseuille flow by closure of a valve, and (2), the initiation of a nearly rectangular pressure pulse at the end of the pipe. In problem (1), radial as well as axial pressure variations were found; nearly periodic damped waves exist at the centerline and at the wall, and are approximately 180 deg out of phase. Essentially plane waves are found for problem (2), regardless of whether the fluid is flowing or not, provided that the initial pulse magnitude is not too large; the results show that the viscous effects are concentrated in a thin boundary layer.

Introduction

The analysis of pressure wave propagation in liquid-filled tubes has received considerable attention due to engineering interest in the behavior of fluid transmission lines and the design of hydraulic control systems. According to the linear theory of sound, pressure waves are propagated with constant energy and uniform wave velocity. The influence of viscosity tends to alter the acoustic waveform from that predicted by this linear theory. Firstly, the wave amplitude is damped due to wall shear resistance, and secondly, the viscous effects related to velocity gradients in the direction of flow smooth out any exceptionally steep portions of the wave. The former effect is usually referred to as dissipative and the latter is dispersive.

In the early investigations the dissipative effect was modelled by the addition of a "quasi steady state" frictional resistance term to the wave equation. Numerical solutions based on the method of characteristics are applicable to the modified wave equation, as shown by Wylie and Streeter [1]. Zielke [2] discussed the shortcomings of this model and modified the resistance for frequency dependent viscous effects resulting from time-dependent pressure gradient. Brown [3], D'Souza and Oldenburger [4], and Holmboe and Rouleau [5] solved the continuity and the axial momentum equation. This theory describes the frequency-dependent viscous effects but does not include the dispersive viscous effects related to the axial velocity gradient. Walker, Kirkpatrick, and Rouleau [6] showed how the dispersive effects smooth out steep wave fronts. In all these investigations the radial variation of pressure is neglected and the nonlinear convective effects are not considered.

In the present paper the complete Navier-Stokes equations are solved numerically together with the continuity equation. The model appropriately includes the dispersive and dissipative effects of viscosity and enables one to gage the effects of nonlinear convection and radial variation of pressure, which in some cases are found to be substantial. Regarding numerical schemes, it has been observed that the stability criterion severely restricts the time steps of explicit schemes, and the solution of large matrix equations is necessary for the implicit schemes. Both result in large amounts of computation time. Here we use the implicit factored scheme proposed by Warming and Beam [7]. In this implicit method the time step is not severely restricted and simultaneously the order of the matrix equations is reduced due to the factorization.

Basic Equations

The equation of mass conservation and the equation of state for a slightly compressible liquid are:

$$\frac{\partial \rho}{\partial t} + u' \frac{\partial \rho}{\partial x} + v' \frac{\partial \rho}{\partial r} + \rho\left(\frac{\partial u'}{\partial x} + \frac{\partial v'}{\partial r} + \frac{v'}{r}\right) = 0, \quad (1)$$

$$\frac{dp'}{d\rho} = \frac{k}{\rho} = a_0^2, \quad (2)$$

where ρ, p', u', and v', respectively, are density, pressure, axial velocity, and radial velocity. t is time, x and r are axial and radial coordinates. In the water hammer problem, x is measured positively from the valve toward the reservoir. a_0 is sonic velocity, which is constant for liquids, and k is the bulk

Contributed by the Fluids Engineering Division and presented at the Symposium on Numerical Methods for Fluid Transients, Houston, Texas, June 1983 of THE AMERICAN SOCIETY OF MECHANICAL ENGINEERS. Manuscript received by the Fluids Engineering Division, May 9, 1983.

*Currently, Assistant Professor, Department of Engineering Science and Mechanics, Iowa State University, Ames, Iowa 50011.

modulus. The equation of state may be used to transform all density derivatives into pressure derivatives. The transformed continuity equation is

$$\frac{\partial p'}{\partial t} + u' \frac{\partial p'}{\partial x} + v' \frac{\partial p'}{\partial r} + k\left(\frac{\partial u'}{\partial x} + \frac{\partial v'}{\partial r} + \frac{v'}{r}\right) = 0. \quad (3)$$

The axial and radial momentum equations are:

$$\frac{\partial u'}{\partial t} + u' \frac{\partial u'}{\partial x} + v' \frac{\partial u'}{\partial r} = -\frac{1}{\rho_0} \frac{\partial p'}{\partial x} + \frac{\mu}{\rho_0} \times \left[\frac{4}{3} \frac{\partial^2 u'}{\partial x^2} + \frac{1}{r} \frac{\partial}{\partial r}\left(r \frac{\partial u'}{\partial r}\right) + \frac{1}{3} \frac{\partial}{\partial x}\left(\frac{1}{r} \frac{\partial}{\partial r}(rv')\right)\right], \quad (4)$$

$$\frac{\partial v'}{\partial t} + u' \frac{\partial v'}{\partial x} + v' \frac{\partial v'}{\partial r} = -\frac{1}{\rho_0} \frac{\partial p'}{\partial r} + \frac{\mu}{\rho_0} \times \left[\frac{1}{3} \frac{\partial^2 u'}{\partial x \partial r} + \frac{\partial^2 v'}{\partial x^2} + \frac{4}{3} \frac{\partial}{\partial r}\left(\frac{1}{r} \frac{\partial}{\partial r}(rv')\right)\right], \quad (5)$$

where ρ_0 is the mean density and μ is the viscosity. Now we construct the dimensionless variables and state the initial and boundary conditions for the water hammer and the pressure pulse problems.

Propagation of Short Pulse

The dimensionless variables are chosen as $u = u' a_0 \rho_0 / p_0$, $v = v' a_0 \rho_0 / p_0$, $p = (p' - p'_e)/p_0$, $\xi = x/R$, $\eta = r/R$ and $\tau = a_0 t/R$ where p_0 is the peak of the input pressure pulse, p'_e is the pressure at $x = 0$, where the input is fed and R is the radius of the pipe. Equations (3), (4), and (5), when written in terms of the dimensionless variables, become

$$\frac{\partial p}{\partial \tau} + \frac{\partial u}{\partial \xi} + \frac{\partial v}{\partial \eta} + \frac{v}{\eta} = -A\left(u \frac{\partial p}{\partial \xi} + v \frac{\partial p}{\partial \eta}\right), \quad (6)$$

$$\frac{\partial u}{\partial \tau} + \frac{\partial p}{\partial \xi} = -A\left(u \frac{\partial u}{\partial \xi} + v \frac{\partial u}{\partial \eta}\right) + H \times \left(\frac{4}{3} \frac{\partial^2 u}{\partial \xi^2} + \frac{1}{\eta} \frac{\partial}{\partial \eta}\left(\eta \frac{\partial u}{\partial \eta}\right) + \frac{1}{3} \frac{\partial}{\partial \xi}\left(\frac{1}{\eta} \frac{\partial}{\partial \eta}(\eta v)\right)\right), \quad (7)$$

$$\frac{\partial v}{\partial \tau} + \frac{\partial p}{\partial \eta} = -A\left(u \frac{\partial v}{\partial \xi} + u \frac{\partial v}{\partial \eta}\right) + H\left(\frac{1}{3} \frac{\partial^2 u}{\partial \xi \partial \eta} + \frac{\partial^2 v}{\partial \xi^2} + \frac{4}{3} \frac{\partial}{\partial \eta}\left(\frac{1}{\eta} \frac{\partial}{\partial \eta}(\eta v)\right)\right). \quad (8)$$

In the above equations $A = p_0/\rho_0 a_0^2$ and $H = \nu/Ra_0$, where ν is the kinematic viscosity.

The no-slip condition at the wall of the pipe is

$$u = 0, \; v = 0, \text{ at } \eta = 1 \quad (9)$$

and the symmetry condition at the axis of the pipe is

$$\frac{\partial u}{\partial \eta} = 0, \; v = 0, \; \frac{\partial p}{\partial \eta} = 0 \text{ at } \eta = 0. \quad (10)$$

Two kinds of initial conditions can be considered. One corresponds to initial stationary fluid in the pipe and is given by

$$u = 0, \; v = 0, \; p = 0 \text{ at } \tau = 0. \quad (11)$$

The other corresponds to initial Poiseuille flow in the pipe and is given by

$$u = 2(\eta^2 - 1), \; v = 0, \; p = 8H\xi \text{ at } \tau = 0. \quad (12)$$

The input pulse at $\xi = 0$ consists of three parts; first is a 4th order rise given by

$$p = 16\left(\frac{\tau}{\tau_0}\right)^2 \left(1 - \frac{\tau}{\tau_0}\right)^2; \; 0 < \tau < \frac{1}{2}\tau_0 \quad (13a)$$

second is a steady top

$$p = 1; \; \frac{1}{2}\tau_0 < \tau < \frac{5}{2}\tau_0, \quad (13b)$$

and third is a 4th order drop given by

$$p = 16\left(\frac{\tau - 2\tau_0}{\tau_0}\right)^2 \left(1 - \frac{\tau - 2\tau_0}{\tau_0}\right)^2; \; \frac{5}{2}\tau_0 < \tau < 3\tau_0. \quad (13c)$$

The total input duration time is $3\tau_0$.

Water Hammer

The dimensionless variables are chosen as $u = u'/u_0$, $v = v'/u_0$, $p = (p' - p'_e)/\rho_0 u_0 a_0$, $\xi = x/R$, $\eta = x/R$ and $\tau = a_0 t/R$, where u_0 is a reference velocity. Although these variables are quite different from the pulse variables the equations in dimensionless form are the same as equations (6), (7), and (8). The parameter H remains unchanged, but A is modified to $A = u_0/a_0$.

The same no-slip condition (9) and symmetry condition (10) apply. The initial condition is Poiseuille flow in the pipe, given by

$$u = 2(\eta^2 - 1), \; v = 0, \; p = 8H\xi \text{ at } \tau = 0. \quad (14)$$

The valve at $\xi = 0$ stops the flow in the pipe as

Nomenclature

a_0 = sonic velocity
A = $p_0/\rho_0 a_0^2$ for pulse problem
= u_0/a_0 for water hammer problem
H = ν/Ra_0
i, j = subscripts, denoting spatial step
k = bulk modulus
n = superscript, denoting time step
p = dimensionless pressure
= $(p' - p'_e)/p_0$ for pulse problem
= $(p' - p'_e)/\rho_0 u_0 a_0$ for water hammer problem
p' = pressure
p'_e = pressure at $x = 0$
p_0 = peak of the input pressure pulse
p^* = see equation (20)
r = radial coordinate
R = radius of the pipe
R_1, R_2, R_3 = functions, see equation (16)
t = time
u = dimensionless axial velocity
= $u' a_0 \rho_0 / p_0$ for pulse problem
= u'/u_0 for water hammer problem
u' = axial velocity
u_0 = reference velocity
u^* = see equation (20)
v = dimensionless radial velocity
= $v' a_0 \rho_0 / p_0$ for pulse problem
= v'/u_0 for water hammer problem
v' = radial velocity
v^* = see equation (20)
x = axial coordinate
ξ = dimensionless axial coordinate
= x/R
η = dimensionless radial coordinate
= r/R
μ = coefficient of viscosity
ν = kinematic viscosity
ρ = density
ρ_0 = mean density
τ = dimensionless time
= $a_0 t/R$
τ_0 = related to input duration time; see equation (13) for pulse problem, equation (15) for water hammer problem

$$u = 2(\eta^2 - 1)\left(2\left(\frac{\tau}{\tau_0}\right)^3 - 3\left(\frac{\tau}{\tau_0}\right)^2 + 1\right);\ 0 < \tau < \tau_0 \qquad (15a)$$

$$u = 0;\ \tau_0 < \tau \qquad (15b)$$

Now we proceed to the solution of equations (6), (7), and (8), subject to the initial and boundary conditions discussed above.

Numerical Solution

The right-hand sides of equations (6), (7), and (8) consist of the nonlinear convection terms and the viscous diffusion terms. The convection and the diffusion contain the dimensionless parameters A and H, respectively. The parameter $H \ll 1$ for both pulse and hammer problems. The parameter $A \ll 1$ for the pulse problem if the peak $p_0 \ll \rho_0 a_0^2$ and for the hammer problem if the reference velocity $u_0 \ll a_0$. As a result, the magnitudes of convection and diffusion terms are much smaller than the left-hand sides of equations (6), (7), and (8). In the numerical scheme the terms on the left-hand side are handled implicitly and the right-hand sides are handled explicitly. In the pulse problem for high p_0 the nonlinear convection should be handled implicitly and iteratively. This aspect is discussed quantitatively in the last section.

Denoting the right-hand sides of equations (6), (7), and (8) by R_1, R_2, and R_3, respectively, we write

$$\frac{\partial p}{\partial \tau} + \frac{\partial u}{\partial \xi} + \frac{\partial v}{\partial \eta} + \frac{v}{\eta} = R_1, \qquad (16a)$$

$$\frac{\partial u}{\partial \tau} + \frac{\partial p}{\partial \xi} = R_2, \qquad (16b)$$

$$\frac{\partial v}{\partial \tau} + \frac{\partial p}{\partial \eta} = R_3. \qquad (16c)$$

The time-derivatives are approximated by three-point backward formula given by

$$3Z^{n+1} - 4Z^n + Z^{n-1} = 2\,\Delta\tau\left(\frac{\partial Z}{\partial \tau}\right)^{n+1} + 0(\Delta\tau^3), \qquad (17)$$

where $\Delta\tau$ is the time-step and $Z(\tau, \xi, \eta) = Z(n\Delta\tau, \xi, \eta) = Z^n(\xi, \eta)$. The advantages of using the three-point backward scheme in the present transient problems are discussed by Mitra and Rouleau [8]. By using (17) we write (16) as

$$\begin{bmatrix} 1 & \frac{2}{3}\Delta\tau\frac{\partial}{\partial\xi} & \frac{2}{3}\Delta\tau\left(\frac{\partial}{\partial\eta} + \frac{1}{\eta}\right) \\ \frac{2}{3}\Delta\tau\frac{\partial}{\partial\xi} & 1 & 0 \\ \frac{2}{3}\Delta\tau\frac{\partial}{\partial\eta} & 0 & 1 \end{bmatrix} \begin{Bmatrix} p^{n+1} \\ u^{n+1} \\ v^{n+1} \end{Bmatrix}$$

$$= \begin{Bmatrix} \frac{4}{3}p^n - \frac{1}{3}p^{n-1} + \frac{2}{3}\Delta\tau\, R_1{}^n \\ \frac{4}{3}u^n - \frac{1}{3}u^{n-1} + \frac{2}{3}\Delta\tau\, R_2{}^n \\ \frac{4}{3}v^n - \frac{1}{3}v^{n-1} + \frac{2}{3}\Delta\tau\, R_3{}^n \end{Bmatrix} \qquad (18)$$

The time marching scheme is started with Euler implicit and then is continued with three-point backward according to equation (18).

The coefficient matrix in the left-hand side of equation (18) is approximately factorized to

$$\begin{bmatrix} 1 & \frac{2}{3}\Delta\tau\frac{\partial}{\partial\xi} & 0 \\ \frac{2}{3}\Delta\tau\frac{\partial}{\partial\xi} & 1 & 0 \\ 0 & 0 & 1 \end{bmatrix} \begin{bmatrix} 1 & 0 & \frac{2}{3}\Delta\tau\left(\frac{\partial}{\partial\eta} + \frac{1}{\eta}\right) \\ 0 & 1 & 0 \\ \frac{2}{3}\Delta\tau\frac{\partial}{\partial\eta} & 0 & 1 \end{bmatrix} \qquad (19)$$

according to Warming and Beam [7]. It is shown by Warming and Beam that the formal accuracy of the time differencing is not upset by the approximate factorization. At this point we define

$$\begin{bmatrix} 1 & 0 & \frac{2}{3}\Delta\tau\left(\frac{\partial}{\partial\eta} + \frac{1}{\eta}\right) \\ 0 & 1 & 0 \\ \frac{2}{3}\Delta\tau\frac{\partial}{\partial\eta} & 0 & 1 \end{bmatrix} \begin{bmatrix} p^{n+1} \\ u^{n+1} \\ v^{n+1} \end{bmatrix} = \begin{bmatrix} p^{*n+1} \\ u^{*n+1} \\ v^{*n+1} \end{bmatrix} \qquad (20)$$

Then

$$\begin{bmatrix} 1 & \frac{2}{3}\Delta\tau\frac{\partial}{\partial\xi} & 0 \\ \frac{2}{3}\Delta\tau\frac{\partial}{\partial\xi} & 1 & 0 \\ 0 & 0 & 1 \end{bmatrix} \begin{bmatrix} p^{*n+1} \\ u^{*n+1} \\ v^{*n+1} \end{bmatrix}$$

$$= \begin{bmatrix} \frac{4}{3}p^n - \frac{1}{3}p^{n-1} + \frac{2}{3}\Delta\tau R_1{}^n \\ \frac{4}{3}u^n - \frac{1}{3}u^{n-1} + \frac{2}{3}\Delta\tau R_2{}^n \\ \frac{4}{3}v^n - \frac{1}{3}v^{n-1} + \frac{2}{3}\Delta\tau R_3{}^n \end{bmatrix} \qquad (21)$$

Effectively, equations (20) and (21) signify the decomposition of a two-dimensional problem into two one-dimensional problems. We first sweep in the ξ-direction and solve (21) to get p^{*n+1}, u^{*n+1}, v^{*n+1}; then we sweep in the η-direction and solve (20) to get p^{n+1}, u^{n+1}, v^{n+1}.

Now it remains to approximate the spatial derivatives in equations (20) and (21) by difference formulas. We use the upwind spatial difference scheme whose development for a one-dimensional system is given by Warming and Beam [7]. The scheme has been tested for the present transient problems by Mitra and Rouleau [8]. They have shown that the combination of three-point backward time differencing and upwind space differencing provides a method in which numerical dissipation is independent of time step size and proportional to space step size, and numerical dispersion is second order in both time and space step sizes. Thus, solutions represent real viscous effects, rather than the effects of

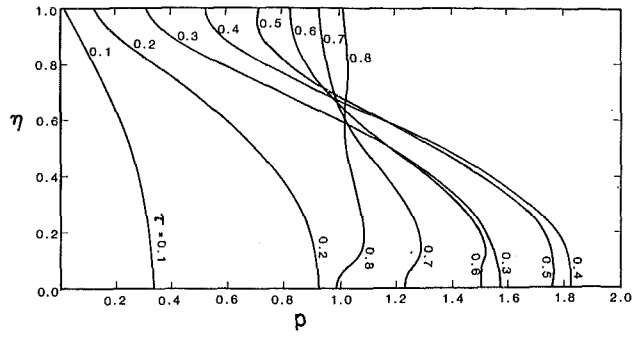

Fig. 1(*a*)

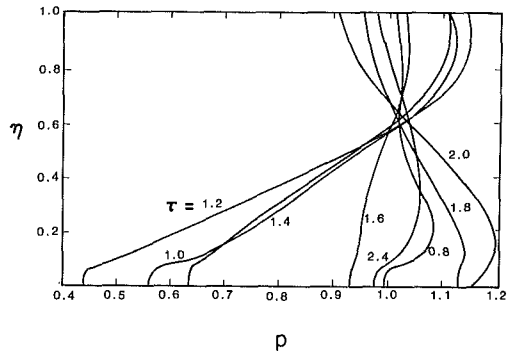

Fig. 1(*b*)

Fig. 1 Radial variation of pressure at $\xi = 0.0$ for the water hammer problem. Re = 100, H = 1.2 × 10^{-4}.

numerical viscosity, when space step size is taken sufficiently small. After factorizing the two-dimensional problem into two one-dimensional problems the use of the upwind scheme closely resembles that due to Warming and Beam. By denoting the right-hand side as $\{T_1^n, T_2^n, T_3^n\}$ we write equation (21) as

$$p^{*n+1}_{i,j} + \frac{1}{3}\Delta\tau\left(\frac{\partial u^{*\,n+1}}{\partial\xi}\right)^{+}_{i,j} + \frac{1}{3}\Delta\tau\left(\frac{\partial u^{*\,n+1}}{\partial\xi}\right)^{-}_{i,j} + \frac{1}{3}\Delta\tau\left(\frac{\partial p^{*\,n+1}}{\partial\xi}\right)^{+}_{i,j} - \frac{1}{3}\Delta\tau\left(\frac{\partial p^{*\,n+1}}{\partial\xi}\right)^{-}_{i,j} = (T_1^n)_{i,j}, \tag{22a}$$

$$u^{*n+1}_{i,j} + \frac{1}{3}\Delta\tau\left(\frac{\partial p^{*\,n+1}}{\partial\xi}\right)^{+}_{i,j} + \frac{1}{3}\Delta\tau\left(\frac{\partial p^{*\,n+1}}{\partial\xi}\right)^{-}_{i,j}, + \frac{1}{3}\Delta\tau\left(\frac{\partial u^{*\,n+1}}{\partial\xi}\right)^{+}_{i,j} - \frac{1}{3}\Delta\tau\left(\frac{\partial u^{*\,n+1}}{\partial\xi}\right)^{-}_{i,j} = (T_2^n)_{i,j}, \tag{22b}$$

$$v^{*n+1}_{i,j} = (T_3^n)_{i,j}. \tag{22c}$$

Similarly equation (20) is written as

$$p^{n+1}_{i,j} + \frac{1}{3}\Delta\tau\left(\frac{\partial v}{\partial\eta}^{n+1}\right)^{+}_{i,j} + \frac{1}{3}\Delta\tau\left(\frac{\partial v}{\partial\eta}^{n+1}\right)^{-}_{i,j} + \frac{2}{3}\Delta\tau\left(\frac{v}{\eta}^{n+1}\right)_{i,j} + \frac{1}{3}\Delta\tau\left(\frac{\partial p}{\partial\eta}^{n+1}\right)^{+}_{i,j} - \frac{1}{3}\Delta\tau\left(\frac{\partial p}{\partial\eta}^{n+1}\right)^{-}_{i,j} = p^{*n+1}_{i,j}, \tag{23a}$$

$$u^{n+1}_{i,j} = u^{*n+1}_{i,j}, \tag{23b}$$

$$v^{n+1}_{i,j} + \frac{1}{3}\Delta\tau\left(\frac{\partial p}{\partial\eta}^{n+1}\right)^{+}_{i,j} + \frac{1}{3}\Delta\tau\left(\frac{\partial p}{\partial\eta}^{n+1}\right)^{-}_{i,j}$$

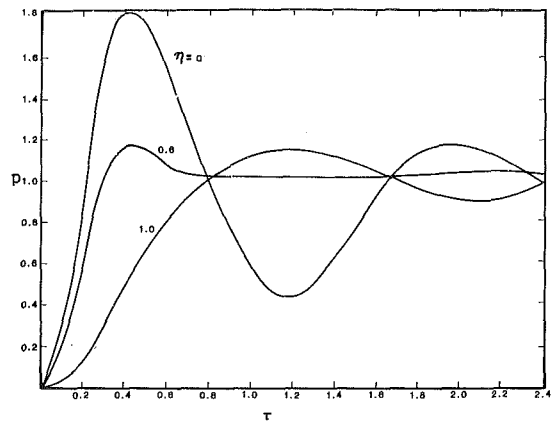

Fig. 2 Temporal variation of pressure at $\xi = 0.0$ for the water hammer problem. Re = 100, H = 1.2 × 10^{-4}.

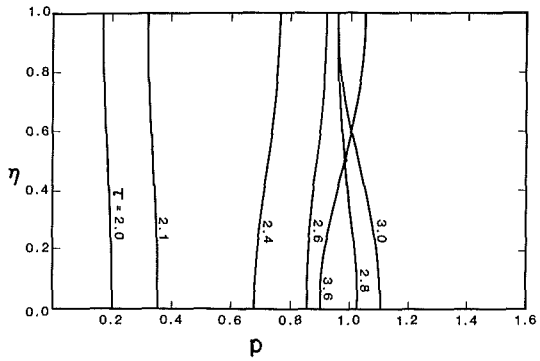

Fig. 3 Radial variation of pressure at $\xi = 2.0$ for the water hammer problem. Re = 100, H = 1.2 × 10^{-4}.

$$+ \frac{1}{3}\Delta\tau\left(\frac{\partial v}{\partial\eta}^{n+1}\right)^{+}_{i,j} - \frac{1}{3}\Delta\tau\left(\frac{\partial v}{\partial\eta}^{n+1}\right)^{-}_{i,j} = v^{*n+1}_{i,j} \tag{23c}$$

In equations (22) and (23) the subscripts i, j mean $Z(\tau, \xi, \eta) = Z(\tau, i\Delta\xi, j\Delta\eta) = (Z(\tau))_{i,j}$ where $\Delta\xi$ and $\Delta\eta$ are step sizes respectively in ξ and η directions. The spatial derivatives in equations (22) and (23) are approximated by the formulas

$$\left(\frac{\partial Z}{\partial\xi}\right)^{+}_{i,j} = \frac{1}{\Delta\xi}(Z_{i,j} - Z_{i-1,j}), \tag{24a}$$

$$\left(\frac{\partial Z}{\partial\xi}\right)^{-}_{i,j} = \frac{1}{\Delta\xi}(Z_{i+1,j} - Z_{i,j}), \tag{24b}$$

$$\left(\frac{\partial Z}{\partial\eta}\right)^{+}_{i,j} = \frac{1}{\Delta\eta}(Z_{i,j} - Z_{i,j-1}), \tag{24c}$$

$$\left(\frac{\partial Z}{\partial\eta}\right)^{-}_{i,j} = \frac{1}{\Delta\eta}(Z_{i,j+1} - Z_{i,j}). \tag{24d}$$

Substituting expressions similar to those in equation (24) in equations (22) and (23) we get a set of simultaneous equations connecting the dependent variables p, u, and v. The right-hand sides of equation (23), which are lumped convection and diffusion effects, are computed by approximating the partial derivatives by central difference formulas.

The above simultaneous equations, which are the conservation equations in the field, are solved at every time step together with the following equations derived from the boundary conditions. At the wall ($\eta = 1$) the no-slip condition (9) is used for u and v, and for p the following condition is derived from the radial momentum equation (16c):

$$\frac{\partial p}{\partial\eta} = R_3 \tag{25}$$

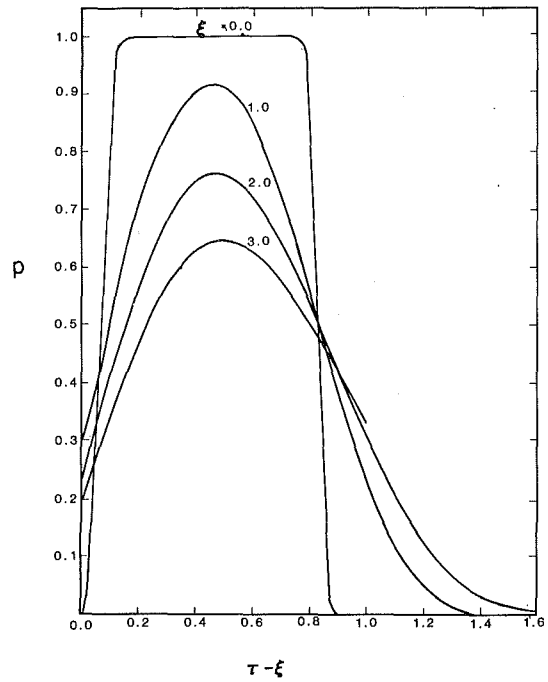

Fig. 4 Temporal variation of pressure at several axial stations for the pulse problem with input duration time 0.9. Peak of the input pulse p_0 = 100 psi, H = 4.0 × 10^{-7}.

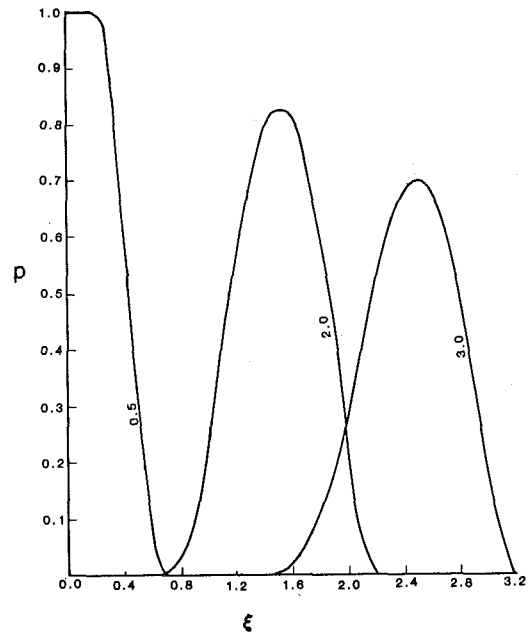

Fig. 5 Axial variation of pressure for the pulse problem with input duration time 0.9. Peak of the input pulse p_0 = 100 psi, H = 4.0 × 10^{-7}.

At the axis of the pipe ($\eta = 0$) the symmetry condition (10) is imposed. For the pulse problem p is specified at $\xi = 0$ according to equation (13) and for u the following condition is derived from the continuity equation (16*a*).

$$\frac{\partial u}{\partial \xi} = -\frac{\partial p}{\partial \tau} + R_1 \tag{26}$$

For the water hammer problem u is specified at $\xi = 0$ according to equation (15) and for p the following condition is derived from the axial momentum equation (16*b*):

$$\frac{\partial p}{\partial \xi} = -\frac{\partial u}{\partial \tau} + R_2 \tag{27}$$

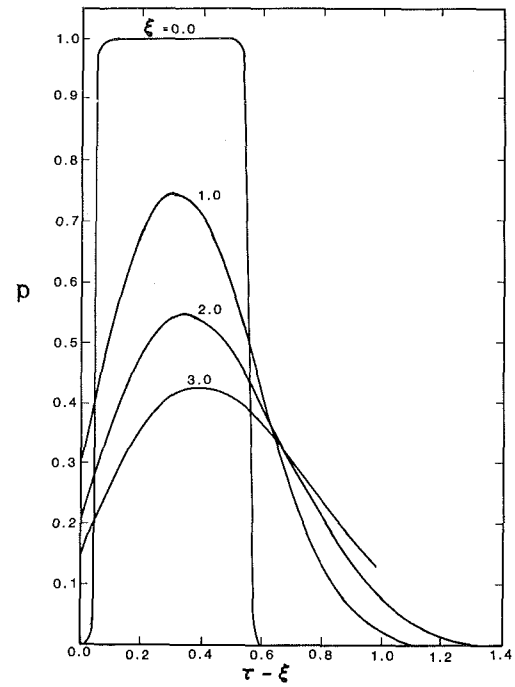

Fig. 6 Temporal variation of pressure at several axial stations for the pulse problem with input duration time 0.6. Peak of the input pulse p_0 = 100 psi, H = 4.0 × 10^{-7}.

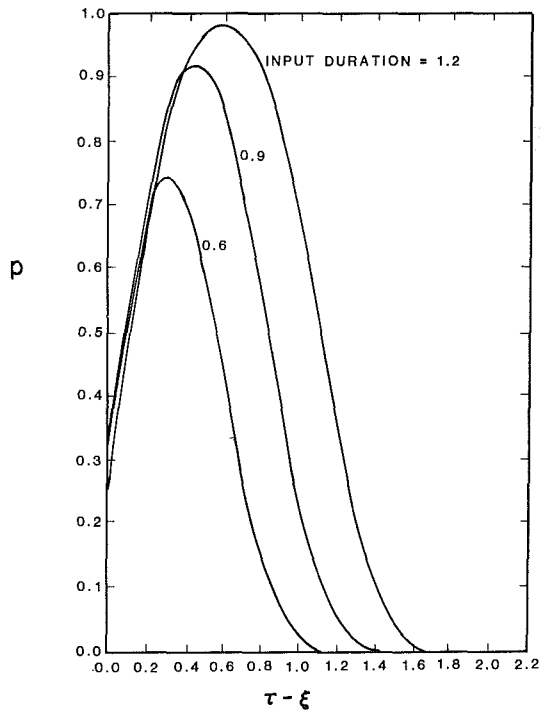

Fig. 7 Effect of input duration time on temporal variation of pressure at ξ = 1.0. Peak of the input pulse p_0 = 100 psi, H = 4.0 × 10^{-7}.

The derivatives in equations (25), (26), and (27) are approximated by suitable forward or backward second-order difference formulas. At any time τ the wave would have propagated from $\xi = 0$ to as far at $\xi = \tau$. For all ξ beyond this point the initial conditions exist. In the present calculations the initial conditions are imposed at $\xi = \tau + 3\Delta\xi$.

All the computations are done with $\Delta\tau = \Delta\xi = \Delta\eta = 0.05$. In the following sections the results are presented. Numerical experiment has confirmed that this value of $\Delta\xi$ is small

Table 1 Comparison of pressure at valve from one-dimensional and two-dimensional models

Re = 100, H = 1.2×10^{-4}

τ	Pressure from one dimensional model of Holmboe and Rouleau [5]	Weighted average p from present two-dimensional model
0.2	1.0008	0.4758
0.6	1.0013	1.0317
1.0	1.0017	1.0202
1.4	1.0020	1.0073
1.8	1.0023	1.0067
2.2	1.0026	1.0140
2.6	1.0028	1.0153
3.0	1.0030	1.0107
3.4	1.0032	1.0092
3.8	1.0034	1.0124

Table 2 Effect of fluid viscosity on the shape of pressure pulse

Input duration time $3\tau_0$ = 3.0, peak of the input pulse p_0 = 100 psi

τ	Pressure at ζ = 1, η = 0		
	Low Viscosity H = 4.0×10^{-7}	Moderate Viscosity H = 3.08×10^{-6}	High Viscosity H = 4.0×10^{-5}
1.0	0.1387	0.1390	0.1390
1.2	0.4417	0.4430	0.4426
1.4	0.7500	0.7523	0.7513
1.6	0.9346	0.9364	0.9349
1.8	0.9936	0.9942	0.9926
2.0	1.0010	1.0010	0.9994
2.2	1.0003	1.0001	0.9986
2.4	1.0	0.9999	0.9983
2.6	1.0	0.9999	0.9983
2.8	1.0	0.9999	0.9983
3.0	0.9996	0.9994	0.9979
3.2	0.9915	0.9913	0.9897
3.4	0.9347	0.9340	0.9325
3.6	0.7521	0.7504	0.7490
3.8	0.4481	0.4460	0.4450
4.0	0.1718	0.1705	0.1702

enough to ensure that the viscous effects are real, rather than numerical [8].

Results

We first present the results of the water hammer problem. We assume a fluid with kinematic viscosity $\nu = 0.427 \times 10^{-3}$ ft^2/s and sonic velocity $a_0 = 4345$ ft/s flowing in a pipe of diameter $D = 1$ in. The reference velocity u_0 is computed for Reynolds number $\mathrm{Re} = u_0 D/\nu = 100$. The velocity at $\xi = 0$ is varied according to equation (15) and corresponds to a valve closure with closing time $\tau_0 = 0.4$. In Figs. 1(*a*) and 1(*b*) the radial variation of p at the valve ($\xi = 0$) is shown for various τ. The pressure at the axis of the pipe increases faster than the pressure at the wall. Axial pressure reaches the maximum value of 1.8 when the valve is completely closed at $\tau = 0.4$. The maximum value of 1.8 is almost twice the value of 1.0 observed for frictionless liquids. This is because axial velocity in a Poiseuille profile is twice the mean velocity. Beyond $\tau = 0.4$ the pressures at the wall and axis start oscillating. This oscillatory behavior is shown in Fig. 2. In Fig. 3 the radial variation p is shown for various τ at $\xi = 2.0$. At this downstream station we observe oscillations similar to those in Fig. 2 but in a much smaller scale because of the viscous dissipation. All water hammer computations were started from an initial Poiseuille flow at $\tau = 0$ and continued up to $\tau = 4$. The time required on a DEC 2060 system is about 150 s.

A comparison of the present results with the earlier one-dimensional solution obtained by Holmboe and Rouleau [5] is desirable. As a purely heuristic procedure, the weighted average pressure $\bar{p}$ at $\xi = 0$ is computed as

$$\bar{p}(\tau, \xi = 0) = 2\int_0^1 p(\tau, \eta, \xi = 0)\eta \, d\eta$$

and compared with Holmboe and Rouleau's solution in Table 1. It should be remembered that their solution is for instantaneous valve closing whereas the present one is for cubic closing. Except for the initial and final portions of the pulse, the results are in close agreement. The weighted average pressure shows a slight oscillatory behavior as a result of the complex wave structures evident in Fig. 2.

When not specified otherwise the pulse problem is considered for a fluid with kinematic viscosity $\nu = 0.44 \times 10^{-4}$ ft^2/s, density $\rho_0 = 1.531$ slug/ft^3, sonic velocity $a_0 = 4420$ ft/s, pipe diameter $D = 0.6$ in., and peak of the pulse input $p_0 = 100$ psi. As mentioned earlier, two kinds of initial conditions, given by equations (11) and (12), can be considered. Although computations have been done for both cases the results presented here correspond to the stationary fluid case of equation (11). However, when the initial Poiseuille velocity of the flowing fluid case, equation (12), is of no larger magnitude than the particle velocity produced by an input pulse, the difference between the flowing fluid case and the non-flow case is negligible. This, of course, is evident from the governing equations. The equations for the flowing fluid case differ from the stationary fluid case by having additional convection terms. These additional convection terms in the axial momentum equation are

$$A\left(u_p \frac{\partial u}{\partial \xi} + v \frac{\partial u_p}{\partial \eta}\right).$$

In the above expression u_p is the initial Poiseuille velocity and u, v are the perturbations over the initial flow. Since A is of the order $0(10^{-4})$ the above effect is quite small unless u_p is very high.

In Fig. 4 the variation of p on the axis of the pipe ($\eta = 0$) with τ is shown for several axial stations. The input pulse fed at $\xi = 0$, given by equation (13), which has the total duration time $3\tau_0 = 0.9$, is also shown in the figure for comparison. Since the pulse duration is short the boundary layer near the pipe wall is extremely thin and the propagating pressure wave is plane except at radial stations very close to the wall. The variation of p at $\xi = 1$, 2, and 3 clearly shows how the pulse amplitude diminishes and width increases as it propagates downstream. In Fig. 5 p at $\eta = 0$ is plotted against ξ for several values of τ for the same pulse duration time of 0.9. Figure 6 is similar to Fig. 4 except the pulse duration time is reduced to 0.6. A comparison of Figs. 4 and 6 reveals that for a pulse of shorter duration the pressure at any downstream station rises to a smaller peak. This effect is implicit in the analytical solution obtained by Holmboe and Rouleau [5]. Figure 7 explicitly shows the effect of input duration time on pressure; for pulse durations less than unity the peak pressure

is considerably less than unity. The effect of fluid viscosity on the shape of pulse has also been investigated and the variation of p at $\eta = 0$ with τ for different fluids is given in Table 2. The overshoot in pressure is purely numerical. The table shows that an increase in viscosity causes a reduction in the peak pressure.

Additional numerical experimentation revealed that if the magnitude p_0 of the input is increased then the parameter A and thus the magnitude of convection increases. For A of the order $0(10^{-2})$ some unusual variations of pressure and velocity were noticed in the results. This probably signifies that the explicit treatment of the convection terms in the numerical treatment is not adequate. For density $\rho_0 = 1.7$ slug/ft^2 and $a_0 = 4700$ ft/s an A of the order $0(10^{-2})$ roughly corresponds to $p_0 = 5000$ psi.

Conclusions

The numerical method developed here, based on implicit factorization, allows, for the first time, a two-dimensional solution for fluid transients in viscous, slightly compressible liquids contained in rigid pipes. The complete axial and radial Navier-Stokes equations have been solved, including the terms which represent convection and dispersion, as well as the dissipative shear terms. With the numerical method it is possible to include all these terms with but little extra effort. However, the explicit treatment of the convective terms limits the magnitude that can be accommodated.

The significance of a complete solution is apparent for the water hammer problem, in which particle velocities are relatively high. Radial pressure variations are large near the valve. Upstream from the valve the radial variations decay, and the pressure wave tends to become plane. Dissipation and diffusion are apparent in the pulse problem, but the results show that an initially plane pressure wave remains essentially plane, for the peak pressures considered. A pulse that is initially rectangular, spreads and decays as it travels. This degradation could be a limiting factor in the design of transmission lines.

The results indicate that the pressure waves tend to become plane in certain instances; that is, the radial pressure variations become small compared to the axial variations. It might seem that in these instances, the radial component of the Navier-Stokes equation could be dispensed with, yielding a degenerate plane wave model that would be simpler to solve numerically. However, close examination reveals that the boundary conditions for a viscous fluid, equation (9), cannot be satisfied by such a plane wave model. It follows that the radial component of the Navier-Stokes equations must be retained in order to incorporate the viscous and kinematic boundary conditions in a numerical solution.

Acknowledgment

This research was partially supported by a grant from the Ford Motor Company Research Fund, administererd by Carnegie-Mellon University.

References

1 Wylie, E. B., and Streeter, V. L., *Fluid Transients*, McGraw-Hill, New York, 1978.

2 Zielke, W., "Frequency-Dependent Friction in Transient Pipe Flow," ASME *Journal of Basic Engineering*, Vol. 90, 1968, pp. 109–115.

3 Brown, F. T., "The Transient Response of Fluid Lines," ASME *Journal of Basic Engineering*, Vol. 84, 1962, pp. 547–553.

4 D'Souza, A. F., and Oldenburger, R., "Dynamic Response of Fluid Lines," ASME *Journal of Basic Engineering*, Vol. 86, 1964, pp. 589–598.

5 Holmboe, E. L., and Rouleau, W. T., "The Effect of Viscous Shear on Transients in Liquid Lines," ASME *Journal of Basic Engineering*, Vol. 89, 1967, pp. 174–180.

6 Walker, M. L., Jr., Kirkpatrick, E. T., and Rouleau, W. T., "Viscous Dispersion in Water Hammer," ASME *Journal of Basic Engineering*, Vol. 82, 1960, pp. 759–764.

7 Warming, R. F., and Beam, R. M., "On the Construction and Application of Implicit Factored Schemes for Conservation Laws," Computational Fluid Dynamics," SIAM-AMS *Proceedings*, (H. B. Keller, ed.), Vol. 11, 1978, pp. 85–129.

8 Mitra, A. K., and Rouleau, W. T., "Implicit Methods for the Solution of the One-Dimensional Wave Equation," ASME Symposium on Advances in Numerical Methods in Fluid Transients, Houston, Texas, June 20–22, 1983.

Prediction of Propeller Cavitation Noise From Model Tests and Its Comparison With Full Scale Data

G. Bark
Research Engineer,
Swedish Maritime Research Centre SSPA,
S-400 22 Göteborg,
Sweden

This paper deals with the prediction of propeller cavitation noise from model experiments in a cavitation tunnel. The purpose was to investigate the validity of a simple scaling formula for high frequency cavitation noise, and to get information about the influence of test parameters and analysis methods. The results indicate that the scaling formula normally used at low frequencies can, as a first approximation, be used also at high frequencies. Concerning analysis methods it is demonstrated that the noise signals in model and full scale may have different statistical properties, implying that the simple root-mean-square value of the model signal is not always a sufficient basis for prediction of full scale noise.

1 Introduction

Methods for prediction of propeller cavitation noise can be of mainly three different types based on, respectively:

1) empirical data from a sample of propellers condensed into simple formulas or diagrams for estimation of the radiated noise,
2) measurements of cavitation noise at model tests in, for example, a cavitation tunnel, or
3) theoretical determination of the cavitation development and the corresponding radiation of noise.

The validity of a method of type 1) is often restricted to configurations similar to those on which the method is based. To overcome this drawback development of more general methods was started and in this paper a method of type 2) is investigated. Important problems arising in such a method are those concerning the

1) similarity of cavitation behavior of model and full scale,
2) scaling formulas transforming model noise to full scale data and
3) similarity of the acoustic properties of the model and full scale configurations.

The purposes of the present investigation were:

1) to test the validity of the theory at high frequencies (up to 300 multiples of the blade frequency f_1),
2) to determine of the influence on the noise of different test parameters (e.g., speed of water at model tests) and
3) to investigate of the similarity of the individual pressure pulses as well as the statistical properties of the complete pressure signals.

Contributed by the Fluids Engineering Division and presented at the International Symposium on Cavitation Noise, Winter Annual Meeting, Phoenix, Ariz., November 9–14, 1982, of THE AMERICAN SOCIETY OF MECHANICAL ENGINEERS. Manuscript received by the Fluids Engineering Division, April 6, 1983.

The model tests, carried out at The Swedish Maritime Research Centre SSPA, were a part of a joint project in which also Det norske Veritas (DnV), Norway, The Ship Research Institute of Norway and The Danish Ship Research Laboratory (SL) took part. The full scale data used in this paper were produced by DnV and SL in cooperation with the East Asiatic Company of Denmark (ship owner) and Nakskov Shipyard, Denmark, that built the ships. The ships were the two single screw 32,000 tdw product carriers *M/T Pasadena* and *M/T Patagonia* built as sister ships, but equipped with different propellers. A summary of the activities within the joint project is given in [1] and the present paper is a developed version of [2].

2 Scaling of Cavitation Noise

2.1 Foundations. Scaling formulas and their relation to bubble dynamics are discussed by several authors in for example the references [3–6]. The scaling formulas applied in this paper are based on the theory of radial motion of an inviscid and incompressible fluid outside a spherical cavity. Using certain assumptions, [3], [4], resonable in a first order model, the following formula for the scaling of the continuous part of the power spectrum is obtained:

$$\frac{G_s(f_s)}{G_m(f_m)} = \left(\frac{r_m D_s}{r_s D_m}\right)^2 \left(\frac{\rho_s}{\rho_m}\right)^{1/2} \left(\frac{\Delta P_s}{\Delta P_m}\right)^{3/2} \lambda \qquad (1)$$

For application to the measured sound pressure $p\ (f, \Delta f)$ in a frequency band Δf around the center frequency f equation (1) transforms to

$$\left(\frac{p_s(f_s,\Delta f_s)}{p_m(f_m,\Delta f_m)}\right)^2 = \left(\frac{r_m D_s}{r_s D_m}\right)^2 \left(\frac{\rho_s}{\rho_m}\right)^{1/2} \left(\frac{\Delta P_s}{\Delta P_m}\right)^{3/2} \lambda \frac{\Delta f_s}{\Delta f_m} \qquad (2)$$

If the analysis bandwidth Δf is a constant percentage of the

center frequency f (i.e., $\Delta f = af$, a = constant) equation (2) is reduced to

$$\left(\frac{p_s(f_s,af_s)}{p_m(f_m,af_m)}\right)^2 = \left(\frac{r_m D_s}{r_s D_m}\right)^2 \left(\frac{\Delta P_s}{\Delta P_m}\right)^2 \tag{3}$$

It can also be shown that equation (3) holds for spectral lines as well as for the continuous part of the spectrum, a fact making spectra with constant percentage bandwidth suitable for analysis of propeller noise.

With certain assumptions about the cavitation process and its scaling, [3], [4], the pressure difference ΔP, driving the cavity collapse, can be substituted by a reference velocity V_0 or by the speed n of the propeller shaft. Equation (3) can then be written:

$$\left(\frac{p_s(f_s,af_s)}{p_m(f_m,af_m)}\right)^2 = \left(\frac{r_m D_s}{r_s D_m}\right)^2 \left(\frac{\rho_s}{\rho_m}\right)^2 \left(\frac{V_{0s}}{V_{0m}}\right)^4 = \left(\frac{r_m D_s}{r_s D_m}\right)^2 \left(\frac{\rho_s}{\rho_m}\right)^2 \left(\frac{n_s D_s}{n_m D_m}\right)^4 \tag{4}$$

Using the Rayleigh formula for the collapse time T of a vapour filled spherical cavity, the following expression for frequency scaling is obtained:

$$\frac{f_s}{f_m} = \frac{T_m}{T_s} = \left(\frac{\rho_m}{\rho_s}\right)^{1/2} \left(\frac{\Delta P_s}{\Delta P_m}\right)^{1/2} \frac{1}{\lambda} = \frac{V_{0s}}{V_{0m}} \frac{1}{\lambda} = \frac{n_s}{n_m} \tag{5}$$

According to this approximation the blade freequency $f_1 = nz$, can be used as frequency unit in the propeller noise spectrum.

In the derivations of equations (1) and (5) it is assumed that the cavitation extents are identical in model and full scale at equal cavitation numbers. At well developed cavitation, this assumption is reasonable, (see [7]), but close to incipient cavitation, most model tests suffer from scale effects so that $\sigma_s > \sigma_m$ at identical cavitation extents. The above formulas have then to be modified in accordance with the ideas presented in [4] and [5]. Owing to the simplifications the present scaling formulas are considered as first approximations at high frequencies, while at the lowest multiples of the blade frequency ($\lesssim 5f_1$) these formulas have shown to be entirely relevant ([7]).

2.2 Application of the Scaling Formulas. By using any of the equations (1)–(4) the desired full scale quantity, as for example $G_s(f_s)$, is obtained directly when the corresponding model quantity is known.

It can also be convenient to use certain nondimensional quantities and in accordance with equation (4) and the standard for low frequencies, the nondimensional pressure coefficient K_p is defined as

$$K_p = \frac{p_{\text{rms}}}{\rho n^2 D^2}, \tag{6}$$

where p_{rms} is the root-mean-square sound pressure. The corresponding level $L(K_p)$ is expressed as

$$L(K_p) = 20 \log 10^6 K_p \tag{7}$$

With these quantities the full scale level $L(p_s)$ in the frequency band $\Delta f_s = af_s$ centered at the frequency $f_s = f_m n_s / n_m$ can be expressed as

$$L(p_s) = 20 \log \frac{p_s(f_s,af_s)}{10^{-6}} = 20 \log \frac{p_m(f_m,af_m)}{10^{-6}} + 20 \log \left[\left(\frac{n_s D_s}{n_m D_m}\right)^2 \frac{\rho_s}{\rho_m} \frac{r_m D_s}{r_s D_m}\right] = L(K_{pm}) + 20 \log \left(n_s^2 D_s^2 \rho_s \frac{r_m D_s}{r_s D_m}\right) dB \text{ relative } 10^{-6}\text{Pa} \tag{8}$$

Sometimes a transformation to levels in bands of 1 Hz bandwidth is made. If, however, the occurrence of spectral lines is not fully known, such transformed levels become uncertain and the data are therefore presented as 1/3 octave band spectra in the present paper. Utilizing the structure of the scaling principle as well as the percentage bandwidth, the results can be presented as in Fig. 1 showing the model as well as the full scale results together with the nondimensional quantities.

3 Full Scale Measurements

The noise signals, registered by the hydrophones protruding from the hull plating, were recorded on tape and analyzed in 1/3-octave bands. No visual observations of the cavitation and limiting velocities for incipient cavitation could be performed at the full scale tests. The measurements were carried out on the Atlantic Ocean with sea state 2 for *M/T Patagonia* and 6 for *M/T Pasadena*. Sea state 2 has no significant influence on the propeller cavitation on a ship of

Nomenclature

a = constant relating bandwidth to center frequency in the case of proportional bandwidth
D = propeller diameter
f = frequency
$f_1 = nz$ = blade frequency
Δf = bandwidth
$G(f)$ = power spectral density of pressure signal $p(t)$
$J = \frac{V_A}{nD}$ = advance ratio of the propeller
$K_p = \frac{p_{\text{rms}}}{\rho n^2 D^2}$ = nondimensional pressure coefficient
$L = 20^{10} \log \frac{p_{\text{rms}}}{p_0}$ = sound pressure level in dB *re* p_0 ($p_0 = 10^{-6}$ Pa)
N = relative number of pulses
n = rate of revolutions of propeller shaft
P_v = vapor pressure of water
P_0 = static pressure in reference point
$\Delta P = P_0 - P_v$
$p(t)$ = pressure disturbance (sound pressure)
p_{rms} = root-mean-square value of $p(t)$
r = distance from source point to field point
T = collapse time of a cavity
t = time
V_s = velocity of the ship
V_A = advance velocity of propeller
V_0 = velocity of water in reference point
V_v = mean velocity in test section measured by the tunnel venturimeter
z = number of propeller blades
α/α_s = relative gas content at atmospheric pressure of the water in the cavitation tunnel
$\lambda = D_s/D_m$ = geometric scale factor
ρ = density of water
$\sigma = \frac{P_0 - P_v}{0.5\rho V_A^2}$ = cavitation number where P_0 is the static pressure in the undisturbed flow at the depth of the propeller hub
σ_i = cavitation number at incipient cavitation

Subscripts

m = refers to model scale
s = refers to full scale

this size, while sea state 6, with the waves on the quarter, may modulate the cavitation process considerably.

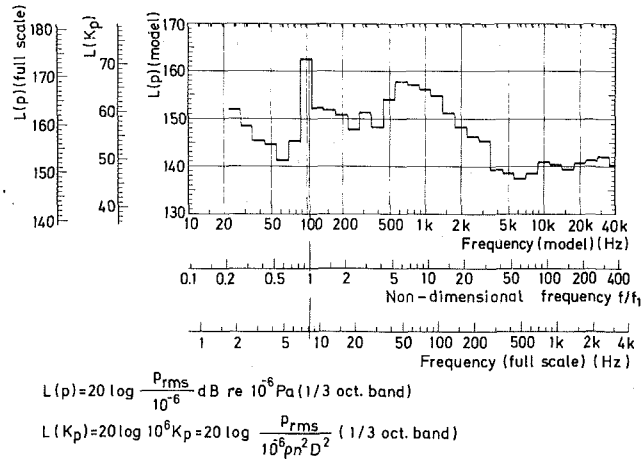

Fig. 1 Example of scaling a 1/3-octave spectrum

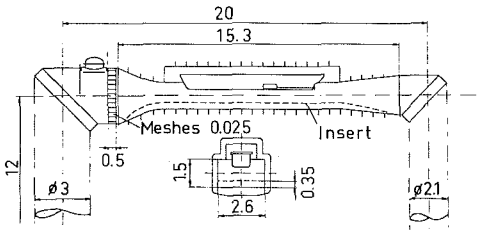

Fig. 2 SSPA cavitation tunnel No. 2. Low speed test section (dimensions in meters)

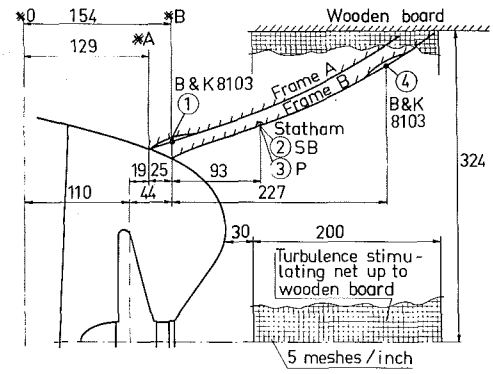

Fig. 3 Ship model. Position of propeller model and pressure transducers (dimensions in millimeters).

4 Model Measurements

4.1 Cavitation Tunnel. The model tests were carried out in SSPA large cavitation tunnel equipped with a test section permitting the use of a complete ship model. In this facility the ship model is completely immersed in water, and the water line is simulated by a 15 mm wooden board. The velocity of the water above the board is zero (Figs. 2 and 3).

4.2 Ship Model. The wooden ship model was 6.89 m long, corresponding to a model scale of 1/23.7.

4.3 Propeller Models. Two propeller models manufactured in bronze, with the diameter 0.236 m, were used at the tests. Propeller P1831 is a model of the conventional propeller used on *M/T Pasadena*, while P1832, used on *M/T Patagonia*, is of a more unconventional design with large blade area, unloaded tips and skew back. Both propellers have 4 blades and a full scale diameter of 5.60 m.

4.4 Measuring Equipment. The propeller-induced pressure pulses were measured by two hydrophones (1 and 4 in Fig. 3) and two strain gauge pressure transducers (2 and 3 in Fig. 3). The pressure transducers were flush-mounted, and the hydrophones were placed with the nose toward the flow direction and mounted in small hollows, so that the acoustic center coincided with the surface of the hull. The transducer positions were identical with those on the ships, where hydrophones of same type were mounted in all four positions. All noise results shown in this paper are obtained from transducer No. 1 close to the center line in frame A. The signals were recorded on an FM tape recorder, and the resulting frequency range of the recorded hydrophone signals was 0.1 Hz - 40 kHz.

4.5 Tests Carried Out. Model tests were carried out at three water velocities and two gas contents α/α_s for the full scale conditions A_1, B_1, D_1, A_2, B_2, and D_2 as shown in Table 1. Some additional tests were also carried out in order to investigate the sensitivity of the cavitation noise to small variations in the cavitation number σ and advance ratio J.

5 Comments on the Experimental Procedure

As is well known, model tests considering cavitation cannot be performed with complete similarity between model and full scale and the development of methods of reducing these discrepancies or "scale effects" is therefore important. Some of these problems will be discussed in this section.

5.1 Cavitation Extent. The discrepancy between model and full scale of the cavitation extents can be expressed by σ_s/σ_m, σ_s, and σ_m being the cavitation numbers at identical cavitation extents in full and model scale respectively. σ_s/σ_m

Table 1 Relative number N of sharp dominating pulses

Ship				*Pasadena* (P1831)			*Patagonia* (P1832)			Mean
Condition				A_1	D_1	B_1	A_2	D_2	B_2	
			σ_{V_A}	19.5	17.9	15.3	17.7	16.3	13.7	
			J	0.390	0.390	0.390	0.412	0.412	0.412	
			V_s(knots)	14.8	15.3	16.3	14.2	14.3	15.8	
			n_s(r/min)	115.5	120.8	132.0	116.6	121.0	132.4	
N	in	Full scale		1.00	1.00	1.00	1.00	1.00	1.00	1.00
		Model	V_v (m/s) α/α_s							
"	"	"	4.5 0.4	0.64	0.47	0.56	0.75	0.71	0.59	0.62
"	"	"	6.0 "	1.09	1.07	0.72	0.67	0.50	0.76	0.80
"	"	"	7.5 "	1.09	1.13	0.89	1.00	1.07	1.00	1.03
"	"	"	4.5 0.7				0.67	0.71	0.47	0.62
"	"	"	6.0 "				0.75	0.71	0.59	0.68
"	"	"	7.5 "				0.83	1.07	1.06	0.99
"	"	"	Mean	0.94	0.89	0.72	0.78	0.80	0.75	

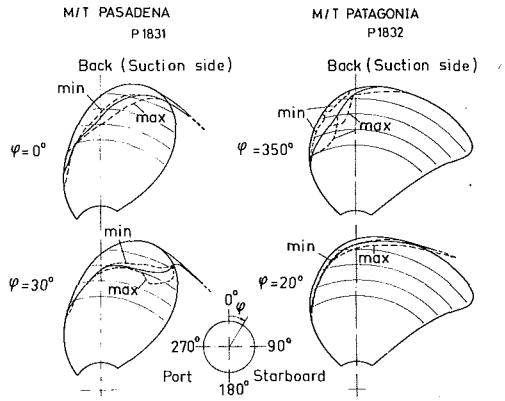

Fig. 4 Cavitation extensions at model tests. Conditions B_1 and B_2, respectively.

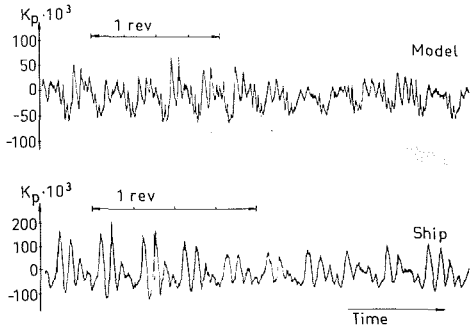

Fig. 5 Pressure signals in the frequency range $f_1 - \approx 300 f_1$ *M/T Pasadena*, (P1831), at full speed, (condition B_1)

$= 1.0$ expresses the vanishing scale effect meaning that the cavitation extents at model and full scale are identical at the same cavitation numbers. For the present facility and the experimental procedure, the upper bound $\sigma_s/\sigma_m \approx 2$ can be expected close to incipient cavitation. At the cavitation extents of the present experiments it can, with reference to [7], be supposed that σ_s/σ_m is much closer to 1 than to the upper bound 2. The approximation $\sigma_s/\sigma_m = 1$ is then reasonable and the scaling formulas (4) and (5) are from this point of view justified.

5.2 Cavitation Number Similarity. Generally Froude number similarity is not maintained in a cavitation tunnel of the present type implying that cavitation number similarity is obtained only at one single depth in the propeller disk. According to SSPA practice this similarity is selected to be at the depth of the propeller hub. As a consequence the model cavitation number at the upper edge of the propeller disk becomes 15 percent too high and hence the cavity volume is slightly reduced in this position.

5.3 Intermittency of Cavitation. It is often observed from films and pressure pulse recordings that the random variations in cavity size from one blade passage to another is larger in model than in full scale. It is also observed that the sizes of the largest cavities in model tests are mostly fairly similar to the largest full scale cavities. In model scale however, these fully developed cavities are more rarely appearing and fewer significant pressure pulses per propeller revolution are therefore generated than in full scale. Since the root-mean-square value p_{rms} of the pressure depends on the pulse height as well as on the occurrence frequency, it is concluded that the use of p_{rms} from model tests in equations (1)–(4) may result in too low predicted full scale levels.

If the insignificant pulses could be identified, the obvious solution would be to exclude them from the analysis. In fact, such a treatment of the signals is performed at SSPA for the prediction of low frequency pressure pulses from propellers [7]. In that method a digital procedure excludes the smallest pulses, resulting from for example noncavitating blade passages and the predicted full scale spectrum then corresponds to model values higher than the root mean squares. The criteria for exclusion of pulses are based on numerous comparisons of model and full scale data.

5.4 Possibilities to Decrease Insignificant Intermittency of Model Signals. Much effort has been made at SSPA to minimize these scale effects and in summary it has been found that the intermittency of the model signal decreases when:

1) a high water velocity is used,
2) the propeller is coated with a matt paint,
3) the ship model is equipped with a net stimulating the turbulence in the wake close to the propeller (Fig. 3) and when,
4) the amount of cavitation nuclei is raised to a certain level by the use of an appropriate gas content of the tunnel water.

5.5 Similarity of the Acoustical Parameters. The present paper deals mainly with the hydrodynamical aspects of cavitation noise prediction and the acoustical similarity problem is only briefly discussed.

The main problem is that certain boundary conditions are hard to realize at model tests. For example the ship and the model were made of different materials (steel and wood, respectively) and the free water surface in full scale was simulated by water-wood-water interfaces at the model tests (Figs. 2 and 3). The corresponding errors, as well as the influence of the relatively distant tunnel walls, can be reduced by an acoustical calibration of the tunnel as well as of the full scale ship. In the present project it was, however, not possible to perform this calibration in full scale, why the method could not be used.

6 Results and Discussion

6.1 Extent of Cavitation. An example of the cavitation extent of the propeller models is shown in Fig. 4. The cavities on P1831 are somewhat larger, and the cavity shape at $\phi = 30$ deg, is such that large voids may break off and collapse violently in the way described in [8].

6.2 Comparison of Pressure Signals. For the estimation of the similarity of individual pulses and their statistical properties the time histories of the signals were traced out on paper. Short sequences of this type are shown in Figs. 5 and 6 in which the amplitude scales are nondimensional according to equation (6).

Figure 5 shows pressure signals corresponding to the frequency range $f_1 - \approx 300\ f_1$, i.e., all significant contributions to the signal are included. In Fig. 6 the low frequency part is subtracted by filtering through the band $50f_1 - 210f_1$, meaning that the individual pulses visible in the clusters correspond to late parts of collapses and early parts of rebounds. On longer recordings it can be seen that for *M/T Pasadena* the full scale signals are less periodic than the model signals. A substantial modulation at frequencies between 0.1 and 0.2 Hz is observed, supporting the assumption that the cavitation is disturbed by the ship motions in the waves (sea state 6). For *M/T Patagonia*, where the full scale measurements were carried out at calm conditions, the resulting signals were more regular than those from the model tests.

By use of long recordings of the type shown in Fig. 6, an estimate was made of the occurrence frequency of sharp and high pressure pulses. The data presented in Table 1 are showing the relative numbers N per blade passage of high

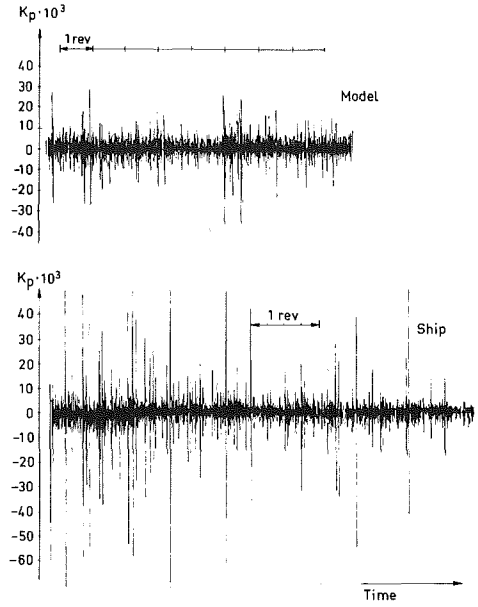

Fig. 6 Pressure signals at high frequencies ($50f_1 - 210f_1$) *M/T Pasadena*, (P1831), at full speed, (condition B_1)

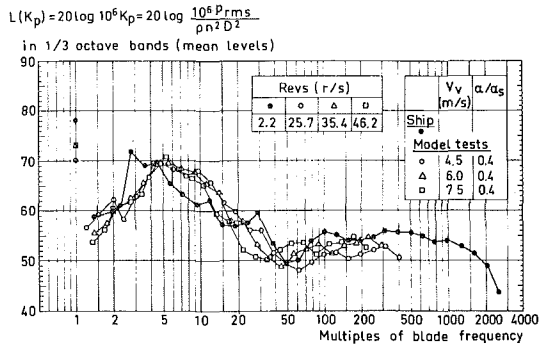

Fig. 7 Nondimensional noise presented as $L(K_P)$ in 1/3-octave bands (mean rms levels). Comparison of full scale data (filled symbols) with model data at three water velocities (open symbols) for *M/T Patagonia* (P1832) at full speed (condition B_2).

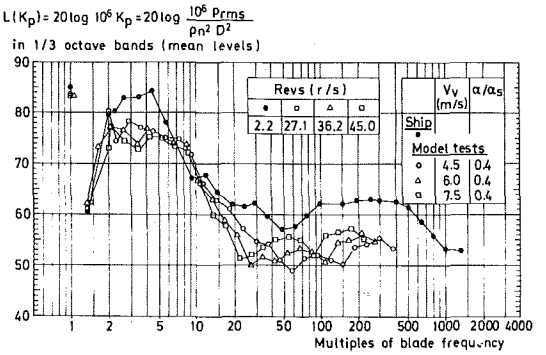

Fig. 8 Nondimensional noise presented as $L(K_P)$ in 1/3-octave bands (mean rms levels). Comparison of full scale data (filled symbols) with model data at three water velocities (open symbols) for *M/T Pasadena* (P1831) at full speed (condition B_1).

pulses divided by the corresponding number in full scale signals (i.e., $N = 1$ at full scale). The conclusion from Table 1 is that there is a significant tendency that the relative numbers N increase towards unity with increasing water velocity, while no effect of the gas content α/α_s is observed. This does however not imply that the number of pulses is independent of the gas content in a wider variation.

6.3 Comparison of 1/3-Octave Band Frequency Spectra. An elimination of effects due to different bandwidths in model and full scale is obtained by using a constant percentage bandwidth at the spectral analysis. 1/3-octave bands were then considered adequate and the analysis was performed with an analog equipment, giving the rms level as a function of time for each frequency band during 5 seconds. The mean value of the rms level over this time is defined as the "mean" rms level, and equals the level normally referred to as the "rms level." The highest rms level during the 5 seconds is referred to as the "maximum" rms level. The introduction of these "maximum" levels is a demonstration of the fundamental idea of using a larger value than the "mean" rms level for the prediction of full scale noise. In future analysis procedures quantities as "mean" and "maximum" should be more sharply defined, and also supplemented by statistical data on the pulse heights obtainable from a pulse height analyzer.

Examples of data made nondimensional according to equations (5) and (7) are presented in Figs. 7 and 8, where "mean" rms levels are used from full scale as well as from model tests at three water velocities. The scaled model levels for *M/T Patagonia* (Fig. 7) are fairly close to the full scale data in a wide frequency range, while the model levels for *M/T Pasadena* are significantly below the full scale levels (Fig. 8). Similar results were also obtained for the conditions *A* and *D*.

An explanation of the difference between the model and full scale levels for *M/T Pasadena* is possible by supposing that the pulse height is amplitude modulated due to ship motions in waves as is proposed in section 6.2. An increase of the rms level in full scale is then predicted by the theory of amplitude modulation also if the mean value of the pulse heights are not changed by the waves.

Referring to the discussion in section 5.3 the full scale levels (mean rms) are finally compared with the "maximum" rms levels from the model tests in Fig. 9. A comparison with Fig. 7 shows a moderate influence of using "maximum" levels for predictions.

6.4 Influence on the Noise Levels of Water Velocity and Gas Content at Model Tests. An inspection of Figs. 7–10 reveals that the levels at blade frequency in most cases increase with water velocity, while the tendency in the rest of the low frequency range varies somewhat. At high frequencies ($\gtrsim 50f_1$) the observations are disturbed by a spectrum waviness not scaling with equation (5). Long recordings of the type shown in Fig. 6 indicate however that the scaled pulse height as well as the occurrence rate (Table 1) increase with the water velocity. An increase is also observed in Fig. 12, where the influence of spectrum waviness is reduced by omitting the frequency scaling (discussed below in section 6.6).

A comparison of Figs. 7 and 10 in the high frequency range indicates that the influence of the gas content of the tunnel water was negligible at 6.0 and 7.5 m/s, while at 4.5 m/s and the higher gas content ($\alpha/\alpha_s = 0.7$), the amount of free gas bubbles in the test section was large enough to disturb the measurements at high frequencies. The conclusion is that $\alpha/\alpha_s = 0.4$ was a sufficiently high gas content in this case, and that a substantial increase above an optimum α/α_s should be avoided.

6.5 Sensitivity of Noise to Variations of Cavitation Conditions. For some reasons the loading condition σ and J of the propeller is only known to a certain approximation, and it is then of interest to know the sensitivity of the noise to variations in σ and J. Such data are given in Fig. 11, showing firstly that the greatest sensitivity of levels to σ-variations occurred between 2 and 6 multiples of the blade frequency, and secondly that the sensitivity at the high frequencies was of

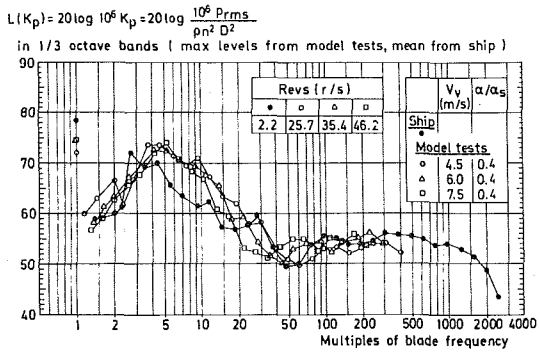

Fig. 9 Nondimensional noise presented as $L(K_P)$ in 1/3-octave bands. "Maximum" rms levels from model scale (open symbols) and mean rms from full scale (filled symbols). *M/T Patagonia* (P1832) at full speed (condition B_2).

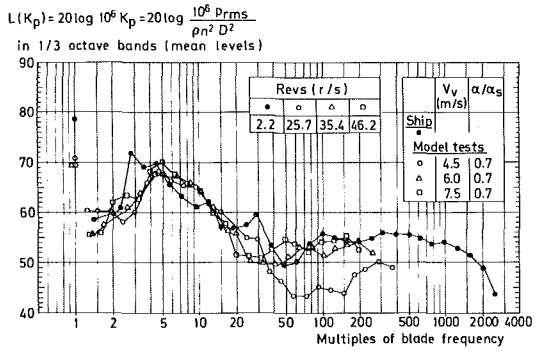

Fig. 10 Nondimensional noise presented as $L(K_P)$ in 1/3-octave bands (mean rms levels). Comparison of full scale data (filled symbols) with model data (open symbols) at three water velocities and extra high gas content ($\alpha/\alpha_S = 0.7$) for *M/T Patagonia* (P1832) at full speed (condition B_2).

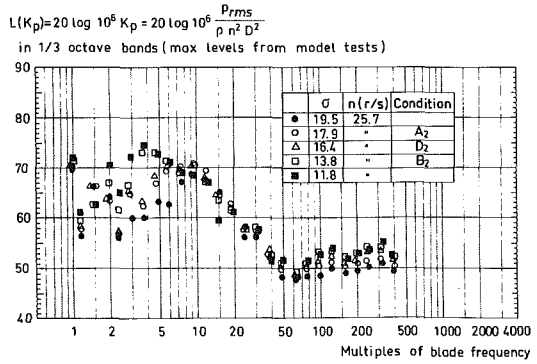

Fig. 11 Variation of σ at $J = 0.412$. Model tests *M/T Patagonia*.

similar order as at the blade frequency. Also the J-variations generated similar results.

These results are expected to be general within certain intervals, but surely they do not hold at conditions close to incipient cavitation or at conditions where the cavity dynamics changes rapidly as for example where break off develops as described in [8].

6.6 Spectrum Form. Figures 7, 8, and 9 demonstrate that the main forms of the model and full scale spectra are fairly similar. In the model results for *M/T Patagonia* it is, however, observed that the peak around five multiples of the blade frequence was wider and shifted to a slightly higher frequency than in full scale. This means that some type of low frequency variations of the cavitation were more developed and faster in the model tests. By comparison of Figs. 7 and 10

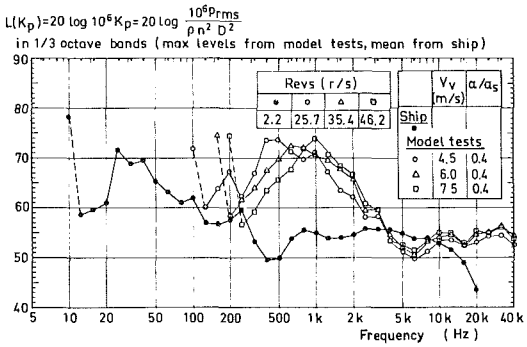

Fig. 12 $L(K_P)$ in 1/3-octave bands. No scaling of frequencies. Condition B_2, *M/T Patagonia*, P1832.

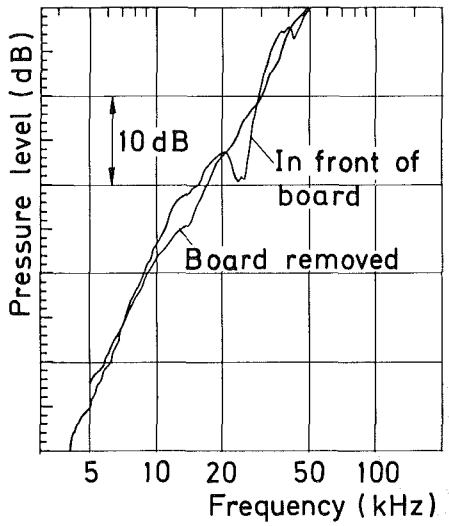

Fig. 13 Reflexion from a wet wooden board (from [9])

it is also noticed that this scale effect on the low frequency peak decreased slightly when the gas content α/α_s was increased from 0.4 to 0.7. Thus it is demonstrated that the highest possible gas content should be used to minimize this scale effect (compare section 6.4).

It is interesting to note that no scale effect of the present type is observed in Fig. 9 showing the *Pasadena* results. In this case the scale effect is however supposed to be masked by the additional fluctuations which the full scale cavitation obtained due to the ship motions in the waves.

The frequency of the peak around five multiples of the blade frequency scales according to equation (5), which is demonstrated in Figs. 7, 8, 9, 10, and 12. This is, however, not true for the wavy pattern between 10 and 30 kHz. In Fig. 12, where no frequency scaling is applied, it is demonstrated that this wavy pattern in fact is independent of the shaft speed.

In principle, this spectrum pattern could have been generated by sound wave reflexions at the model boundary as is demonstrated in Fig. 13 showing the pressure level 10–20 mm in front of a 500 × 500 × 20 mm wet board of wood immersed in a 4 × 3 × 2 m water basin. These levels are compared with levels measured after removing the board. Using a gating system the influence of the reflexions from the basin walls was eliminated. The hull thickness of the present wooden ship model was about 50 mm, and the center of the hydrophone was located 5 mm from the hull surface. Supposing the interference pattern to be dominated by reflexion in the interface closest to the hydrophone, the minimum at 15 kHz can be explained as being a node at a quarter of a wave length from the interface. The frequency and distance

correspond to a velocity of sound of about 300 m/s, which is a rather low, but not an impossible value in the partly bubble filled water. It is also observed that the simple relation of frequency to the shaft speed breaks down already around $15f_1 - 30f_1$ ($\approx 2-4$ kHz) (Figs. 9 and 12), corresponding to a yet lower velocity and sound or a reflexion in another interface.

Another comment to the failure of frequency scaling is that the present way of applying equation (5) relies on the assumption that also the final collapse velocity is firmly related to the shaft speed. Objections may be raised against this assumption, and for example it is noted that Baiter proposed a different behavior of shock pulses in [3] (p. 22).

The conclusion from this discussion is that the non-scaling spectrum waviness was probably caused by wave reflexions but there may also be other explanations.

7 Sources of Error

The following comments are made about the sources of error influencing the present investigation:

1) The instrumentation errors at acoustical measurements were in model as well as in full scale tests typically 1 dB.
2) The reading and plotting errors were typically $\lesssim$ 1 dB for the acoustical data.
3) The scattering of the full scale data at repeated measurements was about 1-2 dB at high frequencies and the blade frequency, while it was 3-5 dB in the range $2f_1 - 5f_1$. The corresponding model data were 1 and 2-3 dB, respectively.
4) J and σ are known within ± 6 and ± 13 percent, respectively, which, according to Fig. 11 and its counterpart for J-variation, corresponds to level errors of about 1 dB.
5) Errors arise when the same standard frequency analysis is applied to model and full scale signals with different statistical properties. The tendency is normally that an rms analysis will provide too low levels for prediction. The difference between the "maximum" and the mean levels shown in Figs. 7 and 9 may indicate the order of magnitude of this error to 1-5 dB.
6) The model levels at high frequencies are decreased by about 1 dB due to the Froude number effect discussed in section 5.2. This type of error can easily be compensated for by measuring at small σ-variations as shown in Fig. 11.
7) The error caused by the lack of similarity in the boundary conditions may be estimated by acoustical calibrations. The standard method is to substitute the propeller by a loudspeaker calibrated in free field and then to compare the signal from this source with the signal from the propeller. Such calibrations have to be performed also in full scale, if the intention is to compare model and ship noise data.

   The importance of calibration also in full scale is demonstrated in [10], showing that the resonant vibration of hull plates may increase the pressure level outside a plate by 10–15 dB.

   From general considerations it can be expected that the simulation of the steel ship by a wooden model would decrease the measured model noise, while an increase would be obtained because the free water surface in full scale was simulated by water-wood-water interfaces. The net effect, depending on for example the transducer position, is not known at this stage.
8) It is also remarked that Mach number similarity cannot normally be obtained in experiments of the present type meaning that relations between distance and wave lengths are not identical in model and full scale. The discrepancies are however moderate, and the effects on directivity and the extent of the near field may then be neglected.
9) No problems occurred due to background noise being 20–30 dB below the noise from the cavitating propeller.

   In estimating the total error it may be expected that those of types 1, 2, 3, and 4 are randomly + or −, while those of types 5, 6, and perhaps 7 lowered the noise in the model tests. Because of the uncertainty in some of the error estimations a summation is however avoided, and the conclusion is that further experience from model as well as full scale measurements is required for an estimation of the total uncertainty.

8 Summary and Conclusions

The following conclusions are made from the present experiments:

1) Concerning the model test parameters it was found that the highest water velocity resulted in the best agreement with the full scale data. This is true for the pulse statistics (Table 1) as well as the spectrum levels (Figs. 7, 8, 9). Two values of the gas content parameter were tested (α/α_s = 0.4 and 0.7). Apart from a slight influence on the low frequency peak (section 6.6) the results were not very sensitive to this variation, indicating that α/α_s = 0.4 was sufficiently high at the present conditions. If however the gas content is too high, the cavitation noise at high frequencies will be damped by the gas bubbles (Fig. 10), and if it is too low, the cavitation will be increasingly intermittent, which will cause difficulties at the analylsis.
2) The shapes of individual pressure pulses were rather similar in model and full scale. The model signal contained however fewer collapse pulses per propeller revolution and then the root-mean-square value is not entirely significant for the prediction of full scale noise. Based on this observation, guidelines are discussed for an analysis procedure disregarding signal parts which according to certain criteria are insignificant.
3) The spectrum shape is fairly similar in model and full scale. Discrepancies were however observed, and for example the peak around five multiples of the blade frequency was slightly shifted towards higher frequencies in the model tests. It was also found that the frequency was scaling with the shaft speed (or blade frequency) up to 20–40 multiples of the blade frequency, while the spectrum pattern was independent of the shaft speed at the highest frequencies. This behavior was attributed to wave reflexions at the hull or possibly to a development of collapse pulses different from that supposed in the scaling formula.
4) Also if more experience is needed, the adopted level scaling seems to be adequate and, supplemented by refined methods of signal analysis and acoustical calibration, model tests of this kind seems to be useful for the prediction of the full scale noise. It is further concluded that, at most conditions, the sensitivity to errors in σ and J was not larger at high frequencies than at the blade frequency.

Acknowledgments

The author is indebted to the Swedish Board for Technical Development for sponsoring the present investigation and to Dr. Hans Lindgren, Director General of SSPA, for the opportunity to carry out this investigation and thanks are also

due to those members of the staff at SSPA who took part in the work and to those who provided the full scale data.

References

1 Nilsson, A. C., and Tyvand, A. P., (ed), "Noise Sources in Ships. I: Propellers," Final Report from a Nordic Co-operative Project: Structure Borne Sound in Ships from Propellers and Diesel Engines. Miljövårdsserien 1981:2. Published by Nordforsk, P.O. Box 5103, S-10243 Stockholm, Sweden.

2 Bark, G., "Prediction of Cavitation Noise from Two Alternative Propeller Designs. Model Tests and Comparisons with Full Scale Results," International Symposium on Cavitation Noise, ASME, Phoenix, Ariz., Nov. 1982, edited by R. E. Arndt and M. L. Billet, pp. 61-69.

3 Baiter, H.-J., "Aspects of Cavitation Noise," Symposium on "High Powered Propulsion of Large Ships," organized by Netherlands Ship Model Basin, Wageningen, Dec. 1974.

4 Strasberg, M., "Propeller Cavitation Noise After 35 Years of Study," *Proc ASME Symposium on Noise and Fluids Engineering*, Atlanta, Ga., pp. 89-99.

5 Blake, W. K., and Sevik, M. M., "Recent Developments in Cavitation Noise Research," International Symposium on Cavitation Noise ASME, Phoenix, Ariz., Nov. 1982, edited by R. E. Arndt and M. L. Billet, pp. 1-10.

6 Ross, D., *Mechanics of Underwater Noise*, Chapters 7, 8, Pergamon Press, 1976.

7 Johnsson, C.-A., Rutgersson, O., Olsson, S., and Björheden, O., "Vibration Excitation Forces from a Cavitating Propeller. Model and Full Scale Tests on a High Speed Container Ship," 11th ONR Symposium on Naval Hydrodynamics, London, 1976 (or SSPA Publication No. 78).

8 Bark, G., and Van Berlekom, W. B., "Experimental Investigations of Cavitation Noise," 12th Symposium on Naval Hydrodynamics, Washington, D.C., 1978 (or SSPA publication No. 83).

9 Munk, T., and Spangenberg, S., "Sammenligning mellem fuldskalaog modelskala-målinger af kavitationsstøj på M/T Patagonia og M/T Pasadena" (in Danish). Skibsteknisk Laboratorium, Lyngby, Denmark. Report SL 78912.30/4, 1980.

10 Nilsson, A. C., "Propeller Induced Hull Plate Vibrations," *Journal of Sound and Vibration*, Vol. 69, No. 4, 1980, pp. 539-557.

due to those members of the staff at SSPA who took part in the work and to those who provided the full scale data.

References

1 Nilsson, A. C., and Tyvand, A. P., (ed), "Noise Sources in Ships. I: Propellers," Final Report from a Nordic Co-operative Project: Structure Borne Sound in Ships from Propellers and Diesel Engines. Miljövårdsserien 1981:2. Published by Nordforsk, P.O. Box 5103, S-10243 Stockholm, Sweden.

2 Bark, G., "Prediction of Cavitation Noise from Two Alternative Propeller Designs. Model Tests and Comparisons with Full Scale Results," International Symposium on Cavitation Noise, ASME, Phoenix, Ariz., Nov. 1982, edited by R. E. Arndt and M. L. Billet, pp. 61-69.

3 Baiter, H.-J., "Aspects of Cavitation Noise," Symposium on "High Powered Propulsion of Large Ships," organized by Netherlands Ship Model Basin, Wageningen, Dec. 1974.

4 Strasberg, M., "Propeller Cavitation Noise After 35 Years of Study," *Proc ASME Symposium on Noise and Fluids Engineering*, Atlanta, Ga., pp. 89-99.

5 Blake, W. K., and Sevik, M. M., "Recent Developments in Cavitation Noise Research," International Symposium on Cavitation Noise ASME, Phoenix, Ariz., Nov. 1982, edited by R. E. Arndt and M. L. Billet, pp. 1-10.

6 Ross, D., *Mechanics of Underwater Noise*, Chapters 7, 8, Pergamon Press, 1976.

7 Johnsson, C.-A., Rutgersson, O., Olsson, S., and Björheden, O., "Vibration Excitation Forces from a Cavitating Propeller. Model and Full Scale Tests on a High Speed Container Ship," 11th ONR Symposium on Naval Hydrodynamics, London, 1976 (or SSPA Publication No. 78).

8 Bark, G., and Van Berlekom, W. B., "Experimental Investigations of Cavitation Noise," 12th Symposium on Naval Hydrodynamics, Washington, D.C., 1978 (or SSPA publication No. 83).

9 Munk, T., and Spangenberg, S., "Sammenligning mellem fuldskalaog modelskala-målinger af kavitationsstøj på M/T Patagonia og M/T Pasadena" (in Danish). Skibsteknisk Laboratorium, Lyngby, Denmark. Report SL 78912.30/4, 1980.

10 Nilsson, A. C., "Propeller Induced Hull Plate Vibrations," *Journal of Sound and Vibration*, Vol. 69, No. 4, 1980, pp. 539-557.

DISCUSSION

H.-J. Baiter[1]

Power density spectra of cavitation noise predicted from a model test will, in general, conform unsatisfyingly with corresponding spectra determined on full scale. As far as experimental faults can be excluded, the applied scaling relations must be blamed for the discrepancy. But it may be allowed to consider the scaling relations principally correct and only affected by some dissimilarity. In this case two questions arise. Can the influence of the dissimilarity be removed in advance by experimental means as surface roughness or artificial cavitation nuclei? And, if the occasion arises, can the dissimilarity be corrected for afterwards by modifications of the scaling relations?

The last mentioned question is a main concern of G. Bark's paper. Based on usage developed at SSPA he suggests to scale the spectral level using a maximum rms sound pressure instead of a mean rms sound pressure. This takes into account that the blades of a model propeller occasionally refuse to produce cavitation noise when passing through the model ship's wake, whereas on full scale the noise production is much the same for each blade passage. Using maximum values of the rms sound pressure means to rate only those blade passages of the model propeller, which can be considered representative with respect to full scale.

To improve this modification to cavitation noise scaling for future practice, G. Bark suggests to base it on a more sophisticated pulse height analysis. However, not only pulse heights should be taken into account but also pulse widths. This appears particularly important with respect to the shape of the spectral hump, which typically appears in the low frequency range (in the results reported by Bark below about the twentieth multiple of the blade frequency).

[1] Fraunhofer-Institut für Hydroakustik, Fed. Rep. of Germany.

To point out this importance, the theoretical model of propeller cavitation noise proposed in [11] may be helpful. Irrespective of how far this model applies in detail, some general conclusions can be drawn from it. Due to these conclusions the width of the spectral hump as well as its location along the frequency scale depend on characteristic time parameters of the cavitation events occurring within the blade passage periods. One of these parameters is in any case the overall duration of the cavitation noise events. In addition, the duration of particulars can be of influence as for instance the duration of noise pulses generated by collapsing bubble clouds. Also typical retardations between different particulars come into question. Besides the mean values of such quantities also their standard deviations have to be taken into consideration. It is not unlikely that the one or other of these parameters does not conform with the assumed scaling rule for the time scale (Bark's equation (5)), and this could explain why the nondimensional plot of the spectral hump attains different shapes and locations for model and full scale (see Bark's comments "Spectrum Form").

Another possible reason for deviations from equation (5) is nonlinear effects during the final collapse phase of the single cavitation bubbles. As conjectured by Bark this influence may be responsible for the considerable spread of the nondimensional spectral plots fo Figs. 7-9 respecting the right-hand flank of the spectral hump. Though this cannot be excluded so far, the above discussed parameters seem to offer a more obvious explanation.

In my opinion the position of the right-hand flank of the spectral hump is mainly defined by the reciprocal of the mean duration of pressure pulses generated by collapsing bubble clouds. According to equation (5) the duration of such pulses should be proportional to the characteristic length. But the model and full scale data of Figs. 7-9 indicate a proportionality to some power of the characteristic length, the power being smaller than unity (in other words: the pulse duration in the model case is likely to be longer than it should be in correspondence with (5)). Similarly, according to equation (5) the pulse duration should be inversely proportional to the flow velocity. But the data of Figs. 7-9 indicate a proportionality to some power of the reciprocal velocity, the power being smaller than unity (in other words: performing model tests at constant cavitation number and increasing the velocity, the pulse duration is likely to be reduced to a smaller extent than predicted by (5)). Do the pressure signals observed in the full scale and model tests give evidence of such trends?

Additional Reference

11 Baiter, H.-J., "An Extended Base for the Statistical Description of Cavitation Noise," *International Symposium on Cavitation Noise*, ASME , Phoenix, AZ, Nov. 14-19, 1982, pp. 93-108.

Author's Closure

I generally agree to Baiter's 1st and 2nd paragraphs and will only add that it often seems necessary to improve the similarity not only by artificial means (surface roughness and a high density of cavitation nuclei) but also by using analysis methods taking account of the remaining dissimilarities. An approach of the latter kind is applied to the data in Fig. 9 of the paper. To obtain in the best similarity for the cavitation process, tests at SSPA are carried out at the highest possible velocity and gas content of the water. A small roughness on the propeller blades is also used as a standard.

As Baiter claims in the 3rd paragraph, it is known from the spectrum theory that the width of the hump centered around five multiples of the blade frequency depends primarily on the pulse duration. Taking account also of scale effects in this parameter would result in more precise predictions of the spectrum form at certain frequencies, which of course is of interest in refined models. The use of a pulse height analysis,

as suggested in the paper, is only a method to reduce the effect of the fact that fewer pulses occur in the model tests than in full scale. To ignore this discrepancy will result in an underprediction of the noise level. Based on observations of the pressure signals, the effect of fewer pulses occurring in model scale can, in the present case, be claimed to be more important than the scale effect on the form of the individual pulses, which was found to be moderate.

In the 4th paragraph, Baiter points out that, according to the additional reference ([11]), the details of the spectrum hump depend on the mean values, as well as on the standard deviations of several parameters. In connection with this remark it should be noted that, in the model results, the peak of the hump is more independent of the water velocity than is the high frequency flank around twenty multiples of blade frequency.

The higher the velocity, the lower is the frequency of the right end of the hump (Figs. 7-10). This result is in accordance with the idea of a stronger random modulation of cavitation events at lower water velocities, as reported in the paper, and hence the standard deviation due to this modulation of pulse parameters may be important in the present case.

Concerning Baiter's last paragraph it can be reported that the dimensionless pulse duration of the *dominant* pulses responsible for the hump, is roughly independent of the water velocity. At the lower velocity (4.5 m/s) there are however a certain amount of pulses of roughly 20-30 percent shorter duration than at 7.5 m/s. The shaft speeds at these velocities were 25.7 and 46.2 r/s, respectively, meaning that the increase in pulse duration is not sufficient to explain the frequency shift of the high frequency flank. (The peak of the hump is not shifted significantly.)

The influence of the scale effect on the pulse duration, combined with the widening of the hump due to modulation as discussed above, may however result in the observed behaviour of the spectrum around twenty multiples of the blade frequency.

As stated in the paper, as well as by Baiter, there are several possible explanations of the deviations from the simple scaling theory. For a better understanding it is thought that specially designed experiments are needed in which the dynamics of the individual cavities, as well as the statistics of the whole process, are investigated with respect to the problems discussed above.

A Limited Role of Separation Bubble in Desinent Cavitation

Y. Ito

Research Assistant.

R. Oba

Professor.

Institute of High Speed Mechanics,
Tohoku University,
Sendai, Japan

In order to clarify whether a separation bubble always plays an important role, the desinence of streamer-cavitation, a kind of attached-cavitation, was carefully investigated in typical internal flows through venturies with and without a 40 μm thin backward facing step under a prescribed cavitation nuclei as well as various hydrodynamic conditions. The following facts have been found: (i) the separation bubble can play an important role in the desinence only when the separation bubble thickness H is larger than the diameter of nucleus d_{np} that may grow up to a critical one [18], (ii) a marked change takes place in the desinent cavitation number σ_d due to the step, i.e., $\sigma_d \cong |C_{ps}|$ for $H > d_{np}$ but $\sigma_d < |C_{ps}|$ for $H \leqq d_{np}$, (iii) for the cavitation there are two geneses, i.e., the nuclei floating within the separation bubble and the bubble-cloud occurring in the reattachment-region.

Introduction

The mechanism of cavitation inception comes up as an essential problem, since the associated vibration, intolerable noise, and structural damage arise immediately when cavitation initiates. Relating to their hydrodynamic environment, there are several types of cavitation-bubbles with their own aspects, behavior, geneses, as well as zones where cavities occur, resulting in a wide scatter in the desinent or the incipient cavitation number.

According to the literature [1, 2], the cavitation does not always initiate at the point of minimum pressure, and often initiates in a region of higher pressure, near the transition or the reattachment-region of the separated laminar boundary layer. Recently, it has been suggested that the laminar separation bubble can play an important role in the inception of attached-cavitation [2–7], and that the cavitation number σ_i should directly be related to the pressure coefficient at boundary-layer separation-point C_{ps} as $\sigma_i \cong |C_{ps}|$ [2, 3]. Meanwhile we have demonstrated somewhat singular facts indicating $\sigma_d < |C_{ps}|$ in the desinence for the streamer-cavitation [7], a kind of the attached-cavitation, in a typical flow through the venturi. It is, therefore, doubtful to the authors whether such a separation bubble plays always an important role in the desinence.

In this paper, therefore, as the first step to clarify more precisely the role of the separation bubble and the cavitation nuclei in the desinent cavitation, the behavior of the separation bubbles and the related streamer-cavitation are carefully observed in typical internal flows through venturies, under prescribed flow conditions.

Experimental Facilities

The test was conducted in the existing closed-type water-tunnel [7, 8] installed with a reservoir of large capacity. In order to control the freestream turbulence, which is known to be one of the powerful factors on the inception [9], a turbulence generating grid was installed 6 mm upstream from the venturi, in which a large number of 3 mm × 3 mm holes formed a net of 4 mm meshes on a 0.5 mm thin brass-plate to prevent cavitation at the grid itself.

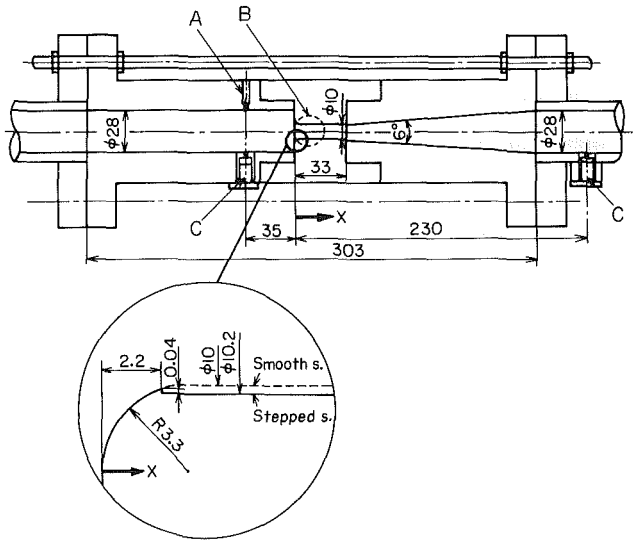

Fig. 1 Test venturies (all dimensions are in millimeters)

Two kinds of perspex-test-venturies were prepared for the present test, i.e., the smooth surface without a step and the stepped surface shown in Fig. 1. The smooth surface venturi had the throat-diameter D_T of 10 mm and the throat length of 29.7 mm, so that the area ratio $(D_T/28)^2 = 0.128$. The stepped surface venturi, however, has a 40 μm thin backward facing step, as large as the cavitation nuclei, which was made slightly upstream from the boundary-layer separation-point measured on the smooth surface, in order to assure separation-bubble-occurrence there.

Contributed by the Fluids Engineering Division and presented at the International Symposium on Cavitation Inception, Winter Annual Meeting, Phoenix, Ariz., November 9–14, 1982 of THE AMERICAN SOCIETY OF MECHANICAL ENGINEERS. Manuscript received by the Fluids Engineering Division, May 17, 1983.

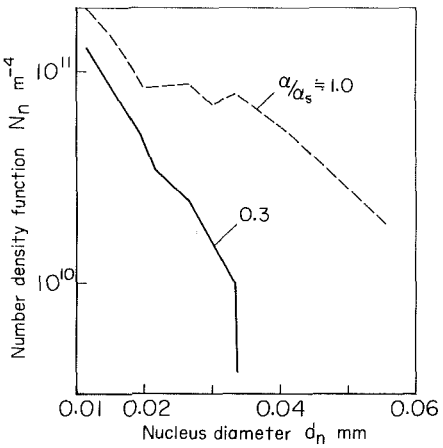

Fig. 2 Nuclei-size-spectra of sample water (Uncertainties of α/α_s and N_n are ± 5 and ± 10 percent, respectively)

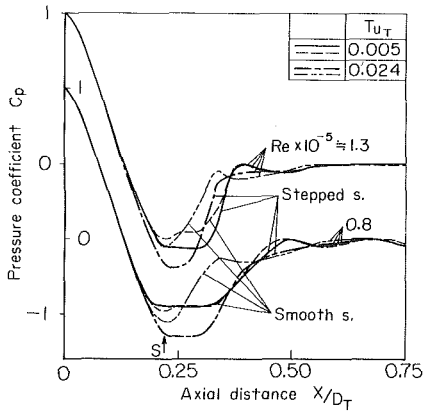

Fig. 3 Axial surface-pressure-distribution of test venturies (Uncertainties of C_p is ± 5 percent)

The upstream static pressure P_1 and the mean velocity U_1 were always monitored at the section "A" by means of pressure transducers "C," which were set through a pressure-hole, 0.6 mm in diameter, 1 mm long, with a kind of silicone-oil inserted to match the acoustic impedance. To detect cavitation events carefully, a PZT-probe "B" was fixed on the outer surface $1D_T$ downstream from the throat [8]. The local mean velocity U, the fluctuating velocity u and the turbulent intensity $T_u = \sqrt{\bar{u}^2}/U$ were measured by a Laser velocimeter. The nuclei-size-spectra in our sample water was measured by a Coulter-counter whose orifice made of ruby, was 0.2 mm in diameter and 0.15 mm long, while the relative air content α/α_s was measured by Numachi's method [10].

Experimental Procedures

The fresh tap water or the degassed one was first poured into the tunnel as described in references [7, 8]. The nuclei, one of the most powerful factors [9], were checked after 3 min of water-recirculation under the constant pressure P_1 of 100 kPa, when the cavitation is expected to be stable, to determine whether or not the spectra fitted the prescribed one shown in Fig. 2. Figure 2 illustrates the typical nuclei-size-spectra, where N_n is the number density function.

By considering the rather small test section as well as the corresponding thin separation-bubble-thickness,the flow patterns, especially the aspects of separation bubbles, were visualized by coating a very thin, 1 mm wide, oil-paint mixture over the venturi-throat-inlet [7].

The local pressure distribution was measured through 26 pressure taps of 0.3 mm in diameter, which were precisely vertically drilled on the throat surface, from the inlet to the exit.

Cavitation-inception was detected in the desinent state, both visually and acoustically, with the PZT-probe, and the cavitation aspects were photographed simultaneously with the corresponding flow-measurements. We used a high speed-camera, whose maximum framing rate was about 44,000 frames per second with a microscope of 10 magnification, and a 35 mm camera with a xenon-flash-lamp, whose exposure time was 3 μs.

The cavitation number σ and the pressure coefficient C_p are, respectively, defined as $\sigma = 2(P_T - P_V)/\rho U_T^2$ and $C_p = 2(P - P_T)/\rho U_T^2$, where the pressure P_T and the velocity U_T were measured at the throat, $X \cong 7$ mm, in which the axial velocity and the turbulent intensity were almost uniformly distributed [7]. And P_v and ρ are the vapor pressure and the density of water, respectively.

The range of test conditions was 0.09 ~ 0.45 for σ, 5 ~ 20 m/s for U_T, so that $R_e = (0.7 \sim 1.93) \times 10^5$ where $R_e = U_T D_T/\nu$ (Reynolds number). The upstream static pressure P_1 was 50 ~ 190 kPa, the turbulent intensity $T_{uT} = \sqrt{\bar{u}^2}/U_T$ was 0.005 or 0.024 and the upstream turbulent intensity T_{u1} was 0.021. The relative air content, α/α_s, was 0.3 or 1.0, so that $(\alpha/\alpha_s)_T$ was 0.9 ~ 6 at the throat and the water temperature t_w was 287 ~ 298 K, where ν was the kinematic viscosity of water.

Results

Basic Flow Pattern. First, we will examine the oil-film

Nomenclature

C_p = pressure coefficient = $2(P - P_T)/\rho U_T^2$
C_{ps} = pressure coefficient at boundary-layer separation-point
C_{pm} = minimum pressure coefficient
D = diameter
d_n = nucleus diameter
d_n,crit = critical nucleus diameter
d_{np} = powerful nucleus diameter
H = separation bubble thickness
h = step height
l = separation bubble length
N_n = number density function of nucleus
P = static pressure
P_v = vapor pressure of water
R_e = Reynolds number = $U_T D_T/\nu$
$R_{e,crit}$ = critical Reynolds number
T_u = turbulent intensity = $\sqrt{\bar{u}^2}/U$
t_w = water temperature
U = freestream velocity
u = fluctuating velocity
X = axial distance
α/α_s = relative air content of water under the standard temperature and pressure
ν = kinematic viscosity of water
ρ = density of water
σ = cavitation number = $2(P_T - P_V)/\rho U_T^2$
σ_d = desinent cavitation number
τ = time

Subscript

1 = upstream from venturi
BE = beads
SB = streamer-bubble
SM = smooth surface without a step
ST = stepped surface
T = venturi-throat

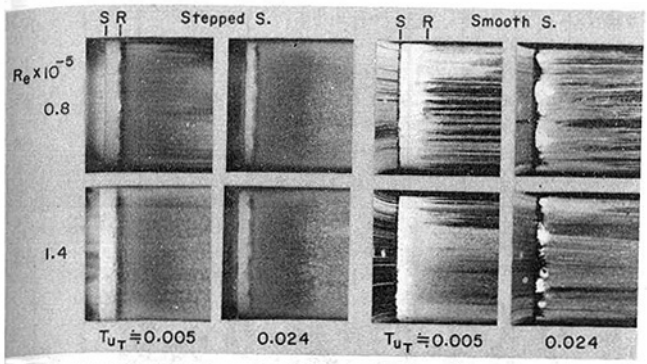

Fig. 4 Oil-film patterns on venturi-throat-surface for various Reynolds numbers R_e and turbulent intensities T_{uT}

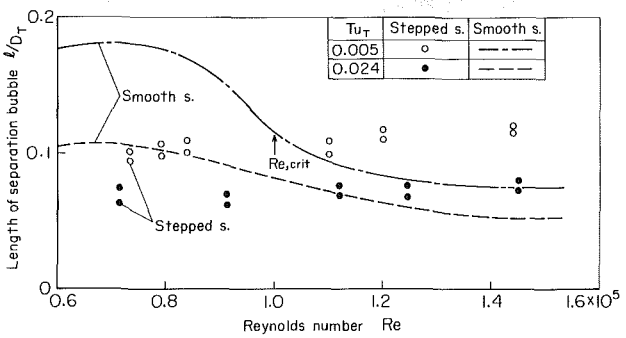

Fig. 5 Length l of separation bubbles (Uncertainty of l is ± 2 percent)

patterns as well as the pressure-distribution on the inner venturi-surface, in order to identify the detailed aspects of the separation bubbles which should be dominantly related to the cavitation inception [2–4]. Figure 3 illustrates, the pressure coefficient C_p versus the axial distance X/D_T, in cavitation-free states for various Reynolds numbers R_e at two typical turbulent intensities $T_{uT} \cong 0.005$ and 0.024. The results include both cases with and without the thin step, where S and R in Figs. 3 and 4 show the boundary-layer-separation and the reattachment, respectively. In Fig. 4 the oil-spots remaining between S and R indicate clearly the existence of a laminar separation bubble, suggesting an evidence of three-dimensional flows. For the lower turbulent flow on the smooth surface illustrated in Fig. 4, a number of streamerlike-slender oil-spots with almost uniform dimensions were circumferentially arranged with almost equal spacing on the throat. This suggests the existence of streamerlike separation bubbles described earlier [7], while for the higher turbulent flow such spots fluctuated somewhat in the positions, sizes and numbers. Especially, for the stepped surface, the patterns seem to be almost independent of R_e or T_{uT}, and the three-dimensional structure within the bubbles almost vanished. While the minimum pressure coefficient[1] C_{pm} was lowered by 0.1 on the average, the lower pressure zone was somewhat lengthened, as is shown in Fig. 3. It is to be emphasized here that the separation bubble is not only three-dimensional and time-dependent in its major features, but also it is not necessarily stationary in space.

Figure 5 shows the bubble-length l evaluated in the oil-film patterns, comparing it with various R_e and T_{uT}. Here we denote the subscripts ST and SM for "with the step" and "without the step." Clearly on the smooth surface, the bubble-length l_{SM} changed rapidly in the range of critical Reynolds number $R_{e,crit}$ from 0.9×10^5 to 1.1×10^5, while l_{ST} on the stepped surface was held roughly constant at a fixed T_{uT} in the entire range of R_e. Notice here that the separation

[1] As expected there is no marked change in C_{pm}.

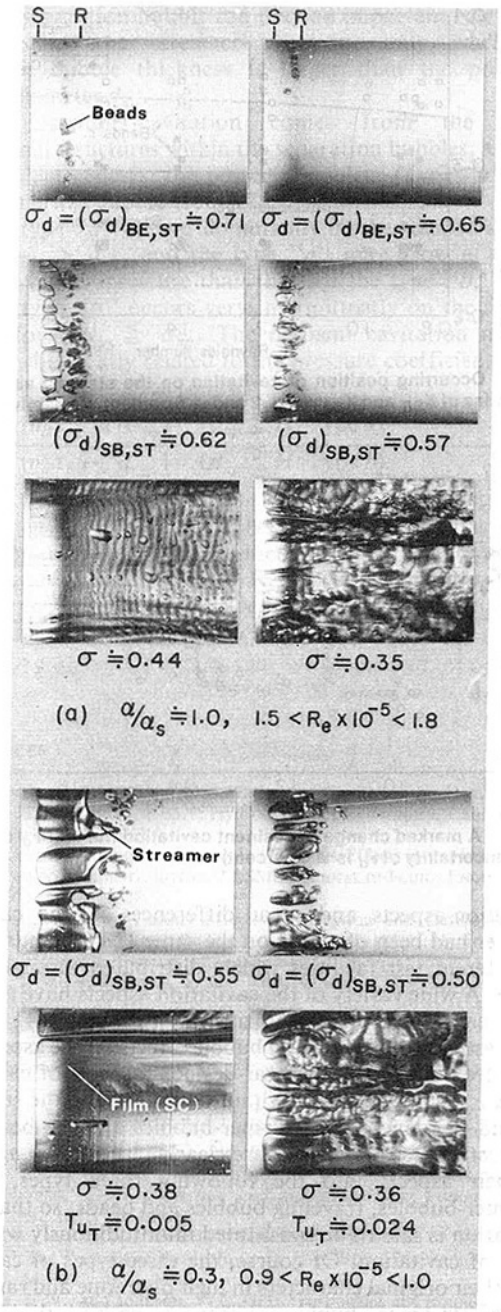

Fig. 6 Near-desinent aspects of cavitation on the stepped surface

bubble has to be a "long" bubble for $R_e < R_{e,crit}$, while it has to be a "short" bubble for $R_e \geqq R_{e,crit}$ [7], because the Brennen-waves [11] showing the transition of boundary layer were clearly observed on the streamer-bubble surfaces for $R_e \geqq R_{e,crit}$.

Such a short-bubble, in which the transition and the turbulent reattachment result in a sufficiently high fluctuating pressure, may play an important role in the cavitation inception [2–7]. Then, we tried to evaluate the separation bubble thickness H defined by the maximum distance from the rigid wall to the separated shear-layer. By using Tani's analyses [12], the thickness for the smooth surface H_{SM} is estimated to be about 0.02 mm, so that the corresponding thickness on the stepped surface $H_{ST} \cong H_{SM} + h$ is 0.06 mm, when we consider the step-height $h \cong 0.04$ mm. Then $H_{ST} \cong 3 H_{SM}$.

Aspects of Desinent Cavitation. A follow-up study by Johnsson [13] demonstrated that a wide variety of incipent

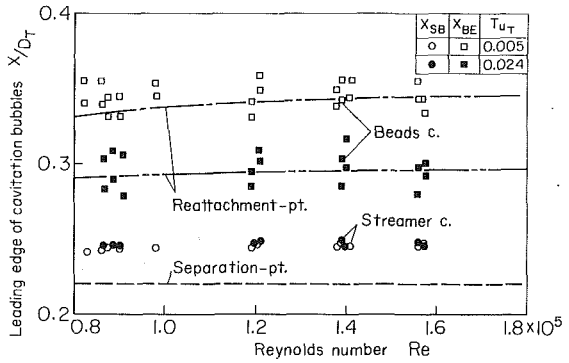

Fig. 7 Occurring position of cavitation on the stepped surface (Uncertainties of X_{SB} and X_{BE} are ± 2 and ± 5 percent, respectively)

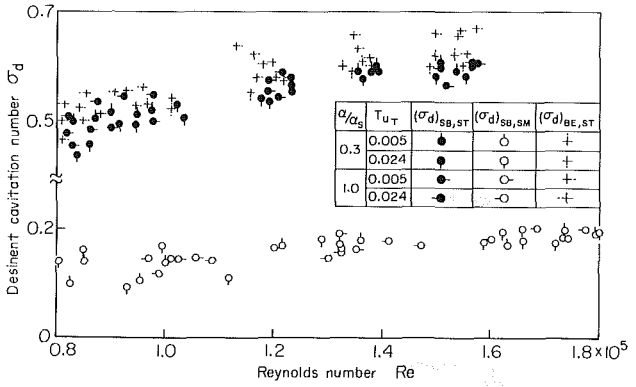

Fig. 8 A marked change in desinent cavitation number σ_d due to the step (Uncertainty of σ_d is ± 5 percent)

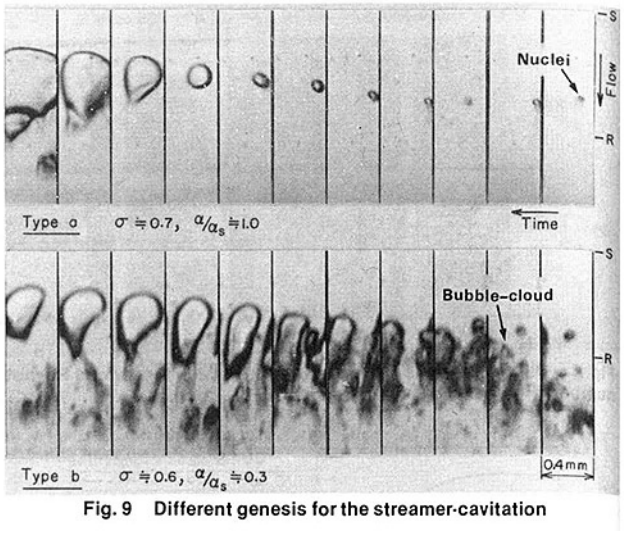

Fig. 9 Different genesis for the streamer-cavitation

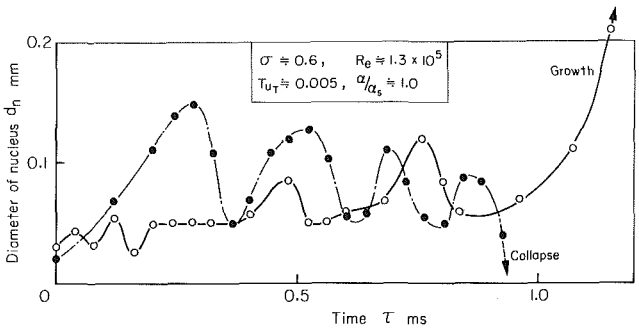

Fig. 10 Critical behavior of powerful nucleus (Uncertainties of d_n and τ are ± 10 and ± 2 percent, respectively)

cavitation-aspects and great differences in the cavitation number had been observed on the same ITTC standard body in different test facilities widely distributed throughout the world. A wide variety of the cavitation aspects have also been observed in the present venturi without the step [14]. Here let us investigate the separation bubble effects on the aspects.

Figure 6 illustrates the near-desinent aspects of cavitation, where σ_d is the desinent cavitation number and the subscripts SB and BE denote the streamer-bubbles and the beads. The desinent cavitation-bubbles are clearly classfied by σ_d as well as their aspects into the following three types, namely streamer-bubbles, traveling bubbles and beads, so that such a cavitation is said to be constituted multitudinously with three types of cavitation. Of course, the three types of cavitation have their original characters in their own zone and range in σ.

The streamer bubbles occurred within the laminar separation bubble for both cases with and without the step. The leading edges were located near the separation point, as shown in Fig. 7. The front portions were transparent, while the surfaces were wavy in the range of $R_e \geqq R_{e,crit}$, breaking up ultimately into a lot of microscopic bubbles immediately downstream. As is shown in Figs. 7 and 8, the aspects and σ_d depend principally on R_e, as is to be expected from the fact that the streamer-bubbles agree well with the oil-spots in width and in number [7] and have highly R_e-dependent features. And it is remarkable that the aspects and σ_d, so that this type of cavitation, are insensitive to the cavitation-nuclei or α/α_s, as is similar to those of the band-or the sheet-type cavitation [1, 2, 4, 5].

As is shown in Figs. 6 and 7, the beads appeared within a very narrow region near the reattachment-point, as microscopic irregularly-shaped bubbles rapidly appeared and disappeared. The beads whose aspects seen to be scarcely affected by nuclei or α/α_s are very similar to the transient bubble-ring on a hemispherical nose [4] and occurred principally on the stepped surface. When the very narrow region was full of the beads, the bubble-cloud with almost uniform dimension came out circumferentially and developed upstream as shown in Fig. 9.

The traveling bubbles observed here are not necessarily spherical. They rapidly grow and collapse in the low pressure region in the throat. The bubbles were observed mainly in the lower velocity and the higher α/α_s range on the smooth surface, while they were scarcely seen on the stepped surface with a higher H. Sometimes the streamer-bubbles were absorbed locally or wholly into the traveling bubbles, resulting in a drastic change into the large massive bubbles, as described elsewhere [8, 15].

Desinent Cavitation Number. We investigate how the thin backward facing step affects the desinent cavitation number σ_d, especially with respect to the streamer-cavitation.

Figure 8 plots the desinent cavitation numbers $(\sigma_d)_{SB,ST}$, $(\sigma_d)_{SB,SM}$ and $(\sigma_d)_{BE,ST}$ against R_e for the two types of cavitation, for various T_{uT}, the nuclei-size-spectra as well as both cases with and without the step. Notice here that the step results in a marked change in $(\sigma_d)_{SB}$. And the numbers tend to increase slowly with R_e, approaching an asymptotic value. It is also remarkable that $(\sigma_d)_{SB}$ is scarcely sensitive to the nuclei-size-spectra or $(\alpha/\alpha_s)_{BE,ST}$ is a little bit sensitive to the nuclei, especially in a lower T_{uT} and a higher R_e. As previously described [7], however, σ_d of the traveling cavitation is very sensitive to the nuclei as well as the velocity U_T, especially in the lower U_T-range.

Let us consider a possible factor of the marked change in $(\sigma_d)_{SB}$, by ignoring the secondary effects of the nuclei-size-spectra or α/α_s. As is clear in Figs. 3 and 8, $(\sigma_d)_{SB,ST} \cong |C_{ps,ST}|$, but $(\sigma_d)_{SB,SM} < |C_{ps,SM}|$. Here, the averaged value of $(\sigma_d)_{SB,ST}$ and $|C_{ps,ST}|$ is respectively 0.62 and 0.58 at $R_e = 1.5 \times 10^5$ for the low turbulent flow where the streamer-

bubbles appear dominantly, while $(\sigma_d)_{SB,SM}$ and $|C_{ps,SM}|$ are 0.18 and 0.47. The fact that $(\sigma_d)_{SB,ST} \cong |C_{ps,ST}|$ corresponds well to the results of a band-or a sheet-cavitation for hemispherical noses [2-4]. Arakeri et al. [16] reported on the hemispherical nose with a step that the incipient cavitation number σ_i increased monotonically with the step-height h, through no information was given on the nuclei-size-spectra or the cavitation aspects.

Two Geneses of Streamer-Cavitation. Let us focus our attention on the desinent process of the streamer-cavitation, from which the marked change results.

Since the nuclei moved comparatively slowly within the separation bubble, we succeeded in taking the nuclei microphtographs by means of the high speed-camera. Figure 9 illustrates the photographs of the near-desinent process occurring on the stepped surface, and clearly shows two geneses for the streamer-bubble. That is to say, one is a fairly large freestream nucleus floating within the separation bubble (see Type "*a*" in the figure), while the other is a streamerlike bubble-cloud arranged circumferentially near the reattachment-point (see Type "*b*"). The type "*a*" and "*b*" appear usually on the stepped surface, and the type "*a*" takes place earlier than the type "*b*," while for the thinner H_{SM} only the type "*b*" occurs very intermittently, corresponding to the suppression of the beads. The bubble-cloud consists of a huge number of extremely fine bubbles, a few micrometer or less in diameter, that might be holes statistically distributed in liquid [17].

Strasberg [18] demonstrated such a critical nucleus diameter $d_{n,\,crit}$ to grow explosively. Here, let us consider the diameter d_{np} of the nucleus that may grow to $d_{n,\,crit}$ under locally fluctuating pressures at acoustic pressures at the pressure within the separation bubble P_s. In the following we call it "powerful nucleus." The pressure P_A, at which the powerful nucleus begins to grow by rectified diffusion, was derived by the Hsieh-Plesset equation [19], as $P_A = 3/2\, P_s[1 + 4S/(d_{np}\, P_s) - (\alpha/\alpha_s)]^{1/2}$. Here S is the surface tension of water, and (α/α_s) is the relative air content at P_s. The values of (α/α_s) are estimated to be $1.1 \sim 1.4$ in the desinent state of interest, when $\alpha/\alpha_s \cong 1.0$, $P_s = 60 \sim 80$ kPa and the measured value of $P_A = 4 \sim 8$ kPa. Then, d_{np} is lying between 20 μm and 30 μm in the separation bubble, so that $H_{ST} > d_{np}$, but $H_{SM} \leqq d_{np}$.

Though numerous nuclei are actually floating within the separation bubble, especially at the higher α/α_s or the higher U_T on the stepped surface, most of the nuclei of $d_n > d_{np}$ or $d_n < d_{np}$ grow explosively or collapse rapidly, while the nuclei of $d_n \cong d_{np}$ behave critically, as shown in Fig. 10.

Since the separation bubble thickness is three or four times larger than the powerful nucleus diameter on the stepped surface, such a separation bubble enables rather small nuclei to grow by rectified diffusion. Then, the necessary number of the powerful nuclei should be available for the inception initiated from the type "*a*." It is easy to find why $(\sigma_d)_{SB} \cong |C_{ps}|$. On the smooth surface where the beads or bubble-cloud was seldom observed, on the contrary, such nuclei could not be available there, since the separation bubble is thinner than the powerful nucleus. Then, the inception principally depends on the type "*b*" which may grow at a considerably lower pressure than that for type "*a*," so that $(\sigma_d)_{SB} < |C_{ps}|$.

Conclusion

The mechanism of cavitation desinence, especially of the streamer-cavitation, is experimentally investigatged in typical internal flows through venturies with and without the step having only height as large as cavitation nuclei, under prescribed nuclei-size-spectra as well as various hydrodynamic conditions. The results are summarized as follows:

1 The separation bubble can play an important role in the desinence of the streamer-cavitation, only when the separation bubble thickness is larger than the powerful nucleus-diameter d_{np}.

2 The streamer-cavitation comes from the three-dimensional structures within the separation bubbles, and has two different geneses: the powerful nucleus (Type "*a*") and the streamerlike bubble-cloud (Type "*b*").

3 The type "*a*" appear dominantly on the stepped surface where $H_{ST} > d_{np}$, and the type "*a*" may grow at a considerably higher pressure than that for the type "*b*," while only the type "*b*" occurs very intermittently on the smooth surface for $H_{SM} \leqq d_{np}$. The desinent cavitation number $(\sigma_d)_{SB}$ is differently related to the pressure coefficient at the separation-point C_{ps}, as follows:

$$(\sigma_d)_{SB} \cong |C_{ps}| \quad (d_{np} \leqq H: \text{Type } a)$$

$$(\sigma_d)_{SB} < |C_{ps}| \quad (d_{np} \geqq H: \text{Type } b)$$

4 The streamer-cavitation has highly R_e-dependent features and $(\sigma_d)_{SB}$ is scarcely sensitive to the nuclei-size spectra or α/α_s, while the desinent caviation number of the traveling cavitation with poor R_e-dependent features is very sensitive to them, as described elsewhere [7]. The beads-cavitation is intermediate in character between the former two.

References

1 Kermeen, R. W., "Some Observations of Cavitation on Hemispherical Head Models," Rep. No. E-35.1, Hydrodynamics Laboratory, California Institute of Technology, 1952.

2 Arakeri, V. H., and Acosta, A. J., "Viscous Effects in the Inception of Cavitation on Axisymmetric Bodies," ASME JOURNAL OF FLUIDS ENGINEERING, Vol. 95, 1973, pp. 519-528.

3 Arakeri, V. H., "Viscous Effects in Inception and Development of Cavitation on Axi-symmetric Bodies," Rep. No. E-183.1, Hydrodynamics Laboratory, California Institute of Technology, 1973.

4 Holl, J. W., and Carroll, J. A., "Observations of the Various Types of Limited Cavitation on Axisymmetric Bodies," ASME JOURNAL OF FLUIDS ENGINEERING, Vol. 103, 1981, pp. 415-424.

5 Kodama, Y., Take, N., Tamiya, S., and Kato, H., "The Effects of Nuclei on the Inception of Bubble and Sheet Cavitation on Axisymmetric Bodies," ASME JOURNAL OF FLUIDS ENGINEERING, Vol. 103, 1981, pp. 557-563.

6 Arakeri, V. H., Carroll, J. A., and Holl, J. W., "A Note on the Effect of Short and Long Laminar Separation Bubbles on Desinent Cavitation," ASME JOURNAL ON FLUIDS ENGINEERING, Vol. 103, 1981, pp. 28-32.

7 Ito, Y., and Oba, R., "Several Types of Cavitation Bubbles, Especially Streamer-Bubbles," *1981 Cavitation and Polyphase Flow Forum, ASME*, Boulder, Colo., 1981, pp. 14-16.

8 Oba, R., and Ito, Y., "Effects of Flowing Down Bubbles on Cavitation in a Venturi," The Reports of the Institute of High Speed Mechanics, Tohoku Univ., Vol. 44, 1981, pp. 1-14.

9 Daily, J. W., and Johnson, V. E., Jr., "Turbulence and Boundary Layer Effects on Cavitation Inception From Gas Nuclei," *Trans. ASME*, Vol. 78, 1956, pp. 1695-1706.

10 Numachi, F., "Über die Kavitationsentstehung mit besonderen Bezug auf den Luftgehalt des Wassers," *Ingenieur-Archiv*, Bd. 7, 1936, S. 369-406.

11 Brennen, C., "Cavitation Surface Wave Patterns and General Appearance," *Journal of Fluid Mechanics*, Vol. 44, 1970, pp. 33-49.

12 Tani, I., "Low Speed Flows Involving Bubble Separations," *Progress in Aeronautical Science*, Vol. 5, 1964, pp. 70-103.

13 Johnsson, C. A., "Cavitation Inception on Head Form. Further Test," *Proceedings of the 12th International Towing Tank Conference*, Rome, 1969, pp. 381-392.

14 Oba, R., and Ito, Y., "Cavitation Aspects in a Venturi ("Johnsson Effects" in a Low Turbulence Flow)," *Transactions of the Japan Society of Mechanical Engineers*, Vol. 45B, 1979, pp. 1428-1434.

15 Ito, Y., and Oba, R., "Cavitation Bubble Observation in a Venturi, Especially, With Respect to Streamer Bubbles," The Reports of the Institute of High Speed Mechanics, Tohoku Univ., Vol.. 45, 1982, pp. 1-18.

16 Arakeri, V. H., and Ramarajan, V., "Inception of Cavitation From a Backward Facing Step," ASME JOURNAL OF FLUIDS ENGINEERING, Vol. 103, 1981, pp. 288-293.

17 Finch, R. D., "Hole Theory of Cavitation Nucleation," *The Physics of Fluids*, Vol. 12, 1969, pp. 1775-1778.

18 Strasberg, M., "Undissolved Air Cavities as Cavitation Nuclei," *Proceedings of NPL Symposium on Cavitation in Hydrodynamics*, London, 1956.

19 Strasberg, M., "Rectified Diffusion: Comments on a Paper of Hsieh and Plesset," *Journal of Acoustical Society of America*, Vol. 33, 1961, p. 359.

DISCUSSION

B. R. Parkin[2]

This discusser wishes to congratulate the authors for presenting a body of useful observations on cavitation desinence and separation bubbles. This work will be a source of information and ideas about the physical aspects of cavitation in the future.

Referring to some of the experimental methods mentioned by the authors, first I ask is the Coulter counter technique used in these experiments the same as that described in the *International Symposium on Cavitation Inception* (1979)[4]? Second, can you offer a comparison of Numachi's method (authors' [10]) of dissolved air content determination and the use of the Van Slyke apparatus commonly used today?

The present discusser questions the idea of liquid holes as cavitation nuclei cites. His reason is that the occurrence and disappearance of liquid holes is associated with time scales typical of the statistics of the liquid state. This characteristic life time is orders of magnitude less than any event associated with cavitation inception. Therefore, how can such holes produce cavitation nuclei?

One last question concerns possible differences between inception and desinence in the separated flows under study. Did the authors observe any that they can discuss? One might suppose that the conditions for sustaining cavitation, once it is underway may be quite different from those required to start it – especially if inception is influenced by distributed nuclei in the flow. Were the terms inception and desinence used as synonyms in this paper?

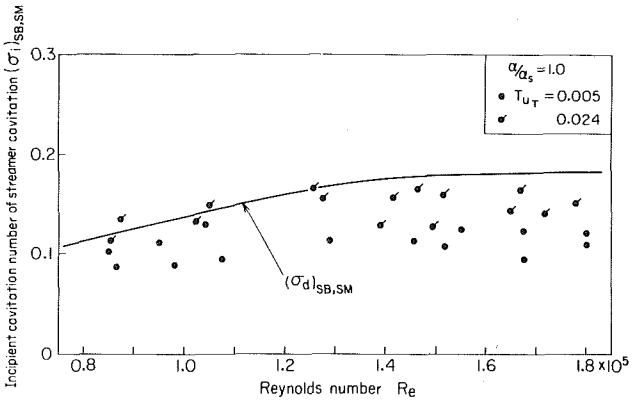

Fig. 11

Authors' Closure

First, the authors would like to Professor B. R. Parkin for his fruitful discussions and helpful comments.

1. Our Coulter-counter apparatus and its characteristics have been described in our previous papers,[3] as you mentioned. The more detailed informations can be seen in reference [A].

2. The Numachi's method [10, B] is the same as the Van Slyke's one [C] in principle. Numachi [B] gave his short comments for the Van Slyke apparatus.

3. We called "the holes" the cavitation nuclei of accumulated holes proposed by Finch [17]. It is not so-called "hole" corresponding to the absence of one molecule whose radius would be one-half of the mean intermolecular spacing and is in the state of the accumulation of holes, that a cavitation nucleus of critical size might arise.

4. As shown in Fig. 11 [D], when comparing the incipient cavitation number $(\sigma_i)_{SB,SM}$ is fairly different from $(\sigma_d)_{SB,SM}$ for our streamer-cavitation, while the difference is relatively small for the present stepped-surface.

Additional References

[A] Oba, R., Kim, K. T., Niitsuma, H., Ikohagi, T. and Sato, R., "Cavitation-Nuclei Measurements by a Newly Made Coulter-Counter Without Adding Salt in Water," The Report of the Institute of High Speed Mechanics, Tohoku Univ., Vol. 43, 1981, pp. 163–176.

[B] Numachi, F., and Shiina, T., "Über die Kavitationsentstehung mit besonderem Bezug auf den Luftgehalt des Wassers," *The Transaction of the Japan Society of Mechanical Engineers*, Vol. 3, No. 10, 1937, pp. 177–185.

[C] Van Slyke, and Neil, J. M., "The determination of gases in blood and other solutions by vacuum extraction and manometric measurement I and II," *Biological Chemistry*, Vol. 61, 1924, p. 523.

[D] Ito, Y. and Oba, R., "Mechanism of Cavitation Inception of Streamer Type," *The Transaction of the Japan Society of Mechanical Engineers*, Vol. 49, No. 442, 1983, pp. 1099–1107.

[2]Applied Research Laboratory, Pennsylvania State University, State College, Pa. 16801.

[3]ASME, New York, p. 147; see also, Oba et al., "Cavitation in an Extremely Limited Flow through Very Small Orifices," ASME JOURNAL OF FLUIDS ENGINEERING, Vol. 104, No. 1, Mar. 1982, pp. 94–98.

The Study of Propeller Cavitation Noise Using Cross-Correlation Methods

L. J. Leggat

N. C. Sponagle

Defence Research Establishment Atlantic, Dartmouth, Nova Scotia, Canada

This paper presents a technique for the study of the mechanisms responsible for the generation of noise from cavitating propellers. The experimental method, which involves the cross-correlation of the pressure gradient in the near-field of the propeller with the far-field sound, allows the determination of the spatial distribution of acoustic source strength on and near the cavitating propeller. The paper describes the mathematical basis for the cross-correlation technique, and then presents some of the results from experiments with propellers specifically designed to produce vortex and bubble forms of cavitation. Cross-correlations performed at a number of points along a track parallel to the axis of the propeller indicate that most of the noise from propellers producing vortex cavitation originates from the region of vortex collapse. A bubble cavitation propeller showed a region of relatively constant source strength distribution from the propeller disk region downstream to the point of vortex collapse.

Introduction

In recent years, the noise produced by hydrodynamic flow past rigid or flexible surfaces has been the subject of considerable interest. It is known that in noncavitating fluid flows the noise is produced by a variety of mechanisms, most notably fluctuating forces caused by variations in the magnitude and incidence of the inflow velocity. Other mechanisms such as incident turbulence, turbulent boundary layers, separated flows and vortex shedding may be important in noncavitating flows. These mechanisms can all be described as dipoles whose acoustic efficiencies are dependent upon the cube of the Mach number.

In flows where cavitation occurs, these dipole mechanisms are of secondary importance to the growth and collapse of cavitation cavities. Cavitation behaves as a monopole mechanism whose acoustic efficiency is dependent upon the Mach number. In circumstances where the Mach number is small such as for the flow past a marine propeller, the monopole and dipole acoustic efficiencies are such that cavitation is the predominant source of noise.

Cavitation on a marine propeller can appear in a number of forms. Three of the more comon types are vortex, sheet, and bubble cavitation. Vortex cavitation is generated in the low pressure regions of the hub and tip vortices. Sheet and bubble cavitation can occur on both the face and the back of a propeller blade. The back, however, is more likely to experience these forms of cavitation owing to the low pressure on this side of the blade. The occurrence and the extent of these forms of cavitation are dependent upon the propeller design, the operating condition of the propeller, and the flow in which the propeller operates. During conditions of moderate to high propeller loading, it is not unusual to find two or more types of cavitation simultaneously present on the propeller.

In reduced-noise propeller design, attempts are made to avoid the noisier types of cavitation, and special design practices are adopted to control the noise produced by the remaining types. However, the effectiveness of the noise control is very much dependent upon the designers notion of the mechanism responsible for the noise generation. While it is generally agreed that cavitation noise is produced by the growth, collapse and rebounding of vapour bubbles, the issue becomes obscure when considering the more intricate sheet and vortex cavitation types. More precise knowledge of the mechanisms responsible for the noise and the distribution of sources on and near the blade should assist present effort in the field of propeller noise reduction.

The study of propeller radiated noise due to cavitation on the propeller is presently carried out using two methods. The first, propeller viewing and sound ranging, is carried out on full scale ships. The propellers are viewed through ports in the bottom of the ship's hull, above the propeller. Ideally, sound ranging is carried out simultaneously. It is a fairly simple procedure to determine the spectral content of the first type of cavitation to occur on the blade. Generally, tip vortex cavitation appears first. However, if more than one form occurs, it is impossible to discriminate the contribution to the far-field signal from the various forms of cavitation on the blade.

The second method used to study propeller cavitation and radiated noise is through model testing in cavitation tunnels and towing tanks. This procedure suffers from the same deficiencies as the full scale experiments; however, it has the added complication that the sound measurements have to be made inside the tunnel or tank. The resulting sound data

Contributed by the Fluids Engineering Division and presented at the International Cavitation on Noise, Winter Annual Meeting, Phoenix, Ariz., November 14-19, 1982, of THE AMERICAN SOCIETY OF MECHANICAL ENGINEERS. Manuscript received by the Fluids Engineering Division, June 13, 1983.

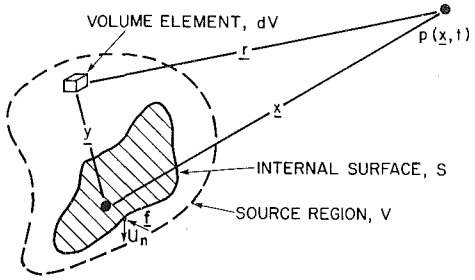

Fig. 1 Terminology for generalized noise source

represent the near field propeller pressure field in a highly reverberant space. It is therefore difficult to obtain meaningful acoustic data over a wide frequency range and to discriminate between the source strengths of the different forms of cavitation.

The present paper describes an experimental method for obtaining the acoustic source strengths of various forms of propeller cavitation and the results obtained from some tests with cavitating propellers. The method, based on Curle's formulation of flow noise theory [1], makes use of the cross-correlation between the normal pressure gradient in the near-field of the cavitation and the acoustic pressure in far-field. The technique is an extension of established methods for determining the acoustic source strength in aerodynamic flows about solid surfaces, in air jets, and on the surfaces of fan blades [2–5]. The method discriminates in favor of that part of the near-field pressure gradient fluctuation which contributes to the far-field acoustic pressure. Because the normal pressure gradient is directly proportional to the cavity normal velocity through Euler's equation, a direct evaluation of the local acoustic source strength, intensity, spectrum, and correlation area is possible. In this way the different forms of propeller cavitation can be studied independently leading to improved concepts of the physical mechanisms responsible for the noise, and to more accurate scaling laws and prediction techniques. The propeller designer, knowing the relative acoustic intensity and cause of each form of cavitation, will be better prepared to produce a design which discriminates against the noisier forms of hydrodynamic cavitation.

Theoretical Development

Application of Curle's General Aerodynamic Noise Equation. The acoustic radiation from a region of unsteady flow containing a surface is given by Curle's generalized solution to the Lighthill equation [6], (see Fig. 1),

$$a_0^2\rho'(\mathbf{x},t) = \int_S \left[\frac{\delta}{\delta t}(\rho u_n)\right]\frac{dS}{4\pi x} - \frac{\delta}{\delta x_i}\int_S [f_i+\rho u_i u_n]\frac{dS}{4\pi x} - \frac{\delta^2}{\delta x_i \delta x_j}\int_V \left[\frac{T_{ij}}{4\pi x}\right]dV \quad (1)$$

where ρ' is the incremental density disturbance relative to the ambient density ρ, and a_0 is the ambient speed of sound. The square brackets denote evaluation at retarded time $\hat{t} = t - x/a_0$. The first two integrals are associated with noise generated by the flow passing over the surface S, which may deform with a velocity u_n. The quantity f_i represents the local stress acting at each point on the surface. The vector $\mathbf{f}$ may comprise both shear stress and normal stress components. The third integral is the Lighthill volume integral for turbulence-generated quadrupole noise where T_{ij}, the effective stress tensor, is given by

$$T_{ij} = \rho u_i u_j + \tau_{ij} + (p - a_0^2\rho')\delta_{ij} \quad (2)$$

where $\rho u_i u_j$ is the Reynolds stress, τ_{ij}, the viscous stress and $(p - a_0^2\rho')\delta_{ij}$ the thermal stress.

In the geometric and acoustic far-field, where $r^2 >> S$, and $r >> \lambda$, the spatial derivatives can be shown to become time derivatives and $r = (\mathbf{x} - \mathbf{y}) \approx x$ such that

$$p(\mathbf{x},t) \approx \frac{1}{4\pi x}\int_S [\rho\dot{u}_n]dS + \frac{x_i}{4\pi x^2 a_0}\int_S \left[\frac{\delta}{\delta t}(f_i+\rho u_i u_n)\right]dS + \frac{x_i x_j}{4\pi x^3 a_0}\int_V \left[\frac{\delta^2 T_{ij}}{\delta t^2}\right]dV \quad (3)$$

For hydrodynamic flow noise, the quadrupole noise is minimal, and so attention is directed to the two surface integrals. For cases where cavitation occurs on the blades and at low Mach numbers, the contributions from the second integral are small giving

$$p(\mathbf{x},t) \approx \frac{1}{4\pi x}\int_S [\rho\dot{u}_n]dS \quad (4)$$

This equation gives the acoustic pressure produced by a monopole with surface velocity u_n. For a propeller, acoustic radiation results from monopoles on and near the surface of the blade associated with the growth and collapse of cavitation. Because the surface velocity of the cavitation is difficult to measure, we substitute the normal pressure gradient by use of Euler's equation of linear momentum,

$$\frac{\delta}{\delta t}u_n = -\frac{1}{\rho}\nabla p_n \quad (5)$$

where ∇p_n is the normal pressure gradient. Substituting equation (5) into equation (4) we obtain

$$p(\mathbf{x},t) \approx -\frac{1}{4\pi x}\int_S [\nabla p_n]dS \quad (6)$$

Nomenclature

a_0 = speed of sound
a_1, a_2 = amplitudes
B = bandwidth
$f_i, \mathbf{f}$ = local surface stress tensor, vector
f_0 = center frequency
p = far-field acoustic pressure or local pressure
∇p_n = normal pressure gradient
$\mathbf{P}$ = distance between source and far-field measuring point
$R_{xy}(\tau)$ = cross-correlation between variables x and y
S = surface
T_{ij} = effective stress tensor
t = time
$\hat{t}$ = retarded time $t = t - x/a_0$
u = velocity
u_i, u_j = velocity vectors
u_n = normal velocity
V = volume
X = dimensionless propeller radius
$\mathbf{x}$ = $\mathbf{x} = (x - y)$ distance from source point to far-field microphone
$x_i, \mathbf{x}$ = space coordinate to indicate point of sound detection in the far-field
$y_i, \mathbf{y}$ = space coordinate used in source region
δ_{ij} = Kronecker delta tensor
λ = wavelength of sound
ρ = ambient density
ρ' = density fluctuation
τ = retarded time delay between two realizations of fluctuating variables
τ_{ij} = viscous stress tensor
= a dot over a symbol indicates derivatives with respect to time

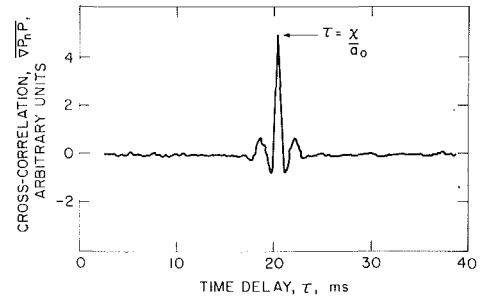

Fig. 2 Cross-correlation function

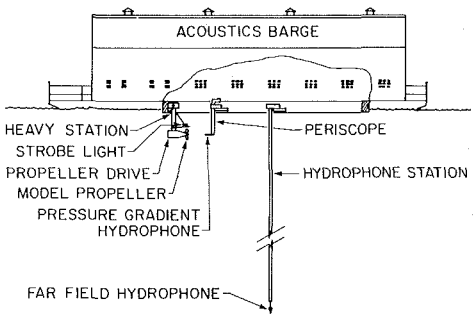

Fig. 3 Propeller drive and hydrophone layout

The Causality Formalism. If both sides of equation (6) are multiplied by the far-field radiated pressure at a new time, t', time averaging yields

$$\overline{p(t)p(t')} \approx -\frac{1}{4\pi x}\int_S [\overline{\nabla p_n(\mathbf{y},\hat{t})p(\mathbf{x},t')}]dS \tag{7}$$

If p and ∇p_n are stationary random variables,

$$\overline{pp(\mathbf{x},\tau)} \approx -\frac{1}{4\pi x}\int_S [\overline{\nabla p_n p}]_{\tau+x/a_0}\,dS \tag{8}$$

where $\tau = t - t'$

The expression for the mean square acoustic pressure is given when $\tau = 0$. Thus,

$$\overline{p^2}(\mathbf{x}) \approx -\frac{1}{4\pi x}\int_S [\overline{\nabla p_n p}]_{x/a_0}\,dS \tag{9}$$

and,

$$\frac{\overline{dp^2}}{dS} \approx -\frac{1}{4\pi x}[\overline{\nabla p_n p}]_{x/a_0} \tag{10}$$

Thus the contribution to the mean square sound pressure at a far field point $\mathbf{x}$ arriving from an element above the blade surface $dS(\mathbf{y})$ where ∇p_n is being measured is given by the integrand of equation (9). The quantity $\overline{dp^2}/dS$ (equation (10)) may be viewed as the strength of the acoustic source at a near-field point, and for the case where the monopole sound radiation is dominant, it will be called the surface monopole source strength.

Typically, the cross-correlation function will be similar to that shown in Fig. 2. The amplitude of the correlation function is evaluated at the appropriate time delay, thus yielding a source strength associated with the monopole strength in the region of the measurement.

The magnitude and phase of the source region's pressure intensity spectrum may be evaluated simply by performing the Fourier transform of the cross-correlation function in the vicinity of the appropriate time delay x/a_0. By performing many cross-correlations between the near-field pressure gradient and far-field sound at various points near the propeller and in its wake, it is possible to determine the distribution of acoustic source strength produced by a cavitating propeller.

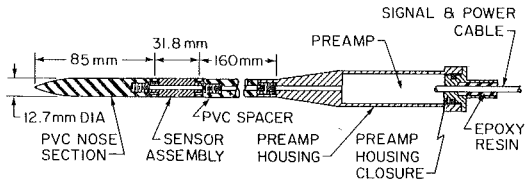

Fig. 4 Pressure gradient hydrophone

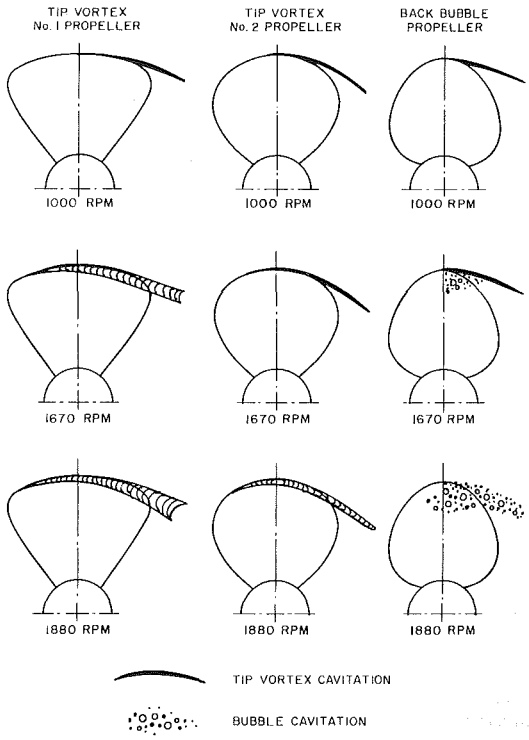

Fig. 5 Cavitation patterns for the three research propellers

Experimental Method

Apparatus. A complete description of the Defence Research Establishment Atlantic (DREA) propeller noise facility and its capabilities is given in reference [7]. A shortened version is presented here. The experiments are carried out in the well of the DREA Acoustic Barge [8], located in Bedford Basin. The Basin has a mean depth of 50 m and the bottom is covered with a deep layer of silt, giving it good acoustic absorption properties.

Model propellers designed to produce various forms of cavitation are driven by a stationary drive pod suspended 2.67 m below the water surface as shown in Fig. 3. The 26.5 kW electric motor installed in the pod will drive a 250 mm diameter propeller at revolution rates in excess of 2000 rpm. Instrumentation installed in the pod allows the measurement of propeller revolution rate and torque.

The propeller cavitation state is observed or photographed through a periscope fitted to one of the barge well cross-trollies. Lighting is provided by two high intensity strobe lamps mounted in water tight containers and fixed to a frame above the drive pod.

A pressure gradient hydrophone was designed and built at DREA to enable measurement of the $\overline{\nabla p_n p}$ term of equation (10) [9]. This hydrophone, shown in Fig. 4, consists of two ceramic cylinders mounted to a cylindrical probe. The two elements are gain and phase matched. The pressure dif-

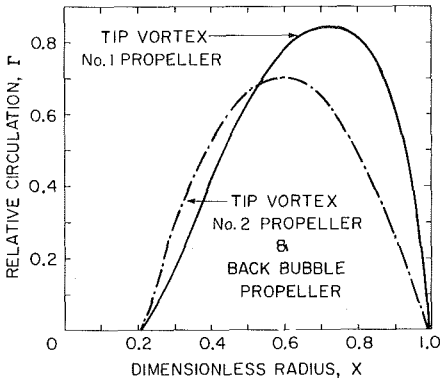

Fig. 6 Propeller circulation distribution

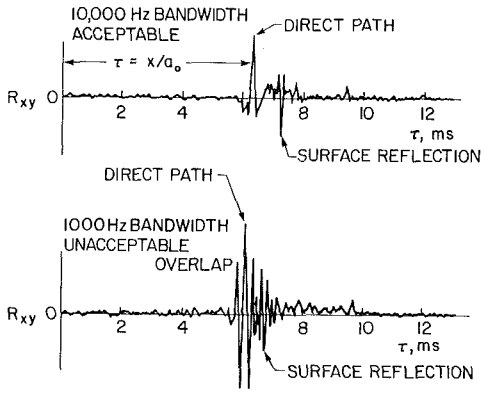

Fig. 7 The effect of bandwidth on correlation function overlap

ference, $\Delta p/\Delta x$, an approximation of the pressure gradient, is measured by differencing the signals from the two elements. The spacing between the two elements (31.8 mm) makes the hydrophone effective over the frequency range of 1 to 20 kHz.

The hydrophone was calibrated using the substitution technique. The sensitivity of the hydrophone is -200 dB re 1 V/μPa at 1.0 kHz, and increases at 6 dB per octave to 20.0 kHz, where the response deteriorates as a result of the half wavelength of the sound approaching the ceramic crystal spacing. The directivity of the hydrophone is the expected cosine pattern with broad-side rejection varying from 10 dB at 1.0 kHz to 32 dB at 10.0 kHz.

Propellers. Three propellers were designed for the initial experiments. They are two-bladed fixed-pitch propellers, 250 mm in diameter, and were designed especially for the bollard pull condition. Experiments were carried out with the three propellers, which are shown in Fig. 5 along with their associated cavitation patterns. One was designed to produce extreme tip vortex cavitation, a second to produce normal tip vortex cavitation simultaneously with hub vortex cavitation, and a third to produce bubble cavitation. These will be referred to as the Tip Vortex No. 1 propeller, Tip Vortex No. 2 propeller and Back Bubble propeller, respectively.

The Tip Vortex No. 2 propeller and the Back Bubble propeller were designed with a spanwise circulation distribution that would normally be associated with reduced noise propellers, while the Tip Vortex No. 1 propeller has a circulation distribution biased toward the tip as shown in Fig. 6. The two tip vortex propellers were designed so that bubble and sheet types of cavitation would be avoided, and only vortex types of cavitation would be present. The Back Bubble propeller was given excessive camber to encourage the development of bubble cavitation.

Some Geometry Considerations. The theory developed

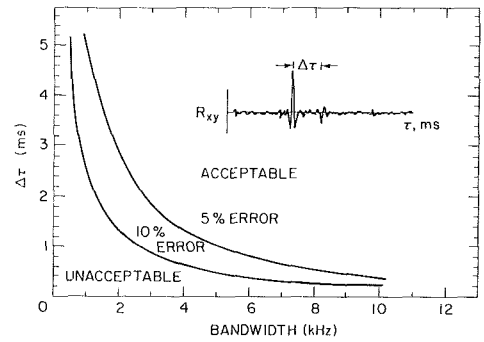

Fig. 8 Criterion for minimizing correlation function overlap

earlier, which allows the determination of acoustic source strength distribution near the propeller depends upon being able to evaluate the magnitude of the cross-correlation function $\nabla p_n p$ at the correct time delay. The typical cross-correlation function shown in Fig. 2 is representative of one obtained in an anechoic environment. The time delay of the peak corresponds to the time required for the sound to travel from the near-field pressure gradient hydrophone to the far-field hydrophone.

With the experimental arrangement shown in Fig. 3, reflections of the sound from the propeller occur at the water surface and at the barge well side walls. The time taken for the sound travelling by these reflective paths to arrive at the far-field measuring point is greater than that for the direct path. As a result, additional peaks occur in the correlation function. When the arrival time of the direct path is close to that of the reflected paths, overlap of the peaks can occur. This generally results in errors being introduced into the direct path information. Also, as the bandwidth of the source signal decreases, the correlation function becomes more like a damped periodic function. The limit of zero bandwidth corresponds to a sine wave, the correlation of which is a cosine wave. For these cases where the source signal contains significant amounts of periodic information, it is virtually impossible to differentiate between the direct and reflected paths of the correlation function. Thus to obtain meaningful results from this technique in a non-anechoic environment, the geometry of the source and hydrophones must be selected so that the error from the reflective contribution to the correlation function is minimized.

Before commencing experiments with model propellers, an analysis of this problem was carried out. Experiments were conducted using a J-11 projector as a source driven by a white noise generator. Through filtering, the bandwidth of the source signal was varied for various source to receiver spacings. This allowed an investigation of the effect on the correlation function overlap of both source bandwidth and source to receiver spacing.

A typical result showing the effect of bandwidth on the correlation function is shown in Fig. 7. The top trace, which shows a correlation function with adequate time difference between the direct and reflected paths, allows a confident evaluation of the magnitude of the correlation function corresponding to the direct path. Note in this trace that the surface reflection appears as a negative-going peak owing to the pressure-release surface. In the bottom trace, the direct and surface reflected functions overlap as a result of the reduction in bandwidth of the source signal. Clearly this situation does not allow a confident evaluation of the peak-level associated with the direct path.

A simple mathematical model of the cross-correlation function for the direct and surface reflected paths was developed by combining expressions for bandwidth-limited correlation functions given by equation (11). Here τ_1 is the time for the sound to travel between the near and far-field sensors by the direct path and τ_2 the time for the reflected

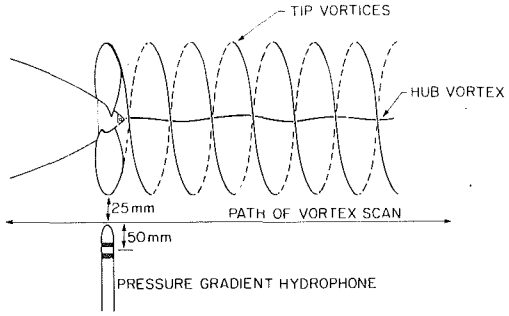

Fig. 9 Arrangement for wake axial traverse

path. This model agreed well with results obtained using the J-11 projector driven with bandwidth-limited white noise, and so was used

$$R_{xy}(\tau) = a_1 B\left[\frac{\sin \pi B(\tau-\tau_1)}{\pi B(\tau-\tau_1)}\right]\cos 2\pi f_0(\tau-\tau_1)$$

$$+ a_2 B\left[\frac{\sin \pi B(\tau-\tau_2)}{\pi B(\tau-\tau_2)}\right]\cos 2\pi f_0(\tau-\tau_2) \quad (11)$$

to develop criteria based on bandwidth and time delay for acceptable correlation functions.

A critical time delay ($\Delta\tau_{crit}$) is defined as the time required for one of the correlation functions to decay to 10 percent of the peak value. Thus, when combining direct and surface reflected path correlation functions, this critical time delay represents a criterion which poses a maximum 10 percent error on the peak value of the direct path correlation function. Using this criterion, a plot of the effect of source bandwidth and time delay on the correlation function overlap was generated, and is shown in Fig. 8. This graph gives combinations of time delay difference, $\Delta\tau$ (a function of the positioning of near and far-field sensors) and source bandwidth which will produce a correlation function with errors of less than 10 and 5 percent. Clearly as the bandwidth of the source signal is reduced, the correlation function becomes more periodic and the required time delay difference becomes large. For a signal bandwidth of 1 kHz, $\Delta\tau_{crit} = 2.50$ ms, which corresponds to a path length difference between the surface and reflected paths of 3.75 m.

The effective frequency range of the pressure gradient hydrophone designed for the cross-correlation experiments is in excess of 10 kHz. For these tests, the near-field pressure gradient hydrophone and far-field hydrophone were positioned to give a $\Delta\tau$ of 4 ms, giving an expected overlap error of less than 1 percent.

Propeller Wake Scans. Wake scans were carried out with the three experimental propellers to determine the location of noise sources along the propeller axis. To perform this experiment, the length of the hydrophone nose was reduced from 85 mm to 34 mm so that the pressure difference pair of elements could be positioned as close as possible to the propeller blade tips. The hydrophone was positioned 25 mm from the blade tip as shown in Fig. 9, and moved axially, starting upstream of the propeller, in 50 mm steps from nominally 350 mm upstream to 1500 mm downstream. This distance spanned the propeller, wake development, and cavitation collapse sectors of the cylindrical control volume around the propeller and its wake.

At each measurement point, the pressure gradient and far-field signals were measured, amplified, filtered between 1 and 18 kHz, and recorded for later analysis. A portable correlation computer and spectrum analyzer were available to verify data as they were being recorded.

Two wake scans were carried out with the Back Bubble propeller while only one was done with each tip vortex propeller. The cavitation states for the propellers were observed and photographed through the periscope. Table 1 lists the conditions for each of the three propellers.

Table 1 Test conditions

Propeller	rpm	Cavitation States
Tip Vortex No. 1	1667	Tip Vortex
Tip Vortex No. 2	1667	Tip Vortex Hub Vortex
Back Bubble	1667	Bubble Tip Vortex Hub Vortex
Back Bubble	1433	Tip Vortex Hub Vortex

All propellers were tested at 1667 rpm. The Back Bubble propeller was also tested at a lower rate to investigate the influence on pressure gradient and source strength distribution of the disappearance of bubble cavitation.

The recorded data were analyzed using a Saicor correlation computer linked to a PDP 11/34 mini-computer. The results included averaged spectra of the near-field pressure gradient and the far-field noise, and the acoustic source strength at each discrete location along the cylindrical control volume surface where measurements were taken. These latter values were plotted as a function of the axial distance to give a source strength distribution.

Results

Pressure Gradient and Acoustic Spectra. Typical spectra for the near-field pressure gradient and far-field sound power for each propeller are shown in Figs. 10 and 11, respectively. The pressure-gradient spectra were measured at a point 254 mm downstream of the propeller plane with the propellers turning at a rate of 1667 rpm. The spectra are relatively flat between 1 and 18 kHz, except at 6 kHz where a dip of about 5 dB occurs consistently in all curves. This is an anomaly inherent in the measurement system. However, because it was consistent in all spectra, and because it occupied a relatively narrow band, it does not affect the end results.

The high pressure gradient amplitude associated with the Tip Vortex No. 1 propeller is consistent with the results from the far-field hydrophone (Fig. 11). As can be seen from Fig. 11, the level from this propeller exceeds those of the other two by as much as 19 dB. It also absorbed about 30 percent more power than the other two. This factor alone cannot explain the large difference between the level of its spectrum and those of the other two. Comparisons of spectrum levels at conditions of equal power showed that the Tip Vortex No. 1 propeller was consistently noisier in the range of revolution rates from 1250 to 1800 rpm. The biasing of the loading toward the tip of this propeller would result in a stronger tip vortex, a greater amount of cavitation, and more noise.

Near-Field Pressure Gradient. In the near-field of the propeller, the pressure gradient receives contributions from both hydrodynamic and acoustic pressure fluctuations. Generally, the hydrodynamic pressures are dominant, but do not propagate acoustically. Thus, the pressure gradient measurements alone will not necessarily reveal the true distribution of acoustic source strength in the propeller near-field. However, when used together, the pressure gradient and acoustic source strength information provide a powerful means of investigating cavitation noise generation.

The variation of near-field pressure gradient with axial distance along the propeller wake for the Tip Vortex No. 1, Tip Vortex No. 2, and Back Bubble propellers are shown in Figs. 12, 13, and 14. The distances are referenced to the plane of the propeller. Negative numbers indicate distances upstream of the propeller plane, and positive numbers downstream.

The pressure gradient curve for the Tip Vortex No. 1 propeller rises to a broad peak 250 mm downstream of the

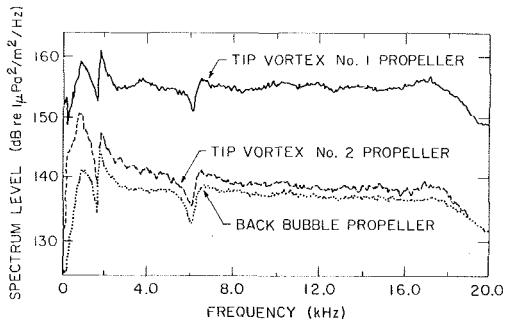

Fig. 10 Pressure gradient spectra, 1667 rpm. Uncertainty in spectrum level is ±0.5 dB at 20:1 odds. Filter bandwidth is 50 Hz.

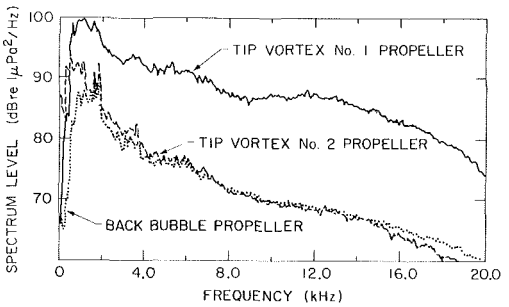

Fig. 11 Far-field sound spectra, 1667 rpm. Uncertainty in spectrum level is ±0.5 dB at 20:1 odds. Filter bandwidth is 50 Hz.

propeller. The rise to and decay from this peak are rapid, indicative of a localized region of significant pressure gradient. Observations of the development of the cavitation revealed that this region of high pressure gradient occurred at the point where the tip vortex cavitation collapsed.

The near-field pressure gradient for the Tip Vortex No. 2 propeller are shown in Fig. 13. As shown in Table 1, the curve corresponds to a condition with both tip and hub vortex cavitation on the propeller. The curve shows a rise in the pressure gradient at the point downstream where the cavitating vortices were observed to collapse. The curve decays rapidly with increasing axial distance beyond the region of vortex collapse.

The difference in the pressure gradient curves for the Back Bubble propeller with and without bubble cavitation are shown in Fig. 14. The top curve, which has two distinct peaks, corresponds to the condition with bubble, and tip and hub vortex cavitation present on the blades. The first peak occurs adjacent to the plane of the propeller and is probably associated with the bubble cavitation collapse on the back of the blades. The pressure gradient associated with the back bubble cavitation is greater than that for the vortex cavitation. The second peak, 350 mm downstream of the propeller plane, is produced by the collapse of the cavitation in the tip and hub vortices. The lower curve, which shows the results from a condition with no bubble cavitation present, has only one peak which is associated with the collapse of the tip and hub vortex cavitation.

Taken collectively, these curves suggest that the regions of high pressure gradient are associated with the collapse of cavitation voids. These regions appear to be relatively localized considering the resolution capabilities of the pressure gradient hydrophone. The pressure gradient rises and decays quickly outside the region of high pressure gradient.

Acoustic Source Strength. The results of the cross-correlation between the near-field pressure gradient and the far-field acoustic pressure were employed with equation (10) to derive values for the acoustic source strength at a number of points in the near-field of the propeller. The results of the calculations are shown in Figs. 15, 16, and 17, for the Tip Vortex No. 1 propeller, Tip Vortex No. 2 propeller, and Back Bubble propeller, respectively.

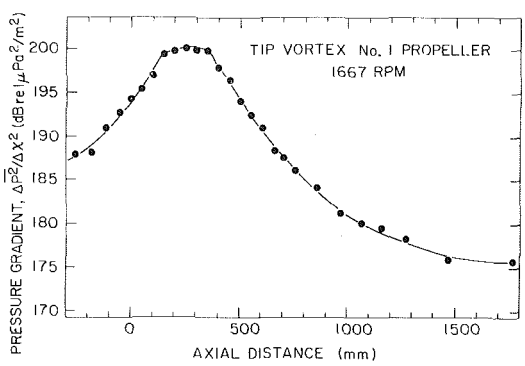

Fig. 12 Pressure gradient, Tip Vortex No. 1 Propeller. Uncertainty in ∇p^2 is ±0.2 dB, in axial distance is ±20.0 mm at 20:1 odds.

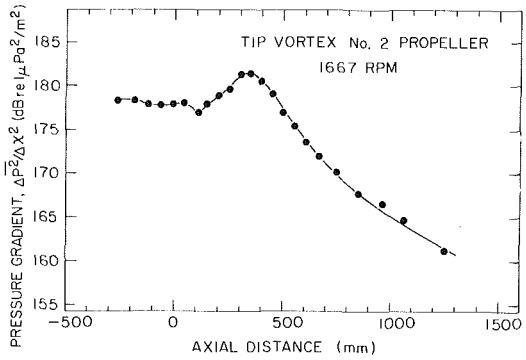

Fig. 13 Pressure gradient, Tip Vortex No. 2 Propeller. Uncertainty in ∇p^2 is ±0.2 dB, in axial distance is ±20.0 mm at 20:1 odds.

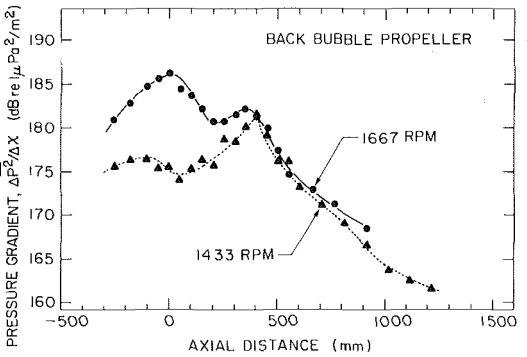

Fig. 14 Pressure gradient, Back Bubble Propeller. Uncertainty in ∇p^2 is ±0.2 dB, in axial distance is ±20.0 mm at 20:1 odds.

The acoustic source strength distribution for the Tip Vortex No. 1 propeller (Fig. 15) shows that the majority of sound from this propeller originates from a narrow region downstream of the propeller where the tip vortices were observed collapsing. This region, located at an axial distance of between 250 and 400 mm, corresponds to the area of maximum pressure gradient in Fig. 12. The shape of the two curves differ, however, with Fig. 15 showing a much more localized source than Fig. 12.

The spatial resolution of the two measurements is probably the cause of the different shapes of the pressure gradient and acoustic source strength curves. The spatial resolution of the pressure gradient measurement is governed only by the dipole directivity of the pressure gradient hydrophone, which is rather coarse; typically 360 mm for these wake scans, based on the 3 dB down point. The spatial resolution of the acoustic source strength measurement is enhanced by the use of the appropriate time delay in the determination of the magnitude of the cross-correlation function. The combination of the

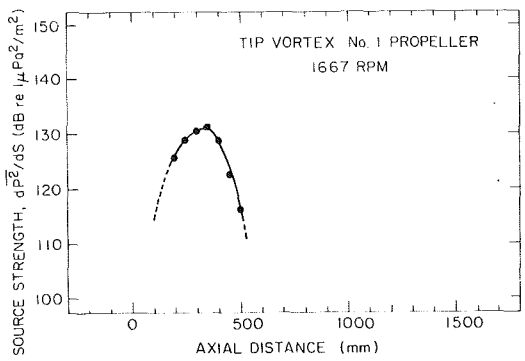

Fig. 15 Source strength distribution, Tip Vortex No. 1 Propeller. Uncertainty in dp^2/dS is ±0.5 dB, in axial distance is ±20.0 mm at 20:1 odds.

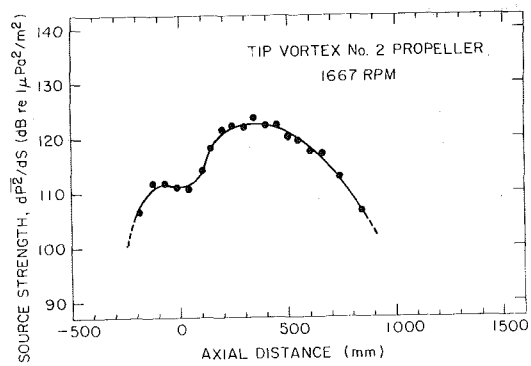

Fig. 16 Source strength distribution, Tip Vortex No. 2 Propeller. Uncertainty in dp^2/dS is ±0.5 dB, in axial distance is ±20.0 mm at 20:1 odds.

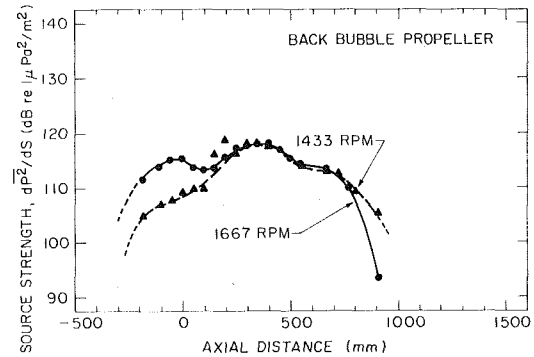

Fig. 17 Source strength distribution, Back Bubble Propeller. Uncertainty in dp^2/dS is ±0.5 dB, in axial distance is ±20.0 mm at 20:1 odds.

directivity of the pressure gradient hydrophone and the use of time delay yields a spatial resolution of about 100 mm.

The results for Tip Vortex No. 2 propeller (Fig. 16) show that the noise in the far-field originates downstream of the propeller. However, in this case the acoustic source strength is more evenly distributed with distance, has a lower maximum, and falls off more slowly than that of Tip Vortex No. 1 propeller.

As shown in Table 1, the cavitation conditions of Tip Vortex No. 1 and Tip Vortex No. 2 differed by the presence of a hub vortex on the Tip Vortex No. 2 propeller. The acoustic source strength results suggest that the hub vortex behaves as more of a line source which contributes to a distributed acoustic source strength (Fig. 16).

The acoustic source strength distributions for the Back Bubble propeller are shown in Fig. 17 and should be compared with the pressure gradient curves of Fig. 14. The main difference between the two sets of curves is that the change in acoustic source strength at the propeller plane location when the bubble cavitation disappears is small relative to the change in pressure gradient. The difference in acoustic source strength is 4 dB as opposed to 12 dB for the pressure gradient. Further, the acoustic source strength of the bubble cavitation is slightly less than that for vortex cavitation collapse. This result also seems to be at variance with the pressure gradient data. However, hydrodynamic and acoustic pressure fluctuations contribute to the pressure gradient. The results suggest that the bubble cavitation produces high hydrodynamic pressure gradient levels, which do not propagate acoustically, and that the source strength of the vortex and bubble cavitation are of the same order for this condition.

The curve in Fig. 17 for 1433 rpm has a similar broad shape to that of Fig. 16. In each of these cases only tip and hub vortices are present on the propeller. Thus it would appear that the hub vortex of the Back Bubble propeller is contributing to the distribution of the acoustic source strength in the propeller wake as was the case for the Tip Vortex No. 2 propeller.

Concluding Remarks

This paper has described a method for determining the distribution of acoustic source strength in the near-field of a cavitating propeller by the use of cross-correlation. The technique described offers a powerful method for finding the mechanisms and locations of sound generation on and near the propeller.

Results indicate that for propellers producing vortex types of cavitation, the noise is produced by the collapse of the cavitating vortices at points downstream of the propeller plane with the tip vortex producing a very localized point source, and the hub vortex producing a distributed line source.

Propellers which develop both bubble and vortex types of cavitation produce an acoustic source strength distribution which is nearly constant from the propeller plane to the point of vortex cavitation collapse. Such a result could be explained by bubbles produced at the blade rebounding near the propeller, and by the tip and hub vortices collapsing farther downstream.

The bubble cavitation produces high levels of pressure gradient compared to the pressure gradients associated with the vortex collapse region. However, as the acoustic source strength of the two regions are of the same order, the strong pressure gradient field of the bubble cavitation is relatively inefficient acoustically compared to the region of the vortex collapse.

References

1 Curle, N., "The Influence of Solid Boundaries on Aerodynamic Sound," *Proc. Roy. Soc.* (London), Series A231, 1955, pp. 505-514.

2 Siddon, T. E., "Surface Dipole Strength by Cross-Correlation Method," *JASA.*, Vol. 53, No. 2, Feb. 1973, pp. 619-633.

3 Leggat, L. J., and Siddon, T. E., "Experimental Investigations of the Aeroacoustic Mechanism of Rotor-Vortex Interactions," *JASA.*, Vol. 64, No. 4, Oct. 1978, pp. 1070-1077.

4 Regan, D. R., and Meecham, W. C., "Multiple Turbojet Noise-Suppression Studies Using Cross-Correlation Techniques," *JASA.*, Vol. 63, No. 6, June 1978, pp. 1753-1767.

5 Pan, Y. S., "Cross-Correlation Methods for Studying Near and Far-Field Noise Characteristics of Several Flow-Surface Interaction Problems," Presented to the 57th meeting of the ASA, Apr. 1974.

6 Lighthill, M. J., "Sound Generated Aerodynamically," *Proc. Roy. Soc.*, A267, 1962, pp. 147-182.

7 Leggat, L. J., "Propeller Cavitation Noise Investigations in a Free-Field Environment," Presented to the DRG Seminar on Advanced Hydrodynamic Testing Facilities, The Hague, Apr. 1982.

8 McMahon, G. W., "New Floating Laboratory Facilities Underwater Acoustic Measurement," *Canadian Electronics Engineering*, Feb. 1961.

9 Fanning, B. L., "A Pressure Gradient Hydrophone for Propeller Noise Studies," DREA Informal Communication, Oct. 1981.

10 Bobber, R. J., *Underwater Electroacoustic Measurement*, Naval Research Laboratory, Washington, D.C., July 1970.

A. Shima
Professor.
Mem. ASME

T. Tsujino
Research Assistant.

H. Nanjo
Graduate Student.

N. Miura
Technical Official.

Institute of High Speed Mechanics,
Tohoku University,
Sendai, Japan

Cavitation Damage in Polymer Aqueous Solutions

Cavitation damage tests in polymer solutions are made with a vibratory cavitation apparatus. It is possible for this device to suppress the degradation of polymer by ultrasonic cavitation. Polymer solutions used are 100 wppm, 500 wppm, and 1000 wppm solutions of Polyox. The weight loss in 100 wppm Polyox solution is larger than that in water, but in 500 wppm and 1000 wppm Polyox solutions the weight losses after 60 min exposure to cavitation are relatively small. It is indicated that the cavitation damage in polymer solutions is subject to the effective influence of elastic properties of liquids.

1 Introduction

Cavitation damage is one of the major problems encountered in the operations of hydraulic structures, water turbines and pumping machinery. Hitherto, cavitation damage in Newtonian fluids (mainly water) have been surveyed from various viewpoints, furthermore much information about the effects of properties of liquids and hydrodynamic parameters on the damage has been obtained [1, 2].

Since it has been found that the addition of small quantity of drag-reducing polymers suppresses cavitation occurrence [3, 4], the cavitation phenomena in polymer solutions have drawn a great deal of attention, and relatively much literature has been reported [5–10]. However, there has been only a little amount of information about cavitation damage in polymer solutions. So far as our knowledge goes, there are papers by Shapoval and Shal'nev [11] and Ashworth and Procter [12]. Shapoval and Shal'nev performed an experiment of cavitation damage generated after a circular cylinder in a cavitating pipe, and found that the weight loss decreased by an addition of 300 wppm polyacrylamide into water. Ashworth and Procter reported the results of vibratory tests with small separation in 100 wppm and 1000 wppm polyacrylamide solutions, where the cavitation erosion rates were increased. Unfortunately the degradation rates of the polymer solutions used in their experiment were large, so it may be assumed that rheological properties of their polymer solutions were appreciably changed.

The purpose of the present study is to clarify the effect of an addition of polymer on cavitation damage by using vibratory cavitation damage test apparatus. To suppress the degradation of polymer during test duration, the present experimental device has a unique system of which fresh polymer solutions are supplied to the test vessel by a pump, at the same time, the polymer solutions degraded by cavitation are drained away. Polymer used in this experiment is Polyox WSR-301 which is often used in cavitation experiments. In the present experiment, the effects of polymer concentration and degradation on the weight loss are made clear, and the cavitation clouds and the damage patterns on the surface of test specimen are demonstrated. Comparisons between these results and the cases of water-glycerol solution are made.

2 Experimental Equipment and Procedure

Figure 1 shows schematically the arrangement of the vibratory cavitation facility used to study the effect of polymer additives on cavitation damage. The basic equipment comprised a commercial electrostrictive transducer driven at a nominal frequency of 19.5 ± 0.5 kHz with a peak-to-peak

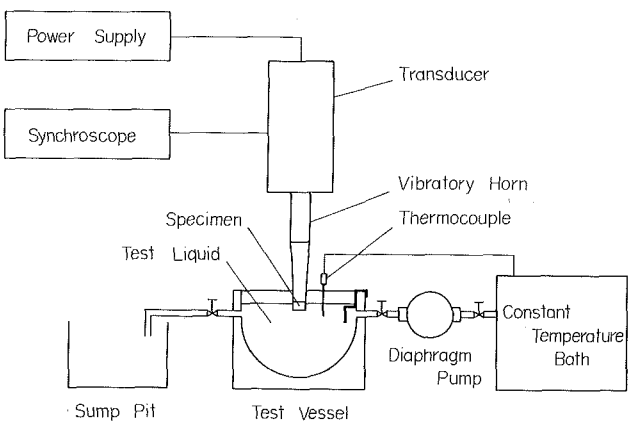

Fig. 1 Schematic block diagram of the vibratory cavitation test facility

Contributed by the Fluids Engineering Division and presented at the Winter Annual Meeting, New Orleans, La., December 9–14, 1984, of THE AMERICAN SOCIETY OF MECHANICAL ENGINEERS. Manuscript received by the Fluids Engineering Division, January 30, 1984. Paper No. 84-WA/FE-1.

Table 1 Values of liquid viscosity η

($\eta \times 10^3$ [Pa·s], t_ℓ = 295 K)

Liquids	Water	100 wppm Polyox solution	500 wppm Polyox solution	1000 wppm Polyox solution	water-glycerol solution (70:30, v/v)
Viscosity of fresh solution	0.955	1.12	1.95	3.57	2.80
Equilibrium viscosity at $Q=0.5\times10^{-3}$ m^3/min	—	1.03	1.58	2.72	—
Viscosity of completely degraded solution	—	—	—	1.04	—
Uncertainty	±0.5 percent	±2 percent	±3 percent	±5 percent	±0.5 percent

amplitude 38 ± 1 μm. Simultaneously with the damage of the test specimen, the ultrasonic cavitation also degrades the polymer. In the present experimental system, cavitating liquids in the test vessel are suitably discharged to suppress the polymer degradation as far as possible. At the same time fresh polymer solutions adjusted to constant temperature in a bath are supplied into the test vessel by a diaphragm pump. To make a drainage of test liquids easy, the bottom of the vessel was made hemispherical in shape. The volume of test liquids in this vessel was 0.9×10^{-3}m^3, the liquid temperature was maintained at 295 ± 1 K. The water-soluble polymer used in our paper was Polyox WSR-301 (Union Carbide Co., Ltd.). The concentrations of polymer solutions tested were c = 100, 500, and 1000 wppm. For estimation of the degree of degradation of polymer solutions, the viscosities of fresh polymer solutions and degraded polymer solutions were measured using a capillary viscosimeter with thermostatic control. The test specimen is a cylinder which is 15.9 mm in diameter and 12 mm in height, whose material is 5056 aluminum (tensile strength 2.45×10^8 N/m^2, proof stress 1.18×10^8 N/m^2, Rockwell hardness H_{RB} = 41.0). The specimen surfaces were polished with No. 3000 emery paper. The flow rate Q supplied into the test vessel was maintained at 0.5×10^{-3} m^3/min (the uncertainty is ± 2 percent). The submergence of the test specimen tip was 10 mm. Weights were measured before and at various intervals throughout the tests to an accuracy of 0.1 mg. Each measurement was repeated at least 5 times to assure consistency of results. For comparison, the tests for the cases of water and water-glycerol solution (70:30, v/v) were also made. Moreover, photographs were taken of the cavitation cloud with an exposure time of 0.7 microsecond.

3 Results and Discussion

3.1 Effect of Polymer Addition on Weight Loss. Figure 2 shows the weight loss W_L-test time t curves in water (0 wppm) and 100 wppm, 500 wppm, and 1000 wppm Polyox solutions. For reference, the change in viscosities of the test liquids due to exposure to cavitation is shown on Table 1. Also, the values of air content a/a_s of liquids were 1.07 for water, 1.16 for 100 wppm Polyox solution, 1.11 for 500 wppm Polyox solution and 1.13 for 1000 wppm Polyox solution, respectively, a_s being the saturated concentration in water. As is seen in the figure, the tendency of $W_L - t$ curve in 100 wppm Polyox solution is similar to the case of water, however the weight loss is large as compared with that in water. The tendency in 500 wppm Polyox solution considerably differs from the tests in water and 100 wppm Polyox solution. That is, the weight loss is larger during the earlier period of the test, but afterward the increasing rate of the weight loss decreases, and the weight loss after 60 min exposure to cavitation is one half of that in water. It may be regarded that the result of 1000 wppm Polyox solution is roughly similar to the case in 500 wppm Polyox solution. In this case the weight loss in the initial stage is largest, but the damage rate decreases rapidly with the elapsed time, and consequently the weight loss at 60 min is smallest.

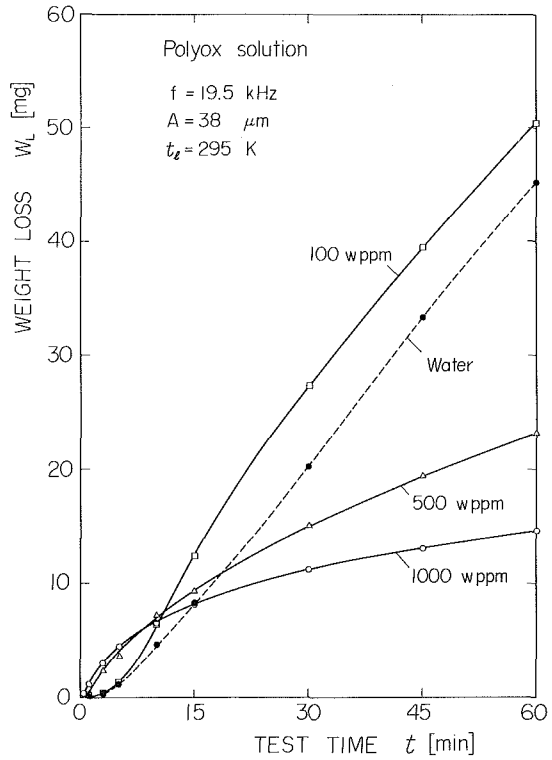

Fig. 2 Effect of addition of polymer on the weight loss

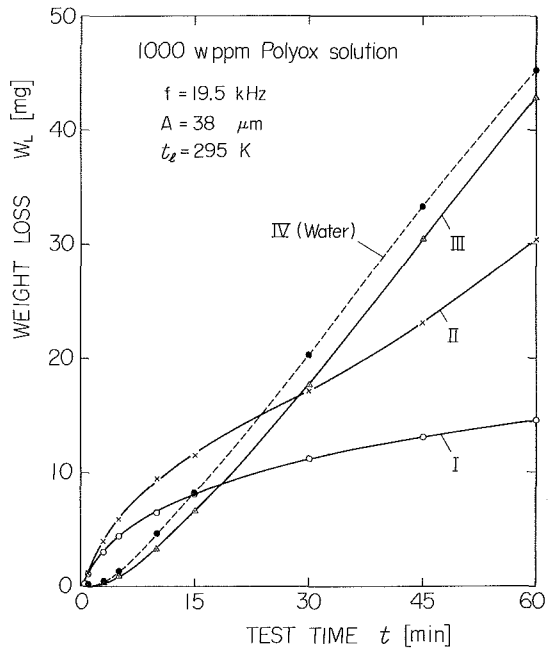

Fig. 3 Effect of polymer degradation on the weight loss I: Case of Q = 0.5×10^{-3}m^3/min, II: Case of Q = 0, III: Case of completely degraded polymer solution, IV: Case of water

Also, the data in this figure were obtained within experimental uncertainty of ± 9 to ± 14 percent.

3.2 Effect of Degradation of Polymer. As stated in the former section, during the experiment of cavitation damage in polymer solutions, it it impossible to remove completely the

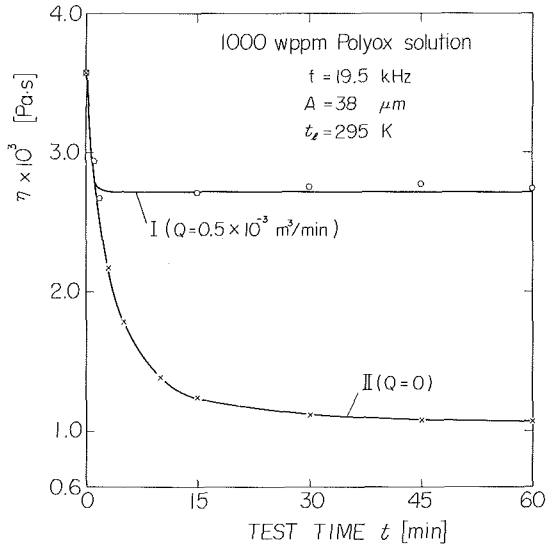

Fig. 4 Changes in viscosity of 1000 wppm Polyox solution with exposure time

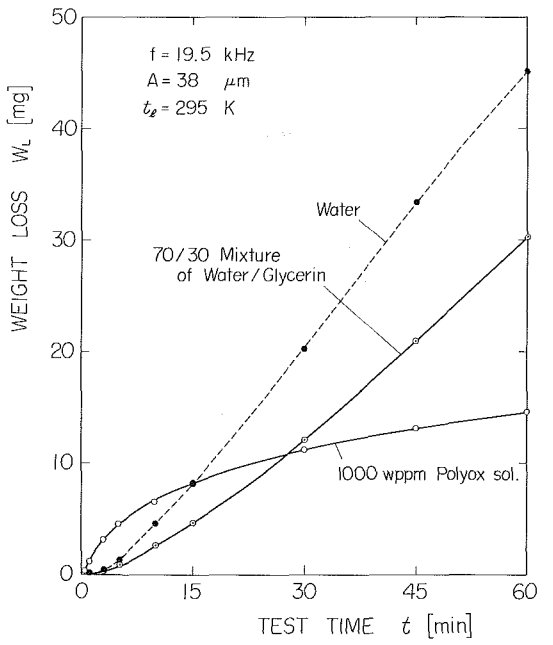

Fig. 5 Comparison of case of water-glycerol solution with polymer solution

effect of degradation of polymer. This implies that the degree of degradation of polymer is one of the important parameters against cavitation damage. Hence the tests of 1000 wppm Polyox solution, as an example, were undertaken to determine the influence of degradation on the damage. The result is shown in Fig. 3. The changes in viscosities of the testing solutions are thereupon represented in Fig. 4 and Table 1. Case I in the figure corresponds to the case where the flow rate is $Q = 0.5 \times 10^{-3}\text{m}^3/\text{min}$. In this case, the value of the viscosity falls rapidly within about 2 min after beginning the test and then remains almost constant. In case II for $Q = 0$, the viscosity decreases markedly during first 15 min, and afterwards it approaches monotonically to a certain constant value with time. Case III is the result in Polyox solution previously exposed to cavitation during a long enough time, so that it can be regarded as completely degraded polymer solution. Case IV is for water. These results indicate that polymer degradation has a great influence on the cavitation

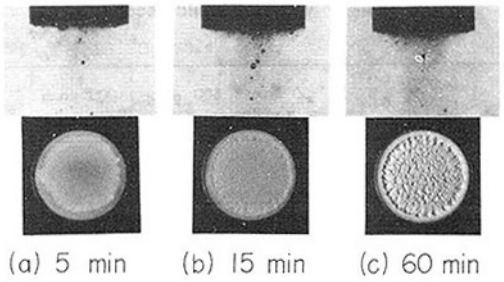

Fig. 6 Cavitation clouds and damage patterns of test specimen in water

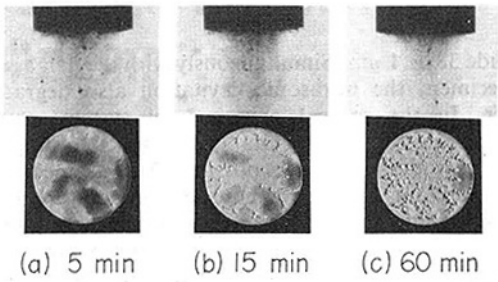

Fig. 7 Cavitation clouds and damage patterns of test specimen in 100 wppm Polyox solution

damage. The $W_L - t$ curve in case III for degraded polymers differs entirely from case I where the degradation of polymer was suppressed, and has the same tendency as in case IV of water (Newtonian fluid). The increasing rate of damage in case II during which the degradation was not controlled is similar, in earlier test period, to case I, because the rheological characteristics of the polymer solution are sustained. But due to a progressive degradation with the exposure time, at a later stage the tendency of the $W_L - t$ curve is rather nearer to case III than case I.

Also, an experiment under the condition where the flow rate was $Q = 1.0 \times 10^{-3}\text{m}^3/\text{min}$ was carried out. Its weight loss-time relation was quite similar to the case for $Q = 0.5 \times 10^{-3}\text{m}^3/\text{min}$.

The uncertainty of the results presented in Fig. 3 is ± 10 percent maximum, whereas the uncertainty of data in Fig. 4 is ± 5 percent.

3.3 Comparision With the Case of Water-Glycerol Solution. Figure 5 shows a comparison with the case of a 70/30 mixture by volume of water and glycerol with the same viscosity as 1000 wppm Polyox solution ($Q = 0.5 \times 10^{-3}\text{m}^3/\text{min}$). Although the weight loss in the water-glycerol solution is smaller than that in water, due to an increase of viscosity of the liquid, the tendency of the $W_L - t$ curve is similar to water. It is evident, however, that the result differs appreciably from that in 1000 wppm Polyox solution with the same viscosity. This fact suggests that the cavitation damage in polymer solutions is greatly influenced by the elastic properties of the liquids.

The experimental uncertainty in this figure is ± 10 percent maximum.

3.4 Observations of Cavitation Clouds and Damaged Patterns of Specimen Surface. For clarification of the results, photographic observations of cavitation clouds and damaged patterns of specimen surface were made.

3.4.1 Cases of Water and 100 wppm, 500 wppm and 1000 wppm Polyox Solutions. First, Fig. 6 shows the result of water for comparison with the cases of the polymer solutions.

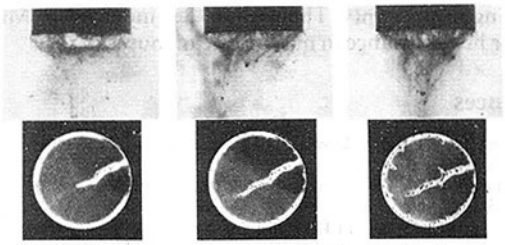

Fig. 8 Cavitation clouds and damage patterns of test specimen in 500 wppm Polyox solution

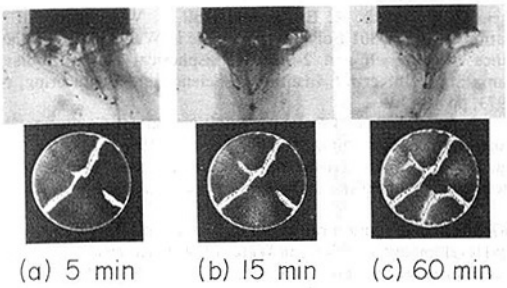

Fig. 9 Cavitation clouds and damage patterns of test specimen in 1000 wppm Polyox solution

Fig. 10 Damage patterns of test specimen in 1000 wppm Polyox solution under the condition of $Q = 0$

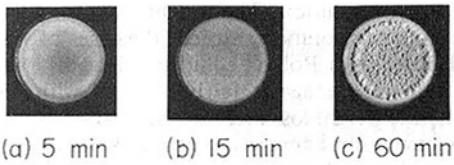

Fig. 11 Damage patterns of test specimen in completely degraded 1000 wppm Polyox solution

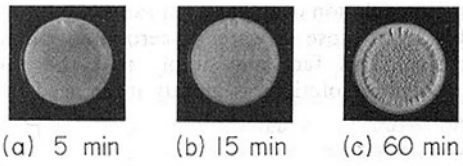

Fig. 12 Damage patterns of test specimen in water-glycerol solution (70/30 : v/v)

The specimens in water were uniformly eroded with pits surrounded by undamaged rims.

Figure 7 shows flash photographs of the cavitation clouds and the specimen surfaces after being exposed to cavitation in 100 wppm Polyox solution for 5, 15, and 60 min. The damage patterns in 100 wppm Polyox solution, unlike those in water, have some stringy forms in the earlier stage. The neighborhood of rim is also eroded. A number of stringy forms increase with the elapsed time and their shapes are extended. Consequently, the more heavily damaged region spreads on the specimen surface. This fact may be responsible for the result that the weight loss in 100 wppm Polyox solution is larger than in water.

Figure 8 is for 500 wppm Polyox solution. It is found that in this solution dish shaped cavitation clouds occur, unlike the case of water. As a result, the damage patterns also differ remarkably from the cases of water and 100 wppm Polyox solution. In a short period after beginning the test, stringy damage patterns with deeper pits are generated and the rim of the specimen is also eroded. This may be a cause for an increase of weight loss in the earlier stage. After that, although the stringy damage progresses in depth and size and the damage near the rim increases, considerably large undamaged region was maintained. It is possible that this fact results in the weight loss at $t = 60$ min decreasing (Fig. 2).

Figure 9 shows the case of 1000 wppm Polyox solution. Similar results are found to the series shown in Fig. 8 for the specimen in 500 wppm Polyox solution. That is, the damage with stringy form on the specimen and the erosion of the rim are produced. Larger undamaged region, that has only lost its luster, remains. However the damage near the rim is small compared with the case of 500 wppm Polyox solution. This may be a reason why the weight loss at $t = 60$ min in 1000 wppm Polyox solution was least.

3.4.2 Case of Degraded 1000 wppm Polyox Solution. Figure 10 shows the damage patterns exposed to cavitation in 1000 wppm Polyox soluton for which the degradation was not controlled, that is, the flow rate $Q = 0$. The damage pattern at 5 min is similar to the result shown in Fig. 9 ($Q = 0.5 \times 10^{-3} m^3/min$). That is, the damage of the rim and the stringy damage pattern appear, and the undamaged area on the specimen remains fairly large. Since the degradation of polymer progresses with exposure to cavitation, the damage patterns are also changed with the elapsed time. As a result the damaged area increases and then a large number of pits are produced. This may be responsible for an increase of weight loss (Case II in Fig. 3).

Figure 11 is for completely degraded 1000 wppm Polyox solution. As is seen in these photographs, the damage pattern in this solution has no characteristics as observed in fresh Polyox solution at all, which is almost similar to the case of Newtonian fluid (water). As noted above, it is evident that the damage patterns change remarkably with degradation of the polymer.

3.4.3 Case of Water-Glycerol Solution. Figure 12 shows for the damage patterns in a water-glycerol solution. These damage patterns are similar in form to the case of water, but markedly differ from those in 1000 wppm Polyox solution with the same viscosity. From a comparison of the results for the polymer solution with water-glycerol solution, it may be concluded that the cavitation damage in polymer solutions is subject to the effective influence of the elastic properties of liquids.

4 Conclusions

Damage tests of aluminum specimens in 100 wppm, 500 wppm, and 1000 wppm Polyox solutions, water and water-glycerol solution were made using a vibratory cavitation damage apparatus. The effects of polymer additives on the cavitation damage were made clear. It was quite possible for the present device with flowing system to suppress degradation of polymer. Results obtained were summarized as follows:

(1) Case of 100 wppm Polyox solution: the weight loss is larger than that in water. Initially, stringy damage pattern appears on the test specimen. As time elapses, the form of the damage becomes large and the damaged region extends all over the specimen surface.

(2) Case of 500 wppm Polyox solution: The weight loss in the initial is large compared with the cases of water and 100 wppm Polyox solution. This is attributed to the appearance of a stringy damage pattern with relatively large pits. The stringy form elongates with the exposure time, but with little increase of the damaged area, as a result the weight loss after a test time of 60 min is less than for the cases of water and 100 wppm Polyox solution.

(3) Case of 1000 wppm Polyox solution: The results for the weight loss and the damage pattern are similar to those in 500 wppm Polyox solution. The weight loss, for times up to about 10 min in this solution, exceeds the cases of water, 100 wppm and 500 wppm Polyox solutions. But afterwards the increasing rate of damage is fairly reduced with test time, consequently the weight loss after 60 min is least.

(4) The cavitation damage in polymer solutions is greatly affected by polymer degradation. The results for completely degraded 1000 wppm Polyox solution show similar trends to a Newtonian case.

(5) The damage patterns of the specimen surface and the weight loss-time relation in 1000 wppm Polyox solution differ considerably from those in water-glycerol solution with the same viscosity. This fact may imply that the cavitation damage in polymer solutions is greatly influenced by elastic properties of liquids.

Acknowledgments

The authors wish to express their thanks to Professor S. Kamiyama and Dr. K. Koike of the Institute of High Speed Mechanics, Tōhoku University for their cooperation with measuring instruments. The authors are indebted to Miss M. Sekii for her assistance in making the manuscript.

References

1 Knapp, R. T., Daily, J. W., and Hammitt, F. G., *Cavitation*, McGraw-Hill, New York, 1970.

2 Hammitt, F. G., *Cavitation and Multiphase Flow Phenomena*, McGraw-Hill, New York, 1980.

3 Hoyt, J. W., "Effect of High-Polymer Solutions in a Cavitating Body," *Proceedings of 11th International Towing Tank Conference*, Tokyo, 1966, pp. 233–234.

4 Ellis, A. T., Waugh, J. G., and Ting, R. Y., "Cavitation Suppression and Stress Effects in High-Speed Flows of Water with Dilute Macromolecule Additivies," ASME *Journal of Basic Engineering*, Vol. 92, 1970, pp. 459–466.

5 Brennen, C., "Some Cavitation Experiments with Dilute Polymer Solutions," *Journal of Fluid Mechanics*, Vol. 44, 1970, pp. 51–63.

6 Baker, C. B., Arndt, R. E. A., and Holl, J. W., "Effect of Various Concentrations of WSR-301 Polyethylene Oxide in Water upon the Cavitation Performance of 1/4-inch and 2-inch Hemispherical Nosed Bodies," The Pennsylvania State University, Institute of Science and Engineering, No. TM 73-257, 1973, pp. 1–13.

7 Hoyt, J. W., "Effect of Polymer Additives on Jet Cavitation," ASME JOURNAL OF FLUIDS ENGINEERING, Vol. 98, 1976, pp. 106–112.

8 Ting, R. Y., "Characteristics of Flow Cavitation in Dilute Solutions of Polyethylene Oxide and Polyacrylamide," *Physics of Fluids*, Vol. 21, 1978, pp. 898–901.

9 Oba, R., Ito, Y., and Uranishi, K., "Effect of Polymer Additives on Cavitation Development and Noise in Water Flow Through an Orifice," ASME JOURNAL OF FLUIDS ENGINEERING, Vol. 100, 1978, pp. 493–499.

10 Murai, H., Watanabe, H., and Katagiri, K., "Suppression of Cavitation Inception in Water by Additives," *Proceedings of 10th Symposium IAHR*, Tokyo, Vol. 1, 1980, pp. 65–76.

11 Shapoval, I. F., and Shal'nev, K. K., "Cavitation and Erosion in Aqueous Solutions of Polyacrylamide," *Soviet Physics Doklady*, Vol. 22, 1977, pp. 635–637.

12 Ashworth, V., and Procter, R. P. M., "Cavitation Damage in Dilute Polymer Solutions," *Nature*, Vol. 258, 1975, pp. 64–66.

An Analytical Model for Prediction of Two-Phase (Noncondensable) Flow Pump Performance

Okitsugu Furuya
Tetra Tech, Inc.,
Pasadena, Calif. 91107
Mem. ASME

During operational transients or a hypothetical LOCA (loss of coolant accident) condition, the recirculating coolant of PWR (pressurized water reactor) may flash into steam due to a loss of line pressure. Under such two-phase flow conditions, it is well known that the recirculation pump becomes unable to generate the same head as that of the single-phase flow case. Similar situations also exist in oil well submersible pumps where a fair amount of gas is contained in oil. Based on the one dimensional control volume method, an analytical method has been developed to determine the performance of pumps operating under two-phase flow conditions. The analytical method has incorporated pump geometry, void fraction, flow slippage and flow regime into the basic formula, but neglected the compressibility and condensation effects. During the course of model development, it has been found that the head degradation is mainly caused by higher acceleration on liquid phase and deceleration on gas phase than in the case of single-phase flows. The numerical results for head degradations and torques obtained with the model favorably compared with the air/water two-phase flow test data of Babcock and Wilcox (1/3 scale) and Creare (1/20 scale) pumps.

1 Introduction

1.1 Background. During operational transients or a hypothetical LOCA (loss of coolant accident) condition, the recirculating coolant of PWR (pressurized water reactor) may flash into steam due to a loss of line pressure. The pressurized water will now contain vapors, the amount of which will depend upon the extent of the transient or accident condition. With such a two-phase flow medium as a coolant, it is well known that the recirculation pump becomes unable to generate the same head as that of the single-phase flow case. The degree of head degradation depends on physical, geometrical and thermal conditions, but it was indicated in various experiments that the head was almost totally lost under certain conditions. From a PWR's safety point of view, it is therefore essential to understand such phenomena and develop an analytical capability for accurately predicting the performance of PWR's cooling pump under the two-phase flow conditions. Such an analytical model can then be integrated into PWR system thermalhydraulic analysis codes.

Similar situations also exist in submersible pumps for deep oil well pumping where a fair amount of gas is contained in oil. The head of each pump in the multistage pump configuration is substantially lower than that of single-phase flow, thus resulting in many hundred stages of pumps. The same head degradation phenomena is prevalent, but in this case the two-phase flow media consists of oil and noncondensable gas, unlike the above PWR cooling systems. Since the mechanism of pump head degradation has not been well understood, effort has simply been made on separation of gas from oil. It is again desirable to understand the basic mechanism of head degradation so that proper pumps can be used for pumping gaseous oil from deep wells with a higher efficiency.

1.2 Review of Past Test Programs. Extensive two-phase pump tests have been conducted to date (see Table 1 and a recent review article by Kim [1]), but the geometric and physical conditions were different in these testings. These include (i) scale and pump geometry, (ii) pump type (radial, mixed, or axial flow type) and, thus, specific speed, (iii) two-phase flow media (condensable or noncondensable), (iv) pump operational conditions, and (v) line pressure. Due to the different pump features and test conditions existing in these tests, the results substantially differed from one to another.

(i) Scale and Pump Geometry. As has been shown in Table 1, the scales of C-E (Combustion Engineering, see reference [2]) and Creare pumps [3] are 1/5 and 1/20, respectively. There existed some difference in homologous head between the C-E tests and Creare tests (see [3]). It is quite possible that the scaling of bubble size to pump size plays an important role in the head degradation mechanism. Another important factor related to the pump geometry will be that of detailed pump blade profile shape, as was pointed out by Chen and Quapp [4]. Although the specific speeds of the pumps tested in the Fast Loop Facility [4] and C-E were almost the same (see Table 1), the number of blades, exit blade angle, breadth ratio and diameter ratio were quite

Contributed by the Fluids Engineering Division and presented at the Winter Annual Meeting, New Orleans, La., December 19-13, 1984 of THE AMERICAN SOCIETY OF MECHANICAL ENGINEERS. Manuscript received by the Fluids Engineering Division, July 8, 1983. Paper No. 84-WA/FE-8.

Table 1 Review of past experiments

COMPANIES / CHARACTERISTICS	B&W[1]	C-E[2]	CREARE[3]	EG&G (FAST LOOP FACILITY)	EG&G (SEMI-SCALE FACILITY)	KWU	PWR PRIMARY COOLANT PUMP (BYRON JACKSON)
Scale	1/3	1/5	1/20		Not Scaled	1/5 of German KWU	1/1
Pump type	Mixed Type	Mixed Type	Mixed Type	Mixed Type	Radial Flow Type	Axial	Mixed Type
Specific speed	4,317	4,200	4,200	4,150	926	6,705	4,200
Two-phase test condition	Air/Water (20–120 psi)	Steam/ Water (15–1250 psi)	1) Air/Water (90 psi) 2) Steam/ Water (400 psi)	Nitrogen/ Water (800 psi)	Steam/ Water (200–900 psi)	Steam/ Water (15–1200 psi)	Steam/ Water (15–2250 psi)
Flow rate (GPM)	11,200	3,500	181	4,500	180	3,145	87,000
Speed (rpm)	3,580	4,500	18,000	3,600	3,560	8,480	900

1) Babcock & Wilcox
2) Combustion Engineering
3) These pumps are geometrically similar, modeled after the Palisades LWR pumps.

different. As a result, the head degradation of these two pumps exhibited quite different characteristics (see [4]).

(*ii*) *Pump Type and Specific Speed.* The type of hydraulic pump is usually classified into three categories, radial, mixed and axial flow type. The pumps tested in the Semiscale facility [4], C-E/Creare and C-E for KWU (Kraft Werk Union of West Germany [5]) represent each of these three categories, as is shown in Table 1. Figure 1 shows the test results of these three different pumps at design condition,

Nomenclature

a_b, a_l = accelerations of bubble and liquid
C_d = drag coefficient
dn, ds = infinitesimal increments in the n- and s-coordinates
dm_b, dm_l = mass in the control volume, for bubble and liquid, respectively
dK, dP_s = centrifugal force and pressure force acting on the control volume
F_s = forces acting on the bubble
g = gravitational constant
h = normalized head ($\equiv H/H_R$)
$\Delta H_b, \Delta H_l$ = energy or head increase for bubble and liquid, respectively
$\Delta H_{SP}, \Delta H_{TP}$ = energy or head increase for the single-phase and two-phase flows, respectively
$\dot{m}_b, \dot{m}_l, \dot{m}_{TP}$ = mass flow rate of bubble phase, liquid phase and two-phase mixture, respectively
$\Delta H_w, \Delta H_\alpha, \Delta H_s$ = head losses attributable to the exit flow velocity increase, void fraction change and slip velocity, respectively
n = coordinate normal to the streamline coordinate, s
N = pump rotational speed (rpm)
p = static pressure
p_0 = total pressure
Q = volumetric flow rate
Q_l, Q_b = volumetric flow rate for liquid and bubble, respectively
r = radial distance measured from the center of rotation
r_b = bubble radius
s = streamline coordinate
t = time
T = torque
u = tangential velocity
v = absolute velocity
v_u = tangential component of the absolute velocity
$v_u^{1\phi}$ = tangential component of the absolute velocity under the single phase condition
V_b = volume of bubble $\left(= \frac{4}{3}\pi r_b^3\right)$
w_b, w_l = flow velocity relative to the rotating blades in the s-direction
$\bar{x}$ = $\dot{m}_b/\dot{m}_{TP}$
α = void fraction
α_N = N/N_R (normalized speed)
β' = geometric angle of the s-coordinate made with the circle whose center is the center of rotation
β = nondimensional torque ($\equiv (T/T_R)\cdot(\rho_R/\rho)$)
ν = Q/Q_R (normalized volumetric flow rate)
ρ_b, ρ_l = densities of bubble and liquid, respectively
ρ_{TP} = two-phase flow density in homogeneous flows ($= (1-\alpha)\rho_l + \alpha\,\rho_b$)
ρ_{TP}^* = two-phase flow density in separated flows ($= \dot{m}_{TP}/(Q_l + Q_b)$)

Subscripts

b, l = denotes the qualities related to the bubble phase and liquid phase, respectively
1,2 = denotes the qualities related to the suction side and discharge side, respectively
R = denotes the quantities at the rated condition

showing remarkably different characteristics in head degradation, i.e., larger head degradation for the radial-flow pumps and smaller head degradation for mixed/axial flow pumps (see also the paper of Lea and Bearden [6]). This seems to indicate that the blade-through flow dynamics have a significant contribution to the basic mechanism of pump head degradation under two-phase conditions.

(*iii*) *Two-Phase Flow Media (Condensable Versus Noncondensable).* There existed again a large difference in the pump performance test results between the noncondensable gas/water tests and condensable steam/water tests (see Fig. 1 and also the report of Creare [3]). Heidrick, et al. [7] presented important evidence which seemed to have provided an explanation for the difference. The reading of gamma-densitometers installed at the inlet and outlet of the pump showed that the steam injected at the inlet entirely condensed through the blades and did not appear at the outlet up to the steam-to-water mass flow ratio, $x=0.015$ (equivalent to $\alpha_1=0.2$). It means that any adverse effect due to the existence of bubbles will only appear around the blade inlet area and then disappear towards the blade exit for low inlet void fraction cases. Therefore, the head degradation in condensable steam/water media is much less than that of the noncondensable gas/water media.

(*iv*) *Pump Operational Conditions.* Every pump is designed to operate with the best efficiency at the design condition. At a LOCA condition, the recirculation loop loses a substantial amount of coolant and also the pump-motor rotation speed may change. This will result in an off-design operation of the cooling pump where the blade-through flow pattern entirely changes. It was shown in various test results, e.g., see the paper of Runstadler and Dolan [8], that the degree of head degradation changed depending upon operational conditions.

(*v*) *Line Pressure.* The upstream line pressure also seems to have a significant impact on the head degradation characteristics of two-phase flow pumps (see the report of C-E [2] and also the paper of Lea and Bearden [6]). Generally speaking, the extent of head degradation is smaller for the higher line pressure. The reason for this fact may be three-fold, one related to possible cavitation appearance, the second due to the condensation effect and the third due to the density change of gas or steam phase.

1.3 Data Analysis and Existing Semi-Empirical Correlations

1.3.1 Data Analysis. It was pointed out in the report of Creare [3] that there existed difficulty in analyzing the data taken by C-E and Creare to define the head increase across the pump. In their report, the total head increase H_{total} was defined as

$$\frac{g}{g_c}H_{total}=\left(\frac{p_{out}}{\rho_{out}}-\frac{p_{in}}{\rho_{in}}\right)+\frac{1}{2g_c}[v_{out}{}^2-v_{in}{}^2]$$

where p, ρ, v denote the static pressure, average density and velocity, respectively, and the subscripts, "in," and "out" identify the quantities at the pump inlet and outlet, respectively. When this formula was used to plot the data of C-E and Creare, it was found that the head became negative even at near design point. As a result, Creare used a simpler form, i.e, static head increase:

$$\frac{g}{g_c}H_{static}=\frac{p_{out}-p_{in}}{\rho_{in}}.$$

With this definition, the data became a little more positive and thus understandable (see [3]). A question now arises as to whether or not the above definition is a right formula for the real pump head increase of the two-phase flow condition.

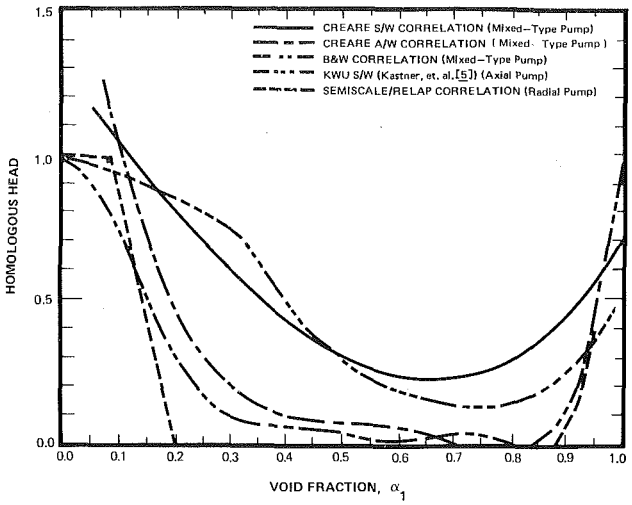

Fig. 1 Comparison of Creare A/W and S/W head correlations with B&W and Semiscale/ RELAP head multiplier correlations (after Creare Report [3]) (A/W and S/W stand for air/water and steam/water)

This question should be clearly answered before even reducing the experimental data for comparisons with theories.

1.3.2 Semi-Empirical Correlations. Based on the tests conducted to date, various empirical curves were constructed to characterize the pump performance operating under two-phase flow conditions. Such curves include those of Babcock and Wilcox [9], Semiscale [4], C-E [2], and Creare [3]. All these curves are more or less similar in that the head and torque degradation of the pump are expressed by only one parameter, i.e., inlet void fraction α_1. The approach of Wilson, et al. [10] was based on the single-phase ideal Euler's head equation in combination with various empirical head loss data for both single and two-phase flow media. It was, however, shown by Wilson that the correlation between the model and test data was rather limited.

The work by Zakem [11] is similar to the method of Hench and Johnston [12], who used a one-dimensional control-volume method for solving two-phase diffuser flow problems. Zakem applied the method to rotating machinery and then simply identified a nondimensional parameter. Data reduction with this new parameter for the test data of Babcock and Wilcox [9] resulted in some success.

2 Analytical Model Development for Two-Phase Flow Pumps

Based on the discussions provided above, it is apparent that the development of a new analytical model for characterizing the performance of two-phase flow pumps is in order. This should clarify the mechanism of pump head degradation under two-phase flow conditions by including compressibility, line pressure, condensation effect, flow regime, slippage of two-phase flow, and, of course, void fraction. A new analytical model which has been developed here is a first step for such a complete work. Although it neglects some of the above aspects (as will be stated in the following section), it is believed that the new method is the most rigorous and versatile one ever developed to date in this field. Furthermore, the final formula obtained from this new analytical model development conveniently reveals several important features for understanding the basic mechanism of two-phase flow pump head degradation. These features also serve as pertinent information concerning what type of new two-phase flow pump tests are to be conducted in the future.

2.1 Mathematical Formulation. The method used here is somewhat similar to that of Zakem [11], but the solution methods are quite different. Zakem applied the results of two-

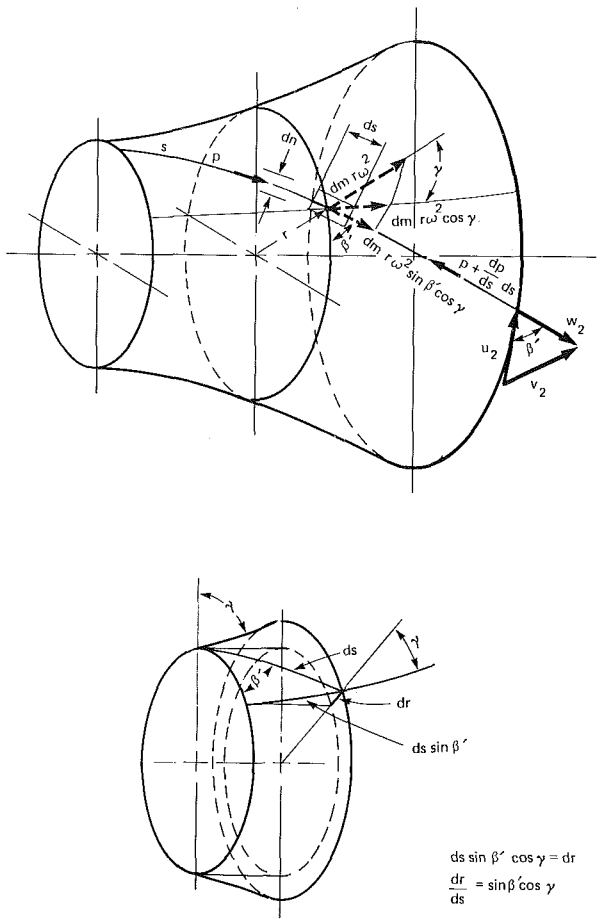

Fig. 2 Control volume method for rotating machines and force diagrams

phase flow equations only to a nondimensional analysis without investigating the basic mechanism of head degradation, whereas the present work defined the head degradation, and then analytically calculated it by solving the governing equations.

A control volume method is employed to investigate the head degradation for the flow going through the blades of a pump under the two-phase flow conditions. In order to apply such a method we need to make the assumption that the trajectory of liquid be identical to that of bubbles so that we can use a control volume bounded by two streamlines. It is also assumed that the slip between the two phase flows be allowed. Furthermore, the effects of condensation and compressibility are neglected for simplicity so that ρ_l and ρ_b are assumed to be constant.

The control volume used in the analysis is shown in Fig. 2 where the streamline, s, and the line normal to the streamline, n, are used as the curvilinear coordinates. The control volume is composed of dn, ds and a unit thickness in the direction normal to the stream surface.

The masses in the liquid phase and bubble phase, dm_l and dm_b contained in this control volume are given

$$dm_l = (1-\alpha)\cdot dn\cdot ds\cdot \rho_l \tag{1a}$$

$$dm_b = \alpha\cdot dn\cdot ds\cdot \rho_b \tag{1b}$$

where α is void fraction; ρ_l, ρ_b are the densities of liquid and bubble, respectively, and the subscripts l and b are used to represent the quantities for liquid and bubbles. Then, the momentum balance applied to this control volume in the direction of flow, i.e, s-direction, is expressed as follows,

$$\frac{d}{dt}(dm_l\cdot w_l + dm_b\cdot w_b) = F_s \tag{2}$$

where

F_s = external force acting on the control volume in the s-direction,

w_l, w_b = relative flow velocities of liquid and bubble, respectively in the s-direction.

The external force, F_s, consists of two components, namely the centrifugal force, dK, and pressure force, dP_s,

$$F_s = dK - dP_s, \tag{3}$$

where

$$dK = dm\cdot r\cdot \omega^2\cdot \sin\beta'\cdot\cos\gamma \tag{4a}$$

$$dP_s = \frac{\partial p}{\partial s}\cdot ds\cdot dn, \tag{4b}$$

$$dm = dm_l + dm_b \tag{4c}$$

and r is the radial distance of the control volume center measured from the center of rotation, ω is rotational speed, β' and γ are the local geometric angles of the stream surface shown in Fig. 2 and p denotes the static pressure. From equations (2) to (4), assuming a steady state flow so that dm_l and dm_b do not change along the streamline, we find

$$dm_l\frac{dw_l}{dt} + dm_b\frac{dw_b}{dt} = dm\cdot r\cdot\omega^2\cdot\sin\beta'\cdot\cos\gamma - \frac{\partial p}{\partial s}\cdot ds\cdot dn \tag{5}$$

through the transport theorem. Equation (5) will become

$$(1-\alpha)\rho_l\frac{\partial w_l}{\partial s}w_l + \alpha\rho_b\frac{\partial w_b}{\partial s}w_b = [\rho_l(1-\alpha)+\rho_b\alpha]r\omega^2\frac{dr}{ds} - \frac{\partial p}{\partial s} \tag{6}$$

where $dr/ds = \sin\beta'\cdot\cos\gamma$, see Fig. 2 and equations (1a), (1b), and (4c) have been used. Based on the assumption that all the quantities in the above equation (6) change along the streamline direction, s, we will be able to write (6) as

$$\frac{d}{ds}\left[(1-\alpha)\rho_l\frac{{w_l}^2}{2} + \alpha\rho_b\frac{{w_b}^2}{2} - \{\rho_b\alpha+\rho_l(1-\alpha)\}\frac{(r\omega)^2}{2} + p\right] + \left[\rho_l\frac{{w_l}^2-(r\omega)^2}{2} - \rho_b\frac{{w_b}^2-(r\omega)^2}{2}\right]\frac{d\alpha}{ds} = 0. \tag{7}$$

Integration of equation (7) from the suction side to discharge side, denoted by subscripts 1 and 2, respectively, yields

$$\left[(1-\alpha_2)\rho_l\frac{w_{2l}^2-u_2^2}{2} + \alpha_2\rho_b\frac{{w_2}_b^2-u_2^2}{2} + p_2\right] - \left[(1-\alpha_1)\rho_l\frac{w_{1l}^2-u_1^2}{2} + \alpha_1\rho_b\frac{{w_1}_b^2-u_1^2}{2} + p_1\right] + \int_1^2\left(\rho_l\frac{w_l^2-u^2}{2} - \rho_b\frac{w_b^2-u^2}{2}\right)\frac{d\alpha}{ds}\cdot ds = 0. \tag{8}$$

The relationship obtained here is considered to be the Bernoulli equation for the rotating machinery operating under two-phase flow conditions. There exists a slip velocity between the liquid and bubbles and therefore the void fraction is allowed to change. It must be pointed out, however, that in equation (8) any nonmechanical head loss existing in actual pump operations, such as head loss due to the frictional drag, has been neglected. However, such an assumption will not affect the final results in determining the two-phase flow head degradation, as will be explained later.

We now determine the head degradation of the pump operating under the two-phase flow condition. The energy

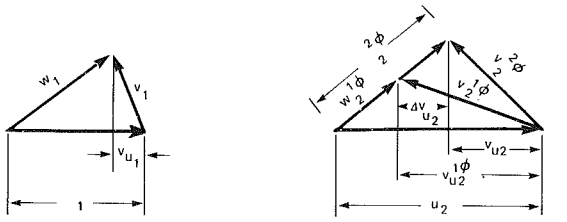

Fig. 3 Velocity triangles

increase in the two-phase flow, ΔH_{TP}, can be expressed as a sum of the energy increase in the liquid phase, ΔH_l, and that in the bubble phase, ΔH_b,

$$\Delta H_{TP} \cdot \dot{m}_{TP} = \Delta H_l \cdot \dot{m}_l + \Delta H_b \cdot \dot{m}_b \tag{9}$$

where $\dot{m}_{TP}$, $\dot{m}_l$ and $\dot{m}_b$ denote the mass flow rate of the overall two phase flow, liquid and bubbles, respectively, and

$$\dot{m}_{TP} = \dot{m}_l + \dot{m}_b \tag{10a}$$

$$\dot{m}_l = dn \cdot (1-\alpha) w_l \cdot \rho_l \tag{10b}$$

$$\dot{m}_b = dn \cdot \alpha \cdot w_b \cdot \rho_b. \tag{10c}$$

Assuming that the flow is inviscid and incompressible with no thermodynamic effects, we can write ΔH_l and ΔH_b in terms of the difference in the total pressures between the suction and discharge sides,

$$\Delta H_l = \frac{p_{02l} - p_{01l}}{\rho_l g} = \frac{p_2 - p_1}{\rho_l g} + \frac{v_{2l}^2 - v_{1l}^2}{2g}, \tag{11a}$$

$$\Delta H_b = \frac{p_{02b} - p_{01b}}{\rho_b g} = \frac{p_2 - p_1}{\rho_b g} + \frac{v_{2b}^2 - v_{1b}^2}{2g}, \tag{11b}$$

where g denotes the gravitational constant.

From equations (9) and (11),

$$\Delta H_{TP} = \frac{p_2 - p_1}{\rho_{TP}^* g} + \frac{v_{2l}^2 - v_{1l}^2}{2g} \cdot (1-x) + \frac{v_{2b}^2 - v_{1b}^2}{2g} \cdot x \tag{12}$$

where

$$\rho_{TP}^* = \frac{\dot{m}_{TP}}{Q_l + Q_b}, \tag{13}$$

$$Q_l = dn \cdot (1-\alpha) \cdot w_l, \tag{14a}$$

$$Q_b = dn \cdot \alpha \cdot w_b, \tag{14b}$$

$$x = \dot{m}_b / \dot{m}_{TP}, \tag{15a}$$

$$1 - x = \dot{m}_l / \dot{m}_{TP}. \tag{15b}$$

ρ_{TP}^* is an average density in the separated two-phase flow condition, which will be reduced to the two-phase density, ρ_{TP}, of the homogeneous flow if $w_l = w_b$, where

$$\rho_{TP} = (1-\alpha) \cdot \rho_l + \alpha \cdot \rho_b. \tag{16}$$

It should be noted that ρ_{TP}^* is constant since $\dot{m}_{TP}$, Q_l and Q_b are constant owing to the conservation law of the mass and flow rate under the incompressible flow assumption. Equation (12) should represent the head increase of the two-phase flow pump and should be compared with the one used by Creare [3] see Section 1. It can be seen that the formula used by Creare for test data reduction more or less agrees with equation (12) except for the dynamic head terms since at far upstream $\rho_{TP}^* = \rho_{lN}$. It means that as long as the dynamic head terms are negligibly small compared to the static pressure term, the formula lof Creare [3], intuitively derived, is acceptable.

The term $(p_2 - p_1)$ in the Bernoulli equation (8) is substituted into the same term in equation (12),

$$\Delta H_{TP} = -\left\{ \frac{(1-\alpha_2)\rho_l}{\rho_{TP}^* g} \frac{w_{2l}^2 - u_2^2}{2} + \frac{\alpha_2 \rho_b}{\rho_{TP}^* g} \frac{w_{2b}^2 - u_2^2}{2} \right\}$$

$$- \left\{ \frac{(1-\alpha_1)\rho_l}{\rho_{TP}^* g} \frac{w_{1l}^2 - u_1^2}{2} + \frac{\alpha_1 \rho_b}{\rho_{TP}^* g} \frac{w_{1b}^2 - u_1^2}{2} \right\}$$

$$+ \frac{v_{2l}^2 - v_{1l}^2}{2g} \cdot (1-x) + \frac{v_{2b}^2 - v_{1b}^2}{2g} \cdot x$$

$$- \frac{1}{\rho_{TP}^* g} \int_1^2 \left(\rho_l \frac{w_l^2 - u^2}{2} - \rho_b \frac{w_b^2 - u^2}{2} \right) \frac{d\alpha}{ds} ds. \tag{17}$$

Use of equations (10), (14), and (15) and of velocity relationship $w^2 - v^2 = (u - v_u)^2 - v_u^2$ (see Fig. 3), provides

$$\Delta H_{TP} = \Delta H_{SP} - \Delta H_w - \Delta H_s - \Delta H_\alpha, \tag{18}$$

where

$$\Delta H_{SP} = (1-x) \cdot \frac{v_{u2l}^{1\phi} u_2 - v_{u1l}^{1\phi} u_1}{g} + x \cdot \frac{v_{u2b}^{1\phi} u_2 - v_{u1b}^{1\phi} u_1}{g} \tag{19}$$

$$\Delta H_w = (1-x) \frac{\Delta v_{u2l} u_2}{g} + x \cdot \frac{\Delta v_{u2b} u_2}{g} \tag{20}$$

$$\Delta H_s = (1-x) \cdot \left\{ \alpha_2 \cdot \left(\frac{w_{2b}}{w_{2l}} - 1 \right) \cdot \frac{w_{2l}^2 - u_2^2}{2g} - \alpha_1 \cdot \left(\frac{w_{1b}}{w_{1l}} - 1 \right) \frac{w_{1l}^2 - u_1^2}{2g} \right\} + x \cdot \left\{ (1-\alpha_2) \cdot \left(\frac{w_{2l}}{w_{2b}} - 1 \right) \frac{w_{2b}^2 - u_2^2}{2g} - (1-\alpha_1) \cdot \left(\frac{w_{1l}}{w_{1b}} - 1 \right) \frac{w_{1b}^2 - u_1^2}{2g} \right\} \tag{21}$$

$$\Delta H_\alpha = \frac{1}{\rho_{TP}^* g} \int_1^2 \left(\rho_l \frac{w_l^2 - u^2}{2} - \rho_b \frac{w_b^2 - u^2}{2} \right) \frac{d\alpha}{ds} ds, \tag{22}$$

and

$$v_{u1} = v_{u1}^{1\phi} - \Delta v_{u1}, \text{ tangential component of } v_2$$

$$v_{u2} = v_{u2}^{1\phi} - \Delta v_{u2}, \text{ tangential component of } v_1 \tag{23}$$

In the above equations, all velocity components are those of the two-phase flow conditions except for the ones with the superscript "1ϕ." They designate quantities belonging to the single phase conditions. It means that the velocity component, e.g. $v_{u2}^{1\phi}$, is different from $v_{u2}^{1\phi}$ by Δv_{u2} due to the two-phase flow condition as is shown in Fig. 3. It must also be mentioned that the definition of ΔH_w, ΔH_s and $\Delta H\alpha$ in equation (18) has been arbitrarily made. Although we can name ($\Delta H_w + \Delta H_s + \Delta H_\alpha$) as ΔH_{total}, it was decided to use these three separate terms; ΔH_w is due to the increase of the relative speed w of liquid portion at pump exit caused by two-phase flow condition, ΔH_s is attributable to the slip velocity between the liquid and bubble phases and ΔH_α is due to the variation of void fraction along the flow passage between the blades. Equation (18) will then be written

$$\frac{\Delta H_{TP}}{\Delta H_{SP}} = 1 - \frac{\Delta H_w + \Delta H_s + \Delta H_\alpha}{\Delta H_{SP}}. \tag{24}$$

This relation in equation (24) provides the ratio between the two-phase flow pump head and single-phase flow pump head. It must be pointed out here that since actually measured ΔH_{SP} will be used in obtaining the ratio of ΔH_{TP} to ΔH_{SP} in equation (24), the previously omitted nonmechanical, head loss which was not included in Euler's formula, has now been recovered. It should also be noted that if there exists no slip velocity (i.e., $w_l = w_b$ and consequently $d\alpha/ds = 0$), $\Delta H_w = \Delta H_s = \Delta H_\alpha = 0$. For such a homogeneous two-phase flow case, $\Delta H_{TP}/\Delta H_{SP}$ becomes unity, indicating no head degradation within the framework of current assumptions.

This new formula for the head degradation rate should be compared to the one previously given by Creare [13], i.e.,

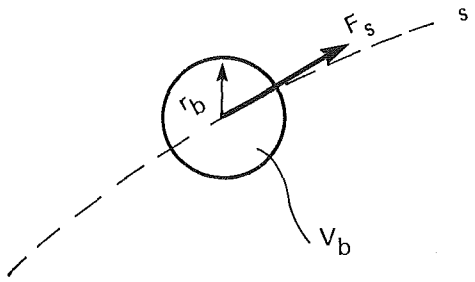

Fig. 4 Bubble geometry and force

$$\frac{\Delta H_{TP}}{\Delta H_{SP}} = \frac{\dfrac{\Delta p}{\rho_{TP}}}{\dfrac{\Delta p}{\rho_l}(1-x)+\dfrac{\Delta p}{\rho_b}x} \tag{25}$$

where Δp is the static head increase between the pump suction and discharge sides and ρ_{TP} is the two-phase flow density under the homogeneous flow condition. The above formula of Creare was simply based on the intuitive definition, not reflecting any pump flow phenomena.

In order to calculate the quantities of ΔH_w, ΔH_s and ΔH_α in equation (22), we should know the detailed data for the relative velocities for both the liquid and bubbles, as well as the void fraction along the path of blade-through flow. Hench and Johnston [12] applied the momentum equation to the bubble for this purpose, when they solved the problem of two-phase diffuser flows. Applying the same philosophy to the present rotating machinery problem,

$$\rho_b V_b \frac{dw_b}{dt} = \sum F_s \tag{26}$$

where

$$\sum F_s = \text{(Pressure Force)} + \text{(Centrifugal Force)} + \text{(Drag Force)} + \text{(Virtual Mass Force)} \tag{27}$$

and V_b denotes the volume of bubble. Each force acting on the bubble can be written in the following form (see Fig. 4);

$$\text{(Pressure Force)} = -\frac{\partial p}{\partial s}\cdot V_b \tag{28a}$$

$$\text{(Centrifugal Force)} = \rho b V_b r\omega^2 \sin\beta'\cdot\cos\gamma \tag{28b}$$

$$\text{(Drag Force)} = C_d\cdot\frac{1}{2}\rho_l\cdot(w_l-w_b)\cdot|w_l-w_b|\pi {r_b}^2 \tag{28c}$$

$$\text{(Virtual Mass Force)} = -\frac{1}{2}\rho_l\cdot V_b\cdot(a_b-a_l) \tag{28d}$$

where

r_b = radius of bubble, assuming that the bubble is spherical,

$$a_b = \frac{dw_b}{dt} = \frac{\partial w_b}{\partial t} + w_b\frac{\partial w_b}{\partial s} \tag{29a}$$

$$a_l = \frac{dw_l}{dt} = \frac{\partial w_l}{\partial t} + w_l\frac{\partial w_l}{\partial s}. \tag{29b}$$

Assuming the steady-state flow condition and substituting equations (28) and (29) into equations (26) and (27), we obtain

$$\rho_b w_b\frac{\partial w_b}{\partial s} + \frac{1}{2}\rho_l\left(w_b\frac{\partial w_b}{\partial s} - w_l\frac{\partial w_l}{\partial s}\right) = -\frac{\partial p}{\partial s} + \rho_b r\omega^2\sin\beta' \cdot\cos\gamma + \frac{C_d}{r_b}\frac{3}{8}\cdot\rho_l\cdot(w_l-w_b)|w_l-w_b|. \tag{30}$$

Equation (30) is now combined with the momentum equation for the two-phase mixture, equation (6), to eliminate $\partial p/\partial s$ term,

$$\frac{\dot m_l^2}{\rho_l\cdot(dn)^2}\frac{1}{(1-\alpha)}\left[\frac{1}{(1-\alpha)}\frac{d\alpha}{ds} - \frac{1}{(dn)}\frac{d(dn)}{ds}\right] + \frac{\dot m_b^2}{\rho_b(dn)^2}\cdot\frac{1-\alpha}{\alpha^2}\cdot\left[\frac{1}{\alpha}\frac{d\alpha}{ds} + \frac{1}{(dn)}\frac{d(dn)}{ds}\right] + \frac{1}{2}\rho_l\cdot\left[\left(\frac{\dot m_b}{\rho_b\cdot dn\cdot\alpha}\right)^2\left(\frac{1}{\alpha}\frac{d\alpha}{ds} + \frac{1}{(dn)}\frac{d(dn)}{ds}\right) + \left(\frac{\dot m_l}{\rho_l\cdot dn\cdot(1-\alpha)}\right)^2\left(\frac{1}{1-\alpha}\frac{d\alpha}{ds} - \frac{1}{(dn)}\frac{d(dn)}{ds}\right)\right] = (\rho_l-\rho_b)(1-\alpha)r\omega^2\sin\beta'\cdot\cos\gamma - \frac{C_d}{r_b}\frac{3}{8}\rho_l\left[\frac{\dot m_l}{\rho_l\cdot dn\cdot(1-\alpha)} - \frac{\dot m_b}{\rho_b\cdot dn\cdot\alpha}\right]\cdot\left|\frac{\dot m_l}{\rho_l\cdot dn\cdot(1-\alpha)} - \frac{\dot m_b}{\rho_b\cdot dn\cdot\alpha}\right|, \tag{31}$$

where the mass conservation equations (10*a*) and (10*b*) have been used.

This differential equation contains only one variable, i.e, α, and all other quantities here are either constant or known as a function of s. The quantities which belong to the former category include $\dot m_l$, $\dot m_b$, ρ_l, ρ_b, and ω, whereas those which belong to the latter category include (dn), $r\sin\beta'$ and $\cos\gamma$. Therefore, if the boundary conditions at the suction side are known, the ordinary differential equation of (31) can be solved for α along s. Once $\alpha(s)$ is obtained, $p(s)$ can be solved by using either equation (6) or (30). Furthermore, w_l and w_b will be determined from the mass conservation equations in (10*b*) and (10*c*). Now all quantities necessary for calculating ΔH_w, ΔH_s, and ΔH_α are made available.

Torque. The calculations of torques corresponding to the degraded heads of the pumps operating under two-phase flow conditions will be made possible with a simple assumption as follows. For the case of single-phase flow, the relationship between the torque, head and flow rate is written

$$T_{1\phi}\cdot\omega = (H_{1\phi}+\Delta H_{1\phi})\cdot Q\cdot\rho\cdot g \tag{32}$$

where $H_{1\phi}$ is the actually measured single-phase flow head and $\Delta H_{1\phi}$ is the head loss, corresponding to a portion of the input torque not converted into head. Assuming that the same amount of head loss, $\Delta H_{1\phi}$, can be applied to the two-phase flow cases, we can define the torque for two-phase flow conditions

$$T_{2\phi}\cdot\omega = (H_{2\phi}+\Delta H_{1\phi})\cdot Q\cdot\rho^*_{TP}\cdot g. \tag{33}$$

By eliminating $\Delta H_{1\phi}$ from equations (32) and (33),

$$T_{2\phi}\cdot\omega = (H_{2\phi}-H_{1\phi})\cdot Q\cdot\rho^*_{TP}\cdot g + T_{1\phi}\cdot\omega.$$

Normalization of each term in the above equation will yield

$$\frac{\beta_{2\phi}}{{\alpha_N}^2} = \left(\frac{h_{2\phi}}{{\alpha_N}^2} - \frac{h_{1\phi}}{{\alpha_N}^2}\right)\cdot\frac{\nu}{\alpha_N}\cdot\eta_R + \frac{\beta_{1\phi}}{{\alpha_N}^2}, \tag{34}$$

where

η_R = hydraulic efficiency of the pump at the rated condition for the single phase flow

$$= \frac{H_R Q_R \rho g}{T_R\omega_R}$$

h = normalized head ($\equiv H/H_R$)
α_N = normalized rotational speed ($\equiv N/N_R$)
β = normalized torque ($= (T/T_R)\cdot(\rho_R/\rho)$)
ν = Q/Q_R
H = head
N = rotational speed
T = torque
Q = volumetric flow rate,

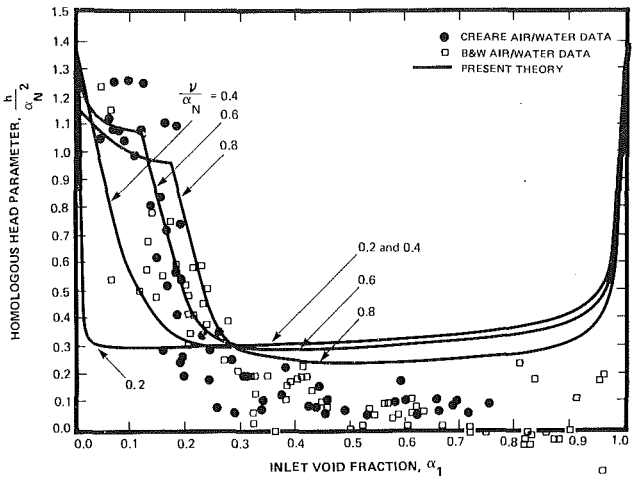

Fig. 5 Comparison of present theory for homologous heads with Creare and B&W data for ν/α_N between 0.2 and 0.8

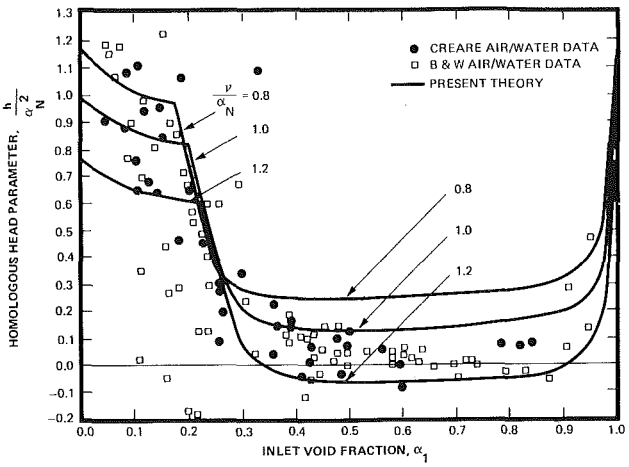

Fig. 6 Comparison of present theory for homologous heads with Creare and B&W data for ν/α_N between 0.8 and 1.2

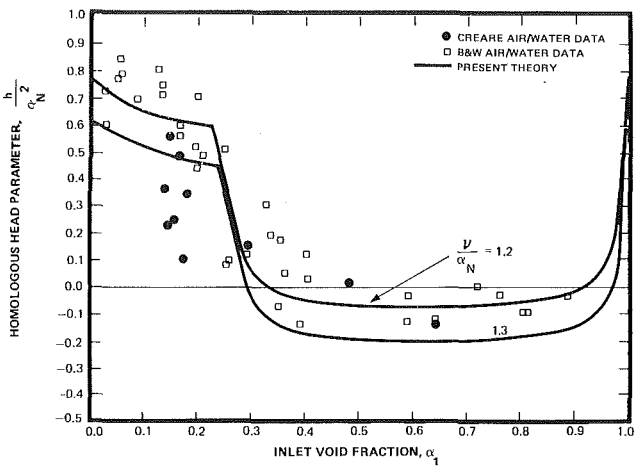

Fig. 7 Comparison of present theory for homologous heads with Creare and B&W data for ν/α_N between 1.2 and 1.3

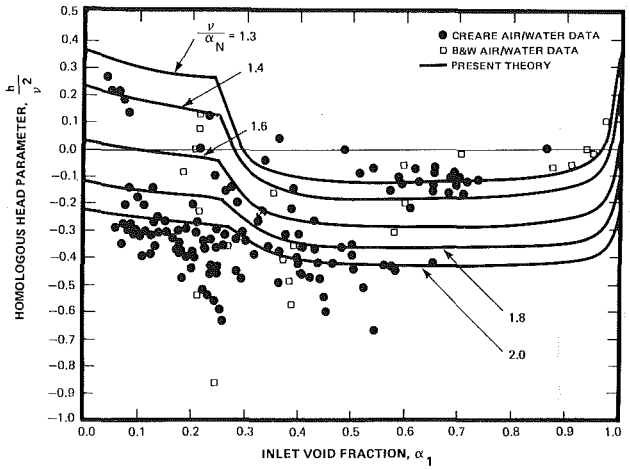

Fig. 8 Comparison of present theory for homologous heads with Creare and B&W data for ν/α_N between 1.3 and 2.0

and subscripts "R" denote the quantities at the rated condition. All the quantities necessary for the above equations are available either from the single-phase pump test results or from the results obtained with the present analytical model *calculations*.

3 Comparisons Between the Theory and Test Data

The analytical model developed here was used to calculate the head degradation and torque for the pump tested by Babcock and Wilcox (1/3 scale) and Creare (1/20 scale), operating under air/water two-phase conditions. The input data necessary for such calculations included in the single-phase flow performance of the pump, pump geometry, rated conditions, physical parameters of air and water, drag coefficient, C_d and bubble size, r_b.

The last two values, C_d and r_b, employed in the present calculations were the same as those used by Hench and Johnston [12]. First, they classified the flow into two regimes depending upon the local void fraction, α, i.e., bubbly flow regime for $\alpha \leqq 0.3$ and churn-turbulent flow regime for $\alpha \geqq 0.4$. In the bubbly flow regime, it was found in their experiments that the bubble radius was about 0.0625″ (= 1.59 mm) and thus the corresponding drag coefficient was determined to be 0.54 based on the experimental data of Haberman and Morton [14]. Regarding the choice of C_d and r_b for the bubbly flow regime, it was reported in the paper of Hench and Johnston [15] that the relative sensitivity of the results of this analysis to bubble size and drag coefficient in the range of interest was shown to be small. For the churn-turbulent flow regime, the drag coefficient is drastically reduced. A combined relationship between C_d and r_b was empirically obtained by Zuber and Hench [16]

$$\frac{C_d}{r_b} = 2.79(1-\alpha)^3(\text{in}^{-1}), \text{ or } .11(1-\alpha)^3(\text{mm}^{-1}).$$

It must also be mentioned that the added mass term was dropped from equation (31) since the term applies only to spherical bubbles and therefore is not appropriate for the two-phase flow of churn-turbulent regime. Hench and Johnston also pointed out that this term is negligibly small compared to other terms in the equation. The values for C_d/r_b between $\alpha = 0.3$ and 0.4 were those of linear connection between these two points.

Figures 5 to 8 show the homologous heads calculated from the present analytical model in comparison with Babcock and Wilcox (1/3 scale) and Creare (1/20 scale) air/water test results. It is seen that the overall agreement is excellent, particularly for the homologous flow parameter, $\nu/\alpha_N \approx 1$, i.e., near the rated condition. The trend of measured head degradations is well represented by the present analytical model, i.e., a relatively mild head degradation up to α_1 (inlet void fraction) $\leqq$ 0.2, then a sudden drop between α_1 = 0.2 and 0.3, followed by a fairly flat low head for $0.3 \leqq \alpha_1 \leqq 0.9$ and a return to the single-phase homologous heads as α_1 reaches unity.

It must be mentioned that the test data shown here were

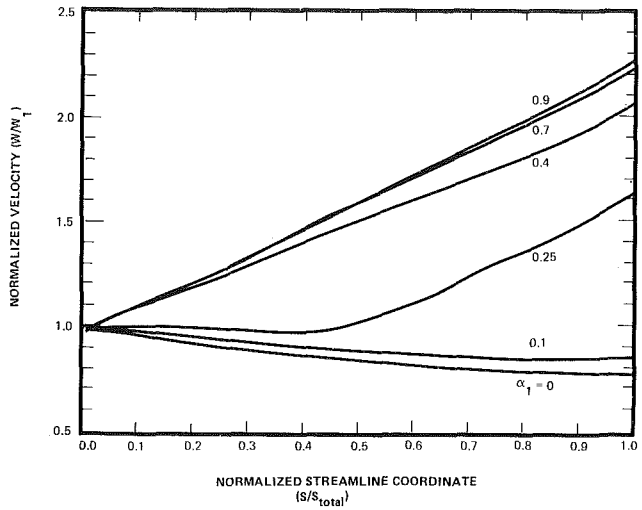

Fig. 9 Relative liquid velocity changes along the flow passage for $\nu/\alpha_N = 1.0$

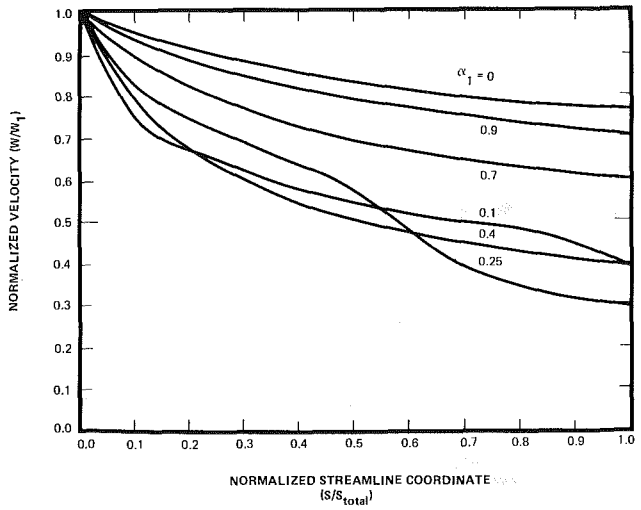

Fig. 10 Relative gas velocity changes along the flow passage for $\nu/\alpha_N = 1.0$

taken from the report of Creare [3] in which the data were classified as a function of wide range of ν/α_N values, except for $1.2 \leqq \nu/\alpha_N \leqq 1.3$. The test data for $0 \leqq \nu/\alpha_N \leqq 0.8$, $0.8 \leqq \nu/\alpha_N \leqq 1.2$ and $1.2 \leqq \nu/\alpha_N \leqq 2.0$ were all lumped together, as seen from Figs. 5 to 8. Although the report of Creare [3] stated the insensitivity of head degradation to the homologous flow parameter ν/α_N, theoretically there exists a clear distinction in head degradation for different values of ν/α_N. It seems that the difficulty in classifying the test data as a function of ν/α_N is attributable simply to wide scattering of the test data.

The basic mechanism of these head degradations shown in Fig. 5 to 8 has already been explained in the previous section. However, it will more clearly be understood by investigating the detailed quantities of blade-through flow obtained in the present calculations. Figures 9 to 11 show change of liquid and gas flow relative velocities and local void fraction, respectively, along the flow passage. Homologous flow parameter is $\nu/\alpha_N = 1.0$ and the inlet void fractions were $\alpha_1 = 0.1, 0.25, 0.4, 0.7$ and 0.9. Due to the difference of flow media densities between water and air, the former is subject to larger external force, in this case, centrifugal force, than the latter. Consequently, the water is accelerated faster and the air is decelerated slower than in the case of single-phase flow. This acceleration of the water contributes to the major part of head degradation, i.e., in terms of ΔHw.

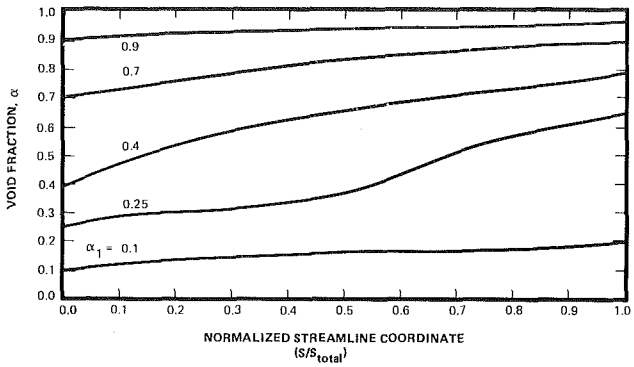

Fig. 11 Void fraction changes along the flow passage for $\nu/\alpha_N = 1.0$ for the inlet void fractions, $\alpha_1 = .1, .25, .4, .7$, and .9

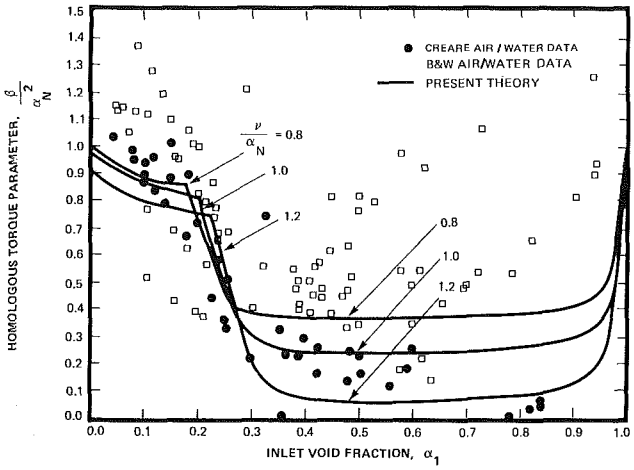

Fig. 12 Comparison of present theory for homologous torques with Creare and B&W data for ν/α_N between 0.8 and 1.2

Figure 11 shows a continuous increase in local void fraction along the flow passage, indicating larger population of air bubbles towards the pump outlet. Patel and Runstadler reported in their paper [17] that the large void in the impeller was observed in air/water pump tests. Murakami and Minemura [18] pointed out the association of large void formation with an extensive degradation of pump head. Photographs taken by Manzano-Ruiz and Wilson [19] also showed some evidence of bubble agglomeration. The effect of centrifugal force on the head degradation also seems to explain the more severe head degradation for the radial flow pumps in which the centrifugal force is the major head generation force. The fact indicates that use of axial-flow pumps may provide better performance than radial- or mixed-flow pumps in two phase flow conditions (see Fig. 1).

For extreme off-design condition cases, such as $\nu/\alpha_N \leqq 0.4$ (Fig. 5) or $\nu/\alpha_N \geqq 2.0$ (Fig. 8), some discrepancy between the analytical results and test data exists. It is not surprising to find the discrepancy at such extreme conditions. Despite the physical fact that the streamline profile shapes may be substantially different near the blade inlet area between the design condition and off-design conditions, the present model only used those of the design condition. It is indicative based on this fact that the future analytical model may need to employ flow passages at off-design conditions different from that of design condition.

Figure 12 shows the calculated homologous torques corresponding to the cases of Fig. 6. Again the overall agreement with test data, particularly with those of Creare, is good. It is not known why the test data of Babcock & Wilcox are so scattered. The limiting values of homologous torque test data as $\alpha_1 \rightarrow 0$ do not match with the single-phase measured data which are shown by the analytical results at $\alpha_1 = 0$. This fact indicates substantial error in measurements.

Although such errors were observed in the homologous head measurements (see Figs. 5 to 8), the degree of the errors was much smaller. As far as torque measurements are concerned, those by Creare are less scattered and compare favorably with the analytical results.

4 Conclusions

Based on the one dimensional control volume method, an analytical model has been developed to determine the performance of pumps operating under two-phase flow conditions. The analytical method developed here has incorporated pump geometry, void fraction, flow slippage and flow regime (implicitly through the bubble diameter and drag coefficient) into the basic formula, but neglected the compressibility and condensation effects.

During the course of model development the basic mechanism of head degradation was identified. Three separate terms contributing to the head degradation are called here ΔH_w, ΔH_s, and ΔH_α. ΔH_w is due to the relative flow speed increase of liquid particles at pump exit, ΔH_s is attributable to the slip velocity between two phases at inlet and exit and ΔH_α stems from the void fraction change along the flow passage. It has been found in the numerical calculations that the ΔH_w's contribution to the head degradation is much larger than the sum of $(\Delta H_s + \Delta H_\alpha)$.

The numerical results for head degradations and torques were obtained and favorably compared with the test data of air/water two-phase flow conditions obtained by Babcock & Wilcox (1/3 scale) and Creare (1/20 scale). The overall agreement is excellent despite the fact that the test data were so scattered and inconsistent.

For the extreme off-design conditions, some discrepancy existed in the above comparison. It seems that the predetermined stream-surface used in the analysis will need modification for such extreme off-design conditions.

Furthermore, in order for the analytical model to be able to determine the performance of steam/water two-phase flow pumps, the condensation and compressibility effects will have to be properly incorporated.

Acknowledgment

The author had many useful discussions with Prof. A. J. Acosta of Caltech and this is gratefully acknowledged. He also thanks Drs. J. H. Kim and Bill K. H. Sun of EPRI, for their various support as well as encouragement during the course of the project. The author thanks Mr. Shin Maekawa for carrying out all numerical computations for the present work.

References

1 Kim, J. H., "Perspectives on Two-Phase Flow Pump Modeling for Nuclear Reactor Safety Analysis," presented at Cavitation and Multiphase Flow Forum of ASME Conference, Houston, June 1983, edited by J. Hoyt, pp. 29–33.

2 Combustion Engineering, Inc., "Pump Two-Phase Performance Program" Vol. I through VIII, EPRI NP-1556, Sept. 1980.

3 Creare, Inc., "Two-Phase Performance of Scale Models of a Primary Coolant Pump," EPRI NP-2578, Sept. 1982.

4 Chen, T. H., and Quapp, W. J., "Centrifugal Pump Performance Under Simulated Two-Phase Flow Conditions," The Symposium on Polyphase Flow and Transport Technology, Aug. 1980.

5 Kastner, W., and Seeberger, G. J., "Pump Behavior and its Impact on a Loss-of-Coolant Accident in a Pressurized Water Reactor," *Nuclear Technology*, Vol. 60, Feb. 1983.

6 Lea, J. F., and Bearden, J. L., "Effect of Gaseous Fluids on Submersible Pump Performance," *Journal of Petroleum Technology*, Vol. 34, Dec. 1982.

7 Heidrick, T. R., et al., "Centrifugal Pump Behavior in Steady and Transient Steam-Water Flows," The Symposium on Polyphase Flow and Transport Technology, The Winter Annual Meeting of the ASME, Dec. 1978.

8 Runstadler, P. W., Jr., and Dolan, F. X., "Two-phase Flow Pump Data for a Scale Model NSSS Pump," ASME Symposium on Polyphase Flow in Turbomachinery, Dec. 10–15, 1978, San Francisco.

9 Babcock & Wilcox, "One-Third-Scale Air-Water Pump Program, Test Program and Pump Performance," EPRI NP-135, July 1977.

10 Wilson, D. G., et al., "Analytical Models and Experimental Studies of Centrifugal-Pump Performance in Two-Phase Flow," EPRI NP-677, May 1979.

11 Zakem, S., "Analysis of Gas Accumulation and Slip Velocity in a Rotating Impeller," ASME Cavitation and Polyphase Forum, 1980.

12 Hench, J. E., and Johnston, J. P., "Two-Dimensional Diffuser Performance with Subsonic, Two-Phase, Air-Water Flow," ASME *Journal of Basic Engineering*, Mar. 1972.

13 Creare Inc., "Review and Analysis of State-of-the-art of Multiphase Pump Technology," EPRI NP-159, Feb. 1976.

14 Haberman, W. L., and Morton, R. K., "An Experimental Investigation of the Drag and Shape of Air Bubbles Rising in Various Liquids," DWTN-SRDC, Report 802, Sept. 1953.

15 Hench, J. E., and Johnston, J. P., "Two-Dimensional Diffuser Performance with Subsonic, Two-Phase, Air-Water Flow, General Electric Report APED 5477, Jan. 1968.

16 Zuber, N., and Hench, J. E., "Steady State and Transient Void Fraction of Bubbling Systems and Their Operating Limits. Part I, Steady State Operation," General Electric Report No. 62GL100, 1962.

17 Patal, B. R., and Runstadler, P. W., Jr., "Investigation into the Two-Phase Flow Behavior of Centrifugal Pumps," ASME Symposium on Polyphase Flow in Turbomachinery, Dec. 10–15, 1978, San Francisco.

18 Murakami, M., and Minemura, K., "Effects of Entrained Air on the Performance of a Centrifugal Pump," *Bulletin of the Japanese Society of Mechanical Engineers*, Vol. 17, No. 110, Aug. 1974.

19 Manzano-Ruiz, J. J., and Wilson, D. G., "Experimental Study of Two-Phase, Two-Component Flow in Centrifugal Pumps," 2nd International Topical Meeting on Nuclear Reactor Thermal-Hydraulics, Jan. 1983.

Journal of Fluids Engineering

Discussion

Correlation of Cavitation Erosion and Sound Pressure Level[1]

F. G. Hammitt.[2] This investigation of correlation between cavitation erosion rate and cavitation noise in several flow situations, even for only single material (commercially pure aluminum), I believe is most useful and helpful to the overall field of damage prediction. We have done some similar work (1,eg.), emphasizing single-bubble collapse noise energy spectra rather than overall noise, and have also found quite linear correlations with the same material. Though some tests have been made, less information is available at this time for other materials.

In any case, I want to strongly encourage continued similar work elsewhere. I still believe, however, that more general correlations can be obtained only if high-frequency collapse pulses are considered.[3]

Authors' Closure

The authors are grateful for Professor Hammitt's encouragement and, from more recent work, can confirm that the use of high frequency sound gives a better linear correlation between sound level and erosion rate. However, we doubt that the use of pulse counting techniques will offer any significant improvement unless a suitable threshold level is introduced. It is hoped to offer the new work for publication in the JOURNAL OF FLUIDS ENGINEERING in the near future.

[1]By P. A. Lush and B. Angell, published in the September 1984 of the JOURNAL OF FLUIDS ENGINEERING, Vol. 106, No. 3, pp. 347-351.

[2]Professor, Mechanical Engineering Department, University of Michigan, Ann Arbor, Mich. 48109

[3]F. G. Hammitt, *Cavitation and Multiphase Flow Phenomena*, McGraw-Hill, 1980.